Middlesex
University
London

**Middlesex University Research Repository:**
an open access repository of
Middlesex University research
**http://eprints.mdx.ac.uk**

MacLean, L A H, 1993.
The structure of manganese dioxide-hydrogen insertion compounds and some related stability studies.
Available from Middlesex University's Research Repository.

**Copyright:**

Middlesex University Research Repository makes the University's research available electronically.

Copyright and moral rights to this thesis/research project are retained by the author and/or other copyright owners. The work is supplied on the understanding that any use for commercial gain is strictly forbidden. A copy may be downloaded for personal, non-commercial, research or study without prior permission and without charge. Any use of the thesis/research project for private study or research must be properly acknowledged with reference to the work's full bibliographic details.

This thesis/research project may not be reproduced in any format or medium, or extensive quotations taken from it, or its content changed in any way, without first obtaining permission in writing from the copyright holder(s).

If you believe that any material held in the repository infringes copyright law, please contact the Repository Team at Middlesex University via the following email address:
eprints@mdx.ac.uk

The item will be removed from the repository while any claim is being investigated.

# The Structure of Manganese Dioxide-Hydrogen Insertion Compounds and Some Related Stability Studies

L.A.H.MacLean

A thesis submitted to Middlesex University in
partial fulfilment of the requirements for the degree of
Doctor of Philosophy

March 1993

The work was carried out at the Energy Technology Centre, Middlesex University,
School of Mechanical Engineering, Bounds Green Road, London N11 2NQ
and was funded by the N.A.B. Research Initiative 2 and British Ever Ready.

To Cristina

# Abstract.

Six synthetic manganese dioxides (coded SBPA, Faradiser WSZ, IBA no.14, IBA no.19, R2 and Faradiser M) covering the range of crystal structures exhibited by battery active materials were studied by XRD (X-Ray Diffraction) and FTIR (Fourier Transform Infra-Red) spectroscopy when H was inserted with organic reductants. Initial x-ray diffraction patterns (i.e. before H insertion) indicated a structural series, the $\gamma$-$\gamma_t$-$MnO_2$ series, where $\gamma$-$MnO_2$ designates the phase defined by de Wolff's intergrowth model. This model described $\gamma$-$MnO_2$ as a random alternation of two types of layers derived from the known structures of the minerals ramsdellite and pyrolusite. $\gamma$-$MnO_2$ may be characterised by one parameter, p, the pyrolusite type layer fraction. $p=0$ corresponds to ramsdellite whereas $p=1$ corresponds to pyrolusite. The additional structural defect responsible for the $\gamma$-$\gamma_t$-$MnO_2$ series was found to be that of microtwinning in accordance with the model proposed by Pannetier *et al.* Material SBPA possessed a low degree of microtwinning with $p=0.20_4\pm0.005$ whereas typical battery active manganese dioxides IBA no.19 and R2 possessed x-ray diffraction patterns consistent with a high degree of microtwinning and $p\sim0.2$. The other materials, except Faradiser M, displayed x-ray diffraction patterns intermediate between those of SBPA and IBA no.19/R2. Faradiser M possessed a high degree of microtwinning but with $p\sim0.7$.

The most H inserted compounds (i.e. of composition $MnOOH_{1.0}$) also formed an analogous structural series, the $\delta$-$\delta_t$-MnOOH series. $\delta$-MnOOH may be described as a random alternation of two types of layers derived from the known structures of the minerals groutite and manganite which are reduced isostructural derivatives of ramsdellite and pyrolusite. $\delta$-MnOOH was successfully analyzed for the concentration of (presumed) manganite type layer defects (m) in an analogous manner to that required to determine p, which confirmed the existence of reduced intergrowth structures. m was found to be less than p unless the H insertion reaction temperature was lowered ($\sim$2°C) in which case m=p. This was consistent with the observed precipitation of small amounts of $\gamma$-MnOOH when H was inserted with chemical reductants in non-aqueous solvents.

The level of H insertion may be represented by the formula r in $MnOOH_r$, where $\sim0.1\leq r\leq1.0$ (r starts at a value greater than zero due to the non-stoichiometry of battery active materials). H insertion into EMD (Electrodeposited Manganese Dioxide) R2 led to approximate isotropic lattice expansion in the H insertion region $0.11\leq r\leq0.80$. This observation was consistent with a homogeneous solid state reduction with formation of a solid solution in which $H^+$ and $e^-$ were mobile. In the region $0.80\leq r\leq1.01$ 'new' non-moving peaks emerged characteristic of the final product while the original lines continued to move. The line shift indicated anisotropic lattice expansion. The 'new' non moving peaks could not be interpreted on the basis that a new phase was emerging. An explanation for this behaviour based on the properties of the defect crystal structure of the original material has been found. It involved identification of a type of x-ray line shift characteristic of random layer structures. The effects observed were consistent with random precipitation of $\delta$-MnOOH micro-domains within the solid solution. The 'new lines' which emerged represented a re-emergence of lines originally overlapped with other lines due to the particular effects of microtwinning. The appearance of micro-domains of the end product crystallizing within the solid solution implied that $H^+$ and $e^-$ were no longer mobile in the crystal structure but located or 'frozen' in position. The presence of 'frozen' H (i.e. $\delta$-MnOOH micro-domains) was supported by measurements of FTIR band areas at wavenumber regions where OH vibration modes occurred. The onset of OH vibration modes with increasing H insertion supported the interpretation of the x-ray patterns.

Interpretation of the FTIR spectra of material SBPA indicated no OH bond formation in the H insertion region $0.068\leq r\leq0.35$ and OH bond formation in the region

$0.35 \leq r \leq 0.882$. Examination of the XRD patterns indicated heterogeneous solid state reduction had occurred in the H insertion region $0.40 \leq r \leq 0.882$. The onset of OH bond formation at $r=0.35$ was interpreted as a necessary precursor to heterogeneous reduction starting at $r=0.40$. Heterogeneous reduction was presumed to have occurred by H location in an outer particulate layer which propagated into the bulk.

H insertion into the remaining materials was interpreted in a similar manner. That is beyond a certain r in $MnOOH_r$ H location, as indicated by OH bond formation, led to crystallization of $\delta$-MnOOH micro-domains which either randomly precipitated in the solid solution or they associated in such a way that led to heterogeneous reduction. The r in $MnOOH_r$ at which H started to locate appeared to depend on the relative rates at which H was inserted and diffused into the solid. H location occurred at $r \approx 0.20$ for Faradiser M in contrast to R2 in which it located at $r=0.80$.

A complementary study of the stability of the H inserted compounds in 7M KOH was carried out. Results from potential measurements, x-ray diffraction and SEM were obtained. Over a period of six weeks potential measurements indicated development of a heterogeneous potential at deep H insertion levels. X-ray diffraction and SEM signified formation of $\delta$-$MnO_2$ and $\gamma$-MnOOH. The results confirm the proposition of Holton *et al.* that H inserted compounds are unstable in KOH and disproportionate into $\delta$-$MnO_2$ and $\gamma$-MnOOH. This work removes doubt concerning the above proposition since formation of $\delta$-$MnO_2$ in their work was not simply the result of instability. The H insertion level at which instability was observed appeared related to the formation of $\delta$-MnOOH micro-domains, particularly for R2 in which instability occurred between $0.80 \leq r \leq 1.0$. This coincides with the oxidation state, $MnO_{1.6}$, beyond which alkaline manganese batteries cease to deliver useful power on prolonged intermittent discharge. Faradiser M possessed the largest instability region ($0.48 \leq r \leq 1.0$) and would, on this basis, be unsuitable for alkaline manganese batteries.

## Acknowledgements

It is a pleasure to acknowledge the support and guidance of my principal supervisor Professor Frank L.Tye, which without, I would never have completed the work.

I would also like to express my gratitude for the help provided by my other supervisor Dr Elizabeth Mayer-Abraham and the following people.

My parents who always encouraged and supported me.

Colleagues at the Energy Technology Centre particularly José Larcin who I owe a great deal to for my understanding of chemistry and electrochemistry and Etienne D.Gehain who convinced me, amongst many other things, of the usefulness of computers.

I wish also to acknowledge the contribution of John Fitzpatrick, a previous researcher at this Institute, whose chemically prepared H inserted samples form an important part of this study.

Technical staff throughout Middlesex University.

Finally I would also like to mention Dr Jean Pannetier and his colleagues Dr Yves Chabre and Dr Christiane Poinsignon, who greatly influenced and accelerated my understanding of the structure of manganese dioxide during an enjoyable visit to Grenoble.

# Contents

# 1 Introduction

This study was primarily concerned with structural changes which occurred when $H^+$ and $e^-$ (or H) was chemically inserted via a solid state reaction into synthetic battery active manganese dioxide. This term, as shall become clear, accurately refers to a series of materials whose structure is the subject of considerable debate. The interest in such (hydrogen insertion) materials is not unrelated to their widespread application in the dry cell battery industry. Furthermore, the possibility of increasing usage in for example $Li/MnO_2$ and rechargeable alkaline manganese batteries means that continued research into the properties of this material is ensured. Considering that it is well over 100 years since G.L.Leclanché patented[1] the 'Leclanché cell', which first made use of manganese dioxide in the cathode, it is perhaps surprising that the crystal structure of modern high performance materials is still in doubt. It may thus be inferred that the crystal structure of the H inserted derivatives is also a matter which is not satisfactorily understood. By way of introduction the author proposes to review the classification of $MnO_2$ and MnOOH polymorphs. MnOOH is considered the theoretical limiting composition when H is inserted in a solid state reaction process such as is generally accepted to occur during discharge of a dry cell battery, be it of the Leclanché or alkaline manganese type.

## 1.1 Manganese dioxide polymorphs.

A preliminary classification is presented here which adheres to an extent to the schemes presented by Giovanoli[2] and Burns and Burns[3]. A recent important discovery concerning a new polymorph[4] of $MnO_2$ is included. The final classification, however, will need to take into account the results of this study. This question is returned to in chapter 9.

Polymorphism is the rule rather than the exception for $MO_2$ metal oxides[5]. The reason for the large number of forms of $MnO_2$ is currently attributed to the ability of $[MnO_6]$ octahedra to form endless chains (by sharing octahedral edges) which can be linked at octahedral corners with other chains[3]. It is convenient to divide the polymorphs of manganese dioxide[†] into two categories; namely (1) perfectly periodic (or 'crystalline') stoichiometric phases and (2) not perfectly periodic (or not perfectly 'crystalline') non-stoichiometric phases. It is in the latter category which battery active synthetic manganese dioxide falls. Members of the above classes are as follows:

(1) $\beta$-$MnO_2$ or pyrolusite,
ramsdellite,
$\lambda$-$MnO_2$.
(2) $\gamma$-$MnO_2$.

Members of classification (1) are now described with the objective of providing an introduction to the structure of $\gamma$-$MnO_2$, which, as shall be revealed, is crucial to the understanding of battery active materials.

### 1.1.1 $\beta$-$MnO_2$.

In common with many other transition metals which have incompletely filled d sub-shells (namely Ti, Cr, Os, Ru, Ir, Sn and Ta) the dioxide crystallizes with the tetragonal rutile structure[6]. This is $\beta$-$MnO_2$ or pyrolusite (which is the mineral name). Figure 1-1(a) and (b) contain representations of this structure. Both are idealisations of the actual structure. In figure 1-1(b) the oxygens are hexagonally close packed (h.c.p.) so that the octahedra formed are perfect or undistorted. Each occupying Mn has a coordination number (c.n.) of 6 and each O a c.n. of 3. The *sphere* coordination number of a hypothetical (i.e. containing no manganese) h.c.p. oxygen structure is 12. Recently a new packing arrangement of spheres has been identified[7,8] with a sphere c.n. of 11. The packing density is somewhat less than h.c.p. (74.05%) at 71.87%. This arrangement may be used to produce an idealised rutile structure[8] as shown in figure 1-1(a). This new packing scheme, named primitive tetragonal packing[9] (p.t.p.), contains an equal number of two types octahedra of which metal atoms occupy one type. They appear as either squares or parallelograms on projection. The parallelograms represent undistorted octahedra (see figure 1-1(b)) and the squares heavily distorted octahedra. This results in the creation of a fourfold axis perpendicular to the plane of paper missing in a h.c.p. arrangement[8]. This structure represents much better the actual rutile (i.e. $TiO_2$) structure

---

[†] This description concentrates exclusively on those phases not containing any foreign ions in their structure. At one time compounds, now known to contain variable amounts of other elements, were believed to be polymorphs of manganese dioxide eg. "$\delta$-$MnO_2$". Giovanoli[2] has reviewed and elucidated this problem.

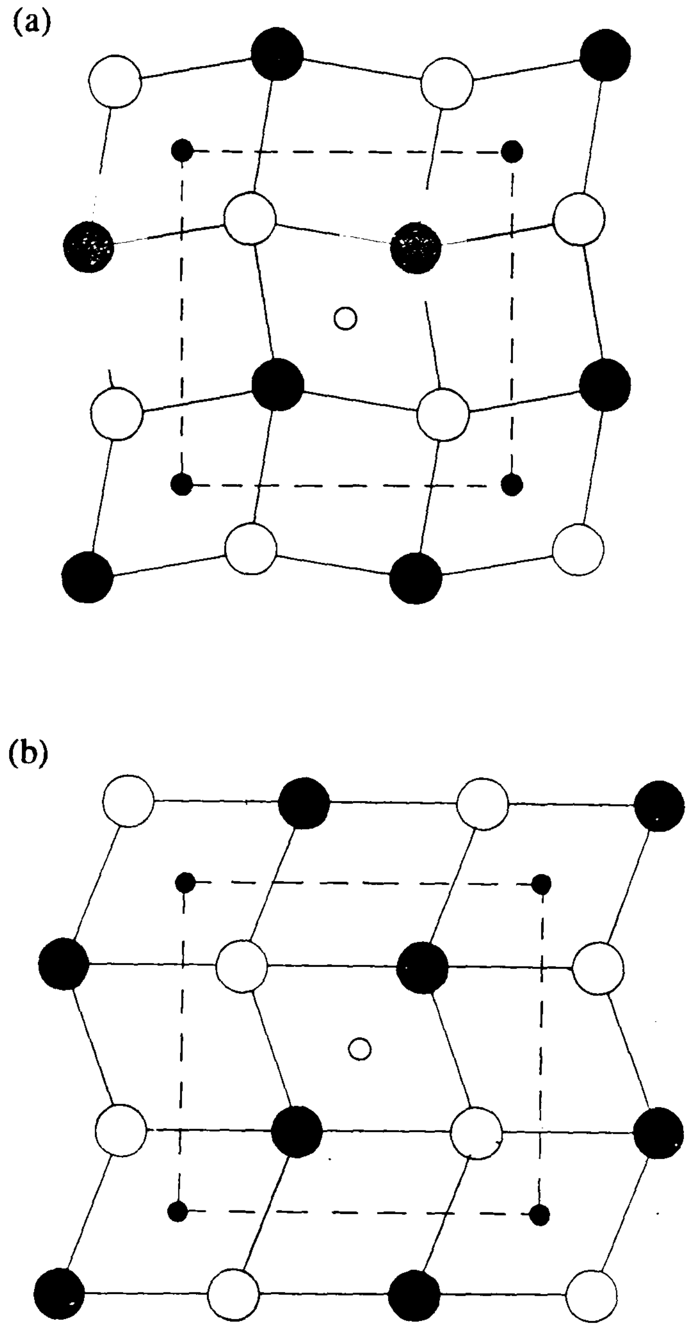

Figure 1-1 (a) Projection on the (a,a) plane of the ideal tetragonal rutile structure based on p.t.p. of oxygens. (b) Projection on the (a,b) plane of an approximate rutile structure based on h.c.p. of oxygens. Note that the structure is orthorhombic since $b=3/(2\sqrt{2})a \approx 1.06_1 a$. Large circles represent an oxygen atom and small circles a metal atom. Open and filled circles represent z levels of 0 and ½ respectively. Infinite occupied chains of octahedra extend in the c direction (i.e. perpendicular to the plane of the paper).

than an approximation such as that in figure 1-1(b). Since it is based on an exactly p.t.p. arrangement of oxygens it is justifiably regarded as the ideal structure of rutile. One reason for showing both the approximated (figure 1-1(b)) and the ideal structure (figure 1-1(a)) is to emphasize the close relationship between their oxygen arrangements. The ideal rutile structure may be regarded as resulting from 'distorting' the h.c.p. oxygen framework[†] of the approximated structure.

It is noted that $\beta$-$MnO_2$ does not crystallize in the ideal rutile structure as described, which predicts an ideal c/a ratio[8] of 0.5858 whereas the ratio calculated from published data[6,10], indicates that it is 0.653 (which is close to rutile[6] in which c/a=0.644).

Both the approximated structure and the ideal p.t.p. based structure may be described as consisting of infinite single chains of Mn occupied edge sharing oxygen octahedra extending in the **c** direction with chains joined at their octahedral corners.

### 1.1.2 Ramsdellite.

Ramsdellite, named[11] after Ramsdell who first noted its occurrence[12], occurs as a rare mineral the structure of which has been determined by Byström[49]. It essentially crystallizes in the diaspore structure but with elongated O-O bond lengths due to the lack of H bonding[13]. In terms of the simplified description of manganese dioxide polymorphs, it may be regarded as infinite double chains of edge sharing octahedra with the double chains linked by corners to other double chains. Figure 1-2(b) indicates a projection on the (001) plane of this simplified scheme. Evidently the oxygen arrangement in figure 1-2(b) is h.c.p. if the structure is formed from perfect octahedra and is therefore an analogous approximate structure to that represented in figure 1-1(b).

An analogous ideal ramsdellite structure to the idealised rutile structure may be obtained, figure 1-2(a). Conceptually this follows[9] by regarding p.t.p. as an "intergrowth"[‡] of body centred tetragonal packing (b.c.t.p.) and h.c.p. rather than a

---

[†] It is noted that the structure shown in figure 1-1(b) is orthorhombic . It is interesting that claims for the existence of an orthorhombic form of pyrolusite[105,94] have been made when it is found as a pseudomorph after manganite. Comparing the oxygen arrangements in figures 1-1 and 1-4 it appears that the h.c.p. arrangement is more closely related to the manganite structure than that of the p.t.p. arrangement. However, forming the axial ratios from published data[105] on 'orthorhombic pyrolusite' indicates that the structure does not have h.c.p. oxygens.

[‡] The use of this term does not imply any connection with the de Wolff intergrowth model of $\gamma$-$MnO_2$ to be described in the next section.

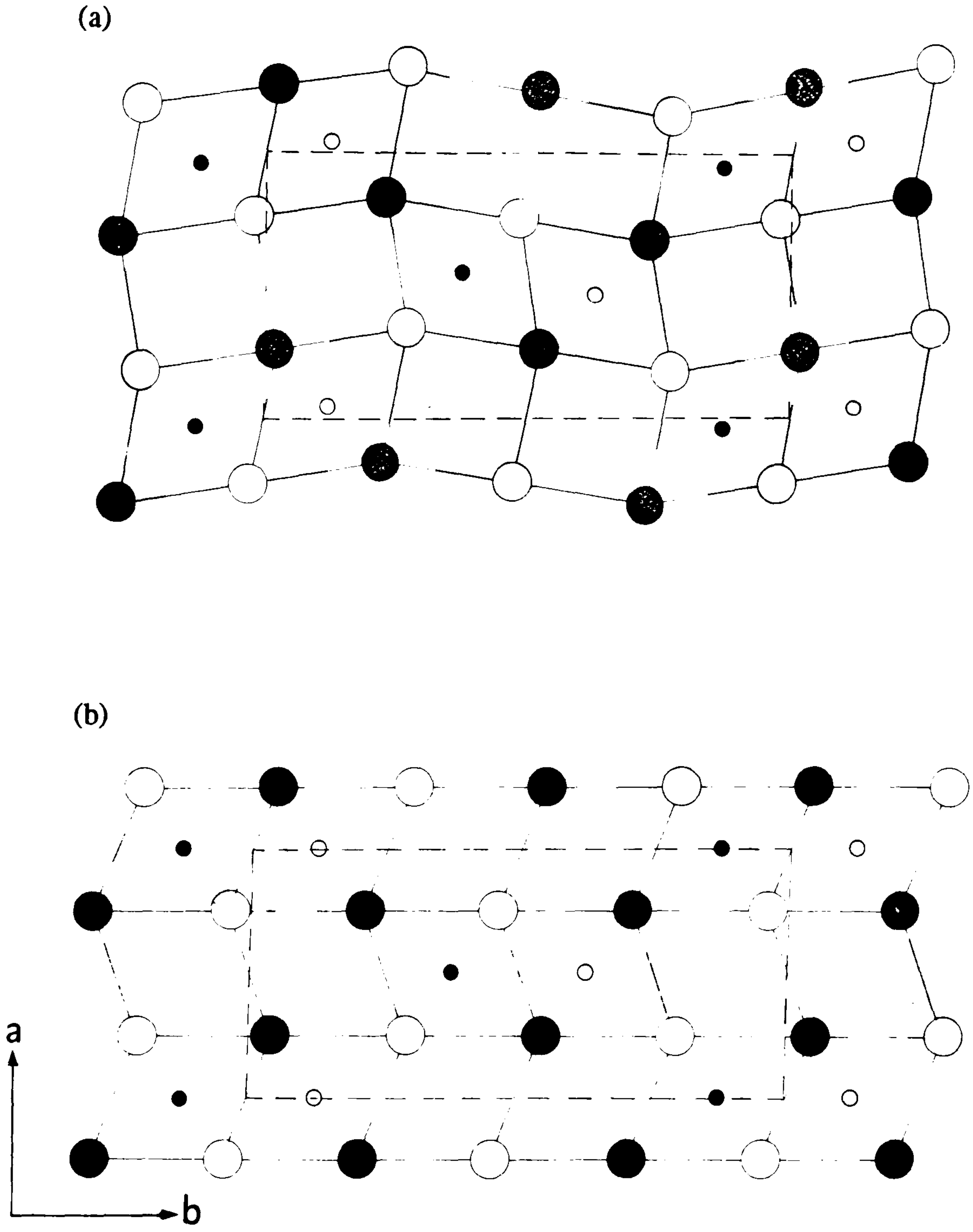

Figure 1-2 (a) Projection on the (a,b) plane of the ideal ramsdellite structure based on a combination of b.c.t.p. and h.c.p. of oxygens. (b) Projection on the (a,b) plane of an approximate ramsdellite structure based on h.c.p. of oxygens. Large circles represent oxygen atoms and small circles metal atoms. Open and filled circles represent z levels of 0 and ½ respectively. Infinite occupied chains of octahedra extend in the c direction (i.e. perpendicular to the plane of the paper).

distorted h.c.p. network. Essentially b.c.t.p. corresponds to a structure composed (in the same projection as figure 1-1) entirely of squares and h.c.p. entirely of parallelograms therefore p.t.p. may be regarded as an alternation of squares and parallelograms. It is therefore a simple matter to construct other "intergrowth" structures such as the ramsdellite structure presented in figure 1-2(a). The orthorhombic unit cell is indicated in the figure. If t designates tetragonal and o orthorhombic then as noted earlier

$$\frac{c_t}{a_t} = 2-\sqrt{2} = 0.5858, \quad \text{for ideal rutile.}$$

$$\Rightarrow c_t = (2-\sqrt{2})a_t = c_o, \quad \text{for ideal ramsdellite.}$$

From geometrical considerations it may be deduced that

$$b_o = 2a_t$$

$$\therefore \frac{b_o}{c_o} = \sqrt{2} + 2 = 3.414$$

$$\text{and since } a_o = a_t$$

$$\text{then } \frac{b_o}{a_o} = 2.$$

These values may be compared with those derived from the ramsdellite lattice[49] parameters which indicate that $b_o/c_o = 3.24_1$ and $b_o/a_o = 2.04_5$. It is noteworthy that the ideal ramsdellite lattice parameters are very close to those of the 'h.c.p. ramsdellite' which may easily be derived to be (see section 2.4.3).

$$\frac{b_o}{c_o} = 2\sqrt{3} = 3.464$$

$$\text{and } \frac{b_o}{a_o} = \frac{3}{\sqrt{2}} = 2.12.$$

The closeness of these ratios to that of the 'ideal' ramsdellite structure is a reflection of the intimate relation between p.t.p., b.c.t.p. and h.c.p.

### 1.1.3 λ-MnO$_2$.

This phase has only recently been synthesized[4]. It is based on cubic close packing (c.c.p.) of oxygens rather than h.c.p. The structure is closely related to the spinel structure $LiMn_2O_4$ from which it was synthesized (by removing Li ions from the tetrahedral sites). The existence of a phase with c.c.p. of oxygens raises the interesting possibility of c.c.p. stacking faults occurring in an otherwise h.c.p. oxygen arrangement of a manganese dioxide. Such a suggestion has been made previously[14]. In the normal notation for designating close packed layers if ABAB... represents h.c.p. and ABCABCABCABC... c.c.p. then a C layer occurring (randomly) in an otherwise perfect h.c.p. arrangement represents a random stacking fault structure. The x-ray diffraction effects from such stacking faults have been theoretically treated by Wilson[15] and are exemplified (for instance) in cobalt.

### 1.1.4 $\gamma$-$MnO_2$.

This phase may be precisely defined as an infinite structural series of related materials characterised mainly by their x-ray powder diffraction pattern, the end members of which are ramsdellite and pyrolusite. This is the modern description of $\gamma$-$MnO_2$ which originates with the fundamental work of de Wolff[48]. In the original paper[48], a structural intergrowth of ramsdellite type infinite double chains of octahedra randomly interspersed with pyrolusite type infinite single chains of octahedra was proposed following the suggestion of Byström and Byström[50] (cf. section 2.3), see figure 1-3(a) and (b). The plausibility of such a model was ascertained by examining the structures of both ramsdellite (figure 1-2) and pyrolusite (figure 1-1) and by noting similarities of certain actual diffraction patterns with that of ramsdellite and pyrolusite. Note that figure 1-3(b) is an intergrowth structure based on the approximated ramsdellite and pyrolusite structures (i.e. h.c.p. packing of oxygens) and figure 1-3(a) is the analogous ideal intergrowth structure based on a combination of b.c.t.p and h.c.p. of oxygens. The original model was valid only for small instances of p (fraction of pyrolusite type infinite octahedral chains). This restriction was removed in a later paper[57], which clearly indicated that p may and does vary from p=0 (ramsdellite) to p=1 (pyrolusite), and thus justifies the above definition of the collective name $\gamma$-$MnO_2$.

It is often stated that the de Wolff model of $\gamma$-$MnO_2$ is a structural intergrowth of alternating layers of pyrolusite and ramsdellite[16]. Such a statement is at best informative and at worst misleading since, as may be deduced from figure 1-3, 'unit cells' of pyrolusite do not necessarily occur except at high p values in which case

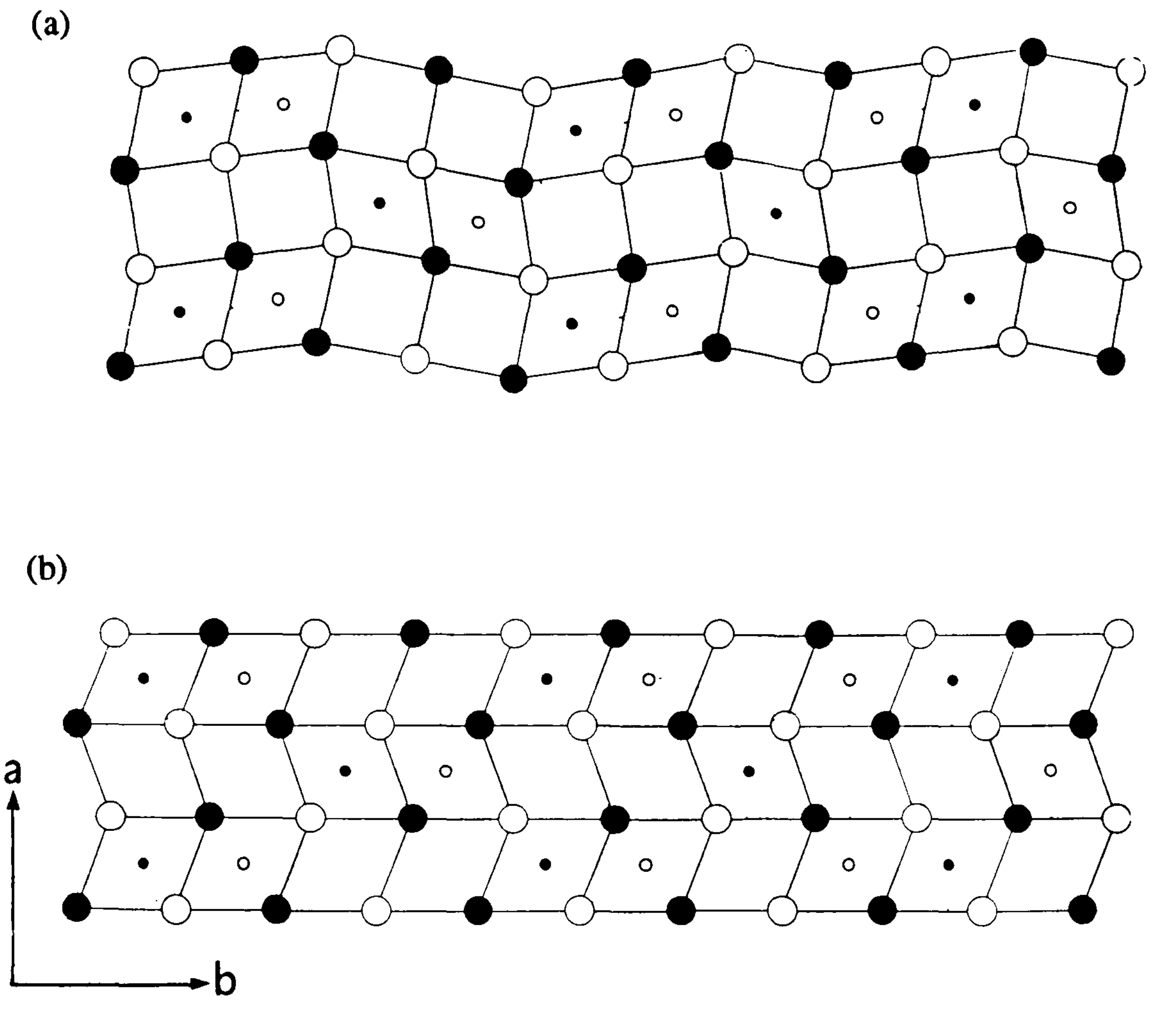

Figure 1-3 (a) Projection on the (a,b) plane an ideal de Wolff intergrowth structure based on a combination of b.c.t.p and h.c.p. of oxygens. (b) Projection on the (a,b) plane of an approximate intergrowth structure based on h.c.p. of oxygens. Large circles represent oxygen atoms and small circles metal atoms. Open and filled circles represent z levels of 0 and ½ respectively. Infinite occupied chains of octahedra extend in the c direction (i.e. perpendicular to the plane of the paper).

ramsdellite 'unit cells' do not necessarily occur. Failure to recognise that $\gamma$-$MnO_2$ is a random layer structure has led to erroneous deductions concerning crystallite size and strain[17].

It is interesting to note that, apart from the end members, gamma manganese dioxide[†] is always non-stoichiometric[18,19,20,55]. If the stoichiometry is expressed as x in $MnO_x$, x is always less than 2. Typically $x=1.96_6\pm0.003$, (this work sample SBPA) whereas the stoichiometry of crystalline $\beta$-$MnO_2$ and ramsdellite are very[21] close[‡] to x=2. Explanations for the observed non-stoichiometry has not attracted very much attention in the literature (see however the work of Parida[18,19] and co-workers[§]). Chemical formulas for gamma manganese dioxide, for example[22]

$$(2x-3)MnO_2.(4-2x)MnOOH.mH_2O,$$

nearly always assume that in fact manganese dioxide is stoichiometric and that the measured x is due to 'partial reduction' of the $Mn^{4+}$ to $Mn^{3+}$ due to the presence of H in the structure. Since these materials may accommodate H with a decrease in the value of x in $MnO_x$ it seems odd and rather unsatisfactory that they always initially contain a residual H content. Why is it that the non-stoichiometry, as with many other binary metal dioxides, is not due to (for instance) interstitial manganese or oxygen vacancies?

With regard to the above statement it is worth noting that the recently proposed[23] "cation-vacancy model for $MnO_2$" does not provide an answer to this question. This is because the presence of a $Mn^{4+}$ vacancy, with 4 protons replacing lost charge, does not alter the stoichiometry as measured, since what is actually measured is the average valence of Mn (expressed as x in $MnO_x$) rather than the Mn/O ratio. The decrease in valency is accounted for in this model, as before, by postulating that a fraction of $O^{2-}$ are replaced by $OH^-$ with the consequential presence of $Mn^{3+}$ (i.e.

---

[†] It is clear that oxides referred as "Nsutite" or "$\rho$-$MnO_2$" are members of the $\gamma$-$MnO_2$ structural series[10,20,105].

[‡] For $\beta$-$MnO_2$ see for example reference 21 page 22 where chemical analysis of IBA common sample no.6 ($\beta$-$MnO_2$) are given with an average $x=1.99_6$ see also reference 6 where $x=2.00\pm0.02$. In the case of ramsdellite an average composition corresponding to $x=2.00_7$ may be calculated from the values listed in table 1 reference 11.

[§] Their work, which consistently concludes in favour of oxygen vacancies as the cause of the non-stoichiometry in what they call "gamma manganese dioxide", may be doubted due to their reliance on calculation of the 'unit cell' volume which depends on the correct interpretation of the crystal structure of battery active materials.

'partial reduction'). Thus although this model is conceptually attractive from the point of view of explaining, in particular, how large quantities of 'structural water' may be accommodated in $MnO_2$ it fails to provide an insight into why $\gamma$-$MnO_2$ is inherently non-stoichiometric.

## 1.2 $Mn^{III}$ oxyhydroxide polymorhps.

"Oxyhydroxides may be described as compounds of metals in which the coordination group around the metal is composed of O and OH ligands."[24] The following shall restrict itself to oxhydroxides which have a composition approaching MnOOH. In which case the known polymorphs are α-MnOOH, γ-MnOOH, β-MnOOH and δ-MnOOH. Apart from β-MnOOH, the others form compounds which may be described as reduced isostructural counterparts of the manganese dioxide polymorphs. They can be divided similarly, without however, any corresponding implications concerning deviations from stoichiometry (this question appears to have received even less attention in the literature than noted previously for manganese dioxide).

MnOOH polymorphs are analogously divided into two categories; (1) perfectly periodic (or crystalline) modifications and (2) not perfectly periodic ('non-crystalline') modifications. Members of these classes are:

(1) γ-MnOOH (or manganite),
α-MnOOH (or groutite),
β-MnOOH (or feitknechtite)
(2) δ-MnOOH

As before members of each class are described, with a view to gaining an understanding of the H insertion compounds produced in this work.

### 1.2.1 γ-MnOOH.

The crystal structure of this modification has been determined by Buerger[93] and the positions of H within the structure located (using neutron diffraction) by Dachs[25]. A non-primitive B centred unit cell was chosen which preserved the previous convention for adopting the 'unique axis' as the b axis. A non-standard space group results i.e. $B2_1/d$. The structure has a monoclinic unit cell with $\beta=90°$ (which leads to it being referred to as 'pseudo-orthorhombic'). Using the general coordinates listed by

Wyckoff[26], the fractional coordinates given by Dachs and the lattice parameters determined by Buerger a projection of the structure in the same orientation as previous figures was constructed, figure 1-4. The structure is intimately related to that of β-$MnO_2$, compare figure 1-4 with figure 1-1(a). To quote Buerger "To the first approximation, it may be said that the structure is rutile-like. The manganese atoms occupy the centres of oxygen octahedra which form strings along the c axis by sharing edges." Oxygen atoms could not be considered as equivalent in terms of a number characteristics, including radii, such that the a and c unit cell dimensions become (approximately) doubled in manganite compared to β-$MnO_2$. (cf. section 4.1). The position of H within the structure is associated with one of the two types of oxygen, as suggested in the figure.

### 1.2.2 α-MnOOH.

The preliminary crystal structure determinations by Gruner[27] and Colin and Lipscomb[28] of this modification have been refined using single crystal techniques by Dent Glasser and Ingram[92]. It essentially crystallizes in the diaspore (i.e. α-AlOOH) structure[27] but with bond lengths reflecting Jahn-Teller distortion of the octahedra having $Mn^{3+}$ at the centre[92]. The structure is closely related to ramsdellite, which belongs to the same space group. The orthorhombic $a_0$ and $c_0$ unit cell dimensions are similar but $b_0$ is 15% larger in groutite (see figure 4-1).

H has not been located in this structure but Dent Glasser and Ingram suggested their location by analogy with diaspore (in which neutron diffraction studies have determined the H positions). Essentially hydrogen is bonded to one of two types of oxygens in the structure. Further discussion on the relation between groutite and ramsdellite may be found in section 4.1.1, in which it is noted that the approximately h.c.p. oxygen framework possesses a 'puckering' which is inverted in groutite with respect to ramsdellite.

### 1.2.3 β-MnOOH.

This material, first synthesized by Feitknecht and Marti[29], appears to be metastable, of variable stoichiometry, displaying a total of only 5 broadened reflections in its x-ray diffraction pattern. Because of the difficulty in synthesizing this material[29,30], knowledge concerning its structure is limited. It has been

PAGE
MISSING
IN
ORIGINAL

### 1.2.4 δ-MnOOH.

This phase[†] is directly analogous to that of γ-$MnO_2$. That is it say δ-MnOOH may be regarded an infinite but bounded series of related materials the end members of which are groutite and manganite. The plausibility of such a series existing is not simply a consequence of the intimate relation between ramsdellite and groutite and pyrolusite and manganite but the plausibility as to whether an *intergrowth* structure of double and single infinite chains of manganese occupied octahedra could be constructed from the chains existing in groutite and manganite. This question is discussed in section 4.1.

Evidence for members of this series was first recognised by Feitknecht[32] *et al.* in their study of the reduction of disordered γ-$MnO_2$ by $N_2H_4$. Giovanoli[33] *et al.* extended this work in a later study in which members of the γ-$MnO_2$ series were reduced by cinnamic alcohol in xylene. The conclusions reached therein, however, (stated in the next section and discussed in chapter 4) require, it shall be argued, substantial modification.

Despite the fact that x-ray diffraction patterns of reduced γ-$MnO_2$ have been reported[33] to contain qualitatively similar line shifts to that of γ-$MnO_2$ (from the positions of ramsdellite or pyrolusite, explainable by the de Wolff intergrowth model) no analysis for the 'p' layer fraction has been attempted and therefore the existence of reduced intergrowth counterparts has not been theoretically tested by the only method available. This work removes this deficiency by successfully analyzing compounds close to the composition of MnOOH in the manner of de Wolff. Evidently the δ-MnOOH intergrowth structure will appear very similar to the γ-$MnO_2$ intergrowth structures shown in figure 1-3 (a) and (b) though with different 'unit cell' dimensions.

The above conformation has added importance in that recent *in situ* neutron diffraction evidence[34] has suggested that such reduced intergrowth structures do not occur during discharge of γ-$MnO_2$ in 7N KOD. Analogously it has been suggested that synthetic active battery materials do not form intergrowth structures. In contrast it is also claimed they reduce sequentially, that is ramsdellite type double chains are first reduced during insertion of H (or D) and then pyrolusite type single chains. The insertion of H into the pyrolusite type layers is not favoured, however, and the structure breaks. The breaking of the structure is associated with the appearance of $Mn(OH)_2$. This has led

---

[†] The name δ-MnOOH was first proposed by Maskell *et al.*[73] It is preferred to the use of "α-MnOOH" introduced by Giovanoli[2].

Pannetier *et al.*[34,39] to produce a crystallographic phase diagram in which the formation of reduced intergrowth structures based on groutite type double chains and manganite type single chains is explicitly disallowed.

## 1.3 Other manganese dioxide and oxyhyrdoxide polymorphs.

It is interesting to note that, as yet, no corresponding H inserted $\lambda$-$MnO_2$ compound has been reported.

Not included in the above classification of manganese dioxides (at odds with both Giovanoli and Burns and Burns) is the phase named $\varepsilon$-$MnO_2$. The characteristic feature of this material is the (apparent) hexagonal symmetry of the powder x-ray diffraction pattern. De Wolff[43] *et al.* have described this modification as consisting of h.c.p. $O^{2-}$ with $Mn^{4+}$ occupying half the available octahedral sites (with the additional condition that face sharing of adjacent occupied octahedra be disallowed). Claims have been made for naturally occurring[35] $\varepsilon$-$MnO_2$ as well as the synthetic fibrous material investigated by de Wolff *et al.* It has been suggested recently[36] that materials previously thought to exhibit hexagonal symmetry, and therefore classed as $\varepsilon$-$MnO_2$, do not in fact posses this symmetry but rather an *apparent* hexagonal symmetry due to the particular diffraction effects caused by a structural defect, which shifts the line positions from those of $\gamma$-$MnO_2$ (cf. section 2.5). The validity of $\varepsilon$-$MnO_2$ as a separate polymorph of $MnO_2$ is therefore in doubt. This work will provide further evidence that it is not a separate modification and therefore its non-inclusion is to some extent preemptive.

## 1.4 Current state of the debate concerning the crystal structure of synthetic battery active manganese dioxide and their H inserted derivatives.

Electrodeposited manganese dioxide (EMD) and chemical manganese dioxide (CMD), as manufactured for the Leclanché and alkaline Mn battery industry, are normally prepared in bulk and ground to finely divided powders. The exact appearance of the particles appears to reflect the history of the process[138]. One reason for the lack of agreement on the structure of these materials is that single crystals large enough for conventional x-ray diffraction analysis do not occur in the aforementioned processes.

Furthermore the powder x-ray diffraction pattern contains essentially only five broadened reflections (see section 2.1).

As reviewed above, there are only three well established crystalline stoichiometric modifications of $MnO_2$. Namely, $\beta$-$MnO_2$, ramsdellite and $\lambda$-$MnO_2$. Then there is the infinite but bounded series of materials forming $\gamma$-$MnO_2$, which are always non-stoichiometric and elucidated by de Wolff[48] as members of a structural intergrowth of double and single octahedral chains. The debate concerning synthetic battery active materials, which are themselves always non-stoichiometric in a similar manner to $\gamma$-$MnO_2$, has focused on whether they belong to the $\gamma$-$MnO_2$ structural series or $\varepsilon$-$MnO_2$.

Preisler[51] has shown that EMD, grown by the suspension bath process (SBP), can produce a continuous series of materials (in terms of x-ray diffraction, and other properties) from those of line rich $\gamma$-$MnO_2$ to that of conventional EMD depending on the effective current density of deposition. Freund[37] *et al.*'s x-ray diffraction experiments on orientated blocks of fibrous EMD (which has a powder x-ray diffraction pattern similar to conventional EMD), led to apparent inconsistencies if the de Wolff model of $\gamma$-$MnO_2$ were adopted. This led de Wolff[43] *et al.* to determine the structure of this material as $\varepsilon$-$MnO_2$. Giovanoli[2] has subsequently claimed that conventional EMD is better represented by the $\varepsilon$-$MnO_2$ structure where $\varepsilon$-$MnO_2$ is considered to be an end member of $\gamma$-$MnO_2$ due to increasing structural disorder, whereas $\beta$-$MnO_2$ and ramsdellite are the 'true' end members.

Although single crystals of EMD have not been synthesized in a large enough size for single crystal x-ray diffraction, single crystal electron diffraction patterns have recently been reported[44]. The authors claim that their results are consistent with the de Wolff intergrowth model (rather than $\varepsilon$-$MnO_2$). EXAFS spectroscopy appears to support this conclusion[38].

Recently a new model for the structure of electrochemically active manganese dioxide has been proposed[39,40,34] by Pannetier *et al.* It introduces the concept of microtwinning into the de Wolff model of $\gamma$-$MnO_2$ (cf. section 2.5) as the structural fault which characterises battery active forms. Evidence for this fault comes from a comparison with simulated diffraction patterns produced using computerised numerical methods. The results appear to account for many perplexing features of battery active manganese dioxide diffraction patterns, which, until this model had been introduced had not received satisfactory explanation. If confirmed, this model represents a breakthrough in the understanding of the structure of battery active manganese dioxide.

An important technique, so far excluded from the discussion, which *inter alia* provides structural information, is the reduction of $MnO_2$ by the insertion of H into the structure. This is the most important reaction for dry cell batteries and occurs by insertion of $H^+$ and $e^-$ in a single phase reaction (see chapter 8). Study of the accompanying 'lattice dilation', first reported by Brenet[41], has already provided structural information (see introduction to chapter 4). It is not surprising (in view of the preceding discussion) that the structure of the most H inserted derivatives (i.e. close to composition MnOOH) and their relation to the initial material, particularly concerning the origin of 'new' lines[73] at deep H insertion levels, is also a matter which is not well understood. Thus in view of the uncertainty mentioned, the conclusions in particular reached by Giovanoli[2] that insertion of H into $\gamma$-$MnO_2$ leads to $\alpha$-MnOOH and $\varepsilon$-$MnO_2$ leads to $\gamma$-MnOOH deserves re-examination, especially for EMD and CMD. The '$\alpha$-MnOOH' produced, however, was meant to bear the same relation to $\alpha$-MnOOH and $\gamma$-MnOOH that $\gamma$-$MnO_2$ bears to ramsdellite and $\beta$-$MnO_2$. The term $\delta$-MnOOH is preferred in this work (see the footnote on page 13).

## 1.5 Aim of work.

The aim of this work was to gain an insight into the crystal structure of the initial and H inserted forms of synthetic battery active manganese dioxide primarily by examining the structural changes undergone when H is inserted in a solid state reaction. This has been attempted by studying a range of materials possessing differing 'crystallinities' forming a series similar to that reported by Preisler[51]. A secondary aim was to study a property of the H inserted derivatives which may reasonably be expected to be connected with their structure, and thus attempt to correlate any determined structural differences with the property referred to. In this case the stability of the H inserted forms in concentrated KOH was considered a suitable candidate. This topic has additional interest in that, though not generally recognised as such, it may be of importance both in attempts to understand the lower than expected performance of alkaline manganese batteries on extended intermittent discharge regimes and also for endeavours to produce fully rechargeable alkaline manganese cells.

# 2 The Structure of Synthetic Battery Active Manganese Dioxide.

## 2.1 Introduction

This chapter is concerned with the crystal structure of commercially available synthetic battery active manganese dioxide. Such materials are widely used in the dry cell battery industry due to their superior discharge performance compared to natural materials[42]. The x-ray diffraction pattern is typified by that shown in figure 2-1 which is of IBA (International Battery Association) common sample no.19. There are five main peaks in this pattern labelled A,B,C,D,E (peak X1 is a β-$MnO_2$ impurity and X2 is due to the aluminum sample holder. cf. section 2.3.1). The broad reflection at about[†] 22°2θ is characteristic and diagnostic of this type of material. It should be pointed out that although peaks A to E are prominent other reflections are present. If the scale in the region 70 - 140 °2θ is expanded these become apparent as shown in figure 2-1 (b). In structure analysis no piece of information should be left out, however these reflections add little new information because they appear to be mostly weak higher orders of the peaks observed in the lower region of °2θ and therefore will not be considered further.

In order to introduce the subject of the crystal structure of $MnO_2$ a simple model shall be described which, although failing to describe the actual material, serves as a good starting point for the discussion to follow. The simplest description of the structure of $MnO_2$ must be that of a close packed $O^{2-}$ lattice with $Mn^{4+}$ ions occupying 50% of the octahedral sites. It is assumed that the ionic radii[23] of $Mn^{4+}$ would not permit it to occupy the other type of site available[23] (tetrahedral sites). This description is very similar to the model proposed by de Wolff *et al.*[43] for ε-$MnO_2$. The generalisation of the above simple view of the manganese dioxides (not containing any foreign cations) is that of an approximately h.c.p. framework of oxygen ions interspersed in a regular or statistical manner with half the number of manganese ions.

As has been reviewed earlier (chap.1) essentially three rival structures have been proposed to account for the x-ray diffraction pattern of EMD. Two of these were originally proposed by the authors for different materials than that of figure 2-1. In the

---

[†] All °2θ values refer to CuKα radiation unless otherwise stated.

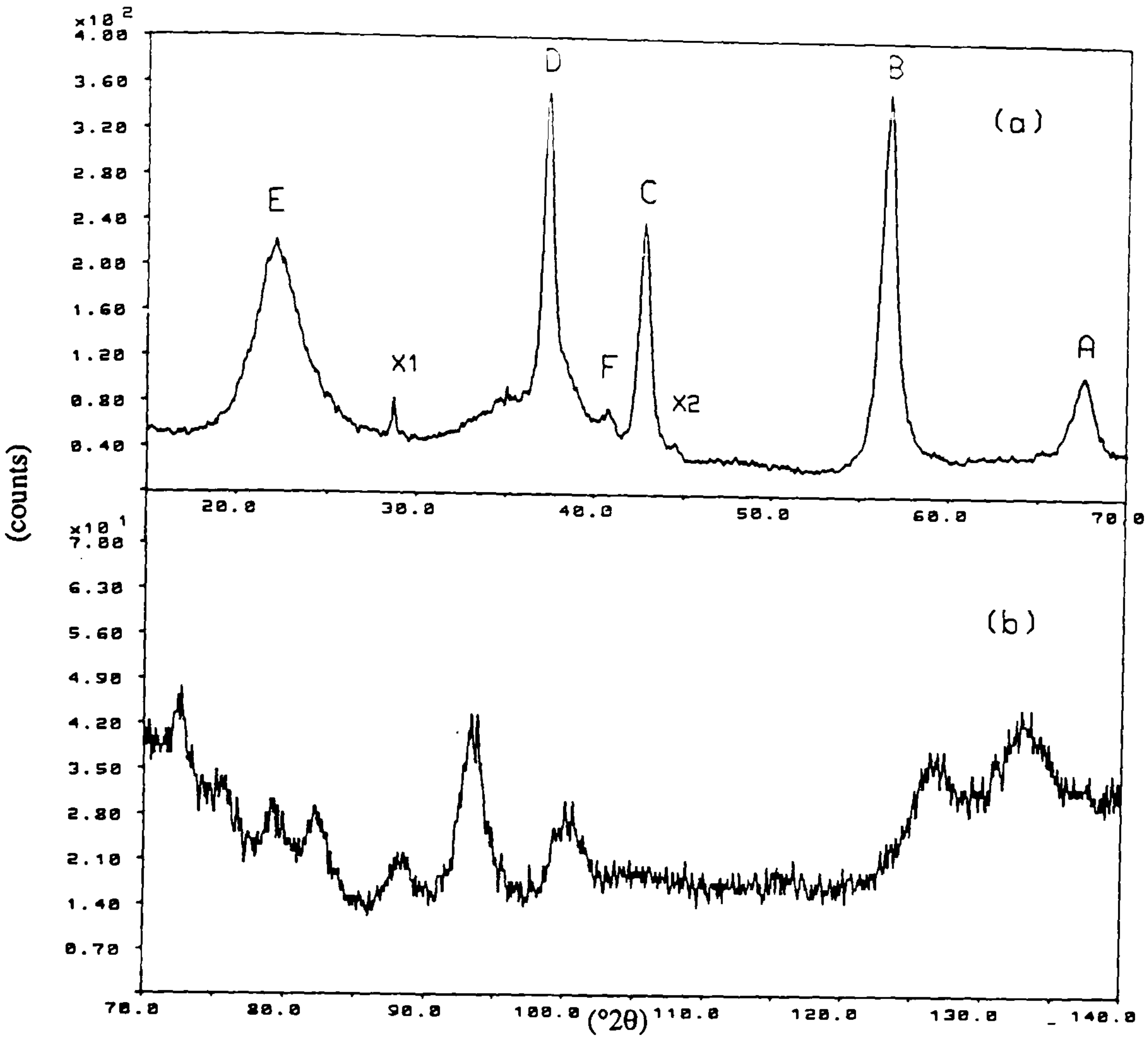

Figure 2-1 X-ray diffraction pattern of IBA no.19. (a) main diffraction peaks A, B, C, D, E, F (15-70°2θ, CuKα) (b) weak peaks (70-140°2θ). X1 and X2 are due to impurities.

absence of any other theory these have subsequently been applied by various authors[44,32,22] to materials with similar x-ray diffraction patterns to that of figure 2-1. It is proposed here to attempt to resolve the conflict by examining each carefully in turn. Because of it's conceptual simplicity the ε-$MnO_2$ model is considered first. The de Wolff intergrowth model and will then subsequently be examined together with the a radical modification of it proposed by Pannetier *et al.* (see section 1.4).

## 2.2 The ε-$MnO_2$ model.

Figure 2-2 is a diagram indicating the relationship of a simple hexagonal unit cell, composed of oxygen ions, to one of the two possible octahedra with centres in the unit cell. There are thus two possible sites that a manganese atom could occupy as indicated in the diagram. An occupation of 0.5 manganese in each site would correspond to a completely random occupation of the available sites. For the description to correspond to the ε-$MnO_2$ model an important condition needs to be made clear. That

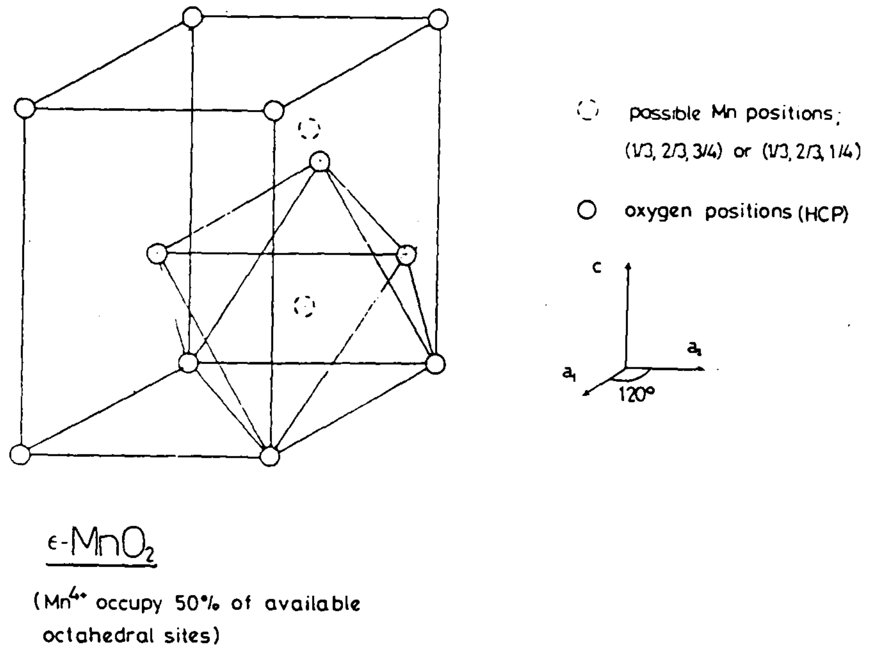

Figure 2-2 Simple hexagonal structure of ε-$MnO_2$ showing possible positions of manganese atoms and relation to [$MnO_6$] octahedra.

is that the occupation of the octahedral sites is 'pseudo-random' because 'face sharing' of $Mn^{4+}$ in two adjacent octahedra is disallowed (because the "Mn-Mn distance would be improbably small"†). Face sharing corresponds to the two octahedra in figure 2-2 their centres being the possible manganese sites.

Randomness is assumed to exist in a 'layer', that is perpendicular to the $c^{\ddagger}_{hex}$ direction, in the simple hexagonal cell defined by the close packed $O^{2-}$ framework (figure 2-2). No face sharing implies a separation of $c_{hex}$ in the direction perpendicular to a layer for any two manganese atoms. If one imagines filling a h.c.p. oxygen framework with Mn layer by layer then once the initial distribution has been (randomly) chosen the distribution of Mn in subsequent layers is completely determined.

In order to elucidate the validity of the ε-$MnO_2$ model for EMD some simple considerations are worth discussing. If the structure is hexagonal the d (or interplanar) spacings are given by equation (2.1) and the ideal ratio of the a and c axis by equation (2.2).

$$\frac{1}{d^2}=\frac{4}{3}\frac{(h^2+k^2+hk)}{a^2}+\frac{l^2}{c^2} \qquad (2.1)$$

---

† Quoted from a translation of the original paper (ref.43).

‡ The subscript hex is introduced to distinguish hexagonal axis.

where $d$ = interplanar spacing (Å)
$h,k,l$ = Miller indices
$a,c$ = hexagonal axis (Å)

$$\frac{c}{a}=\left(\frac{8}{3}\right)^{\frac{1}{2}}=1.633 \qquad (2.2)$$

If the ionic radius[45] of $O^{2-}$=1.40 (Å) then $a_{hex}$=2.80(Å) and from above $c_{hex}$=4.57$_2$(Å). In order to discover which of these reflections are present for ε-$MnO_2$ the effect of adding manganese to the h.c.p. $O^{2-}$ framework must be considered. This is partly achievable by the appropriate structure factor calculation. It is the structure factor ($F_{hkl}$) which determines whether a given line appears even if the Bragg condition is satisfied. $F_{hkl}$ can be calculated from equation (2.3).

$$F_{hkl}=\sum_{n=1}^{N} f_n \exp(2\pi i(hu_n+kv_n+lw_n)) \qquad (2.3)$$

$u_n,v_n,w_n$ = fractional coordinates of element n
$f_n$ = atomic scattering factor of element n

Equation (2.3) is basically a summation of harmonic waves emanating from each atom in the unit cell for a particular direction or (hkl) satisfying the Bragg condition. It should be noted that the atomic scattering factors ($f_n$) depend both on 2θ (the scattering angle) and the incident x-ray wavelength. At 2θ=0 $f_n$ is defined such that it equals the atomic number of the element concerned.

The structure factor for a random model (i.e. with 0.5 Mn in each site of figure 2-2), is designated $F_R$. It should be noted that $F_R$ does not reflect the 'pseudo randomness' of the ε-$MnO_2$ model as discussed above. Ultimately the test as to the validity of this calculation is whether it can reproduce the observed line intensities. The approximate relative intensities expected for a real powder pattern were calculated with equation (2.4).

$$I=|F|^2 p\left(\frac{1+\cos^2 2\theta}{\sin^2\theta\cos\theta}\right) \qquad (2.4)$$

$p$ = multiplicity factor
$2\theta$ = Bragg angle
$F_{hkl}$ = structure factor

The factor in brackets makes the calculation applicable to the particular geometry of a diffractometer (employing a flat powder sample). The above expression does not include the so called 'temperature factor'. Following Cullity[46] (p.132) the calculation was performed for the random model and a hypothetical close packed $O^{2-}$ lattice. The results are given in tables 2.1 and 2.2. The calculated intensities are actually the relative 'integrated intensities' (total reflected energy), and so to compare these with the actual pattern it is necessary to integrate the counts under the peaks rather than use peak heights since in this case the relative peak heights are different from the relative peak areas due to the differing broadnesses of peaks A,B,C,D,E,F (see figure 2-1). For reference the values of the peak and background values used are contained in table 2.3.

It should be noted that although a close packed $O^{2-}$ arrangement has no physical reality it would give the general appearance of any h.c.p. structure with an ionic (or otherwise) radius of about 1.40 (Å). The calculated relative integrated intensities are

Table 2.1 Calculated 'random' $\varepsilon$-$MnO_2$ model powder x-ray diffraction pattern, using equation (2.4), with $a_{hex}=2.77_4$ and $c_{hex}=4.40_6$.

| No | h | k | l | $F_R^2$ | °2θ | d (Å) | p | $I/I_1$ |
|---|---|---|---|---|---|---|---|---|
| 1 | 0 | 0 | 1 | 0 | 20.16 | 4.406 | 2 | 0 |
| 2 | 1 | 0 | 0 | 158.9 | 37.43 | 2.402 | 6 | 44.5 |
| 3 | 0 | 0 | 2 | 54.6 | 40.96 | 2.203 | 2 | 4.3 |
| 4 | 1 | 0 | 1 | 71.1 | 42.88 | 2.109 | 12 | 31.2 |
| 5 | 1 | 0 | 2 | 363.2 | 56.69 | 1.624 | 12 | 100 |
| 6 | 1 | 1 | 0 | 410.7 | 67.53 | 1.387 | 6 | 43.7 |
| 7 | 1 | 0 | 3 | 22 | 75.93 | 1.253 | 12 | 4 |
| 8 | 2 | 0 | 0 | 100.6 | 79.85 | 1.201 | 6 | 8.7 |
| 9 | 1 | 1 | 2 | 53.8 | 82.11 | 1.174 | 12 | 9 |
| 10 | 2 | 0 | 1 | 18.9 | 83.4 | 1.159 | 12 | 3.1 |
| 11 | 0 | 0 | 4 | 274.8 | 88.84 | 1.102 | 2 | 7.2 |
| 12 | 2 | 0 | 2 | 186.3 | 93.94 | 1.055 | 12 | 27.9 |
| 13 | 1 | 0 | 4 | 76.6 | 100.69 | 1.001 | 12 | 11.1 |
| 14 | 2 | 0 | 3 | 11.8 | 112.01 | 0.93 | 12 | 1.7 |
| 15 | 2 | 1 | 0 | 65.4 | 116.21 | 0.908 | 12 | 9.4 |
| 16 | 2 | 1 | 1 | 11 | 120.18 | 0.889 | 24 | 3.2 |
| 17 | 1 | 1 | 4 | 176.8 | 126.68 | 0.863 | 12 | 27 |
| 18 | 1 | 0 | 5 | 9.6 | 137.43 | 0.827 | 12 | 1.7 |
| 19 | 2 | 1 | 2 | 123.9 | 133.36 | 0.839 | 24 | 40.5 |
| 20 | 2 | 0 | 4 | 53.6 | 143.46 | 0.812 | 12 | 10.4 |
| 21 | 3 | 0 | 0 | 154.5 | 148.6 | 0.801 | 6 | 16.8 |

Table 2.2 Calculated powder x-ray diffraction pattern for a hypothetical h.c.p. $O^{2-}$ structure with $a_{hex}=2.77_4$ and $c_{hex}=4.40_6$.

| No | h | k | l | $F^2_{O2-}$ | °2θ | d (Å) | p | $I/I_1$ |
|---|---|---|---|---|---|---|---|---|
| 1 | 0 | 0 | 1 | 0 | 20.16 | 4.406 | 2 | 0 |
| 2 | 1 | 0 | 0 | 28.7 | 37.43 | 2.402 | 6 | 25.7 |
| 3 | 0 | 0 | 2 | 101.7 | 40.96 | 2.203 | 2 | 25.8 |
| 4 | 1 | 0 | 1 | 71.2 | 42.88 | 2.109 | 12 | 100 |
| 5 | 1 | 0 | 2 | 13.8 | 56.69 | 1.624 | 12 | 12.1 |
| 6 | 1 | 1 | 0 | 39.3 | 67.53 | 1.387 | 6 | 13.4 |
| 7 | 1 | 0 | 3 | 22.1 | 75.93 | 1.253 | 12 | 12.9 |
| 8 | 2 | 0 | 0 | 6.8 | 79.85 | 1.201 | 6 | 1.9 |
| 9 | 1 | 1 | 2 | 25.9 | 82.11 | 1.174 | 12 | 13.9 |
| 10 | 2 | 0 | 1 | 18.9 | 83.4 | 1.159 | 12 | 10 |
| 11 | 0 | 0 | 4 | 22.6 | 88.84 | 1.102 | 2 | 1.9 |
| 12 | 2 | 0 | 2 | 5.1 | 93.94 | 1.055 | 12 | 2.4 |
| 13 | 1 | 0 | 4 | 4.4 | 100.69 | 1.001 | 12 | 2 |
| 14 | 2 | 0 | 3 | 11.8 | 112.01 | 0.93 | 12 | 5.4 |
| 15 | 2 | 1 | 0 | 3.8 | 116.21 | 0.908 | 12 | 1.7 |
| 16 | 2 | 1 | 1 | 11 | 120.18 | 0.889 | 24 | 10.3 |
| 17 | 1 | 1 | 4 | 13.9 | 126.68 | 0.863 | 12 | 6.8 |
| 18 | 1 | 0 | 5 | 9.6 | 137.43 | 0.827 | 12 | 5.3 |
| 19 | 2 | 1 | 2 | 3.3 | 133.36 | 0.839 | 24 | 3.5 |
| 20 | 2 | 0 | 4 | 3.1 | 143.46 | 0.812 | 12 | 1.9 |
| 21 | 3 | 0 | 0 | 11.9 | 148.6 | 0.801 | 6 | 4.1 |

compared diagrammatically with the actual measured values from IBA no.19 in figure 2-3.

Table 2.3 Peak and background boundaries for integrated areas of IBA no.19.

| No | Label | Peak (°2θ) | low backgr (°2θ) | High backgr (°2θ) |
|---|---|---|---|---|
| 1 | Peak E | 17.57-28.08 | 16.57-17.57 | 29.38-30.38 |
| 2 | Peak D | 35.61-40.02 | 35.61-35.61 | 40.02-40.02 |
| 3 | Peak F | 40.02-41.41 | 40.02-40.02 | 41.41-41.41 |
| 4 | Peak C | 41.70-44.00 | 41.40-41.70 | 44.00-44.30 |
| 5 | Peak B | 53.7-60.00 | 52.70-53.70 | 60.00-61.00 |
| 6 | Peak A | 66.00-70.05 | 65.00-66.00 | 69.05-70.05 |

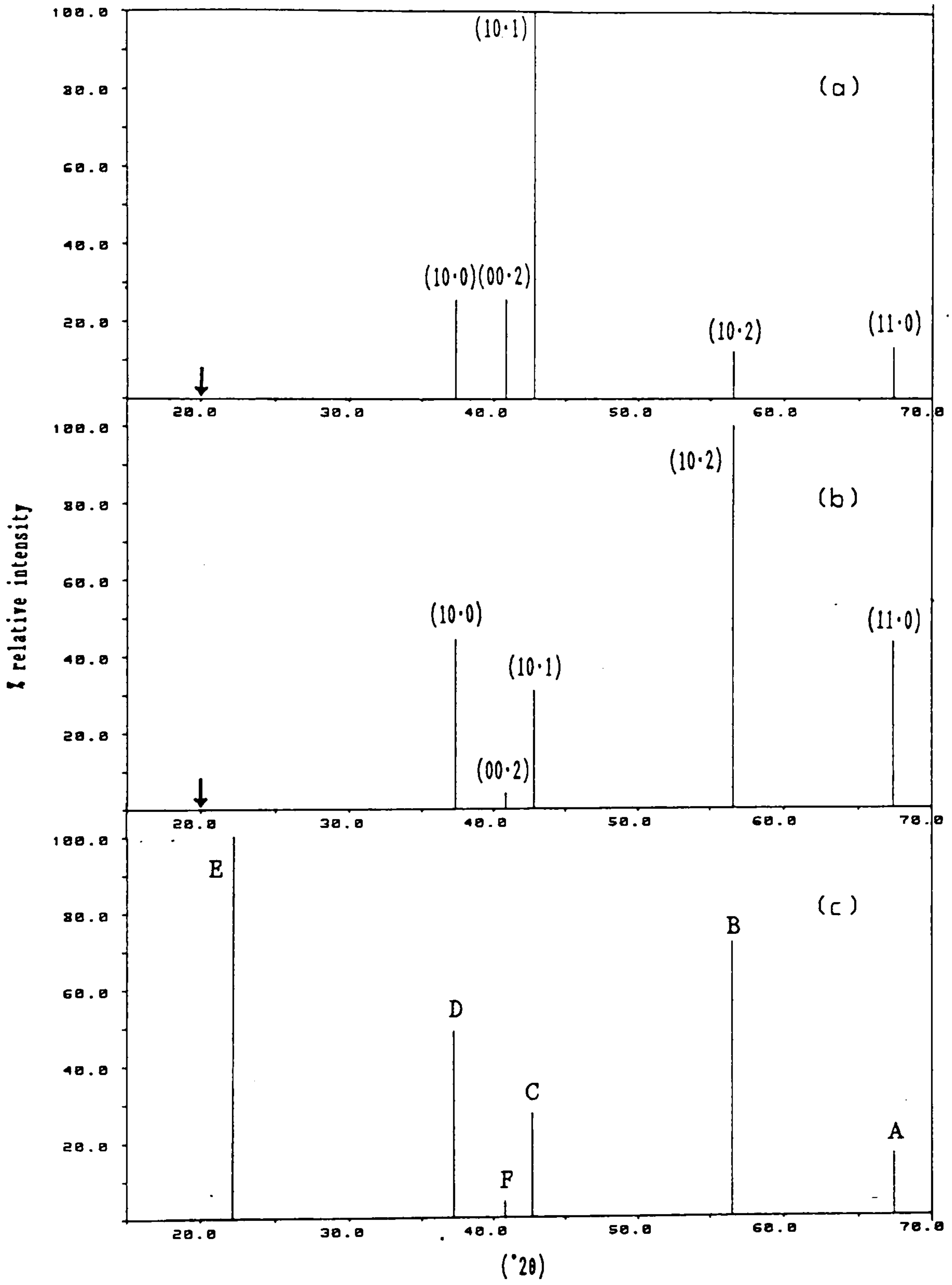

Figure 2-3 Effect of adding manganese to hypothetical h.c.p. $O^{2-}$ structure on calculated intensities and comparison with those measured from IBA no.19. (a) Calculated relative intensities of hypothetical h.c.p. $O^{2-}$structure, (b) 'random' ε-$MnO_2$ model (Mn atoms randomly occupy 50% of available octahedra), (c) measured IBA no.19 integrated relative intensities. Hexagonal indices are indicated in (a) and (b) and position of the forbidden (00·1) reflection is marked by an arrow. The peak labels in (c) are as given in figure 2-1.

For the calculated intensities in figure 2-3 the lattice parameters $a_{hex}$, $c_{hex}$ were re-evaluated to produce a better match to the observed line positions. This was achieved by combining the Bragg condition and the equation for plane spacing (equation (2.1)) and equating the result to the observed $\sin^2\theta$ values for the two most intense peaks (i.e. lines (10.0) and (10.2)). Solving these two equations simultaneously produces $a_{hex}=2.77_4$(Å) and $c_{hex}=4.40_6$(Å). The effective $O^{2-}$ radius now becomes 1.387(Å) and from equation (2.2) the axis ratio 1.588. This is below the value for a perfect h.c.p. arrangement, (see equation (2.2)) but is comparable to the deviations from the ideal shown by metals having a h.c.p. structure[47].

The h.c.p. $O^{2-}$ calculation (figure 2-3 (a)) is in considerable error compared to the observed intensities (figure 2-3 (c)). The random model calculation reflects much better the observed intensities (figure 2-3 (b)) apart from the complete absence of a line at approximately 22°2θ. The d spacing of this broad line is approximately 4(Å). There are incidentally no 'extra' lines due to the incorporation of $Mn^{4+}$ in the h.c.p. $O^{2-}$ structure. (i.e. $F_R$ and $F_{O2-}$ structure factors are zero at the same d spacing).

To summarise, it has been shown the ε-$MnO_2$ model proposed by de Wolff *et al.* for fibrous EMD allows calculation by the classical structure factor method of the intensity and position expected for any line of EMD except the '4(Å) ' peak. The authors propose an explanation of this peak which occurs near (but obviously displaced) from the position of the forbidden (00·1) reflection (see table 2.1 and figure 2-3). Thus whether this model is correct appears to rest on the explanation for this diffraction maxima.

## 2.3 The de Wolff intergrowth model of γ-$MnO_2$.

This model[48] was originally proposed to account for the diffraction patterns of synthetic manganese dioxides showing a resemblance to the diffraction pattern of the rare mineral ramsdellite. Byström[49] earlier had determined the structure of ramsdellite and had also suggested that the differences between ramsdellite and γ-$MnO_2$ were probably because γ-$MnO_2$ was "an intermediate product between pyrolusite and ramsdellite" and later Byström and Byström[50], directly anticipating de Wolff's intergrowth model state that, "The structure of γ-$MnO_2$ has not been definitely established, but it seems that the structure is partly disordered, and possibly the arrangement of the Mn ions changes from ramsdellite to pyrolusite at random. The cell dimensions of $\gamma$-$MnO_2$ indicate that the ramsdellite arrangement dominates." The differences between ramsdellite and $\gamma$-$MnO_2$ , later quantitatively stated and explained by de Wolff[48] (using the intergrowth model briefly described in section 1.1.4), were a broadening and shift of certain lines from the breadth and position of pure ramsdellite. The remaining 'sharp' lines matched an orthorhombic lattice of similar dimensions to ramsdellite.

The question here is whether the model proposed by de Wolff could be applied to EMD. A cursory inspection of figure 2-1 compared with the diffraction pattern of de Wolff's $\gamma$-$MnO_2$ (see table 1 in reference 48) indicates no obvious relation apart from those lines associated with the approximately h.c.p. $O^{2-}$ framework which appears common to nearly all forms of $MnO_2$ ($\lambda$-$MnO_2$ being the obvious exception with a c.c.p. $O^{2-}$ lattice). Only six lines (counting peak F) are present in EMD in the region 0-70 °2$\theta$ compared to 15 in the specimen of $\gamma$-$MnO_2$ used by de Wolff. The situation is not lost however.

### 2.3.1 The series $\gamma$-$MnO_2$ to $\gamma_t$-$MnO_2$.

De Wolff's model is a structural intergrowth between ramsdellite and pyrolusite[†]. The basis of the model is that both minerals contain well defined structural units which can plausibly be introduced into one another without any major distortions of either crystal lattice. A continuous series of intergrowth crystals therefore ought to exist from ramsdellite to pyrolusite. Such a series indeed seems to exist, as is shown by heat treatment experiments[57] on $\gamma$-$MnO_2$. For EMD, however, another series exists the end members of which are neither ramsdellite or pyrolusite. This series is known to exist because of the variation of x-ray diffraction pattern with the conditions of deposition of the manganese dioxide. The usual process of EMD production is by anodic oxidation of manganese ions from an acidic manganous sulphate bath at elevated temperature[51] (90-95°C). Depending on the current density of deposition it is known that a range of manganese dioxides is produced[51]. At low current densities a 'high structured' EMD is formed while at higher current densities a 'lower structured' EMD is formed which has the typical six lines of commercial EMD (i.e. similar to that of figure 2-1). Intermediate current densities produce intermediate structured products. The author is

---

[†] See however section 1.1.4 as to why such a statement should not be taken as definitive.

fortunate† to have materials representative of this phenomena produced by the Suspension Bath Process[51] (SBP). This process enables higher current densities to be used with titanium electrodes which would otherwise be sensitive to passivation. It consists of adding particles of $MnO_2$ (or even lower oxides) in the form of a neutral suspension to the suspension bath. The results have been explained on the basis of absorbtion of these particles on the surface of the deposition electrode increasing its active surface and therefore lowering the effective current density of deposition. Figure 2-4 shows four materials all produced under the same conditions except that different concentrations of suspended particles (expressed in $mgl^{-1}$) were introduced. Figure 2-4 (a) has the highest concentration of suspended particles and thus was produced by the lowest effective current density of deposition. The powder x-ray diffraction pattern strongly resembles the mineral nsutite, and has many more lines than the material of figure 2-1. Figure 2-4(d) has the lowest concentration of suspended particles and therefore according to the theory the highest effective current density of deposition. Its pattern looks similar to that of figure 2-1 except for the stronger line at 28.4°2θ. As has been mentioned already this is believed to be a $\beta$-$MnO_2$ impurity produced by a chemical (rather than electrochemical) reaction in the deposition bath. The break up of peak A into two separate peaks is also observed as a difference between figures 2-1 and 2-4. The x-ray diffraction pattern of EMD with no added particles is of course that of figure 2-1.

To summarise, it appears that a continuous series of related x-ray diffraction patterns are produced from a pattern resembling the mineral nsutite at low current densities, to that of the conventional six peak pattern of commercial EMD formed at higher current densities.

Giovanoli[2] has considered that while ramsdellite and pyrolusite are the true end members of the $\gamma$-$MnO_2$ group increasing crystalline disorder of $\gamma$-$MnO_2$ leads to another series between $\gamma$-$MnO_2$ and $\varepsilon$-$MnO_2$. This is the series exemplified in figure 2-4. $\varepsilon$-$MnO_2$ is then a pseudo end-member of the $\gamma$-$MnO_2$ group. It is however meant to be disorder of the crystal structure not just the results of small crystallites. As Giovanoli states "the disorder is such that the space group alters from the diaspore type to NiAs type." It shall become clear in the following discussion that this definition is not adequate and, for reasons which shall become clear, the terminology adopted here

---

† Kindly donated by E.Preisler.

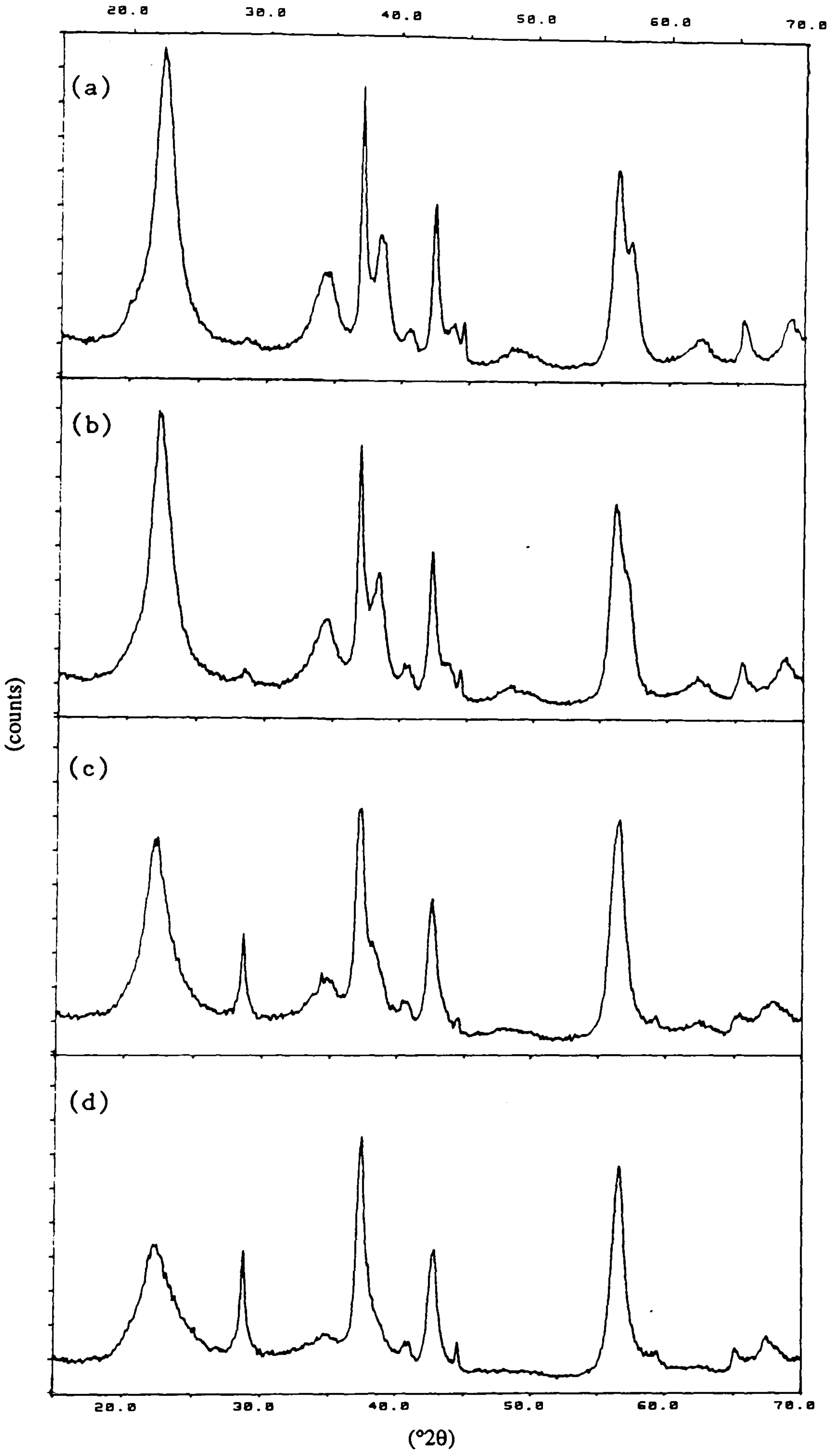

Figure 2-4 Effect on x-ray diffraction pattern of increasing effective current density of deposition for SBP-EMD. (a) 1000, (b) 500, (c) 200, (d) 100 ($mgl^{-1}$) all at 120 ($Am^{-2}$) 'geometrical' current density.

is of a structural series extending from $\gamma$-$MnO_2$ to $\gamma_t$-$MnO_2$.

In this study five materials were chosen which represent the range of structures found in the commercially available synthetic manganese dioxides for primary batteries[52]. It is of interest to see whether these materials are members of the series $\gamma$-$MnO_2$ to $\gamma_t$-$MnO_2$. Figure 2-5 displays the x-ray diffraction patterns of these materials. Two are CMDs (Chemical Manganese Dioxide) (b) and (d) and two are EMDs (a) and (c) (the fifth material is the SBP-EMD of figure 2-4 (a), labelled SBPA). From the appearance of these patterns it is clear that (a),(b) and (c) fit into the above mentioned series while (d) is distinctly different. The pattern of (d), however, can be reproduced exactly by heat treatment of (c) for one day at 300°C in air[53]. Faradiser M therefore does not represent an unknown structure of $MnO_2$ provided an explanation for (c) can be found.

For the moment the following question shall be addressed: given that EMD deposited at low effective current density of deposition possesses more x-ray diffraction lines, or is more 'structured', does it in fact fit the intergrowth model proposed by de Wolff?

### 2.3.2 Does SBP-EMD fit the intergrowth model of de Wolff?

Firstly a short description of the model shall be given with the aid of figure 2-6 (a reproduction of fig.2 from the original paper[48]). Figure 2-6 (a) which is a projection on the (001) plane shows a simplified ramsdellite structure together with a pyrolusite layer type (cf. figure 1-3). The double chains of $MnO_2$ octahedra extend in the c direction and share opposite edges with their neighbours. Between chains only the corners of the octahedra are shared. Similarly single chains of $MnO_2$ octahedra distinguish pyrolusite. The diagram is simplified because the oxygen frameworks of pyrolusite and ramsdellite are not strictly the same (compare figure 1-1 (a) and figure 1-2 (a)), nor are they perfect octahedra as shown in the figure. Perfect octahedra are formed if the oxygen (or strictly speaking the $O^{2-}$) framework is h.c.p. (or just hexagonal).

The introduction of the pyrolusite type layer can be described as a local shortening of the b axis. Figure 2-6 (b) indicates that a transverse component is also introduced. This description works only if single layers occur in isolation and so the model (in this version) is valid only for small pyrolusite type layer concentrations. If p

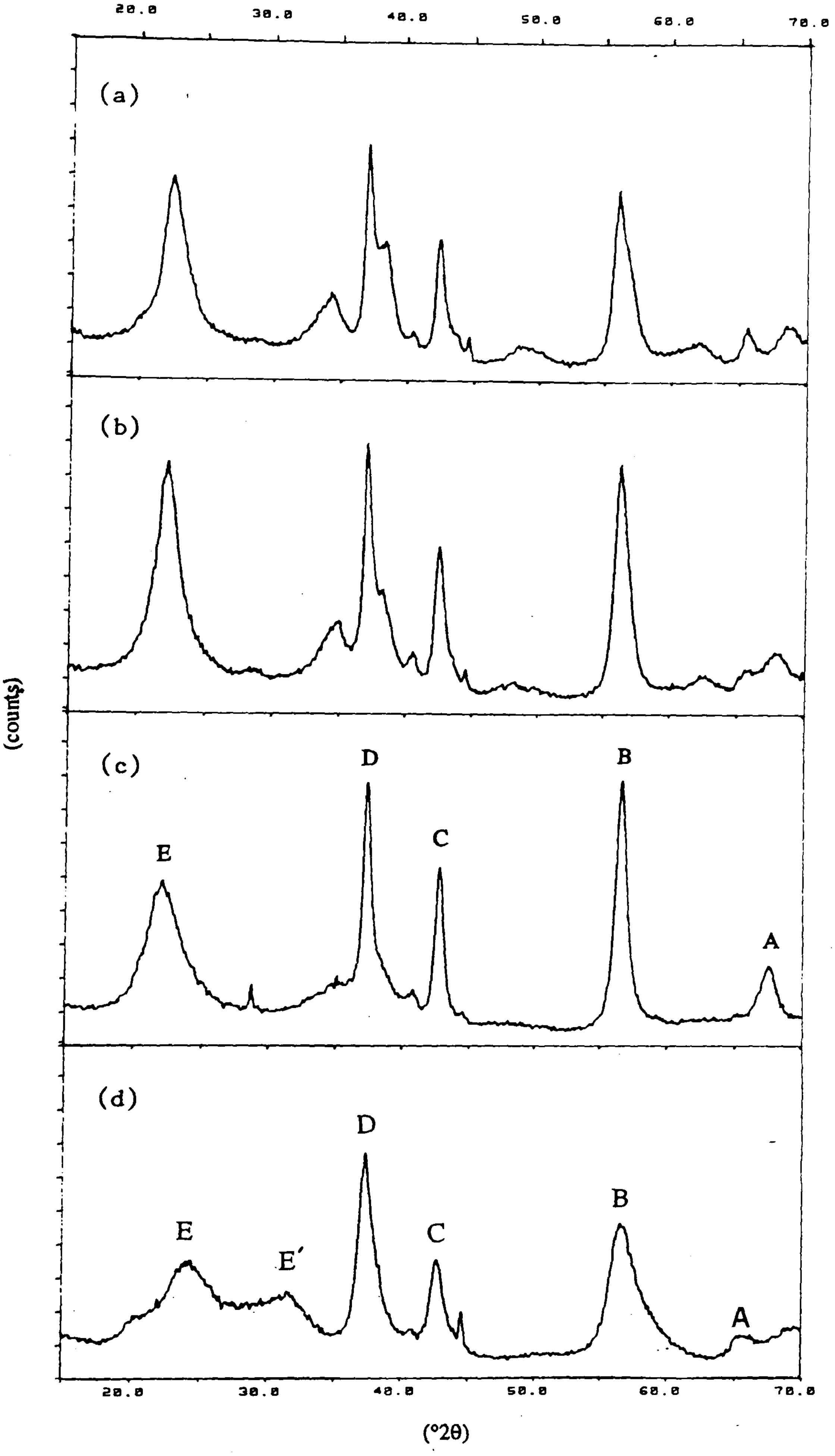

Figure 2-5 Powder x-ray diffractograms of materials used in this study. (a) Faradiser WSZ (b) IBA no.14 (c) IBA no.19 (d) Faradiser M. (a)-(c) apparently members of the structures series presented in figure 2-4. (d) similar to heat treatment of (c) at 300°C for 24 hrs. Peak labels of (d) are those suggested by a comparison with (c).

is the probability of a pyrolusite type layer, p=1 for pyrolusite and p=0 for ramsdellite. The model is thus reduced to a succession of two kinds of infinite layers having at the boundary a layer phase shift caused by the local shortening of the b axis. (There is also the question of the layer form factor but this is neglected in this simplified model which deals with the effect on the positions of lines rather than their intensities.)

The effect on the diffraction conditions is clearly indicated in figure 2-6 (c). This

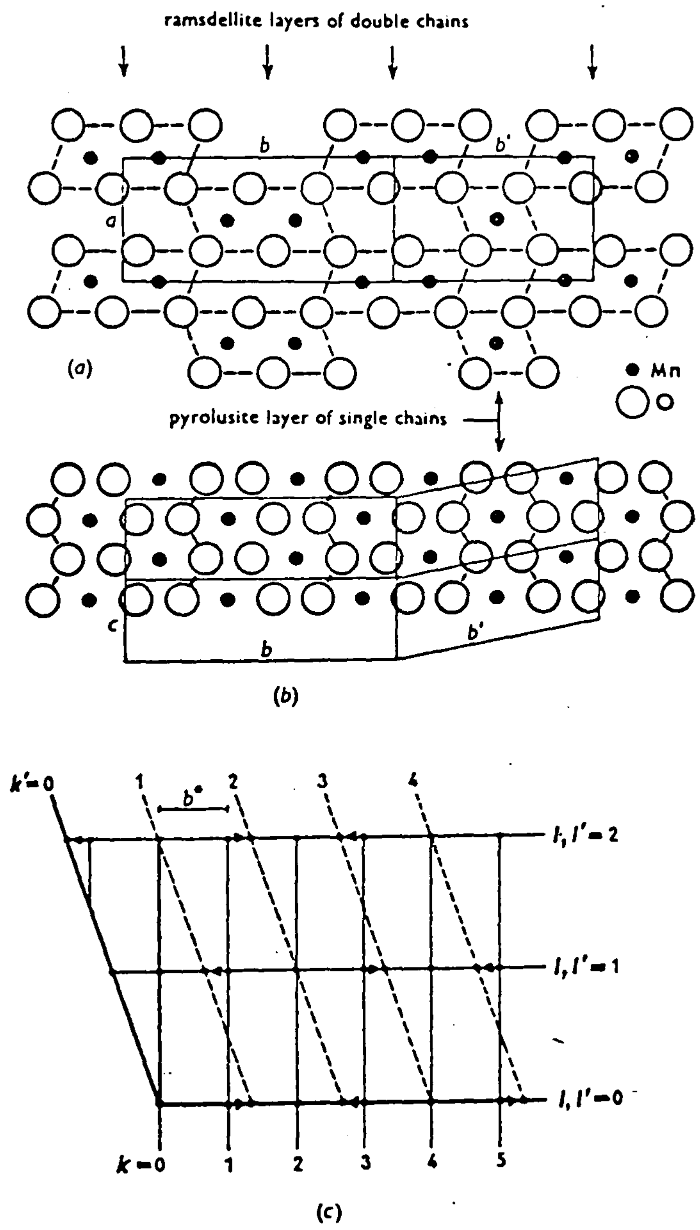

Figure 2-6 (reproduced from de Wolff[48] ) (a) Schematic drawing of part of the proposed random layer model for $\gamma$-$MnO_2$, viewed along c. (b) Same, viewed along a. (c) Section h = constant of the reciprocal lattice of this model. Lines with k = odd are shifted in the direction of the arrows.

diagram is of a section of the reciprocal lattice and can be constructed from the section of the 'real' lattice of figure 2-6 (b). Recalling the definition of the reciprocal lattice[54] "The point hkl in the reciprocal lattice representing the plane (hkl) in the real lattice lies on the normal from the origin to the plane, and at a distance ρ from the origin, where

$$\rho = \frac{k^2}{d_{(hkl)}} \tag{2.5}$$

, and k is a constant,..." . Here $k^2$ has been chosen such as to produce a convenient size for the diagram. Also $k^2$ for the two perpendicular directions in reciprocal space are not equal in order to exaggerate the displacement of the reciprocal lattice points (in fact $b^*=2.25/b$ and $c^*=1.25/c$). In the diagram the reciprocal lattice for ramsdellite ($a^*,b^*,c^*$) and the 100% fault lattice ($a^*,b^{*\prime},c^*$) are drawn in the same space. In general a reciprocal lattice point is shifted in the direction of the k axis towards its neighbouring point in the reciprocal fault lattice and the corresponding peak is shifted and broadened. Certain points coincide with fault lattice points and are therefore not shifted nor broadened. The precise conditions have been found by de Wolff to be the following. Those points with ($\frac{1}{2}k+l$) even in the reciprocal ramsdellite lattice are neither shifted nor broadened. Those with k odd are shifted by a constant amount in reciprocal space. The sign of the shift is given by the arrow in figure 2-6 (c) and results in either a higher or lower d spacing compared to the perfect ramsdellite lattice.

Returning now to the question posed at the beginning of this section a table similar to table 1 in de Wolff's paper was constructed for the sample labelled SBPA, table 2.4. The indices have been assigned to SBPA using de Wolff's table. Unambiguous indices for the 'sharp' lines are marked with a hash. These were used to calculate the lattice parameters a,b,c of an orthorhombic lattice similar to ramsdellite. This is achieved as follows: recalling that

$$\frac{1}{d^2} = \frac{h^2}{a^2} + \frac{k^2}{b^2} + \frac{l^2}{c^2} \tag{2.6}$$

is the equation for the d spacing of an orthorhombic unit cell, in order to find a,b and c a linear regression analysis can be performed. This is in preference to solving the equations simultaneously as in section 2.2 which may be unduly biased if one d spacing happens to have a large error. The independent variables are $h^2$, $k^2$, and $l^2$ and the dependent is $1/d^2$. The regression analysis was performed using a spreadsheet software package and provides† $1/a^2$, $1/b^2$ and $1/c^2$ which can be solved to obtain a,b and c. The results are a=4.427, b=9.32 and c=2.846. In this case it is convenient to represent d spacings by $q=10^4/d^2$ in which case from eqn.2.6

$$q_c=508.02h^2+115.07k^2+1234.56l^2 \qquad (2.7)$$

If $q_o$ represents the observed d spacing then $q_o - q_c$ is the shift from the orthorhombic lattice. The theoretical shift ($\Delta q$) now has to be worked out. This is computed from the constant shift in reciprocal space $r_f\underline{b}^*$ where $r_f$ is the fraction of the $b^*$ axis. Recalling that

$$\underline{b}.\underline{b}^* = 1 \Rightarrow |1/\underline{b}^2| = |\underline{b}^*|^2$$

and from equation 2.6

Table 2.4 Observed d and $q=10^4/d^2$ for pattern SBPA; calculated $q=q_c$ for indices hkl; observed $q_o$-$q_c$ and calculated $\Delta q$ shifts; *hkl* related to ramsdellite indices hkl.

| No | d | $q_o$ | $q_c$ | h | k | l | $q_o$-$q_c$ | $\Delta q$ $b^*/8$ |
|---|---|---|---|---|---|---|---|---|
| 1 | 3.956 | 639 | 623 | *1* | *1* | *0* | 16 | 31 |
| 2 | 2.606 | 1472 | 1544 | *1* | *3* | *0* | -72 | -85 |
| 3 | 2.421 | 1706 | 1695 | 0 | 2 | $1^{\#}$ | 11 | 0 |
| 4 | 2.338 | 1830 | 1858 | *1* | *1* | *1* | -28 | -27 |
| 5 | 2.218 | 2033 | 2032 | 2 | 0 | 0 | 1 | 0 |
| 6 | 2.127 | 2211 | 2203 | 1 | 2 | $1^{\#}$ | 8 | 0 |
| 7 | 2.064 | 2348 | 2349 | 1 | 4 | $0^{\#}$ | -1 | 0 |
| 8 | 1.861 | 2887 | 2778 | *1* | *3* | *1* | 109 | 88 |
| 9 | 1.635 | 3739 | 3727 | 2 | 2 | $1^{\#}$ | 12 | 0 |
| 10 | 1.610 | 3859 | 3873 | 2 | 4 | $0^{\#}$ | -14 | 0 |
| 11 | 1.491 | 4501 | 4619 | *1* | *5* | *1* | -118 | -142 |
| 12 | 1.424 | 4929 | 4938 | 0 | 0 | $2^{\#}$ | -9 | 0 |
| 13 | 1.363 | 5380 | 5377 | 0 | 6 | $1^{\#}$ | 3 | 0 |
| 14 | 1.337 | 5590 | 5561 | *1* | *1* | *2* | 29 | 31 |
| 15 | 1.303 | 5888 | 5885 | 1 | 6 | 1 | 3 | 0 |
| 16 | 1.303 | 5888 | 5907 | 1 | 2 | 2 | -19 | 0 |
| 17 | 1.251 | 6391 | 6482 | *1* | *3* | *2* | -91 | -85 |
| 18 | 1.214 | 6781 | 6779 | 0 | 4 | 2 | 2 | 0 |
| 19 | 1.198 | 6966 | 6970 | 2 | 0 | 2 | -4 | 0 |
| 20 | 1.164 | 7375 | 7409 | 2 | 6 | 1 | -34 | 0 |
| 21 | 1.065 | 8818 | 8811 | 2 | 4 | 2 | 7 | 0 |

---

† This method is directly analogous to the two dimensional problem of finding the best straight line through a set of points by the method of least squares.

$$q'_o = 10^4/d^2 = 10^4(h^2/a^2 + b_s^{*2} + l^2/c^2)$$

where $$|\underline{b}_s^*| = k|\underline{b}^*| \pm r_f|\underline{b}^*|$$

then $\Delta q = q_o' - q_c$ as before. Regarding $r_f$ as an adjustable parameter it was found that a shift of $b^*/8$ (see appendix A) gives an approximate fit to the observed $q_o - q_c$ (see table 2.4). Appendix A contains a method for finding $r_f$ based on optimisation of a function which reflects the closeness of the observed to the calculated shifts. Note the considerable error for those values which theory predicts to be zero. The worst is -34 for peak 20. This however occurs high up in the °2θ range (88°2θ in CuKα radiation) where the peaks are very weak and overlapped and the assigned indices in doubt. The weakness of the peaks could be due to additional crystallite broadening compared to de Wolff's material.

The shift fraction is less than de Wolff's ($b^*/8$ compared to $b^*/7$). From de Wolff the shift fraction in reciprocal space is related to the pyrolusite concentration by equation 2.8.

$$(1-2p)\sin r_f.2\pi - 2p\cos r_f.3^2\pi = 0 \tag{2.8}$$

which implies with $r_f$=1/7 that p=0.25 and with $r_f$=1/8 p=0.23. It is better to compute a p fraction for each instance of a diffraction pattern measured rather than to average the d spacings of a number of patterns and then determine p. This is because p depends on relative line shifts and thus to a good approximation, its determination is unaffected by specimen height displacement (the main source of error in diffractometer line position measurements, see chapter 3, section 3.5). An average p=0.20±0.005 has been determined from four measures of the diffraction pattern for sample SBPA (see appendix A).

The answer to the question posed at the beginning of this section 2.3.2 is that SBPA does fit the de Wolff model for γ-$MnO_2$. A shift in reciprocal space corresponding to p=0.20 accounts for the broadened peaks. Only one peak is missing from those listed by de Wolff down to d=1.06(Å). Other peaks beyond this exist and could be used to check further the above statement.

This conclusion accords with recent important work on the same subject[44]. These authors used single crystal electron diffraction to confirm 'directly' the ramsdellite pyrolusite intergrowth model for various samples of EMD & CMD. This conclusion reversed some of their earlier structure determinations[55] using the same technique which favoured a hexagonal structure. Their statements in general need to be qualified and one in particular rejected.

The two laboratory made EMDs, EMD1 and EMD2, on which single crystal electron diffraction patterns were observed, were both deposited in conditions which " correspond to those reported for the deposition of "$\varepsilon$-$MnO_2$" ". The most notable difference is the use of a chloride bath, which is known to produce fibrous[56] EMD. The number of lines for these two EMDs is reported as 11 in the case of EMD1 (deposited at higher current density than EMD2) and 18 in the case of EMD2. It is not known over what range of °2$\theta$ (CuK$\alpha$ radiation) that this information refers to. It seems clear, however, that these materials must correspond to the low effective current density region of the series indicated in figure 2-4. The fraction of pyrolusite domains p=0.10 - 0.18 for EMD2 corresponds to a (0.04 - 0.09)$b^*$ shift in reciprocal space. In the case of EMD1, however, the shift in reciprocal space of $b^*/3$ does not correspond to p=0.5 (via equation (2.8)) as stated. This is because the model does not apply in this region. In order for the model to apply there must be a prevailing lattice (either ramsdellite or pyrolusite) where faults, in the form of b', can be introduced. In the case of equal fractions of pyrolusite and ramsdellite domains it is clear that this description no longer applies. There is no longer two kinds of translations but many others. For example a translation corresponding to a succession of two or more pyrolusite type layers. All these possibilities would need to be considered. In the case of low p, however, one can assume that isolated layers of pyrolusite occur and the description in terms of randomly alternating b and b' translations is valid. De Wolff attempts to illustrate this point by considering the consequences of the model for pyrolusite concentrations approaching p=0.5. ".....the simplified model is indeed only an approximation. If it were exact, larger pyrolusite concentrations than that of pattern D (p=0.25) would yield patterns converging to that of an ab'c-lattice (for which p=0.5), with the shifted lines gradually sharpening to normal powder lines." In other words it is imagined that because of the large frequency of pyrolusite type layers, on average, only one type of lattice exists (namely the ab'c-lattice) and all the powder lines are normal i.e. sharp.

Because of the above, the findings of Strobel *et al.* can be questioned. EMD1 is <u>not</u> fully compatible with the de Wolff model as stated. Similarly it follows that neither is ICS2, an IBA common sample with an x-ray diffraction pattern similar to figure 2-1, or CMD9 a home made CMD. The results for EMD2 remain valid however.

The restriction that the simplified model introduced by de Wolff did not apply at higher p concentrations was removed in a following paper with Laudy[57]. In the authors opinion this paper has been overlooked to a substantial extent especially considering its wider application compared to the original paper. In order to distinguish the models the following abbreviations shall be used. SdWIM ≡ Simplified de Wolff Intergrowth Model; GdWIM ≡ Generalised de Wolff Intergrowth Model.

### 2.3.3 The Generalised de Wolff Intergrowth Model (GdWIM).

In this section the GdWIM shall be briefly described. It succeeds in removing the restriction of the SdWIM model to low values of p only. This means that the restriction that a pyrolusite type layer must follow a ramsdellite type layer (or vice versa) is removed. The succession of the two types of layers is random (but with important built in restrictions, see section 2.4.3).

The GdWIM is described fully in the paper but it is important for the following sections to state again the approximations it requires. A formula for the scattered intensity I for an infinite random succession of the two types of layers ramsdellite and pyrolusite described by the single parameter p (fraction of pyrolusite type layers) was sought. The approximations are as follows:

a) The diaspore structure $O^{2-}$ framework in ramsdellite and the (very nearly, see section 1.1.1) p.t.p. $O^{2-}$ lattice in pyrolusite do not fit ideally in a possible layer intergrowth of the two. This also applies to the metal ions. Such differences are neglected and the coordinates in each layer are imagined to be uninfluenced by surrounding layers.

b) the sequence of pyrolusite (P) and ramsdellite layers (R) is random.

c) The contribution of the $O^{2-}$ lattice is neglected.

d) The fractional coordinate x of a Mn atom in the ramsdellite layer is set to zero. $x=0.022$ (with respect to the ramsdellite unit cell) in the mineral, note that x necessarily would be zero if the oxygens were h.c.p. (see figure 1-2).

The formula found by Laudy and de Wolff[57] describes all the main features of their $\gamma$-$MnO_2$. This material strongly resembles, in its x-ray diffraction pattern, figure 2-4 (a) that of SBPA which has been shown to fit the SdWIM. $p=0.30$ in their case compared with an average $p=0.20\pm0.005$ for SBPA. Increasing p in the GdWIM produces changes in the calculated pattern which are qualitatively similar to the effects of heat treating the actual material[57]. $p=1$ corresponds to pyrolusite, which was also the final product obtained by heat treatment (the temperature was 490°C for the final product, beyond this transformation into $Mn_2O_3$ occured) though the pattern obtained was observed to be still somewhat broadened compared to mineral samples.

It is clear that the GdWIM accounts for the series $\gamma$-$MnO_2$ to $\beta$-$MnO_2$ when the $\gamma$-$MnO_2$ is described by the SdWIM. The next question that presents itself is whether any modification of the GdWIM could account for the series $\gamma$-$MnO_2$ to $\gamma_t$-$MnO_2$ as described in section 2.3.1.

## 2.4 Extending the GdWIM.

An extension of the of the GdWIM is proposed here which could plausibly explain the series $\gamma$-$MnO_2$ to $\gamma_t$-$MnO_2$. It is based on the findings of Turner and Busek[58] who used high-resolution microscopy (HRTEM) to examine specimens of nsutite.

Orientated grains of nsutite were imaged and found to consist mainly of a random layer structure with layer dimensions consistent with that of a ramsdellite pyrolusite intergrowth structure. A few grains, however, contained layers with dimensions consistent with three [$MnO_6$] octahedra forming chains in the c direction as before. The structure consisting solely of layers of triple octahedra has not been discovered and thus has no analogue to ramsdellite or pyrolusite layers. The effect of this defect in such small concentrations on the x-ray diffraction pattern of nsutite must be small since nsutite is adequately described by the GdWIM, but it seems at least possible that an increasing concentration of this hitherto unknown defect may be responsible for the diffraction patterns $\gamma$-$MnO_2$ to $\gamma_t$-$MnO_2$. Introduction of another layer would further disrupt the phase relations between neighbouring layers leading in general to further broadening and extinction of x-ray peaks.

### 2.4.1 Predicting the effects on the x-ray diffraction pattern of triple octahedral layers.

An exactly similar treatment to that originally proposed in the SdWIM (section 2.3.2) can be applied to the extension of the GdWIM for the case of defects of triple octahedral layers. In other words if q is the probability of a triple octahedral layer then the diffraction effects for the case of low q concentration in an otherwise perfect ramsdellite matrix can be demonstrated by consideration of the ramsdellite reciprocal lattice and the 100% faulted lattice ($a^*, b^{*''}, c^*$). In this case $\underline{b}''$ is now a local lengthening of the b axis to 5/4 of its normal length. The transverse component in this case is

$$\underline{b}'' = \frac{5}{4}\underline{b} + \frac{1}{2}\underline{c} \tag{2.9}$$

Sharp reflections are predicted for b/4 +1/4 = 0,1,2,3,4... or k/2 + 1/2 even which can be deduced from drawing the reciprocal lattice for ramsdellite and the completely faulted lattice on one another as in figure 2(c) (figure 2-6, this work) of de Wolff's paper. Further detailed consideration of this proposal is unnecessary as from the above it is predicted that lines (140) and (240) remain sharp and unshifted with increasing concentration of q or p (since they are the only lines in the $\gamma$-$MnO_2$ pattern with both k/2+1 and k/2+1/2 even). This however is at odds with the observed diffractograms which indicate either a shift or a shift and broadening of both lines (see figure 2-12) when traversing the $\gamma$-$\gamma_t$-$MnO_2$ series.

Although there is no experimental evidence to justify introducing larger layers in the b direction of four times (or greater) a pyrolusite type layer it appears worth pursuing this notion given that triple octahedral layers do at least broaden and shift the remaining lines of $\gamma$-$MnO_2$ including the remaining sharp lines. The suggestion that the $\gamma_t$-$MnO_2$ may contain layers of greater dimensions has been made by Burns[59].

Consideration of the resulting diffraction effects of many simultaneous defects in the way contemplated for pyrolusite layers or triple octahedral layers (i.e. by means of the reciprocal space lattice) would become increasingly complex and impracticable. A better approach is to calculate directly the diffraction pattern resulting from a random sequence of layers of unlimited variety of width concentration and layer form factor. The layer form factor is an entity introduced to enable such a description to be meaningful. It represents the scattering power of a layer and is analogous to the atomic form factor for an atom (as used in equation (2.3)). Layer form factors are calculable by summing up the contribution of atoms in a layer repeating unit. The problem of calculating the diffracted intensity from a random layer crystal thus reduces to summing up the layer form factors characteristic of each layer taking into account their phases which in this case bear a constant relation to adjacent layers.

If the radiation scattered from a mixture of r *kinds* of layers in a crystal of n layers is considered then the scattering from the k^th layer may be represented as $\underline{V}^{(r)}e^{ik\theta}$

where $\underline{V}^{(r)}$ is the scattering vector of the $r^{th}$ layer the magnitude of which is equal to the layer form factor. $e^{ik\theta}$ contains the phase shift between layers and is normally determined by the magnitude of the vector connecting neighbouring layers. An equation for the case outlined (and other variations) was found by Hendricks and Teller[60]. The GdWIM represents one particular case of these more general equations. Originally the author attempted a similar treatment by adapting the H&T (Hendricks and Teller) equations to the hypothetical $MnO_2$ crystal containing random layers of integral widths of $[MnO_6]$ octahedra. A more convenient and flexible method however has recently been discovered. A short digression on this method is presented in the next section.

### 2.4.2 Computation of the diffraction pattern of $\gamma$-$MnO_2$.

In this section a method for computing the diffraction pattern of $\gamma$-$MnO_2$, which as before, is best represented by the pattern of SBPA (figure 2-4(a)) is presented. It relies on a program which has become available to calculate the diffraction patterns of random layer crystals. The program makes use of the algorithm described in a paper by Treacy Newsam and Deem[61] titled "A General Recursion Method for Calculating Diffracted Intensities From Crystals Containing Planar Faults". The FORTRAN version obtained[†] here was successfully run on a Vax mainframe computer[‡]. Great care is required when specifying input for this program (see appendix B).

Consider figure 2-7(a) which is analogous to figure 2-6(a). Here the $\gamma$-$MnO_2$ crystal is imagined to be composed of four types of layers designated R and R' (ramsdellite type layers) and P and P' (pyrolusite type layers). The oxygen lattice in this case is imagined to be ideally h.c.p. The projection is on (001) as in figure 2-6(a). Figure 2-7(a) represents a possible sequence of the four types of layers consistent with the GdWIM described in section 2.3.3. The reduction of this description to a model containing only two types of layers is possible because of condition (c) in the GdWIM, which states that the contribution of the oxygen lattice is ignored. This means that the layers RR' and PP' are related by unit cell translations and thus are equivalent.

The case of an RR' translation is illustrated in figure 2-7(c). If the origin of an R layer is considered to be on a Mn atom then the translation (indicated by the dotted

---

[†] I am grateful to Dr J.Pannetier for bringing this program to my attention.

[‡] Located at Middlesex University Computing Centre.

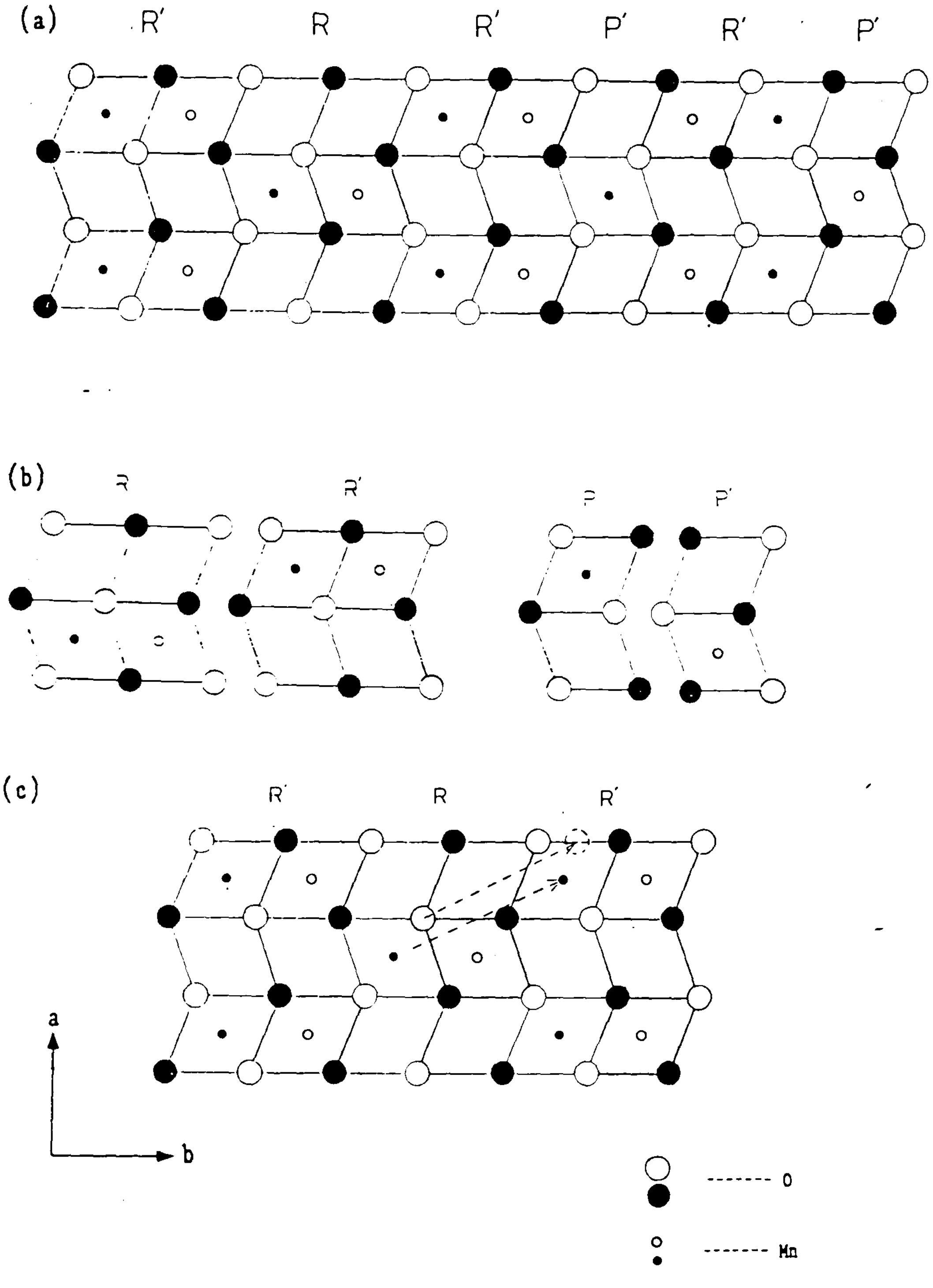

Figure 2-7 (a) projection on (001) of idealised ramsdellite pyrolusite intergrowth structure showing possible sequence of RR'PP' layers. (b) atoms considered for layer form factors (c) representation of why R and R' are not related by a translation unless oxygens atoms are neglected. Open and filled circles indicate z-levels of 0 and ½ respectively.

line) connects this atom with the origin of an R' layer. Applying the same translation to an oxygen atom in the R' layer however does not translate to an equivalent oxygen atom in the R' layer (as indicated again by the dotted line). Thus R and R' are *not* connected by a translation unless the oxygen framework is ignored. Obviously neglect of the oxygen framework in the GdWIM meant that the greatest error in the computed patterns occurred for those lines heavily contributed by oxygen. Since it appears that the related lines are prominent in EMD this approximation is no longer appropriate for testing modifications to the model and therefore the oxygen lattice must be included.

### 2.4.3 Including the oxygen framework.

The crystal now needs to be considered as a random sequence of the four layers RR'PP'. In this notation RR'RR'..... represents ramsdellite and PP'PP'..... pyrolusite. The sequence of layers is arbitrary apart from the following conditions on the next layer.

If R then R' or P ; If R' then R or P'
If P then P' or P'; If P' then P'or R'

Combinations such as RR are disallowed. One can see why this is by examining figure 2-7(b). This indicates the atoms chosen to represent layers RR'PP' which are the atoms required to calculate the layer form factors. It should be noted that the composition of a R or R' layer is $Mn_2O_4$ and that of a P or P' layer $MnO_2$ since for example atoms at the corners of the layer repeating units are shared by four such units. Extending any of these repeating units in the a and c direction produces the corresponding layer. Combination of these layers in the b direction then produces the entire crystal. However the combination such as RR will not correspond to the ramsdellite pyrolusite intergrowth model. Similarly RP' for example would be disallowed whereas RP is allowed. It might be thought that PR is also disallowed since adjacent manganese across the layer boundary are not at the same level of c and thus corresponding octahedra would not share corners as is required by the model. This however is dealt with in the connections between layers which specify a translation vector between the origins of the given layers. Thus the translation vector joining PR has a component in the c direction of -½c, which in effect converts a 'black atom' into a 'white atom' (and vice versa) in figure 2-7(b).

The computed pattern with the orthorhombic lattice parameters and p value determined in section 2.3.2 for sample SBPA is presented in figure 2-8. It should be

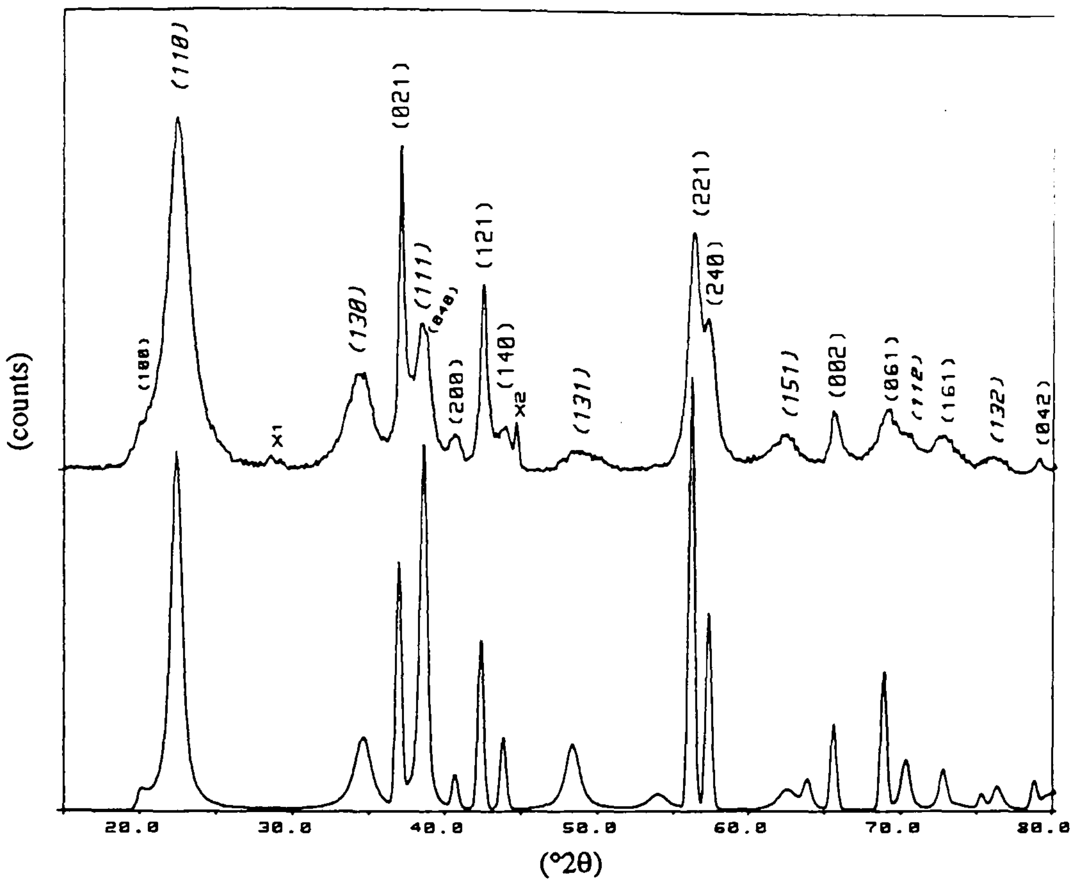

Figure 2-8 Comparison of calculated (according to the GdWIM) and observed $\gamma$-$MnO_2$ x-ray diffraction patterns with p=0.20. Orthorhombic indices are indicated. (hkl) marks the unshifted 'sharp' lines and (*hkl*) marks lines related to (hkl) but broadened and shifted.

noted that adopting these lattice parameters means that the oxygen lattice is not perfectly h.c.p. as previously supposed. This is because the ratios of the orthorhombic lattice parameters are fixed by a h.c.p. oxygen lattice. The relationship between hexagonal and orthorhombic parameters is easily deduced to be

$$a_o = c_{hex}$$

$$b_o = 2\sqrt{3}a_{hex}$$

$$c_o = a_{hex}$$

which implies that $b_o/c_o=2\sqrt{3}\approx 3.464$ whereas the actual ratio of $b_o/c_o$ for SBPA is 3.281.

The background has been stripped from the pattern of figure 2-8(a) and the pattern displaced vertically relative to the calculated pattern in order to facilitate comparison. All the features of the actual pattern (excepting the weak maxima labelled X1 and X2 due to $\beta$-$MnO_2$ and the Al sample holder) contain peaks in the calculated pattern. However, the relative intensity, exact positions of the broad peaks and number of diffraction maxima are not precisely duplicated. In view of the approximations the model contains, however, the correspondence seems reasonable.

The difference in relative intensity between observed and calculated patterns is

Table 2.5 Calculated ramsdellite pattern using Byström's fractional coords. and those derived from an h.c.p. O lattice plus effect on the calculation of replacing $f_{O2-}$ with $f_{O1-}$.

| A<br>no. | B<br>h | C<br>k | D<br>l | E<br>2θ<br>(°2θ) | F<br>d spac.<br>(Å) | G<br>p | H<br>int.<br>Bystr. | I<br>int.<br>h.c.p. | J<br>diff.<br>H-I | K<br>int.<br>$f_{O1-}$ | L<br>diff.<br>I-K |
|---|---|---|---|---|---|---|---|---|---|---|---|
| 1 | 1 | 0 | 0 | 19.991 | 4.4414 | 2 | 0 | 0 | 0 | 0 | 0 |
| 2 | 1 | 1 | 0 | 22.165 | 4.0105 | 4 | 100 | 100 | 0 | 100 | 0 |
| 3 | 1 | 2 | 0 | 27.726 | 3.2174 | 4 | 3.2 | 0 | 3.2 | 0 | 0 |
| 4 | 1 | 3 | 0 | 35.216 | 2.5484 | 4 | 38.1 | 32 | 6.1 | 32 | 0 |
| 5 | 0 | 2 | 1 | 36.949 | 2.4328 | 4 | 28.7 | 27.6 | 1.1 | 26.4 | 1.2 |
| 6 | 1 | 0 | 1 | 37.488 | 2.399 | 4 | 0.5 | 0 | 0.5 | 0 | 0 |
| 7 | 1 | 1 | 1 | 38.755 | 2.3235 | 8 | 28.7 | 49.2 | -20.5 | 49.2 | 0 |
| 8 | 0 | 4 | 0 | 38.578 | 2.3337 | 2 | 5.8 | 12.4 | -6.6 | 11.9 | 0.5 |
| 9 | 2 | 0 | 0 | 40.625 | 2.2207 | 2 | 5.7 | 3.8 | 1.9 | 3.3 | 0.5 |
| 10 | 2 | 1 | 0 | 41.811 | 2.1604 | 4 | 0 | 0 | 0 | 0 | 0 |
| 11 | 1 | 2 | 1 | 42.361 | 2.1336 | 8 | 16.5 | 18.5 | -2 | 20.5 | -2 |
| 12 | 1 | 4 | 0 | 43.821 | 2.0659 | 4 | 2.7 | 8.1 | -5.4 | 9 | -0.9 |
| 13 | 2 | 2 | 0 | 45.217 | 2.0053 | 4 | 1.3 | 0 | 1.3 | 0 | 0 |
| 14 | 1 | 3 | 1 | 47.878 | 1.8999 | 8 | 17.3 | 26.4 | -9.1 | 26.4 | 0 |
| 15 | 2 | 3 | 0 | 50.489 | 1.8076 | 4 | 3.4 | 0 | 3.4 | 0 | 0 |
| 16 | 0 | 4 | 1 | 50.543 | 1.8058 | 4 | 1.8 | 0 | 1.8 | 0 | 0 |
| 17 | 2 | 1 | 1 | 53.196 | 1.7218 | 8 | 0.3 | 0 | 0.3 | 0 | 0 |
| 18 | 1 | 5 | 0 | 53.219 | 1.7211 | 4 | 1.5 | 9.5 | -8 | 9.5 | 0 |
| 19 | 1 | 4 | 1 | 54.884 | 1.6728 | 8 | 0.4 | 0 | 0.4 | 0 | 0 |
| 20 | 2 | 2 | 1 | 56.071 | 1.6401 | 8 | 31.6 | 49.7 | -18.1 | 51.1 | -1.4 |
| 21 | 2 | 4 | 0 | 57.266 | 1.6087 | 4 | 17.3 | 23.1 | -5.8 | 23.8 | -0.7 |
| 22 | 0 | 6 | 0 | 59.405 | 1.5558 | 2 | 0.7 | 0 | 0.7 | 0 | 0 |
| 23 | 2 | 3 | 1 | 60.663 | 1.5265 | 8 | 3.6 | 0 | 3.6 | 0 | 0 |
| 24 | 3 | 1 | 0 | 63.636 | 1.4622 | 4 | 1.5 | 5.3 | -3.8 | 5.3 | 0 |
| 25 | 1 | 6 | 0 | 63.339 | 1.4683 | 4 | 0.1 | 0 | 0.1 | 0 | 0 |
| 26 | 1 | 5 | 1 | 63.097 | 1.4734 | 8 | 19.5 | 11 | 8.5 | 11 | 0 |
| 27 | 3 | 2 | 0 | 66.224 | 1.4112 | 4 | 0.9 | 0 | 0.9 | 0 | 0 |
| 28 | 2 | 5 | 0 | 65.292 | 1.429 | 4 | 0.7 | 0 | 0.7 | 0 | 0 |
| 29 | 0 | 0 | 2 | 65.486 | 1.4253 | 2 | 8.7 | 10.3 | -1.6 | 10.8 | -0.5 |
| 30 | 2 | 4 | 1 | 66.767 | 1.401 | 8 | 0.5 | 0 | 0.5 | 0 | 0 |
| 31 | 0 | 2 | 2 | 68.878 | 1.3631 | 4 | 0.1 | 0 | 0.1 | 0 | 0 |
| 32 | 0 | 6 | 1 | 68.735 | 1.3656 | 4 | 11.9 | 17.3 | -5.4 | 18.2 | -0.9 |
| 33 | 3 | 3 | 0 | 70.431 | 1.3369 | 4 | 4 | 3.8 | 0.2 | 3.8 | 0 |
| 34 | 1 | 1 | 2 | 70.061 | 1.343 | 8 | 6.8 | 7.8 | -1 | 7.8 | 0 |
| 35 | 3 | 0 | 1 | 71.853 | 1.3138 | 8 | 3.8 | 0 | 3.8 | 0 | 0 |
| 36 | 3 | 1 | 1 | 72.674 | 1.301 | 8 | 10.2 | 6.9 | 3.3 | 6.9 | 0 |
| 37 | 1 | 2 | 2 | 72.536 | 1.3032 | 8 | 0.3 | 0 | 0.3 | 0 | 0 |
| 38 | 1 | 6 | 1 | 72.396 | 1.3053 | 8 | 0.2 | 0 | 0.2 | 0 | 0 |
| 39 | 3 | 2 | 1 | 75.115 | 1.2647 | 8 | 0.1 | 1.7 | -1.6 | 2 | -0.3 |
| 40 | 2 | 5 | 1 | 74.233 | 1.2775 | 8 | 0 | 0 | 0 | 0 | 0 |
| 41 | 2 | 6 | 0 | 74.458 | 1.2742 | 4 | 0.8 | 0 | 0.8 | 0 | 0 |
| 42 | 1 | 7 | 0 | 74.253 | 1.2772 | 4 | 4 | 3.2 | 0.8 | 3.2 | 0 |
| 43 | 3 | 4 | 0 | 76.145 | 1.2501 | 4 | 0.3 | 0.8 | -0.5 | 0.9 | -0.1 |
| 44 | 1 | 3 | 2 | 76.59 | 1.244 | 8 | 6.9 | 5.9 | 1 | 5.9 | 0 |
| 45 | 3 | 3 | 1 | 79.124 | 1.2104 | 8 | 1.4 | 5.4 | -4 | 5.4 | 0 |
| 46 | 0 | 4 | 2 | 78.658 | 1.2164 | 4 | 2 | 3.4 | -1.4 | 3.3 | 0.1 |

most likely due to the approximation of adopting fractional coordinates derived from a h.c.p. oxygen lattice. That this may be so is indicated in table 2.5 which shows the calculation of the relative integrated intensities (using the structure factor as in section 2.2) of ramsdellite using the coordinates found by Byström[49] and those determined from the idealised h.c.p. oxygen framework. The most striking differences are for peaks (111) and (221). Furthermore it is (111) and (221) (and (140) which appears as a shoulder on the (111) peak in the actual pattern but as a combined single peak in the calculated pattern) which are larger in the idealised ramsdellite case. Thus adoption of coordinates approaching that of ramsdellite would lower the intensities of (111) and (221) as required to produce a better match in figure 2-8. It should be noted that the oxygen lattice cannot have the same fractional coordinates as that of ramsdellite since this produces peaks which are otherwise absent in an intergrowth structure as shown in table 2.5. It suggests rather that a small distortion from the h.c.p. could provide a way of optimising the calculation to produce a better match. Since typical commercial EMD displays apparent hexagonal symmetry (neglecting (110)) it may be advantageous not to carry out such an optimisation if modification of the de Wolff model is to explain this x-ray diffraction pattern and so further refinement was not pursued.

Another possible source of error in the computed patterns was the adoption of the form factor for $O^{1-}$ rather than $O^{2-}$. This is because the data DIFFaX draws upon[62] contains no values for $O^{2-}$. That the error introduced is small (less than 1.5%) is demonstrated in table 2.5 columns K and L. It is interesting to note that many of the peaks are unaffected by this change indicating that they are heavily contributed by Mn (alternatively it provides an indication of those peaks dominated by oxygen).

Table 2.5 explains the origin of the small peak at 53.2°2θ in the calculated pattern which is now seen to be an enhanced (150) peak. The table also corroborates the implication of figure 2-12 that many peaks assigned single indices (following de Wolff) above sixty °2θ are actually combinations of other small peaks. Finally it should be noted that (100) has a calculated intensity of zero in both ramsdellite calculations and nevertheless appears in the calculated random intergrowth structure and in the actual x-ray diffraction pattern (although it is only just discernable in the actual pattern).

Discrepancies in the positions of the broad lines are of course related to the correct determination of the value of p for the structure which further refinement of p could reduce. The value of p determined in section (2.3.2) was used to generate the pattern in figure 2-8(b).

Finally to conclude this section a visual demonstration of the fact that increasing p does not reproduce the structural series presented in figure 2-4 but rather the $\gamma$-$MnO_2$ series is demonstrated in figure 2-9. This figure contains a sample of computed x-ray diffraction patterns from the infinite range (i.e. from p=0.0 - p=1.0) defined as $\gamma$-$MnO_2$. The lattice parameters used for ramsdellite (p=0.0) were those from Byström[49] (see also JCPDS card 39-375) and those for pyrolusite (p=1.0) from JCPDS card 24-735 (which are incidentally the same as given for pyrolusite by Byström). The slight misfit (in terms of producing an intergrowth structure) between these two sets of data was handled by linearly interpolating the 'lattice parameters' of the intergrowth structure such that at p=0.0 and p=1.0 the values were consistent with the lattice parameters stated. Figure 2-10 compares the computed end members with the JCPDS cards referred to. In the case of p=0.0 (figure 2-10 (a)) small peaks which are not duplicated in the calculated pattern are apparent. As previously explained these absences and other discrepancies in the intensities are due to the adoption of 'h.c.p.' fractional ramsdellite coordinates. Intriguingly the adoption of 'h.c.p.' fractional coordinates in the calculated pattern with p=1.0 produces an almost perfect match with JCPDS card 24-735 (i.e. pyrolusite), figure 2-10 (b).

The most dramatic effect observed in the calculated $\gamma$-$MnO_2$ patterns (see figure 2-9) is the rapid broadening and shift of the lowest $2\theta$ peak (i.e. (110), see figure 2-10) with increasing p. This is a consequence of the H-T effect (cf. section 4.3.2). Eventually this peak appears to emerge as the lowest $2\theta$ pyrolusite peak at p=1.0 in figure 2-9.

The computed patterns of figure 2-9 lend an insight into the relation of Faradiser M (abbrv. F.M) to that of a typical commercial EMD, such as IBA no.19. As previously mentioned (section 2.3.1), the x-ray diffraction pattern of F.M may be exactly duplicated by heating EMD for one day at 300°C in air. The peaks in figure 2-5(d) were labelled by analogy with figure 2-5(c) (or figure 2-1), despite the large shift in position required for peak E. The origin of this shift is now evident from figure 2-9. It is due to an increased fraction of pyrolusite type layers compared to the material with the diffraction pattern in 2-5(c). Furthermore the origin of the characteristic 'bump' (labelled E') between peaks E and D is also due to the increased p value. Consider figure 2-11. In this figure a calculated $\gamma$-$MnO_2$ x-ray diffraction pattern with p=0.7 is compared with the actual F.M pattern. Clearly the positions of peaks E and E' (figure 2-11(a)) compare

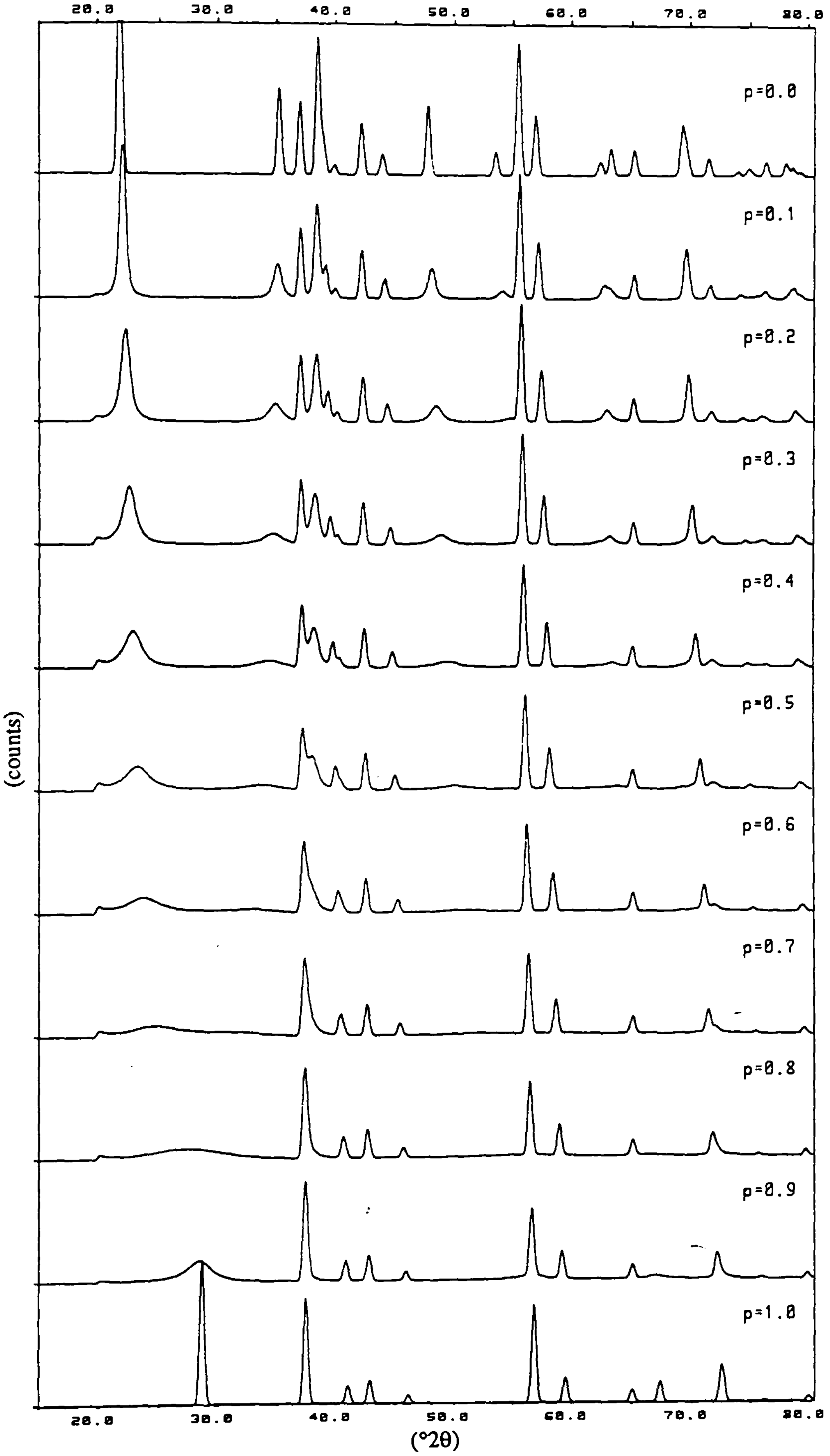

Figure 2-9 Selection of computed (based on the GdWIM ) γ-$MnO_2$ patterns spanning the p (fraction of pyrolusite type layers) range p=0 (ramsdellite) to p=1 (pyrolusite).

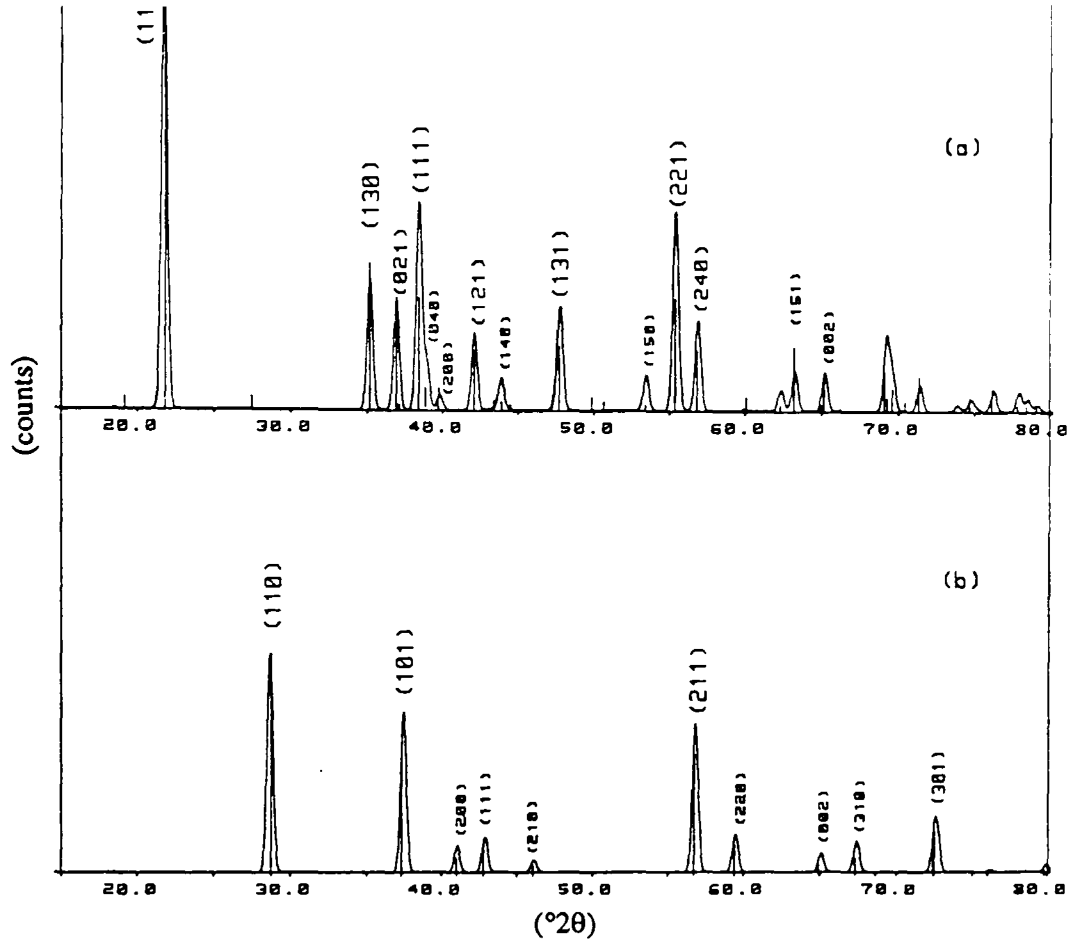

Figure 2-10 Comparison of computed ramsdellite and pyrolusite x-ray diffraction patterns with published position and intensity data. (a) comparison with stick diagram constructed from the data in JCPDS card 39-375 (ramsdellite). (b) comparison with stick diagram constructed from the data in JCPDS card 24-735 (pyrolusite).

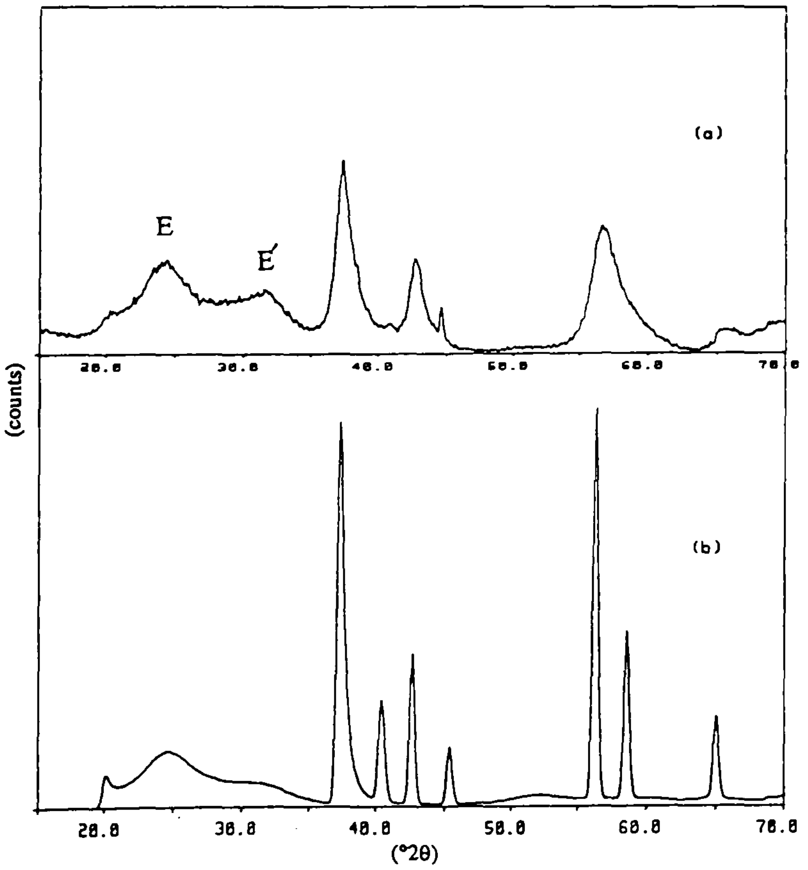

Figure 2-11 Comparison of computed GdWIM and actual x-ray diffraction patterns. (a) Faradiser M. (b) computed pattern with p=0.70.

favourably with their calculated analogues (figure 2-11(b)) the position of which strongly depend on p. Note that the position of E' does not correspond to the 100% pyrolusite peak (which occurs at 28.7(°2θ)) and is therefore *not* due to a small proportion of finely divided β-$MnO_2$. Note also the clear analogue of the (100) peak occurring at 20.0(°2θ) in figure 2-11(a). Concerning this peak de Wolff[57] states that it is "Perhaps the most striking proof of the random layer structure". Clearly large discrepancies are apparent for the remaining diffraction maxima when comparing figure 2-11 (a) and (b), particularly in the broadness and position of the calculated pattern if the displayed peaks are to overlap in such a way as to produce the pattern of F.M. However, it may be stated that whatever structural defect is responsible for producing the $\gamma$-$\gamma_t$-$MnO_2$ series must still be present in F.M since the end member ($\gamma_t$-$MnO_2$, represented by IBA no.19) and F.M are intimately related. This defect must therefore be responsible for the remaining discrepancies.

Thus to conclude, F.M is a material possessing a high p fraction (~0.7) and is therefore more closely related to pyrolusite rather than ramsdellite.

Before returning to the suggestion in section 2.4.1 and trying to introduce into the calculation layers with larger widths it seems appropriate at this stage to specify more precisely the x-ray diffraction effects that any model would need to account for in reproducing the $\gamma$-$\gamma_t$-$MnO_2$ series. This is now described in section 2.4.4.

### 2.4.4 Description of the x-ray diffraction effects observed in the $\gamma$-$\gamma_t$-$MnO_2$ series.

Consider figure 2-12 which contains the materials which are now believed to fully represent the $\gamma$-$\gamma_t$-$MnO_2$ series. Thus it contains the diffraction patterns of figure 2-4 plus that of IBA no.19 which is believed to be the end members of this series[†]. Superimposed on this figure (the dashed lines) are the line positions of the orthorhombic lattice as determined from the sharp lines of figure 2-12(a). (i.e. sample SBPA, see section 2.3.2). Only those lines with non-zero structure factors in column I of table 2.5 are included since other possible positions (as mentioned earlier) do not occur in $\gamma$-$MnO_2$.

Those peak positions, represented by solid lines in figure 2-12, that coincide with the dashed lines are the 'sharp' lines of SBPA (i.e. those with k/2+l even). A slight

---

[†] It is not implied that the end members are perfect crystals but rather that they contain a low and high concentration of one or more structural faults.

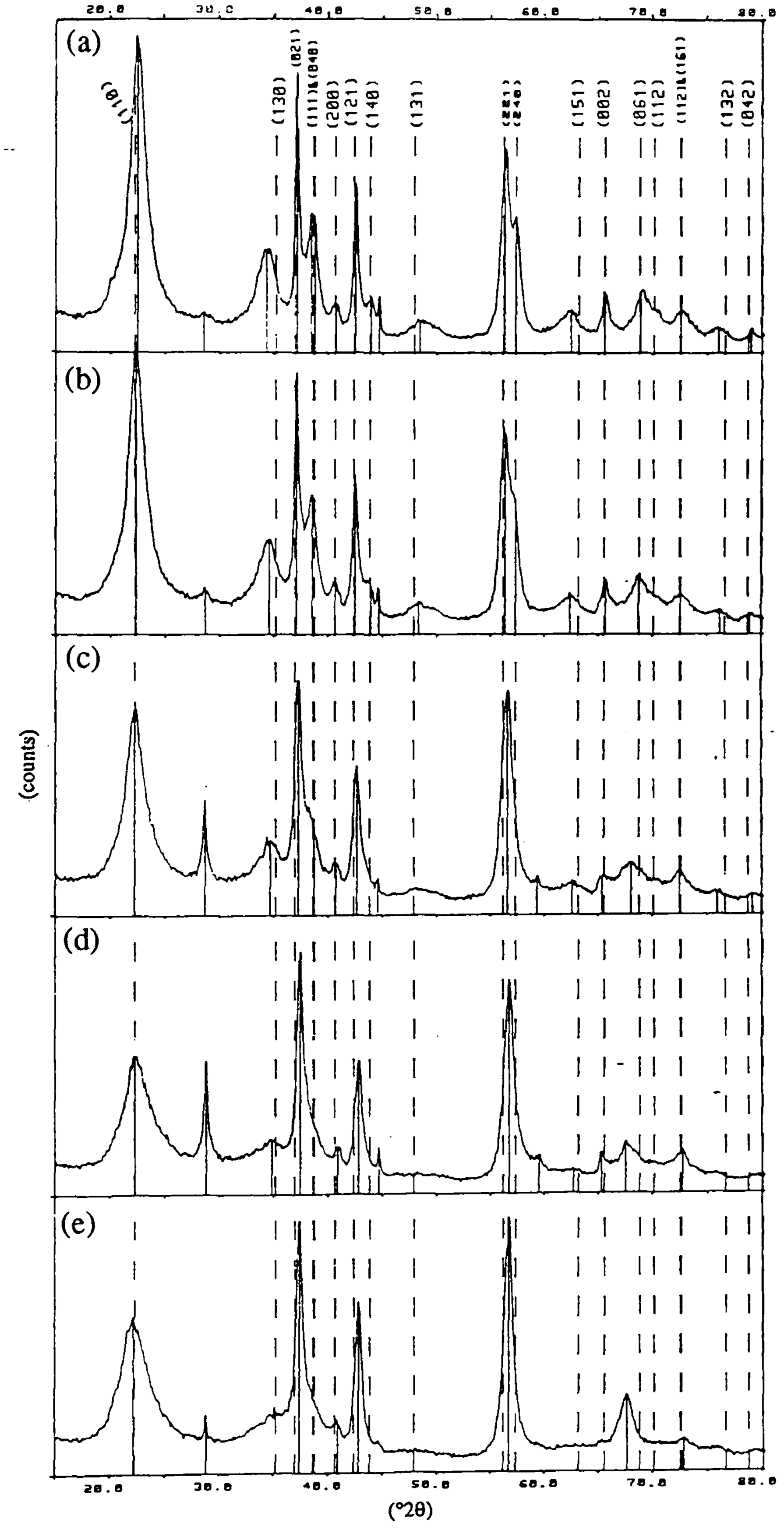

Figure 2-12 X-ray diffraction representation of the $\gamma$-$\gamma_t$-$MnO_2$ series. (a)-(d) SBP-EMD with suspended particle concentrations (a) 1000, (b) 500, (c) 200, (d) 100 ($mgMnO_2l^{-1}$) all deposited at 120 ($Am^{-2}$) 'geometrical' current density. (e) IBA no.19, no suspended particles, current density of deposition unknown. ------ indicates the orthorhombic positions determined from the sharp lines (i.e. those with k/2+1 even) of (a).

discrepancy is apparent in that the line (021) (at 37.2°2θ), which is evidently the sharpest line present, does not quite match the nearest dashed line. This is because of errors in determining the line positions of the sharp lines produce a less than perfect fit for the orthorhombic unit cell parameters subsequently determined (see section 2.3.2). No account was taken in this procedure of the fact that (021) is considerably sharper than for instance (061).

The remaining peaks are the shifted and broadened lines of the de Wolff intergrowth model. The direction of the shifts are apparent in figure 2-12(a). Starting from these positions it is now apparent when following certain peaks from figure 2-12(a)-(e) that the shift direction becomes reversed (i.e. in the opposite sense to the de Wolff shifts), presuming that is, that the orthorhombic lattice has the same unit cell dimensions in all five patterns. Thus for example the broad line (130) (at 34.3°2θ) shifts to higher angles apparently back towards its original orthorhombic position as well as broadening further producing the characteristic 'hump' in the EMD of figure 2-12(e).

The 'sharp' lines are in general broadened and shifted from their orthorhombic positions. (002) appears to fade completely from the series but whether this is the case for (040) (and (111), which occur almost at the same °2θ) and (240) is not clear since they shift into neighbouring peaks.

It is now possible to make a reasonable index assignment of typical EMD (having the x-ray diffraction pattern of figure 2-12(e) or figure 2-1), this is presented in table 2.6. Included in this table is the direction of the shift from the orthorhombic position which is assumed to be the same as for figure 2-12(a). Since the shifts are not consistent with the shifts expected from the GdWIM (or SdWIM) it is reasonable to assume that the p value of EMD must be similar to that of SBPA and therefore that the observed diffraction effects are chiefly due to an increasing concentration of some other type of defect.

### 2.4.5 The effect on the x-ray diffraction pattern of layers of triple octahedra and greater.

In this section brief consideration is given to the statement in the title of this section. Only brief consideration is necessary since it will be demonstrated that the introduction of layers greater than those of triple octahedral layers does not have the desired effect on the x-ray diffraction pattern due to the production of an enhanced (100) peak absent in the $\gamma$-$\gamma_t$-$MnO_2$ series.

Firstly the introduction of triple octahedral layers is considered on the computed pattern. This may be achieved merely by relaxing some of the constraints on the next layer in a random sequence of RR'PP' layers as specified in section 2.4.3. A triple layer then corresponds to RP' or PR'. PR' and P'R must remain disallowed if longer chains are not to be realised.

What is actually specified in the input to DIFFaX are the layer transition probabilities $\alpha$. In a hypothetical crystal with two layers $\alpha_{11}=0.5$ for example means that the probability that layer 1 is followed by layer 1 is 50%. The transition probability corresponds to first neighbour interactions. Thus the layer transition probability is only equal to the probability of existence (or fraction of the layer in the total number of layers, for a large number of layers, here designated B) of the layer when near neighbour interactions are neglected. This is equivalent in a two layer model (which has four possible $\alpha$) to specifying that $\alpha_{11}=\alpha_{21}$, and that $\alpha_{22}=\alpha_{12}$. If this is not the case then the model is no longer truly a random one and corresponds to a separating out of the layers rather than a statistical ensemble, with the layer transition probabilities no longer equal to the probability of existence of a layer. For example if

$$\alpha_{11}=0.99,\ \alpha_{12}=0.01$$
$$\alpha_{21}=0.01,\ \alpha_{22}=0.99$$

then it can easily be shown that the existence probability is 50% for each type of layer. General relations may be derived for a two layer case but for the purposes of this section it is not necessary to state them. With four types of layers RR'PP' the conditions for a random sequence of these layers is obviously

$$\begin{aligned}
\alpha_{RR} = \alpha_{R'R} = \alpha_{PR} &= \alpha_{P'R}\\
\alpha_{RR'} = \alpha_{R'R'} = \alpha_{PR'} &= \alpha_{P'R'}\\
\alpha_{RP} = \alpha_{R'P} = \alpha_{PP} &= \alpha_{P'P}\\
\alpha_{RP'} = \alpha_{R'P'} = \alpha_{PP'} &= \alpha_{P'P'}
\end{aligned}$$

or in other words the probability of the next layer being R or R' or P or P' is independent of the layer preceding it. As stated previously the GdWIM (section 2.3.3) does not fulfil this requirement since for example the probability of an P' layer following a R layer is zero. Relaxing this constraint makes the model 'more random'. So in order to produce triple layers $\alpha_{P'R}$ and $\alpha_{RP'}$ were allowed to be greater than zero. The computation was performed giving existence probabilities $B_R=0.27$, $B_{R'}=0.27$ and

$B_P=0.23$, $B_{P'}=0.23$, which means a probability of an R or R' layer of 0.54 and the probability of a P or P' layer (analogous to p in the GdWIM) of 0.46, obtained from the output of DIFFaX for the transition probabilities specified ($\alpha_{RR'}=\alpha_{R'R}=0.4$, $\alpha_{RP}=\alpha_{RP'}=\alpha_{R'P}=\alpha_{R'P'}=\alpha_{PP'}=\alpha_{P'P}=0.3$, $\alpha_{PR}=\alpha_{P'R'}=0.7$, and the remaining transitions set to zero). The probability of a triple layer can be calculated using the relation

$$B_{R'P}=B_R\alpha_{RP'}=0.27*0.30=\underline{0.081}$$

and similarly for $B_{RP'}$ giving the probability of a triple layer to be 0.16. The computed powder x-ray diffraction pattern is shown in figure 2-13(b). The effect on the x-ray pattern of triple layers is readily assessed by comparison with figure 2-13(a) which is a GdWIM calculation with p=0.20. This effect has already been considered theoretically on a ramsdellite pattern which is related to the case considered (see section 2.4.1). However a noticeable effect, not previously predicted, is the occurrence of an enhanced (100) peak which aside from the other conclusions already reached makes it more apparent that this suggestion is not leading to the end member of the $\gamma$-$\gamma_t$-$MnO_2$ series. It is possible, however, that a small concentration of this defect may account for some of the features of a typical $\gamma$-$MnO_2$ pattern such as that in figure 2-4(a) (which is of sample SBPA). For instance the (150) peak which occurs at 53.2°$2\theta$ in the computed patterns and not in figure 2-4(a) (see also figure 2-8) disappears with the introduction of triple layers (this phenomena could also be due to the oxygen framework cf. section (2.4.3)). Further, the discrepancy found when measuring p could be due to additional shifts of triple layers (see section 2.3.2), though this would be very difficult to prove without an exhaustive program of refinement since there is probably another reason for additional shifts, which will become apparent in section 2.5, that could possibly mask the observable displacements. Further work in this area would involve such refinements on a large selection of $\gamma$-$MnO_2$ patterns and was not attempted here.

The origin of the enhanced (100) occurring at 20.0°$2\theta$ peak is not well understood (by the author). It is noted that it occurs in the ramsdellite to pyrolusite transition, figure 2-9, and in de Wolff's paper[57] where the calculation was performed with manganese only.

Relaxing the constraint that $\alpha_{RP'}$ and $\alpha_{P'R}$ are zero produces layers with increasing dimensions which produced little further change in the calculated pattern for the values of $\alpha_{RP'}$ and $\alpha_{P'R}$ introduced (see figure 2-13(c)). Finally the calculation of a random sequence of RR'PP' layers is displayed in figure 2-13(d). In this case all

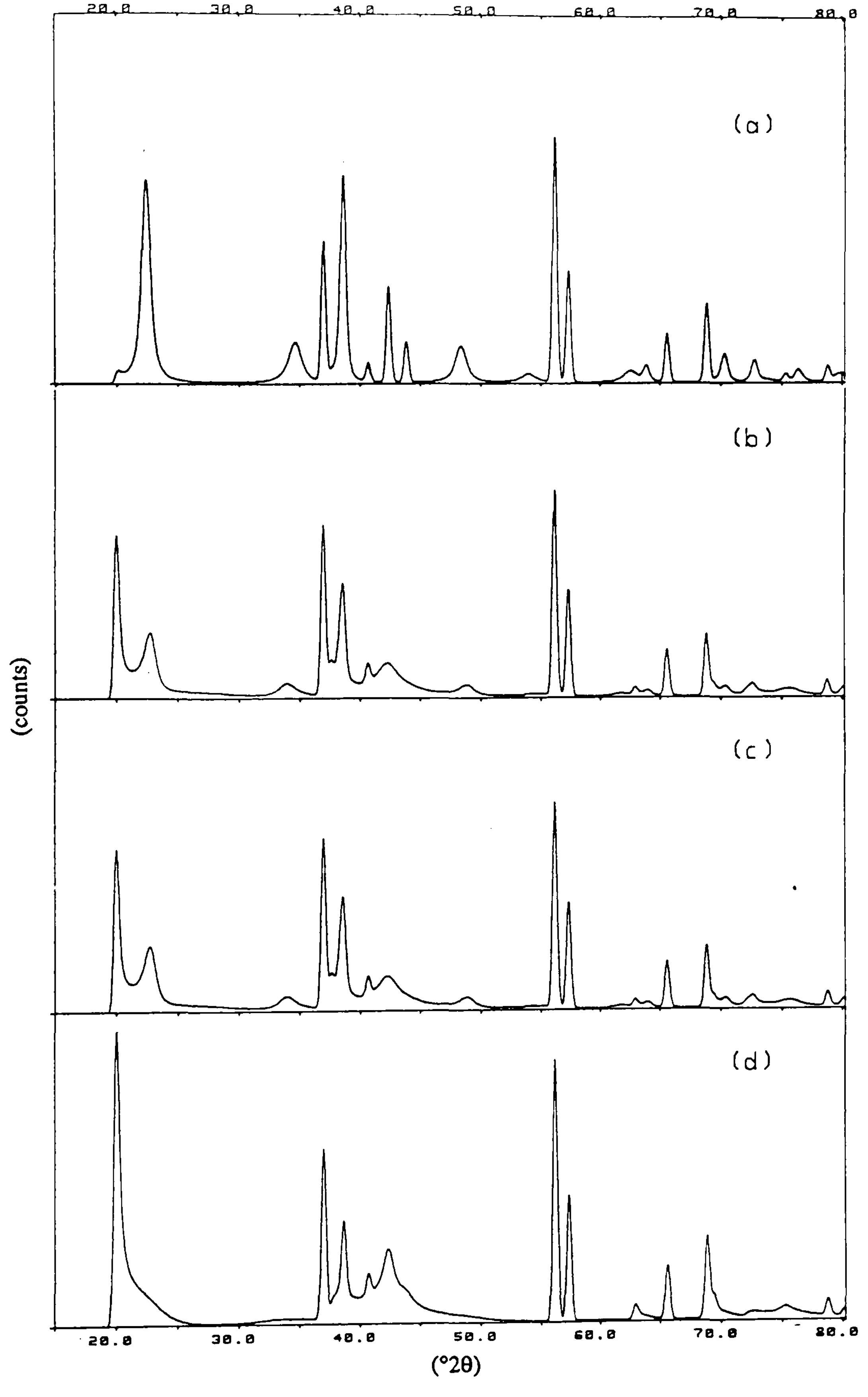

Figure 2-13 Effect of layers of triple octahedra and greater on the computed x-ray diffraction pattern of $\gamma$-$MnO_2$. (a) GDIM with p=0.2 (b) effect of triple octahedral layers (c) effect of triple and greater octahedral layers. (d) random sequence of RR'PP' layers.

possible transitions are allowed and the conditions for a random sequence, as specified above, were met. The probability of each layer was

$$B_R=B_{R'}=0.4$$
$$B_P=B_{P'}=0.1$$

which is analogous to p=0.2. Since in this case layers with large dimensions are likely to exist (for instance the probability of a layer with dimensions four times a p layer is 0.32) the presence of an even stronger (100) peak suggests that they are related to this and/or to the increased 'randomness' of the four layers.

To conclude this section it may be stated that introduction of layers with dimensions associated with triple octahedra (in the b direction, and infinite chains in the c direction) or layers with greater dimensions consistent with multiples of single octahedra produces diffraction phenomena inconsistent with those observed when traversing the $\gamma$-$\gamma_t$-$MnO_2$ series and therefore need not be discussed further.

## 2.5 Further discussion and conclusion in support of Pannetier *et al.* 's recently proposed structural model.

The two structural models widely quoted in the literature in connection with the crystal structure of battery active EMD have been reviewed and discussed. Attention has been focused on the ability of the $\varepsilon$-$MnO_2$ model to account for the characteristic 100% broad line at ~22°2θ (CuKα). Neglecting this peak the model accounts reasonably well for the apparent hexagonal symmetry of the other peaks as well as their integrated intensities. However, the explanation proposed by de Wolff *et al.* that this peak is a shifted forbidden $(001)_{hex}$ reflection due to partial ordering of the manganese in the $c_{hex}$ direction is unsatisfactory. One reason is the following observation. It has been noted[illegible] that the 4.1 (Å) (or 22°2θ) peak, apparent in x-ray diffraction, is absent in room temperature neutron diffraction patterns. This, if one accepts the above explanation for its occurrence, should not occur.

With neutron diffraction there are two types of scattering phenomena. Namely nuclear scattering, which, as the name suggests occurs from interactions of the incoming neutrons with the nuclei in the irradiated sample and magnetic scattering which is the name given to scattering from atoms or ions possessing a net magnetic moment and is caused by interactions with unpaired electrons (neutrons though they have no charge also have a magnetic moment). As $MnO_2$ at room temperature is paramagnetic[64,18] (all forms) the magnetic moments of the manganese point in random directions (the $O^{2-}$ are not magnetic) and thus magnetic scattering results only in a contribution to the background. For nuclear scattering Mn posses an uncommon property amongst the elements. It is one of the few which exhibit a phase change of $\pi$ (or half a wavelength) in the scattered radiation compared to other elements. The consequence of this is that Mn and O scatter $\pi$ out of phase. Thus the disappearance of the 4.1(Å) peak must be due to this fact. That is, it happens that the addition of form factors weighted by the appropriate amount (i.e. for this particular (hkl)) produces a large peak in x-ray diffraction but because of the phase change mentioned they annul each other in neutron diffraction. This, however, could not occur for a peak produced solely by manganese as in the $\varepsilon$-$MnO_2$ model. A peak would occur, though considerably reduced in intensity compared to other peaks in the pattern since the magnitude of the neutron coherent scattering amplitudes[65] are $a_{Mn}$=-3.7±0.2 and $a_O$=+5.80±0.05, and therefore the neutron diffraction pattern is dominated by the oxygen contribution (the reverse is

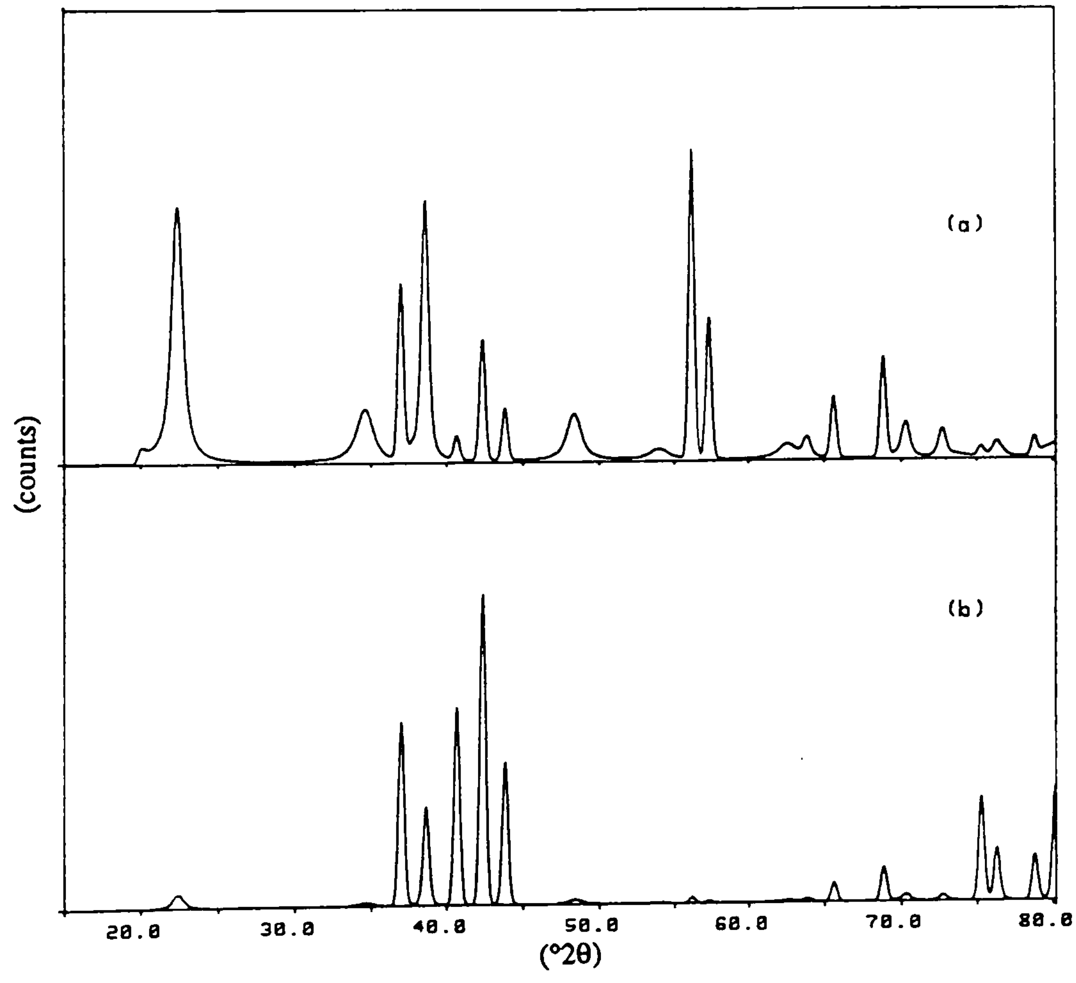

Figure 2-14 Comparison of computed x-ray and neutron diffraction patterns of $\gamma$-$MnO_2$ (with p=0.2). (a) powder x-ray diffraction pattern. (b) powder neutron diffraction pattern ($\lambda$=1.5418(Å)).

approximately true in x-ray diffraction since (at 0°2θ) $f_{O2-}$=10 and $f_{Mn4+}$=21).

The phenomena of a disappearing 4.1(Å) peak, significantly, is easily produced in the de Wolff model of $\gamma$-$MnO_2$ as illustrated by the calculated patterns in figure 2-14 where the striking absence of the (110) peak (and also (221) and (240)) is obvious.

Aside from the above argument convincing evidence is presented in section 6.3 that typical battery active EMD (near the $\gamma_t$ end of the $\gamma$-$\gamma_t$-$MnO_2$ series) does not posses hexagonal symmetry as deduced from line movements of peaks other than that of the 4.1(Å) peak when H is inserted into the structure (and therefore is not described by the $\varepsilon$-$MnO_2$ model).

A clue to the correct structural model is provided by the $\gamma$-$\gamma_t$-$MnO_2$ series represented in figure 2-12, in which it is apparent that typical battery active EMD is the end member of a structural series and not a separate phase unconnected with $\gamma$-$MnO_2$. If this is the case then introduction of one or more other structural faults, it is suggested, into the de Wolff model ought to in principle be able to account for such a series. The author has investigated this and tried to introduce plausible faults in computed x-ray diffraction patterns. The faults introduced produced modifications of the de Wolff model x-ray diffraction patterns inconsistent with those observed in the actual $\gamma$-$\gamma_t$-$MnO_2$ series. The observed diffraction effects are, however, in almost complete agreement with those expected from a new model proposed by Pannetier[39,40,36] *et al.* This model introduces just such a modification of the de Wolff model which enables reproduction of the observed diffraction effects present in the $\gamma$-$\gamma_t$-$MnO_2$ series.

The implementation of this proposal requires a radically different approach to the problem since the structural fault introduced is no longer simultaneously calculable with programs that simulate planar type defects (such as DIFFaX). Rather Monte Carlo simulation of the crystal in a computer and subsequent numerical calculation of the diffraction pattern by Fourier transform was required. The structural fault introduced was a microtwinning on the (021) and or (061) planes. This may be visualised on the (100) plane as a ramsdellite or pyrolusite chain bending at 60° or 120° (the only two possible directions which do not require a re-arrangement or the oxygen sub-lattice), the bending taking place in the plane, see figure 2-15. A full description of this model is not attempted here and the reader is referred to the original papers [39,40,36], but the following aspects will demonstrate that this model is sufficient to account for the diffraction effects observed in the $\gamma$-$\gamma_t$-$MnO_2$ series, described in section (2.4.4).

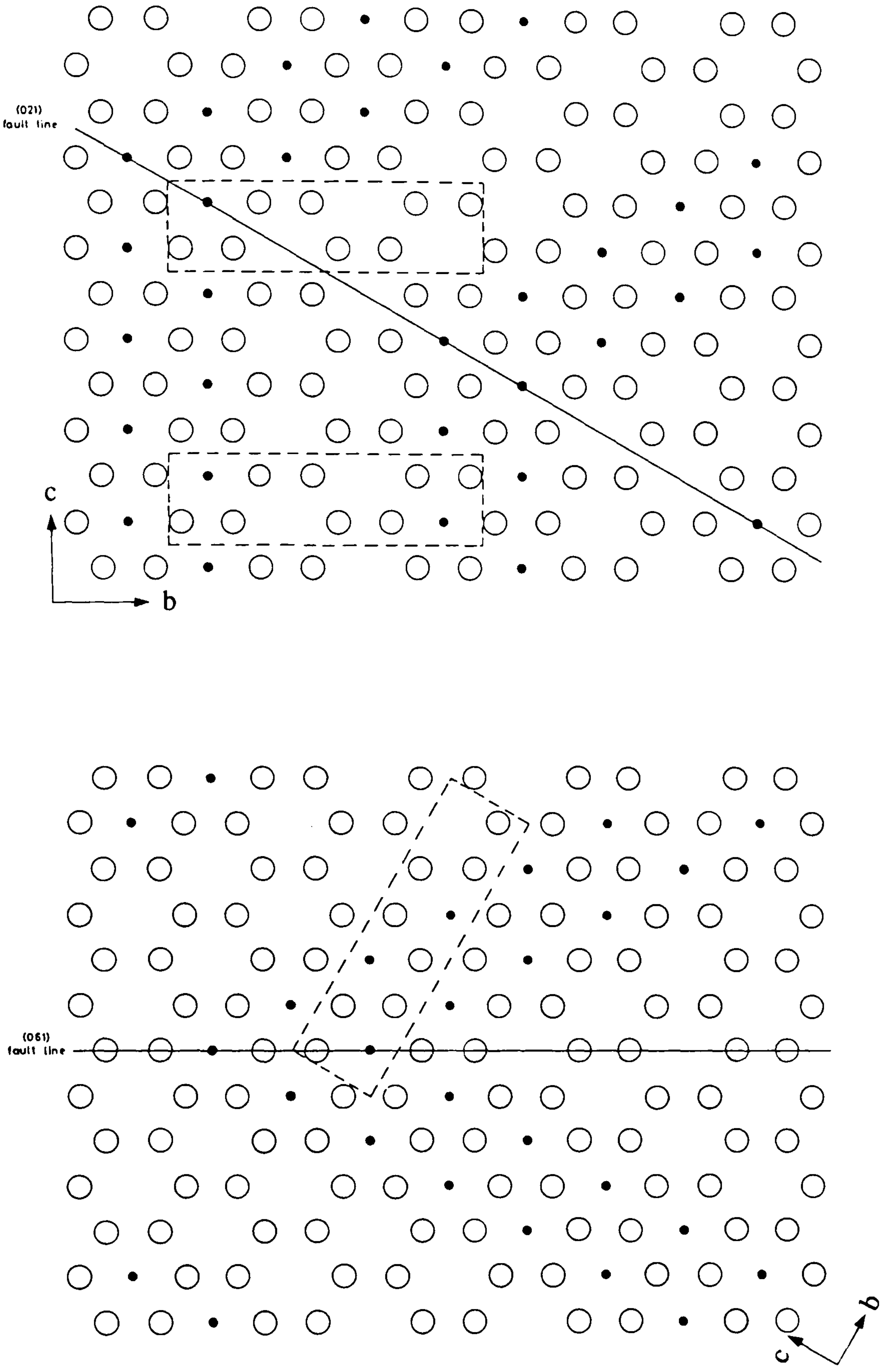

Figure 2-15 Projection on the (b,c) plane of possible microtwinning faults occurring in 'h.c.p. ramsdellite', (cf. section 1-2). Top bending of ramsdellite double chain at 60° at a (021) fault and bottom bending of ramsdellite double chain at 120° at a (061) fault. Perfect 'h.c.p. ramsdellite' unit cells are indicated in the figure. Unfaulted crystal has straight double chains extending in the c direction.

Table 2.6 Suggested indices of EMD in fig.2.10(e) from observed shifts and broadening in fig.2-12(a)-(e) and comparison with effects predicted due to microtwinning only.

| Peak label from fig.2-1 | Sugg. assgn. from fig.2-12 | Orthorhom. indices, fig.2-12 | Observed $\Delta$°2$\theta$ from orthorhom. positions. | Direction of shift due to microtwinning[66]. |
|---|---|---|---|---|
| E | (110) | (110) | $\theta\downarrow$ | - |
| | | (130) | - | - |
| D | (021) | (021) | $\theta\uparrow$ | $\theta\uparrow$ |
| | → | (111) | * | - |
| | → | (040) | * | $\theta\downarrow$ |
| F | (200) | (200) | $\theta\uparrow$ | - |
| C | (121) | (121) | $\theta\uparrow$ | $\theta\uparrow$ |
| | → | (140) | * | $\theta\downarrow$ |
| | | (131) | - | - |
| B | (221) | (221) | $\theta\uparrow$ | $\theta\uparrow$ |
| | → | (240) | $\theta\downarrow$ | $\theta\downarrow$ |
| A | (061) | (061) | $\theta\downarrow$ | $\theta\downarrow$ |
| | | (151) | - | - |
| | → | (002) | - | $\theta\uparrow$ |
| | | (061) | $\theta\downarrow$ | $\theta\downarrow$ |
| | | (112) | - | - |

Notes:

→ means that the corresponding peak in column three probably contributes to the last peak labelled above in the first column. (eg. (002) probably contributes to peak A.)

* means that the shift is not measurable.

Referring to table 2.6 the predicted direction of shifts due *only* to microtwinning are compared with those observed from figure 2-12. The agreement is quite remarkable considering that there is at least six other parameters which could vary so as to mask the shifts due only to microtwinning. These are the variation in p, variation in $\alpha$ the layer transition probability (altering the randomness of the model, as discussed in the previous section), the prevailing orthorhombic 'lattice parameters' a,b,c, and particle size broadening (which may preferentially broaden peaks if the particles have a definite morphology). The instrumental factors are constant in this instance and therefore do not need to be included. The main discrepancy in table 2.6 involve lines (110) and (200), which show small shifts where none are predicted for microtwinning and (002) which does not appear to shift as predicted. The first discrepancy is probably related to small changes in the orthorhombic lattice parameters since (200) is unaffected by variations in p or microtwinning. The second is not so much a discrepancy but due to a lack of x-ray diffractograms between figures 2-12(d) and (e) in which (200) could still be observed to comply with the expected shift.

Detailed descriptions of the effects of microtwinning on x-ray and neutron diffractometer traces are described in the original papers of Pannetier et el and are summarised in the following.

Consideration of the reciprocal lattice due to a perfect ramsdellite orthorhombic lattice and a completely twinned example (in a completely analogous way to sections 2.3.2 and 2.4.1) enable one to group the diffraction lines into three categories[66].

(a) lines (h00), are unaffected.

(b) lines with indices (k/2+l) even which are broadened and displaced in reciprocal space, the direction of the displacement depending on the indices and the broadening of an observed line on the probability of microtwinning.

(c) the remaining lines broaden and fade with increasing microtwinning the amount depending on their displacements from their twinned companions in reciprocal space.

It is remarkable that just those lines that are broadened and shifted by microtwinning (i.e. those with (k/2+l) even) are unaffected in the de Wolff model (except (h00) lines). This means that the determination of p for heavily twinned samples (from the diffraction pattern) a complicated task. The apparent symmetry (neglecting the 22°2θ peak) displayed by EMD is now seen to be an artifact. It is incidentally not the case that the apparent hexagonal lattice is a direct reflection of the oxygen sub-lattice since this is directly calculable by the relations in section 2.4.3, if one knows the orthorhombic lattice parameters. However, these are determined from the sharp lines in the de Wolff model which are shifted due to microtwinning and therefore not known and hence neither are the lattice parameters of the approximately h.c.p. oxygen sub-lattice. It is not suggested that they are not related but rather that the relationship is a complicated one determined by the effects of microtwinning and not directly a reflection of the d spacings of the diffraction pattern.

Thus to summarise, the structural fault required to modify the de Wolff model of $\gamma$-$MnO_2$ is the concept of microtwinning. It has been brought to my attention by Dr Pannetier that such twinning is known to occur in rutile[67] (which has the same structure as pyrolusite) and so its introduction is not just attractive from the viewpoint of explaining the observed diffraction patterns but probably has determinable origins in chemical crystallographic science. Other faults, such as triple octahedral layers, which are believed to have been observed in specimens of nsutite, play only a small role in explaining the diffraction pattern of EMD but may nonetheless provide a way of optimising $\gamma$-$MnO_2$ calculated patterns.

## 2.6 Conclusions.

The conclusions for this chapter are summarised as follows:

(a) Observations on the diffraction patterns of battery active manganese dioxides clearly indicate that they form a structural series.

(b) A class of possible planar structural faulting, one member of which has been observed to occur in specimens of nsutite, has been investigated as to the effects on the computed x-ray diffraction patterns of $\gamma$-$MnO_2$. The results indicate that such faults do not account for the observed structural series stated in (a).

(c) The structural fault required to modify the GdWIM is the concept of microtwinning in accordance with Pannetier *et al.*'s model.

(d) Faradiser M has been found to be structurally related to EMD. It has a similar structure but with a vastly increased proportion of pyrolusite type layers ($p \approx 0.7$). It is thus more closely related to $\beta$-$MnO_2$ rather than ramsdellite (which is the case for EMD ($p \approx 0.2$)).

(e) $\varepsilon$-$MnO_2$ is not a separate polymorph of manganese dioxide nor is its structure described by de Wolff *et al.*'s $\varepsilon$-$MnO_2$ model.

(f) Battery active manganese dioxides are members of the $\gamma$-$\gamma_t$-$MnO_2$ structural series. It is emphasized that this includes EMD's and CMD's.

# 3 Development of Experimental Procedures.

## 3.1 Manganese dioxides investigated.

The manganese dioxides investigated in this study were an SBP-EMD (cf. section 2.3.1) labelled SBPA, Faradiser WSZ (a commercial material obtained from the company Sedema, labelled WSZ), IBA international common samples number 14 and 19 (EMDs from the International Battery Material Association, labelled IBA no.14 and IBA no.19), and Faradiser M (also a commercially available material from Sedema, labelled F.M). The reasons for choosing these materials are given in section 2.3.1. Essentially they were chosen because their structural properties span those displayed by battery active materials as evidenced by their x-ray diffraction patterns.

## 3.2 Chemical insertion of H into manganese dioxides.

The purpose of chemically inserting H in a non-aqueous environment was to produce a range of H insertion materials reflecting as far as possible a solid state reaction process without subsidiary complicating chemical reactions[125,95]. These arise due to the re-establishing of equal concentrations of H in each particle when smaller particles (with a higher surface to volume ratio) are unavoidably inserted to a greater degree *whatever* the chemical H insertion technique used. Establishment of equilibrium may involve soluble intermediates, particularly in an aqueous medium, with the consequent possible appearance of phases not fundamentally characteristic of the H insertion process[68] (see also chapter 8).

To accomplish non-aqueous insertion of H a range of chemical reductants have been employed. These include cinnamyl alcohol in xylene and hydrazine hydrate. Hydrazine hydrate has been employed both in aqueous and non-aqueous solvents, further discussion of methods using this substance shall be reserved until section 3.4. Recent published work by Fitzpatrick and Tye[68] reported on the reduction of manganese dioxide with 'inert' solvents xylene and acetone. Various mixtures of these were used to effect a particularly mild reduction of the EMD coded R2. These samples have been made available to the author who has conducted further x-ray diffraction studies, the results of which are reported in chapter 6. In order to arrive at a more systematic approach acetone alone was investigated as a suitable reducing agent.

The presumed advantages of using acetone are as follows: (a) It is a relatively low molecular weight compound (compared to cinnamyl alcohol) and therefore its oxidation products may be expected to evaporate easily from the oxide surface. (b) If the reaction is 'slow' and occurs at room temperature this could mean more likelihood of homogeneous reduction. Consider figure 3-1 which shows the reaction rate behaviour of IBA no.14 with increasing temperature. Evidently impractical reaction times are required to reach the theoretical H insertion limit corresponding to r=1.0 in $MnOOH_r$ (cf. section 8.1). Increasing the temperature would require increasing the pressure since the maximum temperature stated in figure 3-1 is that of the boiling temperature of acetone (56°C). The quantities used, estimated on the basis of equation (3.1), indicate a large excess of acetone.

$$CH_3COCH_3 + 6MnO_2 + 3H_2O \rightarrow CH_3COOH + CHOOH + 6MnOOH \quad (3.1)$$

This equation was arrived at by writing acetic acid and formic acid as the oxidation products from the reaction and balancing the equation with water[†]. A strong odour of acetic acid was produced when acetone was introduced into a vessel containing manganese dioxide, the presence of which was confirmed by FTIR spectroscopy of the solution product. With this technique no other oxidation product could be unambiguously identified. Equation (3.1) suggests that the reason that the reaction does not proceed completely[‡] is because the reaction is limited by water, which has been deliberately excluded from the system ("Analar" acetone was used which had 0.2% water initially present, this was further dried with a molecular sieve type 4A). Note that a typical EMD contains a total of around 5% of water, which varies according to the history of its storage conditions. However, adding small quantities of water (or increasing the amount of acetone) did not cause the reaction to proceed further. Therefore there seems no reason to suppose water is involved in the reaction which could be written, for example as equation (3.2).

$$2CH_3COCH_3 + 2MnO_2 \rightarrow 2MnOOH + CH_3COOH + C_4H_6 \quad (3.2)$$

$C_4H_6$ could be many different compounds for instance butyne or 1,2-butadiene (which

---

[†] This equation was suggested by J.Larcin.

[‡] It is easy to show by substituting in Gibbs free energy of formation for the reactants and products, available in the literature, that the reaction strongly favours the products.

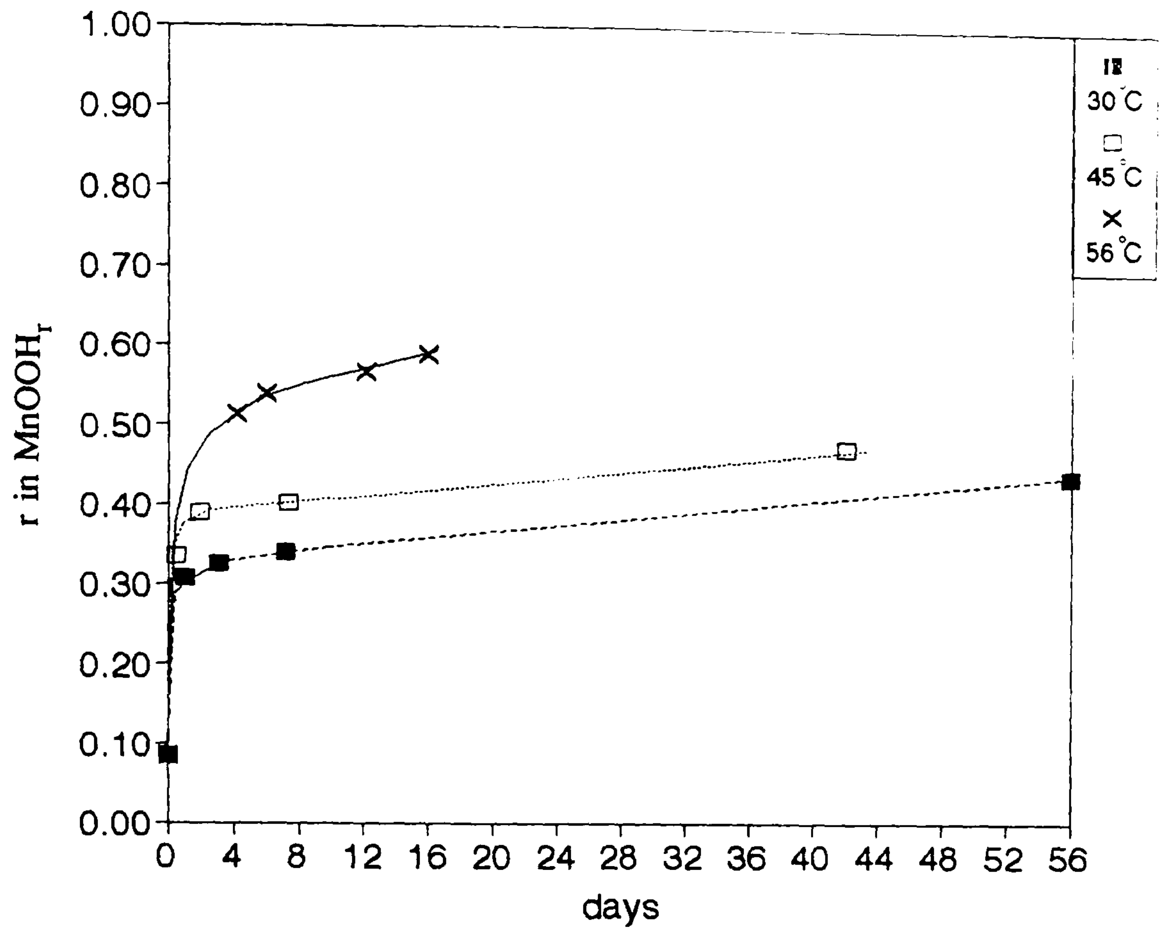

Figure 3-1 r in MnOOH$_r$ versus reaction time in acetone for material IBA no.14 at three different temperatures. 56(°C) corresponds to the boiling temperature of acetone.

is a gas). The reason that the reaction does not proceed completely is probably kinetic, perhaps due to an activated complex formed on the surface of the oxide. This was not investigated further, instead, a different reductant was chosen.

Manganese dioxide has been used in organic chemistry to prepare allylic aldehydes from allylic alcohols[69,70]. Low molecular weight alcohols were considered for the reason given above in (a). 1-propanol was considered a natural choice. Primary alcohols can be oxidised to the corresponding aldehyde[71] therefore the reaction stoichiometry is probably as given in equation (3.3):

$$MnO_2 + CH_3CH_2CH_2OH \rightarrow MnOOH + CH_3CH_2CH_2O \qquad (3.3)$$

Usually, however, such oxidations do not end with the aldehyde[71] which could be further oxidized to propanoic acid. Figure 3-2 compares the reaction rate behaviour of four materials used in this study. The reaction conditions used represent an (approximately) five times excess of propanol on the basis of equation (3.3). Analar 1-propanol (99.5% pure, 0.2% water) dried with a molecular sieve type 4A was used under reflux (97°C). The top of the reflux condenser was protected with a tube containing silica gel to stop ingress of water. Figure 3-3 schematically represents the reaction

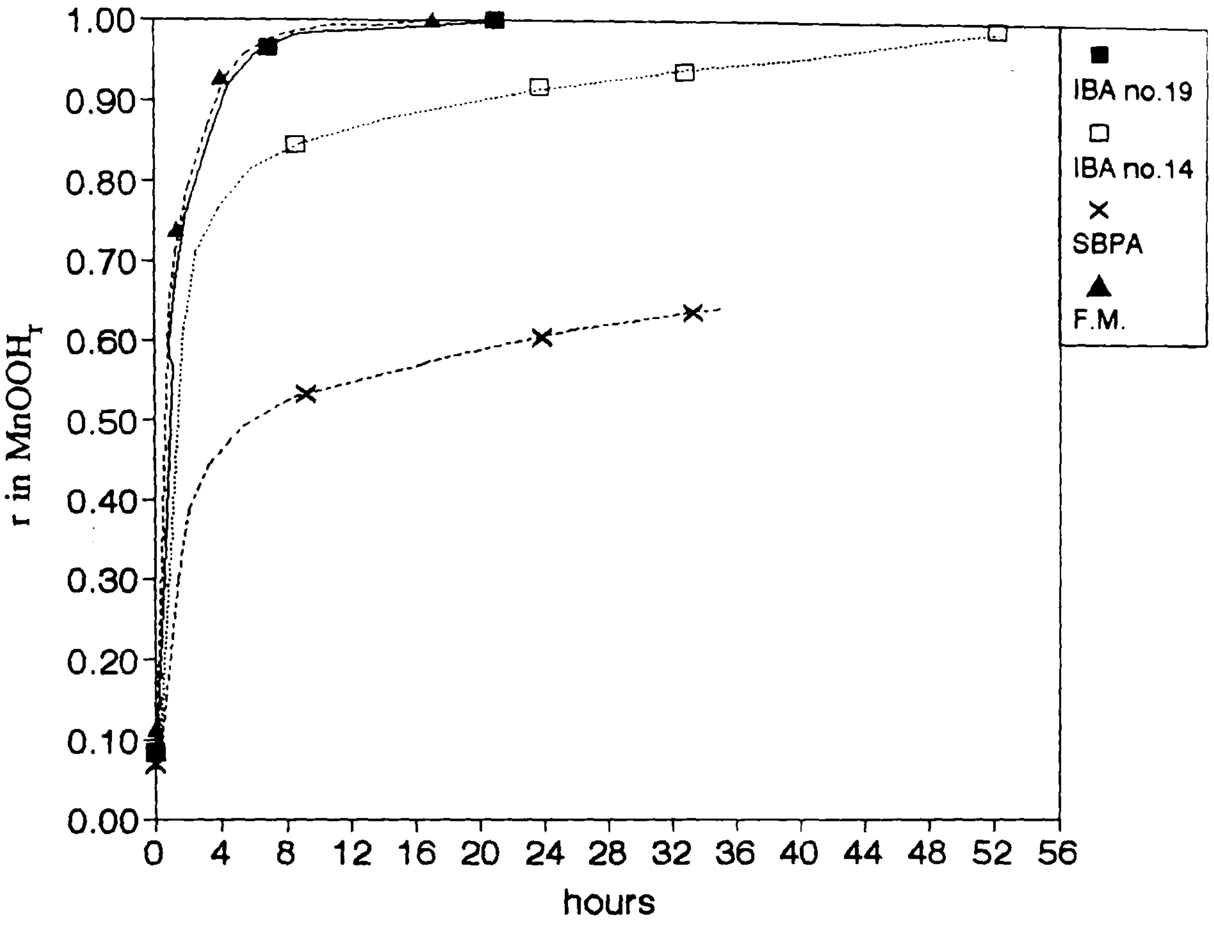

Figure 3-2 r in MnOOH$_r$ versus reaction time in boiling 1-propanol (97(°C)) for materials IBA no.19, IBA no.14, SBPA and F.M.

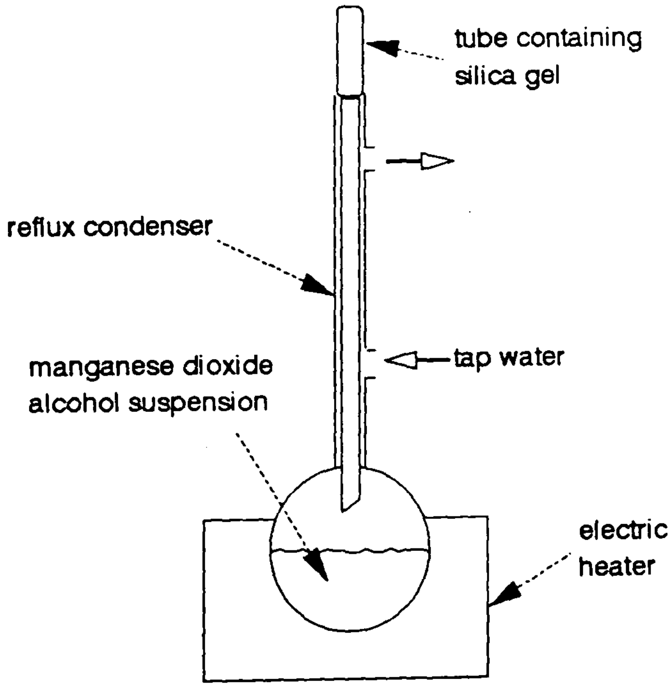

Figure 3-3 Reflux conditions for propanol or butanol reactions with synthetic battery active manganese dioxide.

conditions. At periodic intervals small $MnOOH_r$ samples were removed and analyzed by the 'method 1' analysis technique (see section 3.3). From figure 3-2 it may be seen that 1-propanol is an effective reductant for all the materials except material SBPA. Use of a higher boiling temperature alcohol (1-butanol, b.p[72].=117°C) was required to produce high H insertion levels for this material. By referring to figure 3-2 it is possible to predict the reduction level obtained for a given contact time of a particular material in boiling 1-propanol. By such a method approximately 25 samples for each material covering the so called one electron range (i.e. from the initial reduction level to the theoretical level corresponding to the stoichiometry MnOOH) of a battery were produced.

### 3.2.1 Discussion.

Although propanol is a suitable reductant in terms of its reactivity, a complicating feature compared to the samples produced by Fitzpatrick was observed in the x-ray diffraction pattern. Compare (a) and (b) of figure 3-4. A relatively large line at 26°2θ coincident with the 100% γ-MnOOH line is observed in the propanol reduced sample. Since reduction by $MnCl_2$ + $NH_4OH$ in aqueous solution is known to produce a well defined γ-MnOOH pattern[73], this suggests that soluble Mn species were not totally absent (and thus the reaction conditions were not ideal). Changing to 2-propanol, which might be thought less likely to solubilise Mn (because the oxidation products are less likely to be an acid), produced no difference in the x-ray diffraction pattern. This may be because acetone, which is the expected oxidation product from oxidizing 2-propanol, reacts to give acetic acid as was noted earlier.

The problem was investigated by scanning electron microscopy (SEM). Figure 3-5 and figure 3-6 show the unground starting material (IBA no.19) and its most reduced derivative (also unground). It appears that the small particles have vanished. Other regions (not shown), however, contain agglomerates of small particles. This is probably caused by the method of filtration since a porosity no.4 (pore radius 5-10 μm) sintered glass funnel was used (under vacuum) which would mean the small particles, approximately 1-2 μm in diameter, would pass through the filter unless they agglomerated. A similar effect is observed if the unreduced material is filtered from water by the same method. It is apparent from figures 3-5 and 3-6 that no obvious rounding or cementation of the particles has occurred (i.e. no obvious dissolution has

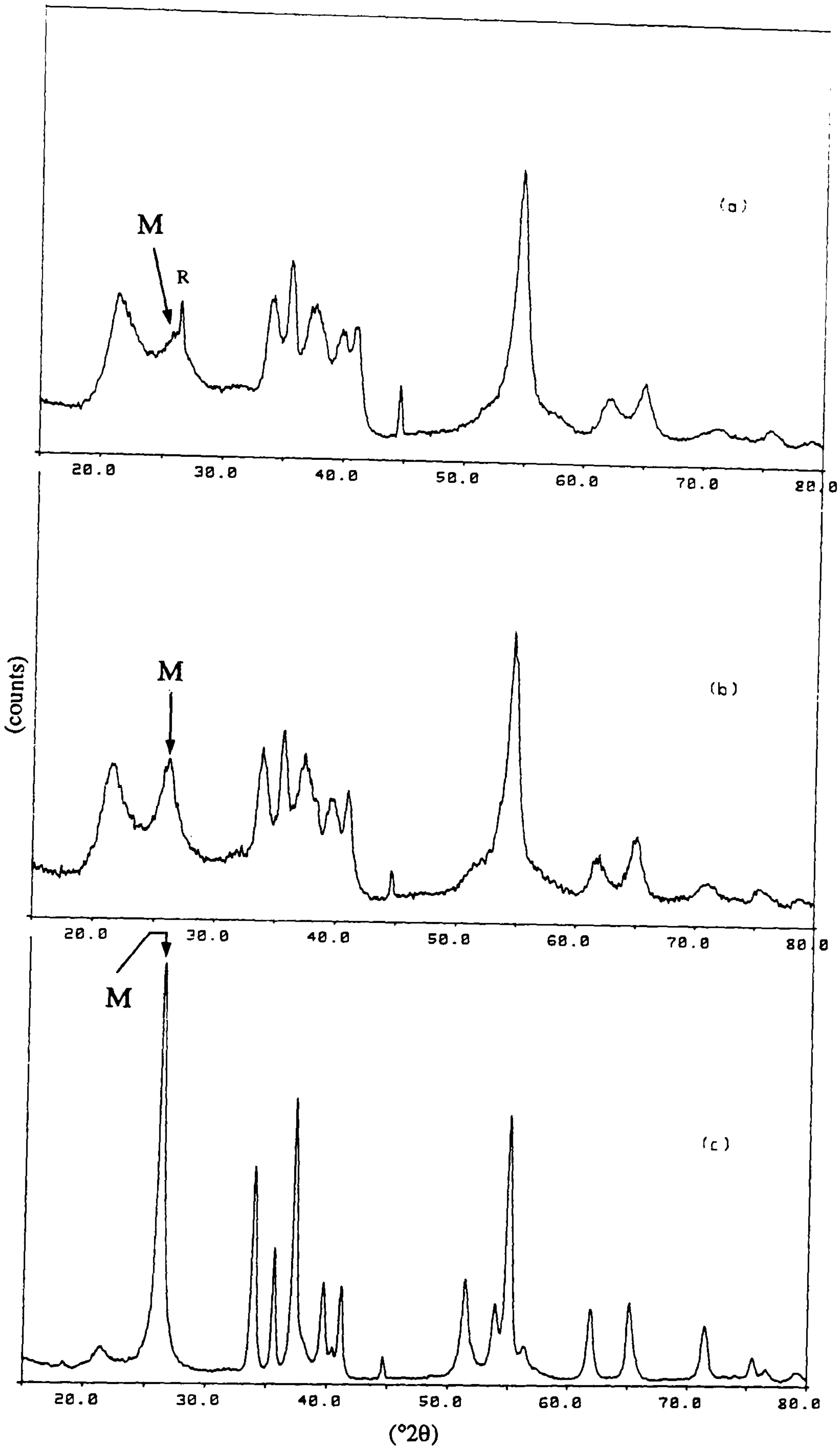

Figure 3-4 X-ray diffraction comparison of (a) most H inserted R2, $MnOOH_{1.0}$, prepared by reaction with cinnamyl alcohol in xylene, (b) most H inserted IBA no.19, $MnOOH_{1.0}$, prepared by reaction with propanol, (c) refluxed material of (b) in distilled water for 20 hours. (Note, full scale double that of (a) and (b)). (c) was identified as manganite. M marks the most intense manganite peak, which is stronger in (b) compared to (a) indicating an increased proportion of manganite. R marks graphite impurity.

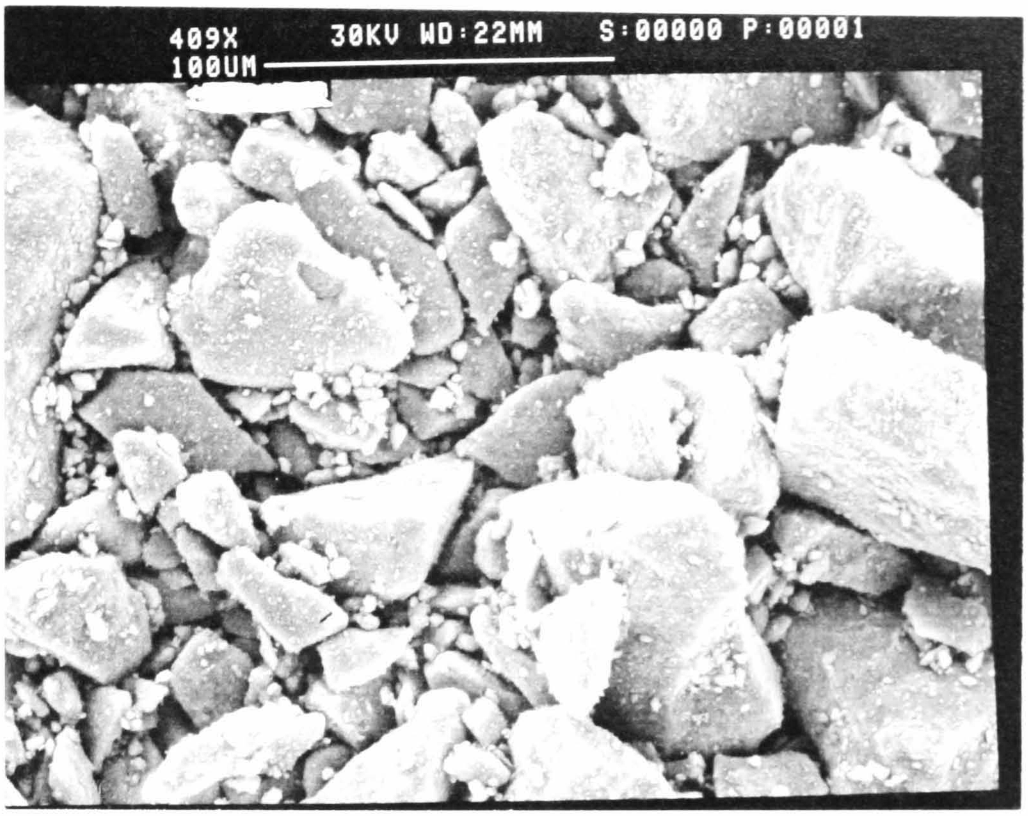

Figure 3-5 SEM photograph of as received EMD IBA no.19.

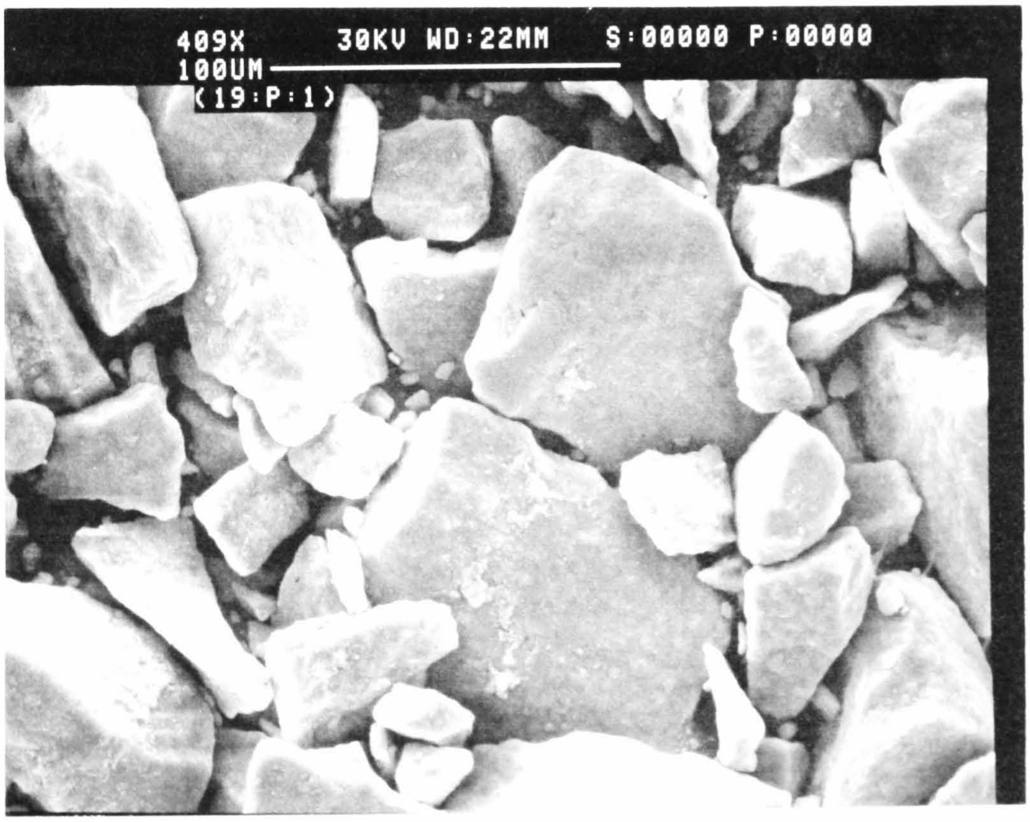

Figure 3-6 SEM photograph of 1-propanol most reduced IBA no.19, $MnOOH_{1.0}$.

occurred).

It is known that refluxing a reduced material in water produces[73] γ-MnOOH. Figure 3-4 displays the effect of refluxing a reduced IBA no.19 sample ($MnOOH_{1.0}$) for 20 hours in water. The SEM picture of this product at the same magnification as figures 3-5 and 3-6 again shows no obvious change in the habit of the particles. Examination at much higher magnification, figure 3-7, indicates new rod shaped crystal growth characteristic of γ-MnOOH. Subsequent investigation of the product obtained from reaction with propanol at the same magnification, figure 3-8, indicates no observable rod shaped growths despite having the broad 'manganite' line. The appearance is very similar to the starting material, figure 3-9. Probably the γ-MnOOH growth is too small to be observed using SEM. Further evidence in favour of this conclusion is a slight brown discolouration of the deeply reduced material (which starts as dark grey) particularly when ground in preparation for x-ray diffraction. The corresponding water refluxed material turns a distinct rust brown colour on grinding.

Another complication was only observed in the deeply reduced SBPA materials. It took approximately six weeks of continuous reflux in 1-butanol to produce the most H inserted samples. In this time period a small amount of reduced manganese dioxide must have been exposed to the air when the level of butanol fell in the manganese dioxide butanol suspension despite the reflux conditions and occasional topping up. This resulted, in one sample, a small quantity of $Mn_2O_3$, probably due to decomposition of the H inserted manganese dioxide[74] in the local hot conditions produced when no butanol covers the oxide.

### 3.2.2 Conclusions.

Propanol and butanol by the method described in section 3.2 have been used to successfully insert H into the manganese dioxides studied.

The complication produced by the appearance of γ-MnOOH is undesirable when measuring interplanar spacings versus r in $MnOOH_r$ as it will effect the slope of these graphs (see for example section 7.2). Whether γ-MnOOH formation was by the suggested dissolution precipitation mechanism is a speculative point, though if this was the case it is likely to have been enhanced by heating. The samples produced by Fitzpatrick under milder conditions (lower temperature) by reacting cinnamyl alcohol dissolved in various 'inert' solvents still show evidence of a broad line at 26°2θ. The

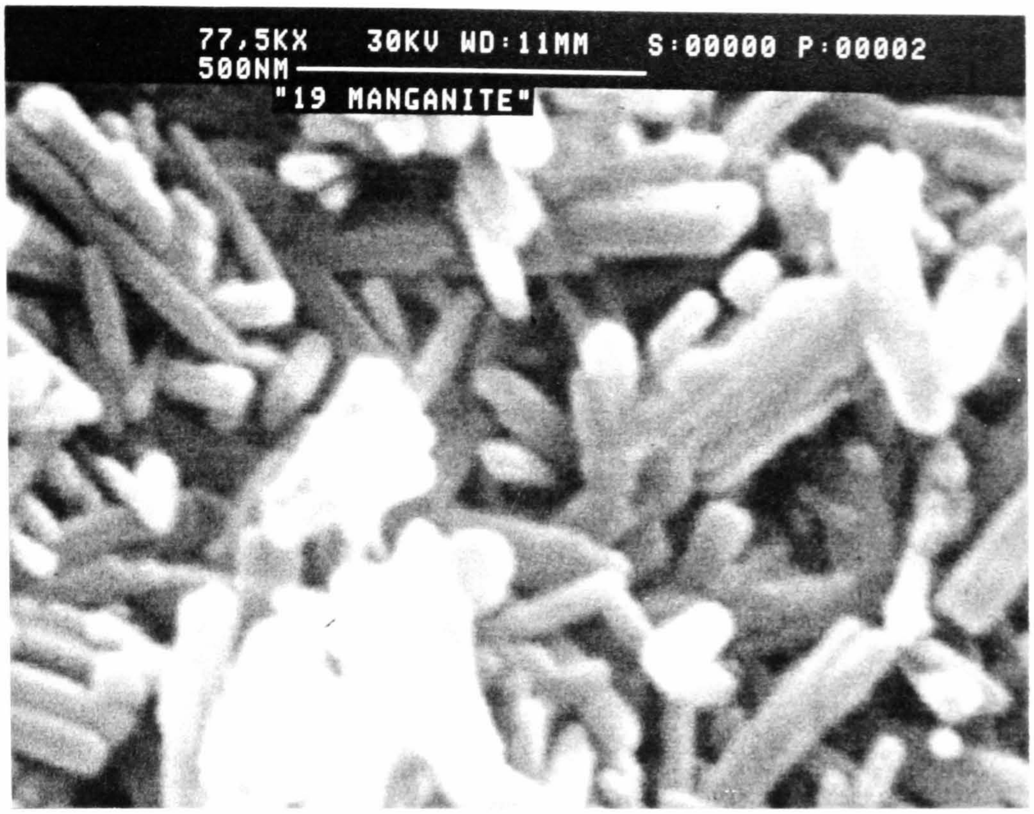

Figure 3-7 SEM picture of most reduced IBA no.19 (MnOOH$_{1.0}$) refluxed in water for 20 hours.

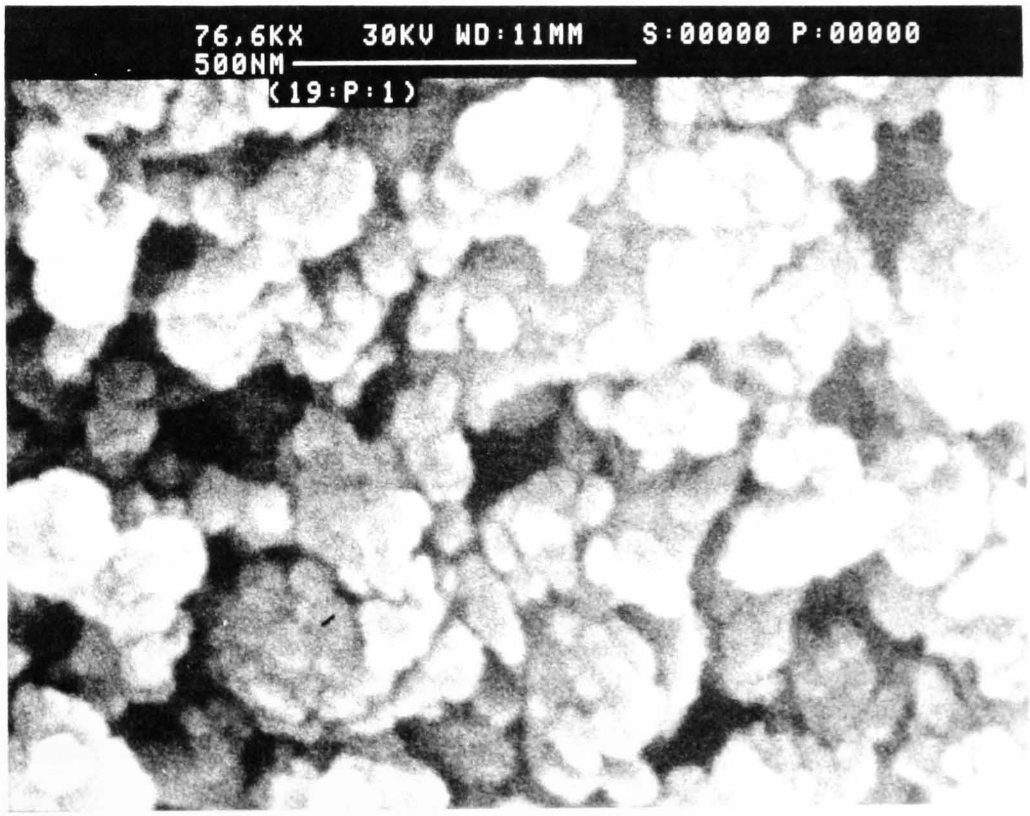

Figure 3-8 SEM photograph of 1-propanol reduced IBA no.19 (MnOOH$_{1.0}$) at same magnification as figure 3-7.

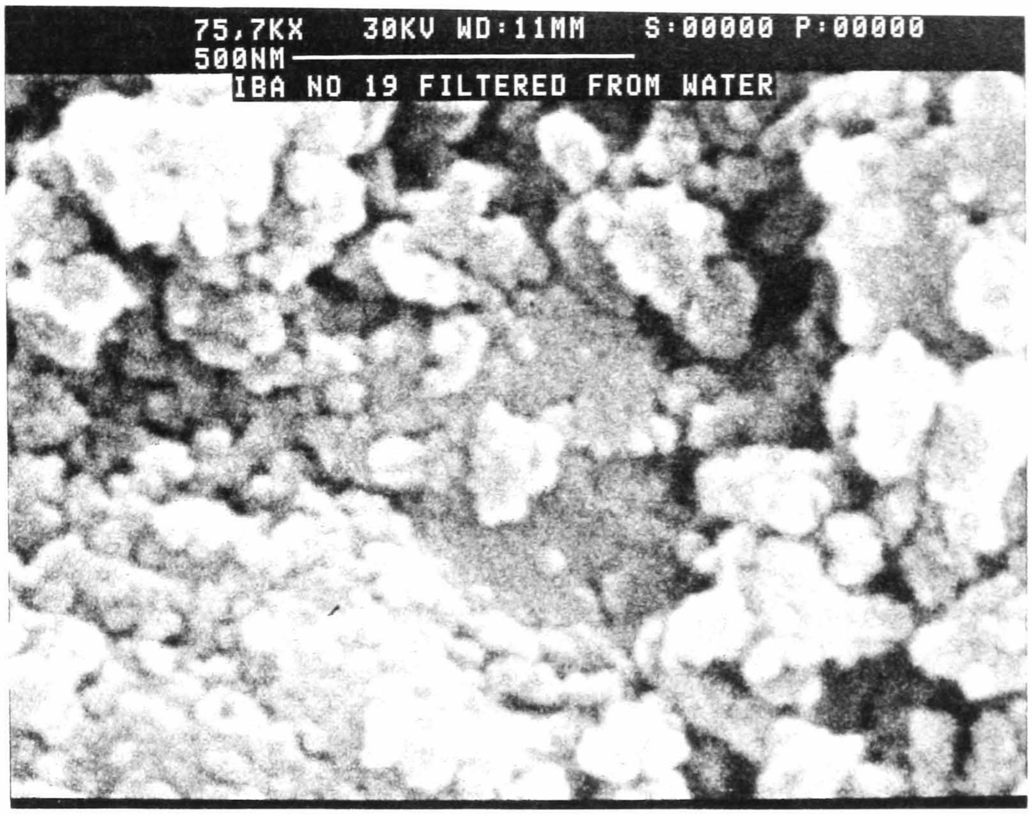

Figure 3-9 SEM picture of IBA no.19 at same magnification as figures 3-7 and 3-8.

problem may therefore be one of degree between the two set of samples (Fitzpatrick's and the samples produced in this work).

The order of reactivity of the manganese dioxides in 1-propanol was found to be (see figure 3-2):

Faradiser M > IBA no.19 > IBA no.14 > SBPA

This order correlates with the order of their BET specific areas as listed in table 8.2.

### 3.2.3 Chemical insertion of H by hydrazine hydrate suspended in hexane.

Chemical insertion of H into manganese dioxide by hydrazine hydrate in hexane was performed by J.Larcin as part of his PhD study[137] and is fully described therein. H inserted Faradiser WSZ samples produced by this method were made available to this study to form part of the x-ray diffraction analyses presented in section 7.1. The reaction of manganese dioxide with hydrazine is described by the following equation:

$$4MnO_2 + N_2H_4.H_2O \rightarrow 4MnOOH + N_2 + H_2O \qquad (3.4)$$

Although the reaction is carried out in a non-aqueous solvent evidently it cannot be a totally non-aqueous reduction of manganese dioxide since water is produced in the reaction. Despite this, the proportion of manganite in the WSZ samples was not noticeable higher than that found for the propanol reduced samples (see section 7.1).

## 3.3 Chemical analysis.

The purpose of chemical analysis in this instance was to determine the value of x in $MnO_x$ or equivalently r in $MnOOH_r$. It is easy to show that r=4-2x. The value of r or x reflects the average valence of the manganese. It was found by determining the available oxygen and total manganese content. Two methods are outlined here, both determine the manganese content by the method of Lingane and Karplus[75]. This involves titration of the manganous ion by the permanganate ion in neutral pyrophosphate solution.

### 3.3.1 Method 1, based on the method of Vetter and Jeager[76].

Approximately 0.1(g) of $MnO_x$ was dissolved for ~½ hour in $A_1$(ml) of acidified Mohr's salt solution† (~0.045(M)$(NH_4)SO_4.FeSO_4.6H_2O/4\%H_2SO_4$). The dissolution equation can be represented:

$$MnO_x + (2x-2)Fe^{2+} + 2xH^+ \rightarrow Mn^{2+} + (2x-2)Fe^{3+} + xH_2O \qquad (3.5)$$

Note that the excess ferrous ions are proportional to the oxidation state. This excess was titrated potentiometrically with ~0.01(M)$KMnO_4$ solution using to the experimental arrangement shown in figure 3-10. When not in use the calomel electrode was kept in saturated KCl solution and the platinum wire in dilute sulphuric acid. Occasionally the platinum wire was dipped in a solution of aqua regia for a few minutes in order to maintain a clean surface.

Solid sodium pyrophosphate (~15(g)) was next added to the solution and allowed to dissolve. The solution pH was now between 6 and 7. The total manganese content was titrated as $Mn^{2+}$ with same $KMnO_4$ solution, the $Mn^{2+}$ being oxidised and $MnO_4^-$ reduced to a $Mn^{3+}$ complex. The titration was performed potentiometrically (with the same apparatus) the potential jump being due to the potential of the platinum wire changing from the value determined by $Mn^{2+}/Mn^{3+}$ couple to that determined by the $Mn^{3+}/Mn^{4+}$ couple. Both of these are strongly pH dependent with the maximum

---

† Designated AMSS from now on.

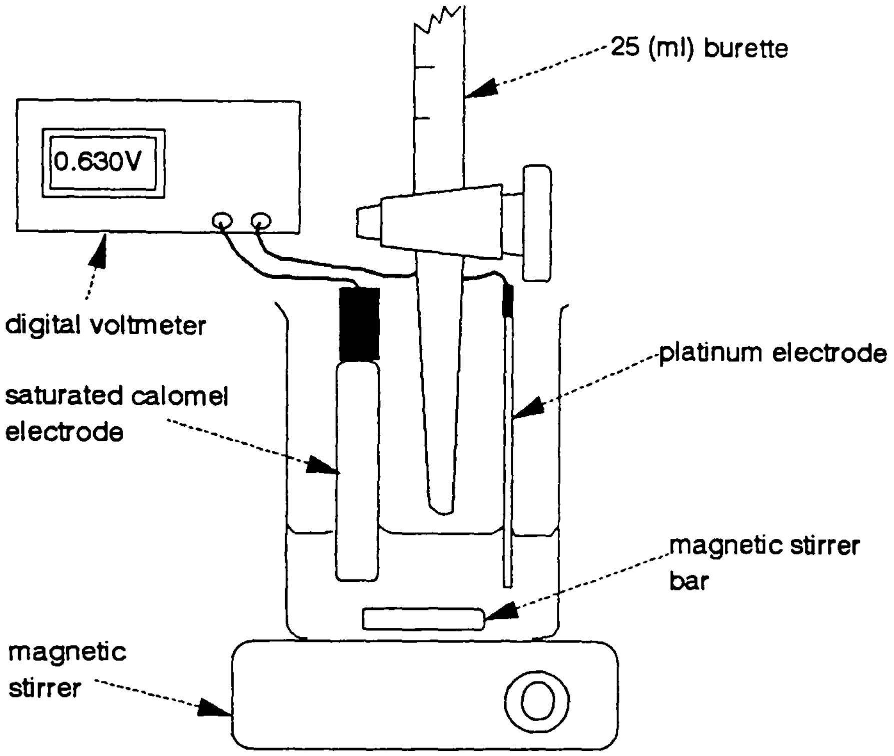

Figure 3-10 Schematic representation of titration apparatus, used in the determination of x in $MnO_x$.

potential jump occurring between pH 6 and 7. The titration equation can be represented:

$$4Mn^{2+} + MnO_4^- + 8H^+ + 15(H_2P_2O_7)^{2-} \rightarrow 5Mn(H_2P_2O_7)_3^{3-} + 4H_2O \quad (3.6)$$

If

$V_o$ = vol. of $KMnO_4$ to titrate $A_1$(ml) of AMSS

$V_1$ = vol. of $KMnO_4$ to titrate the excess $Fe^{2+}$

$V_2$ = vol. of $KMnO_4$ to titrate the total $Mn^{2+}$ content

Then it may be shown that,

$$x = 1 + \frac{5}{8}\frac{(V_o - V_1)}{(V_2 - V_1/4)} \quad (3.7)$$

If $V_0(1)$ is the volume of $KMnO_4$ which titrates $A_o$ of AMSS then the amount $V_o$ is given by

$$V_o = \frac{A_1 V_o(1)}{A_o}(\text{ml}) \quad (3.8)$$

$A_1$ was chosen such that there was a 10% excess of ferrous ions in all determinations, which can be estimated if the approximate oxidation state is known. In which case $A_1 \approx 590.4 \times (\text{mass of sample (g)}) \times (x-1)$.

### 3.3.2 Precision of x.

Regular determinations were performed with a class A 25(ml) burette and accompanying volumetric glassware. Table 3.1 collects together a series of four determinations for a number of IBA materials† and indicates that the standard deviation is such that x in $MnO_x$ is meaningfully stated e.g. for IBA no.14 x=1.957±0.003 (quoted to 2 standard deviations, which will be the practice in this work unless stated otherwise).

### 3.3.3 Accuracy of the method.

Following Maskell[77] the accuracy of the method can be checked without

Table 3.1 Four determinations of initial (i.e. as received) x in $MnO_x$ for a selection of IBA manganese dioxide common samples.

| IBA sample no. | x in $MnO_x$ | x in $MnO_x$ | x in $MnO_x$ | x in $MnO_x$ | Average x | $\delta$¶ | %rel. std. dev. |
|---|---|---|---|---|---|---|---|
| 14 | 1.959 | 1.960 | 1.955 | 1.954 | 1.957 | 0.0015 | 0.07 |
| 15 | 1.965 | 1.964 | 1.951 | 1.958 | 1.960 | 0.0032 | 0.16 |
| 17 | 1.956 | 1.955 | 1.958 | 1.949 | 1.955 | 0.0019 | 0.10 |
| 18 | 1.961 | 1.962 | 1.960 | 1.951 | 1.959 | 0.0025 | 0.13 |
| 19 | 1.965 | 1.966 | 1.963 | 1.964 | 1.965 | 0.0006 | 0.03 |
| 20 | 1.966 | 1.964 | 1.967 | 1.966 | 1.966 | 0.0006 | 0.03 |
| 23 | 1.954 | 1.954 | 1.949 | 1.954 | 1.953 | 0.0013 | 0.06 |
| 24 | 1.946 | 1.945 | 1.945 | 1.942 | 1.945 | 0.0007 | 0.04 |
| 25 | 1.947 | 1.949 | 1.950 | 1.948 | 1.949 | 0.0006 | 0.03 |
| 30 | 1.958 | 1.959 | 1.957 | 1.952 | 1.957 | 0.0015 | 0.08 |
| 31 | 1.960 | 1.961 | 1.959 | 1.959 | 1.960 | 0.0005 | 0.02 |

¶ Unless otherwise stated $\delta$ refers to the standard deviation of the mean.

---

† Undertaken as part of a round robin survey composed by the IBA to determine the reproducibility of a number of laboratory regular analysis procedures.

reference to external standards. The net ionic equation for the titration of ferrous ions in acid solution by permanganate is:

$$5Fe^{2+} + MnO_4^- + 8H^+ \rightarrow 5Fe^{3+} + Mn^{2+} + 4H_2O \tag{3.9}$$

Thus a stoichiometric quantity of $Mn^{2+}$ is produced (which is taken into account in equation (3.7)). This can be titrated with the same permanganate solution in neutral pyrophosphate solution as previously. From the stoichiometry implied by equations (3.9) and (3.6), if $M_4$ is the mass required to titrate an amount of AMSS and $M_5$ the amount titrate the $Mn^{2+}$ produced then:

$$M_4 = 4M_5 \tag{3.10}$$

Approximately 25(ml) of AMSS was accurately weighed into a clean flask. ~20(ml) of ~0.01$KMnO_4$ was weighed into the same flask and the remainder titrated with a 10(ml) burette of the same solution. Sufficient solid sodium pyrophosphate was then added to adjust the pH to 6.5 and the total manganese titrated potentiometrically with the

Table 3.2 Results for 3 determinations of K.

| $M_4$(g) | $M_5$(g) | $K=M_4/M_5$ |
|---|---|---|
| 21.029 | 5.252 | 4.004 |
| 21.856 | 5.472 | 3.994 |
| 22.739 | 5.688 | 3.998 |
| | Average | 3.999 |
| | $\delta$ | 0.003 |
| | rel. std. dev. | 0.07% |

equipment in figure 3-10 as before. The results are given in table 3.2 and indicate good agreement with the expected value determined from equation 3.10 (i.e. K=4.00±0.006).

### 3.3.4 Method 2.

The reason for presenting a different method was as follows. Method 1 has been employed successfully to a large number of EMDs and other materials. It was decided to re-analyze the set of samples produced by Fitzpatrick from the starting material R2, which also form an important part of this study. The more reduced materials smelled strongly of organic oxidation products. For a sample coded JF33 when dissolved in AMSS a sweet smell of cinnamon emanated. When the titration was performed with $KMnO_4$, as in method 1, a fading end point was observed. That is, the potential becomes increasingly unstable near the end point of the titration. When additions of $KMnO_4$ were made which produced the characteristic pink colour associated with the end point, it rapidly disappeared and the potential correspondingly decreased. Evidently another reaction was competing with the titration reaction the effect of which was enhanced in an oxidizing environment of $MnO_4^-$. This reaction was most probably due to oxidation of organic substances adsorbed on the $MnO_x$ which became dissolved in the AMSS. The result is a less reliable determination of x in $MnO_x$ as indicated by table 3.3 (compare with table 3.1). Note that normally the pink colour disappears just after the end point

Table 3.3 Experimental determinations of x in $MnO_x$ for most reduced R2 sample using method 1.

| Material code | x in $MnO_x$ |
|---|---|
| | 1.587 |
| R2 | 1.526 |
| (sample JF33) | 1.516 |
| Average | 1.543 |
| $\delta$ | 0.022 |
| rel.std.dev. | 1.44% |

if the solution was left standing but the change was slow (of the order of 10-15(mins)) probably due to the autodecomposition of $KMnO_4$ in acid solution[78].

In an attempt to minimise the influence of organics the procedures listed in table 3.4 were tried on the $MnO_x$ sample prior to titration. Surprisingly none of these procedures alleviated the fading end point problem. Instead of treating the sample a different oxidizing agent was tried. The natural choice was potassium dichromate which is less easily reduced by organic matter, it also has the advantage of being a near ideal primary standard[79]. Disadvantages include a smaller potential jump at the end point and no colour change associated with the end point because of the green colour of $Cr^{3+}$ ions (AMSS already having a green/blue colour). The reduction of potassium dichromate in

Table 3.4 Treatment of sample reduced with cinnamyl alcohol prior to x in $MnO_x$ determination by method 1.

| Sample code | Treatment of sample prior to titration. |
|---|---|
| JF33 | Washed with inert solvent ($CCl_2F.CClF_2$) |
| | Outgassed for 2 days with occasional air flushing |
| | Heated at 70(°C) during dissolution. |
| | Boiled after dissolution |

acid solution by ferrous ions may be written :

$$Cr_2O_7^{2-} + 6Fe^{2+} + 14H^+ + \rightarrow 2Cr^{3+} + 6Fe^{3+} + 7H_2O \qquad (3.11)$$

A 0.045(N) solution was prepared and the behaviour of the titration of excess ferrous ions, after dissolution of $MnO_x$, observed. This was seen to be that of a standard titration (i.e. without $MnO_x$ dissolved) but with a slow side reaction decreasing the potential on standing when $K_2Cr_2O_7$ was added beyond the end point. Thus the influence of organic matter was still present but to a lesser extent such that the titration could be performed satisfactorily.

The same fading end point behaviour was observed in the titration of the total Mn content. The following procedure, however, was found to produce satisfactory results: A sample of unknown manganese content was dissolved in excess hydrogen peroxide acidified with hydrochloric acid. The resulting solution was boiled thoroughly to remove excess $H_2O_2$ and HCl. The total manganese was then determined in neutral pyrophosphate solution with potassium permanganate as before. The organics were presumably removed by the boiling procedure.

### 3.3.5 Method 2 procedure (details).

Approximately 0.1(g) of $MnO_x$ was accurately weighed into a clean beaker and dissolved in a known weight of AMSS. The excess ferrous ions were titrated potentiometrically with ~0.045(N)$K_2Cr_2O_7$ with the same electrode arrangement as method 1 (see figure 3-10). A further 0.1(g) of $MnO_x$ was accurately weighed into a clean beaker to which was added ~1(ml) of concentrated HCl and ~2(ml)$H_2O_2$(30%). Rapid dissolution of the $MnO_x$ occurred with evolution of gas (probably $O_2$ and $Cl_2$).

One possible equation is:

$$MnO_x + 2H^+ + (x-1)H_2O_2 \rightarrow Mn^{2+} + (x-1)O_2 + xH_2O \qquad (3.12)$$

After a few minutes the beaker was covered with a wash glass and the solution boiled until only a yellowish residue remained. Care must be taken to boil the solution thoroughly to ensure all the excess $H_2O_2$ (and HCl) was removed since permanganate will oxidise $H_2O_2$. After careful washing (with distilled water) of the wash glass and beaker to ensure all the manganese collected, solid sodium pyrophosphate is added until the pH~6.5 and the manganese content was then determined as in method 1. Finally the AMSS was standardised against the dichromate solution and the permanganate against the AMSS. This procedure removed the need to have further external standards (eg. sodium oxalate) to determine the $KMnO_4$ molarity. Furthermore, since it was the value of x which was of interest and not for example the $Mn^{4+}$ or total Mn content, it does not depend on the absolute value of the $K_2Cr_2O_7$ molarity as by this procedure it effectively cancels in the calculation of x (see section 3.3.7).

### 3.3.6 Check of method 2.

A check that the second part of the method 2 was satisfactorily carried out by reacting a known quantity of $KMnO_4$ $M_4$ (25(ml)) with an excess of $H_2O_2$ which was then boiled of as described above. This in turn was titrated with the same $KMnO_4$ solution ($M_5$). From equation (3.6) this value should be exactly one fourth of the original mass. Table 3.5 presents the results of 3 such measurements.

Table 3.5 Results for 3 determinations of $K=M_4/M_5$.

| experiment | $M_5$(g) | $K=M_4/M_5$ |
|---|---|---|
| 1 | 6.226 | 4.015 |
| 2 | 6.236 | 4.009 |
| 3 | 6.230 | 4.012 |
| | Average | 4.012 |
| | $\delta$ | $0.001_7$ |
| | rel. std. dev. | 0.043% |

The results indicate that method 2 could not be as accurate as method 1 due to a systematic error but was equally reproducible. It can be shown that effect of the systematic error was to change the value of x in a typical analysis by +0.003. Despite this it was still the preferred method for materials reduced with cinnamyl alcohol (see section 3.3.9).

### 3.3.7 Calculation of x in $MnO_x$.

If b is the number of moles of manganese per 100(g) of sample then

$$b = \frac{m \times M_K \times 100 \times 4}{1000 \times W} \tag{3.13}$$

where $M_K$ = molality of $KMnO_4$ solution ($molKg^{-1}$)

m = mass of $KMnO_4$ solution to titrate sample (g)

w = mass of sample (g)

Similarly, a, the available oxygen per 100(g) of sample is given by

$$a = \frac{\Delta V \times M_{K2} \times 100 \times 6}{1000 \times W} \tag{3.14}$$

where $\Delta V$ = the difference between the quantity of dichromate used to titrate the AMSS taken to dissolve the sample and that required to titrate the excess AMSS.

$M_{K2}$ = molarity of the potassium dichromate solution ($moldm^{-3}$).

w = mass of sample (g).

Noting that 2x-2 electrons are transferred for every $MnO_x$ in equation (3.5) then

$$a/b = 2x-2$$

$$\Rightarrow x = \frac{1}{2}\left(\frac{a}{b}+2\right) \tag{3.15}$$

### 3.3.8 Method of end point determination.

In all of the titrations described the end point was determined by noting the volume additions and voltages near the end point and calculating $\Delta E/\Delta V$. The volume reading mid-way between those giving the maximum value of $\Delta E/\Delta V$ was taken as the end point. It was known when the titration was near to the end point by referring to previously obtained graph of E versus V. A curve of a typical titration is shown in figure 3-11 and a plot of $\Delta E/\Delta V$ in figure 3-12.

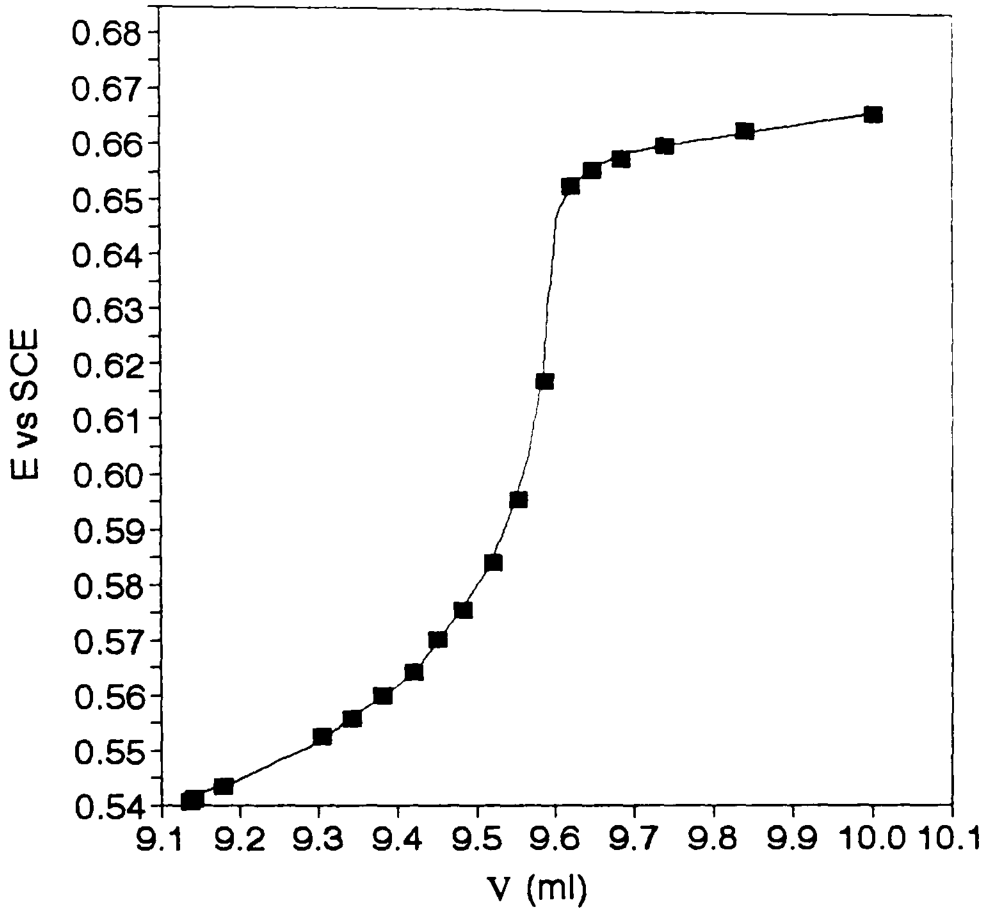

Figure 3-11 Potentiometric titration curve for AMSS (~0.045(M)) with $K_2Cr_2O_7$ (0.01(M)).

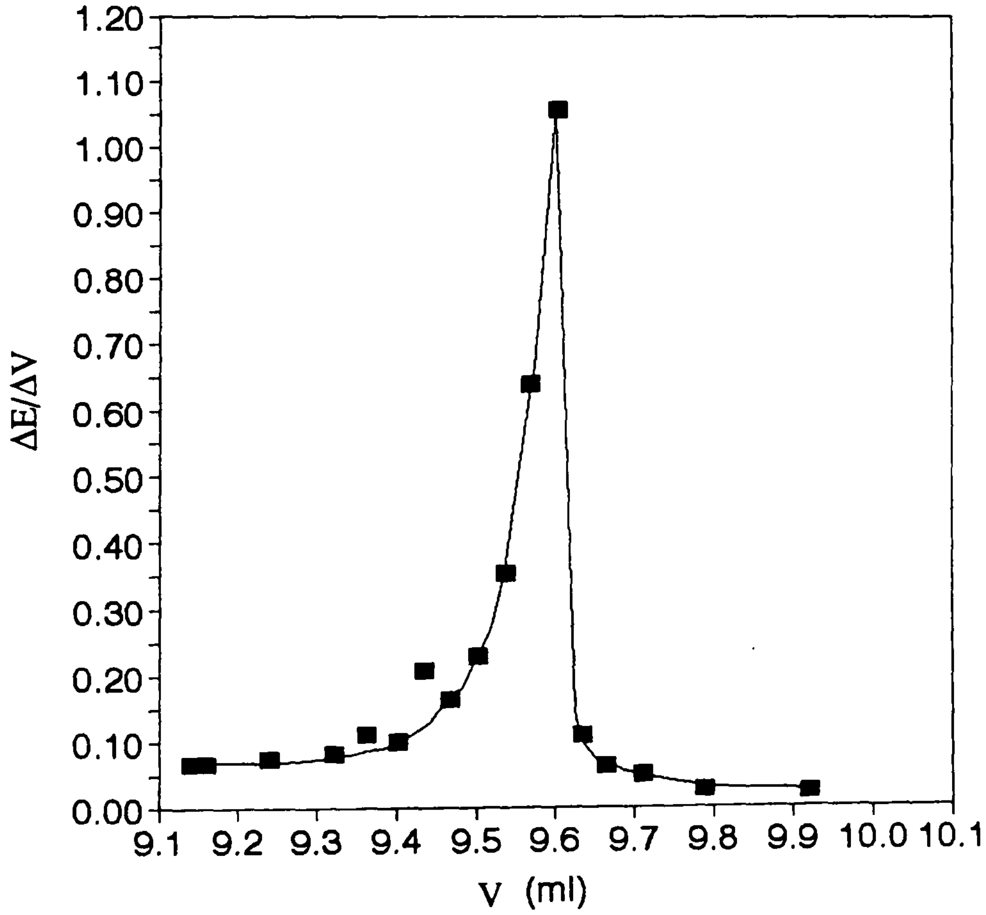

Figure 3-12 $\Delta E/\Delta V$ versus V for the titration of $Fe^{2+}$ with $Cr_2O_7^{2-}$ i.e. 1st derivative of E vs. V curve shown in figure 3-11.

In the calculation of x it has been assumed that the end point, as determined by the above method, corresponded to the stoichiometric end point. Figure 3-12 displays the unsymmetrical shape of the titration curve. Asymmetric curves derive from the fact that the number of ions titrated by the reagent added to the substance to be titrated are unequal[80]. For example equations (3.6) and (3.9) indicate that one $MnO_4^-$ ion reacts with $4Mn^{2+}$ and $5Fe^{2+}$ ions respectively. In methods 1 and 2, however, the titration errors have a tendency to cancel each other in the calculation of x in $MnO_x$ and therefore their effect was considered to be small. Furthermore the titration error is smallest when the potential jump at the end point is large. To increase the potential jump for the available oxygen titration (for methods 1 and 2) phosphoric acid was added which reduced the potential jump of the $Fe^{3+}/Fe^{2+}$ couple by complexation.

### 3.3.9 Results of method 2 analysis on samples prepared by J.Fitzpatrick.

Table 3.6 presents the results of three determinations of x on a selection of reduced R2 samples by the method 2 analysis. From a consideration of the standard deviations of $a_{av}$ and $b_{av}$ the value of x for sample R2 equals $1.95_1 \pm 0.007$ and for sample JF33 $x=1.52_3 \pm 0.004$. The values are thus considerably more precise than that obtained by method 1 analysis of sample JF33 (see table 3.3). The analysis results obtained are compared with the values determined previously by Fitzpatrick (by method 1, see table 3.3). The results are similar for reduced samples down to an oxidation level of $MnO_{1.75}$, indicating that these samples were analyzed by Fitzpatrick a sufficiently greater number times by the less precise method 1 analysis (for cinnamyl reduced samples only, see table 3.3) to compensate for the imprecision. Below $MnO_{1.75}$ an increasing discrepancy between the two sets is observed. The direction of the discrepancy is constant and consistent with aerial oxidation of the deeply reduced samples. It was noticed when plotting the potential versus x in $MnO_x$ that the results determined in this work produced a smoother curve in the potential versus x in $MnO_x$ (see chapter 8) for the deeply reduced samples than if they were plotted against Fitzpatrick's original analysis.

### 3.3.10 Preparation of solutions.

All reagents employed were of 'Analar' grade.

0.05(N) potassium dichromate (accurately).

Table 3.6 Comparison of results to determine x in $MnO_x$ for cinnamyl alcohol reduced R2 samples by method 1 and those determined by Fitzpatrick (method 1).

| sample | a avl.O (moles per 100(g)) | b tot. Mn (moles per 100(g)) | $a_v$ aver. a (moles per 100(g)) | $b_v$ aver. b (moles per 100(g)) | x = ½(a/b+2) | $x_{JF}$ method 1 (from Fitzpatrick) | $x_{JF}$-x |
|---|---|---|---|---|---|---|---|
| R2 | 2.061<br>2.043<br>2.044 | 1.087<br>1.079<br>1.067 | 2.049 | 1.078 | 1.950 | 1.945 | -0.005 |
| JJF16 | 1.920<br>1.923<br>1.942 | 1.071<br>1.075<br>1.067 | 1.928 | 1.071 | 1.900 | 1.888 | -0.012 |
| JJF4 | 1.813<br>1.814<br>1.825 | 1.071<br>1.075<br>1.071 | 1.817 | 1.072 | 1.847 | 1.849 | +0.002 |
| JF14 | 1.688<br>1.693<br>1.695 | 1.067<br>1.065<br>1.061 | 1.692 | 1.064 | 1.795 | 1.801 | +0.006 |
| JF8 | 1.634<br>1.566<br>1.618 | 1.062<br>1.062<br>1.062 | 1.606 | 1.062 | 1.756 | 1.749 | -0.007 |
| JF11 | 1.559<br>2.153<br>1.549 | 1.069<br>1.071<br>1.065 | 1.554 | 1.069 | 1.727 | 1.697 | -0.030 |
| JF22 | 1.458<br>1.478<br>1.488 | 1.076<br>1.074<br>1.084 | 1.475 | 1.078 | 1.684 | 1.646 | -0.038 |
| JF26 | 1.393<br>1.395<br>1.427 | 1.060<br>1.076<br>1.072 | 1.405 | 1.069 | 1.657 | 1.601 | -0.083 |
| JF30 | 1.268<br>1.290<br>1.281 | 1.077<br>1.087<br>1.076 | 1.280 | 1.080 | 1.593 | 1.552 | -0.041 |
| JF33 | 1.117<br>1.104<br>1.101 | 1.067<br>1.049<br>1.061 | 1.107 | 1.059 | 1.523 | 1.496 | -0.027 |

Approximately 6(g) of solid potassium dichromate was heated at 140-150(°C) in an agate mortar for 45 minutes and allowed to cool in a desiccator. 2.45(g) was then accurately weighed into a clean 1 litre volumetric flask with a suitable weighing bottle. The weight delivered was obtained by difference. Distilled water was added and the flask shaken thoroughly before making up to the mark. The resulting normality was calculated from the weight delivered to the flask.

0.01(M) potassium permanganate (approximately).

Sufficient solid potassium permanganate was added to a clean 1 litre beaker and distilled water added. The solution was stirred and boiled gently for about half an hour, allowed to cool, then transferred to a 5 litre volumetric flask and made up to the mark. The resulting solution was then transferred with filtering to two darkened 2.5 litre storage bottles. Homogenisation of the solution for at least 48 hours was allowed before use.

0.05(N) AMSS (approximately)

~88.25(g) of $(NH_4)_2SO_4.FeSO_4.6H_2O$ was dissolved in distilled water in a clean 1 litre flask, to which was slowly added 200(ml) of concentrated $H_2SO_4$. After cooling the solution was transferred to a 5 litre volumetric flask and made up to the mark. The resulting solution was then transferred to two 2.5 litre darkened storage bottles.

Cleaning of glassware

All glassware was cleaned regularly in an ultrasonic bath containing a solution of 5% Decon 90 (in distilled water) and washed thoroughly first with tap water and then with distilled water. Occasional cleaning with 'chromic acid' was also employed. Storage bottles were wetted with chromic acid several hours before washing and drying. Deposits of manganese dioxide (eg. from glassware containing potassium permanganate) were removed with a mixture with hydrogen peroxide and acid.

### 3.3.11 Conclusions.

Although method 2 provided a more accurate determination of x in $MnO_x$ for cinnamyl alcohol reduced R2 samples it was considerably less elegant than the double titration method of Vetter and Jeager[76] (method 1). Method 2 requires two titrations performed on separate accurately weighed samples whereas Vetter and Jeager's method does not require accurate knowledge of the sample weight or the concentration of the reagent solutions.

Fortunately it was discovered that the propanol and butanol reduced samples

Table 3.7 Chemical analysis of IBA no.14 propanol reduced samples to determine x in $MnO_x$ by method 1 (see section 3.3.1).

| Sample No. | 1st analysis of x. | 2nd analysis of x. | average |
|---|---|---|---|
| 1 | 1.958 | 1.958 | 1.958 |
| 2 | 1.934 | 1.933 | 1.933 |
| 3 | 1.906 | 1.903 | 1.905 |
| 4 | 1.891 | 1.884 | 1.887 |
| 5 | 1.882 | 1.879 | 1.881 |
| 6 | 1.849 | 1.848 | 1.849 |
| 7 | 1.830 | 1.827 | 1.829 |
| 8 | 1.849 | 1.848 | 1.849 |
| 9 | 1.806 | 1.805 | 1.805 |
| 10 | 1.804 | 1.798 | 1.801 |
| 11 | 1.797 | 1.797 | 1.797 |
| 12 | 1.779 | 1.779 | 1.779 |
| 13 | 1.779 | 1.778 | 1.779 |
| 14 | 1.763 | 1.763 | 1.763 |
| 15 | 1.755 | 1.753 | 1.754 |
| 16 | 1.738 | 1.735 | 1.737 |
| 17 | 1.719 | 1.713 | 1.716 |
| 18 | 1.710 | 1.708 | 1.709 |
| 19 | 1.708 | 1.707 | 1.707 |
| 20 | 1.692 | 1.692 | 1.692 |
| 21 | 1.695 | 1.680 | 1.687 |
| 22 | 1.680 | 1.679 | 1.679 |
| 23 | 1.656 | 1.657 | 1.657 |
| 24 | 1.653 | 1.652 | 1.653 |
| 25 | 1.629 | 1.631 | 1.630 |
| 26 | 1.594 | 1.593 | 1.593 |
| 27 | 1.595 | 1.592 | 1.593 |
| 28 | 1.586 | 1.587 | 1.587 |
| 29 | 1.513 | 1.516 | 1.515 |
| 30 | 1.503 | 1.507 | 1.505 |

produced in this work did not interfere with the Vetter and Jaeger analysis method to determine x in $MnO_x$. It was therefore considered that two analyses of each sample were sufficient to obtain an accurate determination of the oxidation level for these samples. Table 3.7 collects together an example of a set of analysis performed on propanol reduced IBA no.14 samples.

## 3.4 X-ray diffraction.

### 3.4.1 Instrument description and setup.

Philips PW 1700 series XRD system with the following specifications:

High voltage constant potential generator (PW 1730/10).
Vertical goniometer (PW 1050/81).
Graphite monochromator (PW 1752/00).
Proportional scintillation counter (PW 1711/10)
Automatic sample changer (PW 1170/10).
PW 1700 diffractometer control computer, with link to APD 1700 software running on a Vax mainframe computer.

Instrument setup:

Copper target broad focus x-ray tube (PW 2253/20).
1° divergence slit, 1° scatter slit, 0.1mm divergence slit.
Generator settings, 45kV, 55mA.
Step scans were generally used between 15-80°2θ with a step size of 0.01°2θ and 1s counting time.

The instrument parameters listed above were arrived at after investigating a number of factors which could easily be changed without specialized technical knowledge of the instrument. The above statement assumed that the goniometer was correctly aligned and refers to factors which do not require a complete re-alignment after adjustment. Correct alignment is critical to the attainment of optimum resolution, maximum intensity and correct angular 2θ readings and was performed prior to this investigation by an experienced Philips engineer.

The factors investigated were the type of tube, the receiving slit width and whether or not a β-filter should be employed. The goal was to obtain the best compromise between intensity and the resolution required for the desired measurements on a typical material under study such as EMD IBA no.19. Figure 3-13 is an example of the powder x-ray diffraction pattern of IBA no.19 compared with that of potassium chloride, using the same scan conditions. Compared to KCl, which is a highly crystalline material, the x-ray diffraction maxima of IBA no.19 are weak and considerably broader.

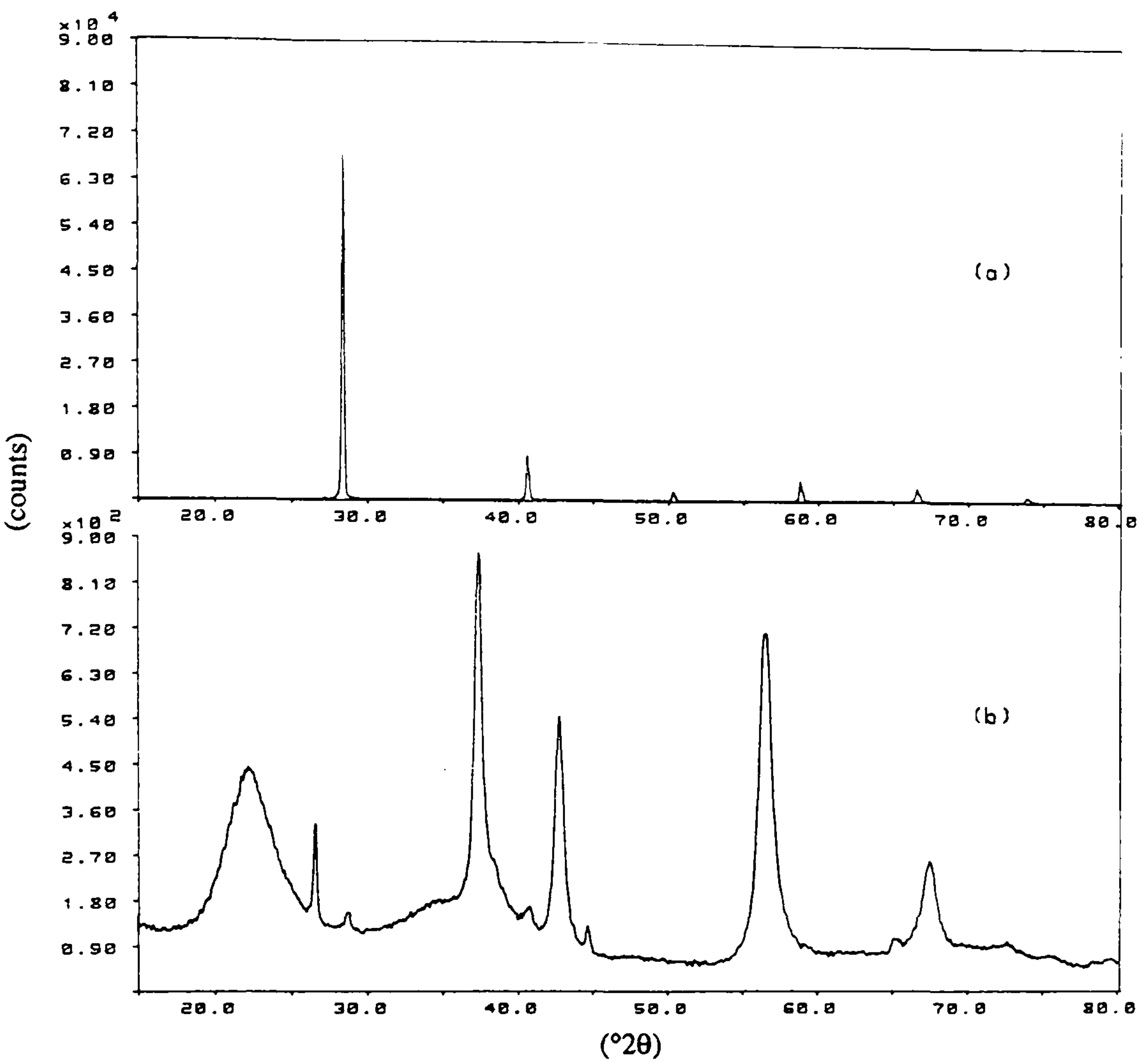

Figure 3-13 X-ray diffraction comparison of (a) 'Analar' Kcl and (b) electrodeposited manganese dioxide, R2, using the same scan conditions. Note counts scale of (a) is 100x that of (b).

The weakness of the pattern is the major concern in determining the instrumental set up.

Two factors which were fixed from the outset were the generator kV and mA settings. The kV was set in accordance with the "optimum kV" for a constant potential generator employing a copper target tube[81]. The mA setting was then adjusted such that the power output was slightly below the maximum rating of the tube (2700W).

The choice of CuKα radiation† is well suited to the study of manganese containing compounds provided a modern crystal monochromator is employed. Thus although Mn fluorescence may be expected from irradiation with CuKα (leading to a contribution to the background radiation) since $\lambda_{CuK\alpha}$=1.5418(Å), which is below the K edge of Mn (1.8964(Å))[82], the monochromator is capable of significantly reducing its effect. That this is so is clearly demonstrated in reference 81 page 17 which compares 3 methods of monochromatisation (namely, β-filtering, pulse height selection,

---

† With regard to this question the ideal type of target for the x-ray tube would be that of Mn since "no element is capable of exciting its own fluorescence"[54].

and a graphite monochromator, similar to the one fixed on the instrument used in this work) when CuK$\alpha$ was used on a sample of high iron content which would be expected to cause considerable Fe fluorescence (as the K edge[82] of Fe is 1.7435(Å) which is only slightly above that of $\lambda_{CuK\alpha}$). The graphite monochromator was clearly superior and leads to a higher figure of merit and intensity compared to the other methods.

In an attempt to optimise the intensity versus resolution of the system smaller and larger receiving slits than a 0.1(mm) were tried. The resolution of the system may be tested by a slow continuous scan (⅛(°2$\theta$min$^{-1}$)) on a strain free powdered wolfram sample[83] at 40(°2$\theta$) with a time constant[†] less than 4(s). At this angle the (110) K$\alpha_1\alpha_2$ doublet should just start to be resolved. In this work it was considered more appropriate to perform slow scans on a well defined $\beta$-MnO$_2$ sample in the angular ranges 37.1 - 38.1 and 40.8 - 41.6 (°2$\theta$) which respectively contain well defined (101) and (111) peaks. These scans were compared with 0.05, 0.1 and 0.2(mm) receiving slits in place.

For a broad focus tube the focal breadth, B, equals 2(mm) and the beam width W=Bsin$\alpha$, where $\alpha$=take off angle. If $\alpha$=6° then W=0.2(mm) which would be the optimum receiving slit size. In this case, however, 0.1(mm) receiving slit produced a intensity similar to that obtained with a 0.2(mm) slit suggesting that the take off angle was less than 6°. With the 0.05(mm) slit in place a dramatic loss in intensity with hardly any observable increase in resolution was observed.

A similar conclusion was reached when the type of tube was changed from a broadfocus example to that of a fine focus design, namely a considerable loss in intensity with no observable benefits to compensate. Thus the only effect was to considerably lengthen scan times to obtain a scan with same statistical accuracy which looked virtually identical to that obtained with a broad focus tube.

### 3.4.2 Sample considerations.

This section is concerned with the necessary groundwork which must be carried out whenever an examination of a previously unencountered material by powder x-ray diffraction is attempted. The object was to determine, in particular, whether the sample

---

[†] This time constant referred to controls the response of the chart recorder device. Later work employed a digital storage system and step scanning which completely removes this possible source of distortion to peak shapes.

suffered from a large degree of preferred orientation, which would obviously affect the reproducibility of peak intensity and position measurements. It was the latter measurement which was of primary importance in this work.

The variables which were changed were the method of sample preparation and the particle size distribution of the powder. The first was fixed by adopting a 'back filling method' similar to that described during a course organised by Philips Scientific (described below). The effect of varying the particle size was then investigated on both the magnitude and reproducibility of intensity measurements. This is known to have a large effect on quartz powders[84]. The easiest way of reducing average particle size is to sieve the material. This procedure was not considered for normal measurement since it risked excluding information due to the possible association of different phases with different particle sizes. Sedimentation procedures were therefore also excluded (sedimentation, for example, was found to lead to an increase in the $\beta$-$MnO_2$ impurity content present in nearly all EMDs). Only the effects of dry grinding were investigated.

### 3.4.3 Sample preparation.

Samples to be analyzed were carefully filled into the back of a standard aluminum diffraction holder (rectangular type) previously fixed with sticky tape against a clean microscope slide. The powder was lightly packed in with a spatula and filled such that a slight even excess protruded from the cavity. This was pressed in firmly with another microscope slide and the excess sliced off with a cover glass and a backplate fitted. Cleaning of the diffraction holders was best carried out with an ultrasonic bath filled with approximately 5% Decon 90. Occasional cleaning with a acid/hydrogen peroxide mixture was also employed.

### 3.4.4 Experimental procedure for grinding experiment.

About 10g of R2 was ground in an agate pestle and mortar for periods of 5 - 30 minutes in steps of five minutes. Ten samples were prepared for each time period and the net intensity of peak B (see figure 6-10) determined by an integration procedure with background subtraction. The time in the peak was 600(s) and in the background 48(s).

### 3.4.5 Results of grinding experiment.

See table 3.8.

Table 3.8 Integrated intensity variation of peak B with grinding time for material R2.

| No. | $G_o$ (0min) | $G_1$ (5min) | $G_2$ (10min) | $G_3$ (15min) | $G_4$ (20min) | $G_5$ (25min) | $G_6$ (30min) | S¶ ≤38μm |
|---|---|---|---|---|---|---|---|---|
| 1 | 24.20 | 40.05 | 43.00 | 40.47 | 34.44 | 33.97 | 34.47 | 61.14 |
| 2 | 30.82 | 41.17 | 38.95 | 40.27 | 29.36 | 30.22 | 31.37 | 59.48 |
| 3 | 31.09 | 40.32 | 36.56 | 38.17 | 30.38 | 32.06 | 30.56 | 59.47 |
| 4 | 28.04 | 40.76 | 41.00 | 41.57 | 33.52 | 31.60 | 29.87 | 59.18 |
| 5 | 26.99 | 38.57 | 40.86 | 40.57 | 31.50 | 32.86 | 30.48 | 62.57 |
| 6 | 30.29 | 38.32 | 43.41 | 35.48 | 33.13 | 30.97 | 28.69 | 60.91 |
| 7 | 28.74 | 39.19 | 37.24 | 33.15 | 32.48 | 29.36 | 28.11 | 61.17 |
| 8 | 29.93 | 43.03 | 38.61 | 30.81 | 34.18 | 34.75 | 32.00 | 58.79 |
| 9 | 30.24 | 38.89 | 38.90 | 32.79 | 33.31 | 31.96 | 32.46 | 60.69 |
| Av. | 28.59 | 39.99 | 39.69 | 35.83 | 32.51 | 31.97 | 30.81 | 60.27 |
| $\delta_{n-1}$‡ | 2.28 | 1.58 | 2.30 | 2.46 | 1.34 | 1.71 | 1.86 | 1.28 |
| %std. dev. | 8.0 | 3.9 | 5.8 | 6.9 | 5.0 | 5.3 | 6.0 | 2.1 |

¶ passed through a 400 mesh sieve. Note $G_o$-$G_6$ carried out with a fine focus tube whereas S was measured with a broad focus tube (higher intensity).

## 3.4.6 Statistical expectations (i.e. expected uncertainty due only to the amount of counts collected).

For sample $G_o$ the average counts collected under the peak was ≈27000 and in the background 768 counts. If

$$\delta_T = \sqrt{27000} = 164.3(c)$$

and

$$\delta_b = \sqrt{768} = 27.7$$

then the standard deviation in the net peak is,

$$\delta_p = (\delta_t^2 + \delta_b^2)^{\frac{1}{2}} = (27000+768)^{\frac{1}{2}} = 166.6(c)$$

and the percentage standard deviation is therefore,

$$\frac{166.6}{27000-768}\times 100 = \underline{0.63\%.}$$

Similarly for $G_1$ the rel.std.dev. = 0.55% and for S it is 0.44%.

---

‡ where $\sigma_{n-1} = \sqrt{\frac{1}{N-1}\sum_{i=1}^{N}(x_i-\bar{x})^2}$

### 3.4.7 Discussion.

Table 3.8 indicates a large contribution to the uncertainty due to the state of the sample material, which may be deduced from comparing the expected standard deviation with the observed value i.e. expected 0.63%, observed 8.0%. It also demonstrates that after an initial increase in reproducibility (after 5 min grinding) no further increase may be expected.

If the sample thickness is thick enough to produce a diffracted beam of maximum intensity (see appendix C) then figure 5-43 in reference 54 for typical experimental conditions is valid. This is a graph of percentage mean deviation (based on a Laplacian probability equation) versus crystallite size. From this graph with $\mu_{MnO2}$ (linear absorption coefficient) equal to 760(cm$^{-1}$) then for a 6% mean deviation the crystallite size is slightly less than 10 microns.

The effect of grinding on the particle size population is clearly seen from figures 3-14, 3-15 and 3-16. The main qualitative effect being to crush the larger particles (~70 - 200μm). Grinding for 5 - 30 mins probably does not affect the crystallite size but may help to increase the 'randomness' of the crystallites by 'freeing' them from large particles. Prolonged grinding would be required to bring the effective crystallite size to less than 5(μm) required for a percentage mean deviation of 1% (see fig.5-43 ref.54). That it is the case that further grinding would increase reproducibility further is supported by the increase obtained from sieving the sample (see table 3.8, column S).

### 3.4.8 Conclusions.

It has been appraised that highly reproducible ($\leq$1%) intensity measurements on a typical commercial EMD cannot be expected when employing a standard sample mounting procedure. The effect of grinding is found to be small probably because although grinding reduces preferred orientation, by 'freeing' crystallites from large particles, it only requires a small amount to be present at the surface exposed to x-rays to have a comparatively large effect on the reproducibility. It is noted that the effects of preferred orientation are in fact small compared to many other materials since the particles do not exhibit any particular external habit as demonstrated in the SEM pictures figures 3-14, 3-15 and 3-16, unlike for example mica. In this work, as it is line position which is of most interest, further investigation into reproducible intensities was not pursued because, as has been demonstrated, large degrees of preferred orientation were

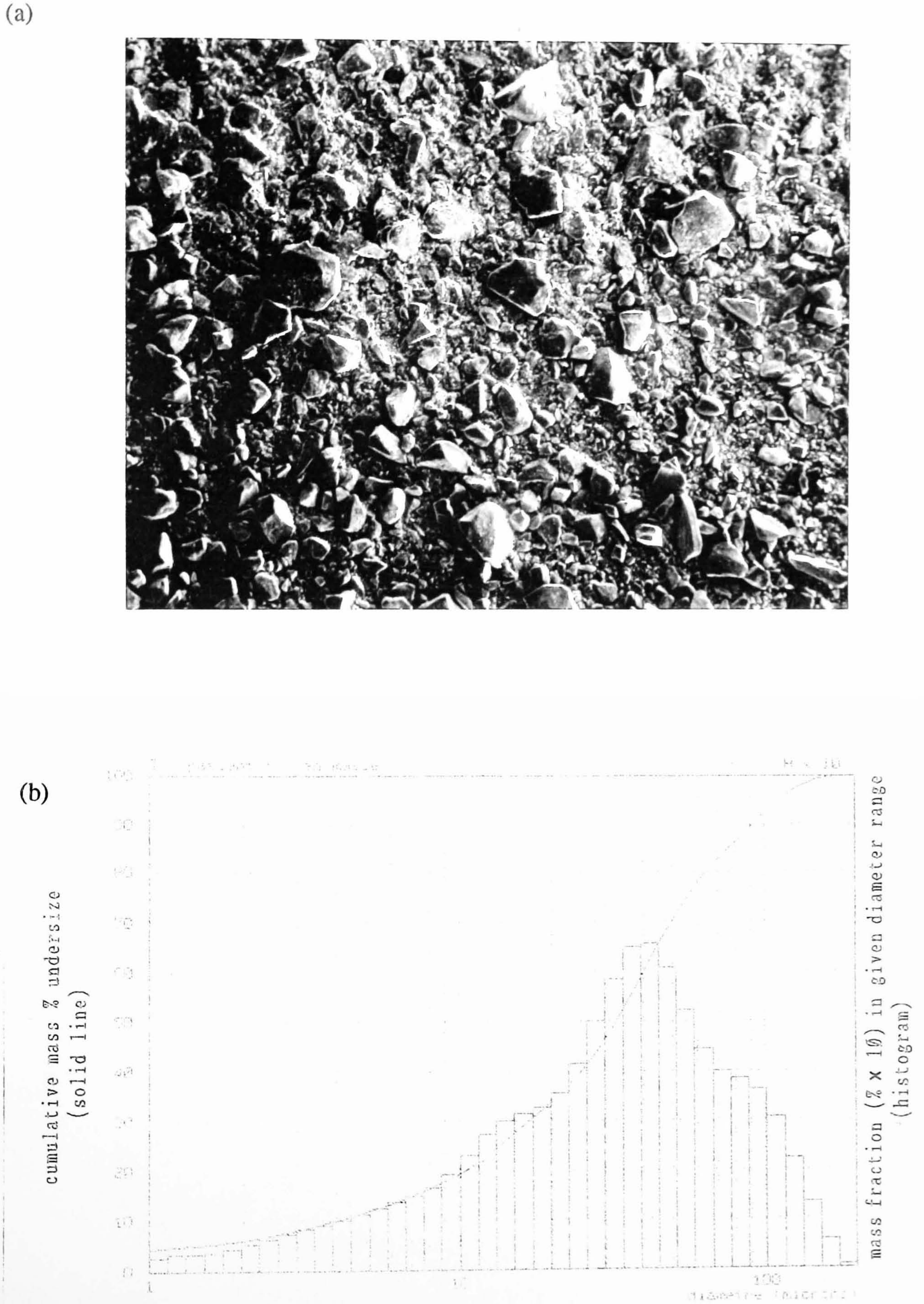

Figure 3-14 Sample $G_o$, unground R2, (see table 3.8) (a) SEM picture, ×50 magnification (b) Particle size distribution.

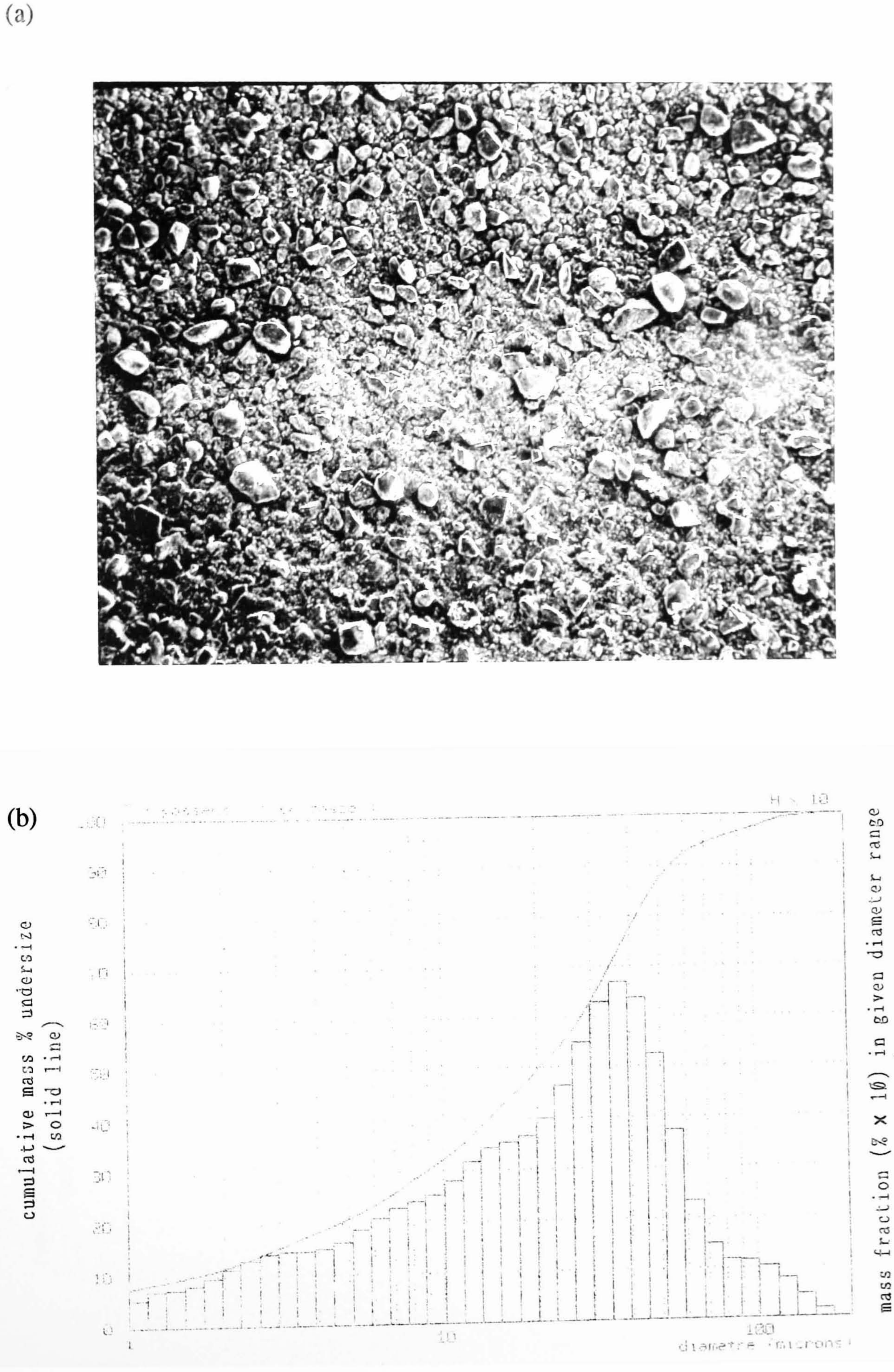

Figure 3-15 Sample $G_3$, R2 ground for 15 minutes, (see table 3.8) (a) SEM picture, ×50 magnification (b) Particle size distribution.

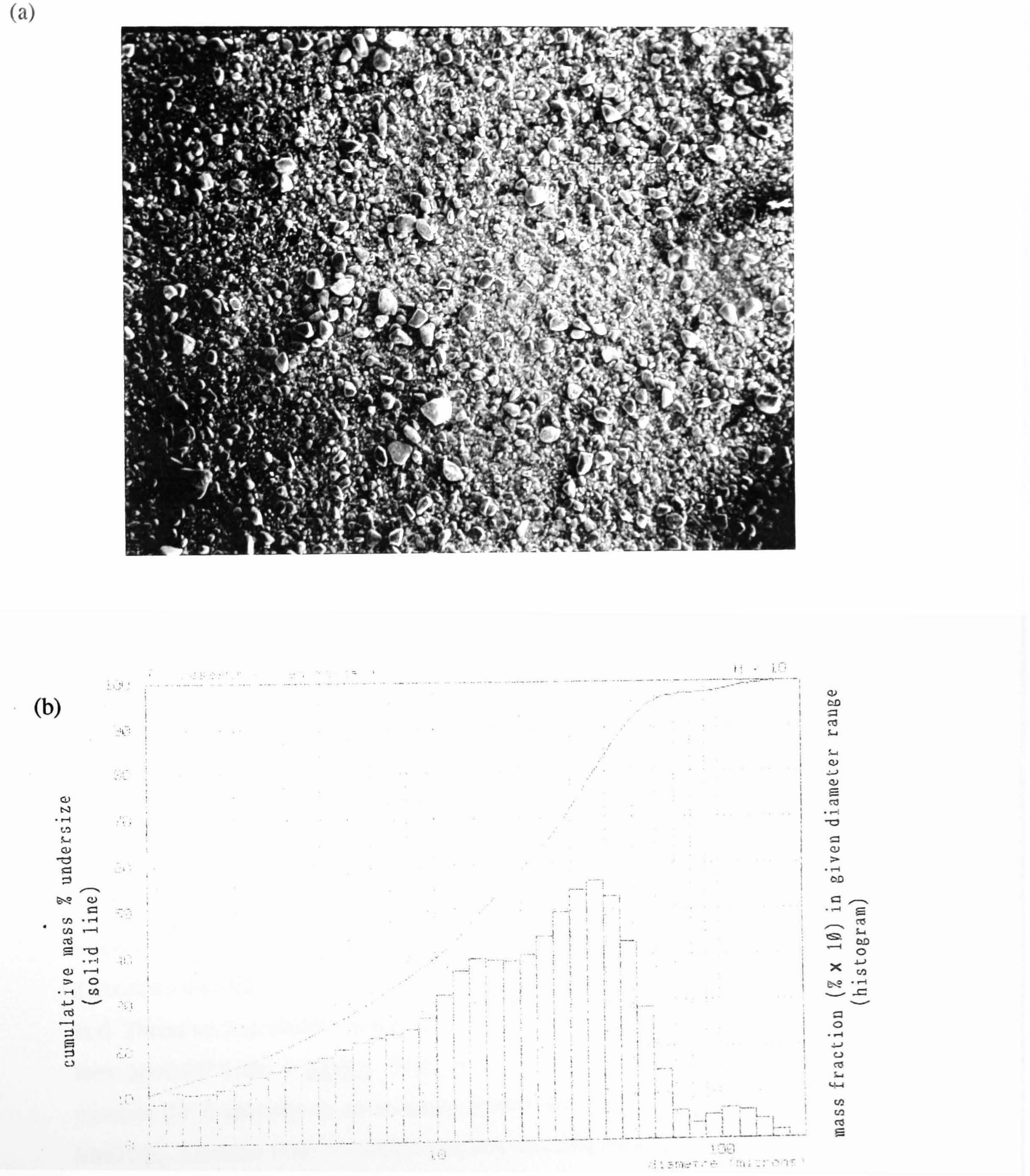

Figure 3-16 Sample $G_6$, R2 ground for 30 minutes (see table 3.8) (a) SEM picture,×50 magnification (b) Particle size distribution.

absent. Powders for analysis were, unless otherwise stated, simply ground for 3 mins.

## 3.5Measurement of d spacings versus H insertion level.

### 3.5.1 Introduction.

d (interplanar spacing) is the fundamental parameter measured by obtaining the angular 2θ position from a powder x-ray diffraction maxima. By measuring d versus x in $MnO_x$ or (r in $MnOOH_r$) insight may be obtained into changes in structure which occur during dilation with H insertion in a manganese dioxide. In general sharp changes in slope or discontinuities in the lattice parameters of a solid solution with composition may be connected with changes in symmetry of the crystal lattice[85]. Evidence of a similar type of behaviour has already been accumulated for a typical commercial manganese dioxide[68] (designated R2 in the publication and here). See chapter 6 for the reasons why in this case the changes in slope cannot be interpreted as symmetry changes.

### 3.5.2 Method of measuring d.

The precision with which lattice constants (or d spacings) can be measured can be reduced to almost negligible proportions (0.003%) if one is prepared to expend enough effort, provided the material has sharp x-ray lines[86]. This is not the case with EMD or CMD which have characteristic broad lines (see figure 3-13). It was therefore necessary to assess what limits of accuracy were required and can be achieved for this study. Neglecting peak E, (whose breadth precludes accurate measurement (see figure 3-13)) for a typical EMD the peaks which were observable throughout the H insertion range fall into two approximate categories. Namely those that shifted approximately 0.05(Å) (peaks A and B) and those that shifted 0.10(Å) (peaks C and D) when H was inserted. Taking the smallest shift, namely 0.05(Å), if a linear relationship between r and d obtained then the error derived in section 3.3.2 for r could be considered as an error in d. Therefore if $\Delta r=0.006$ (as for IBA no.14, see section 3.3.2, as $r=4-2x \Rightarrow |dr|=2dx$) then $\Delta d=0.05*0.006 = \underline{0.0003}$. Thus, as a first estimate, it would be unnecessary to measure the d spacings to an accuracy greater than ±0.0003 due to the error in r in $MnOOH_r$. Consider table 3.9 which indicates that four measures on material IBA no.19 of peak B produced an average in which the error (for twice the standard deviation of

Table 3.9 Four measures of peaks B,C and D with and without correction against an internal KCl standard.

| no. | peak D (Å) | peak D corr. (Å) | peak C (Å) | peak C corr. (Å) | peak B (Å) | peak B corr. (Å) |
|---|---|---|---|---|---|---|
| | | IBA no.19 (x=1.959) | | | | |
| 1 | 2.4090 | 2.4133 | 2.1141 | 2.1167 | 1.6273 | 1.6295 |
| 2 | 2.4107 | 2.4141 | 2.1148 | 2.1171 | 1.6274 | 1.6289 |
| 3 | 2.4104 | 2.4138 | 2.1143 | 2.1164 | 1.6277 | 1.6292 |
| 4 | 2.4099 | 2.4133 | 2.1155 | 2.1176 | 1.6280 | 4.6263 |
| av. | 2.4100 | 2.4136 | 2.1147 | 2.1169 | 1.6276 | 1.6292 |
| δ | 0.0004 | 0.0002 | 0.0003 | 0.0003 | 0.0002 | 0.0001 |
| %dev. | 0.017% | 0.008% | 0.014% | 0.014% | 0.012% | 0.006% |
| | | IBA no.19 (x=1.603) | | | | |
| 1 | 2.4932 | 2.4973 | 2.1861 | 2.1888 | 1.6801 | 1.6816 |
| 2 | 2.4946 | 2.5006 | 2.1852 | 2.1898 | 1.6785 | 1.6805 |
| 3 | 2.4933 | 2.4967 | 2.1872 | 2.1895 | 1.6795 | 1.6808 |
| 4 | 2.4905 | 2.4966 | 2.1863 | 2.1904 | 1.6783 | 1.6808 |
| av. | 2.4929 | 2.4978 | 2.1862 | 2.1896 | 1.6791 | 1.6809 |
| δ | 0.0009 | 0.0009 | 0.0004 | 0.0003 | 0.0004 | 0.0002 |
| %dev. | 0.036% | 0.036% | 0.018% | 0.014% | 0.024% | 0.012% |

the mean) is ±0.0004(Å), which is close to the estimated limit of accuracy required. Note that the measured error increased with reduction as measurements on a reduced sample $MnO_{1.60}$ indicate (see table 3.9). Peak D shows the largest increase in variability with H insertion. The increase in δ with reduction is not unexpected since peak intensity and angular position decreased with increasing r in $MnOOH_r$. Whether or not the accuracy could be improved by employing standard techniques was next investigated.

There are basically two different methods. One involves measuring the d spacings of high angle lines and extrapolating to θ=90° to obtain the 'true' d spacing. This is so because the relative error in d is given by

$$\frac{\delta d}{d} = -\cot\theta\,\delta\theta \qquad (3.20)$$

(from differentiating the Bragg condition), which tends to 0 as θ tends to 90. For EMD there are no suitable high angle peaks with CuKα radiation. Changing the radiation does not alter this conclusion.

The other method is the use of an internal calibration substance with well known lattice parameters. It is the preferred method in this instance because of its simplicity and because very high precision is not required. The previous method is normally chosen for high precision measurements with suitably crystalline materials.

As may be deduced from table 3.9 correcting against KCl (which is mixed in with sample) in general produced a small or sometimes zero increase in the reproducibility of peaks B, C and D for the two sets of measurements. The reason why only a small improvement was observed must be because the largest source of error in the tabulated measurements was not sample height displacement (which use of an internal standard can correct for). Sample height displacement is normally the single biggest source of error in diffractometer measurements[87]. The source of error rather rested with the method of determining the peak position itself from the broad peaks. The method used was a parabola fitting method which fits a parabola to a set of 3 points around the point at which the second derivative was most negative. This was a built in routine in the computer of the diffractometer and was therefore a 'live' routine. It needed to be tuned to the particular peak being measured by setting the so called peak detection width. Herein lies one of the advantages of collecting the data on a magnetic storage disk in which the same routine may be employed but without re-scanning the sample if the peak detection width is not set at its optimum value.

### 3.5.3 Conclusion.

Using an internal position standard does not substantially improve the accuracy of d spacing measures on a typical EMD and therefore was not employed. Furthermore use of an internal standard such as KCl would make it very difficult to measure all of the peaks throughout the whole H insertion because of the large peak movements involved and the inevitable contamination of these peaks with the standard at some point in the H insertion range. This question was not investigated further, and the results of peak determinations were simply averaged over 3 measures. An exception to this procedure were samples SBPA and WSZ, which have significantly sharper peaks, where only 2 replicates produced satisfactory results.

## 3.6 Electrode potential measurements of H inserted synthetic battery active manganese dioxide in KOH solution.

The procedure adopted for this study had the following consideration as a primary objective. To enable a measurement of about 25 samples to be completed in one day such that the potential versus x in $MnO_x$ with time of the whole H insertion range may be measured (see chapter 8). In practice this was not always possible because of the finite time required for potential measurements to stabilise. These times increased considerably for deeply H inserted samples stored in KOH such that only a selection of the available samples were measured. By a matter of trial and error the following equipment and procedure was found to produce satisfactory results.

Refer to figure 3-17 which is a schematic representation of the equipment used. A high impedance digital voltmeter (Solatron model 7150) was employed together an inert electrode constructed with vitreous glassy carbon (obtained from Le Carbon). Potentials were taken as equilibrium values when the following arbitrary criteria was reached, namely that the voltage had not changed by more than 0.0001(V) in five minutes. This often took 20 mins and sometimes considerably longer (1-2 hours). Between measures the glassy carbon electrode was cleaned with an acidified hydrogen peroxide solution, polished with an alumina paste (average micron size 0.01) on a polishing wheel, rinsed with distilled water and dried. Hg/HgO reference electrodes,

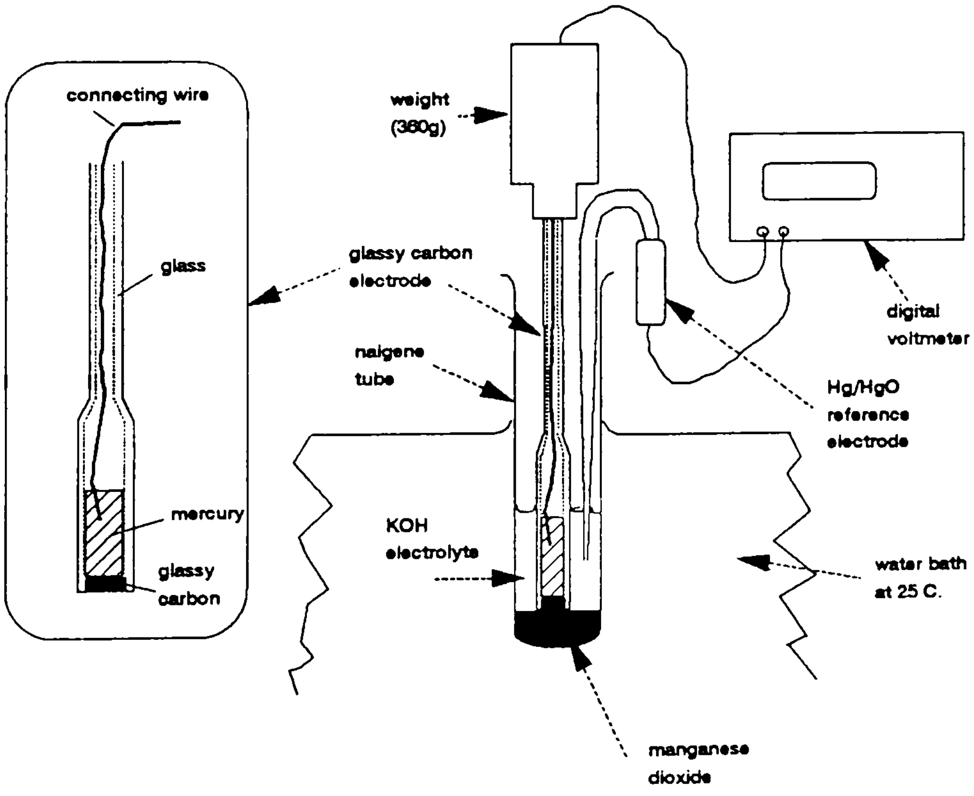

Figure 3-17 Experimental arrangement for measuring electrode potential of manganese dioxide, and reduced forms.

which are particularly suited to measurements in alkaline solution[88], were freshly prepared as required and regularly compared against each other and a commercially available Hg/HgO electrode (Tacussel électronique model XR400) all filled with the same concentration KOH solution (7M).

### 3.6.1 Discussion.

Experimentally, reproducible potentials in alkaline solution have been notably more difficult to achieve than the same measurements in neutral solutions[125]. In this case the simple procedure described above gave satisfactorily reproducible results. For example the initial potential measurements of IBA no.19 averaged over 1,2,3 and 6 weeks indicate a potential of $0.263_2 \pm 0.0004$(V). The accuracy of the results is demonstrated in section 8.7 in which a comparison with those measured from a modified Leclanché cell is presented, from data obtained from Maskell *et al.*[140]

As noted above an arbitrary cut off in the potential versus time had to be imposed, this was because the potential continued to change slowly even after long stabilization times. This slow change may be attributed to the known 'self discharge' tendency of manganese dioxide electrodes in contact with 'inert' electrodes[89,90]. That is, thermodynamically, it may be shown that manganese dioxide should spontaneously decompose in aqueous solution whereas in fact it does not do so unless it is in contact with an electrode (such as Pt, Au or C) which lowers the activation overpotential of the reaction.

### 3.7 FTIR spectroscopy.

All spectra of H inserted manganese dioxide were obtained courtesy of Dr D. Swinkels. The experimental conditions were reported to be the following.

About 3 mg of each sample was mixed with about 450g of CsI and about 200mg used to produce a compressed pellet of known weight (all operations were performed under dry nitrogen). Pellets were scanned with a Perkin Elmer PE 1750 FTIR spectrometer over the wavenumber range 400 - 4000($cm^{-1}$), with each resulting scan being the average of 50 scans. The data were adjusted by subtracting the CsI blank measured during the same run and the spectra were adjusted to a standard 1 $mgcm^{-2}$ loading using the recorded weights. FTIR spectra were saved as Lotus spreadsheet files.

# 4 The Structure of Fully H Inserted Battery Active Manganese Dioxide and Possible Structural Implications for the H Insertion Process.

## 4.1 Does H inserted SBPA also fit the intergrowth model of de Wolff?

It has been speculated previously that if the manganese dioxide in which protons and electrons are inserted contains P(P')[†] layer defects in a framework of R(R') layers then the corresponding H inserted material must also contain M(M') or manganite type layers in a G(G') or groutite framework[73,91]. Manganite and groutite are isostructurally related crystals to pyrolusite and ramsdellite but with the composition MnOOH (see chapter 1). The plausibility of the analogous intergrowth structure (designated δ-MnOOH following Maskell[73] *et al.*) existing is enhanced by noting the following relationships between ramsdellite and groutite, pyrolusite and manganite unit cell dimensions available in the literature. Firstly the relationship between ramsdellite and groutite is summarised in table 4.1 and figure 4-1. Table 4.1 indicates that the main difference in unit cell parameters is an expansion of the b axis in groutite with respect to ramsdellite. In figure 4-1 a unit cell of groutite has been superimposed and centred on a ramsdellite unit cell. The data for ramsdellite was taken from Byström[49] and that for groutite from Dent Glasser and Ingram[92]. It should be noted that in the original

Table 4.1 Comparison of orthorhombic lattice parameters of ramsdellite and groutite.

| Material | $a_0$(Å) | $b_0$(Å) | $c_0$(Å) | Reference |
|---|---|---|---|---|
| ramsdellite | 4.533 | 9.27 | 2.866 | 49 |
| groutite | 4.560 | 10.700 | 2.870 | 92 |
| %increase | 0.60% | 15.43% | 0.14% | |

---

[†] P(P') means P layer and P' layer defects since in the de Wolff model one cannot occur without the other.

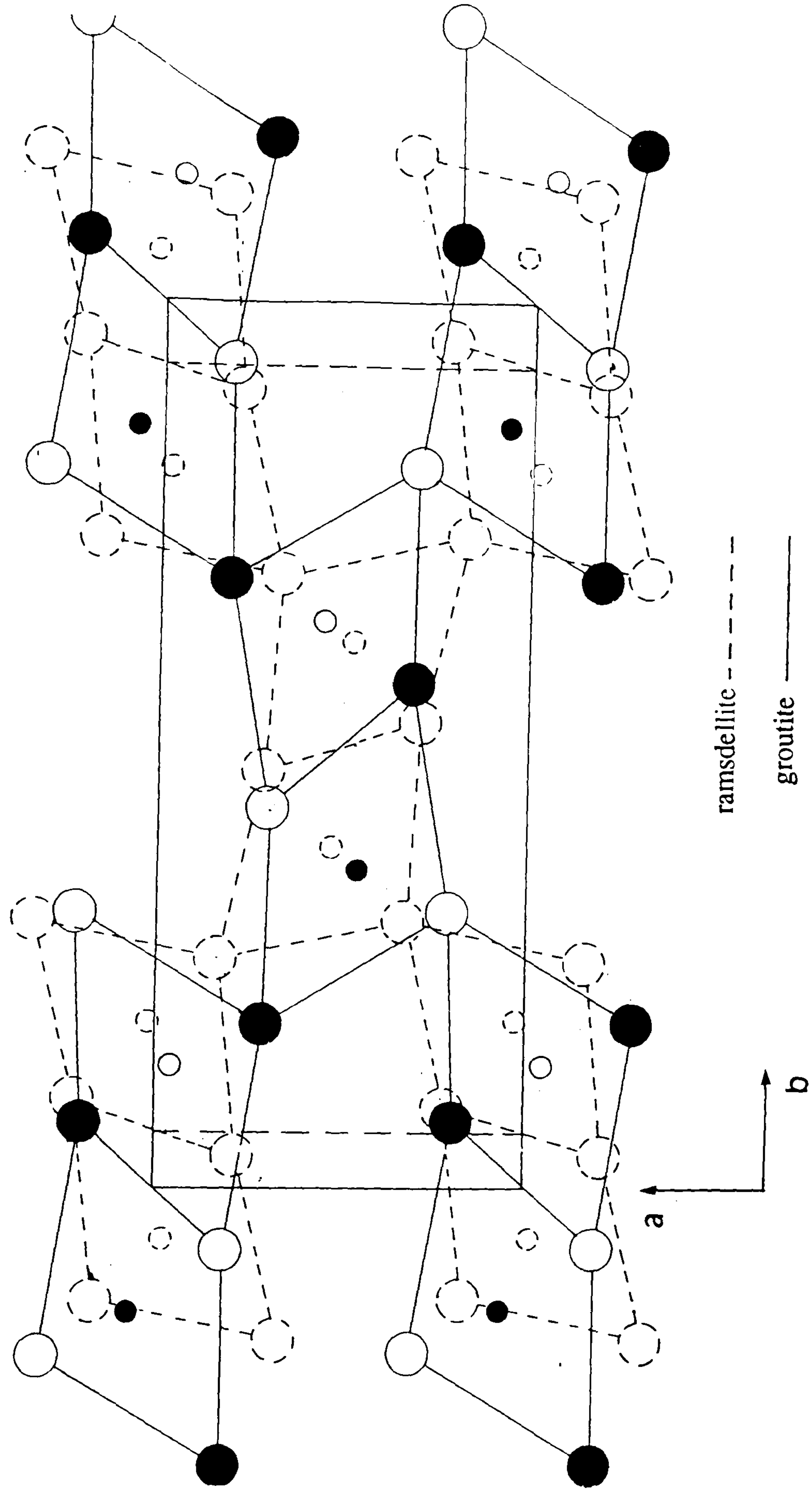

Figure 4-1 Superimposed unit cells of groutite and ramsdellite showing relation between structures. The $\mathbf{a}_0$ unit cell vector appears equal in this diagram whereas $\mathbf{b}_0$ is 15.4% larger in groutite. $\mathbf{c}_0$ is also nearly equal for groutite and ramsdellite. The oxygen arrangement is approximately h.c.p. but 'puckered'. Due to stretching in the $\mathbf{b}_0$ direction the already distorted octahedra are further distorted in groutite with respect to ramsdellite to produce a reversed puckering of the oxygens.

diagrams the viewing directions are different since a$\otimes$b is into the page in figure 1 (Byström) whereas a$\otimes$b points out of the page in figure 1 (Dent Glasser and Ingram)[†]. Figure 4-1 contains both structures viewed such that a$\otimes$b is into the page. The different $b_0$ dimension is observable in the diagram but the small difference in the $a_0$ dimension (see table 4.1) cannot be represented. Apparent in figure 4-1 is the differing distortions of the oxygen sub-lattice. In the **b** direction a string of oxygens would be perfectly aligned in a h.c.p. arrangement (cf. figure 1-2(b)) but for ramsdellite and groutite a 'puckered' arrangement exists. The puckering, however, is reversed for groutite with respect to ramsdellite (see figure 1-2(a) for an idealised puckered arrangement for ramsdellite). The main difference between ramsdellite and groutite could therefore be qualitatively described as an expansion of the lattice in the **b** direction with an accompanying stretching of each $[MnO_6]$ octahedra such as to produce a reversed puckering arrangement of the oxygen sub-lattice (see also section 1.1.2).

Pyrolusite and manganite are not directly comparable however, as for instance there are four formula units contained in the monoclinic[‡] unit cell but only one in present in the tetragonal cell of pyrolusite. Using the assignment of the a,b,c axis adopted for manganite by Buerger[93], division of the manganite a and c axis by two produces a 'unit cell' which may be compared with pyrolusite (see figures 1-4 and 1-1(a) and table 4.2). This is equivalent to noting that the b axis of ramsdellite is approximately twice that of pyrolusite, whereas in this case the a and c axis of manganite are approximately twice that of pyrolusite, as is shown in table 4.2. From

Table 4.2 Comparison of unit cell parameters of pyrolusite and manganite.

| Material | a(Å) | b(Å) | c(Å) | Unit cell type | Reference |
|---|---|---|---|---|---|
| pyrolusite | 4.40 | 4.40 | 2.87 | tetragonal | 49 |
| (manganite) | (8.86) | (5.24) | (5.70) | (monoclinic) | 93 |
| 'unit cell' derived from manganite | 4.43 | 5.24 | 2.85 | N/A | |
| %increase | 0.68% | 19.09% | -0.70% | | |

---

[†] It is further noted that the corresponding JCPDS cards are not reported in the same axis orientation. Ramsdellite (card 39-375) is reported in the conventional orientation for its space group but not in Byström original paper which has the same orientation as Dent Glasser's paper and the corresponding JCPDS card (card 24-713).

[‡] $\beta=90$ in manganite and it is often termed 'pseudo-orthorhombic' for this reason.

table 4.2 it may be seen that similarly to the hypothetical transition ramsdellite to groutite (table 4.1) the main change in unit cell parameters for the transition pyrolusite to manganite is the expansion of the b axis by 19%. Interestingly a figure of 15% (which is the same as that for the transformation ramsdellite to groutite stated in table 4.1) has been determined[94] for the contraction of the b axis during the transformation of manganite to pyrolusite, however, the pyrolusite obtained by this type of transformation is believed to be orthorhombic[94]. An attempt to represent the expansion is provided in figure 4-2 in which half a unit cell in the a direction has been superimposed on a unit cell of pyrolusite. Such a division produces a 'unit cell' which has very nearly the same dimension as that of pyrolusite so that the cells are superimposed on each other in this direction. In the b direction the unit cells are centred to produce equal lattice expansions in the positive or negative direction. It may be ascertained from this diagram that the expansion referred to may essentially be accomplished by stretching of alternative oxygen chains in the positive and negative b directions such as to remove the puckering characteristic of the p.t.p. oxygens (see section 1.1.1) in the pyrolusite structure. Re-examining figure 4-1 one finds that such a mechanism also (approximately) would account for the transition ramsdellite to groutite.

Drawings indicating the relationship between the structures of either ramsdellite/groutite or pyrolusite/manganite are rare in the literature, see however Ohzuku and Hirai[95]. The authors, however, do not draw attention to the obvious relationships stated in this work.

Given that the expansions produced in groutite and manganite are in equivalent directions and of similar size due to incorporation of H, if an intergrowth structure of ramsdellite and pyrolusite type layers exists the corresponding H inserted intergrowth structure would (on this basis) seem possible and reasonable.

Experimental evidence for this structure is provided in figure 4-3(a) which is a powder x-ray diffraction pattern of the most H inserted ($MnOOH_{0.882}$) derivative produced with SBPA. Experimental reasons are given as to why the theoretical limiting composition of MnOOH was not obtained by the H insertion method used plus details of the experimental procedure in section 3.2.1.

Present in figure 4-3(a) are peaks with differing broadness as in figure 2-8 which is of the original SBP-EMD, labelled SBPA. If M(M') layers exist in a matrix of G(G')

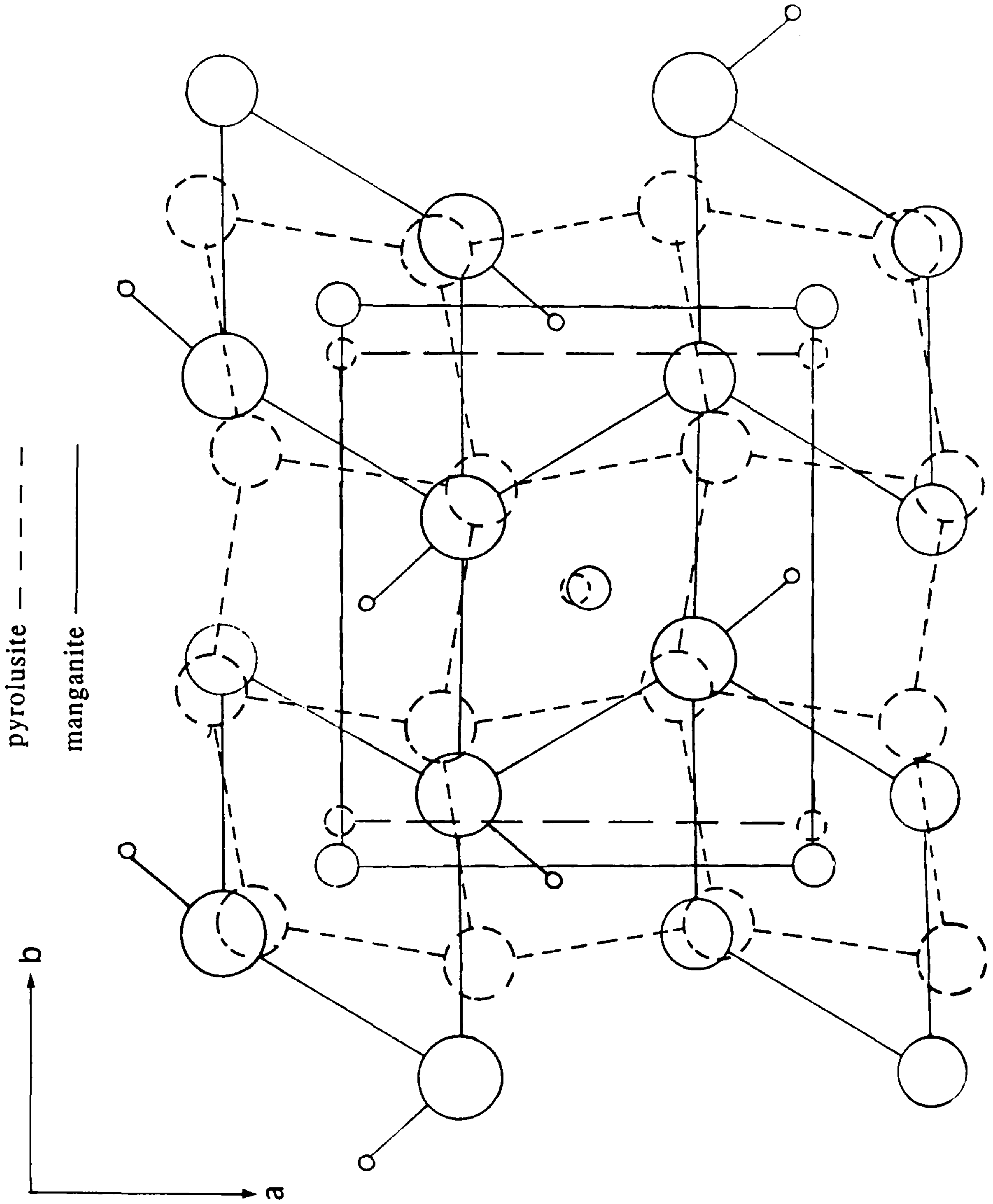

Figure 4-2 Superimposed half unit cell (in the a and c directions) of manganite and unit cell of pyrolusite showing relation between structures. The a 'unit cell' vectors appear equal in this diagram whereas b is 19% larger in manganite. 'c' is also nearly equal for the two 'unit cells'. (cf. figures 1-1(a) and 1-4).

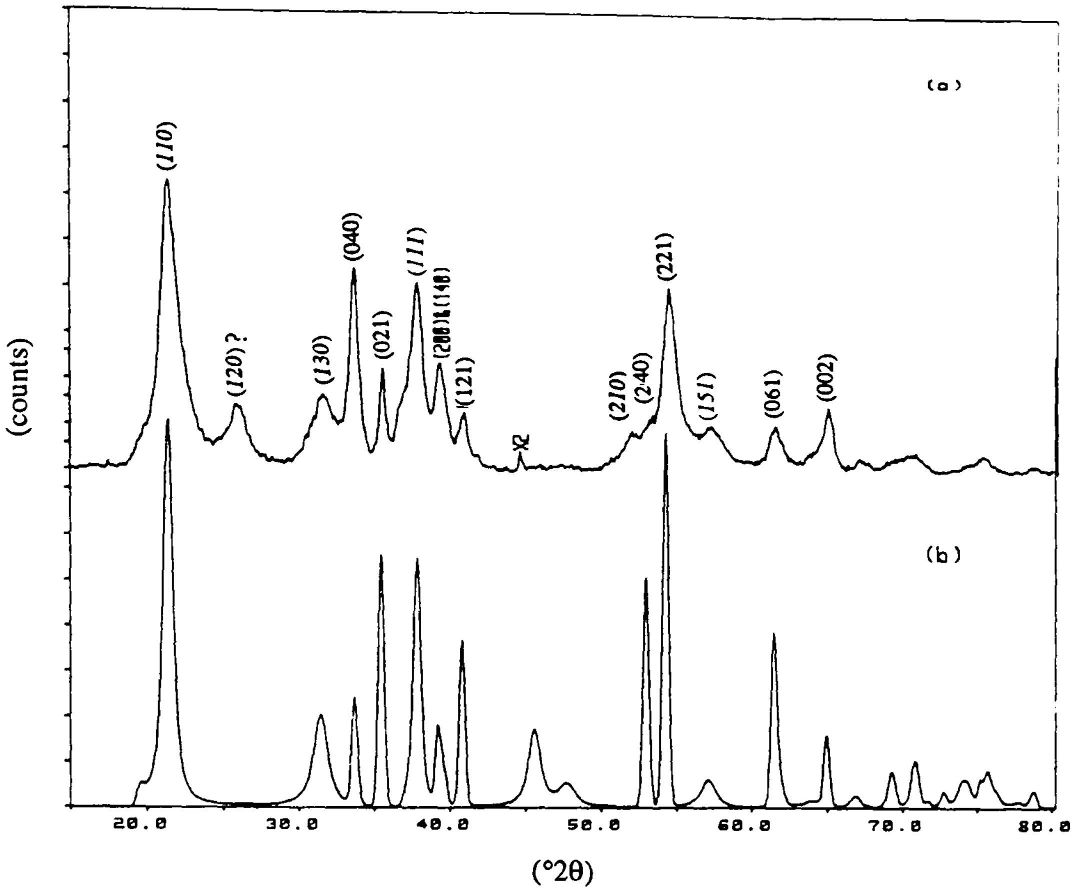

Figure 4-3 Comparison of computed x-ray diffraction pattern, using DIFFaX, of reduced SBPA and actual pattern ($MnOOH_{0.882}$). (a) actual pattern with orthorhombic indices shown. (b) Computed 'random layer' model of G(G') and M(M') layers.

layers analogously to P(P') layers in a predominately R(R') framework then exactly similar conclusions regarding the broadening and shifting of certain lines from their orthorhombic positions ought to apply. In particular those peaks with ½k+l even would be sharp and unshifted and the others in general would be relatively broad and shifted. Referring to figure 4-3, though not as clear as for the initial unreduced material (figure 2-8), this is approximately the case. The indices were determined from the nearest groutite lines when comparing the known positions and intensities[96] of groutite with the observed pattern, figure 4-4. In this figure the correspondence of the lines with the observed positions and intensities is not very satisfactory. This is to be expected, however, since there is no reason to suppose that either the orthorhombic parameters or m (the fraction of M(M') layers, analogous to p) will be the same (note that m=0 for perfect groutite).

In order to determine the m value of the most reduced sample table 4.3 similar to table 2.4 was constructed by exactly the same procedure as outlined in section 2.3.2. The assignment (120) is doubtful (hence the question mark next to its index in figure 4-3) as it occurs very near to the 100% manganite line as shown by comparison with

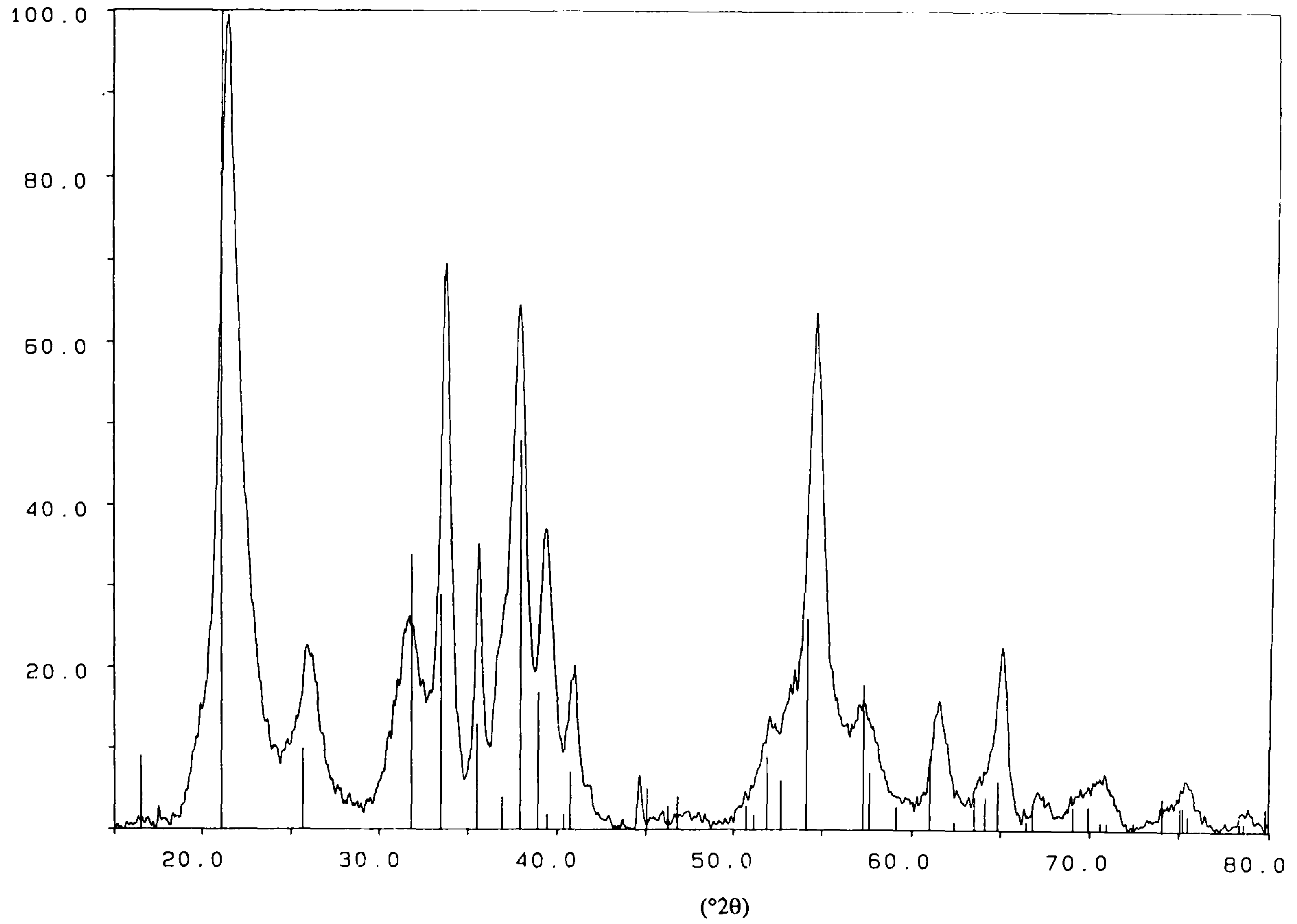

Figure 4-4 Comparison of the powder x-ray diffraction pattern of H inserted SBPA ($MnOOH_{0.882}$) with JCPDs card 24-713, groutite. The stick representing 'integrated intensity' of the 100% groutite line was matched to the 100% $(110)_o$ peak of the H inserted SBPA sample.

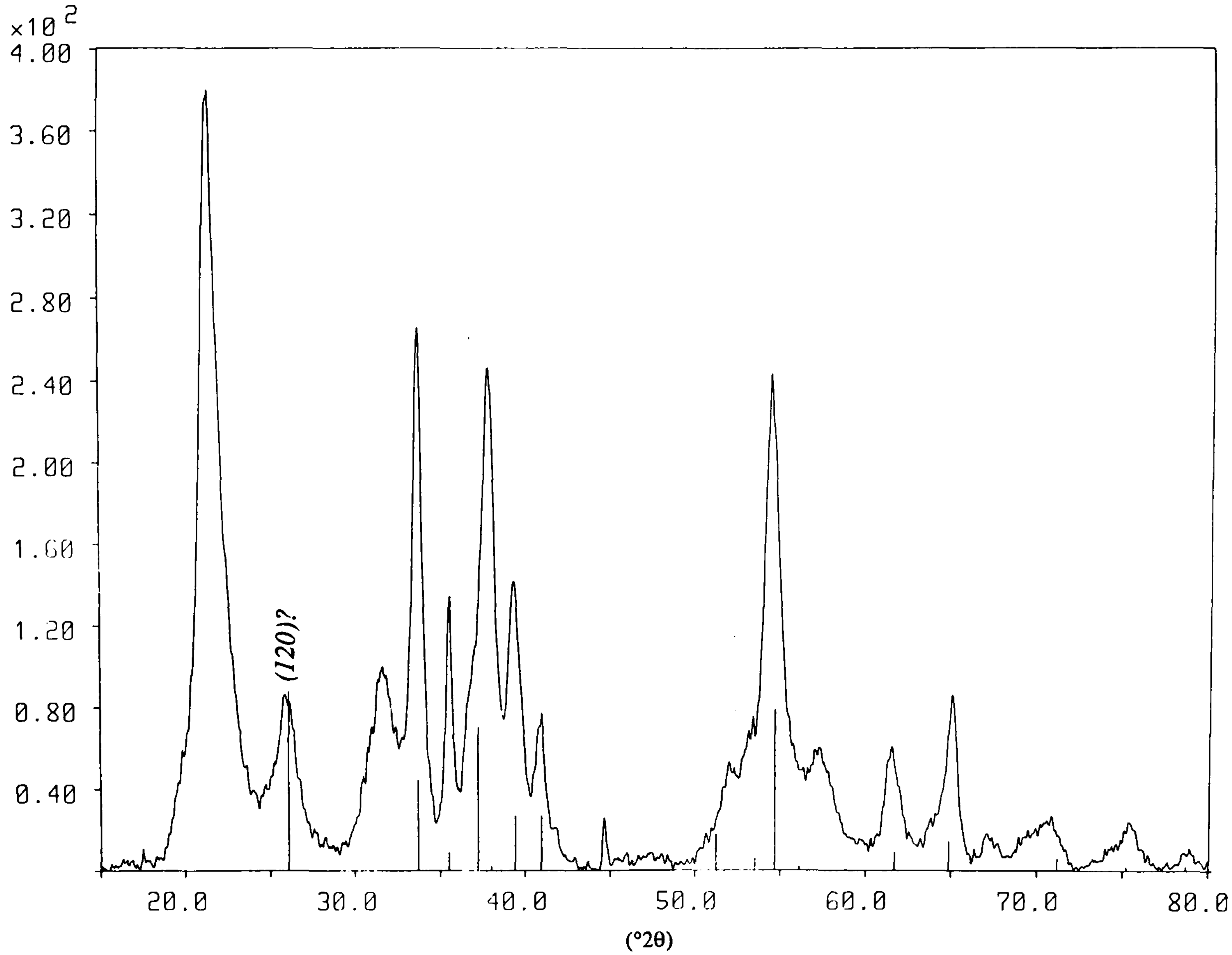

Figure 4-5 Comparison of the powder x-ray diffraction pattern of H inserted SBPA ($MnOOH_{0.882}$) with JCPDs card 18-805, manganite. The stick representing 'integrated intensity' of the 100% manganite line was matched to the 100% *(120)?* peak of the H inserted SBPA sample.

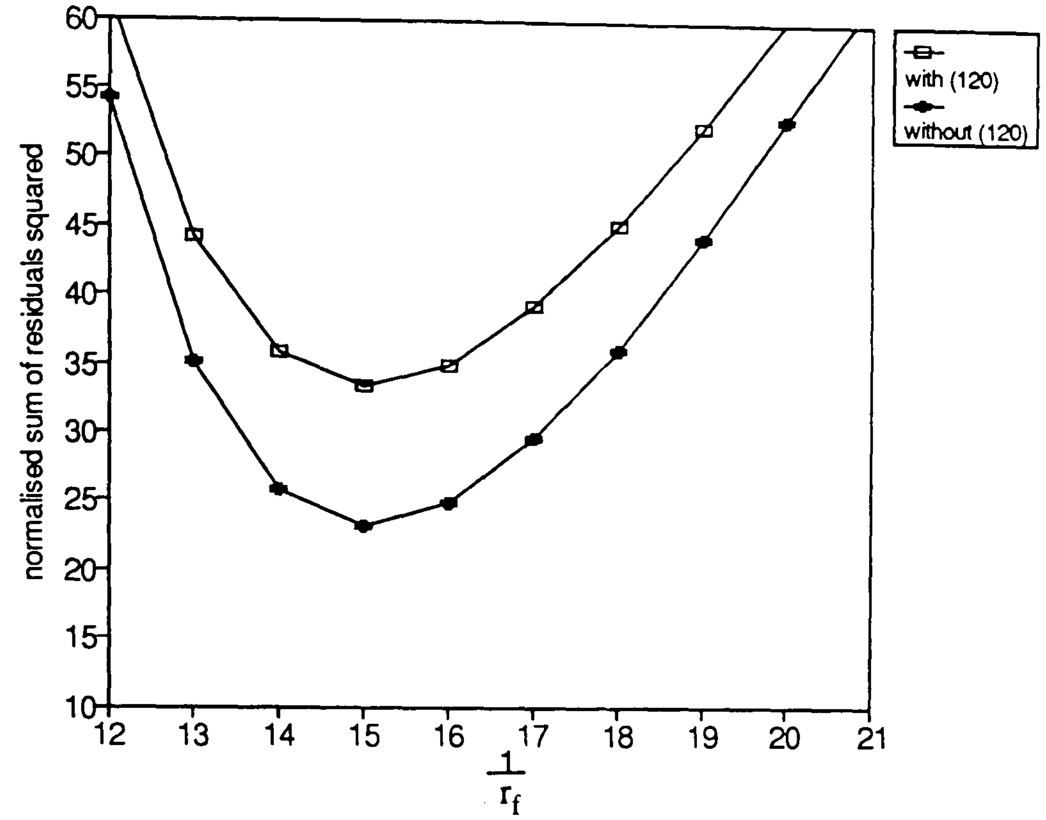

Figure 4-6 Minimisation of the residuals squared (calculated shifted °2θposition - observed shifted position) used in the determination of the pyrolusite layer fraction p. $r_f$=fractional shift in reciprocal space.

Table 4.3 De Wolff analysis of sample A23. Where $q=10^4/d^2$ and subscripts denote o-observed, c-calculated; Calculated $q_c$ and $\Delta q$ shifts for indices hkl; *hkl* related to ramsdellite indices hkl.

| 2θ | d | $q_o$ | $q_c$ | h | k | l | $q_o$-$q_c$ | $\Delta q$ |
|---|---|---|---|---|---|---|---|---|
| 21.365 | 4.159 | 578.2 | 574.8 | *1* | *1* | *0* | 3.4 | 12.2 |
| 26.007 | 3.426 | 852.0 | 839.6 | 1 | 2 | 0† | 12.4 | 0.0 |
| 31.552 | 2.835 | 1243.8 | 1280.9 | *1* | *3* | *0* | -37.1 | -35.0 |
| 35.513 | 2.528 | 1565.1 | 1565.7 | 0 | 2 | 1 | -0.6 | 0.0 |
| 37.824 | 2.378 | 1767.7 | 1787.3 | *1* | *1* | *1* | -19.7 | -11.4 |
| 40.814 | 2.211 | 2045.9 | 2052.2 | 1 | 2 | 1 | -6.3 | 0.0 |
| 39.278 | 2.294 | 1900.7 | 1898.8 | 1 | 4 | 0 | 1.9 | 0.0 |
| 54.375 | 1.687 | 3512.8 | 3511.7 | 2 | 2 | 1 | 1.1 | 0.0 |
| 57.152 | 1.612 | 3850.0 | 3905.8 | *1* | *5* | *1* | -56.0 | -58.6 |
| 64.954 | 1.436 | 4851.7 | 4850.3 | 0 | 0 | 2 | 1.4 | 0.0 |
| 61.435 | 1.509 | 4390.5 | 4390.3 | 0 | 6 | 1 | 0.2 | 0.0 |

†Tentative index, see text.

data[97] for manganite, figure 4-5. Further evidence that the assignment (120) may be wrong occurs when trying to minimise the sum of the square of the residuals when determining the m value (for more information see section 2.3.2 and appendix A). If one includes the (120) peak in the function to be minimised then the minimum of the function is not as low as when it is not included. This is graphically depicted in figure 4-6. Note that the function to be minimised has been normalised by dividing it by the number of terms (i.e. the number of peaks) in the summation.

The minimum occurs at $1/r_f=14.97$ corresponding to m=0.15. An average value for 3 measures has been calculated (see appendix A) m=0.14±0.01. This is below the value of p determined for the initial material, p=0.20±0.005. The following points should however be born in mind concerning the value of m given. Although it has been stated that m, the fraction of manganite type layers, has been determined in fact there is no way in principle of knowing if m or p, or a combination of both has been found (by the method described in section 2.3.2). The analysis only works for the case of a small proportion of one type of layer defect in an otherwise perfect matrix of another layer type. One could perhaps decide the question by recursive (i.e. altering the values of m and p comparing the result with experiment adjusting m and p then repeating the process) simulation of the pattern (with for instance DIFFaX) until the best match with the experimental pattern was found. This, however, would be a difficult task comparable to the task of determining the quantity of triple octahedral layers present in the original material (see section 2.4.1). The fact that the analysis may be performed at all suggests the following. A predominant 'lattice' exists in which layer defects are present (whether they be m or p or both). The lattice must be a groutite type lattice (i.e. that formed by G(G') layers) since the material is reduced. The layer defect concentration of 0.14 is consistent with the earlier suggestion of a slight amount of $\gamma$-MnOOH precipitation, however, it must be noted that the reduction level is only $MnOOH_{0.882}$ so the low value of m (and or p) may be due to a combination of p and m layers co-inhabiting the crystal with subsequent errors in the analysis of the layer defect concentration.

### 4.1.1 Computed x-ray diffraction pattern of reduced SBPA.

To conclude section 4.2 the simulated pattern calculated with DIFFaX is presented. The lattice parameters used were those as determined in the previous section from the procedure to evaluate m (and/or p) and are listed together with those for SBPA in table 4.4 (see also appendix A). This table indicates that the relative expansions of $a_o$, $b_o$ and $c_o$ are comparable to those found given in tables 4.1 and 4.2. In the

Table 4.4 Comparison of initial and final lattice parameters from SBPA and most H inserted product.

| Sample | $a_0$(Å) | $b_0$(Å) | $c_0$(Å) |
|---|---|---|---|
| SBPA | 4.438±0.002 | 9.35±0.01 | 2.850±0.002 |
| Most H inserted product from SBPA | 4.536±0.002 | 10.65±0.01 | 2.870±0.002 |
| %increase | 2.2±0.09% | 13.9±0.2% | 0.7±0.14% |

simulation an R(R') layer was expanded by 14% in the b direction as was a P(P') layer and the other two lattice parameters set equal to those of the most H inserted SBPA given in table 4.4. The expansion was performed on an R(R') layer such that angles between oxygen atoms at a layer boundary remained constant so as to ensure they would continue to match a neighbouring unreduced layer. For details on how this was achieved see appendix B. The calculated pattern is displayed in figure 4-3(b). The agreement with the observed pattern (figure 4-3(a)) is certainly not as good as the original calculation for SBPA (see figure 2-8). However, most peaks in the calculated pattern contain a corresponding peak in the actual pattern, even peak (240), which occurs only as a shoulder on (221) in the actual pattern but as an intense feature in the calculated pattern. The broad maxima in the region 42-52°2θ only corresponds to the remnants of a very broad (130) peak (see figure 2-8) but the most striking disagreement is the complete absence of the '(120)?' peak. This could be due to the simplified oxygen sub-lattice that was adopted for the calculation. Evidence for this is provided by the inspection of the intensities of the peaks in figure 4-3 which are reasonably correlated, where the greatest error with respect to the actual pattern arises for peaks (021), (121), (240) and also perhaps (061) and (221). All those peaks contain a large contribution from oxygen as has been noted earlier, section 2.4.3.

Just as distorting the h.c.p. oxygen sub-lattice in the calculation of the ramsdellite line intensities produces peaks characteristic of ramsdellite distorting the h.c.p. oxygen sub-lattice towards the groutite positions will produce lines characteristic of groutite. The distortion† of the oxygen sub-lattice is different from the ramsdellite case as is

---

† "distortion" here means with respect to the h.c.p. arrangement and does not imply any lack of regularity or infeasibility in such an arrangement.

illustrated in figure 4-1 and noted earlier. Measurement of the peak area of the line at 26.01°2θ (possibly (120)) and *(110)* indicates that this peak is 12% of *(110)* (the 100% peak). This agrees well with the value of 10% for the same ratio in JCPDS card 24-713 (groutite), see figure 4-4. However it is odd that (020) does not also appear with an intensity of 9% as also shown in figure 4-4 (the stick occurring at the lowest 2θ angle). Considering all the evidence presented it is most likely that the peak tentatively assigned (120) represents a small manganite 'impurity' from the reduction process, probably due to the enhanced solubility of Mn species in butanol at boiling temperatures.

## 4.2 An analogous structural series to the $\gamma$-$\gamma_t$-$MnO_2$ series for the H inserted compounds.

The H inserted derivatives formed from the initial battery active materials under consideration in this work form an analogous structural series to the $\gamma$-$\gamma_t$-$MnO_2$ structural series reported in section 2.3.1. That is, whatever structural defect is responsible for the $\gamma$-$\gamma_t$-$MnO_2$ series appears to be retained at the end of the chemical H insertion process, as demonstrated by the x-ray diffraction patterns of the most reduced (i.e. those closest to the theoretical composition MnOOH) products presented in figure 4-7. Since it has been established that the structural fault responsible for the $\gamma$-$\gamma_t$-$MnO_2$ series was that of microtwinning (cf. section 2.5) it may be inferred that it is also responsible for the analogous H inserted structural series or the $\delta$-$\delta_t$-MnOOH series. In this case, however, shifts from the orthorhombic positions determined from the sharp lines of H inserted SBPA, (the dashed lines in figure 4-7) are not explainable solely by microtwinning, nor are they in a consistent direction as in figure 2-12. The following points should, however, be noted concerning figure 4-7. The position of certain maxima depend on the H insertion level i.e. on r in $MnOOH_r$ (if the material reduces in homogeneous phase). Therefore differences may be expected since the materials are not all at exactly the same H insertion level. Furthermore in the case of reduced SBPA the composition indicates that it has an H insertion fill level† of only 87.3% compared to 96.9% or higher for the other materials. However, as shall be presented later, this material was reduced in a heterogeneous process and therefore the positions of the maxima (are in this case) the same as those of the most H inserted product.

---

† Calculated taking into account the initial non-stoichiometry of the manganese dioxide.

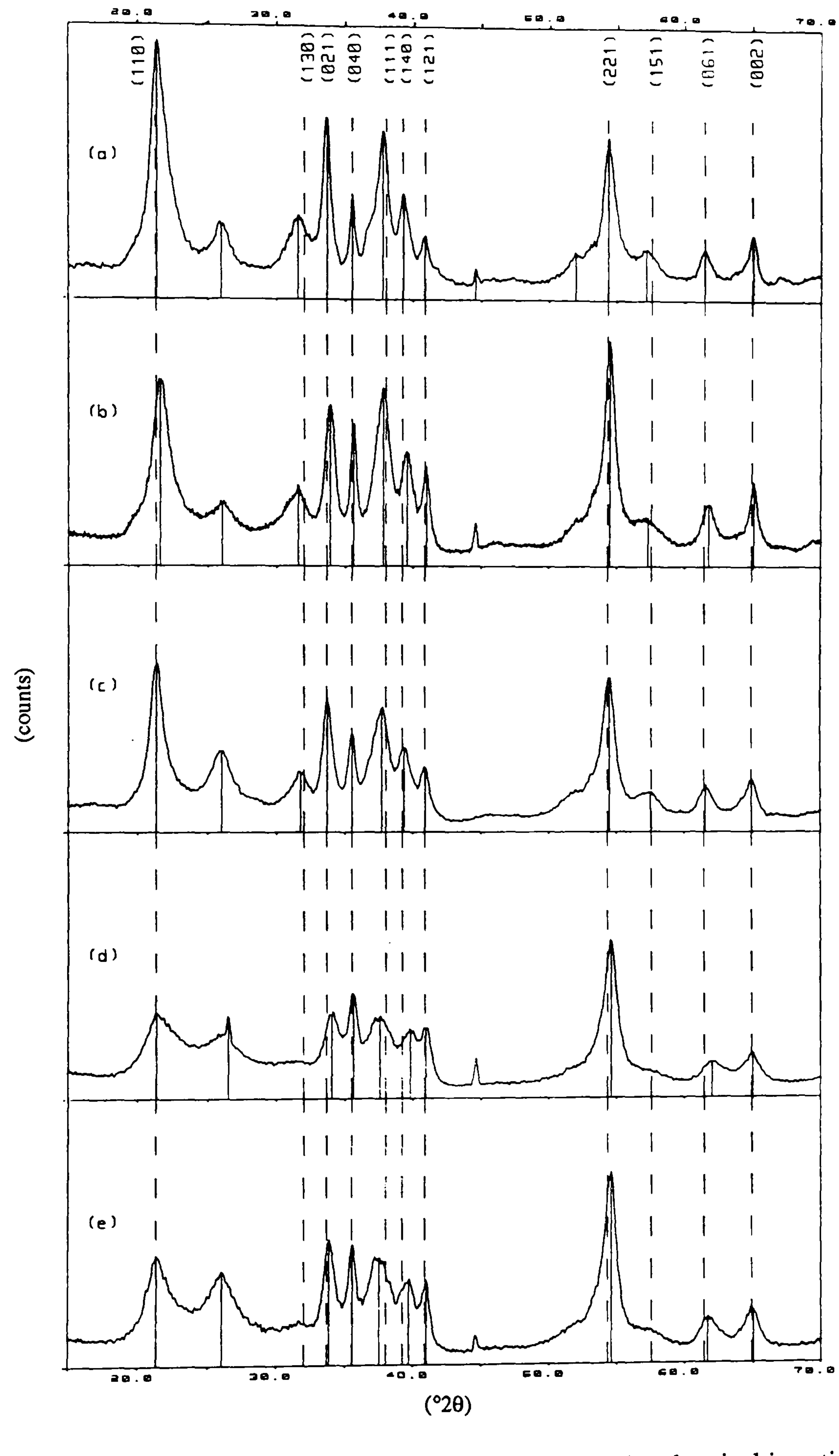

Figure 4-7 Comparison of most reduced materials produced by chemical insertion of H into the starting materials (a) SBPA, composition $MnOOH_{0.882}$, (b) WSZ, $MnOOH_{0.972}$ (c) IBA no.14, $MnOOH_{0.990}$, (d) R2, $MnOOH_{1.008}$ and (e) IBA no.19, $MnOOH_{0.974}$. The dashed lines represent the orthorhombic positions of the groutite type lattice derived from the sharp lines of (a).

## 4.3 Theoretical discussion concerning the nature of line shifts in manganese dioxide due to H insertion.

The previous sections have shown that consideration of the x-ray diffraction patterns of the fully H inserted compounds produced in this work strongly indicate that they posses a random layer structure with additional effects indicative of varying degrees of microtwinning. As is well known, H insertion into (in particular) EMD causes line shifts to occur, which in turn has provided strong evidence to corroborate observations of the electrode potential which indicate that reduction occurs in a single phase, homogeneous process (cf. chapter 8). In the following section it is proposed to consider the possible causes of line shifts when inserting H into manganese dioxide consistent with the structural nature of the reduced derivatives. Such a consideration leads to identification of a new form of line shift which, surprisingly, has elucidated (see section 6.5) the interpretation of the structural changes which occurred when H was inserted into a typical EMD at the $\gamma_t$ end of the $\gamma$-$\gamma_t$-$MnO_2$ series.

### 4.3.1 The causes of x-ray diffraction line shifts due to H insertion into battery active manganese dioxide.

It is well established that insertion of H into battery active manganese dioxide causes the x-ray diffraction lines to shift in a direction consistent with that of an expanding crystal lattice, that is towards lower $2\theta$ values (or higher d values). What has <u>not</u> been established is how insertion of H causes the observed line shifts. Examining the literature one finds that the following argument is propounded. The lattice expansion is the result of replacing the $Mn^{4+}$ ion by the larger $Mn^{3+}$ ion as reduction proceeds. The reduction may be represented by the chemical formula $MnOOH_r$ where r changes from an initial value close to zero (due to the initial non-stoichiometry of the manganese dioxide[†]) to a value of one which corresponds to all $Mn^{4+}$ reduced to $Mn^{3+}$. The author believes what is not stated explicitly is the following. A *shift* in line position with increasing proportion of $Mn^{3+}$ (represented by r) would only result if the distribution of

---

[†] This is not meant to imply that the initial non-stoichiometry is necessarily due to inserted H. A perhaps better notation[107] recognises this distinction by writing $MnO_xH_s$ where x is the initial oxidation state and s varies from zero to $s_{max}$.

$Mn^{3+}$ in the available sites was random, or at least the $Mn^{3+}$ were not confined to a portion of the crystal. If this were the case then a line shift would not result but rather two sets of lines would be apparent one set characteristic of the reduced portion of the crystal and the other set characteristic of the unreduced material.

Increasing H insertion would merely alter the proportions of the two sets of lines according to the composition. This behaviour can be induced to occur in EMD and is further discussed in section 7.3. In this case an apparent line shift would only be observed if the lines were extremely close together such that they overlapped whatever the composition. This type of explanation has been offered[98] to account for the line shifts observed when inserting Li into heat treated EMD (or HEMD). Thus an overall expansion of a crystal lattice would only result if the substituted ion ($Mn^{3+}$ in this case) was distributed 'evenly' amongst the available sites. This is compatible with the idea[99] that a solid solution is formed with $Mn^{3+}$, $Mn^{4+}$, $0^{2-}$, $OH^-$ identified as the thermodynamic components, which in turn only requires independent mobility of $H^+$ and $e^-$. However, it appears necessary for an average expansion of a whole crystal lattice, that not only must the larger ions be distributed randomly amongst the available sites but they must be mobile for it is hard to imagine how a larger unit cell, inhabited by $Mn^{3+}$, could exist 'independently' of other unit cells that are unreduced (or not expanded). Conceptually at least mobility is implied by an average lattice expansion, where the x-ray diffraction lines do not broaden but merely shift with increasing proportion of $Mn^{3+}$.

This is directly analogous to the phenomenon of a random substitutional solid solution which occurs for instance with the ionic salts KCl-KBr. The lattice parameters of the solid solution in this case vary linearly with atomic percentage of solute present. The fact that many random substitutional solid solutions obey an approximately linear relationship is known as[100] Vegard's Law (it is not really a law but an empirical generalisation[101]). Deviations from Vegard's Law include non-linearity (curves showing positive or negative deviations) and abrupt changes in slope[101]. Solid solutions which are not random are termed ordered and may be detected by the presence of superlattice reflections in the x-ray diffraction pattern.

The statements so far in this section have made no reference to the nature of $\gamma$-$MnO_2$ crystal discussed in chapter 2. They rather refer to perfect crystal lattices and an idealised concept of substitutional type solid solutions. As should be apparent from chapter 2 the idea of 'lattice expansion' is strictly speaking not applicable to $\gamma$-$MnO_2$ or members of the $\gamma$-$\gamma_t$-$MnO_2$ series since neither posses a regular crystal lattice. The oxygen framework does posses a sub-lattice† and so the concepts and terms discussed above could be applied to it. Consideration of the nature of the $\gamma$-$MnO_2$ crystal structure leads to a new form of line shift.

### 4.3.2 The Hendricks-Teller effect.

This type of line shift is a consequence of random layer structures and is not deducible from classical x-ray diffraction theory. The example of a random layer structure given in the original paper[60] (concerning random layer structures) by Hendricks and Teller shall be used to illustrate the effect. It is based upon the partially hydrated mineral montmorillonite which contains two layers, one corresponding to the anhydrous material with a 10Å width and the other hydrated layer with a width of 13Å. In the calculation of the x-ray pattern the layer form factor for the two types of layers is set equal (i.e. the influence on the layer form factor of water is neglected). An equation is derived for a random infinite succession of 10Å and 13Å layers with the probability of occurrence of a layer equal to its probability of existence or overall proportion (i.e. it is a genuine random occurrence of each type of layer, see section 2.4.5).

For reference the general equation[60] for the intensity of diffraction I for r different phase shifts phi1, phi2, phi3...phir characteristic of r layers, occurring with probabilities $B^{(1)}$, $B^{(2)}$, $B^{(3)}$, ....$B^{(r)}$ is

$$I=\frac{V^2[1-C^2]}{1-2C\cos\bar{\phi}+C^2} \qquad (4.1)$$

where V=layer form factor

$$C=\sum_{s=1}^{r} B^{(s)}\cos(\phi^{(s)}-\bar{\phi})$$

and $\bar{\phi}$ is defined by $\sum_{s=1}^{r} B^{(s)}\sin(\phi^{(s)}-\bar{\phi})=0$

The phase shift $\phi$ is related to the scattering angle $\theta$ by

---

† it is unlikely that the oxygen sub-lattice could be perfectly regular since local displacements of the oxygen positions probably occur at RP, PR (or R'P', P'R') boundaries.

$$\phi = \frac{4\pi x}{\lambda}\sin\theta \qquad (4.2)$$

$\lambda$=wavelength

x=the width of a layer

Figure 4-8 displays the results for montomorillonite a calculation in which $B_{13Å}=0.5$ (which implies $B_{10Å}=0.5$). In the top part of the figure 4-8 the results are shown for 99% pure forms of the hydrated and anhydrous mineral so that the effect of the random layer calculation may be compared. Thus where two lines overlay a sharp intensity maxima is observed in the random lattice calculation but in other regions where isolated peaks from either spacing occur broad maxima are produced which eventually fade with increasing proportion of the 'other' layer. It should be noted that the intensity calculation only takes into account the effects of the random layer structure since the layer form factor (V) is not evaluated and is therefore regarded as a constant factor. Thus $I/V^2$ is chosen as the ordinate in figure 4-8. V normally depends on the scattering angle $\theta$ in an analogous way to $F_{hkl}$ in section 2.2. The height of the sharp peaks in figure 4-8 have been cut at a value of 10 in $I/V^2$ in order not to intrude into the upper

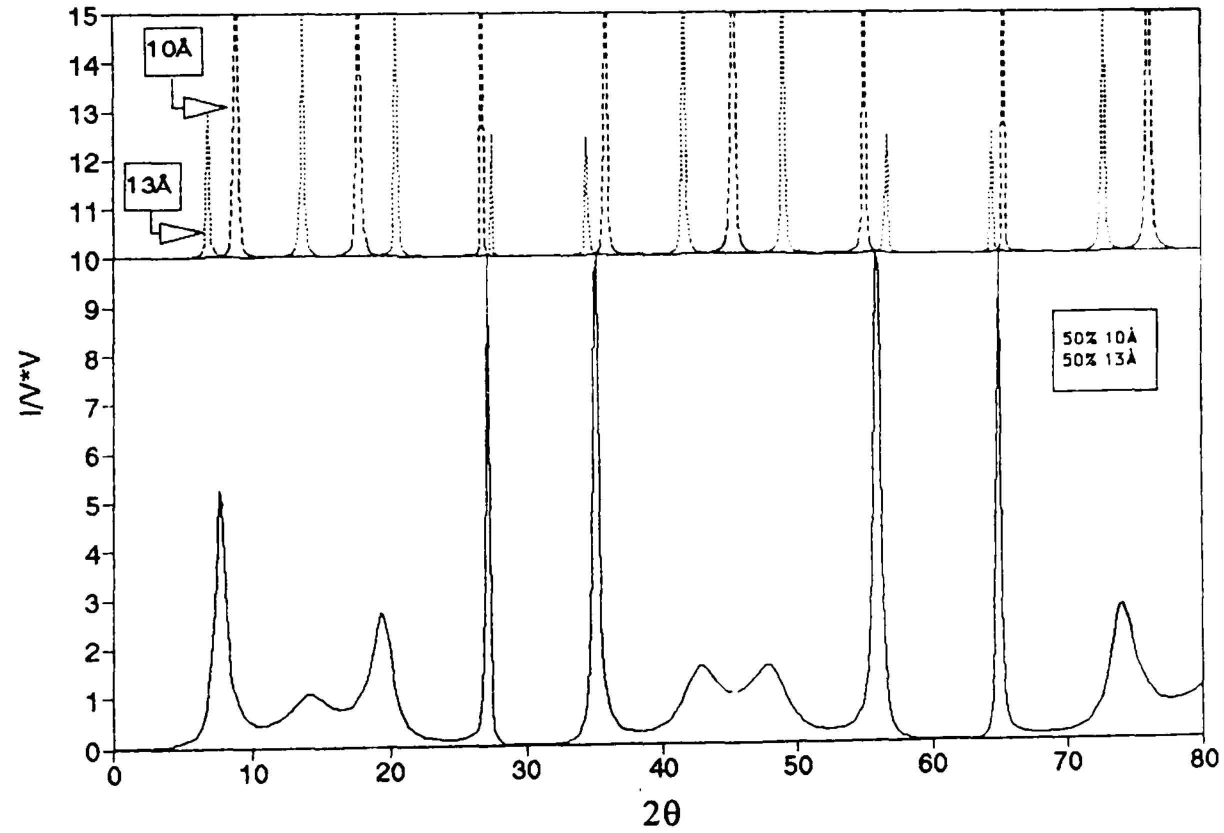

Figure 4-8 Example of a calculated x-ray diffraction pattern for a random layer structure with layer widths 10(Å) and 13(Å). In this case the probabilities of existence of each layer are $B_{13Å}=B_{10Å}=0.5$.

diagram (the peaks of which have been displaced by 10 and similarly cut). Theoretically singularities result where the peaks of the 13Å and 10Å lattice coincide. There are certain peaks which have neighbours sufficiently close to produce a maxima throughout the theoretical composition range from the pure 10Å lattice to that of the pure 13Å lattice. One such peak occurs from the peaks used to identify the 10Å and 13Å patterns in figure 4-8 and results in a maxima at about 8°2θ in the lower random layer calculated spectrum. The data for this maxima calculated with $B_{13Å}$=0.1-0.9 in steps of 0.1 was used to produce the pseudo-3D[†] plot of figure 4-9(a). This plot displays the broadening and shift of the identified x-ray diffraction maxima with increasing proportion of the 13Å layer in the starting 90% pure 10Å phase. The shift is towards lower °2θ values (higher d spacing). Figure 4-10 displays a contour plot of the same data. The dependence of the peak position on composition has an 'S shape' as clearly demonstrated in figures 4-9(b) and 4-10.

To summarise, a new kind of line shift varying with layer composition can be produced by random layer crystal structures. It is observable only when two lines characteristic of the pure layer end members are sufficiently close to interfere with each other. The broadening and dependence of peak position on composition distinguishes this type of line shift from those that may be encountered with perfect crystals (as previously discussed, section 4.3.1).

## 4.4 Simulated effects of H insertion on the computed x-ray diffraction pattern of $\gamma$-$MnO_2$.

In section 4.1 it was shown that the H inserted product of SBPA (which possess a typical $\gamma$-$MnO_2$ x-ray diffraction pattern) has a random layer structure. That is, certain lines are broadened and shifted with respect to those produced from a perfect crystal. The question is how did inserting H into the initial material lead to this structure? The question is addressed from a purely theoretical viewpoint, the actual behaviour is presented in chapter 5.

There are at least three possible cases:

---

[†] This pseudo-3d plot (and all others contained in this work) was produced with the program UNIMAP, part of the series of interactive UNIRAS products available to mainframe Vax users at Middlesex University. The program interpolates a collection of 3D points to produce the regular 3D grid represented in the figure.

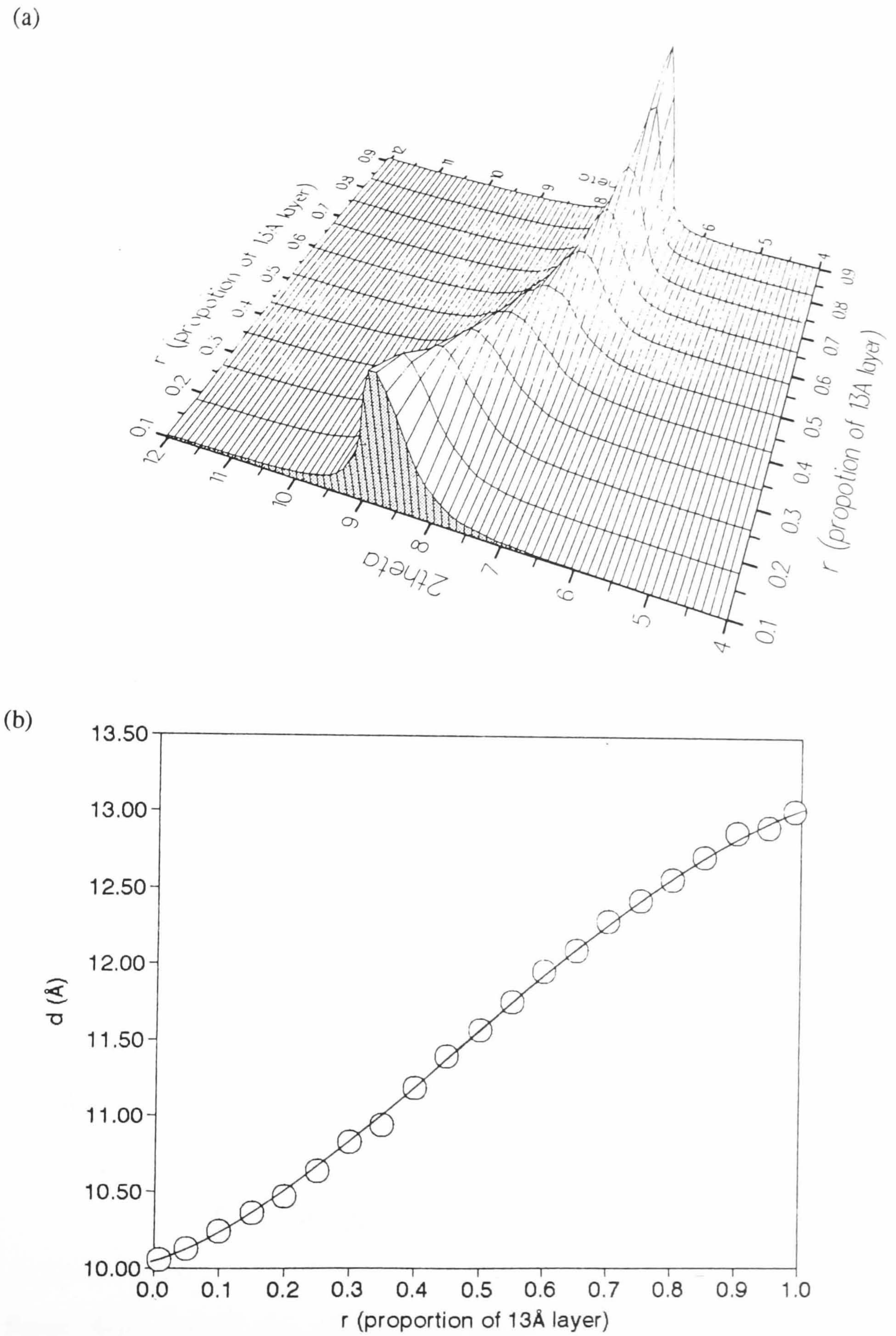

Figure 4-9 (a) Pseudo-3D plot of calculated random layer structure for the mineral montomorillonite. (b) d spacing variation of peak shown in (a) which produces an 'S' shaped shift due to increasing concentration of the hydrated 13(Å) layer in an initial layer structure of the anhydrous 10(Å) layer.

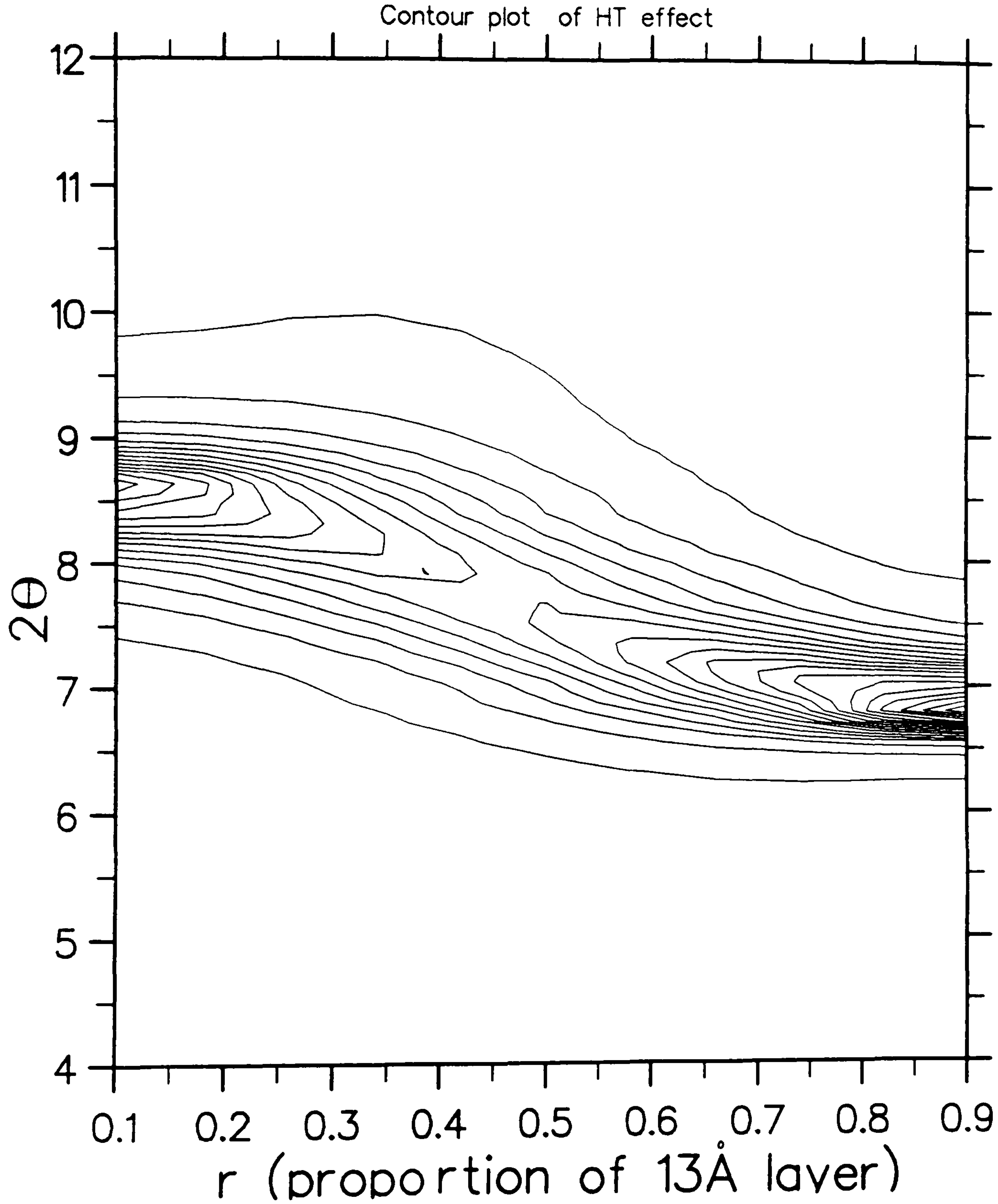

Figure 4-10 Contour plot of calculated random layer structure for the mineral montomorillonite showing a peak which produces an 'S' shaped shift due to increasing concentration of the hydrated 13(Å) layer in an initial layer structure of the anhydrous 10(Å) layer.

Case1 - Overall the oxygen sub-lattice expands in a continuous fashion with accompanying movement of the of the Mn atoms with increasing H insertion level. This is equivalent to a random solid solution, the expansion of the lattice parameters (in this case it is preferable to refer to the oxygen sub-lattice, see section 4.3.1) must be linear (Vegard's Law) or show other deviations as previously discussed (section 4.3.1).

Case 2 - G(G') and/or M(M') layers are formed at the expense of R(R') and/or P(P') layers (i.e. a random intergrowth, with conditions similar to the de Wolff model, of R(R'), P(P'), G(G'), M(M') layers.)

Case 3 - Increasing H insertion produces an x-ray diffraction pattern which is a linear mixture of the initial and final x-ray patterns in direct proportion to the H insertion level. This is an equivalent description to that of a heterogeneous process.

Case 1 implies merely a linear (or otherwise) shift of each diffraction peak towards lower angles, in this case consistent with an expansion in the **b** direction. The results from performing such a simulation do not shed any light on the unusual diffraction effects (reported in the following chapters for the insertion of H into (in particular) the EMD coded R2) observed and are therefore not presented. For similar reasons case 3 is also not presented. In fact, the actual reduction of SBPA was easily realised to be a combination of case 1 and case 3 (chapter 5).

Case 2 is now considered in detail. To do this simulated H insertions were performed and pseudo-3D plots produced of the calculated x-ray diffraction output displaying the same perspective and angular range as those presented in the next chapter (for the actual H insertion process).

### 4.4.1 Case 2, simulated H insertion (random layer model).

Within this case there are many variations in the way that G(G') and M(M') layers may be introduced. Two variations shall be presented which will illustrate that such variations produce small but observable differences in the overall calculated diffraction patterns.

First variation Case 2(a) - sequential reduction. R(R') layers are reduced to G(G') layers followed by P(P') layers to M(M') layers. Twenty patterns were produced with simulated r'in $MnOOH_{r'}$ covering the range r'=0.0 to r'=1.0 in steps of 0.05. $\alpha_{RR'}$ and

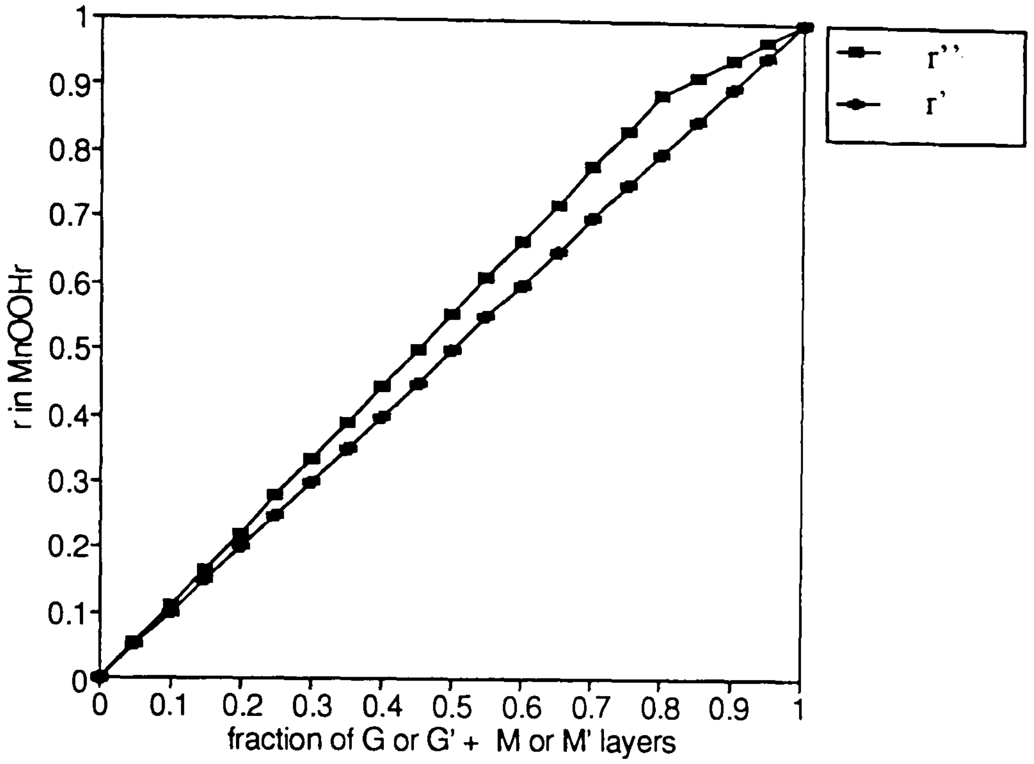

Figure 4-11 Correct relation between layer fraction and stoichiometry expressed as r in $MnOOH_r$. $r'=B_{GorG'}+B_{MorM'}$ and r'', the correct stoichiometry, as given by equation 4.3.

$\alpha_{GR'}$ were decreased from 0.8 to 0.0 at the same time as $\alpha_{RG'}$ and $\alpha_{GG'}$ were increased from 0.0 to 0.8 in steps of 0.05[†]. Thus the existence probability $B_{GorG'}$ was incremented in steps of 0.05. Once all R(R') layers had been replaced (i.e. when $B_{GorG'}=0.8$) then a similar procedure introduces M(M') layers at the expense of P(P') layers until $B_{MorM'}=0.2$ and $r'=1.0$, where $r'=B_{GorG'}+B_{MorM'}$. r' does not reflect the theoretical stoichiometry of the hypothetical random layer model crystal. This is because there are two formula units in R(R') or G(G') layers but only one in P(P') or M(M') layers. It follows therefore that the stoichiometry is given by

$$r''=(2B_{GorG'}+B_{MorM'})/(2(B_{RorR'}+B_{GorG'})+B_{PorP'}+B_{MorM'}) \tag{4.3}$$

The difference between r' and r'' is illustrated in figure 4-11.

Second variation case 2(b) - 'simultaneous' reduction of R(R') and P(P') layers. That is to say G(G') layers were introduced independently from M(M') layers in such a manner that R(R') and P(P') layers are fully replaced at the same moment, which

---

[†] The corresponding transition probabilities beginning with a dashed layer (eg $\alpha_{G'G}$) were similarly varied. Note that the probability of the next layer being a P or P' layer was fixed by maintaining all transition probabilities containing P or P' equal to 0.2=p.

corresponds to r''=1.0. In this case r''=r'. 20 patterns were produced at 0.05 intervals in r''.

The results of case 2(a) are displayed in figures 4-12, 4-13 and 4-14. The following properties are noted. If the d spacing of the initial and final calculated patterns are sufficiently close then an approximately linear shift is observed in the diffraction peak. This applies to for example (021), (111) and (121) in figure 4-12. With the APD program (see section 3.4.1) the peak positions for (021) were determined for each of the calculated patterns. The results are indicated in figure 4-15. This clearly shows an almost perfectly linear relationship until r''=0.8. Thus in this case the S shape of the H-T effect is too small to be detected. Beyond r''=0.8 a change in slope occurs which may be identified with the introduction of M(M') layers. If the d spacing is larger as for example for (*130*) the S shape of the H-T effect is clearly present. When the interplanar spacing is much larger, however, no longer is the diffraction peak continuously visible throughout the r'' range but rather it is only visible at low and high r''. This description applies to (040) and (140) in figure 4-12, and (*151*) and (061) in figure 4-14.

Similar conclusions apply to the results for case 2(b) as illustrated in figures 4-16, 4-17, 4-18. The change in slope for the peak position of (021) versus r'' referred to for case 2(a) due to the introduction of M(M') layers is now no longer visible (see figure 4-15). This is a general conclusion for all peaks showing a continuous shift with r'' and therefore provides a method which in principle could distinguish whether reduction of groutite type layers is sequentially followed by the reduction of pyrolusite type layers or whether they both reduce 'simultaneously'. Comparison of the two variations indicates that the behaviour of peaks (040), (140), (*151*) and (061), which fade rapidly in the initial H insertion range and then re-appear at deep H insertion levels, with hardly any peak movement, is independent of whether the introduction of groutite type layers and pyrolusite type layers is sequential or 'simultaneous'. Figures 4-16 and 4-18 have marked only these peaks which display this phenomena (the other indices are the same as for case 2(a)).

### 4.4.2 Discussion on the 'random layer model' for simulating the x-ray diffraction patterns of reduced $\gamma$-$MnO_2$.

It has been discussed previously that the de Wolff model of $\gamma$-$MnO_2$ is not strictly a random layer model since certain combinations of layers are disallowed. What

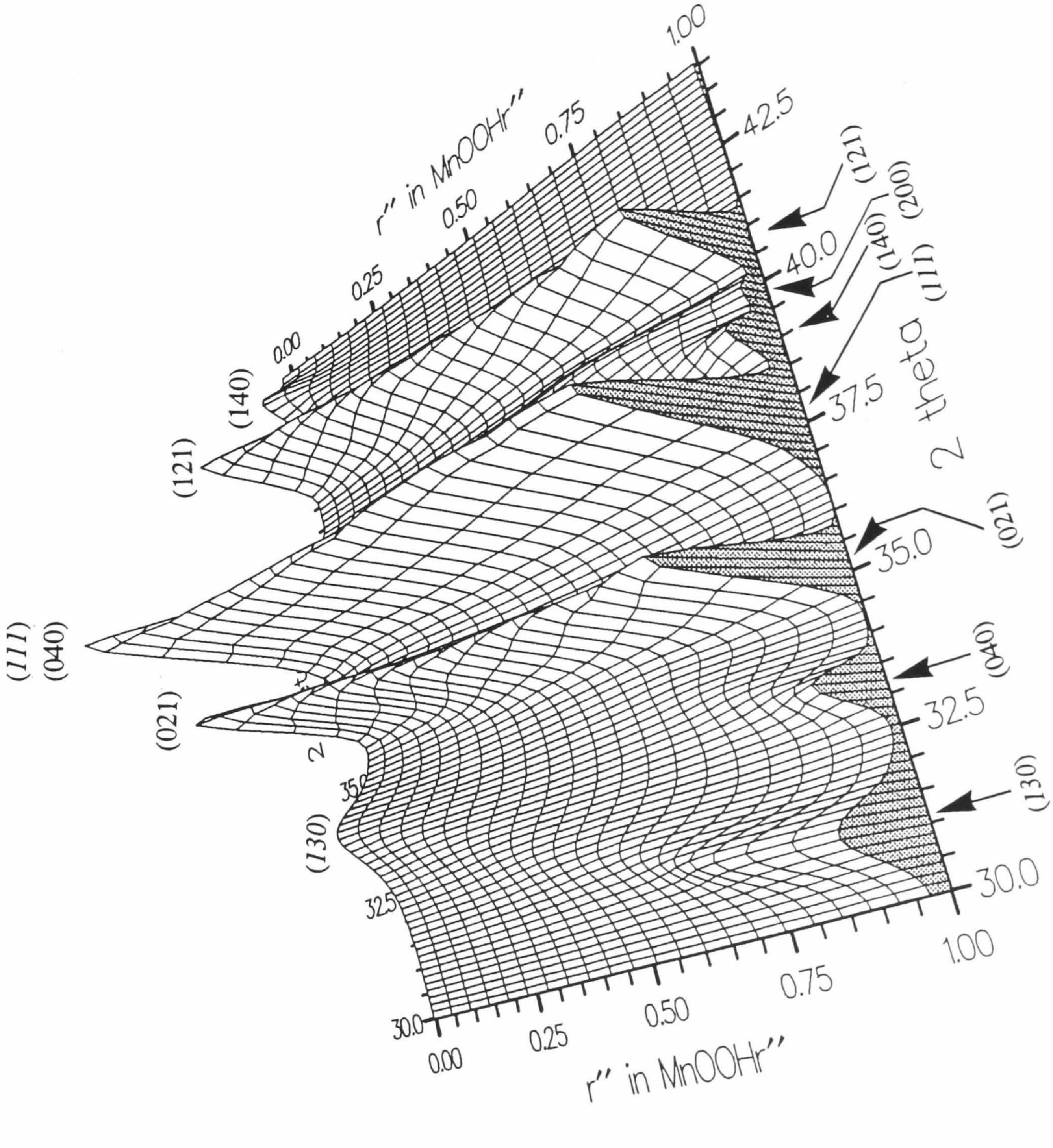

Figure 4-12 Pseudo-3D montage of calculated x-ray diffraction patterns resulting from the replacement of R(R') layers with G(G') layers and P(P') layers with M(M') layers in the manner described by case 2(a) (see section 4.4.1) in the scattering angle range 30-44 (°2θ). The indices marked in italics are shifted from their orthorhombic ramsdellite positions at r''=0.0 and from their orthorhombic groutite positions at r''=1.0.

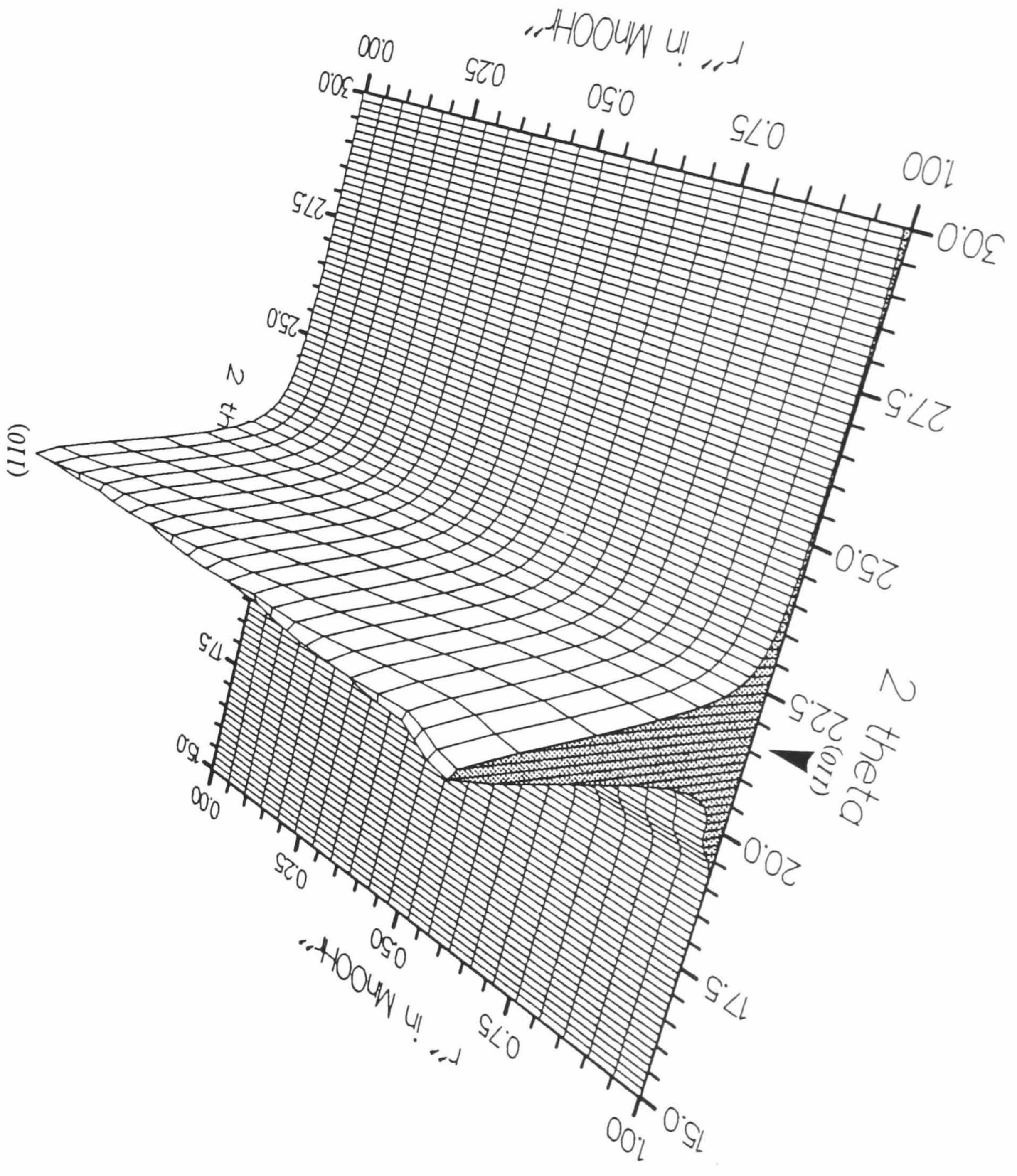

Figure 4-13 Pseudo-3D montage of calculated x-ray diffraction patterns resulting from the replacement of R(R') layers with G(G') layers and P(P') layers with M(M') layers in the manner described by case 2(a) (see section 4.4.1) in the scattering angle range 15-30 (°2θ). The indices marked in italics are shifted from their orthorhombic ramsdellite positions at r''=0.0 and from their orthorhombic groutite positions at r''=1.0.

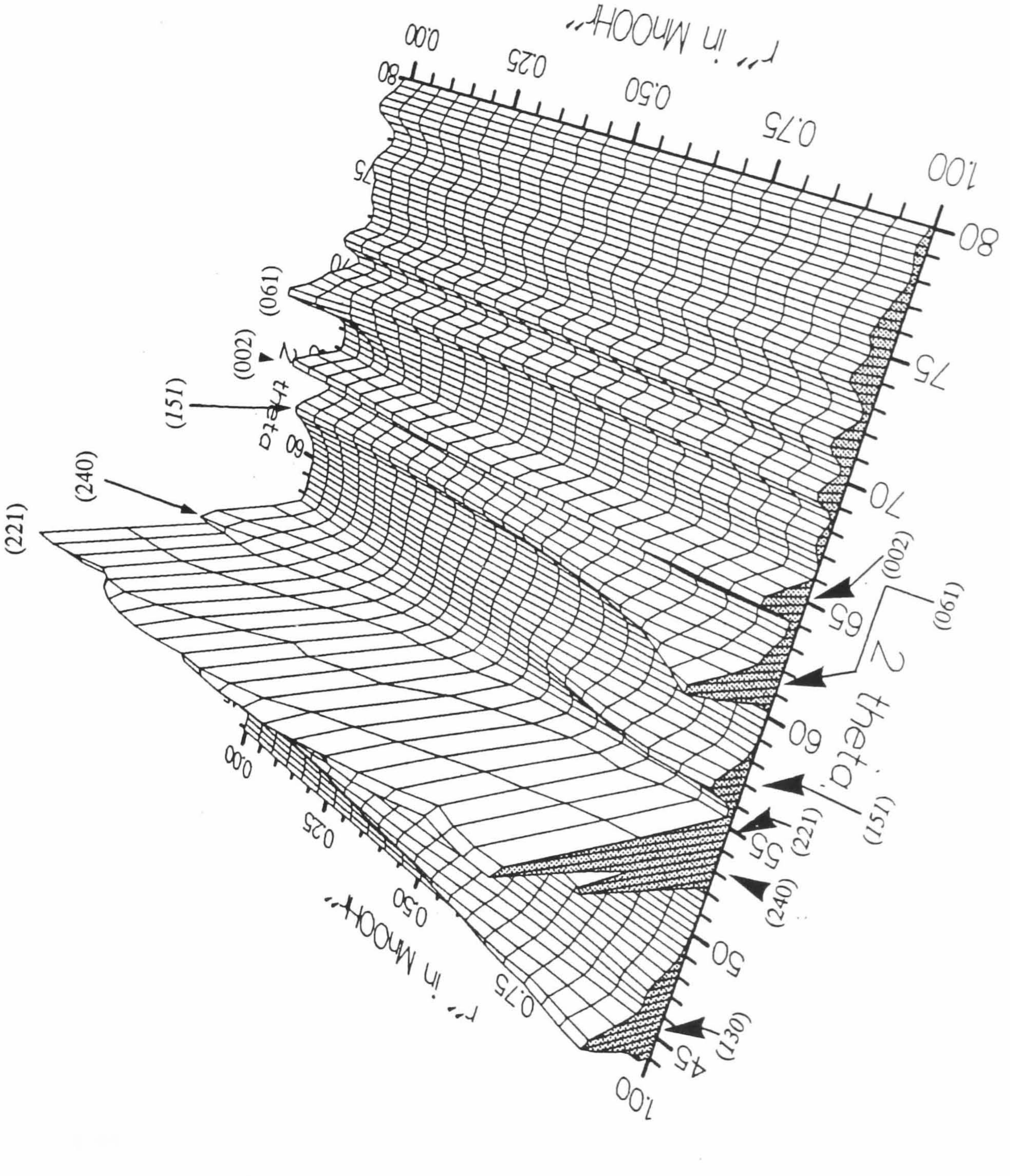

Figure 4-14 Pseudo-3D montage of calculated x-ray diffraction patterns resulting from the replacement of R(R') layers with G(G') layers and P(P') layers with M(M') layers in the manner described by case 2(a) (see section 4.4.1) in the scattering angle range 44-80 (°2θ). The indices marked in italics are shifted from their orthorhombic ramsdellite positions at r''=0.0 and from their orthorhombic groutite positions at r''=1.0.

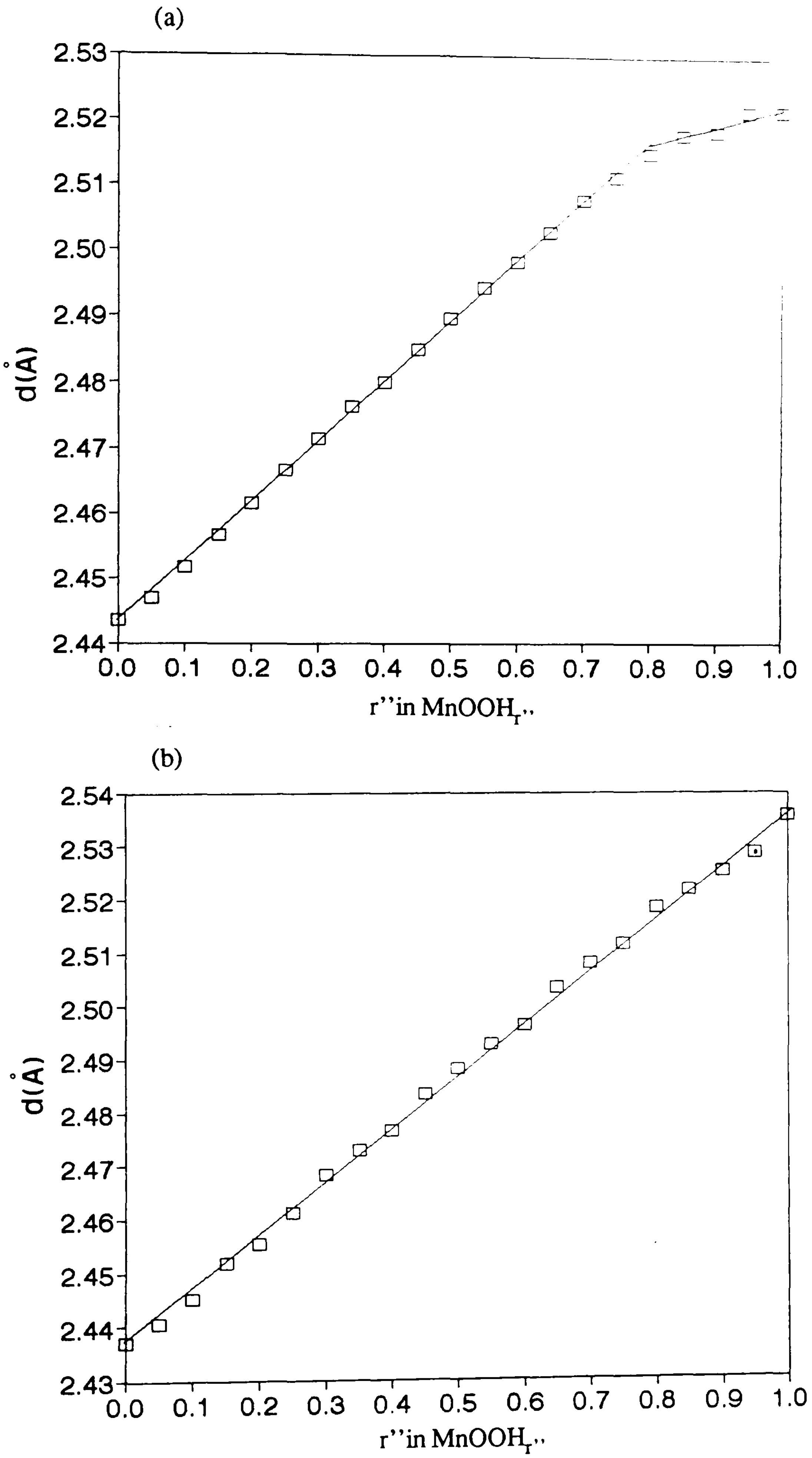

Figure 4-15 $d_{(021)}$ spacing versus theoretical r"in MnOOH$_{r''}$ stoichiometry for calculated diffraction patterns. (a) Case 2(a) (b) Case 2(b).

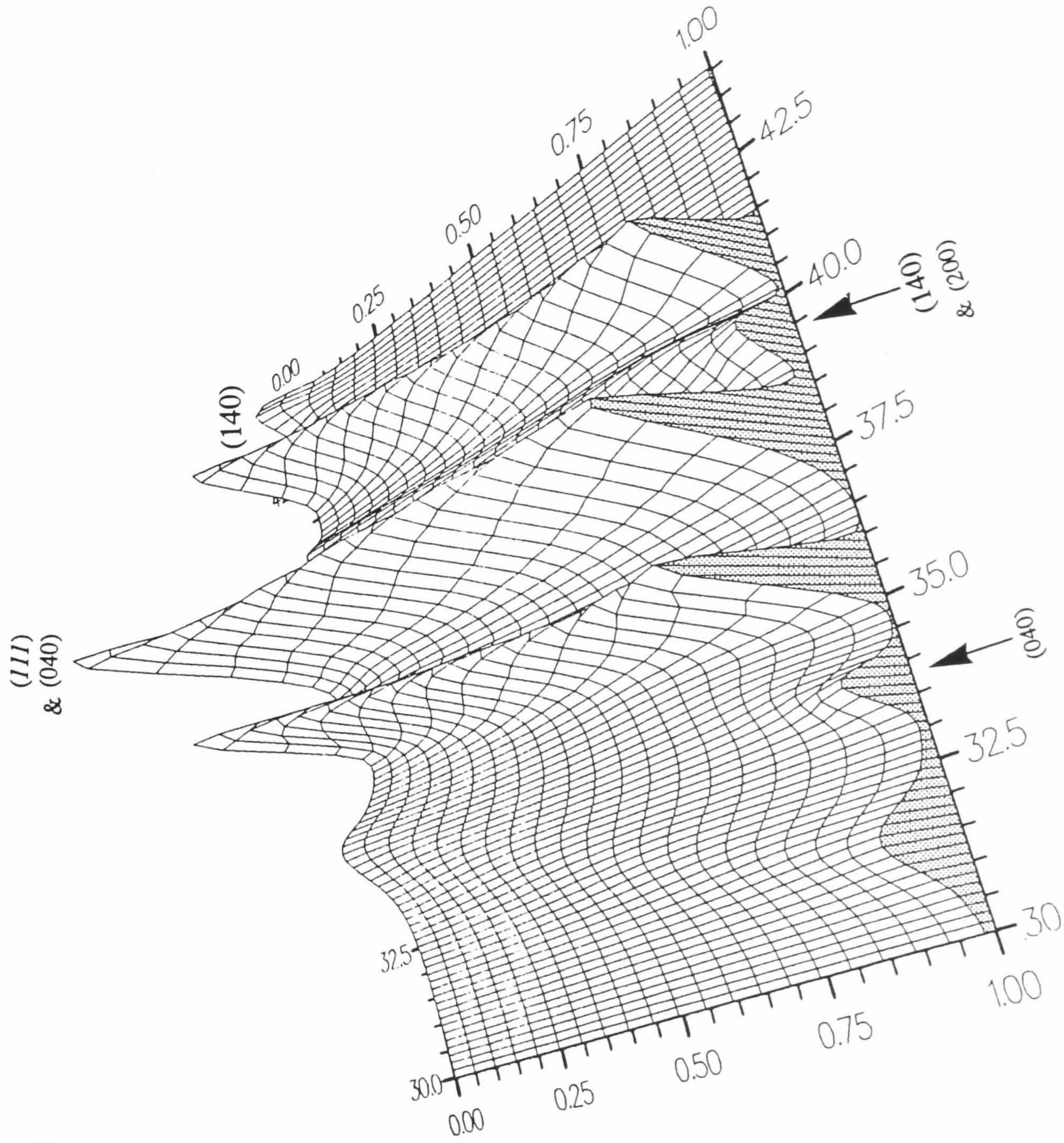

Figure 4-16 Pseudo-3D montage of calculated x-ray diffraction patterns resulting from the replacement of R(R') layers with G(G') layers and P(P') layers with M(M') layers in the manner described by case 2(b) (see section 4.4.1) in the scattering angle range 30-44 (°2θ). The peaks marked fade and re-emerge because of the H-T effect.

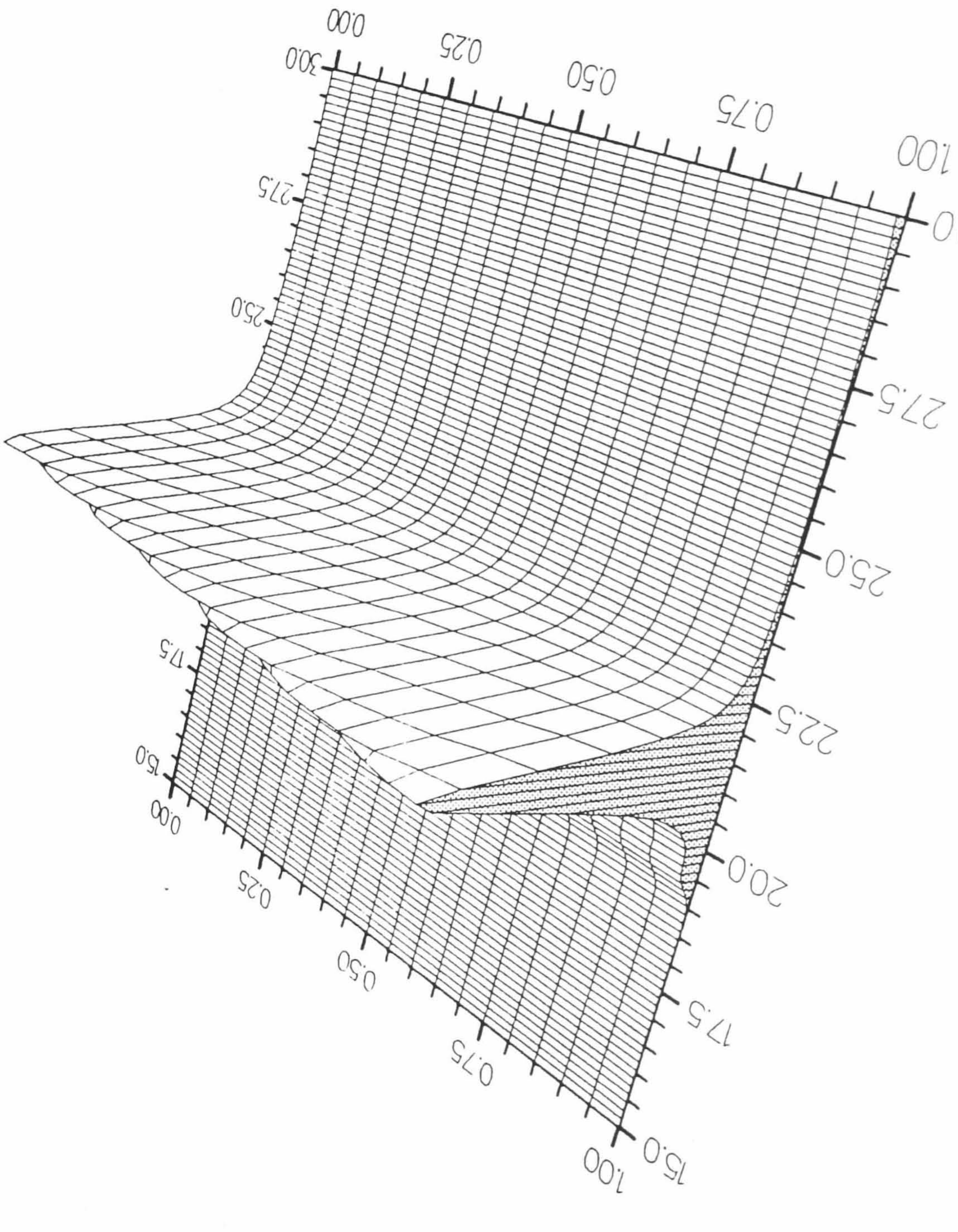

Figure 4-17 Pseudo-3D montage of calculated x-ray diffraction patterns resulting from the replacement of R(R') layers with G(G') layers and P(P') layers with M(M') layers in the manner described by case 2(b) (see section 4.4.1) in the scattering angle range 15-30 (°2θ). Peak indices as given in figure 4-13.

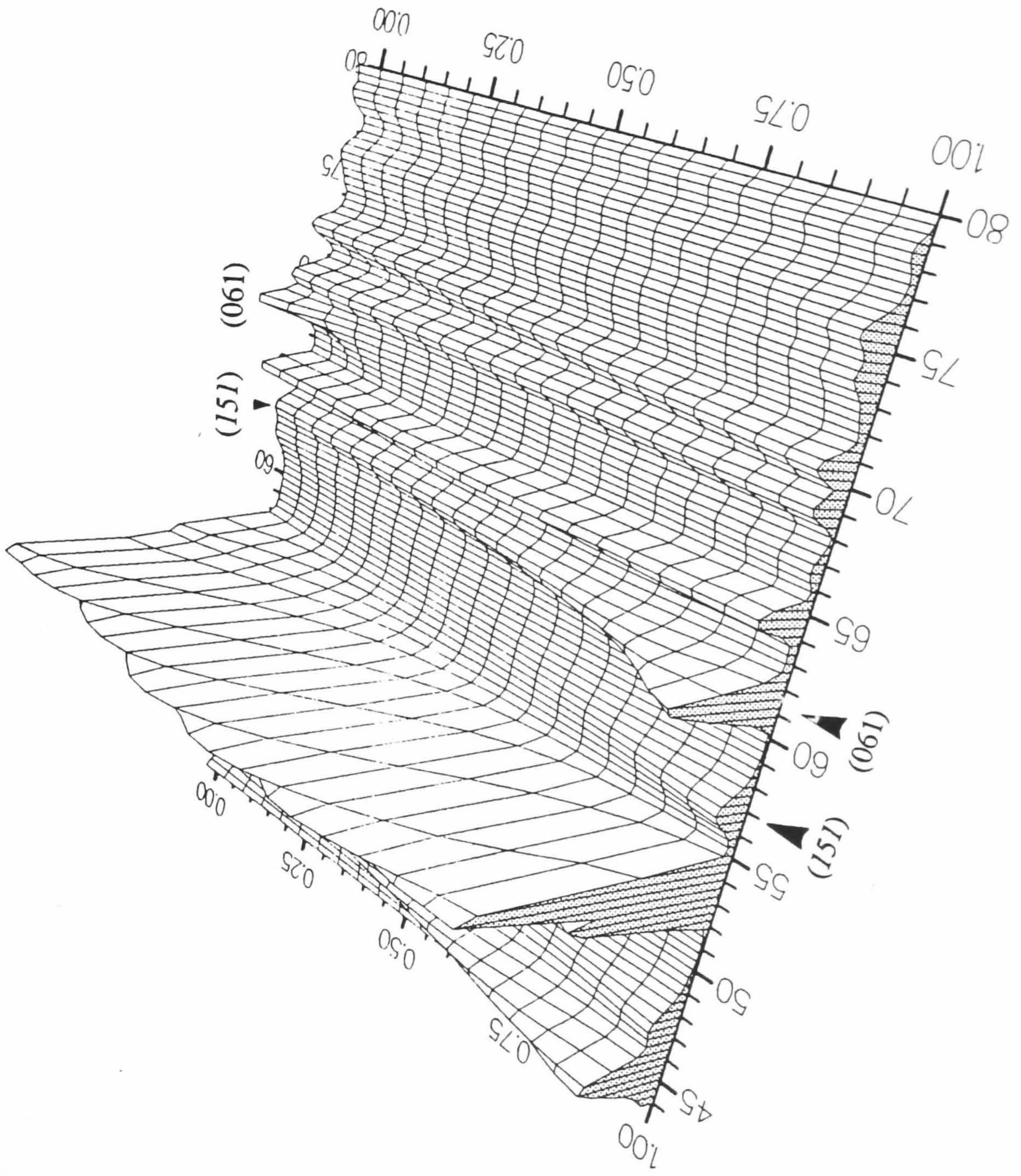

Figure 4-18 Pseudo-3D montage of calculated x-ray diffraction patterns resulting from the replacement of R(R') layers with G(G') layers and P(P') layers with M(M') layers in the manner described by case 2(b) (see section 4.4.1) in the scattering angle range 44-80 (°2θ). The peaks marked fade and re-emerge because of the H-T effect.

enables it to be called a 'random' layer model is that the probability of existence of a layer is equal to its layer transition probability which means that the probability of the next layer being G', for instance, is independent of whether the preceding layer was R, G, P' or M' (which are all the allowed possible layers). Relaxing this restriction allows for a sequence of layers which start to show different effects from the random layer model, as defined. In particular, increasing the layer transition probabilities $\alpha_{GG'}$ and $\alpha_{G'G}$ will mean greater association of these layers and a tendency towards separation of the G(G') layers into groutite portions within the crystal. The next section presents a first attempt at such a model, which demonstrates possible diffraction effects which (it shall be argued) are important to recognise in order to gain a complete understanding of the insertion of H into battery active manganese dioxide (presented in the following chapters).

### 4.4.3 A non-random layer model for simulating the x-ray diffraction patterns of reduced $\gamma$-$MnO_2$.

In this case the model is random to composition $MnOOH_{0.4444}$ corresponding to $B_{RorR'}=0.4, B_{GorG'}=0.4$ and $B_{PorP'}=0.2$. For simplicity M(M') layers were introduced sequentially as in case 2(a) (see section 4.4.1). Beyond this composition instead of $\alpha_{GG'}$ (and $\alpha_{G'G}$) increasing linearly in steps of 0.05 these transition probabilities were arbitrarily set equal to 0.70. That is if one locates a G layer in the crystal there is a 70% chance that the next layer is G'. The probability that the next layer is R' is required to be 10% since the probability of a P layer is maintained at 20% in accordance with the p value of SBPA. The stoichiometry is now no longer simply related to the transition probabilities. A calibration curve[†] of $\alpha_{RG'}$[‡], which now essentially determines the stoichiometry, versus r'' derived from the numerically outputted layer transition probabilities found by DIFFaX was constructed. The departure of the model from the random case is illustrated in figure 4-19 which indicates the probability of finding the pair GG' in the crystal. This is given by $B_{GG'}=B_G\alpha_{GG'}$. At r=0.7778, which corresponds to $\alpha_{RG'}=0.7$, the model reverts to the random case since now the probability of a G layer is independent of the layer preceding it. The remaining R(R') layers are then

---

[†] It is a requirement that $\alpha_{XX'}=\alpha_{X'X}$, where X=R,G,P,M.

[‡] It ought to be possible to derive an analytical relationship relating r,$\alpha$ and B.

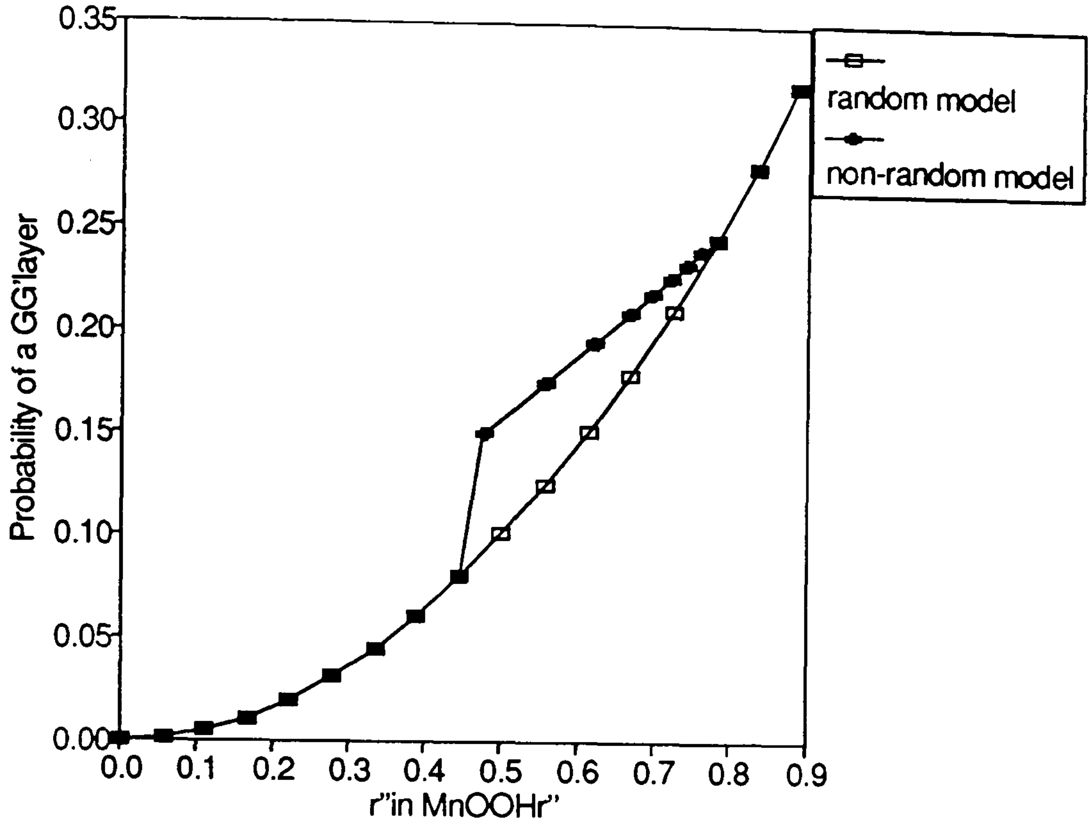

Figure 4-19 Probability of finding a G layer followed by a G' layer, $B_{GG'}=B_G\alpha_{GG'}$, in the a random and non-random layer model of R(R'),G(G'),P(P') layers.

replaced by G(G') layers as in the random model (see section 4.4.1). The final stoichiometry in figure 4-19 of r''=0.889 corresponds to all R(R') layers replaced by G(G') layers. Further reduction introduces M(M') layers at the expense of P(P') layers as in section 4.4.1. The results are again presented as a pseudo-3D montage of the calculated patterns, figure 4-20.

## 4.5 Final comments.

It may seem odd to those familiar with the 'S' shaped electrode potential of battery active manganese dioxide even to consider model in which reduction occurs by random introduction of G(G') (and M(M')) layers in an extended random layer model. That is because this concept appears to be clearly at odds with the concept of a solid solution with $H^+$ and $e^-$ mobile within the crystal structure, since, introduction of G(G') (and or M(M')) layers implies that H is located within a layer. Furthermore it is physically difficult to imagine why reduction should occur by introduction of layers, which extend throughout the crystal, and why they should assume a random distribution.

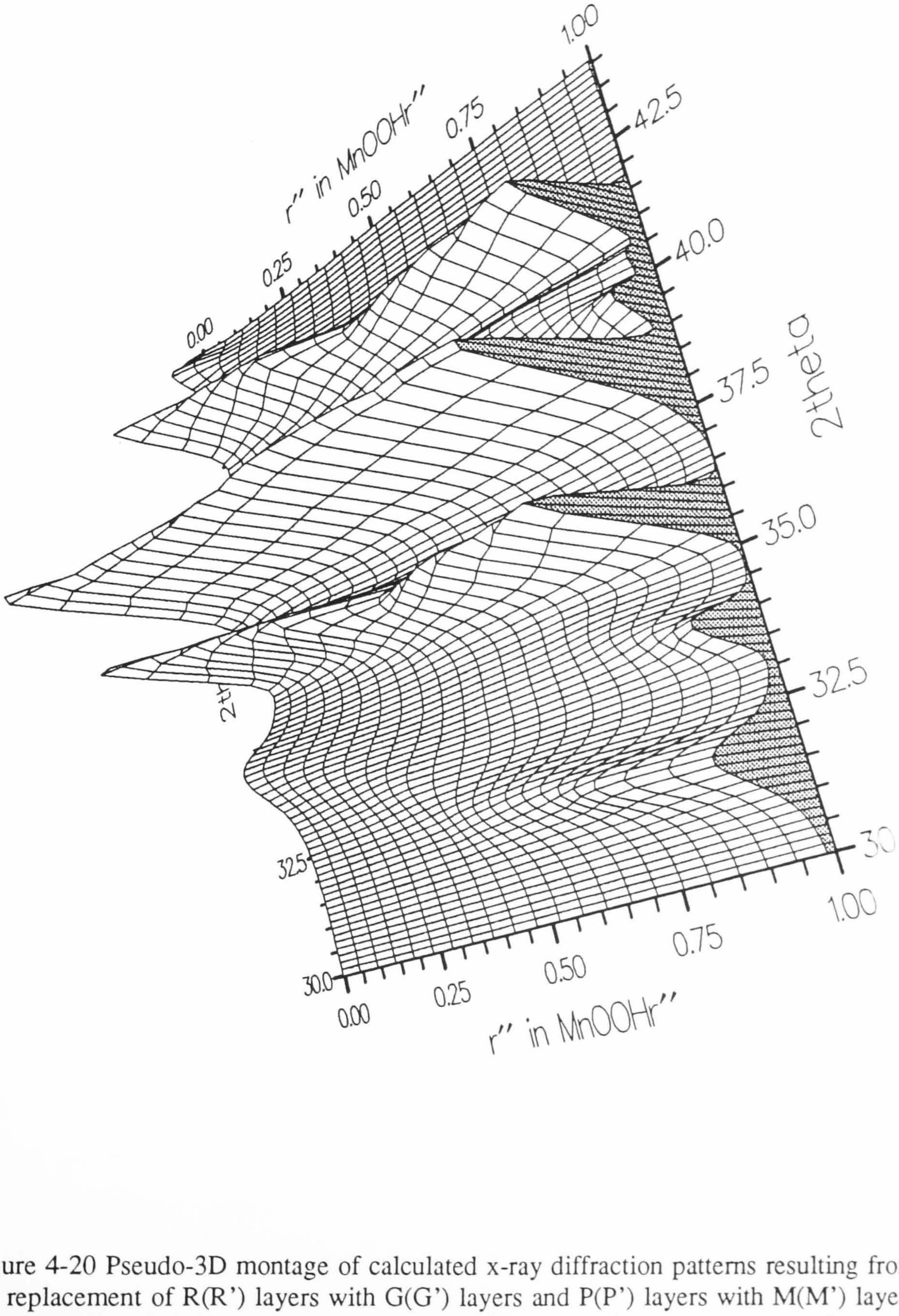

Figure 4-20 Pseudo-3D montage of calculated x-ray diffraction patterns resulting from the replacement of R(R') layers with G(G') layers and P(P') layers with M(M') layers in the manner described by the non-random layer model (see section 4.4.3) in the scattering angle range 30-44 (°2θ). Peak indices as given in figure 4-12.

To this the author accedes to but the following comments may still by worth considering.

If one imagined taking a 'snapshot' of the crystal and locating the positions of $H^+$ and $e^-$, it may be that there is a tendency (the reason for which is unknown) for the protons and electrons to assume positions consistent with the description of an extended random layer model. This admittedly seems quite unreasonable in the case of a member of $\gamma$-$\gamma_t$-$MnO_2$ series towards the $\gamma$-$MnO_2$ end, but not perhaps for heavily microtwinned samples where the notion of a 'layer', in the sense of a random layer model, no longer correctly describes the structure. Essentially, the de Wolff model introduces disorder in a single direction (namely in the $\mathbf{b}_0$ direction) whereas Pannetier's model contains two directions ($\mathbf{b}_0$ and $\mathbf{c}_0$) of disorder.

Quite apart from the above comments, the value of the extended random layer model will become apparent when considering the insertion of H into battery active manganese dioxide near the $\gamma_t$ end of the $\gamma$-$\gamma_t$-$MnO_2$ series (chapter 6) in the region where evidence for restricted mobility of H at deep H insertion levels has already been accumulated[68].

# 5 Interpretation of the X-Ray Diffraction Patterns and FTIR Spectra of Material SBPA with H Insertion Level.

## 5.1 Introduction

In chapters 2 and 4 the structure of the initial (i.e. before H insertion) battery active materials examined in this study and those of the final (i.e. after full H insertion) were discussed. It was concluded that the initial materials are members of the $\gamma$-$\gamma_t$-$MnO_2$ structural series and their reduced counterparts of an analogous H inserted structural series (the $\delta$-$\delta_t$-MnOOH series). Such an observation indicates that structural defect responsible for the $\gamma$-$\gamma_t$-$MnO_2$ series was retained after the H insertion reaction. To a very large extent only phases characteristic of the solid state H insertion reaction were produced by the chemical H insertion technique discussed in section 3.2, that is to say, phases produced through subsidiary chemical reactions via soluble intermediates were minimised. Attempts to do this have been made previously[32,102,22,103,33,73,68,95]. A feature of this investigation was the structural range of battery active materials investigated. Previous investigators have mostly focused on materials at the $\gamma_t$ end of the $\gamma$-$\gamma_t$-$MnO_2$ series. An exception is the work of Giovanoli *et al.*[33] He confirmed the de Wolff model of $\gamma$-$MnO_2$ by selected area electron diffraction of a relatively crystallized $\gamma$-$MnO_2$ obtained from a chemical synthesis procedure[104]. Similar deductions were then made concerning the reduction of such a $\gamma$-$MnO_2$ with cinnamyl alcohol in xylene, a method first introduced by Gabano *et al.*[22] That is the x-ray diffraction pattern of the reduced product was also observed to display qualitativley similar selective line shifts to those of $\gamma$-$MnO_2$ (see section 4.1) or in other words it appeared to be $\delta$-MnOOH. Gabano *et al.* had previously concluded that their final product was $\alpha$-MnOOH. If the $\gamma$-$MnO_2$ was "extremely disperse", however, $\delta$-MnOOH was not produced but $\gamma$-MnOOH in a double phase reaction. It is clear that what Giovanoli meant by "extremely disperse" $\gamma$-$MnO_2$ is what he later recognised[2] as $\varepsilon$-$MnO_2$, which corresponds to the $\gamma_t$ end of the $\gamma$-$\gamma_t$-$MnO_2$ as defined in this work. Such a conclusion has later been shown to be tenable only when the reduction occurred in aqueous solution[73], and as in this work (to be discussed in chap.6), a quite different product is obtained when the reduction was carried out by Gabano *et al.*'s method (or the similar procedure used in this work). This chapter deals with the nature of the changes which occurred when H was inserted into a material near the $\gamma$ end of the $\gamma$-$\gamma_t$-$MnO_2$ series (i.e. material SBPA).

## 5.2 Effect of H insertion on the diffractograms of SBPA.

A convenient representation of the changes in the x-ray diffraction pattern which occurred with H insertion is the pseudo-3d plot of figure 5-1. The number of gridcells in the direction of the r axis was chosen to be equal to the actual number of patterns used to construct the interpolated data (cf. section 4.3.2). The number in the $2\theta$ direction was 100, which by experiment, was found to accurately represent the actual shape of the x-ray diffraction peaks. Reducing this number meant that 'bumps', for instance on the shoulder of the (111)&(040) peak would not be properly followed. Figure 5-2 summarises a selection of the actual data obtained across the H insertion range from which the pseudo-3D plots were constructed. This figure shall be referred to in later sections which present similar summaries of the x-ray diffraction data obtained on other materials in the $\gamma$-$\gamma_t$-$MnO_2$ series.

Figure 5-1 provides a qualitative description of the dramatic changes which are produced with H insertion in a particular range of $2\theta$ values. Initially the maxima move towards lower $2\theta$ angles and from r=0.35 additional peaks start to emerge. At the same point some of the initial maxima (eg $(021)_R$) start to decrease rapidly in intensity. The peaks which emerge (eg $(021)_G$) do not appear to show any peak shifts[†]. Similar pseudo-3D plots are presented for the regions 15-30(°2$\theta$) and 44-80(°2$\theta$) figures 5-3 and 5-4. The notable feature of figure 5-3 is the gradual appearance of the peak at 26°2$\theta$ which has already been identified as belonging to manganite. At high H insertion levels many peaks fade with the appearance of new maxima characteristic of the final reduced product. Some, however, notably (110), (111) and (121) remain visible at all H insertion levels but with intensities which apparently go through a minimum but with a clear

---

[†] Peak shifts may be identified by noting whether the construction lines which are at constant $2\theta$ remain at the same intensity on a peak with increasing r in $MnOOH_r$ or whether they appear to 'climb' up the side of a peak.

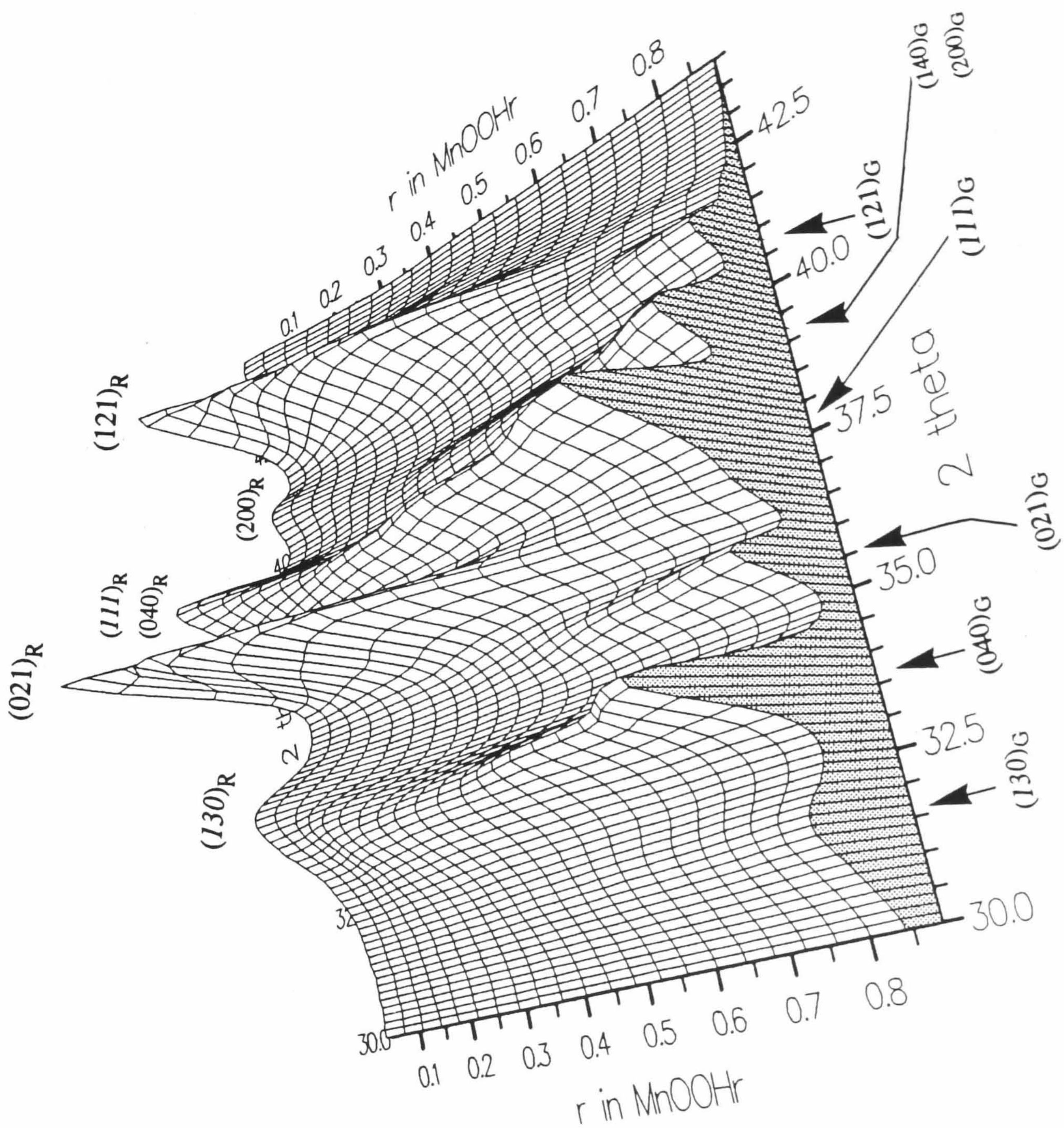

Figure 5-1 Pseudo-3D plot of the x-ray diffraction patterns resulting from H insertion into sample SBPA in the 2θ range 30-44 (°2θ). The subscript R indicates indices derived from a ramsdellite lattice and G those from a groutite lattice.

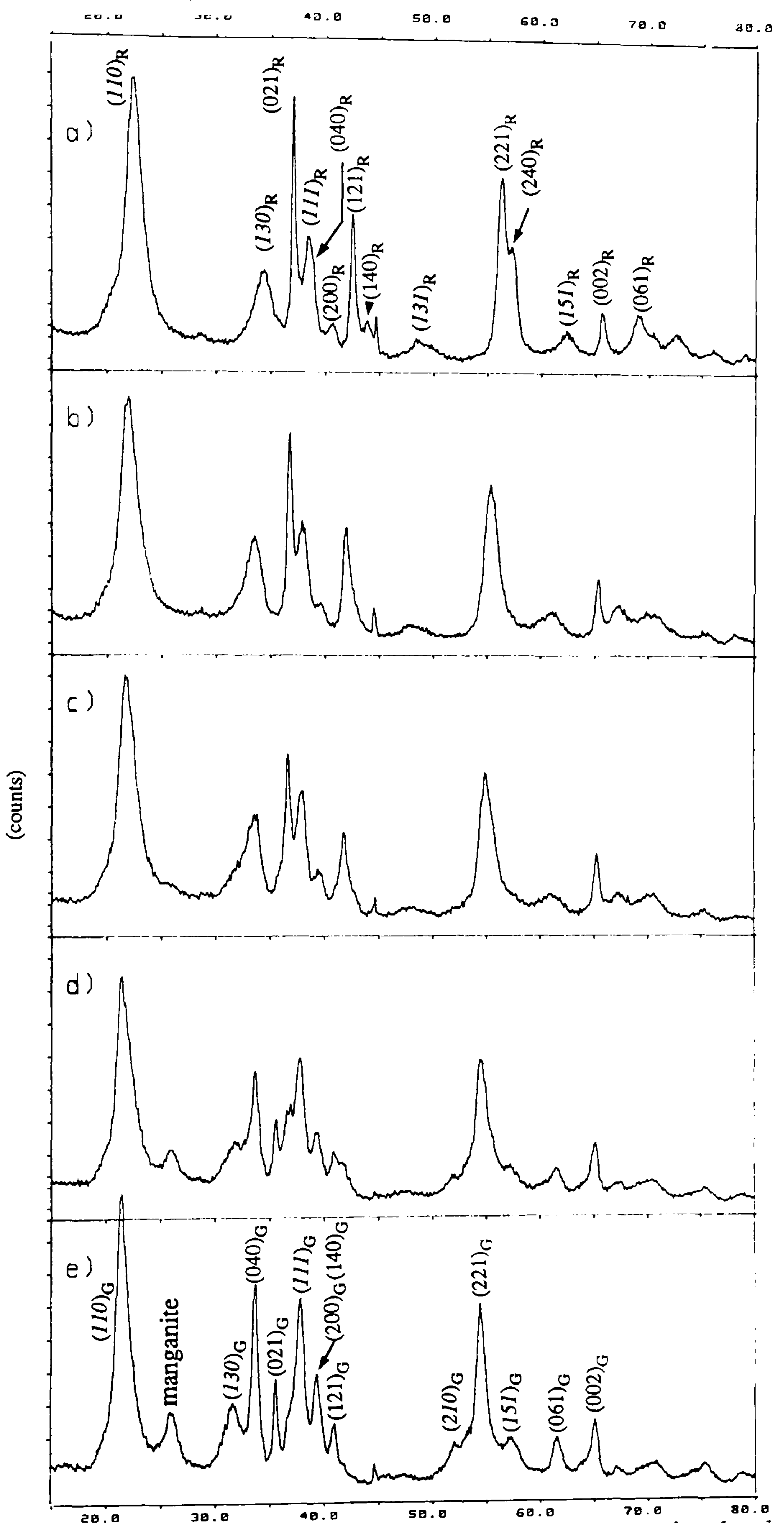

Figure 5-2 Selection of x-ray diffraction patterns representing the changes which occurred with H insertion into material SBPA. (a) $MnOOH_{0.068}$ (b) $MnOOH_{0.346}$ (c) $MnOOH_{0.514}$ (d) $MnOOH_{0.706}$ (e) $MnOOH_{0.882}$. Indices related to ramsdellite $(hkl)_R$ and groutite $(hkl)_G$ are marked.

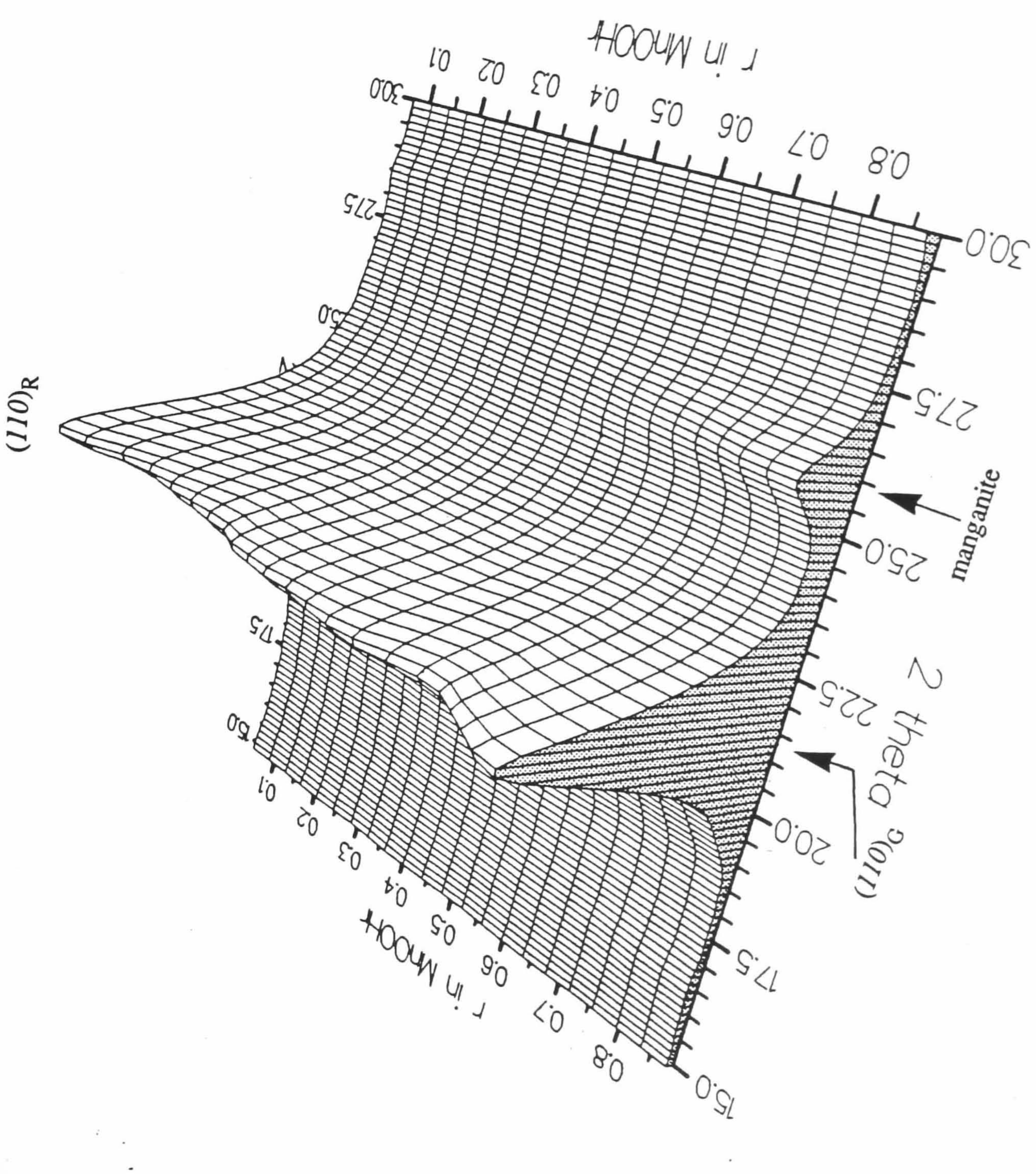

Figure 5-3 Pseudo-3D montage of the x-ray diffraction patterns resulting from H insertion into sample SBPA covering the scattering angle range 15-30 (°2θ). The subscript R indicates indices derived from a ramsdellite lattice and G those from a groutite lattice.

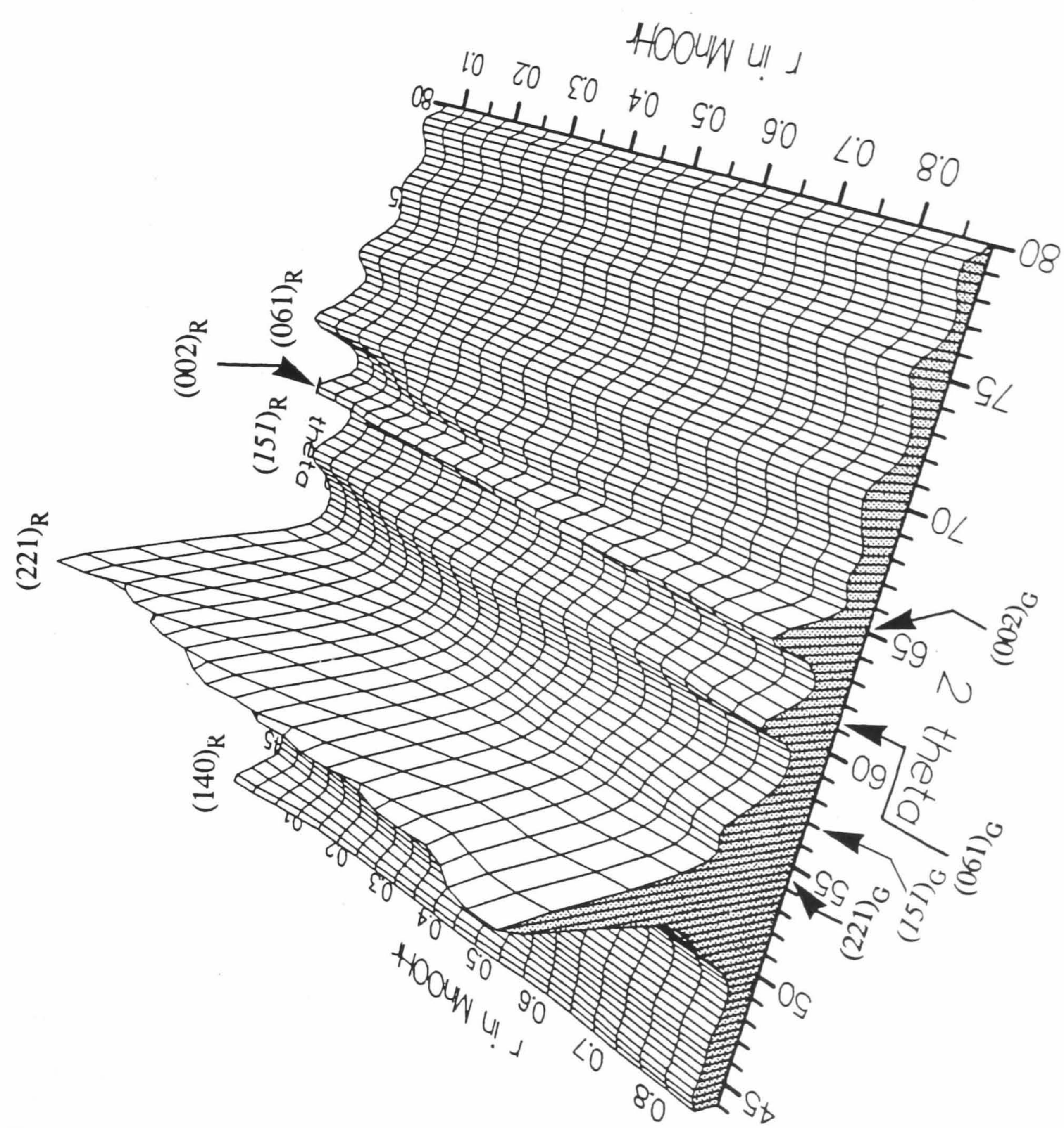

Figure 5-4 Pseudo-3D montage of the x-ray diffraction patterns resulting from H insertion into sample SBPA covering the scattering angle range 44-80 (°2θ). The subscript R indicates indices derived from a ramsdellite lattice and G those from a groutite lattice.

'hump' which would otherwise be the minimum.

The diffractograms presented as pseudo-3D plots admit to a simple unambiguous description. That is of homogenous reduction from $MnOOH_{0.068}$ (starting material) to $MnOOH_{0.35}$ with accompanying lattice dilation in the manner expected for a solid solution (see section 4.3.1) and thereafter heterogeneous reduction from $MnOOH_{0.40}$ to $MnOOH_{0.882}$. That this is so is may be partially appraised by examining the observed peak shifts of any of the available peaks. Consider for example the observed peak shifts of $(021)_R$ and $(121)_R$ of the initial starting material indicated in figures 5-5 and 5-6. Clearly both diagrams signify almost linear peak shifts to an H insertion level corresponding to $r=0.40$ whereby a break occurs and thereafter no subsequent peak shifts. Furthermore the intensity of these peaks beyond $r \sim 0.40$ rapidly decreases and eventually the peaks fade entirely (see figure 5-1). In the same region where both $(021)_R$ and $(121)_R$ start to fade growth of peaks representative of the final reduced product, namely $(021)_G$ and $(121)_G$ emerge (see again figure 5-1), the positions of which are also independent of H insertion level, as displayed in figures 5-5 and 5-6.

In the next section (on FTIR) evidence shall be presented indicating that the solid solution region in fact only extends to $r=0.35$ rather than to $r=0.40$ as suggested from figures 5-5 and 5-6.

Table 5.1 Measured lattice parameter variation in SBPA at H insertion levels marking the boundaries of homogeneous and heterogeneous reduction.

| | r in $MnOOH_r$ | $a_o$ (Å) | $b_o$ (Å) | $c_o$ (Å) |
|---|---|---|---|---|
| | 0.068 | 4.438 | 9.35 | 2.850 |
| %change from those at $r=0.068$ | 0.35 | 2.4% | 1.0% | 0.3% |
| %change from those at $r=0.068$ | 0.882 | 2.2% | 13.9% | 0.7% |

If it is the case that a solid solution exists in the H insertion region $0.068 \leq r \leq 0.35$

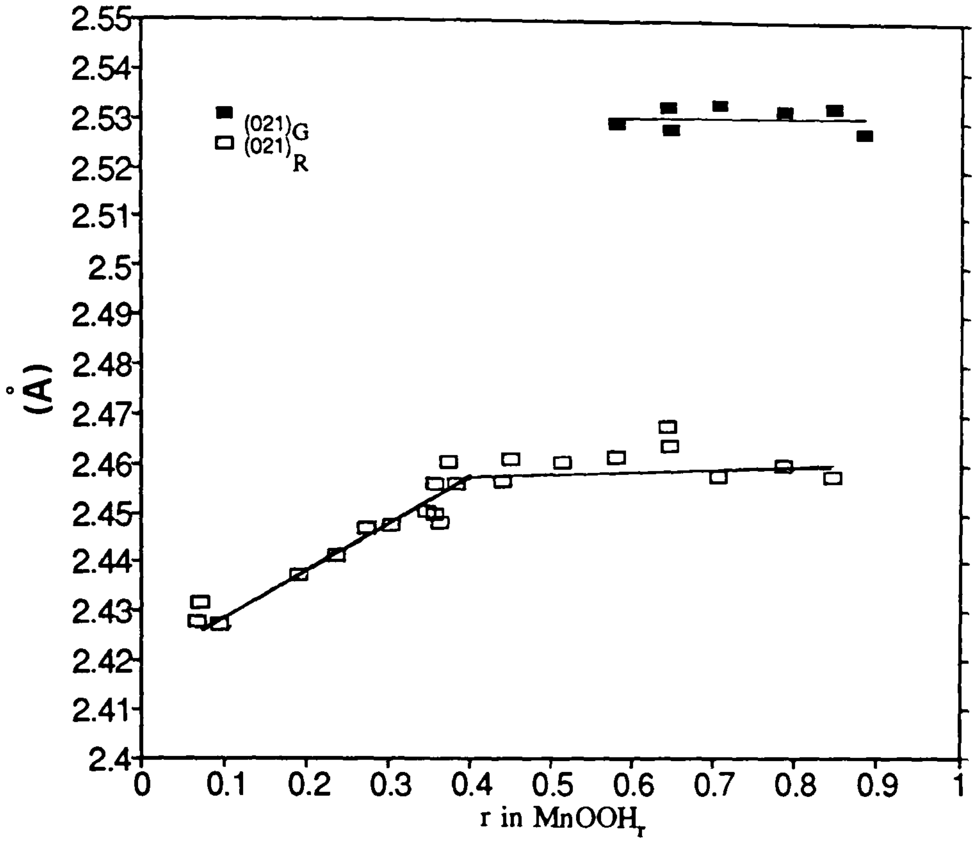

Figure 5-5 d or interplanar spacing variation of peak (021) with H insertion level for SBPA. R - derived from ramsdellite index, G - derived from groutite index.

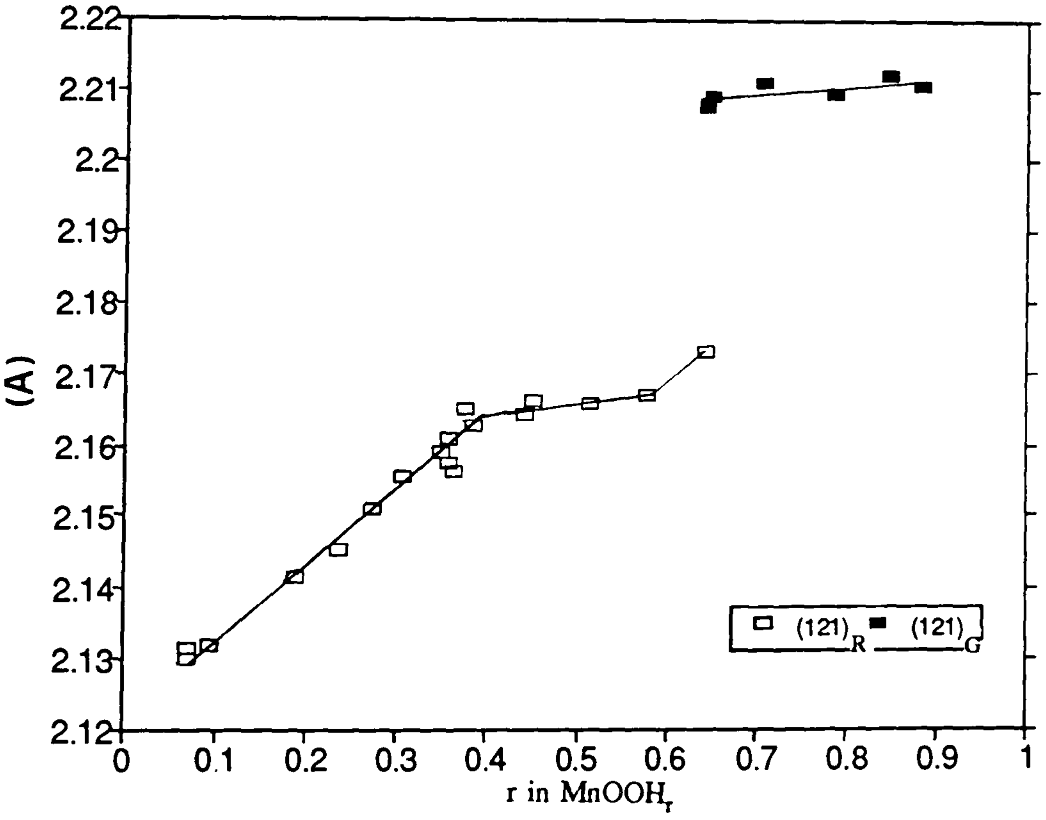

Figure 5-6 d or interplanar spacing variation of peak (121) with H insertion level for SBPA. R - derived from ramsdellite index, G - derived from groutite index.

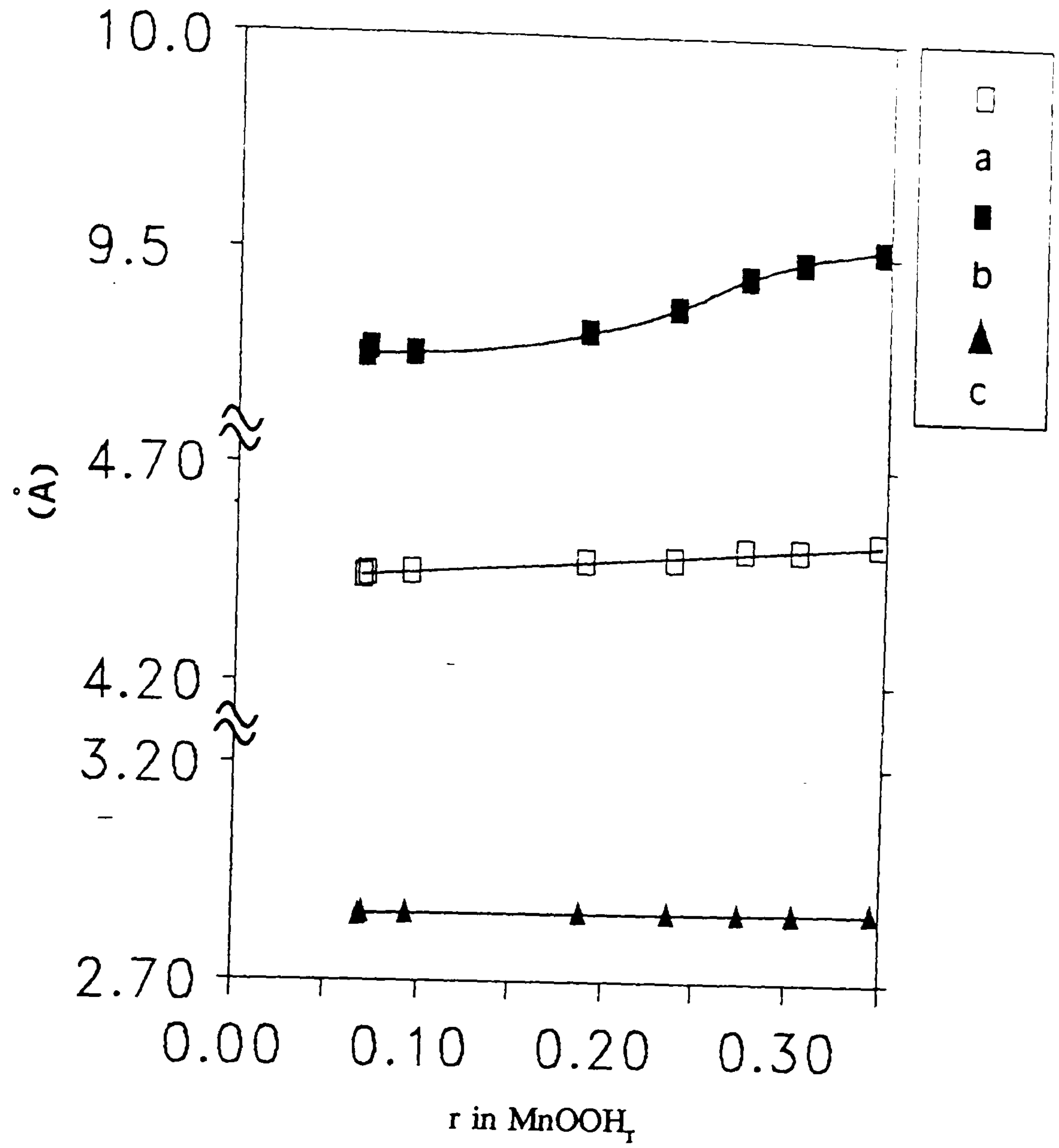

Figure 5-7 $a_0$, $b_0$, $c_0$ lattice parameter variation of SBPA in solid solution H insertion range (0.068<r<0.35). Beyond this level H starts to 'freeze' in position (see sect.5.4).

it is possible to derive lattice parameters in this range from the 'sharp peaks' as was done to find the initial lattice parameters (see section 2.3.2). Figure 5-7 presents results of such an analysis indicating the changes which occurred to $a_0$, $b_0$ and $c_0$ in the solid solution H insertion region. Table 5.1 summarises the overall changes in lattice parameters which occur for the total H insertion range achieved.

There is one question that remains concerning the conclusion that the observed lattice expansion in the region r=0.068 to r=0.35 is the result of a solid solution type lattice expansion. As proved in section 4.4.1 linear changes in peak position can be simulated by an extended random layer model in which G(G') (and/or M(M')) layers are introduced into a R(R') (and/or P(P')) layer matrix. As noted previously, such a model implies that H is immobile within the random layer structure. The next section shall show that supplementary Fourier Transform Infra-red spectroscopy (FTIR) is able to directly reflect H mobility in the manganese oxyhydroxide structure and remove the above doubt concerning the nature of the observed peak shifts.

## 5.3 FTIR spectroscopy of H inserted SBPA.

The presentation of FTIR spectroscopy in this work shall be used only to decide questions such as those posed at the end of the last section. No fundamental analysis leading to peak assignments of the absorption bands present in synthetic battery manganese dioxide was attempted. Since this has not previously been attempted such an analysis would be extremely valuable. The problem is highly complex, however, as battery active manganese dioxide possess a de Wolff random layer structure† (and varying degrees of microtwinning) and thus is not amenable to analysis which requires a perfect crystal.

It is possible following Potter and Rossman[105] to divide the spectra obtained in this instance‡ over the frequency range 400-4000 ($cm^{-1}$) into two approximately distinct regions. In the 400-1400 ($cm^{-1}$) region absorptions are mainly thought to be due to vibrations associated with an [$MnO_6$] octahedra whereas those in the region 1400-4000 are associated with various OH vibrations[105]. Referring to figure 5-8 a large broad absorption is apparent in the 1400-4000 ($cm^{-1}$) region the cause of which is unknown, and in the 400-1400 ($cm^{-1}$) region four sharp absorptions due to vibrational modes of an [$MnO_6$] are distinguishable. As H insertion proceeds broad absorptions are left in the 1400-4000 ($cm^{-1}$) region and in the 400-1400 ($cm^{-1}$) region a general decrease in absorption occurs. If one plots at any wavenumber the absorption versus r as in for example figures 5-9, 5-10 an apparently linear relationship is discerned as indicated by the best straight line. If one plots the slopes of such graphs for all wavenumbers figure 5-11 is obtained. At certain wavenumbers, namely 1038, 974, 654, 622, 522 and 486 the slope becomes zero. That is the absorption at these wavenumbers is independent of r. This suggests that any FTIR pattern is an addition of the final and initial FTIR spectra with those wavenumbers identified representing isobestic points. Indeed synthesising a

---

† It is important to note the distinction as to whether battery active manganese dioxide posses a random layer structure and whether it reduces by introducing G(G') layers in an another (extended) random layer structure. Thus for example although $H^+$ and $e^-$ may be mobile in SBPA it still posses a random layer structure since both the initial and final reduced samples posses it.

‡ All spectra were obtained courtesy of Dr D.Swinkels.

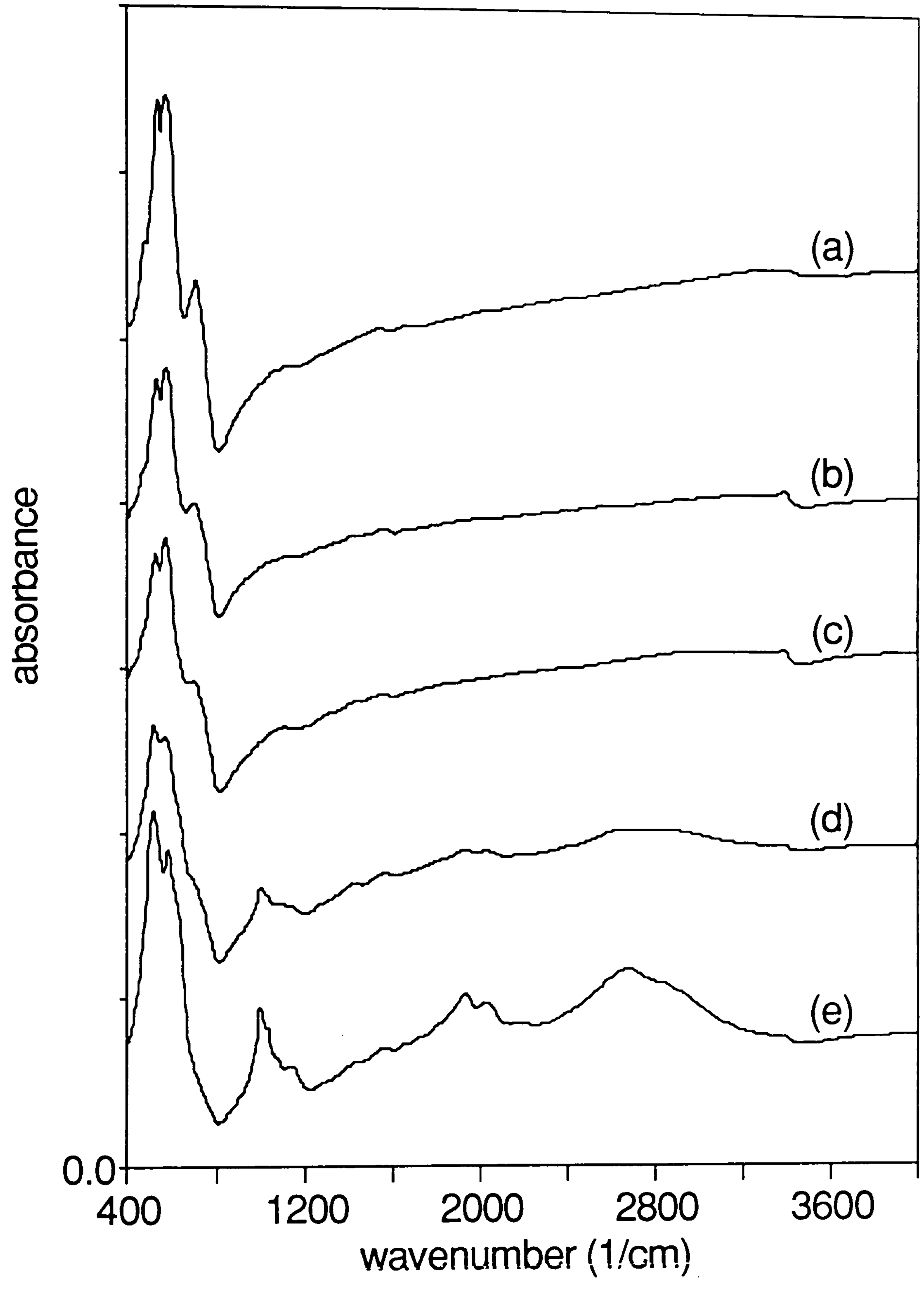

Figure 5-8 Selection of FTIR spectra of material SBPA (a) $MnOOH_{0.068}$ (b) $MnOOH_{0.236}$ (c) $MnOOH_{0.384}$ (d) $MnOOH_{0.642}$ (e) $MnOOH_{0.882}$.

pattern from the initial and final pattern does produce a rough match to an actual pattern of the same composition. Furthermore a very similar shape of graph to figure 5-11 is obtained if one produces the slope derived from the patterns for ramsdellite and groutite

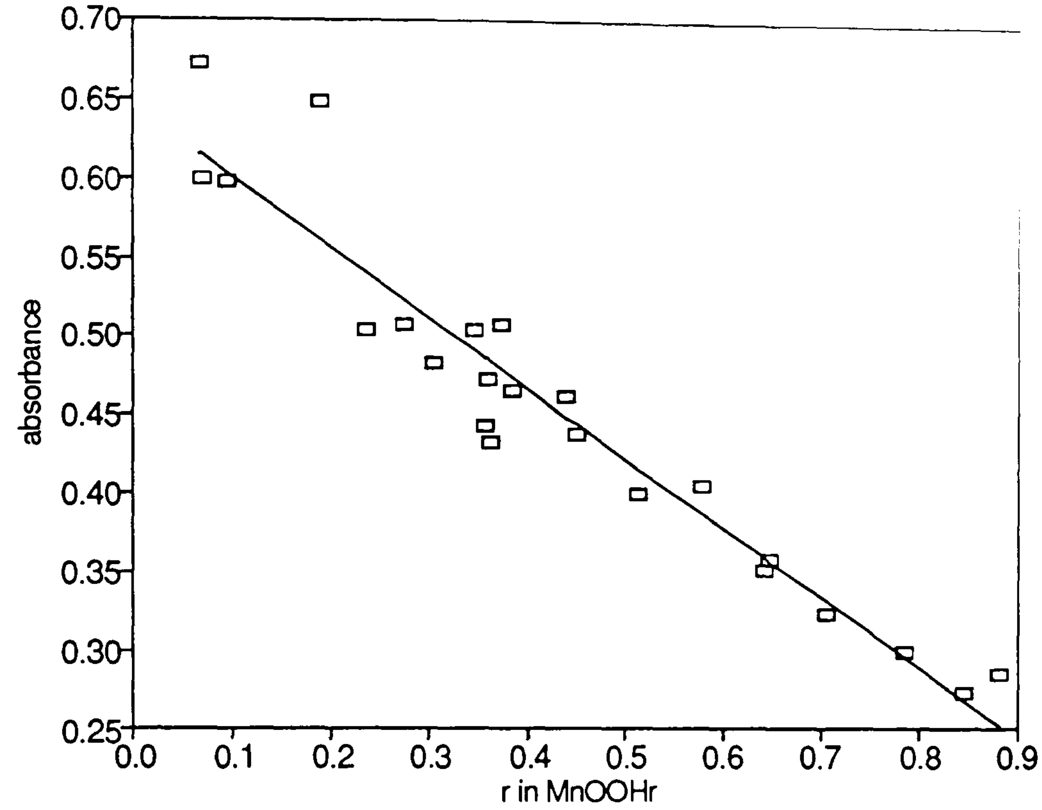

Figure 5-9 Absorbance at wavenumber 704 ($cm^{-1}$) versus r in $MnOOH_r$ for material SBPA.

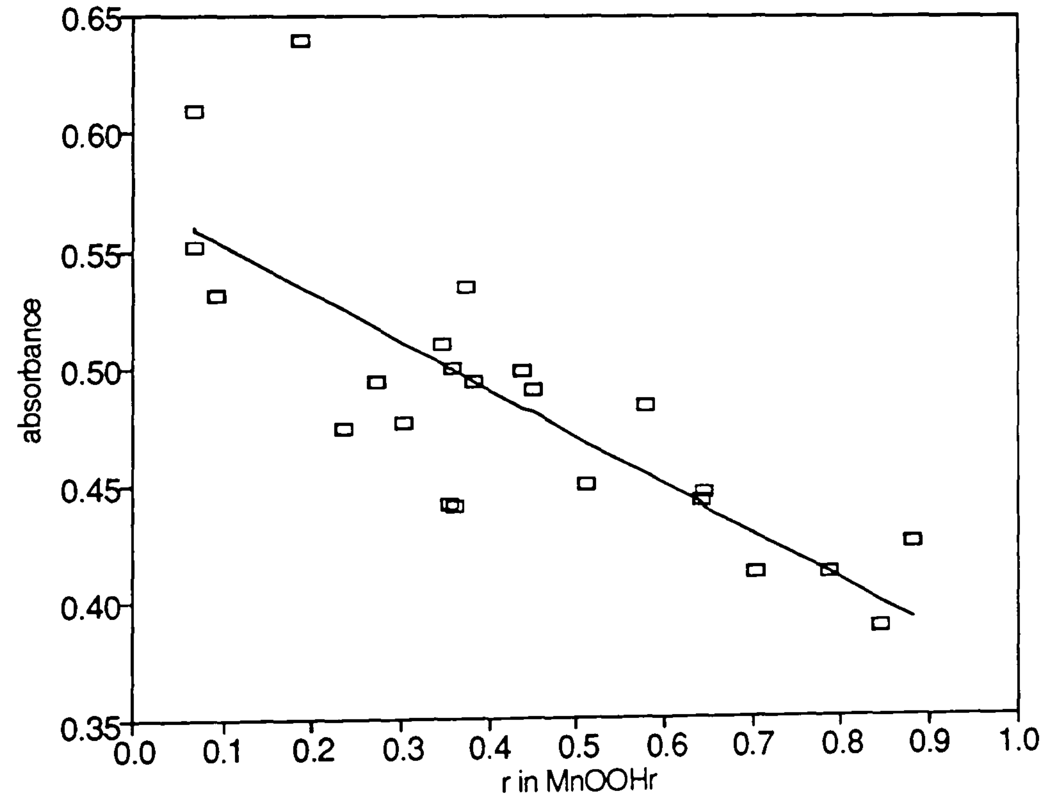

Figure 5-10 Absorbance at wavenumber 2200 ($cm^{-1}$) versus r in $MnOOH_r$ for material SBPA.

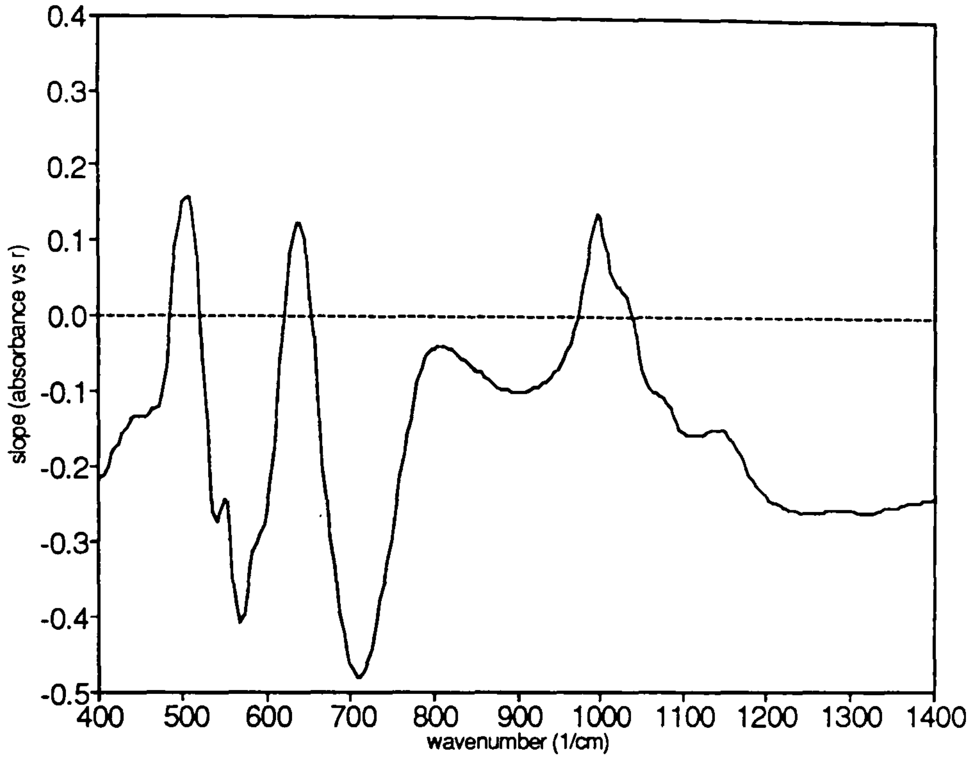

Figure 5-11 Slope of absorbance versus r in the wavenumber range 400-1400 for the FTIR spectra of H inserted SBPA.

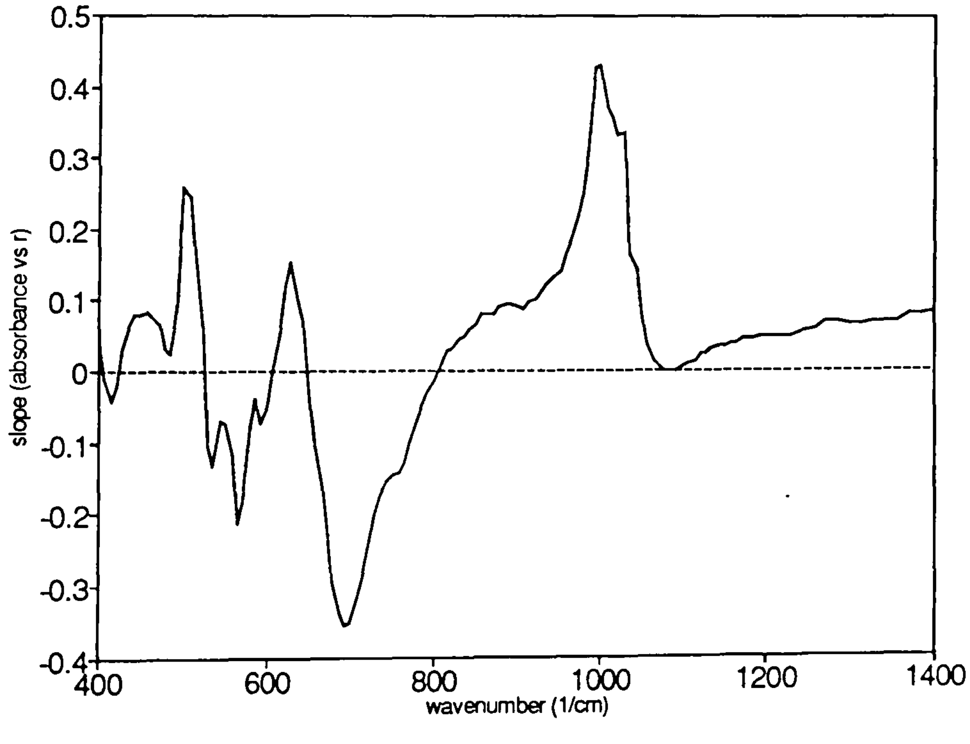

Figure 5-12 Slope of absorbance versus r at all wavenumbers for the FTIR spectra of the hypothetical transition ramsdellite to groutite. Derived from the FTIR spectra available in Potter and Rossman[105].

available in the literature[105] in the region 400-4000 ($cm^{-1}$), figure 5-12. However the relationship is *not* linear between absorption and r as is demonstrated by the following analysis.

Returning to the question of H mobility in the manganese oxyhydroxide structure it is proposed that the absorptions which emerge in the 1400-4000 ($cm^{-1}$) region are caused by OH bonds similar to those observed in groutite and thus associated with restricted mobility of H in the structure. Thus the area of the absorptions which emerge in this region are, it is proposed, a measure of the immobile H in the structure. It was therefore decided to measure the area of the emerging absorptions with increasing H insertion. Since the final reduced products produced by H insertion display very similar FTIR spectra for all the materials under study it was possible to choose boundaries which are independent of the material. Figure 5-13 displays the boundaries chosen together with the FTIR spectra for all the materials. A background area was defined as the area under the line intersecting the points where a peak boundary meets an FTIR curve. This was subtracted from the integrated area under the curve to produce the areas labelled ar1-4. Figures 5-14, 5-15, 5-16, 5-17 were obtained by repeating this procedure on the 23 samples representing the reduction of SBPA over the reduction range r=0.068 to r=0.882. Apart from figure 5-16 these figures clearly demonstrate that a non-linear relationship obtains between absorption and r which is not easily discernable from figures 5-9 and 5-10. A similar conclusion is not obtained for area ar3 because in this case the experimental errors in the area (probably due to slight difference in pellet preparation and/or particle size), mask any non-linear trends in the data. The graphs display a sharp change in behaviour occurring at r=0.35, apparently inconsistent with the x-ray diffraction evidence, which indicated a break at r=0.40. Figures 5-14, 5-15, 5-17 indicate that the area is essentially independent (apart from figure 5-17 which shows a slight downwards trend) of H insertion up to this value. This strongly suggests that H is mobile in this region. Beyond r=0.35 OH bonds are formed as H starts to 'freeze out' or locate within the structure. It is suggested that micro-crystalline domains of δ-MnOOH (cf. 6.4) are formed at the surface of a particle until at r=0.40 a sufficient number are formed and the reaction proceeds heterogeneously as evidenced by the x-ray diffraction results. The interpretation offered here is further enhanced when H insertion into EMD is considered in chapter 6.

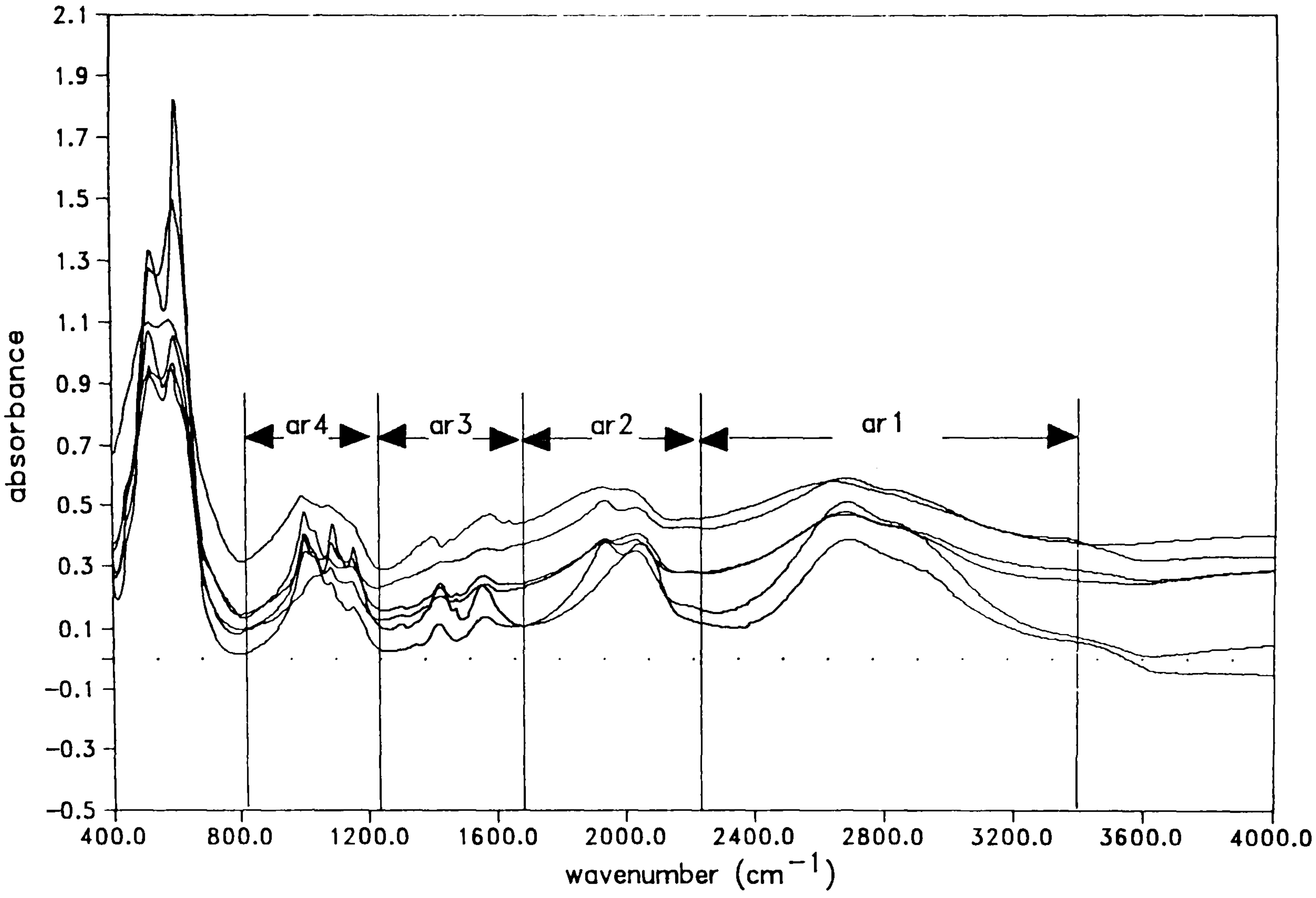

Figure 5-13 FTIR spectra of most reduced SBPA, R2, WSZ, IBA no.14, IBA no.19 and F.M and boundary positions used for areas.

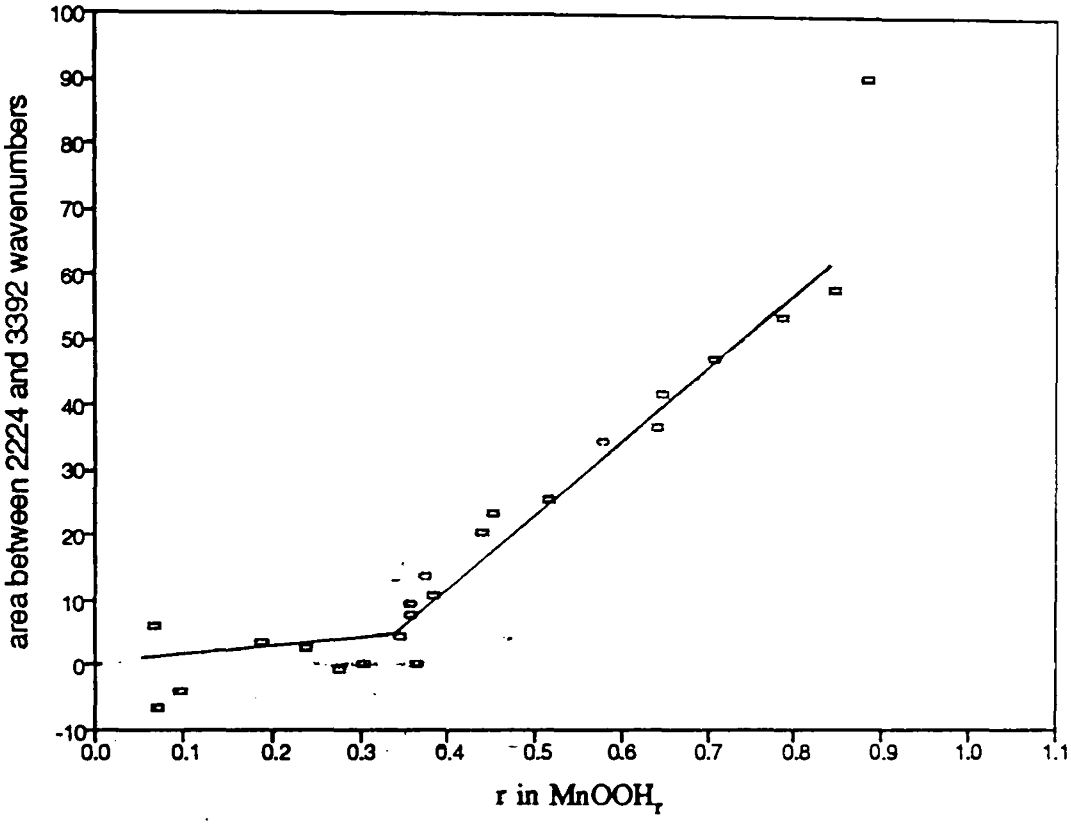

Figure 5-14 Change in integrated area of FTIR spectra minus background area, as defined by the ar1 boundaries shown in figure 5-13, with H insertion into SBPA.

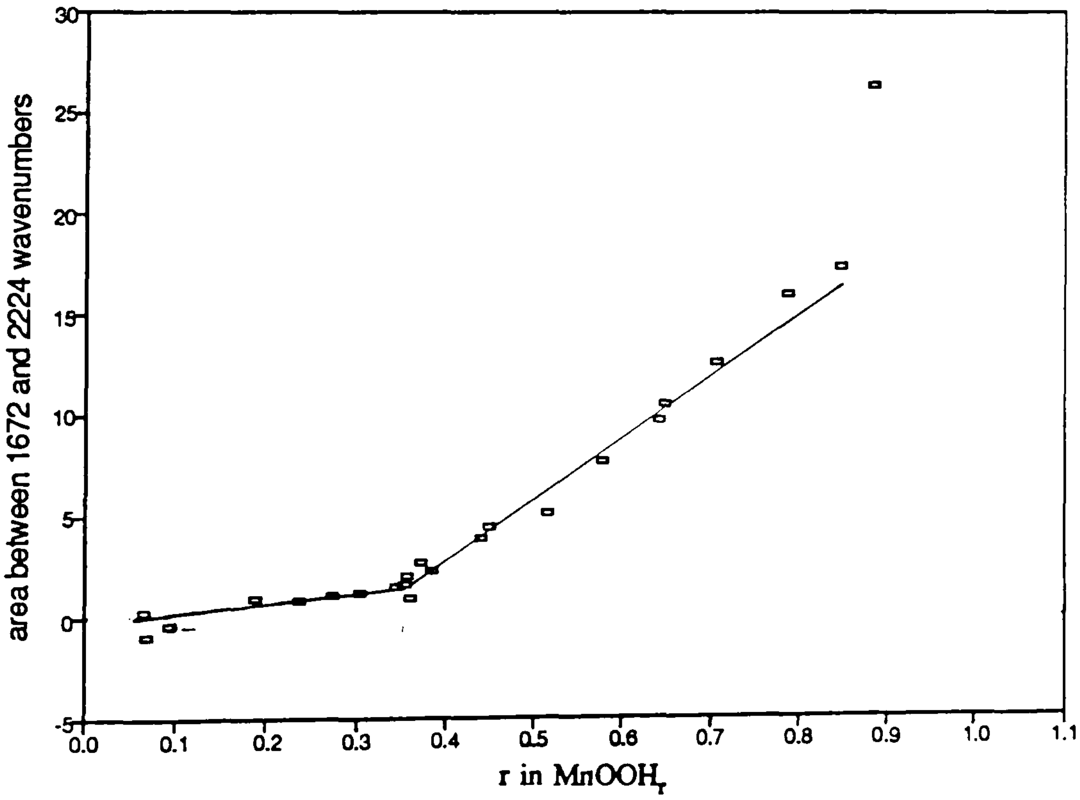

Figure 5-15 Change in integrated area of FTIR spectra minus background area, as defined by the ar2 boundaries shown in figure 5-13, with H insertion into SBPA.

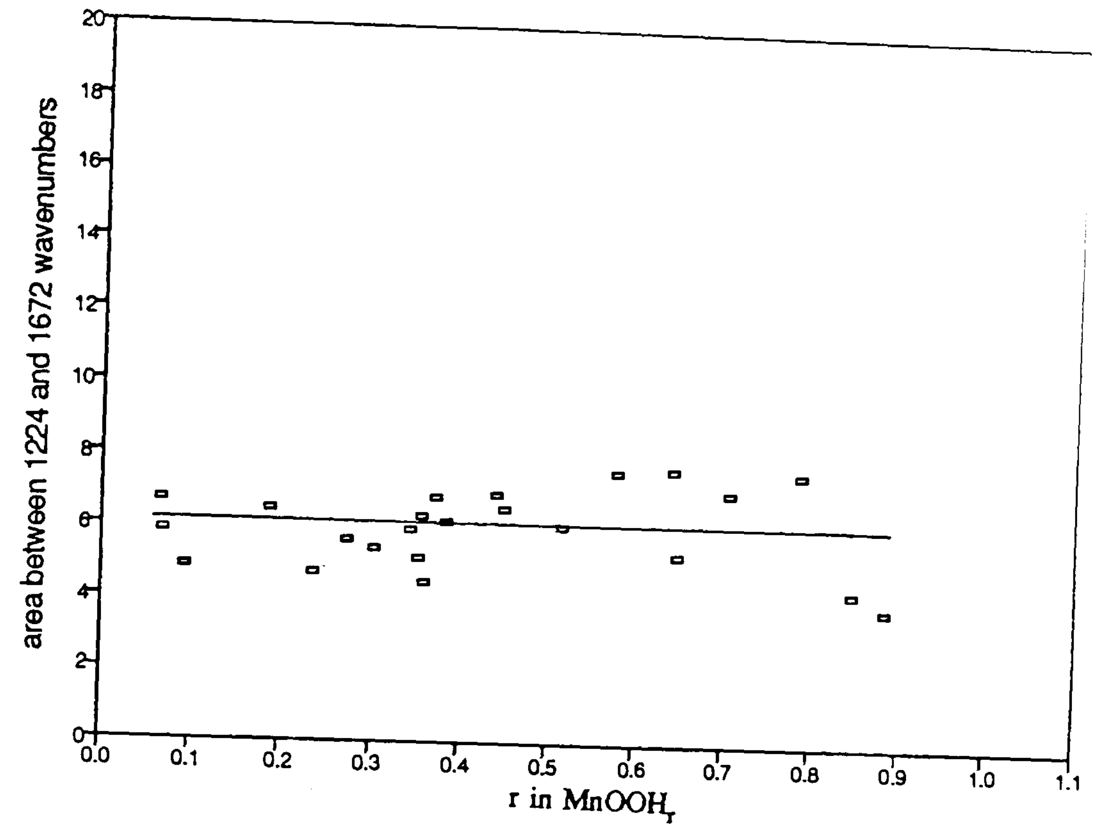

Figure 5-16 Change in integrated area of FTIR spectra minus background area, as defined by the ar3 boundaries shown in figure 5-13, with H insertion into SBPA.

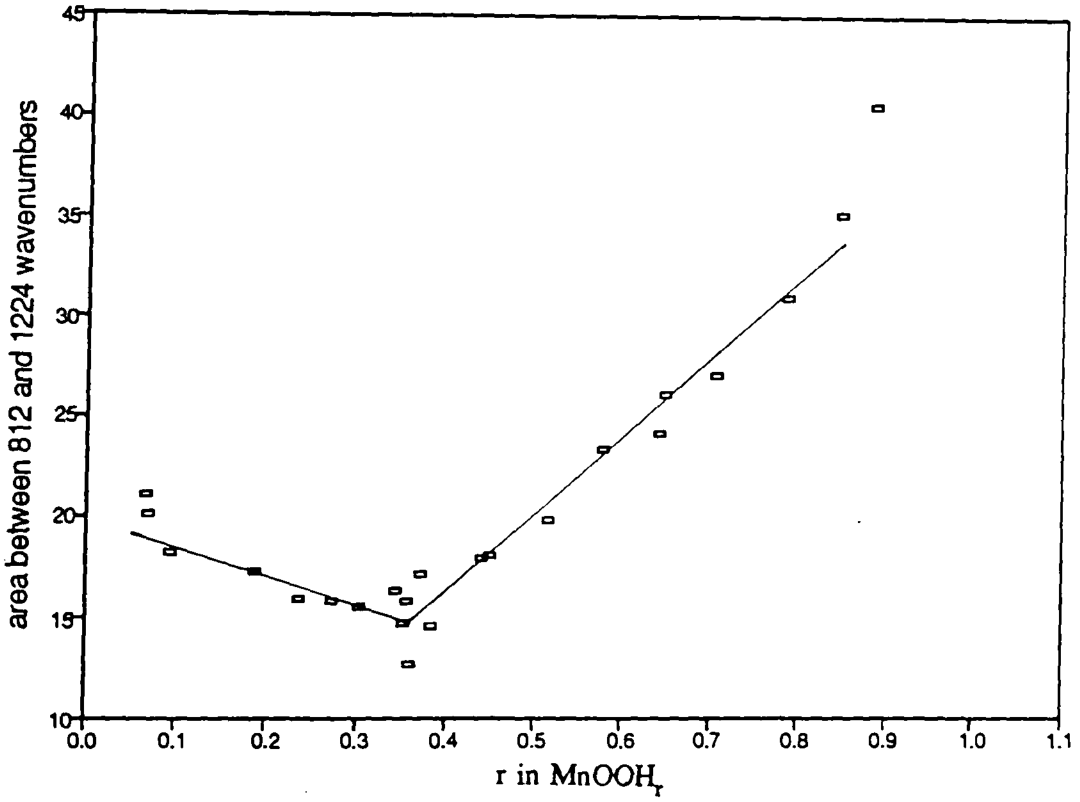

Figure 5-17 Change in integrated area of FTIR spectra minus background area, as defined by the ar4 boundaries shown in figure 5-13, with H insertion into SBPA.

## 5.4 Conclusion.

FTIR and x-ray diffraction evidence point to the following description for H insertion into SBPA. Homogeneous reduction from r=0.068 to r=0.35 with accompanying lattice expansion (see table 5.1) in the manner of a random solid solution. Heterogeneous reduction from $MnOOH_{0.40}$ to $MnOOH_{0.882}$ with the structure of the most reduced product similar to the initial material, that is a random intergrowth structure of G(G') and M(M') (and or P(P')) layers which are expanded analogues of R(R') and P(P') layers, the expansion primarily being in the $\mathbf{b}_0$ direction (see table 5.1).

Before proceeding to consider the structural changes that occur to an EMD (coded R2) the following point should be appraised concerning the above conclusion. The surface area of this material is the lowest of the materials studied (see table 8.2). Thus it is probable that the concentration of inserted H at the surface of the reduced outer particulate layer must be considerably higher than for a similar sized particle with a higher surface area during the same chemical insertion process. Thus it is not necessarily the case that the onset of heterogeneous reduction observed for SBPA is simply a structural characteristic of the material. This question is discussed further in the following chapters (chaps. 6&7) which are concerned with H insertion into the other materials studied.

# 6 Interpretation of the X-Ray Diffraction Patterns and FTIR Spectra of EMD R2 with H Insertion Level.

## 6.1 Introduction.

Attention was focused by Maskell *et al.*[73] on the origin of (apparently) new x-ray diffraction lines which emerge during the later stages of H insertion (beyond $MnOOH_{0.5}$ in their work) when H was inserted into an EMD near the $\gamma_t$ end of the $\gamma$-$\gamma_t$-$MnO_2$ series, whereas the original lines, as had been observed in previous studies, shift over the whole H insertion range. These were ascribed to that of a new phase emerging, namely $\gamma$-MnOOH, even in the case of non-aqueous reduction, where it was believed a slight precipitation on the surface of the oxide had occurred relatively accessible to incoming x-rays (and hence accounting for their relatively large strength). Later work on the same EMD by Fitzpatrick and Tye[68], in which a particularly slow or mild reduction was effected by a combination of various organic reductants, indicated that the new lines could not in fact be attributed to $\gamma$-MnOOH (or $\alpha$-MnOOH) as first thought. They were as suggested by Fitzpatrick[106] an integral part of the solid solution, and were ascribed rather to $\delta$-MnOOH. This view, as shall become clear, is central to the explanation of these lines arrived at in this work.

Undoubtedly one reason for controversy over the origin of these 'new' lines is the remarkable fact, reported by Fitzpatrick and Tye, that the new lines that emerge do not appear to display any peak shifts whereas the original (shifted) lines continue to move though at different relative rates (w.r.t. to H insertion) beyond the H insertion level at which the new lines appear. This fact appears to contradict all the explanations offered to date to account for the new lines. Specifically, if it were the case that insertion of H caused precipitation of $\gamma$-MnOOH (or any other phase) beyond a certain insertion level, then no genuine (that is apart from that caused by overlapping peaks) peak shift would be expected for either those lines associated with the solid solution or those identified with manganite. If on the other hand only a slight amount of $\gamma$-MnOOH precipitation was the cause why should the *relative* rate of expansion of the remaining lines be affected? Finally how could it be that the lines that emerge are an integral part of the solid solution yet emerge with no peak shifts whereas the other lines continue to move?

The first two suggestions have already been shown to be untenable[68]. The ultimate aim of this chapter is to clarify and answer the final question posed above. In so doing it is necessary to draw upon all the previous conclusions concerning the structural nature of battery active manganese dioxide. It shall be shown that the result obtained accords with a new linear cluster model proposed by Tye[107] which accounts for major features of the statistical thermodynamic nature of H in battery active manganese dioxide solid solutions.

## 6.2 Insertion of H into EMD R2, effect on diffractograms.

The author is fortunate to have access to samples prepared by a previous researcher at this institute[†]. They have been prepared under exceptionally mild reducing conditions and to the authors knowledge, contain the largest degree of chemically inserted H without the appearance of new lines characteristic of the final product. The starting EMD has the typical x-ray diffraction pattern of a commercially produced EMD which is virtually identical to IBA no.19 (figure 2-1) with the exception of a small graphite impurity at 26.1°2θ from the deposition process. Referring to figures 6-1, 6-2, 6-3 one can see that the emergence of new lines begins at $MnOOH_{0.80}$ (i.e. $r=0.80$). The lines which emerge do not alter position (°2θ) with H insertion level compared to the 'solid solution' lines, which continue to shift with differing rates (that is d versus r rates) beyond $r=0.80$. That this is so is demonstrated particularly in figure 6-4 in which the position of peak D is compared to the movement of the emerging peak H in the H insertion region $0.8 \leq r \leq 1.0$. Peak H displays the greatest deviation from horizontal amongst the emergent peaks the remaining positions of which are displayed in figures 6-5, 6-6, 6-7 (Note that the scales are half those of figure 6-4). The d spacing of peak J apparently decreases before becoming constant (figure 6-6). This is probably the result of the close proximity of peak F in the decreasing d spacing H insertion region (see figure 6-1). It is tempting to associate the new lines (peaks G, H, I, J, K, see figure 6-10) with that of a new phase emerging. That would be equivalent to suggesting a heterogeneous reaction occurs with the new set emerging at the expense of the original

---

[†] Samples prepared by J.Fitzpatrick.

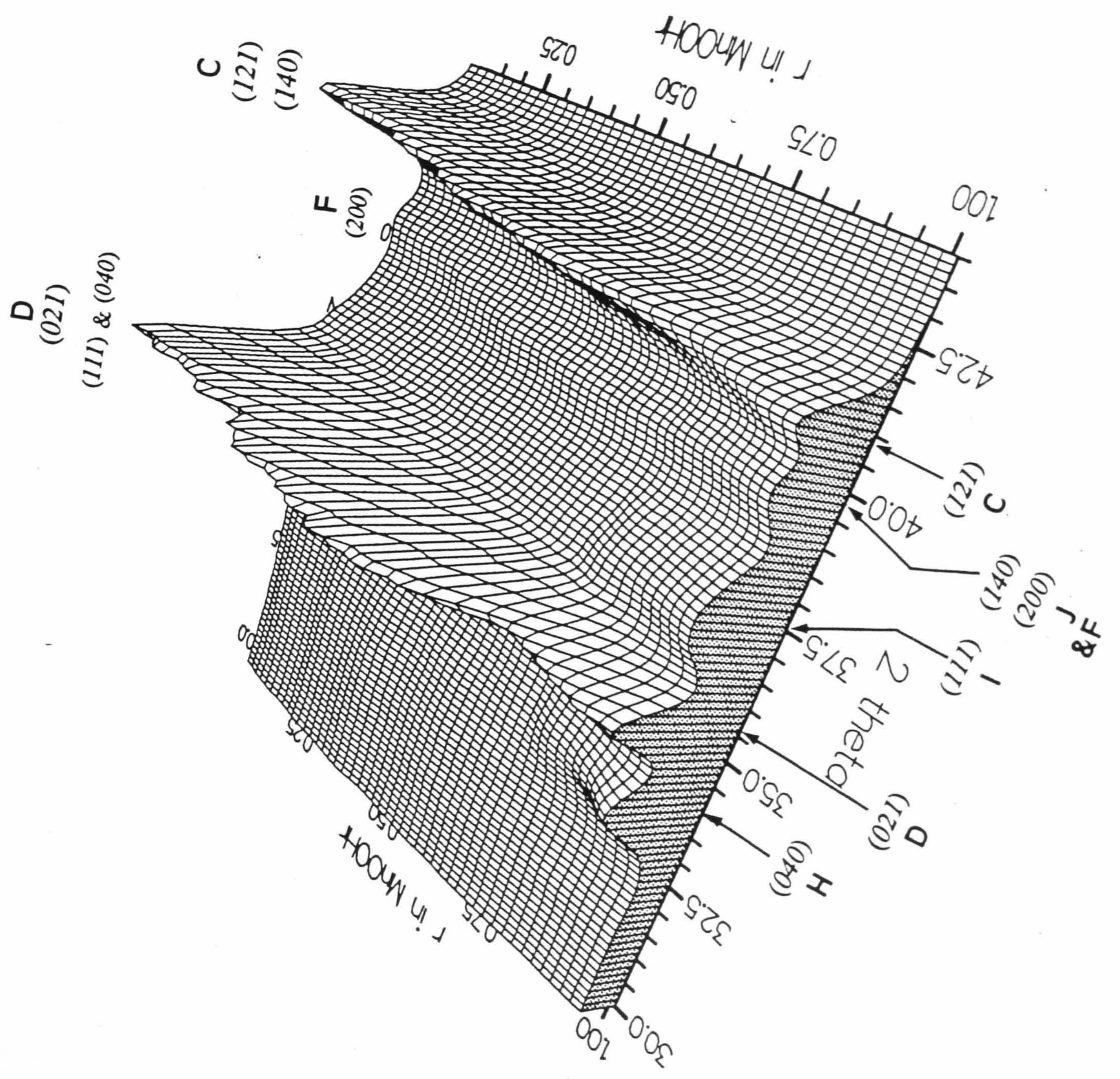

Figure 6-1 Pseudo-3D plot of the x-ray diffraction patterns resulting from H insertion into sample R2 in the 2θ range 30-44 (°2θ).

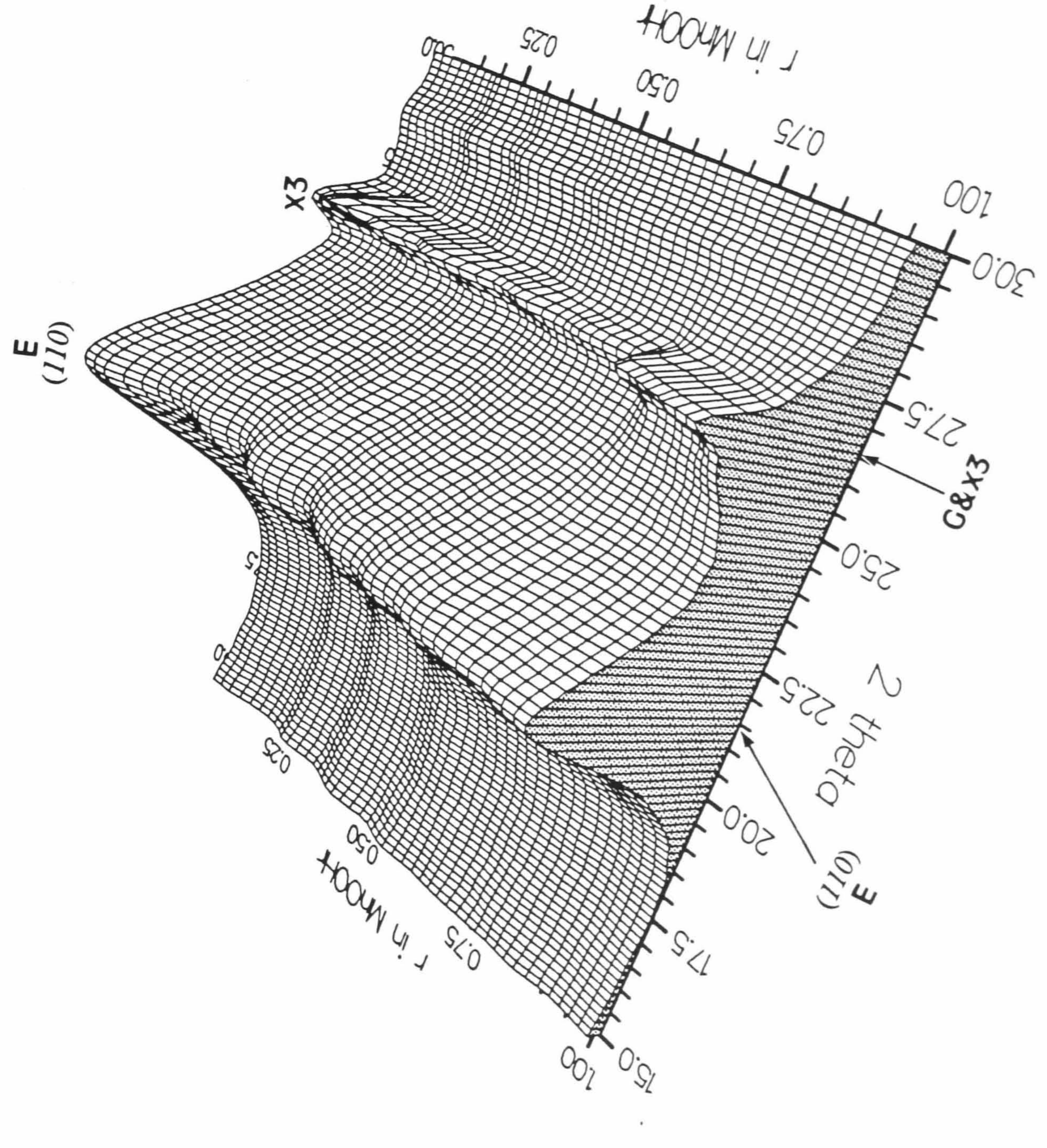

Figure 6-2 Pseudo-3D plot of the x-ray diffraction patterns resulting from H insertion into sample R2 in the 2θ range 15-30 (°2θ).

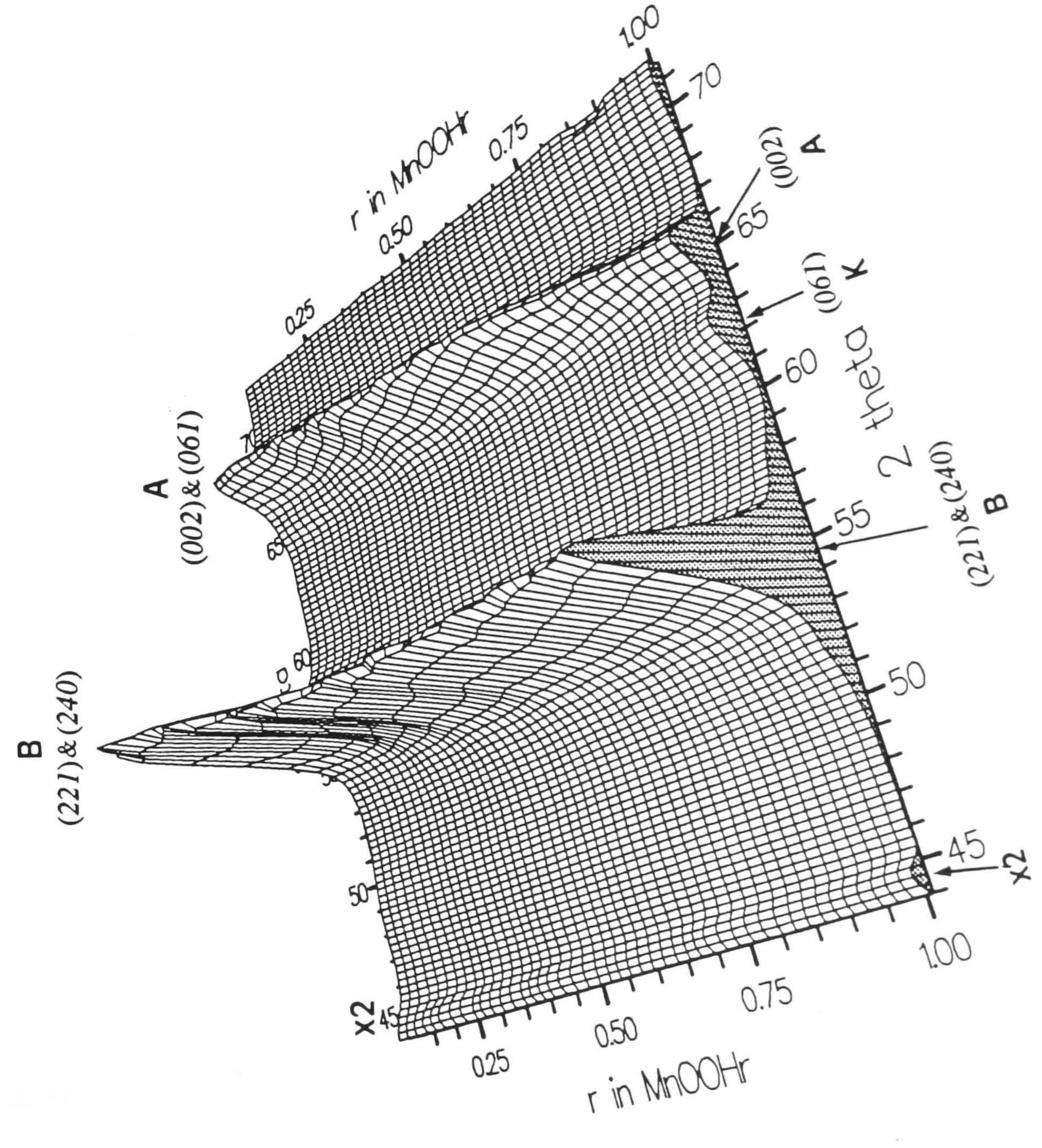

Figure 6-3 Pseudo-3D plot of the x-ray diffraction patterns resulting from H insertion into sample R2 in the 2θ range 44-80 (°2θ).

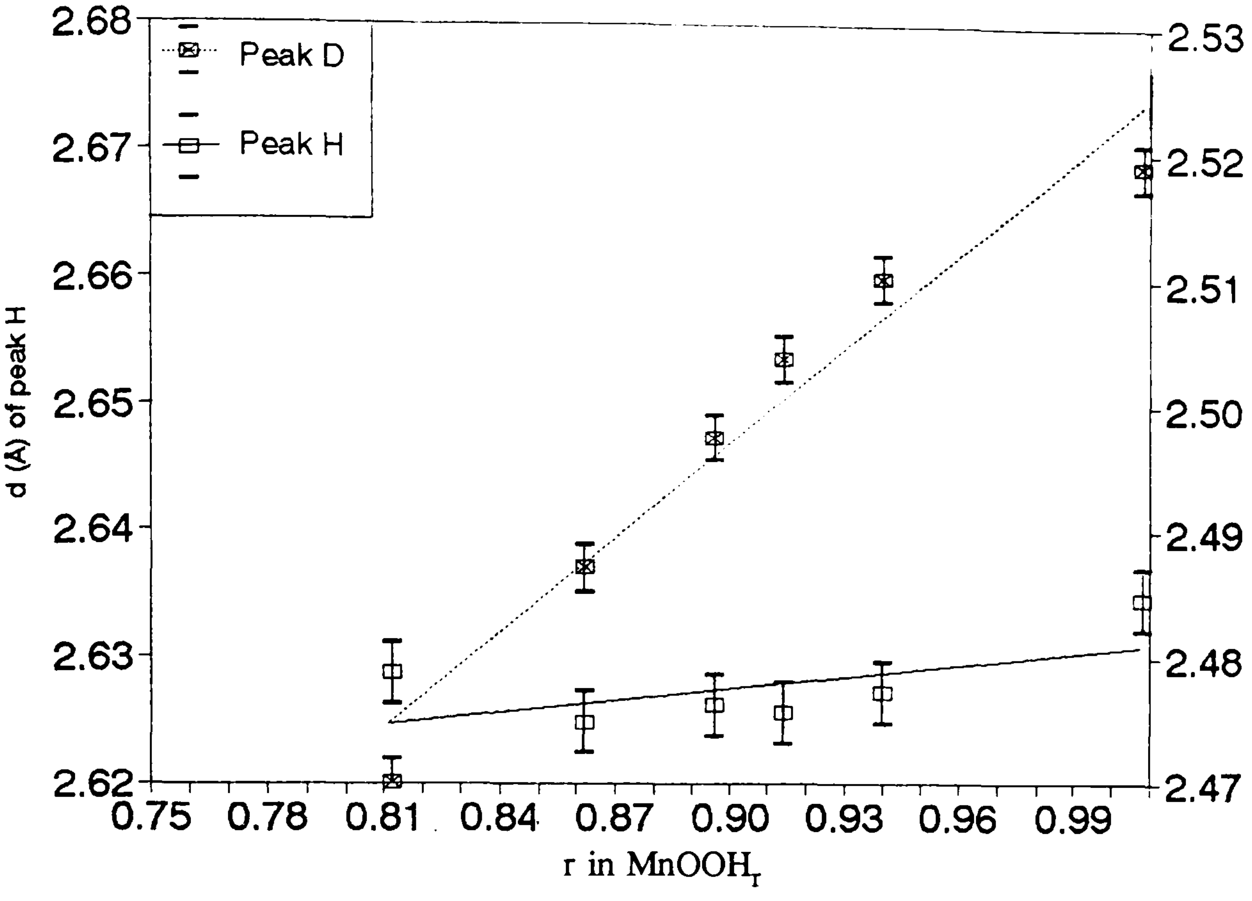

Figure 6-4 d spacing versus r in $MnOOH_r$ for peaks D and H in the region where H starts to become immobile. The scales for both peaks are equal. The lines drawn represent the best straight lines through the experimental points.

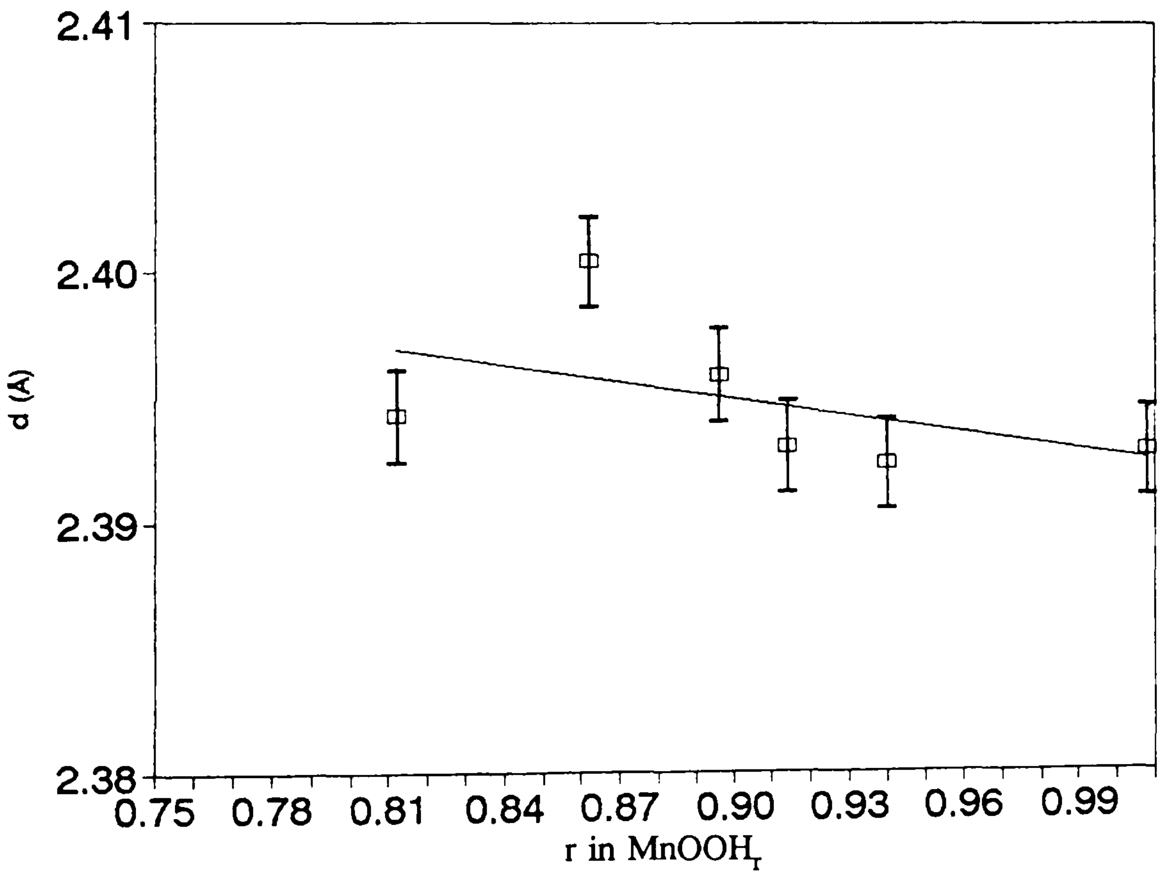

Figure 6-5 d spacing versus r in $MnOOH_r$ for the emergent peak I in the region where H starts to become immobile. The line drawn represents the best straight line through the experimental points.

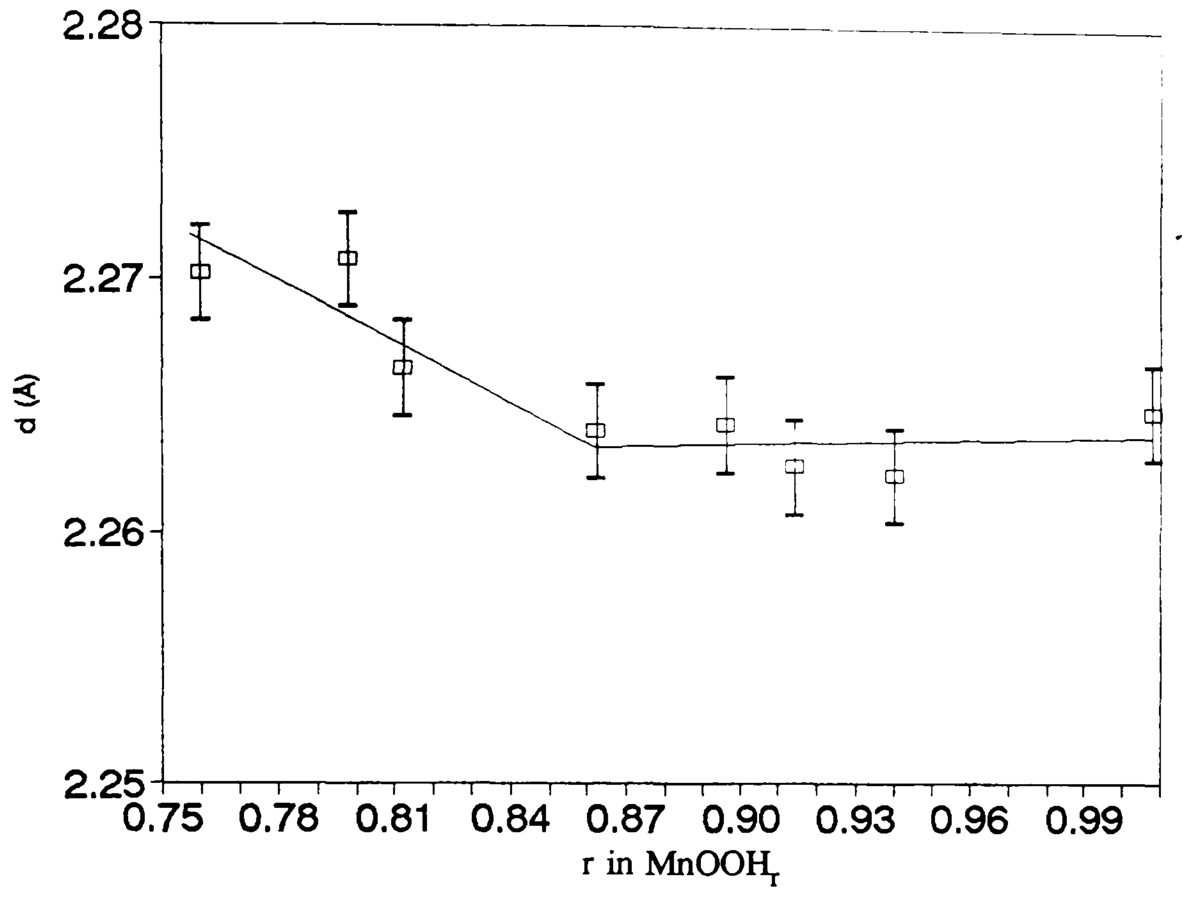

Figure 6-6 d spacing versus r in MnOOH$_r$ for peak J in the region where H starts to become immobile. The nearly horizontal line ($0.86 \leq r \leq 1.0$) represents the best straight line. Before this peak F contributes.

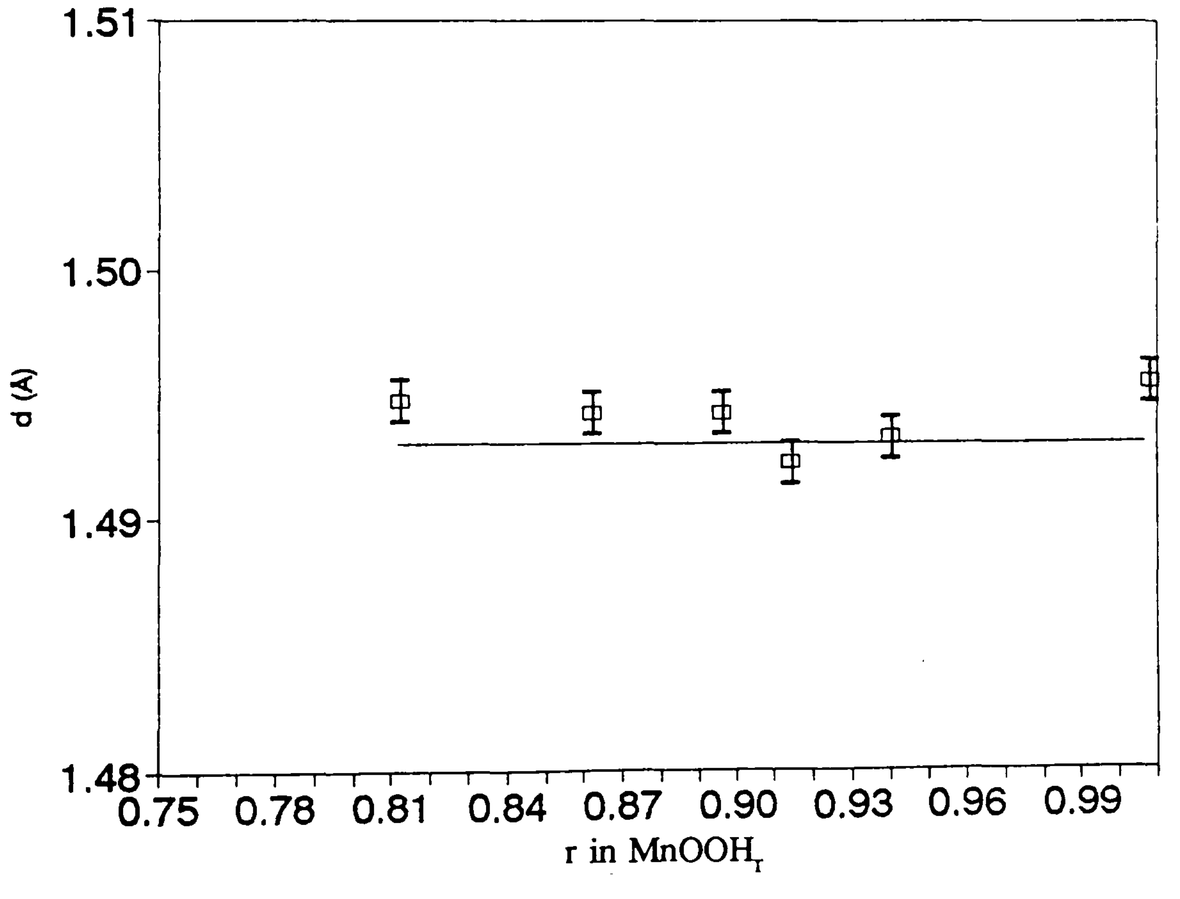

Figure 6-7 d spacing versus r in MnOOH$_r$ for the emergent peak K in the region where H starts to become immobile. The line drawn represents the best straight line through the experimental points.

set. This suggestion is untenable, however, as is demonstrated in figure 6-9. This figure is analogous to figure 7-2 (section 7.1) in which a set of synthesized patterns was generated from adding linear proportions of the initial, in this case at r=0.80), and final patterns (r=1.01) in an attempt to duplicate the observed behaviour (figure 6-8). Whereas this successfully demonstrates heterogeneous reduction in the other case referred to, equally it demonstrates that this is not the process responsible for the observed behaviour in this case. This is because isobestic points, which would manifest themselves as points where all the superimposed graphs cross are not produced in the real case (figure 6-9).

In order to elucidate a process which could account for the observed changes in x-ray diffraction pattern it is necessary to digress slightly and address a question which has already been answered to a considerable extent, that is the question as to whether EMD fits the $\varepsilon$-$MnO_2$ model proposed by de Wolff *et al.*[43] That the following section demonstrates in a concise manner that it does not.

## 6.3 Using the variation of interplanar spacing with H insertion to demonstrate that EMD does not possess hexagonal symmetry and consequently does not fit the $\varepsilon$-$MnO_2$ model.

The aim of this section is to present data showing the anisotropic lattice expansion of an EMD coded R2 and to discuss one particular consequence of this observation.

Figure 6-10 (a) indicates five main diffraction peaks labelled A, B, C, D and E in the starting material. New peaks are present in the most reduced sample and start to emerge at an H insertion level corresponding to r=0.80, peaks G, H, I, J, figure 6-10 (b). As is well established peaks A, B, C, D, E shift to lower Bragg diffraction angles or higher d values with increasing reduction. If the lattice expansion were isotropic then the ratio of any two interplanar spacings would be constant independent of H insertion. As has already been shown by Fitzpatrick and Tye[68] the six ratios representing different combinations from the total possible determined from peaks A, B, C, D show that the lattice expansion is approximately isotropic until r=0.80 beyond which it appears to be anisotropic. The following data was obtained on the same set of samples but with improved precision of the peak positions[107], figures 6-11, 6-12, 6-13, 6-14, 6-15, 6-16.

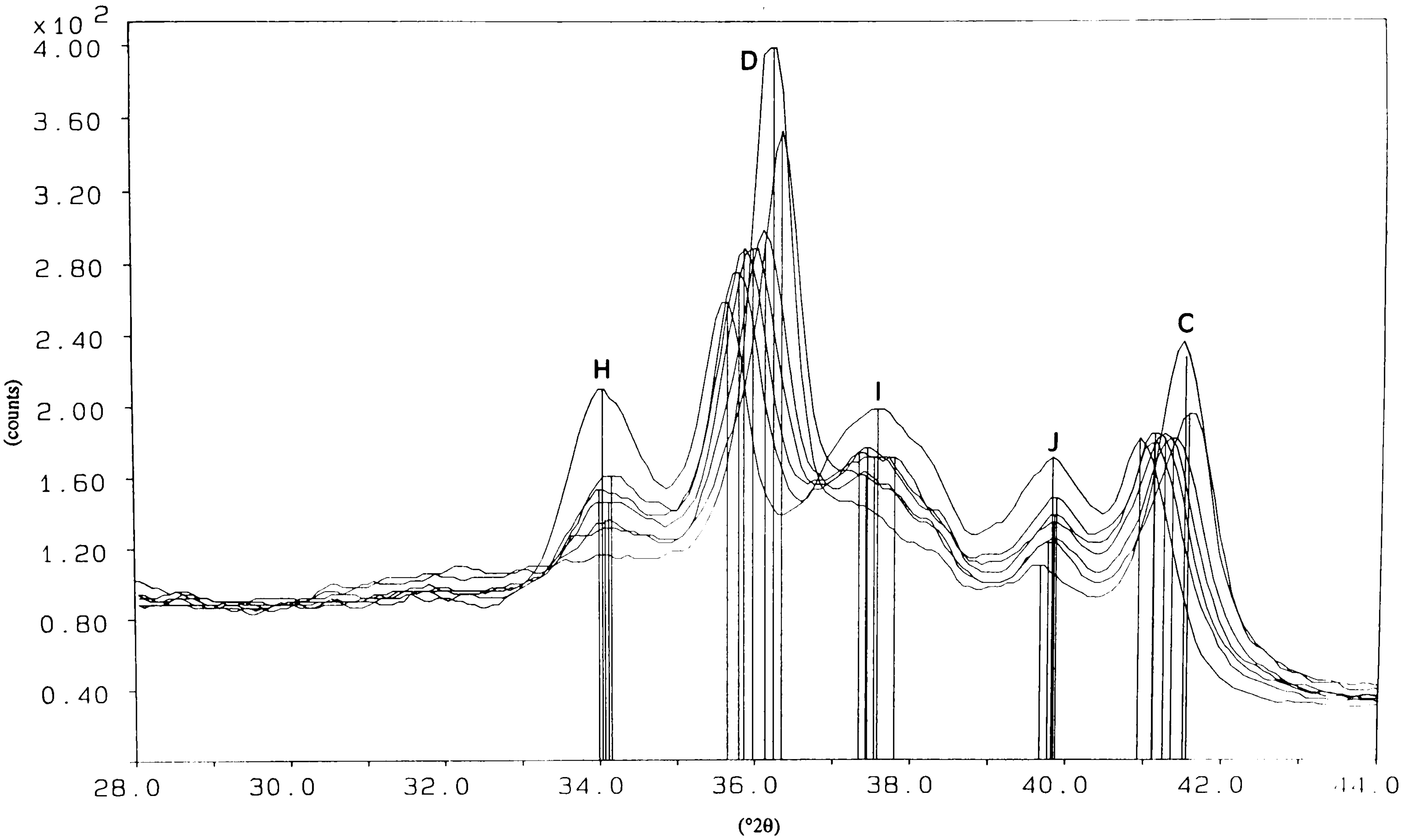

Figure 6-8 Simulated x-ray diffraction of heterogeneous reduction of material R2 from mixtures of samples with compositions $MnOOH_{0.80}$ and $MnOOH_{1.01}$.

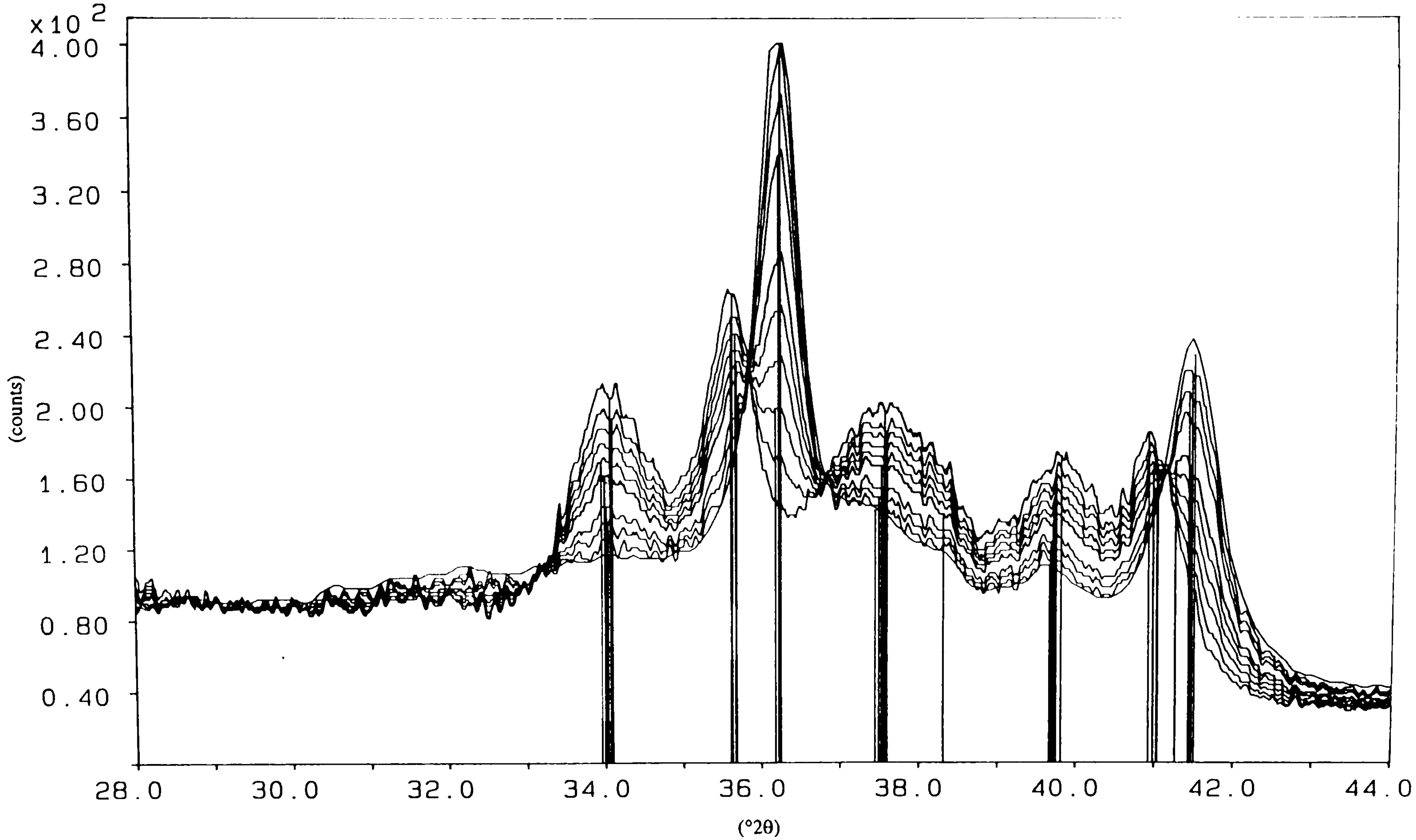

Figure 6-9 Actual x-ray diffraction patterns of material R2 in the composition range $MnOOH_{0.80}$ to $MnOOH_{1.01}$.

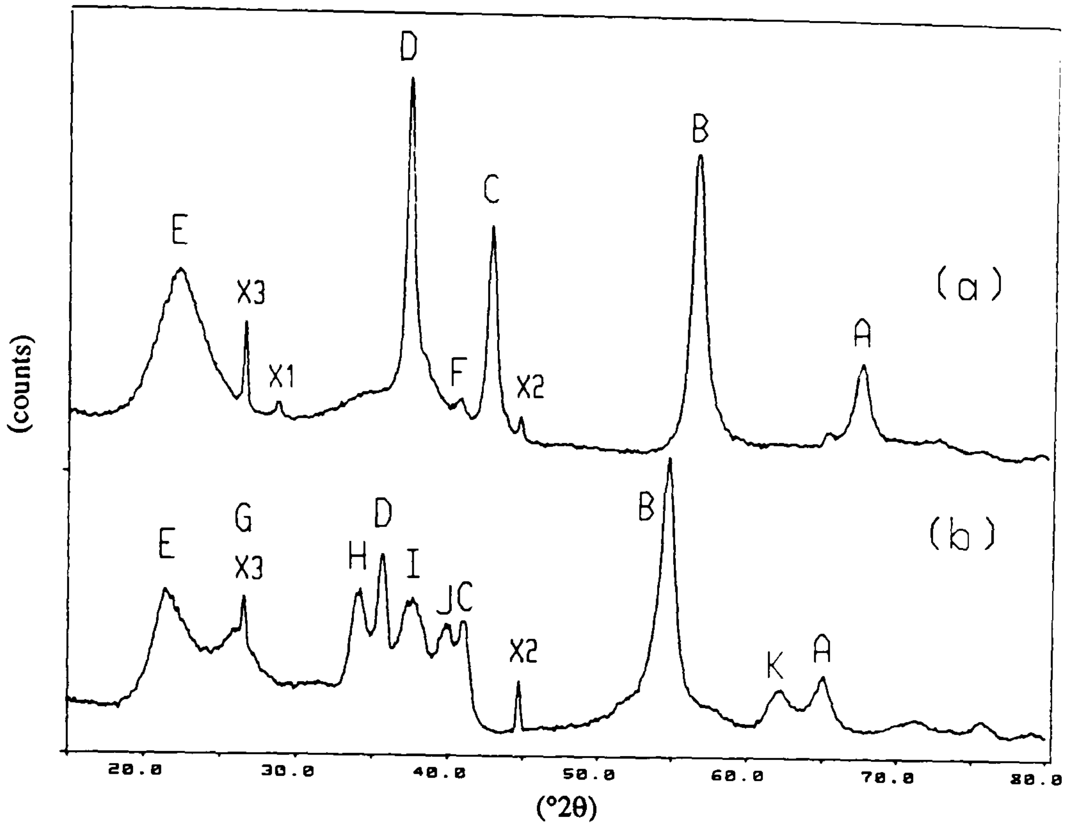

Figure 6-10 X-ray diffraction comparison of R2 and most H inserted R2, indicating original peaks A, B, C, D, E and F, and 'new' peaks G, H, I, J, K.

The broadness and consequent uncertainty in the position of peak E meant that it was disregarded from the possible peak ratio combinations. Drawn on figures 6-11, 6-12, 6-13, 6-14, 6-15, 6-16 are lines corresponding to common breaks in the slopes of the ratios. It is the common break at r=0.80 which shall be focused on in this section.

The effect of anisotropic expansion on a powder x-ray diffraction pattern is now considered in general by referring to a simple example. Figure 6-17 schematically shows the effect on a body centred cubic pattern of expansion in the c direction by 4%. Some lines split and others remain unchanged. This is equivalent to a lowering of symmetry from cubic to tetragonal. Further expansion in the **b** axis direction lowers the symmetry again to that possessed by an orthorhombic lattice, which again produces splitting of x-ray diffraction lines. The powder x-ray diffraction pattern of EMD R2 is not consistent with that of a cubic lattice. It does, however, apparently possess hexagonal symmetry (see section 2.2). (Provided one accepts the ε-$MnO_2$ model which accounts for peak E which is otherwise a forbidden reflection).

The consequences of anisotropic expansion which applied to the cubic structure also apply to a hexagonal structure. Refer to figure 6-18 which indicates a possible

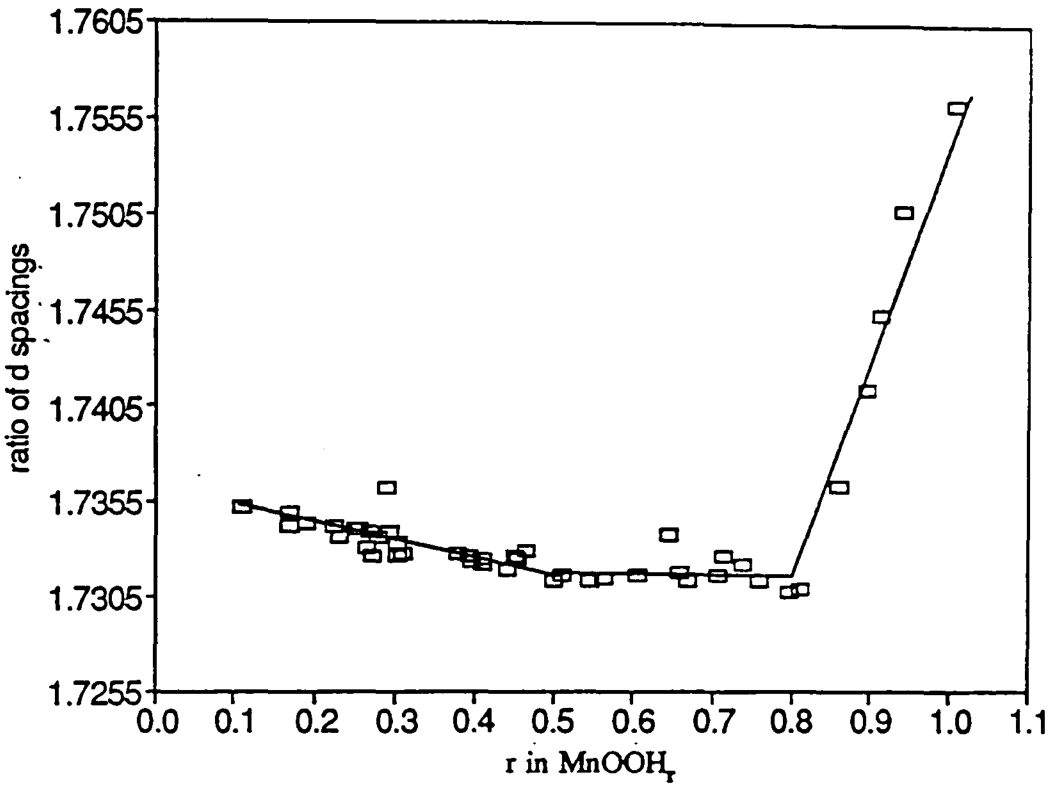

Figure 6-11 Ratio of the d or interplanar spacings for peaks D/A (see figure 6-10) for H insertion into R2.

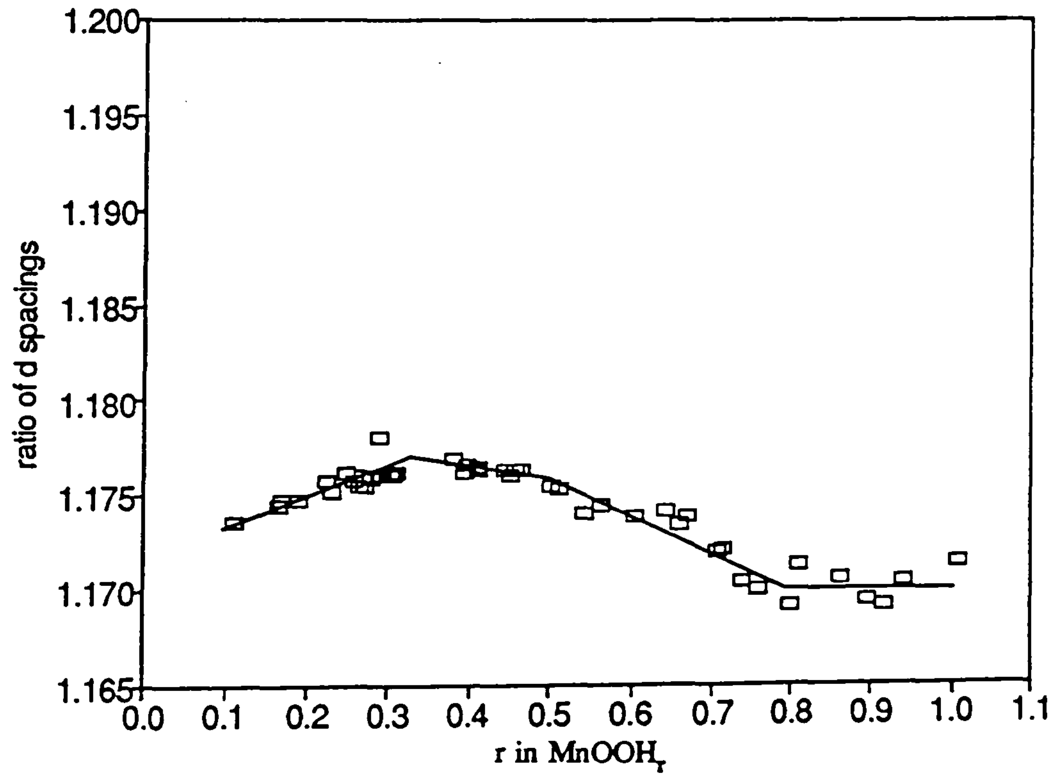

Figure 6-12 Ratio of the d or interplanar spacings for peaks B/A (see figure 6-10) for H insertion into R2.

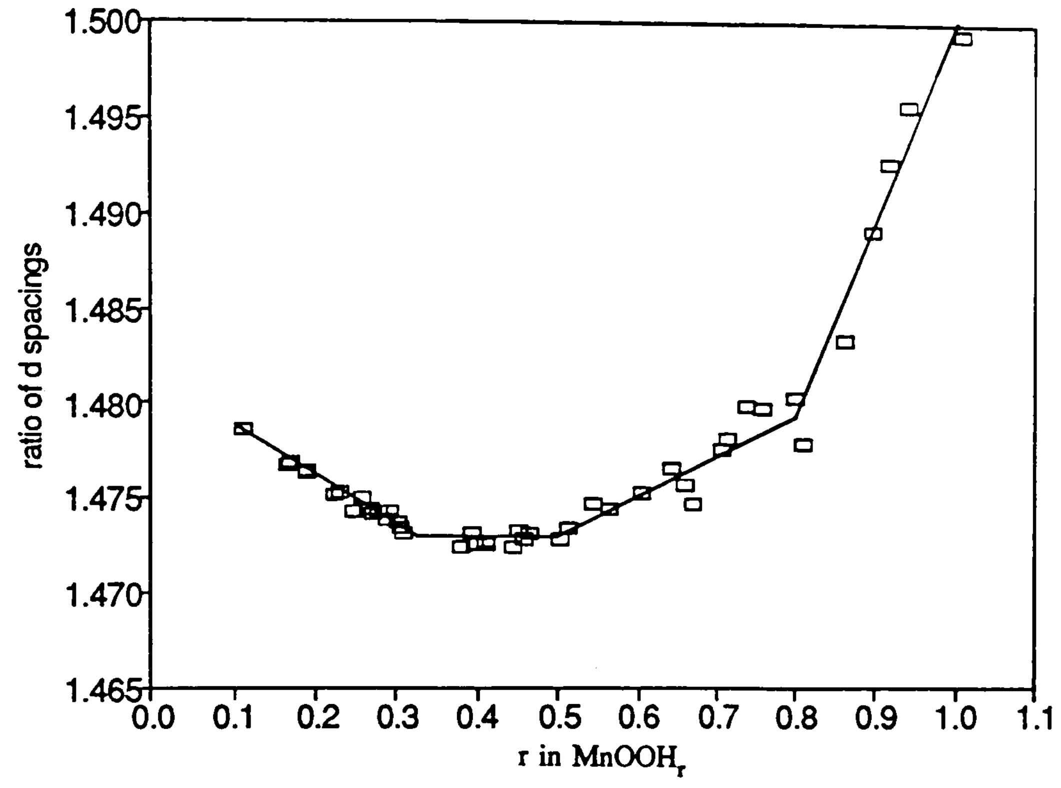

Figure 6-13 Ratio of the d spacings for peaks D/B for H insertion into R2.

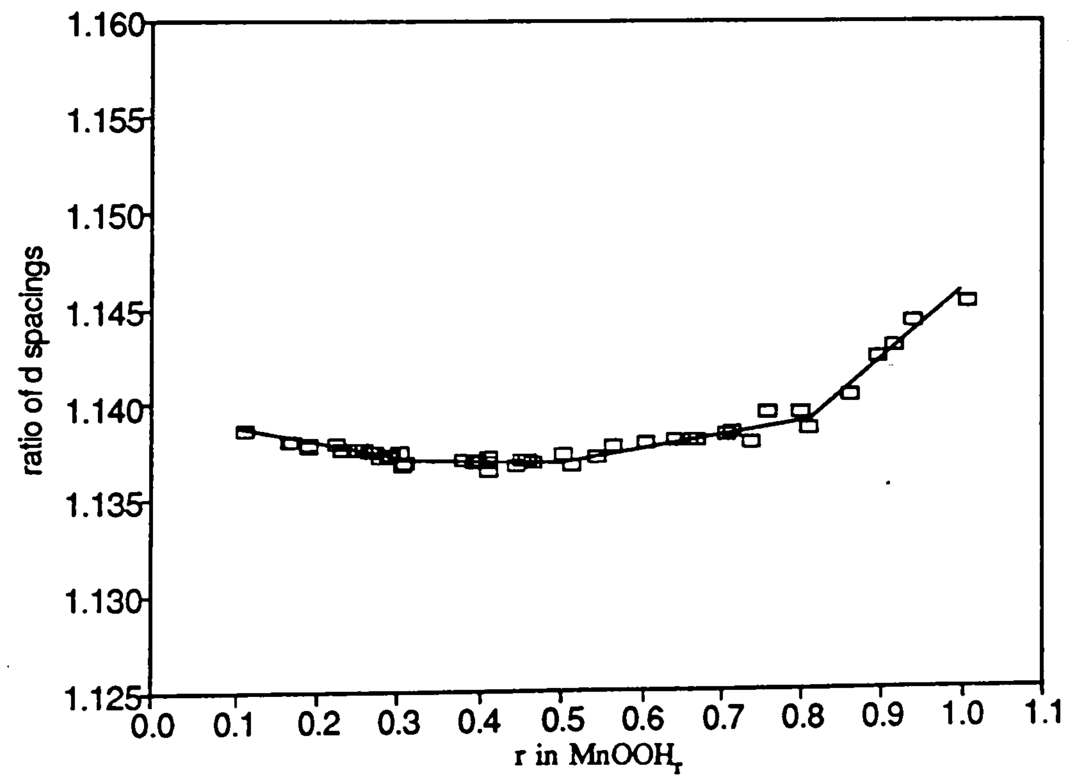

Figure 6-14 Ratio of the d spacings for peaks D/C for H insertion into R2.

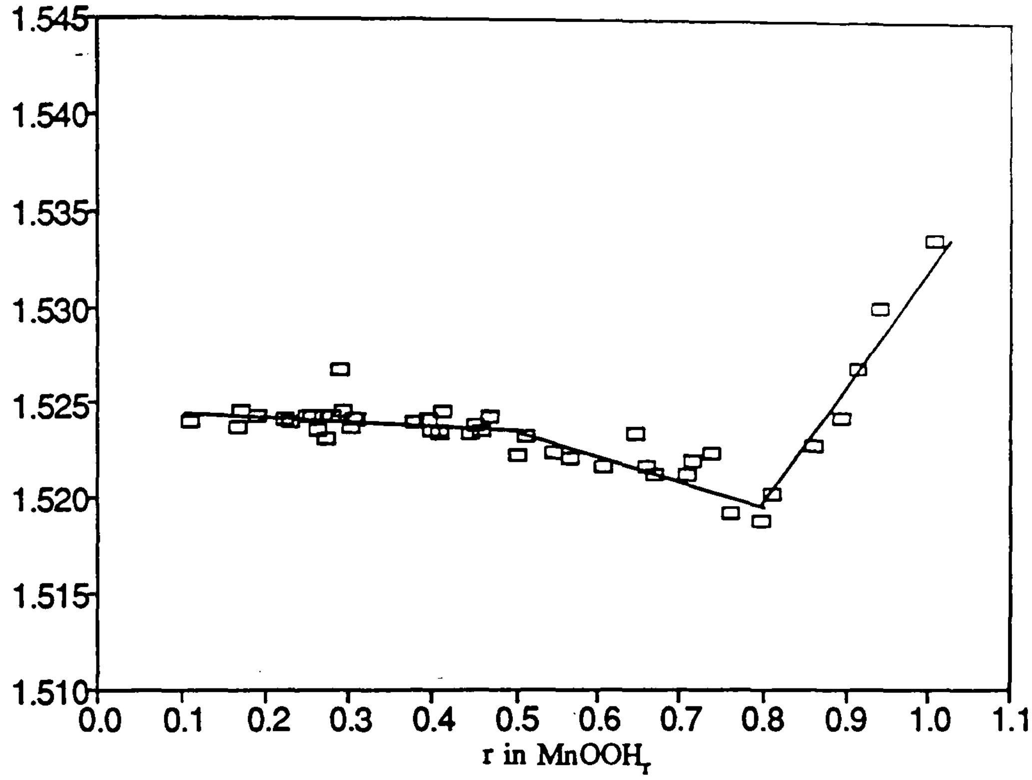

Figure 6-15 Ratio of the d spacings for peaks C/A for H insertion into R2.

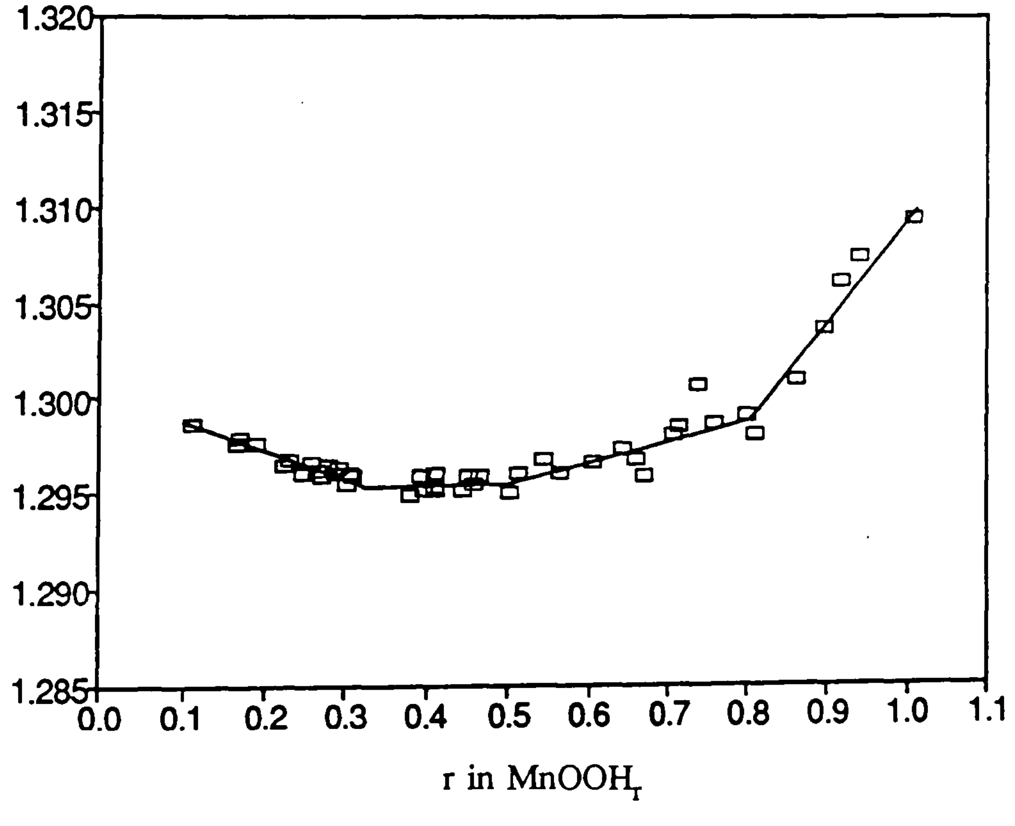

Figure 6-16 Ratio of the d spacings for peaks C/B for H insertion into R2.

hexagonal unit cell with a selection of indices and planes marked. Thus for instance there are six planes of the form {10·0} (the prismatic planes) which contribute to peak D or (10·0) (see figure 2-3 for a list of all the peaks and their hexagonal indices). If expansion with H insertion became greater or less in the direction of $a_1$, $a_2$, $a_3$ then peak D would start to split.

It is tempting at this stage of the discussion to account for the appearance of the new peaks (i.e. peaks G, H, I, J, K) at r=0.80 as a result of a decrease in symmetry due to the observed anisotropic lattice expansion. This however will not work since the new peaks are observed not to be the result of peak splitting of peaks A, B, C, D, or E (see figures 6-1, 6-2, 6-3). Also they do not move with H insertion which in general they would if the lattice was expanding. In other words the new peaks which appear are not the result of symmetry changes to a hexagonal unit cell or indeed any other shape of unit cell as has been suggested[68]. Some other explanation is required excluding that of a new phase emerging which has already been established to be untenable.

The question remains as to whether the movement of peaks A, B, C, D is consistent with a hexagonal lattice in the region beyond r=0.80. This requires the hexagonal lattice to expand anisotropically yet retain hexagonal symmetry. From a study of figure 6-17 there is only one direction in which this is possible, that is in the direction of $c_{hex}$. Thus if it expanded at a different relative rate to $a_1$, $a_2$ and $a_3$ with H insertion the lattice would retain hexagonal symmetry and so produce no peak splitting. One consequence of this would be that the planes parallel to the $c_{hex}$ axis would be unaffected by the anisotropic expansion and therefore their d spacing ratios would remain constant. The observed behaviour, however, is inconsistent with this deduction as peaks D and A which have l=0 in their Miller indices (and so are parallel to $c_{hex}$) show a sharp deviation in their d spacing ratio, see figure 6-11.

The conclusion therefore, on the evidence presented, is that the lattice of EMD R2 cannot have hexagonal symmetry and so the ε-$MnO_2$ model is not the correct structure for EMD.

## 6.4 Precipitation of δ-MnOOH micro-domains within the solid solution as the cause for the observed x-ray diffraction and FTIR behaviour of EMD R2 with H insertion.

A theory is proposed in this section which accounts for the observed x-ray

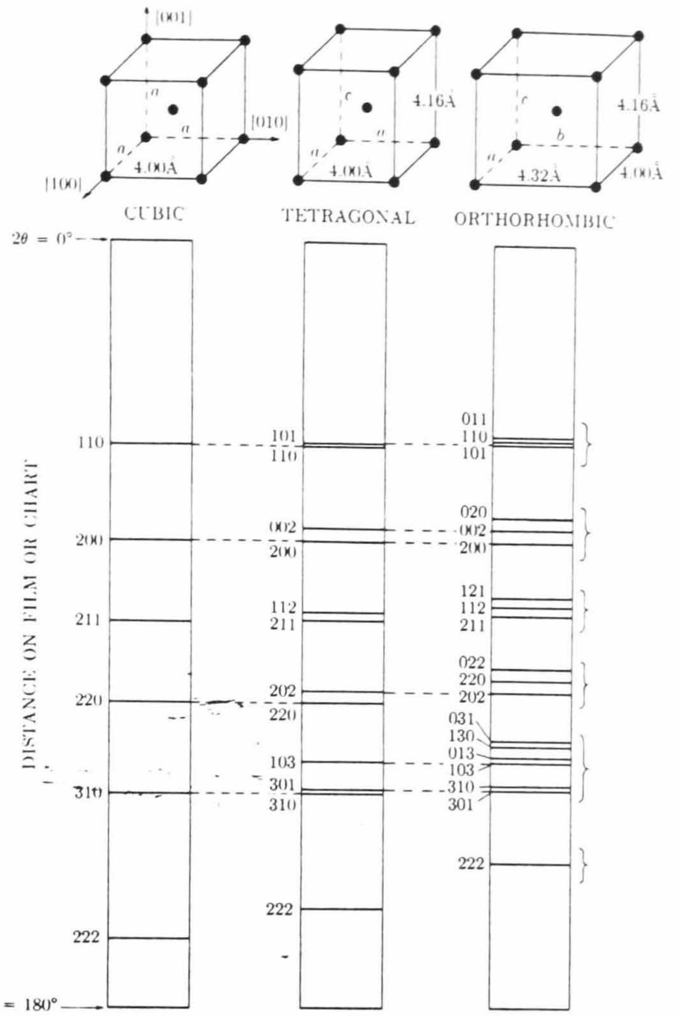

Figure 6-17 Effects of cell distortion on powder patterns. Lines unchanged in position are connected by dashed lines. Reproduced from Cullity[100] (fig. 10-5, p.341).

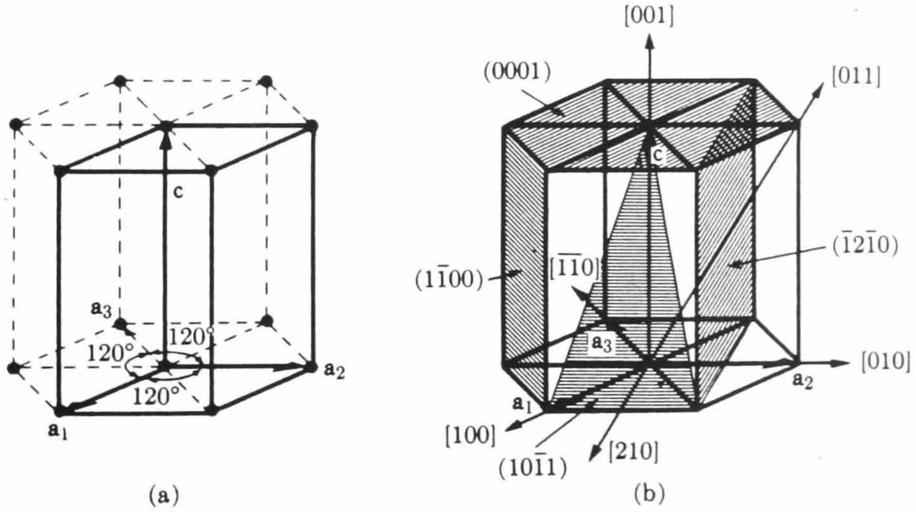

Figure 6-18 (a) The hexagonal unit cell (heavy lines) and (b) indices of planes and directions. Reproduced from Cullity[100] (fig. 2-11, p.44).

diffraction behaviour, as described in the previous section for the EMD coded R2.

Firstly the variation of the interplanar ratios derived from the maxima labelled A, B, C, D as presented in the previous section are reconsidered with respect to an orthorhombic lattice.

It has been established that the 'lattice'[†] expansion of R2 becomes anisotropic beyond a certain level of H insertion (r=0.80). It has also been established that sample SBPA reduces anisotropically by expansion in the $\mathbf{b}_0$ direction. Because the two materials are end members of the same structural series it is natural to suppose that R2 also undergoes lattice expansion in this direction. Using the indices proposed in section 2.4.4 it is possible to predict the effect of expansion in the $\mathbf{b}_0$ direction (only) on the ratios D/A, B/A, C/A, C/B, D/B, D/C for a perfect orthorhombic lattice (i.e. using equation (2.6)). This is achieved using the lattice parameters for SBPA which, it has been argued (see section 2.4.4), are very close to those of sample IBA no.19 and therefore also to sample R2. The following two part calculation was performed in an attempt to reproduce the sharp break which occurs for all but one of the peak d spacing ratios presented in section 6.3.

(a) Isotropic expansion of the SBPA orthorhombic lattice parameters up to a simulated H insertion level of $MnOOH_{0.80}$.

(b) Anisotropic expansion in the region $0.80 \leq r \leq 1.0$ achieved primarily by linear (with respect to H insertion) expansion of the $\mathbf{b}_0$ lattice parameter.

In (a) the percentage increase of each lattice parameter at r=0.80 was chosen to be 2.69% of the initial lattice parameter. This was established from the average relative change of each measured d values for peaks A, B, C and D. In the second part the relative expansions of $a_0$, $b_0$, $c_0$ were chosen so as to produce the best fit to the experimental data. Allowing changes in $a_0$ and $c_0$ explicitly recognises that $a_0$ and $c_0$ are already extended and thus may be expected to decrease if they are to arrive, at r=1.0, without any net expansion, which has previously been established for the relationship between groutite and manganite, and (approximately) for reduced SBPA. A procedure is now described for arriving at the % changes of the orthorhombic parameters required to duplicate the observed variation of the peak ratios D/A, B/A, C/A, C/B, D/B, D/C in the anisotropic reduction region.

---

[†] See section 4.3.1 for more information as to why using the word lattice is not strictly correct.

Firstly it was discovered that assigning peak A as[†] *(061)*$_0$ with the other assignments B *(221)*$_0$, C *(121)*$_0$ and D *(021)*$_0$ could not produce a match to the experimentally derived ratios when expanding $b_0$ by 15% of its initial value (with no change in either $a_0$ or $c_0$). The value of 15% is that observed to occur for H insertion into SBPA (see section 4.1.1, table 4.4). Assigning A as *(002)*$_0$, however, produced a rough match for all ratios with the same 15% expansion of $b_0$. It was then noted that ratio D/A is independent of $a_0$. Thus the percentage increase of $b_0$ was optimised to produce the best fit for this ratio. At the end of this procedure a distinct positive slope for the ratio B/A was obtained whereas the experimental ratio is constant (see figure 6-12). Introducing a small contraction of the $a_0$ axis, however, was able to reproduce this and improve the match for ratio D/A. The overall match obtained for this set of parameters is satisfactory though no adjustment of $c_0$ had been tried. Adjusting $c_0$ produces an opposite effect on B/A ratio. That is to say decreasing $c_0$ increased the slope of ratio B/A whereas decreasing $a_0$ produces a decrease in its slope in the same region. Thus another set of parameters providing an equally satisfactory match is easily arrived at. The parameters used for the first solution together with another example are collected together in table 6.1. It shall be shown in the next section that the first solution provides an explanation for the non-movement of the peaks which appear from r=0.80

Table 6.1 Solution parameters for simulated unit cell axis expansion.

| Solution | % decrease of $a_0$ at r=1.0 relative to value at r=0.80 | %increase of $b_0$ at r=1.0 relative to value at r=0.80 | %decrease of $c_0$ at r=1.0 relative to value at r=0.80 |
|---|---|---|---|
| First | 1.2 | 6.0 | 0.0 |
| Second | 2.2 | 5.0 | 1.0 |
| | overall % change of $a_0$ at r=1.0 relative to value at r=0.0 | overall % change of $b_0$ at r=1.0 relative to value at r=0.0 | overall % change of $c_0$ at r=1.0 relative to value at r=0.0 |
| First | 1.46 | 8.85 | 2.69 |
| Second | 0.43 | 7.82 | 1.67 |

---

[†] Indices in italics refer to lines shifted from their othorhombic positions due to de Wolff disorder and microtwinning.

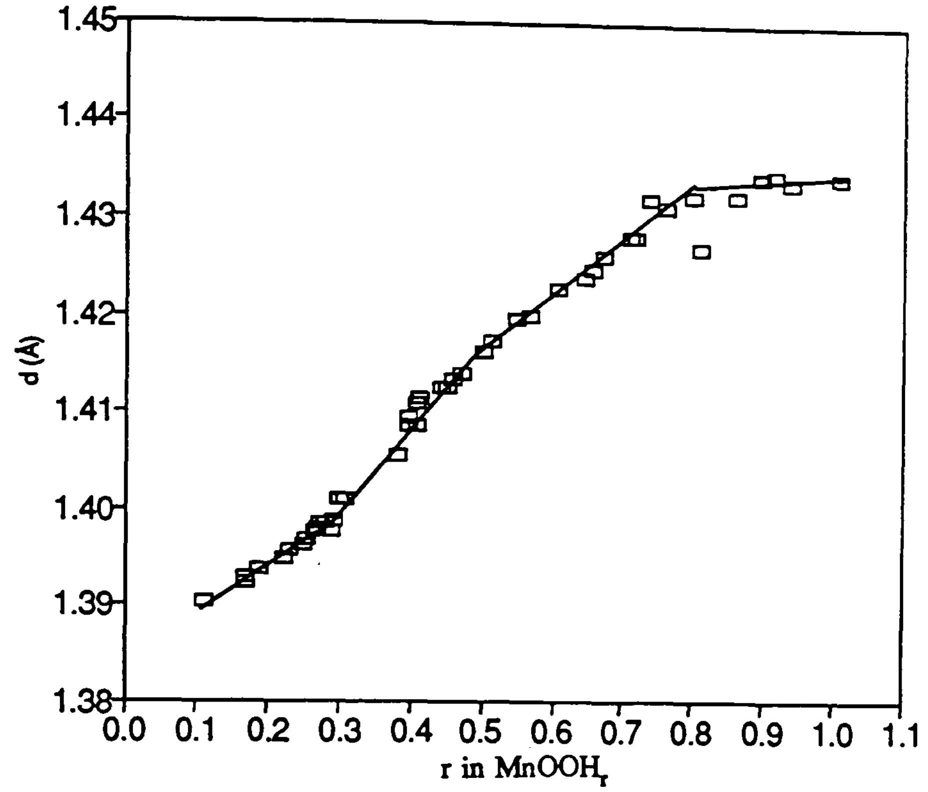

Figure 6-19 Change in d spacing of peak A with H insertion for H insertion into EMD labelled R2.

whereas other solutions do not. Furthermore if the assignment of peak A is correct then the figure 6-19 indicates that the c axis hardly changes beyond r=0.80 since *(002)* reflects directly the change in this parameter (but not directly its value through the Bragg equation). Similar deductions cannot be made for the other lattice parameters since the final reduced product does not contain peaks which directly reflect their variation. The first solution therefore best represents the variation in orthorhombic lattice parameters which produce the required anisotropic lattice expansion. Figures 6-20, 6-21, 6-22, 6-23, 6-24, 6-25 include on the same graph the calculated d spacing ratios based on the parameters listed in table 6.1 for solution 1. The following points must be noted for these graphs. The ratio calculated form a perfect orthorhombic lattice should not be expected to have the same value as those measured form the experimental peak positions. This is because, as discussed previously, every line in the x-ray diffraction pattern is shifted from its orthorhombic position (except (200)) in a direction depending in general on p (the pyrolusite type layer fraction) and the fraction of microtwinning. This indeed was observed to be the case for each ratio calculated. That is a small shift from the observed d spacing ratio (either positive or negative depending on the particular

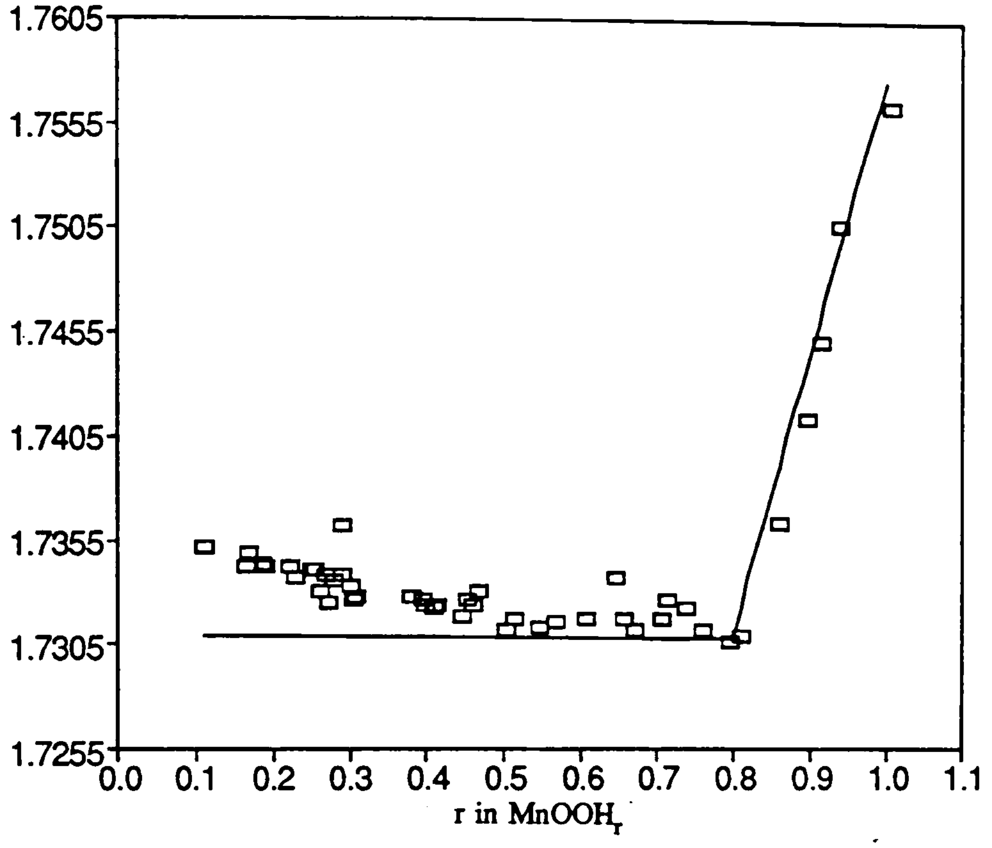

Figure 6-20 Experimental and predicted ratio from expansion of the orthorhombic unit cell as defined in table (3.31) of the d or interplanar spacings for peaks D/A (see figure 6-10) for H insertion into R2.

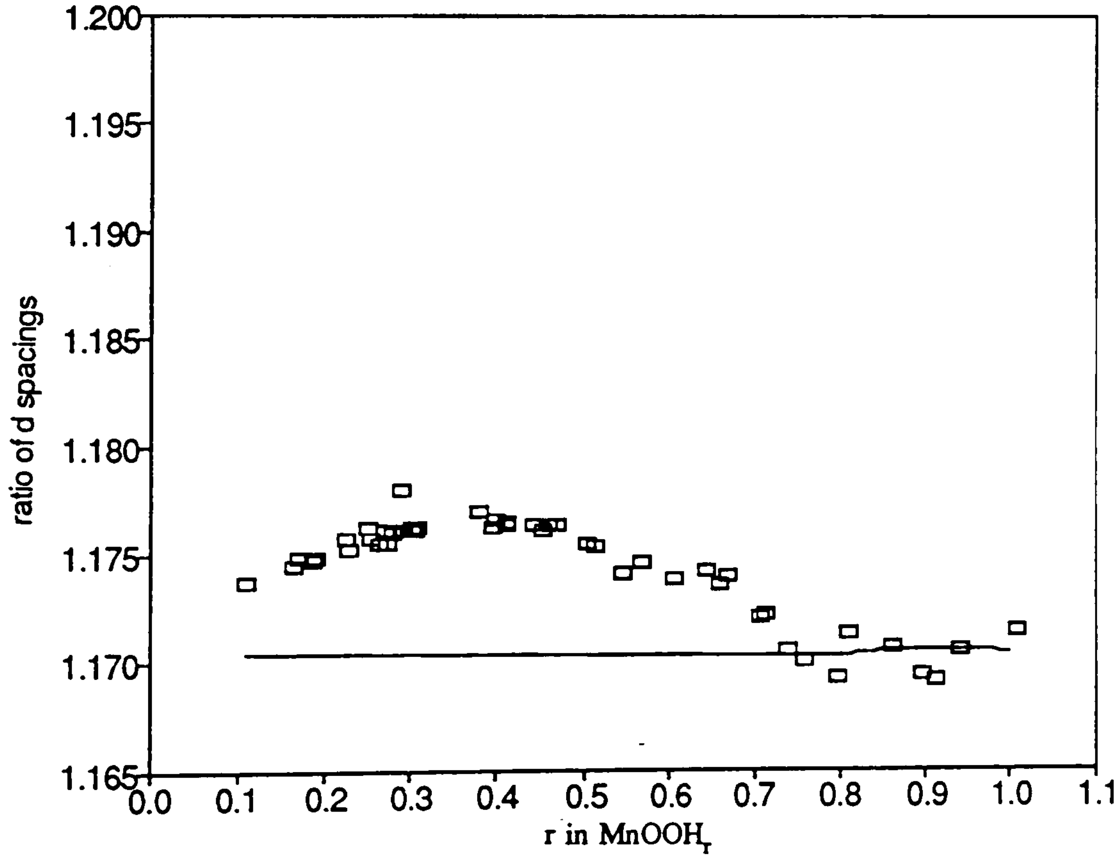

Figure 6-21 Experimental and predicted ratio from expansion of the orthorhombic unit cell as defined in table (3.31) of the d or interplanar spacings for peaks B/A (see figure 6-10) for H insertion into R2.

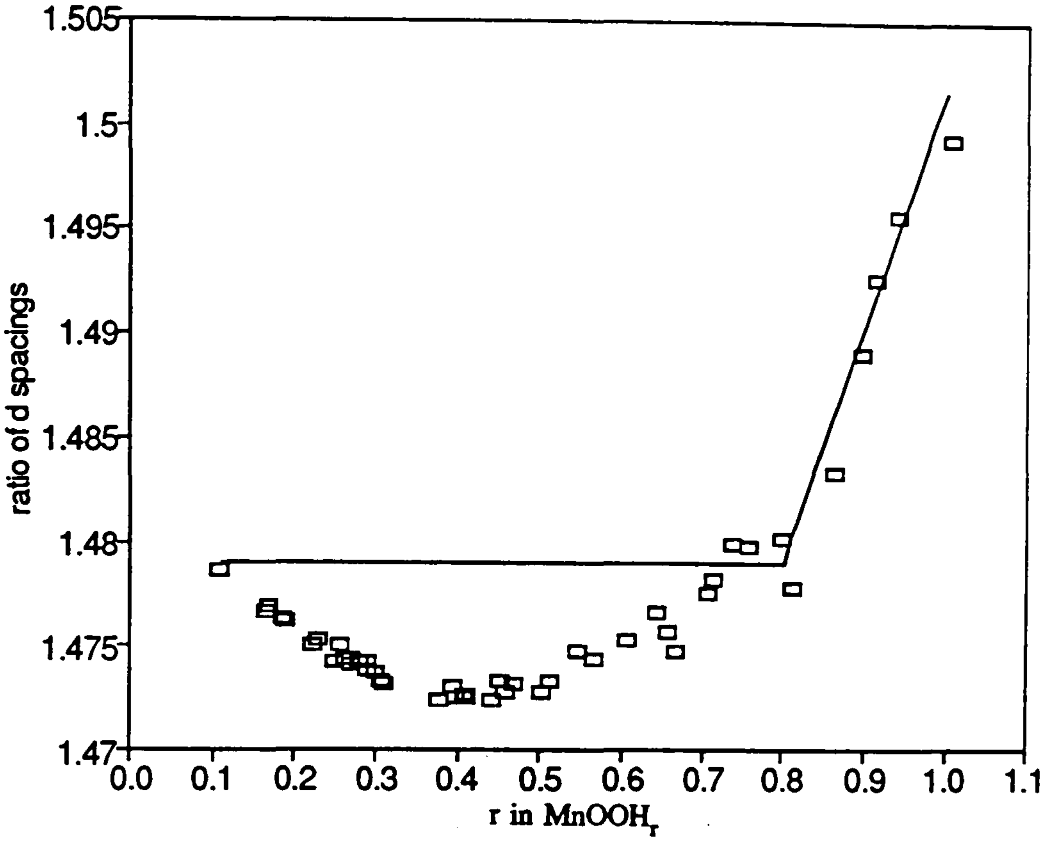

Figure 6-22 Experimental and predicted ratio from expansion of the orthorhombic unit cell as defined in table (3.31) of the d or interplanar spacings for peaks D/B (see figure 6-10) for H insertion into R2.

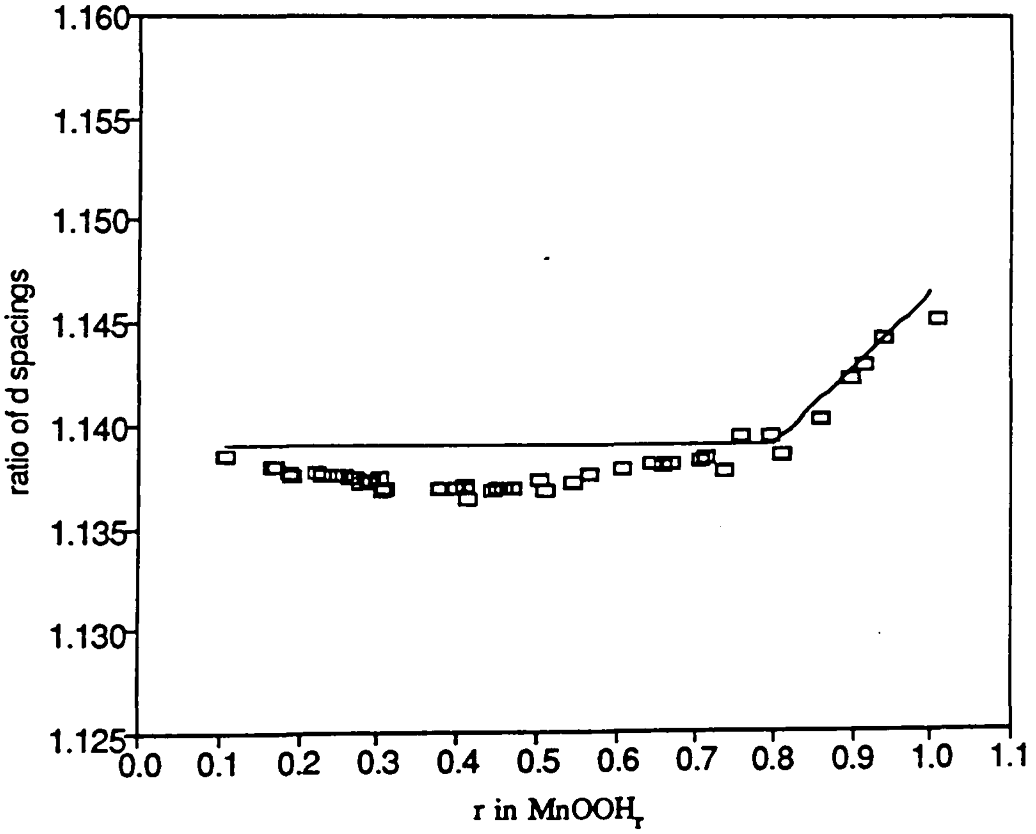

Figure 6-23 Experimental and predicted ratio from expansion of the orthorhombic unit cell as defined in table (3.31) of the d or interplanar spacings for peaks D/C (see figure 6-10) for H insertion into R2.

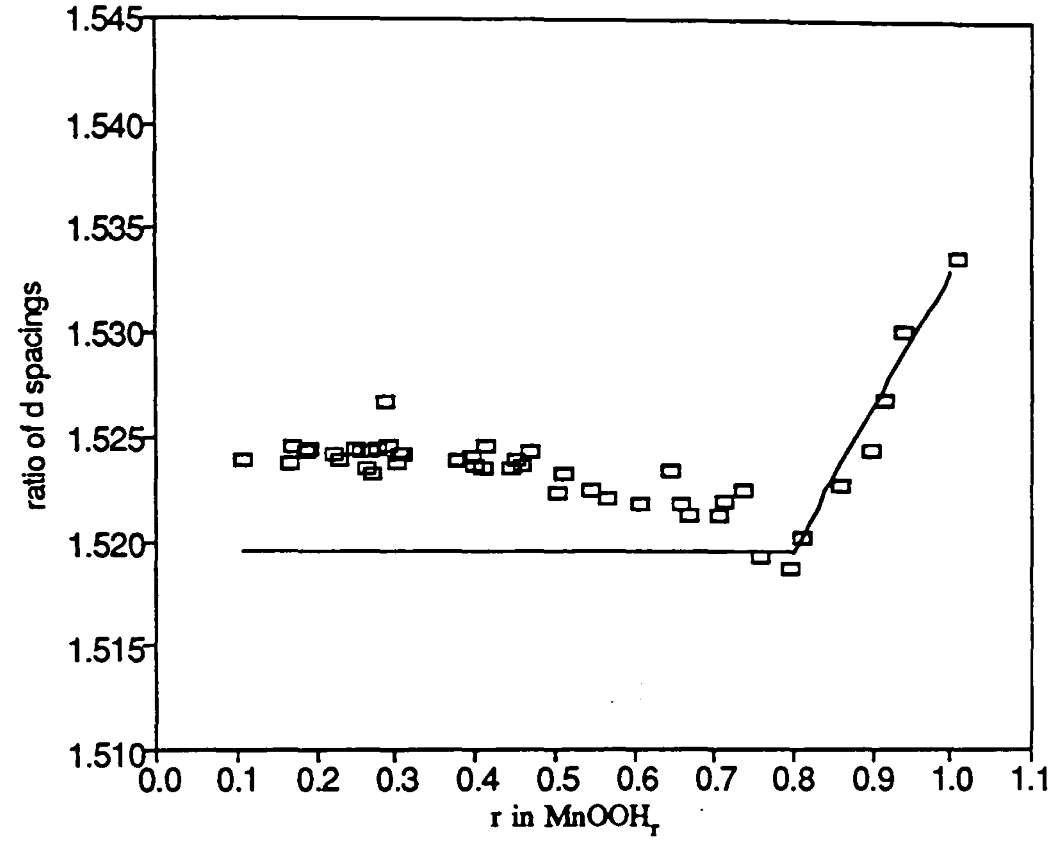

Figure 6-24 Experimental and predicted ratio from expansion of the orthorhombic unit cell as defined in table (3.31) of the d or interplanar spacings for peaks C/A (see figure 6-10) for H insertion into R2.

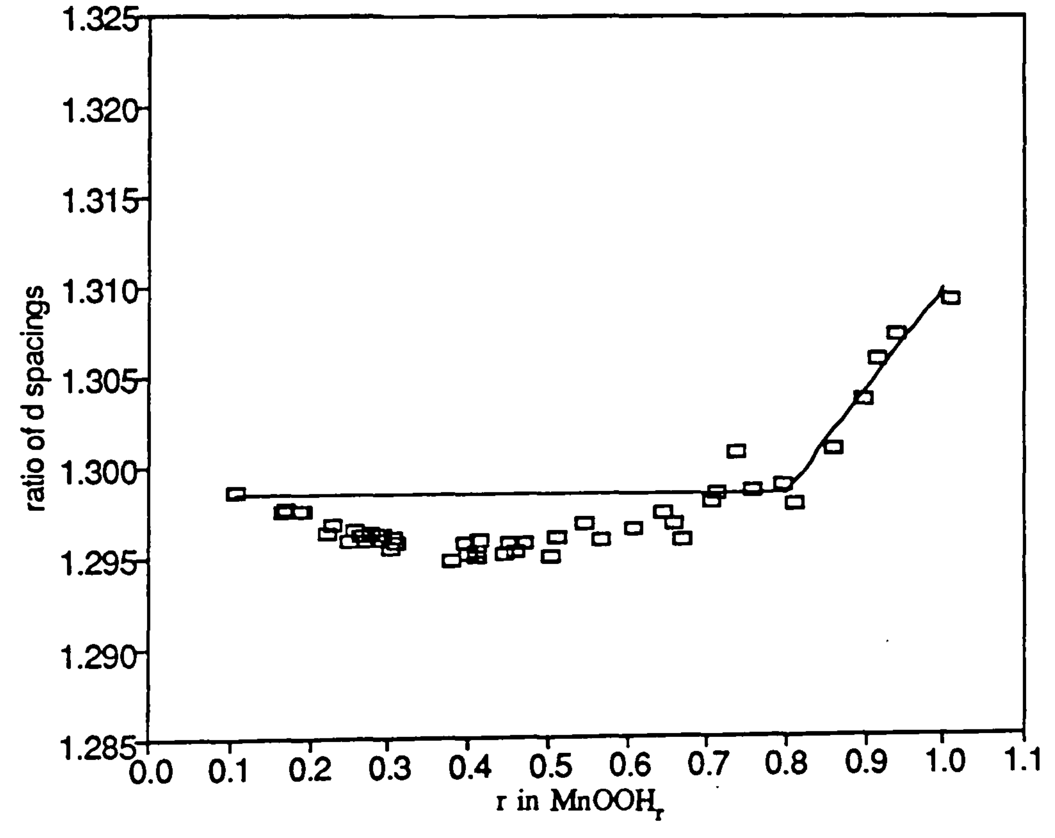

Figure 6-25 Experimental and predicted ratio from expansion of the orthorhombic unit cell as defined in table (3.31) of the d or interplanar spacings for peaks C/B (see figure 6-10) for H insertion into R2.

ratio) was apparent with the indices assigned. Therefore in order to allow direct comparison with the experimental points suitable factors were chosen such as to ensure at r=0.80 the ratios of both experimental and calculated values were the same. This ought to mean, if the unit cell expansion was isotropic in the region r=0.11 to r=0.80, that the value of the ratios also matched at r=0.11. This is true for those ratios not involving peak A. This suggests that peak A is not perfectly described simply as the assignment (*002*) in the H insertion region $0.11<r<0.80$, which is consistent with the previous suggestion that this peak is a combined (*061*), (*002*) peak (see section 2.5). Beyond r=0.80, however, it is described by the single assignment (*002*) as argued above. As shall be shown in the next section this is entirely consistent with the explanation proposed for the 'new' lines which emerge beyond r=0.80. Similar statements apply to the single assignments for peaks B, C and D which are only wholly described by these assignments given above beyond r=0.80. This is because, as shall be explained in the next section, the other peaks which contribute (see table 2.6) rapidly fade beyond r=0.80 and re-appear as separate peaks.

## 6.5 Accounting for new x-ray diffraction lines which emerge in the H insertion region $0.80 \leq r \leq 1.0$.

Table 6.2 Related orthorhombic indices for the most H inserted R2 EMD sample for the emergent lines G,H,I,J,K.

| Peak | Index |
|---|---|
| G | (210) Manganite |
| H | $(040)_0$ |
| I | $(111)_0$ |
| J | $(140)_0\&(200)_0$ |
| K | $(061)_0$ |

So far an account has been given as to how the peaks marked A, B, C, D in figure 6-10 shift with increasing H insertion level. Examining figure 6-10 new peaks emerge labelled G, H, I, J, K. Peak G is almost certainly the result of small a manganite impurity from the reduction process. This peak may be used to determine the fraction of manganite present. The maximum percentage at r=1.0 is equal to 8.3%. It shall become clear from the following sections that this represents a low contribution does not need to be explicitly taken into account in for example correcting the r in $MnOOH_r$ level of the remaining solid solution. The appearance of the manganite peak happens to coincide with the appearance of the other new peaks which otherwise are not correlated. This is demonstrated particularly in section 7.1.1 where it is shown that a material containing peaks H, I, J and K may be synthesized without the appearance of peak[108] G[†]. The indices of peaks H, I, J, and K can be quickly arrived at by comparing the most reduced sample of R2 with that of the most reduced SBPA sample, with the expectation of peak shifts due to microtwinning (see figure 4-7). The indices are almost certainly those given in table 6.2. It is observed that the lines that emerge are, apart from (200), exactly those lines which contribute to the original A, B, C, D peaks in figure 6-10 (see also table 2.6). Note that (200) has been assigned to F the 'sixth' EMD peak). Thus if these assignments are correct, the lines which appear represent a re-emergence of those peaks. To state it another way, the lines which are missing in the original EMD pattern with respect to a perfect ramsdellite structure due to de Wolff P(P') layers and microtwinning are still missing in the most reduced H inserted derivative but now the overlapping lines have become visible. It is tempting to attribute the re-emergence of lines H, I, J, K to a decrease in symmetry of the lattice due to the observed anisotropic expansion[68]. This explanation is, however, not tenable for the following reasons. Firstly there is in fact no decrease in symmetry of the lattice if the theory of the structure of EMD presented in chapter 2 is correct. An analogous situation would be to observe the hypothetical transition ramsdellite to groutite in which there is no decrease in symmetry as both are orthorhombic. Secondly a decrease in symmetry often manifests itself as peak splitting[109] (see also section 6.3) whereas there is no evidence of this type of change when inserting H into R2.

It is an experimental fact that relativley little movement of the re-emergent lines can be detected with increasing H insertion (see section 6.2). The question that presents itself is this. How can this be possible if the lattice continues to expand (anisotropically)? For example peak H should move rapidly with H insertion as it has

---

[†] It may appear that this statement accords with the findings of Stumm and Giovanoli[108] who point out that manganite which precipitates as fine rods sometimes shows no evidence of the 100% line. This is easily accounted for by examining the unit cell of manganite and how it may be orientated in a rod shaped particle. Such rods do indeed form when EMD is refluxed in water (see section 3.2.1). It is obvious, however, that if manganite precipitation was the main reaction beyond r=0.80 this would be a heterogeneous process, which it has been shown is not the case.

Table 6.3 Predicted peak shifts for the anisotropic expansion defined by % lattice parameter changes listed in table 6-30.

| solu-tion. | E<br>*(110)$_o$*<br>(2θ) | H<br>*(040)$_o$*<br>(2θ) | D<br>*(021)$_o$*<br>(2θ) | I<br>*(111)$_o$*<br>(2θ) | J<br>*(140)$_o$*<br>(2θ) | J<br>*(200)$_o$*<br>(2θ) | C<br>*(121)$_o$*<br>(2θ) | B<br>*(221)$_o$*<br>(2θ) | K<br>*(061)$_o$*<br>(2θ) | A<br>*(002)$_o$*<br>(2θ) |
|---|---|---|---|---|---|---|---|---|---|---|
| 1st | -0.004 | -2.197 | -0.559 | -0.002 | -1.841 | -0.500 | -0.375 | -0.007 | -3.237 | -0.000 |
| 2nd | 0.217 | -1.849 | -0.195 | -0.393 | -1.427 | -0.927 | -0.053 | -0.589 | -2.550 | 0.818 |
| Exp. | | | -0.599 | | | | -0.481 | -0.194 | | -0.481 |

an index of (*040*) if the lattice expands only in the $b_0$ direction. Consider table 6.3, which indicates the calculated °2θ shifts expected for anisotropic unit cell expansion defined by the first and second solutions listed in table 6.1. Certain peaks, namely (*040*)$_0$, (*140*)$_0$ and (*061*)$_0$ show tremendous peak shifts compared to the other peaks for both solutions. It is noted that these are all re-emergent peaks. Could it be therefore that precisely those peaks which ought to have large peak shifts actually correspond to the non-moving emergent peaks? Despite the apparent contradictory nature of such a statement it shall be argued this is in fact the case.

To see this it is necessary to consider the random layer model calculation described in section 4.4.1 and figures 4-12 and/or 4-16. In this figure there are two peaks which apparently show different behaviour to the other peaks which merely shift with increasing H insertion. They are (040)$_0$ and (140)$_0$. Both of these fade quickly at low r values and apparently simply re-emerge at high r levels. A similar conclusion for (061)$_0$ and (*151*)$_0$ may be deduced from figure 4-18. (Note that (*151*)$_0$ is not observed in EMD R2 due to the effects of microtwinning). This effect is a consequence of the H-T effect, (cf. section 4.3.2) but instead of the peak in question broadening it completely fades and re-emerges since the d spacings for the initial layer model, i.e. a R(R'), P(P') model, and the reduced model of G(G'), M(M') layers are for these particular Miller indices widely separated in °2θ. Other peaks which have their reduced layer counterparts very much nearer merely show a linear shift (as established in section 4.4.1). It would appear that the emergent non-moving peaks H, J, K may be accounted for by the above suggestion. The remaining peak I does not fit into this category as indicated in table 6.3. However, according to the first solution it is hardly expected to move in the first place. The second solution predicts a positive peak shift hence the further condition which enables one to select the first solution is that of no peak movement for (*111*)$_0$.

A single proposition may now be stated which enables all of the described diffraction effects beyond r=0.80 to be accounted for.

Beyond r=0.80 rapid random nucleation and precipitation of δ-MnOOH micro-domains occurs within the solid solution. These give rise to diffraction effects equivalent to a random layer model with $R_e(R_e)$, G(G'), P(P') and/or M(M') layers. The subscript e denotes isotropically expanded R(R') layers. These are supposed to contain a random distribution of $Mn^{3+}$ determined solely by the reduction level r up to r=0.80 and by the reduction level r and the fraction of δ-MnOOH domains beyond r=0.80. Due to the H-T effect some lines only shift while others emerge without any apparent shift. The shifting lines indicate anisotropic expansion since the nucleating G(G') and/or M(M') layers[†] have a layer spacing essentially much greater in the $b_0$ direction. The δ-MnOOH micro-domains contain $H^+$ and $e^-$ which are no longer mobile within the solid solution. Further evidence for this statement is provided in the next section.

Thus to summarise, from r=0.11 to r=0.80 the orthorhombic lattice (approximately) isotropically expands in the manner of a random solid solution, that is as a consequence of the greater size of $Mn^{3+}$ and the mobility of $H^+$ and $e^-$ within the crystal structure. Beyond r=0.80 $H^+$ and $e^-$ locate within the structure. The resulting diffraction effects observed are broadly those consistent with a random layer model of $R_e(R_e')$, G(G'), P(P'), M(M') layers. $R_e(R_e')$ represents the solid solution, and G(G'), M(M') the regions where protons and electrons have 'frozen out' within the structure. Thus regions of solid solution and δ-MnOOH domains co-exist in the reduced product in the region $0.80<r<1.0$. Increasing H insertion beyond r=0.80 increases the precipitation of δ-MnOOH micro-domains until at r=1.00 the protons and electrons are completely located within the structure.

In the next section FTIR spectroscopy on the same set of samples is presented which strongly supports the idea of solid solution immiscibility in the form of δ-MnOOH micro-domains.

## 6.6 Direct evidence for immobile H in H inserted EMD (sample R2).

Following the previous presentation of FTIR data, integrated areas (with

---

[†] This is what is meant by δ-MnOOH micro-domains i.e. a structure with random layer properties containing $Mn^{3+}$.

background removal) under certain regions of the spectra are determined for each H inserted sample and plotted versus r in $MnOOH_r$. The boundaries of each region are shown in figure 5-13 (cf. section 5.3).

If a solid solution with mobile $H^+$ and $e^-$ is present in the H insertion zone $0.11<r<0.80$ one would expect no major changes in the spectra where OH bonds are normally detected. Beyond r=0.80 absorptions due to OH bonds ought to be detected if δ-MnOOH micro-domains are formed.

Almost exactly this description may be deduced from figures 6-26, 6-27, 6-28 which are the integrated areas for the peaks previously determined to be associated with OH bands. Each figure contains a clear break in the slope of integrated area versus r at r=0.80 before which the area is nearly constant in each case, as expected from the above prediction. The spectra of the final reduced product is very similar to that obtained for the most reduced SBPA sample, which in turn bears a close resemblance to patterns labelled in Potter and Rossman[105] as the mineral groutite.

It may be concluded that FTIR spectra provide a direct means of detecting when H locates in the EMD structure, in this case in the form of δ-MnOOH micro-domains.

## 6.7 Comments and further observations.

The author considers that the argument presented in the preceding sections sufficiently complex for it to re-stated in a slightly different and more general way.

The observed diffraction effects exhibited by R2 in figures 6-1, 6-2, 6-3 are consistent with (essentially) a random layer model of $R_e(R_e')$ layers and G(G') type layers beyond r=0.80. It is analogous to the case calculated in section 4.4.1, in which certain peaks were observed to quickly fade at low H insertion levels (namely (040), (140) and (061))) and re-appear at high insertion levels due to the fact that the d spacings of these peaks are widely separated in d (because G(G') layers are mostly only expanded in the b direction compared to R(R') layers). A similar statement applies in the case proposed but *due to the particular effects of microtwinning*, these peaks are at r=0.80 overlapped with other diffraction maxima, and hence apparently emerge rather than re-emerge, which is the correct description. This statement is further supported by the dramatic loss of intensity observed only for peaks which are proposed to be superpositions of two (or more) diffraction maxima (see figures 6-1 and 6-3). Whereas

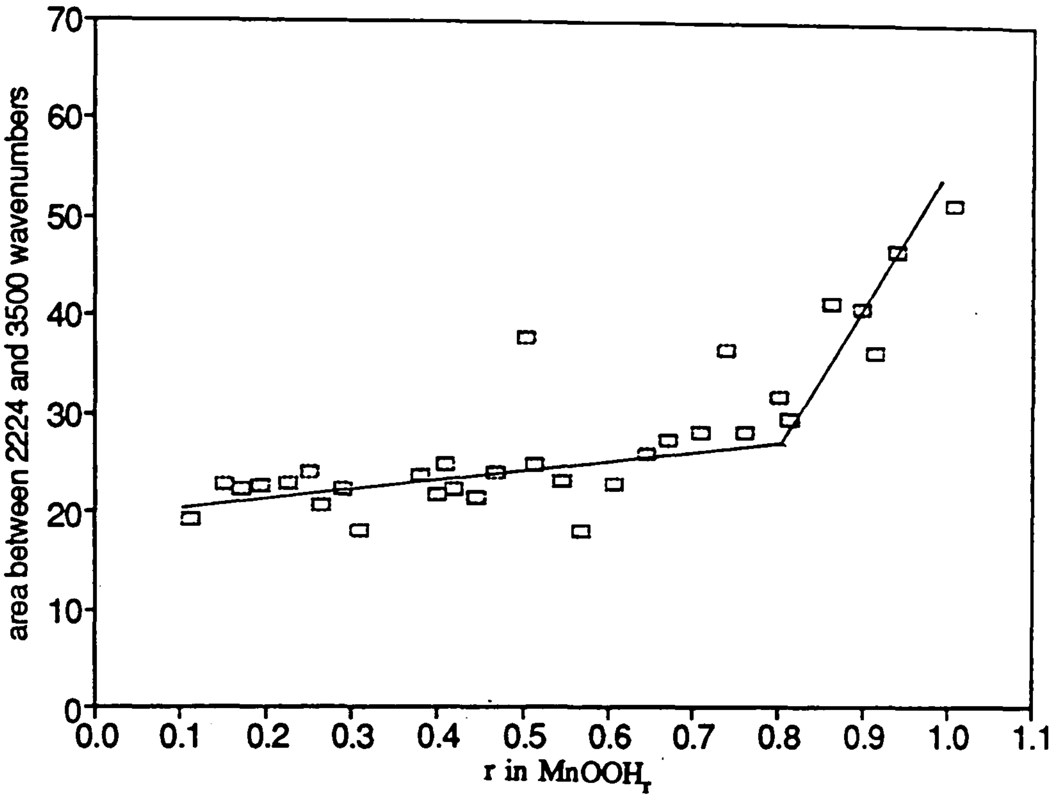

Figure 6-26 Change in integrated area of FTIR spectra minus background area, as defined by the ar1 boundaries shown in figure 5-13, with H insertion into R2.

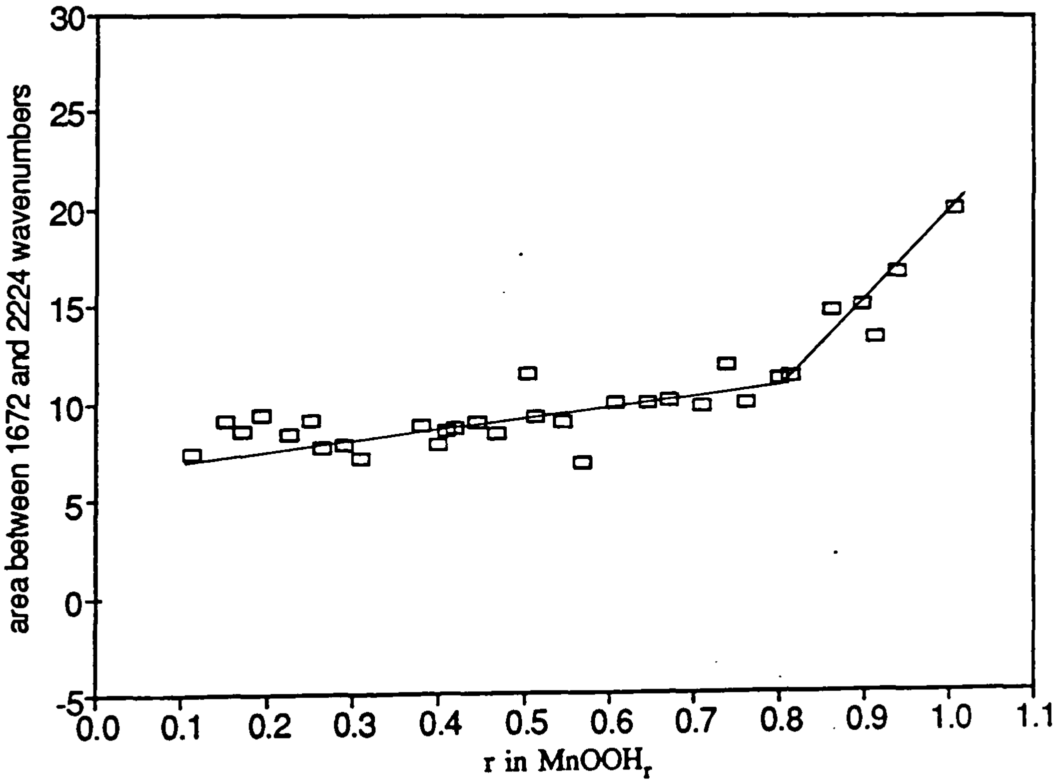

Figure 6-27 Change in integrated area of FTIR spectra minus background area, as defined by the ar2 boundaries shown in figure 5-13, with H insertion into R2.

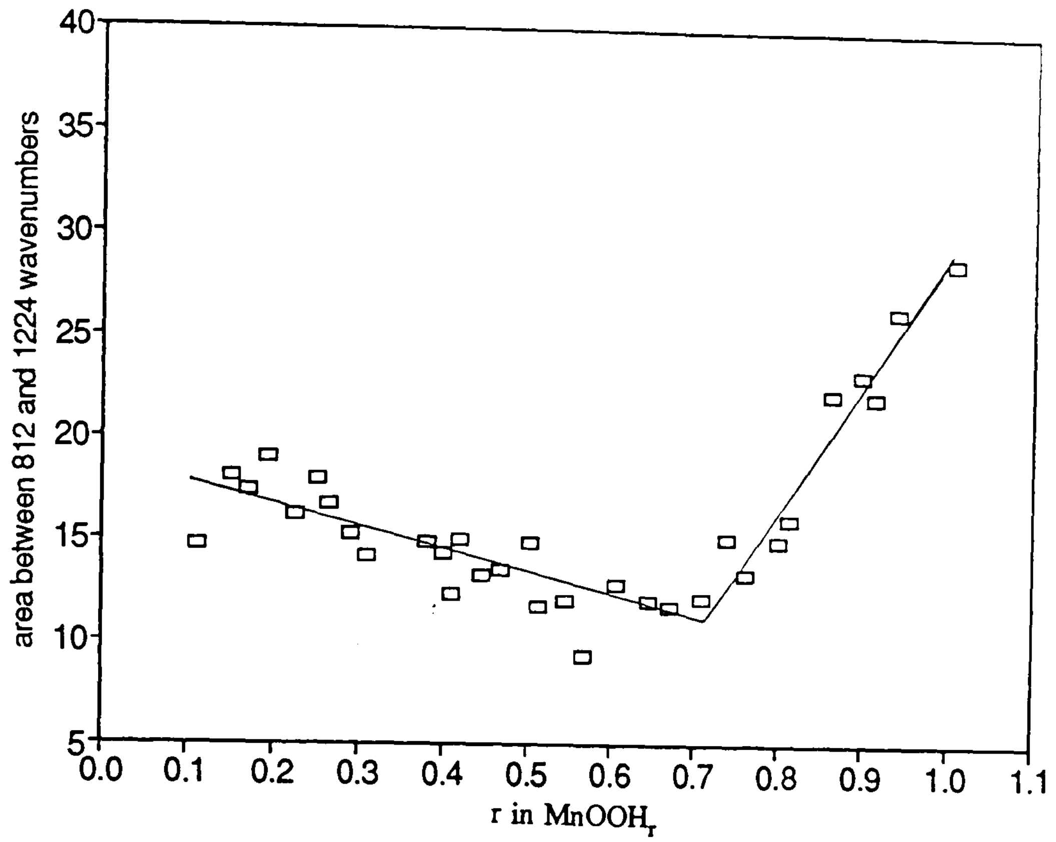

Figure 6-28 Change in integrated area of FTIR spectra minus background area, as defined by the ar4 boundaries shown in figure 5-13, with H insertion into R2.

where this is not the case, notably *(110)* (see figure 6-2) no such loss is observed. Note also peak B which, although a combined peak remains so during H insertion and hence does not display any intensity loss (figure 6-3).

Increasing H insertion beyond r=0.80 causes nucleation of G(G') type layers (or more accurately δ-MnOOH micro-domains) which decrease the proportion of $R_e(R_e')$ layers. $R_e(R_e')$ 'layers' contain mobile $H^+$ and $e^-$ and hence represent the solid solution whereas G(G') type layers have immobile H (see previous section). Thus the cause of the movement of *all the moving* and non-moving peaks beyond r=0.80 is a consequence of a random layer model (or equivalently the H-T effect), since the proportion of G(G') type layers increase at the expense of $R_e(R_e')$ type layers. The reason that anisotropic expansion is observed is because G(G') layers are essentially expanded in the **b** direction compared to $R_e(R_e')$ layers.

The situation of peak *(111)* is apparently more complex but in fact is probably simpler. In this case the peak appears to emerge in a similar way to the other non-moving peaks although it does not belong to the same class as *(040)*, *(140)* and *(061)*. In this case, however, the contribution of *(111)* to peak D must be small if not negligible due to the effects of microtwinning (see figure 2-12). Due to structure factor changes (111) nearly doubles in relative intensity, $I_1/I$=48% compared to $I_1/I$=28.7%, to become the second most intense peak in groutite compared to ramsdellite in the hypothetical transition between the two. Therefore one might expect that as the proportion of G(G') layers increases *(111)* simply emerges† (which in this case is a more accurate description), its non-movement being easily dealt with by the particular lattice shifts required for the isotropically expanded $R_e(R_e')$ layers to move to the dimensions of those governed by G(G') layers (see section 6.5).

Finally, the argument presented represents a first attempt at explaining the observed diffraction effects. It does not match exactly with observation, nor should it be expected to. Thus no presentation of the positions of the calculated peaks (section 4.4.1) which fade and emerge is given. This is because these peaks do in fact display peak shifts, unlike the observed peaks. There are at least two explanations for this discrepancy. Firstly it could be that the peaks which re-emerge are not detected until the have grown to a substantial extent by which time little peak movement has yet to occur. This argument is supported by the 'S' shaped nature of peak shifts due to the H-T effect. Secondly, and more fundamentally, the calculations described in section 4.4.1 assumed a random *layer* crystal with disorder occurring in one spatial direction (**b** direction). Thus the δ-MnOOH micro-domains formed would extend throughout the crystal in the **a** and **c** directions. Clearly if the sample was heavily microtwinned this description does not fully describe the crystal. Disorder would be present in two spatial directions (**b** and **c**) and the domains formed would more accurately be termed $\delta_t$-MnOOH micro-domains. A more complete model would therefore have to simulate the random precipitation of $\delta_t$-MnOOH micro-domains, the results of which may be expected to remove the discrepancy referred to.

## 6.8 Jahn-Teller distortion.

If a transition metal such as $Mn^{3+}$ is surrounded by six negative ions that form a perfect octahedra then by the application of ligand field theory[110] the following deductions have been made.

---

† It could be that the conditions deduced from microtwinning indicating which peaks are faded and shifted are slightly altered in G(G') type matrix enhancing the appearance of *(111)*.

The five d orbitals are split into two groups $e_g$ and $t_{2g}$ with $e_g$ at the higher (less negative) energy. The splitting is a consequence of observing how the orbitals of the free atom can be placed in an octahedra with the Mn ion at the centre. Whether the perfect octahedral coordination is maintained depends on the symmetry with which the four d electrons take up which in turn depends on which energy level they go into. It is not necessarily the case that they will all occupy the lowest energy level of the energy levels $e_g$ and $t_{2g}$ since the electrons also (in this case) want to form the maximum number of parallel spins. The resulting electron arrangement may be viewed as a combination of these two tendencies. If the resulting symmetry is lower than cubic then a more stable arrangement is favoured by distorting the octahedral coordination. This is known as the Jahn-Teller effect.

### 6.8.1 Comments on the Jahn-Teller distortion parameter.

The distortion referred to in the previous section has been expressed[22] as the ratio of two particular edges of an octahedron, in which case for the orthorhombic unit cells of ramsdellite or groutite (or related unit cells of $\gamma$-$MnO_2$) the relation of the sides in mind to the unit cell parameters is

$$a' = c \tag{4.1}$$

$$a'' = \frac{1}{2}\left(\frac{b^2}{4} + c^2\right)^{\frac{1}{2}} \tag{4.2}$$

a''/a'=1 for 'h.c.p. ramsdellite', i.e. one constructed from perfect octahedra of oxygens. This parameter is ~1.05 for $Mn^{3+}$ oxyhydroxides reflecting Jahn-Teller distortion, and lower than 1 (~0.96) for other transition metal oxyhydroxides[73] (not displaying this kind of distortion). Evidently one needs to be able to derive the lattice parameters of the material in order to calculate the value of this parameter. Since the peak positions of a heavily microtwinned sample (i.e. near the end of the $\gamma$-$\gamma_t$-$MnO_2$ series) are all (except peak F) shifted from their orthorhombic positions in direction and magnitude depending on p and the degree of microtwinning it is not valid to calculate the orthorhombic lattice parameters directly from the pattern by fitting an appropriately sized lattice. In the past attempts have been made to do this but since the patterns (very nearly) display apparent hexagonal symmetry, in effect an equation with three adjustable parameters is being fitted to one which apparently only has two. Not surprisingly this may (and has) led to wide discrepancies in the quoted 'lattice parameters' for typical battery active manganese dioxide. In the light of Pannetier *et al.*'s model doubt must be cast over the value of such an exercise. Obviously any derived parameters such as a''/a' are similarly affected.

The numerical values of a''/a' obtained by Maskell[73] *et al.* calculated by such a procedure do not therefore correspond to the ratio of two sides of an octahedra as supposed. Hence the relatively high value of a''/a'$\approx$1.01 for the initial material (EMD R2) is probably not correct. Nonetheless changes in the parameter calculated must surely reflect changes in the octahedral distortion and therefore the conclusions arrived at concerning the type of site occupied by the inserted H may not be affected. The following, however, must be considered.

A sharp and large change in a''/a' (as calculated) was observed at the mid-reduction point as was first reported by Gabano[22] *et al.* (where similar comments to the above apply). Since the graph obtained therein was the result of a number of experiments on the same material but using different reduction methods it seems clear that the sharp change referred to corresponds to the onset of anisotropic expansion (at $r=0.80$) in this work but which was induced to occur at an earlier H insertion level by certain methods of reduction employed (thus overall it appears that a change at $r=0.50$ occurs in a''/a' whereas other methods may have suggested a higher r value). Note that other (smaller) changes[68] in d versus r and other parameters[111] have been reported to occur near the mid-reduction level (also observed in this work as noticeable changes in the d spacings and ratios derived from them in the 'isotropic' H insertion level, see section 6.2). These observations may be reconciled by admitting that slight changes at the mid-reduction level occur which may possibly be masked by other larger changes associated with the precipitation of δ-MnOOH micro-domains within the solid solution. The H insertion level at which this occurs depending on the voracity of the reduction method. The precipitation of δ-MnOOH micro-domains at some high level of H insertion is, however, inevitable.

In the case of material SBPA lattice parameters were derived from the initial x-ray diffraction pattern and those in which a solid solution was formed, namely $0.068<r\leq0.40$. Beyond this H insertion level it was not advisable to calculate lattice parameters from the x-ray diffraction pattern due to the possibility of overlapping peaks because of heterogeneous reduction, (this is particularly true in the case of WSZ, see

section 7.1.1) until that is, the final product was clearly the dominant x-ray diffraction pattern in the mixture.

Consider figure 6-29, which indicates the variation of the Jahn-Teller distortion parameter a''/a'. Clearly considerable change occurs within the solid solution region, which after initially slowly changing, between $0.068<r<0.20$, increases linearly with an increased slope towards $r=0.40$. It is interesting to note that extrapolation of the line in this zone falls below the value calculated for the final reduced product. Thus if the solid solution range could be extended over the whole H insertion range a linear change in this parameter could not be expected in the intervening H insertion levels.

The results obtained may be compared with previous work by Giovanoli and Leuenberger[112] on a material displaying a very similar x-ray diffraction pattern to that of SBPA (i.e. $\gamma$-$MnO_2$, with p=0.2). Figure 6-30 plots the data obtained from the figure in the paper (labelled as in the original) with the data from this work (figure 6-29). In the paper two straight lines intersecting at the mid-reduction point indicating a large change in slope were drawn. In the light of this work, in which heterogeneous reduction has been recognised to occur, considerable doubt must be placed over such an interpretation.

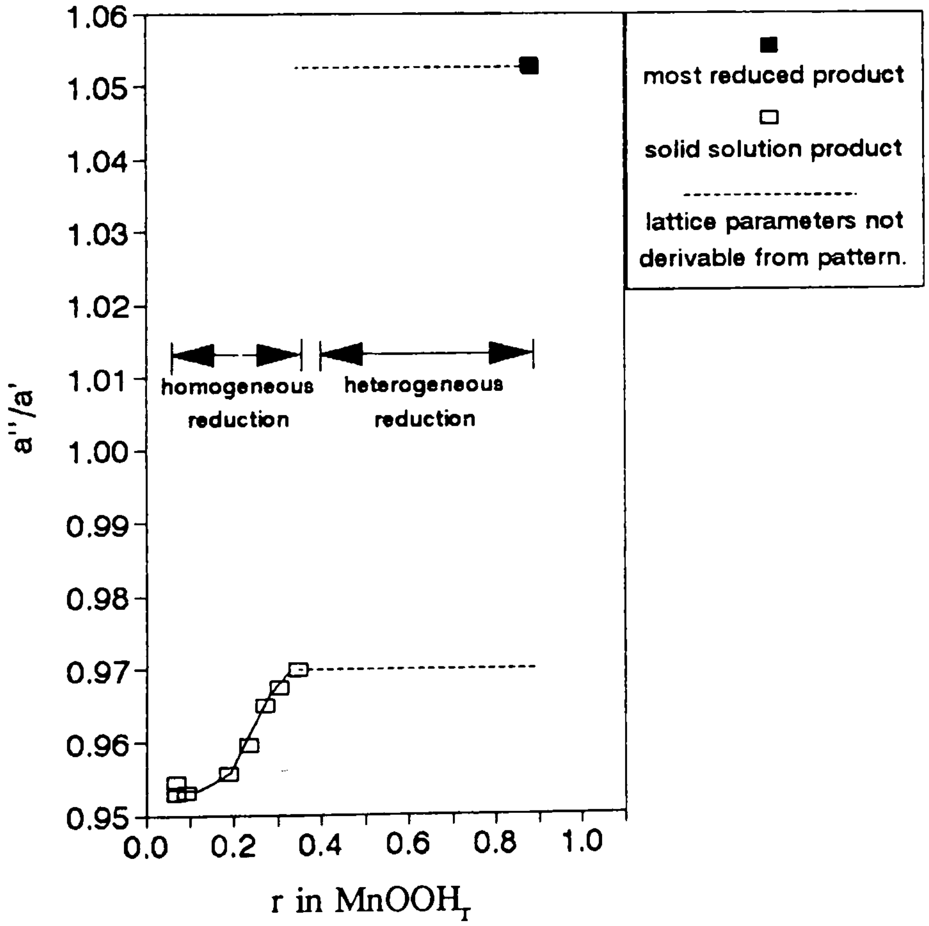

Figure 6-29 Variation of Jahn-Teller distortion parameter versus r in $MnOOH_r$ for sample SBPA. Regions of homogeneous and heterogeneous reduction are marked.

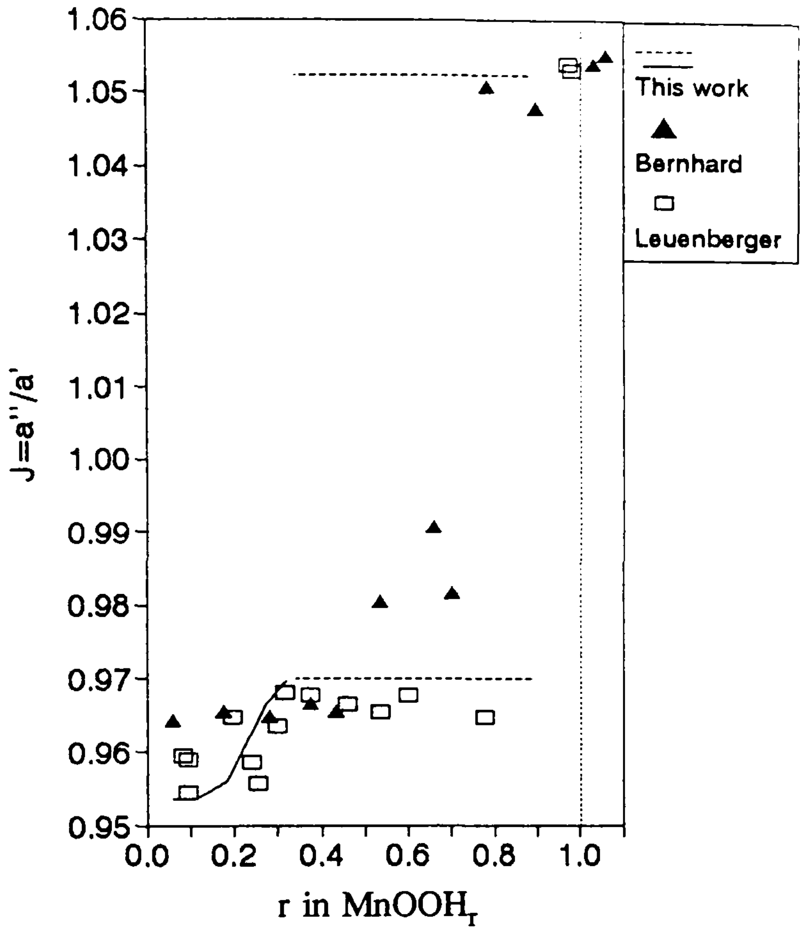

Figure 6-30 Comparison of Jahn-Teller distortion parameter versus r in $MnOOH_r$ obtained from Giovanoli and Leuenberger[112] and from this work. Referenced data labelled as in original.

# 7 Interpretation of the X-Ray Diffraction Patterns and FTIR Spectra of Materials WSZ, IBA no.14, IBA no.19 and F.M with H Insertion Level.

## 7.1 Faradiser WSZ.

In the following sections results for the remaining materials which have also had H inserted chemically are presented. In this section the results for H insertion into Faradiser WSZ (here abbreviated WSZ) are considered. It shall be shown that all the remaining materials in the $\gamma$-$\gamma_t$-$MnO_2$ series may be interpreted with the explanations used to account for the previous two materials. What shall also emerge from the following is a dependence on the reduction mechanism on the choice of chemical reductant.

WSZ, which is characterised by a p fraction equal to 0.24±0.01 (see appendix A), was reduced by hydrazine hydrate in a non-aqueous solvent (see section 3.2.3). This method cannot be totally non-aqueous since hydration water is released in the reaction vessel during preparation. Nevertheless the product obtained at compositions close to MnOOH did not contain an enhanced manganite peak compared to the product obtained from the reduction of SBPA. Figure 7-1 summarises the changes in diffraction pattern which occur. Thus from $r=0.104$ to $r \approx 0.64$ only peak shifts occur. In the region $r \approx 0.64$ to $r=0.972$ new peaks occur and the final diffraction pattern is very similar to that of SBPA reduction (see figure 5-2 and figure 4-7). What is not clear was whether the H insertion reaction was heterogeneous or homogeneous in this region. Figure 7-2 indicates that it was heterogeneous.

Linear proportions of the patterns at $r=0.636$ and $r=0.972$ were added to produce synthesized patterns in steps of $r=0.034$ (which means ten patterns were produced in the H insertion range $r \approx 0.64$ to $r=0.972$). Focusing once again on the $2\theta$ range where most of the new peaks emerge (i.e. 28-44(°$2\theta$)) all the synthesised patterns are plotted on one figure (figure 7-2). This may be compared with the actual patterns in this range plotted in a similar fashion, figure 7-3. This figure indicates very similar behaviour to the synthesized patterns. In particular where there are isobestic points in figure 7-2, identified by places where the intensity is a constant (i.e. where all the lines crossover

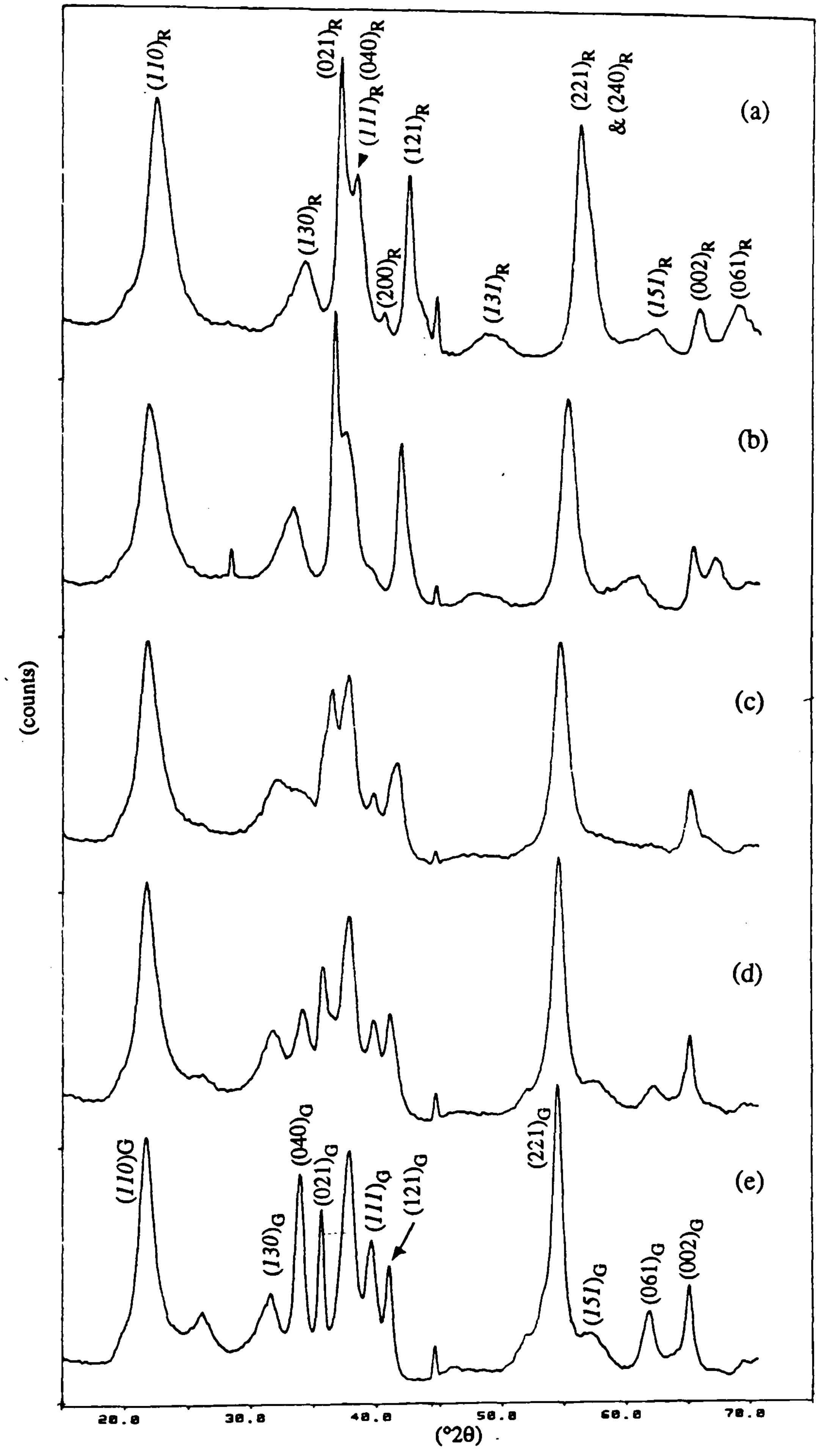

Figure 7-1 Selection of x-ray diffraction patterns representing the changes which occur on H insertion to material WSZ. (a) $MnOOH_{0.104}$ (b) $MnOOH_{0.388}$ (c) $MnOOH_{0.636}$ (d) $MnOOH_{0.784}$ (e) $MnOOH_{0.972}$. Indices related to ramsdellite $(hkl)_G$ and groutite $(hkl)_R$ are marked.

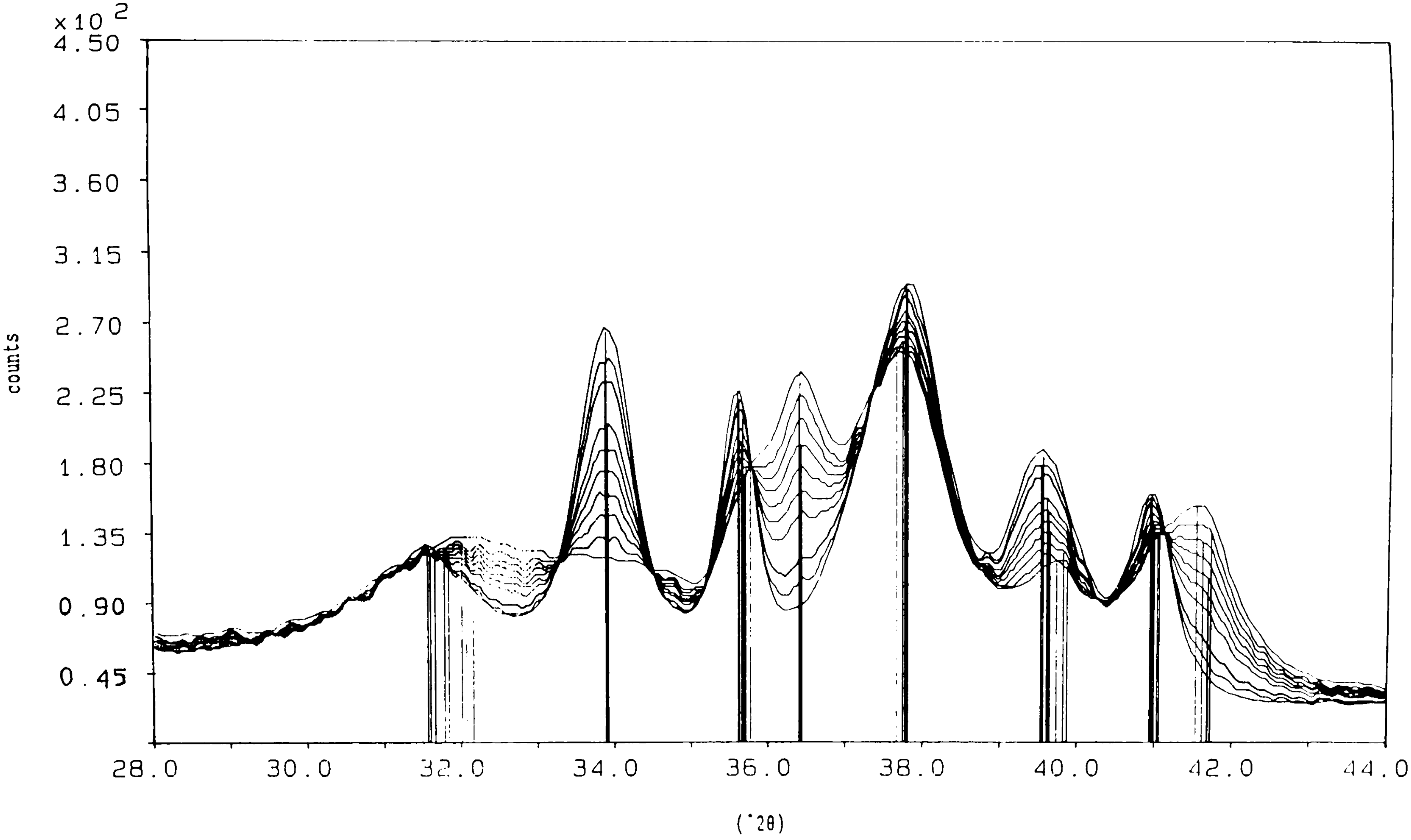

Figure 7-2 Simulated x-ray diffraction of heterogeneous reduction of material WSZ from mixtures of samples with compositions $MnOOH_{0.636}$ and $MnOOH_{0.972}$.

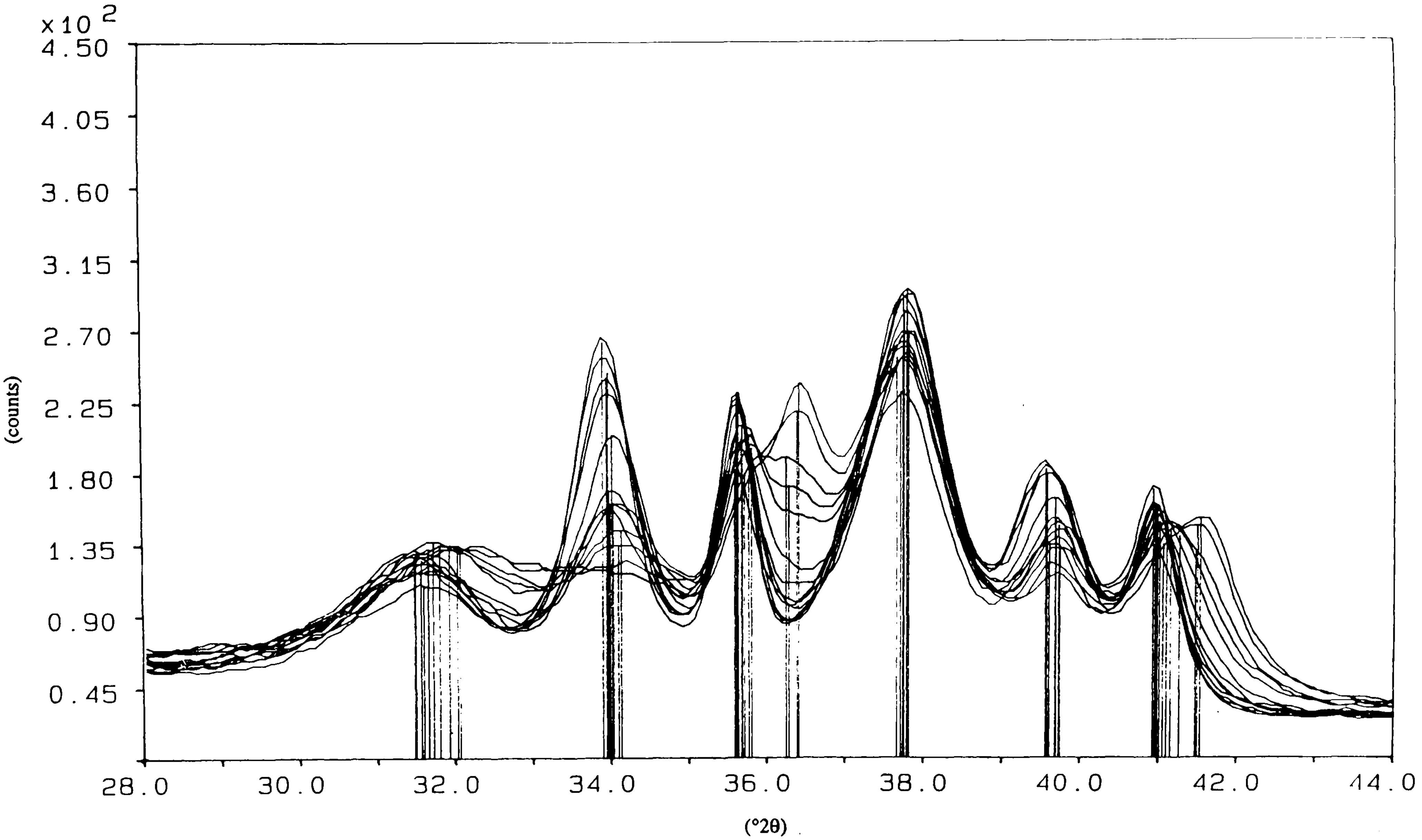

Figure 7-3 Actual x-ray diffraction patterns of material WSZ in the composition range $MnOOH_{0.636}$ to $MnOOH_{0.972}$.

in figure 7-2), corresponding areas of crossover are revealed in figure 7-3. For example the isobestic point at 33.32 (°2θ) in figure 7-2 corresponds to a restricted area in figure 7-3 at the same °2θ angle in which all the lines are present. Such graphs are very dependent on reliable intensities for each pattern, and so the agreement is considered satisfactory.

It is appropriate at this point to discuss the FTIR spectra of the same set of samples. The peak areas ar1, ar2, ar3, (cf. section 5.3) in this case show particularly clear breaks indicating, as previously identified for such evidence, that H locates within the structure from this reduction level onwards, the break in this case occurring at $r \approx 0.40$ (see figures 7-4, 7-5, 7-6). This suggests the homogeneous region is delineated as $0.104 \leq r \leq 0.40$ with location of H occurring thereafter. Note that synthesizing the heterogeneous process from $r=0.40$ does not produce clearly isobestic points by the method described above. This suggests, as for material SBPA, there is a region of H insertion in which H starts to freeze but does not lead to heterogenous behaviour. Rather micro-domains of δ-MnOOH are produced as for material R2 which eventually nucleate heterogeneous reduction. Consideration of graphs indicating d (or interplanar spacing) spacings versus r in MnOOHr for certain peaks supports this idea.

Consider for example figure 7-7 which may be compared with figure 5-5. In these figures the d spacing of $(021)_R$ and $(021)_G$ are plotted. In this case a linear increase in d spacing occurs with a clear change in slope at $r \approx 0.40$. A curve is observed thereafter which is different to the nearly horizontal line observed for material SBPA figure 5-5. This suggests that the curve be associated with the region in which micro-domains of δ-MnOOH precipitate in the solid solution. There is however another reason why a curve may be observed. The peaks representing the final homogeneous reduction and that of the most reduced product are not separated in d spacing as much as in SBPA. The consequence of this is that they are sufficiently close to overlap and appear as one peak. Thus although there is a clear change in slope in $d_{(021)}$ against r in figure 7-7 at $r \approx 0.40$ the slope thereafter is not zero as in the SBPA case. Similarly the slope of $(021)_G$ is not zero either. This argument also applies to that of peak (121), figure 7-8. This figure is of interest because it now appears that a smooth transition between the corresponding reduced analogue of the $(121)_G$ peak and the initial $(121)_R$ peak occurs. It seems clear with reference to the above argument that such a transition is produced by overlapping peaks and the effects of precipitation of δ-MnOOH micro-domains. The

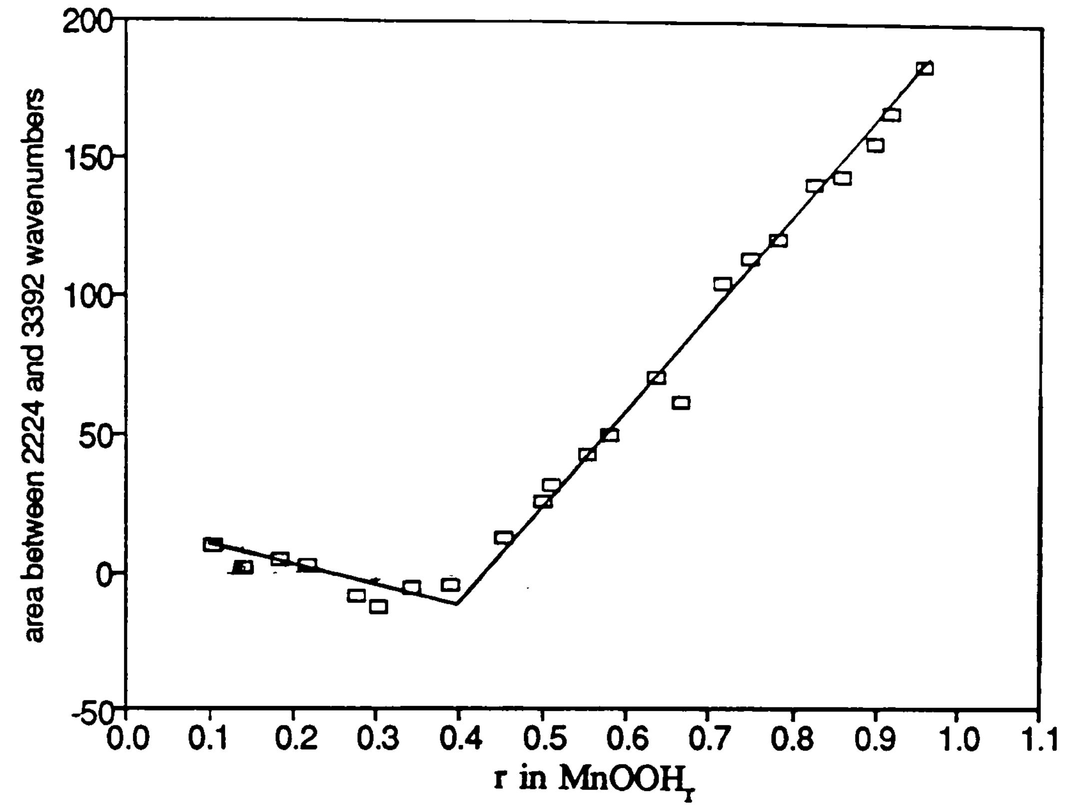

Figure 7-4 Change in integrated area of FTIR spectra minus background area, as defined by the ar1 boundaries shown in figure 5-13, with H insertion into WSZ.

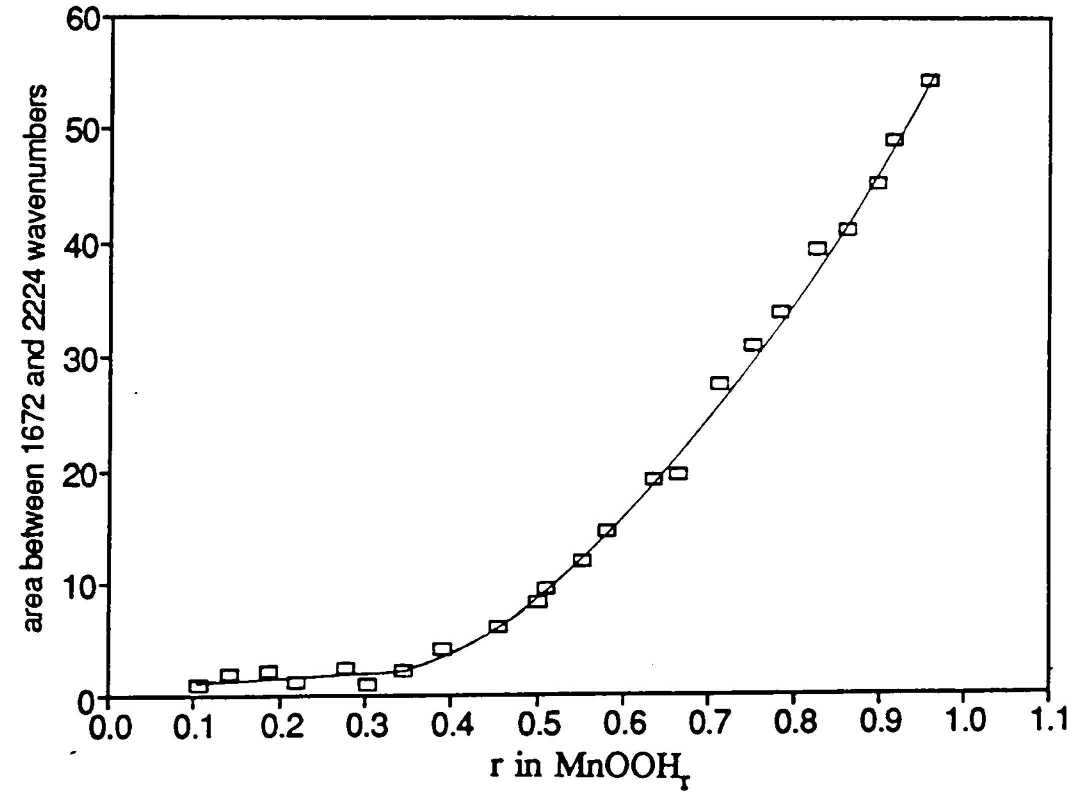

Figure 7-5 Change in integrated area of FTIR spectra minus background area, as defined by the ar2 boundaries shown in figure 5-13, with H insertion into WSZ.

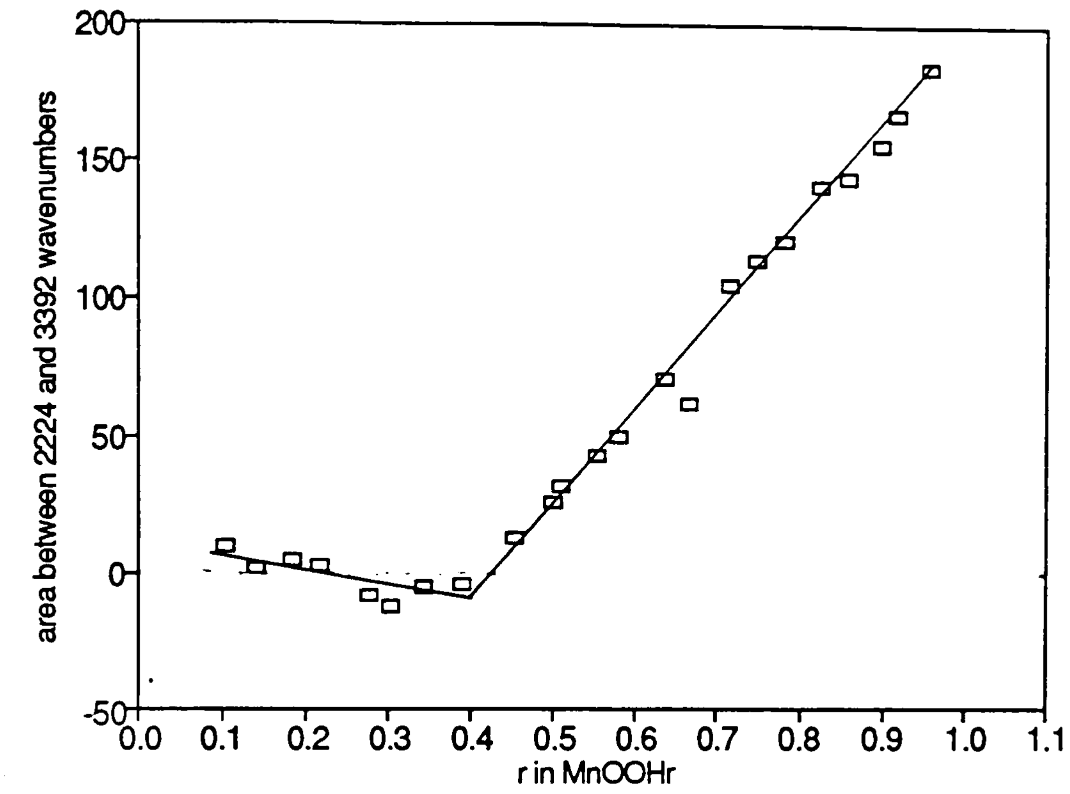

Figure 7-6 Change in integrated area of FTIR spectra minus background area, as defined by the ar4 boundaries shown in figure 5-13, with H insertion into WSZ.

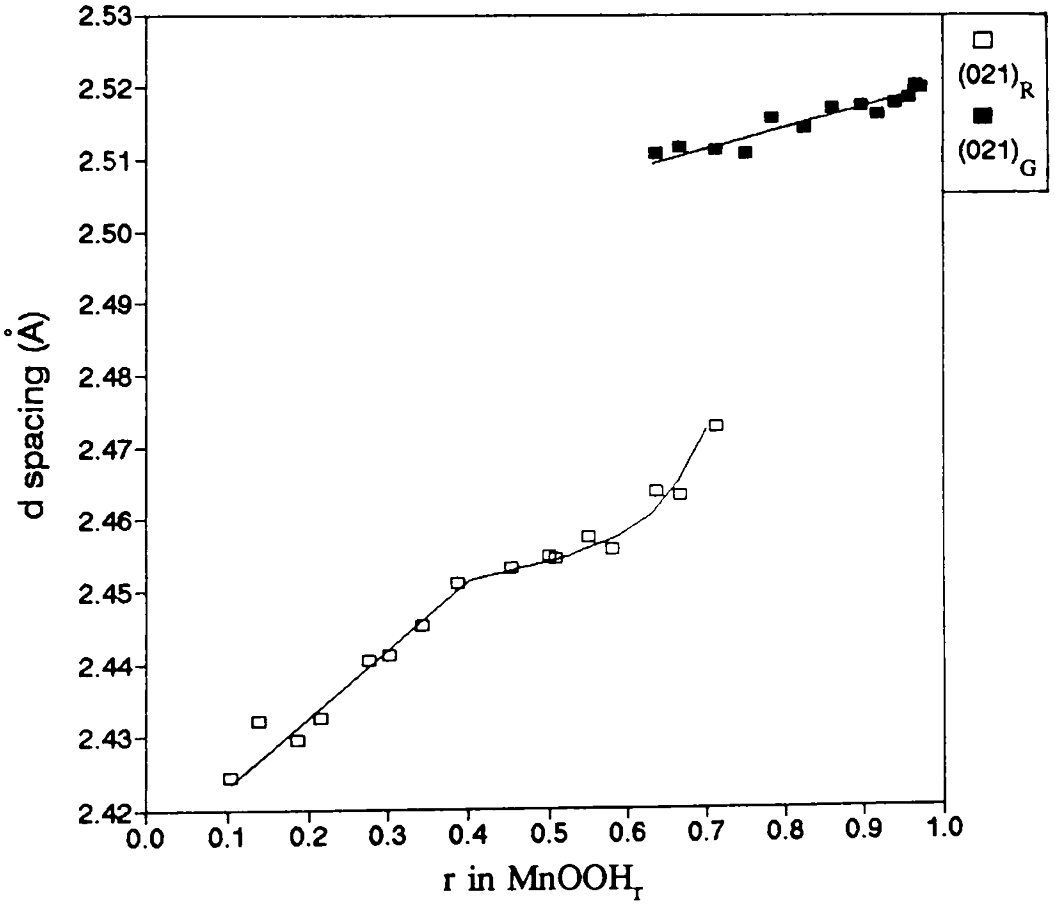

Figure 7-7 d or interplanar spacing variation of peak (021) with H insertion level for WSZ.

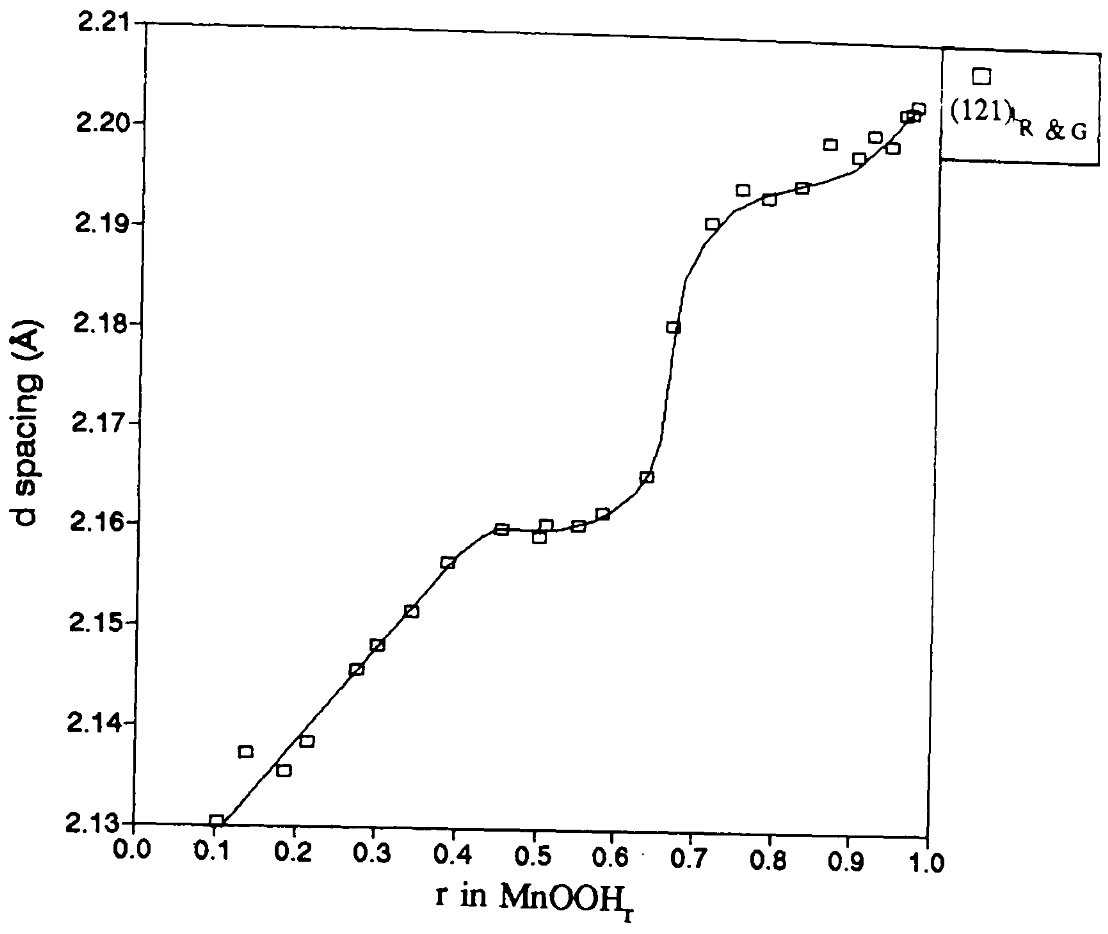

Figure 7-8 d or interplanar spacing variation of peak (121) with H insertion level for WSZ.

reduction in this case becomes heterogeneous at r=0.64 which corresponds to the r in MnOOH$_r$ value at which $(021)_G$ was first detected, see figure 7-7. The corresponding SBPA peak (figure 5-6), because of the greater separation between $d_{(121)R}$ and $d_{(121)G}$ and the relatively short r in MnOOH$_r$ region in which the transition from the first freezing of H occurs and heterogenous reduction, does not show this behaviour.

### 7.1.1 Variation of lattice parameters with H insertion.

It is clear from the previous section that any attempt to derive lattice parameters for the whole H insertion range from the diffraction patterns of WSZ would lead to erroneous results. This is because the reduction is heterogeneous beyond a certain H insertion level and though the two products co-exist in the same crystal each possess different lattice parameters. Within the homogeneous range (i.e. r=0.104 to r=0.40) it is possible to derive the orthorhombic lattice parameters. This was achieved as in previous lattice parameter determinations by using the 'sharp lines' in the pattern. In this instance not so many sharp lines are present because the first effects of micro-twinning (and/or particle size broadening) may be observed. Thus the 'sharp lines' are not so

Table 7.1 Measured lattice parameter variation in WSZ at H insertion levels marking the boundaries of homogeneous and heterogeneous reduction.

| | r in MnOOH$_r$ | $a_o$ (Å) | $b_o$ (Å) | $c_o$ (Å) |
|---|---|---|---|---|
| | 0.104 | 4.458 | 9.27 | 2.846 |
| %change from those at r=0.104 | 0.388 | 1.7% | 2.6% | 0.7% |
| %change from those at r=0.104 | 0.927 | 1.6% | 13.8% | 1.0% |

sharp compared to for instance material SBPA (see figures 2-5 and 2-12) and consequently overlap with neighbouring peaks. For instance the doublet (221)&(240) in figure 5-2 appears as a single peak in figure 7-1. Since (240) is relatively less intense this single peak may be considered as (221) for the purposes of determining its position since the tip of the peak is measured. Lattice parameters determined only from (021), (121), (221) and (002) are presented in figure 7-9. The other two peaks that could have been used, namely (200) and (061), were considered too broad for this purpose especially once reduction proceeds (see figure 7-1). Anisotropic expansion is observed with not unexpectedly the $\mathbf{b_0}$ direction responsible for most of the change. The complete variation in lattice parameters is summarised in table 7.1, which indicates that $b_0$ expands relatively by twice the amount of $a_0$ and six times that of $c_0$ during homogeneous reduction to r=0.40. Beyond this H insertion level 'freezing' of H begins. Solid solution only no longer exists since H begins to locate in the structure at definite sites. Once heterogeneous reduction starts, reduction proceeds presumably by this structure propagating in the crystal from the surface of a particle. The lattice parameters of this material were determined form the most H inserted product by a similar procedure as that for H inserted SBPA (section 4.1). Due to the possibility of overlapping peaks, as explained earlier, the lattice parameters must only be determined form the most H inserted material. The compound in which H locates differs essentially only in the $b_0$ dimension from that of the last solid solution member at r=0.388 as

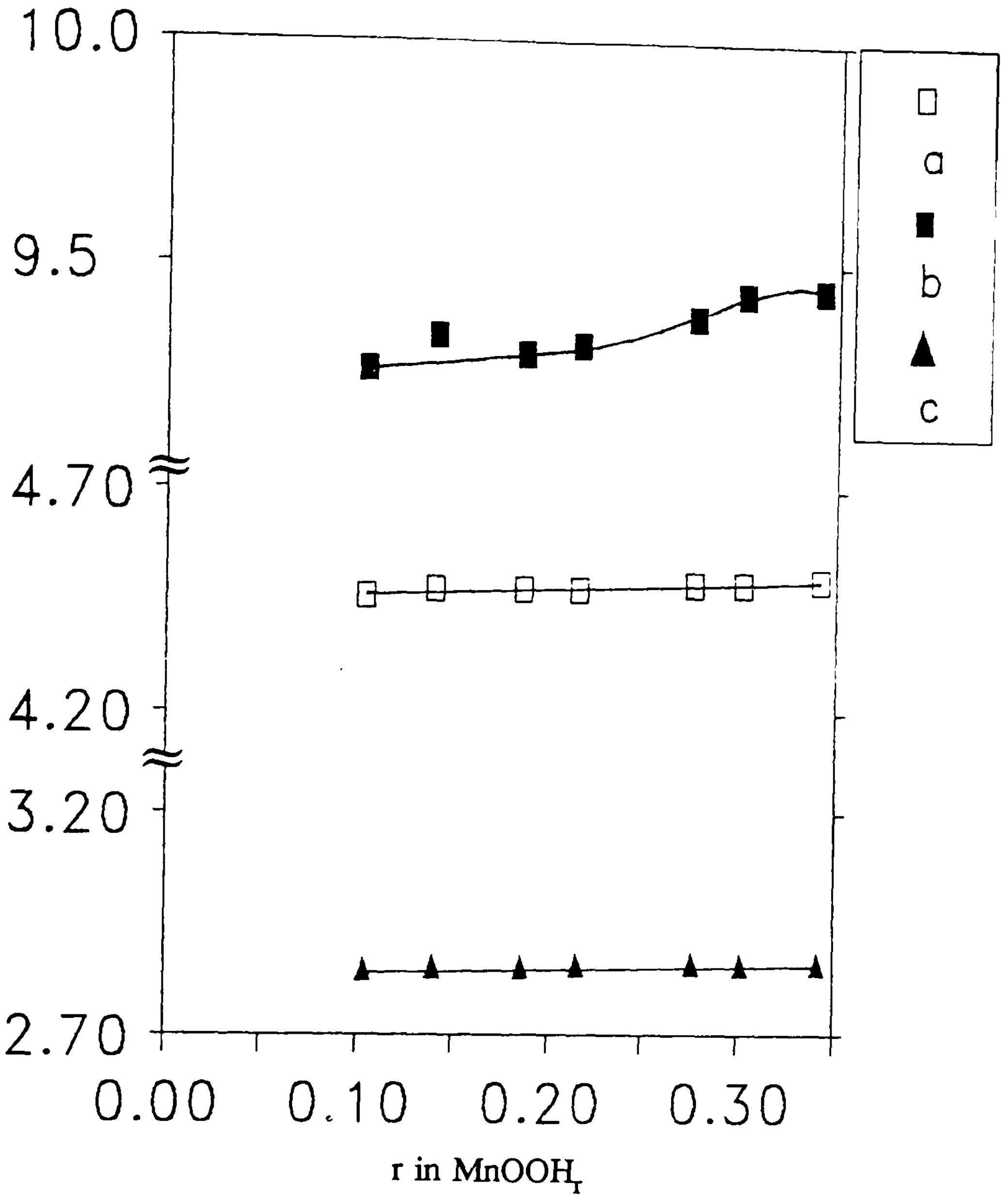

Figure 7-9 $a_0$, $b_0$, $c_0$ lattice parameter variation of WSZ in solid solution H insertion range ($0.104<r<0.40$). Beyond this level lattice parameters cannot be derived (see sect.7.1.1).

indicated in table 7.1. Table 7.1 also shows that the overall percentage lattice expansion of the most H inserted compound compared to the initial material is similar to that of SBPA, see table 4.4, and therefore also similar to that of the hypothetical transition ramsdellite to groutite (cf. section 4.1).

With the same procedure as explained in section 4.1 the 'm' fraction of the most H inserted WSZ material was determined. $m=0.19\pm0.01$ in this instance which is similarly less than the initial p fraction, $p=0.24\pm0.01$, as was noted for SBPA. Similar comments apply (see section 4.1).

Finally to conclude this section evidence is provided which shows that the occurrence of the 'extra' peaks which arise during H insertion are not correlated with the appearance of the 100% manganite line at 26.1°2θ. This is so since it is possible to produce an H inserted compound showing all the new lines except that of the 'manganite line'. Figure 7-10 graphically indicates this. The H inserted material with no manganite line and a composition $MnOOH_{0.956}$, was produced by the same method except that the temperature was kept at ≈2(°C) (by means of an ice bath) throughout the final stages of reduction[†].

Subtracting the area of the x-ray diffraction peak at 26.1°2θ of the low temperature reduced material from one produced at higher temperatures (with the composition $MnOOH_{0.958}$) it is possible to obtain an estimate of the manganite content by comparing this area with a similar area from a sample of pure manganite. A simpler procedure would be to carefully choose the peak boundaries at each side of the manganite peak as close as possible to the beginning of the peak and then obtaining the net area by subtracting the background area obtained by joining the peak boundaries by a straight line. Figure 7-10 indicated such an approximation is valid since the low temperature H inserted pattern has a high background (compared to the other side of the *(110)* peak) in this °2θ region which could easily be approximated by a straight line. The relatively high background on the high angular side of the *(110)* peak is not indicative of residual manganite since patterns at much lower H insertion levels also display this effect (see figure 7-1). The pure manganite sample was obtained by refluxing reduced EMD in water (see section 3.2.1). Taking care to correct the x-ray diffraction intensities for the output of the x-ray tube by measuring a certain line from an external standard sample of quartz (Arkansas stone) one obtains 8.8% of manganite by direct proportion[‡]. The true r in $MnOOH_r$ is obtained by noting that

$$8.8\% \times r_m + (100\% - 8.8\%)r_{wsz} = 0.958$$

assuming that manganite is stoichiometric i.e. $r_m=1.0$, then

$$\Rightarrow r_{wsz} = \underline{0.954}$$

This small error ($\Delta r=0.004$) introduced by a such correction was neglected in previous graphs indicating r as the reduction level of reduced WSZ.

It is interesting to note that the m=0.22±0.01 for the low temperature H inserted WSZ which is within experimental accuracy of the measurement the same as the starting

---

[†] I am grateful to J.Larcin for both suggesting this and actually achieving it.

[‡] This assumes that the absorbtion coefficient of the mixture is the same as the individual components which is true in this case since their elemental constitution is the same.

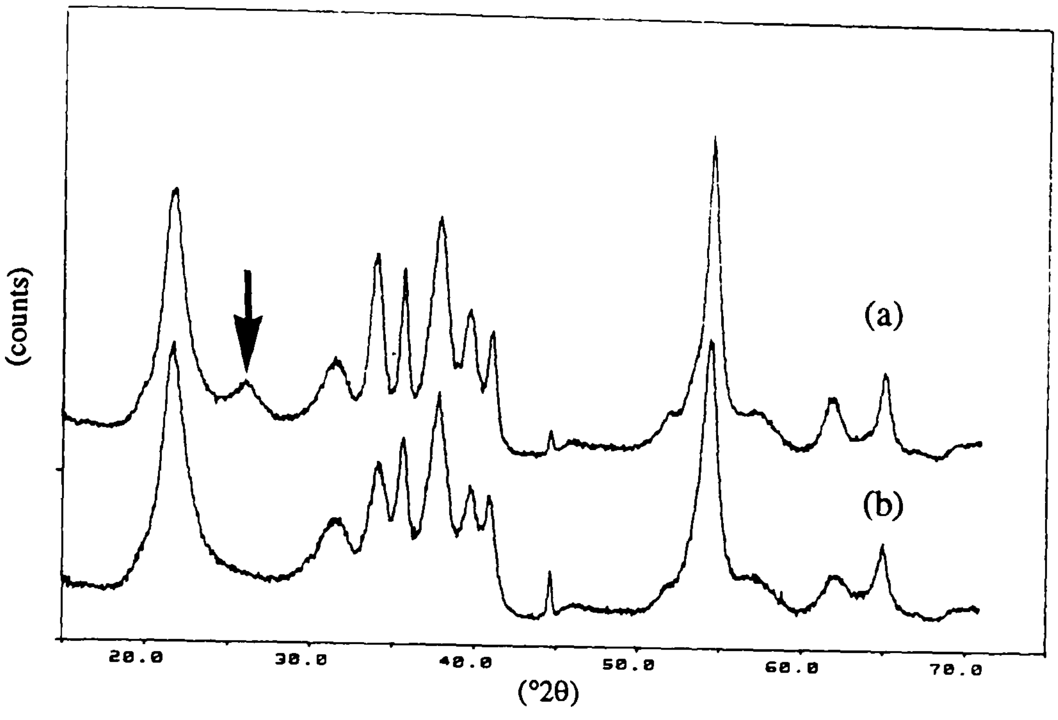

Figure 7-10 X-ray diffraction comparison of 'non-aqueous' hydrazine reduced WSZ. (a) ambient temperature, $MnOOH_{0.948}$ (b) Low temp. (≈2°C), $MnOOH_{0.956}$. (a) shows clear manganite formation, indicated by arrow.

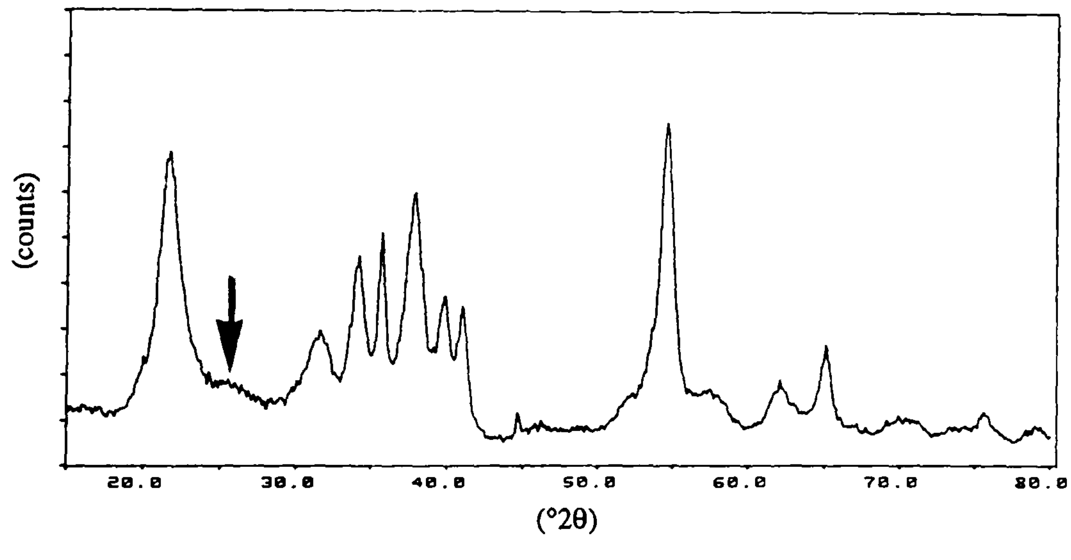

Figure 7-11 X-ray diffraction pattern of low temperature 'non-aqueous' hydrazine reduced WSZ after 1 years storage in air at ambient temperature. Arrow indicates evidence of manganite formation. (compare with figure 7-10 (b)).

material, p=0.24±0.01. This strongly suggests that the manganite precipitated in the normal preparation of an H inserted material was nucleated on manganite type layers at the surface of the crystal and were thus preferentially transformed to manganite with a consequent lowering of m compared to the initial p value. This suggestion is equivalent to that given by Giovanoli (see section 7.5) which, however, was suggested to be the principal reaction in the reduction of $\gamma_t$-$MnO_2$ rather than an unwanted subsidiary reaction.

Finally the instability of δ-MnOOH with respect to γ-MnOOH is confirmed by another observation. Figure 7-11 presents the x-ray diffraction pattern of the same material as in figure 7-10(b) but after one years storage in air at ambient temperature. A slight bump in the vicinity of 26.1°2θ is clearly evident indicating that a slow transformation to γ-MnOOH is underway.

## 7.2 IBA no.14.

The following discussion for the remaining materials will not present clear evidence for a homogeneous or heterogenous H insertion reaction beyond a certain r in $MnOOH_r$ but rather, it shall be argued, support the conclusion that H freezes in the structure in the form of δ-MnOOH micro-domains.

In this section H insertion into IBA no.14 is considered. This material is intermediate between those of the 'high' and 'low structured' manganese dioxides forming the $\gamma_t$-γ-$MnO_2$ series. The diffraction pattern shows effects expected from the presence of micro-twinning. In particular, peaks which are well separated in material SBPA (see figure 5-2) now are combined in broader maxima. This is true for example for peak D (see figure 7-12) which from figure 2-12 is a combination of (021)&(111). The peak labelled A is also clearly separated into two contributions, namely (002)&(061) (see again figure 2-12). This material contains a sufficiently high micro-twinning fraction that it cannot be analyzed successfully for the prevailing orthorhombic lattice parameters and neither therefore for the p fraction.

The changes in x-ray diffraction pattern which occur with H insertion are summarised in figure 7-12. The final product looks similar in its x-ray diffraction pattern

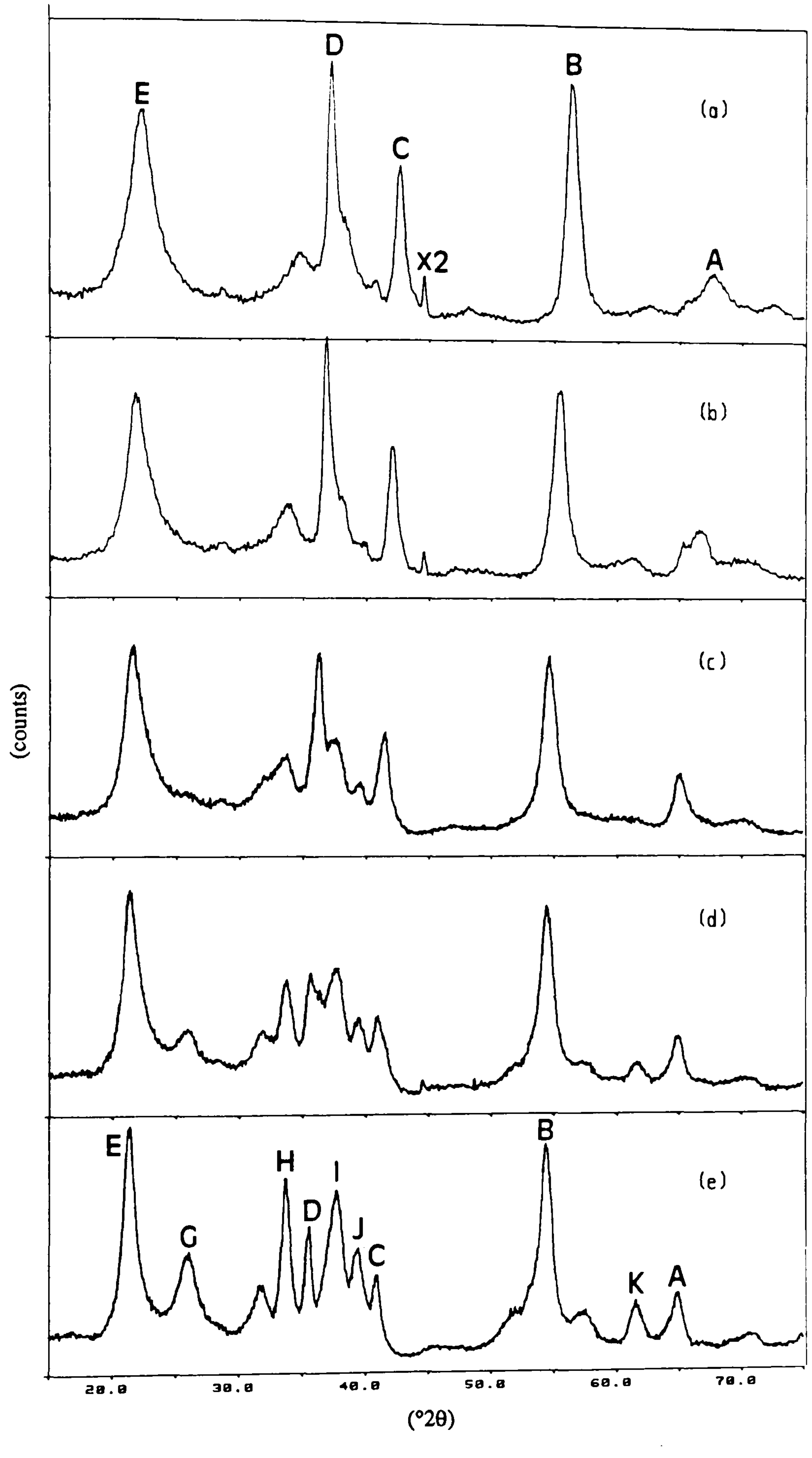

Figure 7-12 Selection of x-ray diffraction patterns representing the changes which occurred with H insertion into material IBA no.14. (a) $MnOOH_{0.084}$ (b) $MnOOH_{0.396}$ (c) $MnOOH_{0.686}$ (d) $MnOOH_{0.826}$ (e) $MnOOH_{0.990}$.

to that of the most H inserted product of SBPA except that the peaks are broader and do not occur quite at the same °2θ positions. As previous evidence has indicated that the most H inserted product of SBPA and WSZ retain the same selective shifts and broadened peaks as that of the parent structure it is stated by analogy that this holds for the other members of the $\gamma$-$\gamma_t$-$MnO_2$ series such as IBA no.14 (cf. section 4.2). In this case the most obvious exception to this general statement is the appearance of an enhanced 'manganite peak' at 26.1°2θ (peak G). Whether its size is sufficient to affect significantly the stoichiometry of the remaining reduced material is now considered.

With the peak and background boundaries given in table 7.2 the integrated area was determined for this peak for all IBA no.14 H inserted samples. At low H insertion levels this procedure produced negative peak areas due to the approximation of the background as the area under a straight line between the peak boundaries. Since this region does not contain manganite the areas obtained in the non-manganite region were shifted by a constant so that their distribution was about zero. The areas in the manganite precipitation region were similarly shifted. Figure 7-13 expresses the results of this procedure as the percentage of manganite, obtained from the measured area as in section 4.1. The maximum percentage of manganite at r=1.0 (~20%) is approximately twice that obtained by a similar procedure (~9%) for H insertion into WSZ (see section 7.1). The effect on the stoichiometry, as expressed in the form r in $MnOOH_r$, considered in the manganite precipitation region, which from figure 7-13 is from r=0.55 to r=1.00, is presented in figure 7-14. An approximately linear increase in the percentage of manganite produces a curve with a maximum correction since the addition of the same mass of manganite of composition MnOOH makes an increasingly small difference to the overall stoichiometry as the overall stoichiometry itself reaches MnOOH. The corrected rc in $MnOOH_{rc}$ does not alter significantly the behaviour of the d versus stoichiometry graphs discussed later.

Table 7.2 Peak and background boundaries used to determine the integrated area of the manganite peak in IBA no.14 reduced samples.

| Low background (°2θ) | Peak (°2θ) | High background (°2θ) |
|---|---|---|
| 24.12-24.17 | 24.17-27.69 | 27.69-27.74 |

Manganite precipitation not only affects the stoichiometry but the x-ray

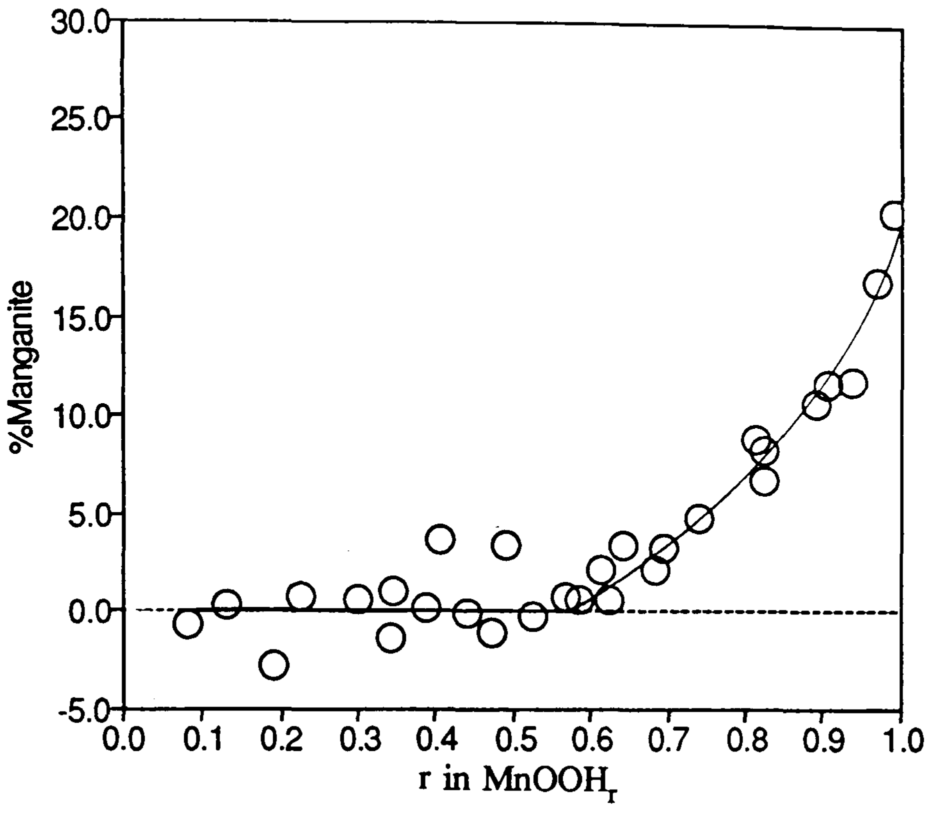

Figure 7-13 Percentage of manganite in H inserted IBA no.14 samples.

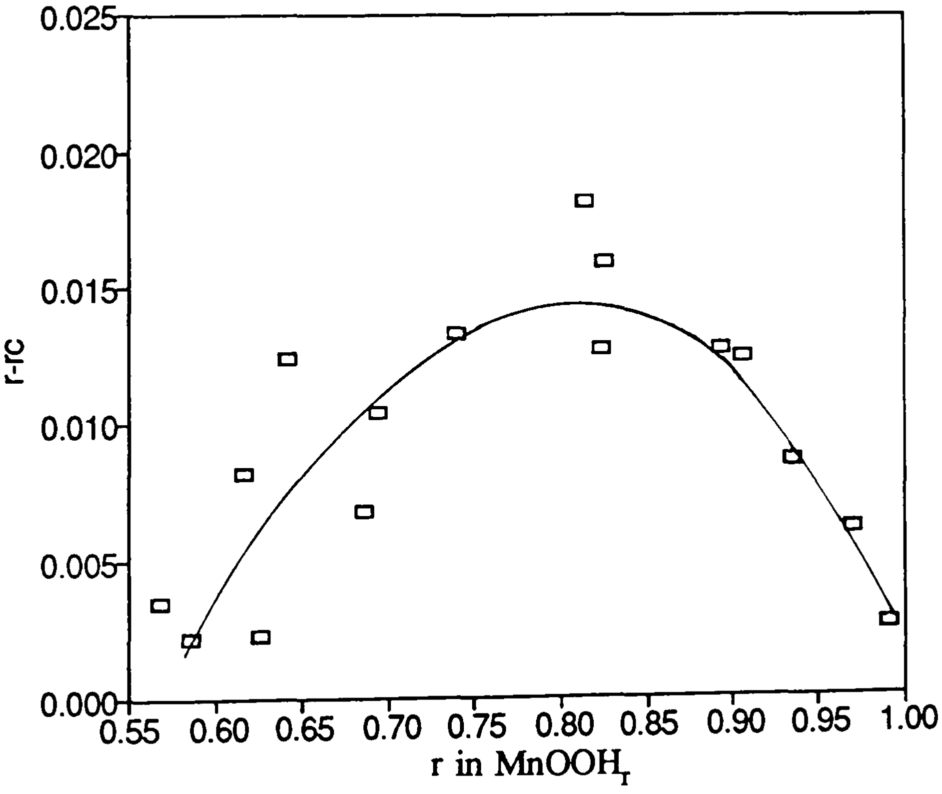

Figure 7-14 r-rc, where rc is the corrected r in MnOOH$_r$ for the amount of manganite, versus the original overall reduction level for H insertion into IBA no.14.

diffraction peaks of the H inserted compounds and their apparent position since it happens to have lines (apart from the 100% peak at 26.1°2θ) which coincide with the peaks which emerge due to non-aqueous solid state H insertion as established by figure 4-5. Before one could asses the affect of manganite precipitation the way in which the material reduced must have been established (in particular whether the reduction was heterogeneous or homogeneous). In this case the evidence does not clearly indicate which process was operating.

Figure 7-12 has been produced with 7-12(c) indicating the pattern at which it is judged new peaks just begin to appear. Concentrating on the 2θ region 28-44(°2θ) the diffraction patterns for all H inserted materials with $r \geq 0.686$ are plotted on top of each other as presented in figure 7-15. For comparison if one synthesizes, as described in section 6.2, a heterogeneous reduction with the end members $rc=0.686$ and $rc=0.990$, figure 7-16 is produced. Whereas figure 7-16 displays clear isobestic points in particular at 35.7 (°2θ) and 36.9 (°2θ) the one at 35.7(°2θ) is not clearly isobestic in figure 7-15. On the other hand comparison of this figure with that of figure 6-8 indicates that they do not shift as expected if random precipitation of $\delta$-MnOOH micro-domains within the solid solution form since remnants of a non-moving peak are observed in the patterns particularly for peak D. The other peaks which emerge also apparently show small peak shifts at odds again with figure 6-8. Although it is not clear which H insertion process is operating beyond $rc \sim 0.70$ an interesting conclusion is obtained by performing an analysis of the ratios for the d spacings of peaks involving peak A.

Firstly it is noted that peak A is split into the components *(061)*&*(002)*. *(002)* occurs only as the small bump at the low angle side, see figure 7-12. Its position is therefore very difficult to determine accurately but because of its importance in determining the way in which the prevailing orthorhombic lattice behaves on H insertion even a relatively imprecise (compared to for example peak D) measure yields useful information.

Figures 7-17, 7-18, 7-19 indicate the peak ratios obtained with H insertion when regarding peak A as either *(002)* or *(061)*. At least two distinct H insertion regions are apparent, $0.084 \leq r \leq 0.55$ and $0.55 \leq r \leq 0.990$. In either case the ratios are not constant and the lattice expansion must be anisotropic in both regions.Beyond $r=0.526$ *(061)* could not be measured as it apparently merges with (002). However at $rc=0.55$ it must be the case that peak A is dominated by *(002)* rather than *(061)* since the direction of the

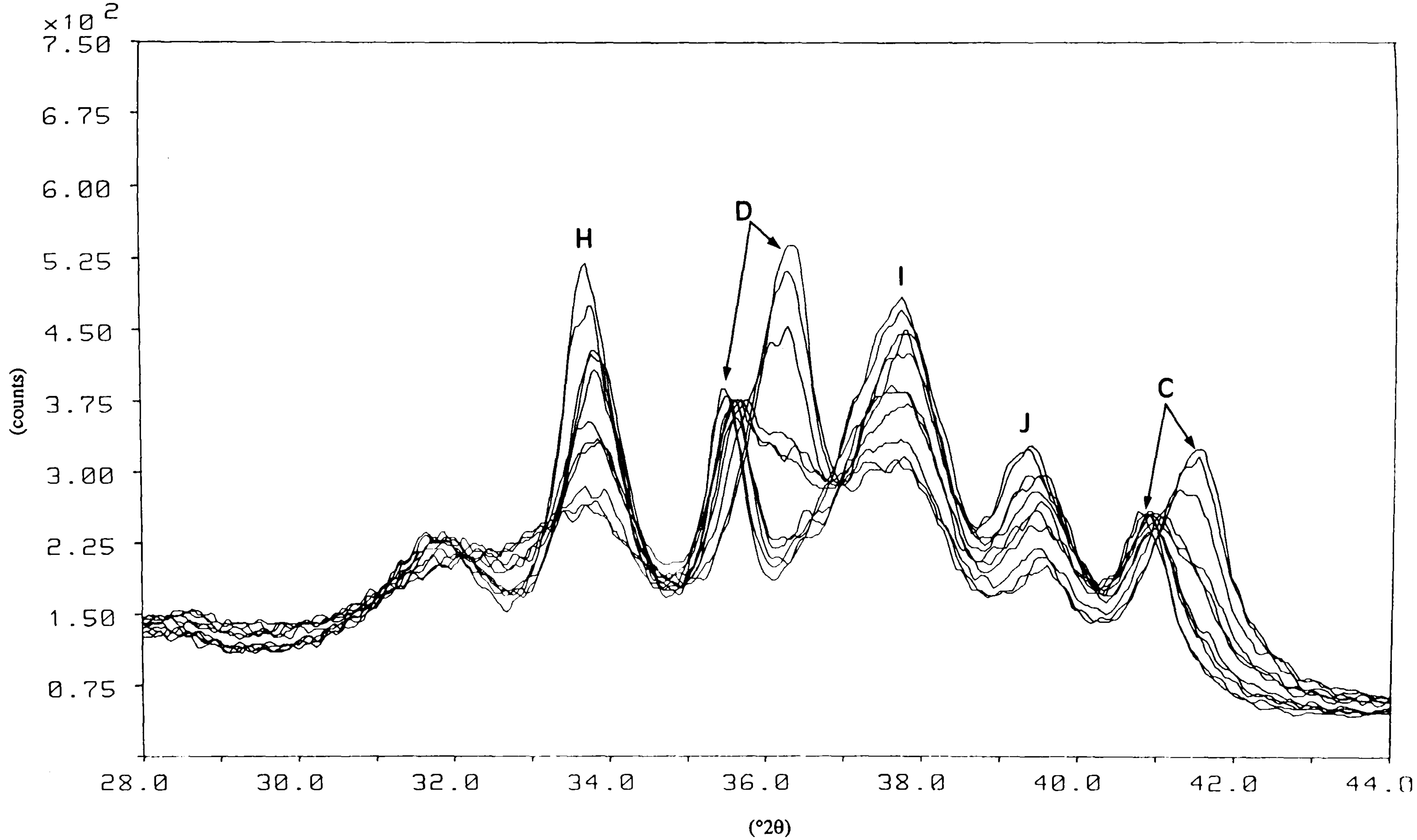

Figure 7-15 Actual x-ray diffraction patterns of material IBA no.14 in the composition range $MnOOH_{0.686}$ to $MnOOH_{0.990}$.

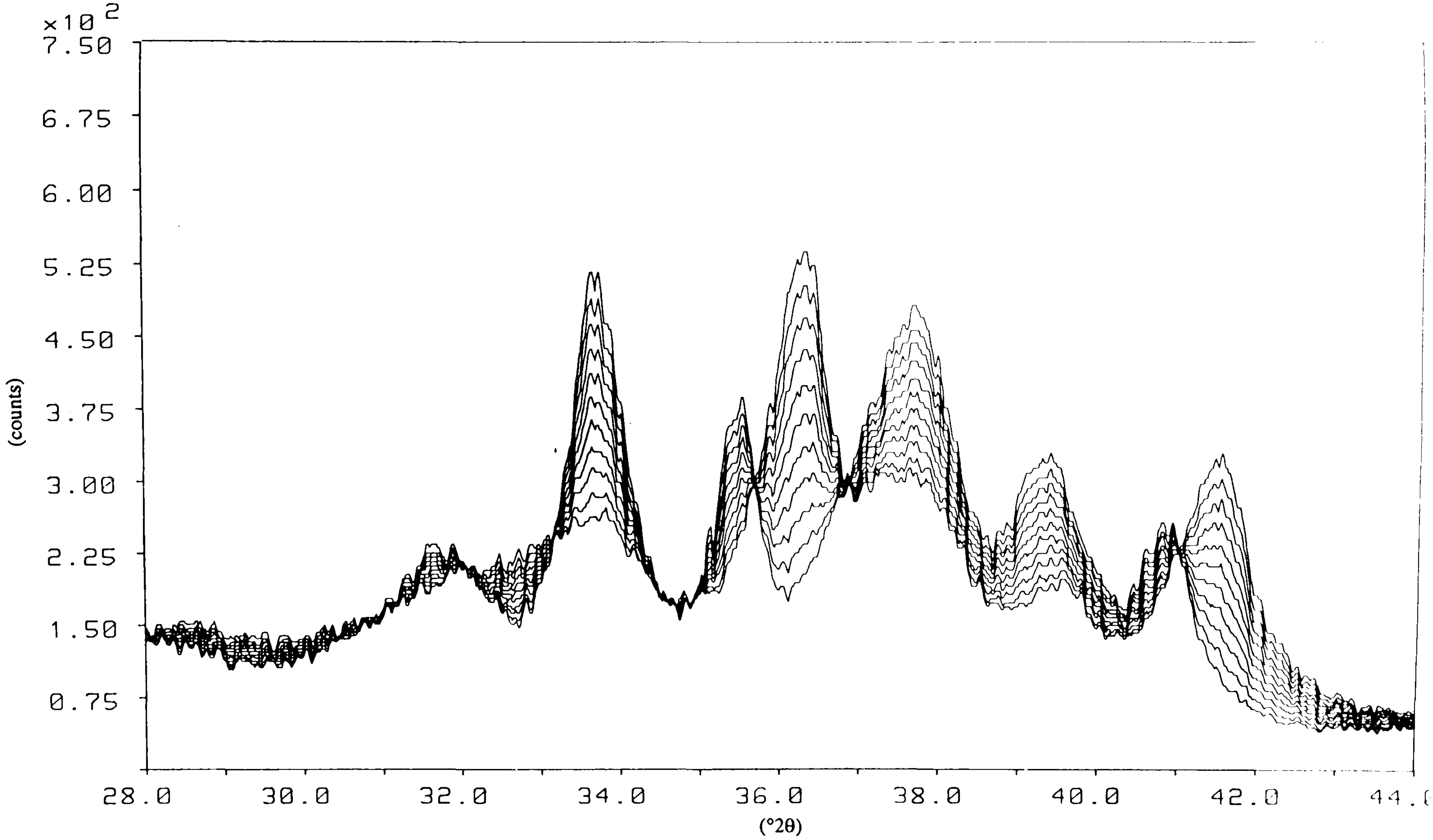

Figure 7-16 Simulated x-ray diffraction of heterogeneous reduction of material IBA no.14 from mixtures of samples with compositions $MnOOH_{0.686}$ and $MnOOH_{0.990}$.

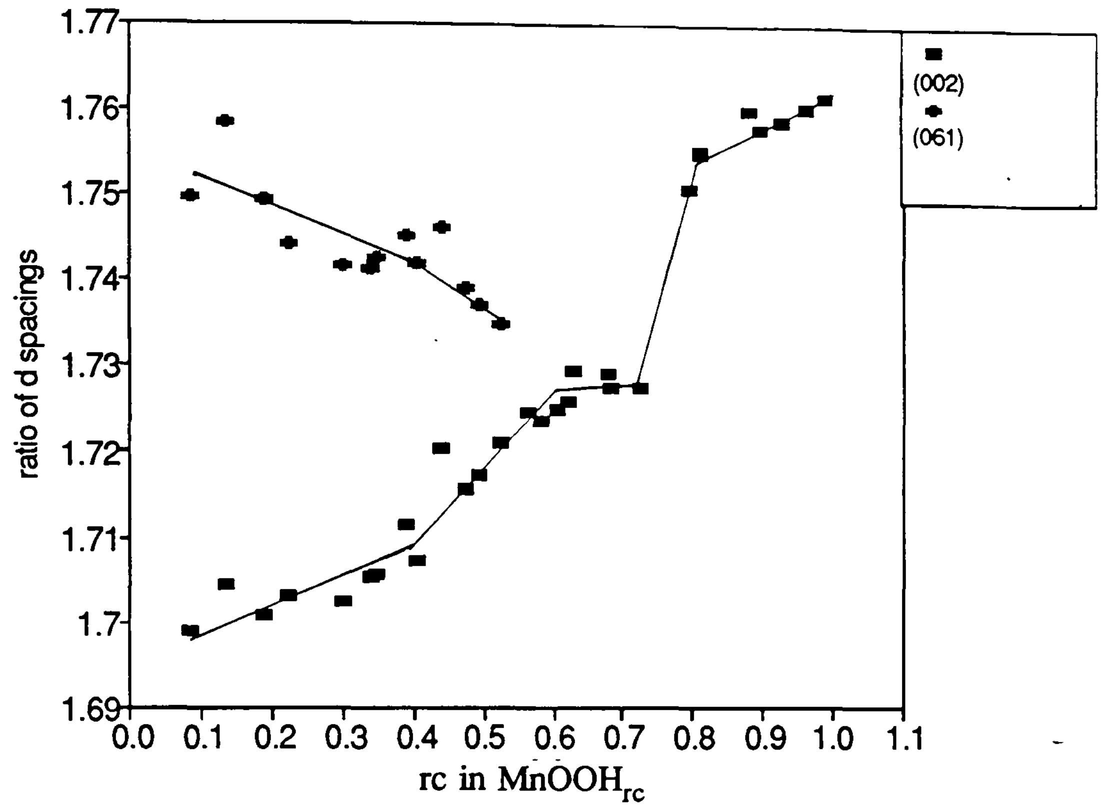

Figure 7-17 d spacing ratio for peaks D/A when regarding A as either (*002*) or (*061*) for H insertion into IBA no.14.

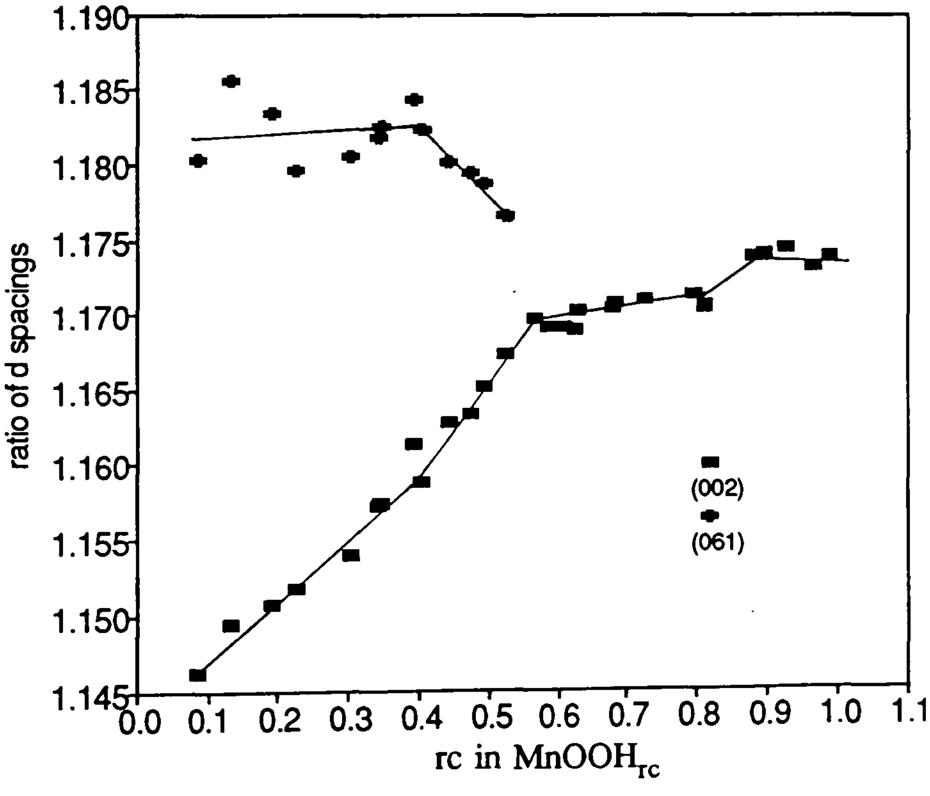

Figure 7-18 d spacing ratio for peaks B/A when regarding A as either (*002*) or (*061*) for H insertion into IBA no.14.

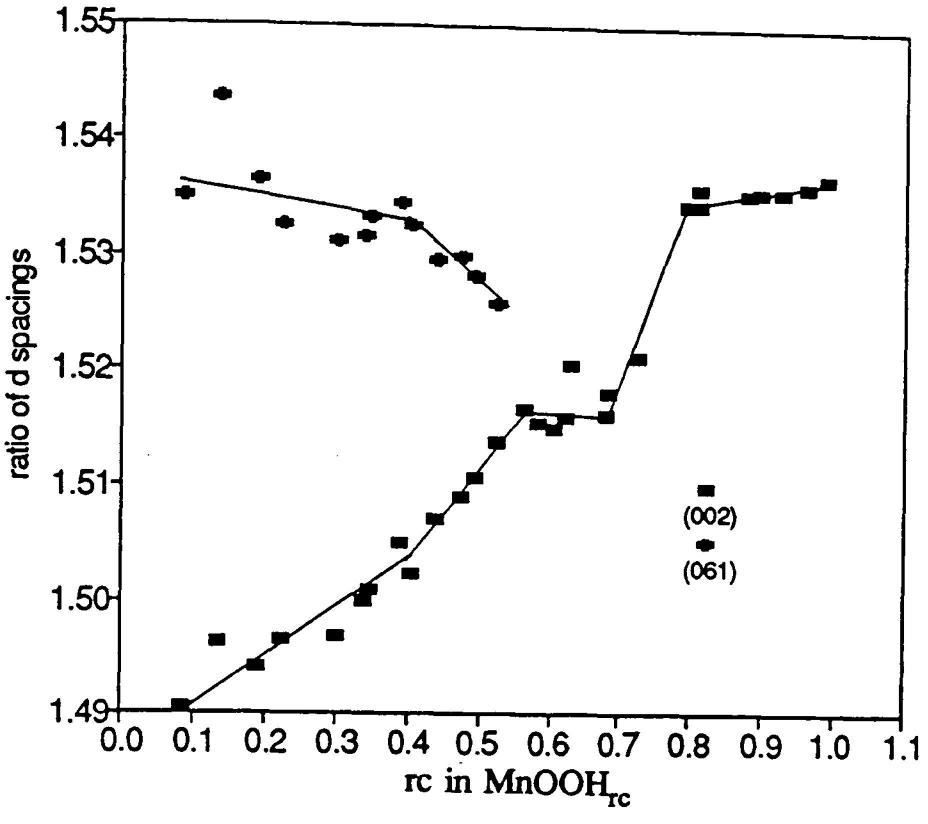

Figure 7-19 d spacing ratio for peaks C/A when regarding A as either (*002*) or (*061*) for H insertion into IBA no.14.

observed change in slopes beyond rc=0.55 in the peak ratios is similar to that of R2 (see section 6.4).

The FTIR peak areas ar1, ar2 and ar4 are presented in figures 7-20, 7-21 and 7-22. As expected location of protons and electrons in the structure gives rise to a distinct break in the peak area against r the lowest break of which occurs at rc=0.45 (figure 7-22). As may be seen from figures 7-17, 7-18, 7-19 smooth change in the d spacing ratios are not observed beyond rc=0.55. This suggests that precipitation of micro-domains occurred as H located but not randomly as described for material R2 and not in a way which led to heterogeneous reduction.

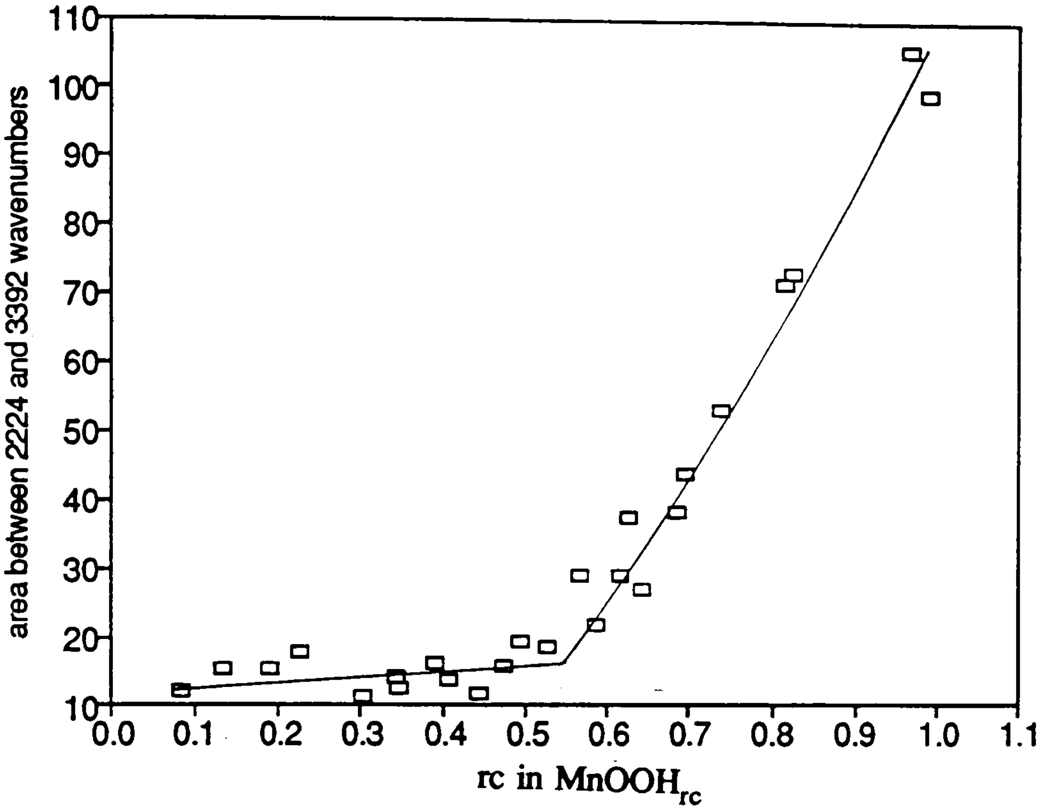

Figure 7-20 Change in integrated area of FTIR spectra minus background area, as defined by the ar1 boundaries shown in figure 5-13, with H insertion into IBA no.14.

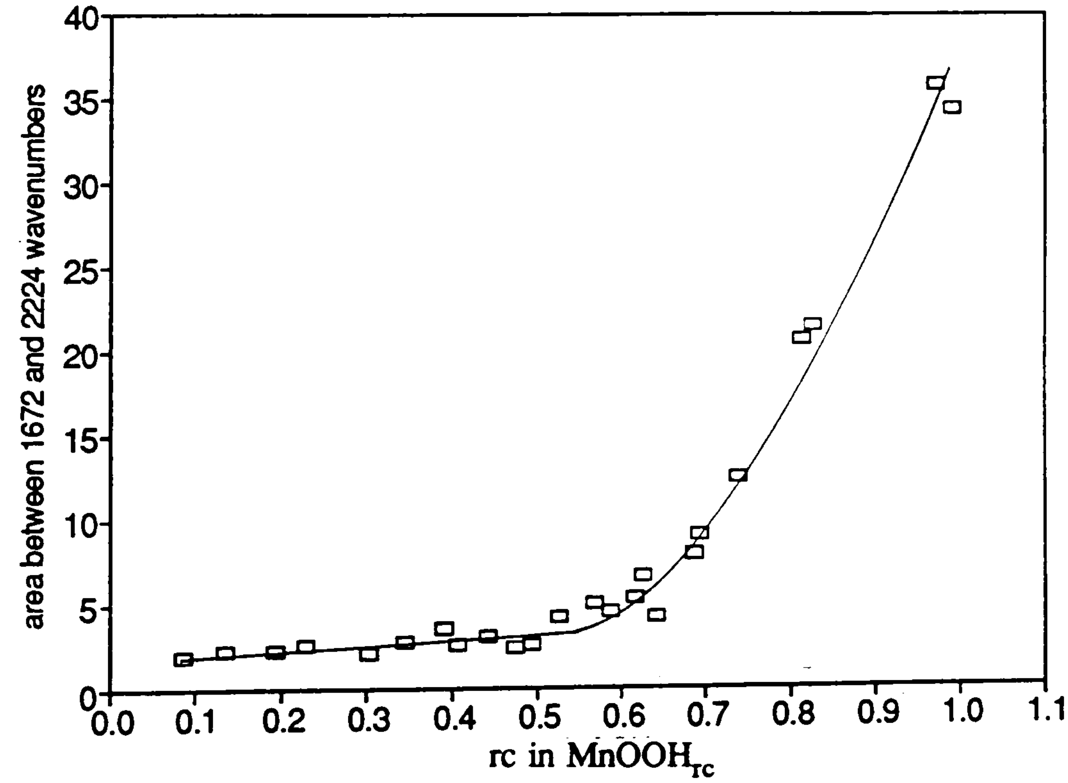

Figure 7-21 Change in integrated area of FTIR spectra minus background area, as defined by the ar2 boundaries shown in figure 5-13, with H insertion into IBA no.14.

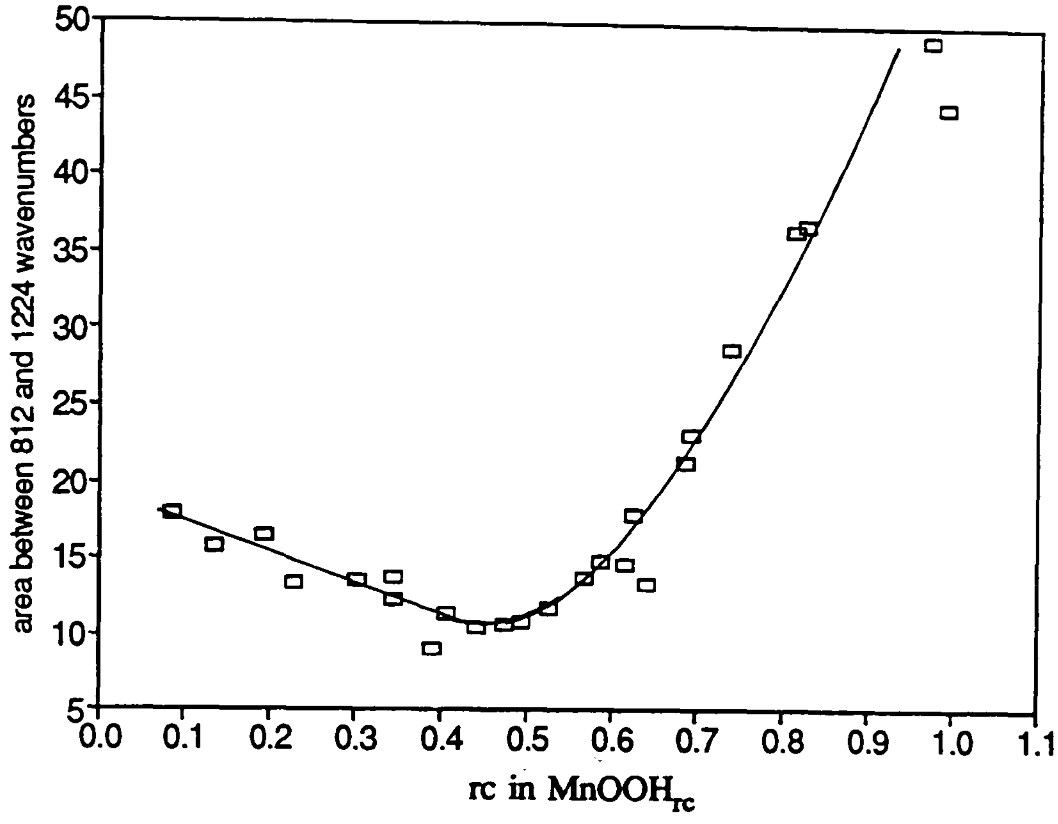

Figure 7-22 Change in integrated area of FTIR spectra minus background area, as defined by the ar4 boundaries shown in figure 5-13, with H insertion into IBA no.14.

Table 7.3 Estimated orthorhombic lattice parameter variation for H insertion into IBA no.14.

|  | r in MnOOH$_r$ | $a_o$ (Å) | $b_o$ (Å) | $c_o$ (Å) |
|---|---|---|---|---|
| overall % from value at r=0.084 | 0.990 | 2.0% | 16.5% | 0.84% |

The overall expansion of an orthorhombic lattice, with the dimensions of those determined from material SBPA, needed to produce the best match to the d spacing ratios at r=1.0, are summarised in table 7.3. This was achieved by a similar procedure as described in section 6.4. The results indicate similar overall expansions to those determined for the other materials when H was inserted.

### 7.2.1 Conclusion.

The previous section has demonstrated that H may be inserted into material IBA no.14 to a H insertion level rc≈0.45 beyond which H starts to locate in position. In the solid solution region the unit cell dilates anisotropically. In this case H location does not clearly lead to either heterogeneous reduction or random internal precipitation of δ-MnOOH micro-domains. It is probable that the δ-MnOOH micro-domains have a clearer tendency to associate such that the reaction becomes almost heterogenous beyond rc≈0.70. This suggests that a non-random de Wolff layer model applies, as described in section 4.4.3, since such a model starts to show the effects expected for a heterogenous process as demonstrated by a comparison of figure 4-20 and figure 5-1, which is of the effect of H insertion into material SBPA (which has shown to be clearly heterogeneous beyond r=0.40, see chapter 5). Thus, for instance, peak $(021)_R$ in figure 5-1 clearly starts to fade beyond a certain H insertion level and re-appears as $(021)_G$. This behaviour has a clear analogue in figure 4-20, though in this case, peak $(021)_R$ does not completely fade but rather goes through a minimum in intensity.

## 7.3 IBA no.19.

A relatively brief account is given of the observed effects on the diffraction and FTIR patterns due to H insertion. The reason is that the behaviour is similar to that discussed for EMD R2 (section 6.4). This is not surprising as the x-ray diffractograms of the starting materials are almost identical, except for the graphite impurity (from the deposition process) in R2 which produces a small peak at 26.1°2θ absent in IBA no.19. Recent work[113] at this Institute has shown that an EMD, again almost identical in x-ray diffraction pattern to R2, may be reduced heterogeneously (heterogeneous reduction setting in at a remarkably low H insertion level ($MnOOH_{0.3}$)) by the 'non-aqueous' hydrazine H insertion method (cf. section 3.2.3) if the reaction is carried out at a sufficiently high reaction rate. It is noted that the final reduced product has the same x-ray diffraction pattern regardless of whether H insertion led to a heterogeneous or homogeneous process. Thus it is not necessarily the case that H insertion by the boiling propanol method (see section 3.2) and room temperature reduction with cinnamyl alcohol (as used in the reduction of material R2) lead to the same x-ray diffraction pattern behaviour even if the starting materials are identical. The main differences are highlighted in the following paragraphs for IBA no.19 with respect to R2. These differences are in all cases attributable to differences in the method of chemical H insertion.

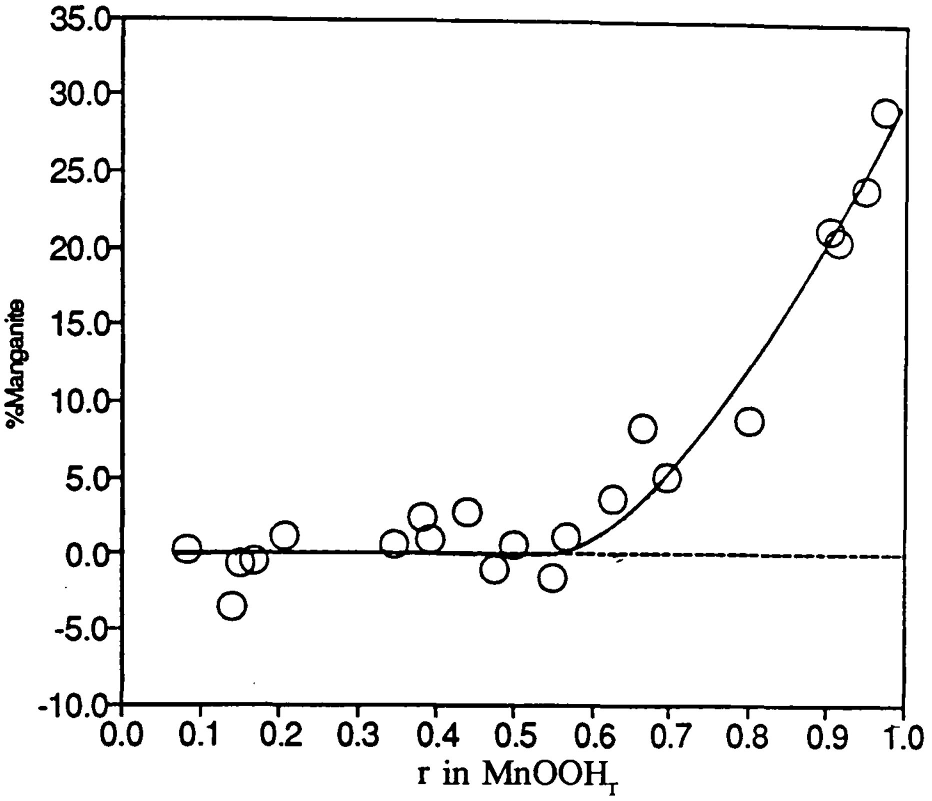

Figure 7-23 Percentage of manganite in H inserted IBA no.19 samples.

H insertion by the propanol method, leads to, as may be seen from figure 4-7, an enhanced manganite contribution which starts to precipitate at about r=0.55. Figure 7-23, which is similar to figure 7-13 (IBA no.14), and shows that manganite begins to precipitate at almost the same overall r in MnOOH$_r$ level but for IBA no.19 the percentage of manganite is larger from that level on. This may be because IBA no.19 has a greater surface area than IBA no.14 (see table 8.2).

As was demonstrated in the previous section the magnitude of the systematic error introduced by the precipitation of manganite on the r in MnOOH$_r$ of the remaining solid solution is not large enough to alter significantly plots of d versus r or ratios of d spacings versus r. More significant but more difficult to assess is the effect on the x-ray diffraction peaks coincident or nearly so with manganite peaks. This has already been mentioned in connection with H insertion into IBA no.14 (section 7.2), similar comments apply. This error together with a tendency for the δ-MnOOH micro-domains to associate may account for the relatively unclear changes in slope compared to those obtained for R2 for d spacing ratios formed from the peaks labelled A, B, C, D, figures 7-24, 7-25, 7-26, 7-27, 7-28 and 7-29. This tendency for the δ-MnOOH micro-domains

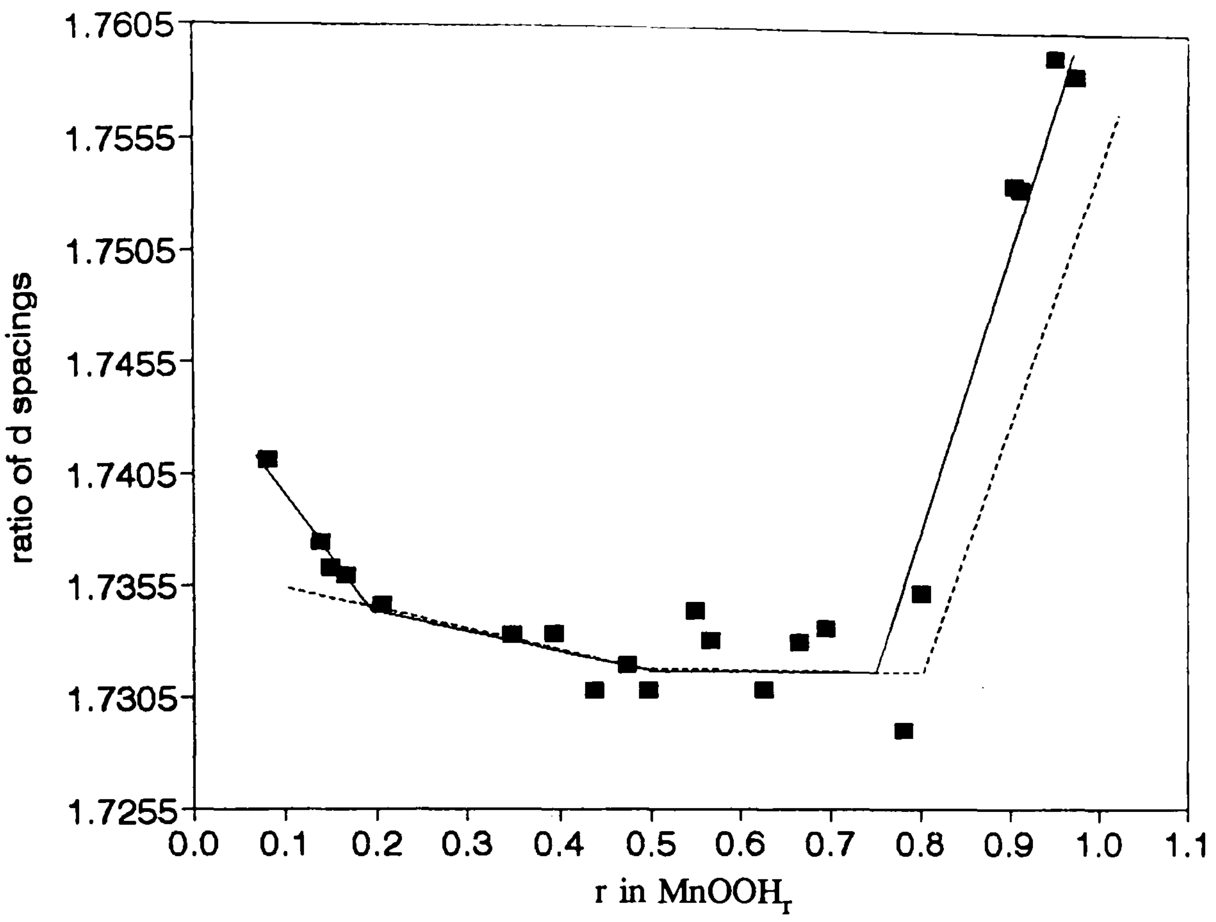

Figure 7-24 Ratio of the d or interplanar spacings for peaks D/A (see figure 6-10) for H insertion into IBA no.19. The dotted line indicates the same ratio derived from material R2.

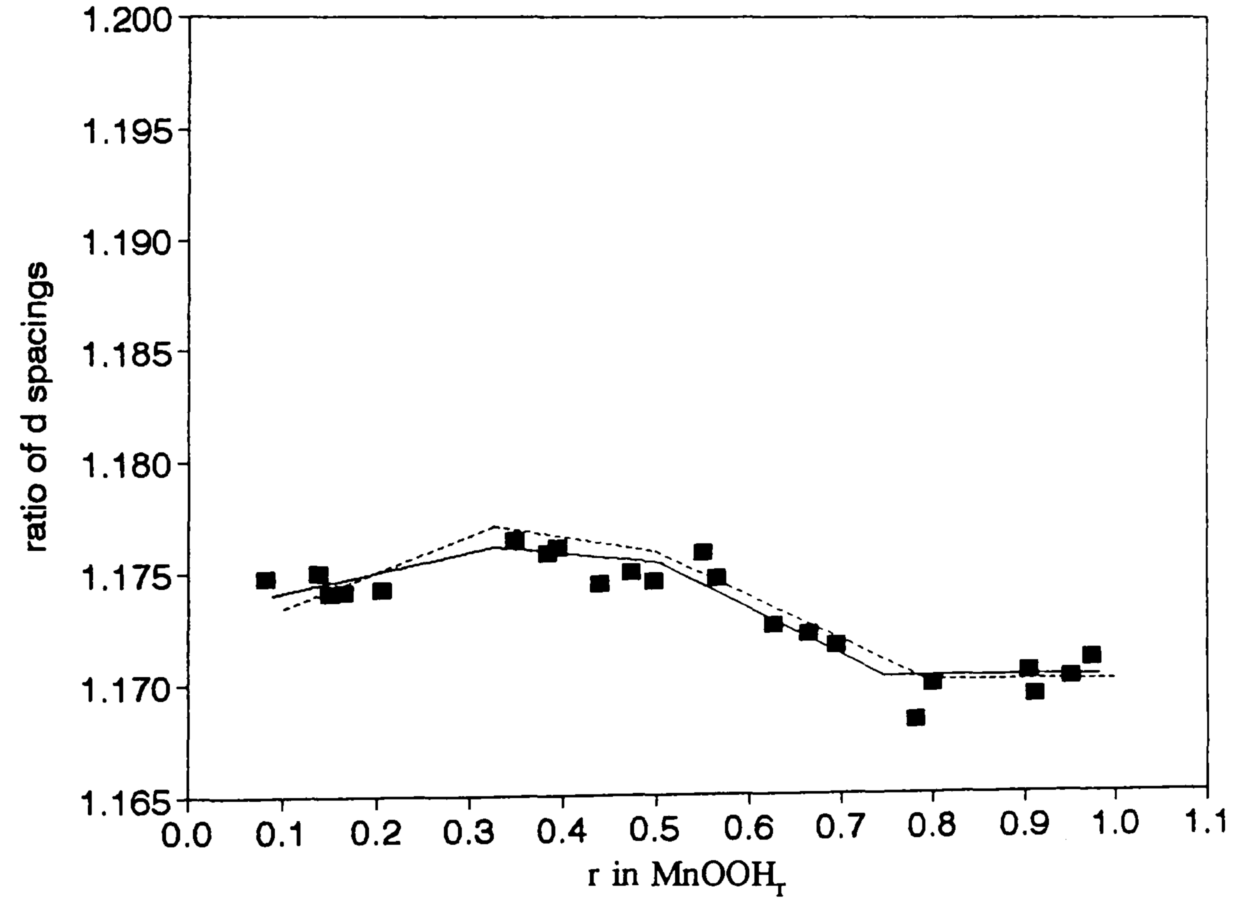

Figure 7-25 Ratio of the d or interplanar spacings for peaks B/A (see figure 6-10) for H insertion into IBA no.19. The dotted line indicates the same ratio derived from material R2.

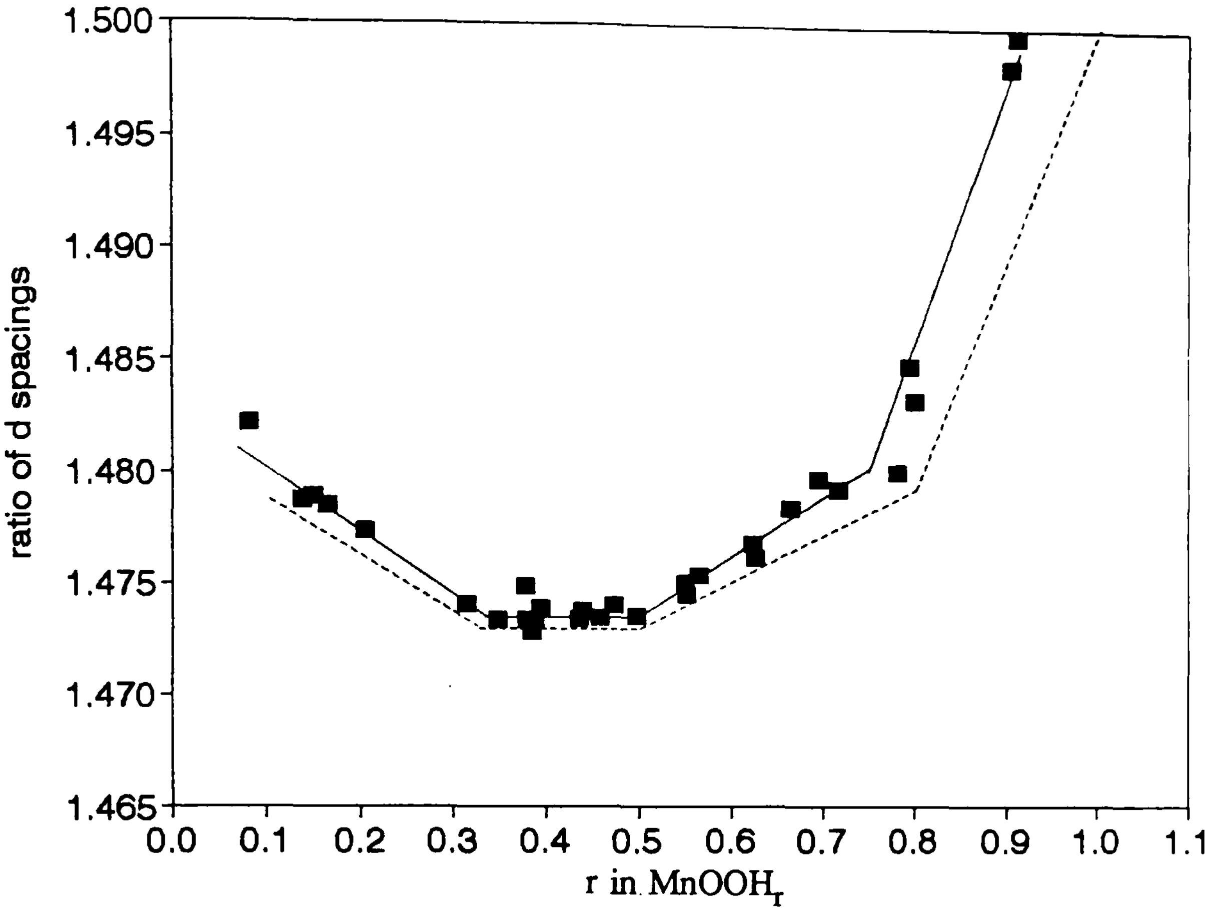

Figure 7-26 Ratio of the d spacings for peaks D/B for H insertion into IBA no.19. The dotted line indicates the same ratio derived from material R2.

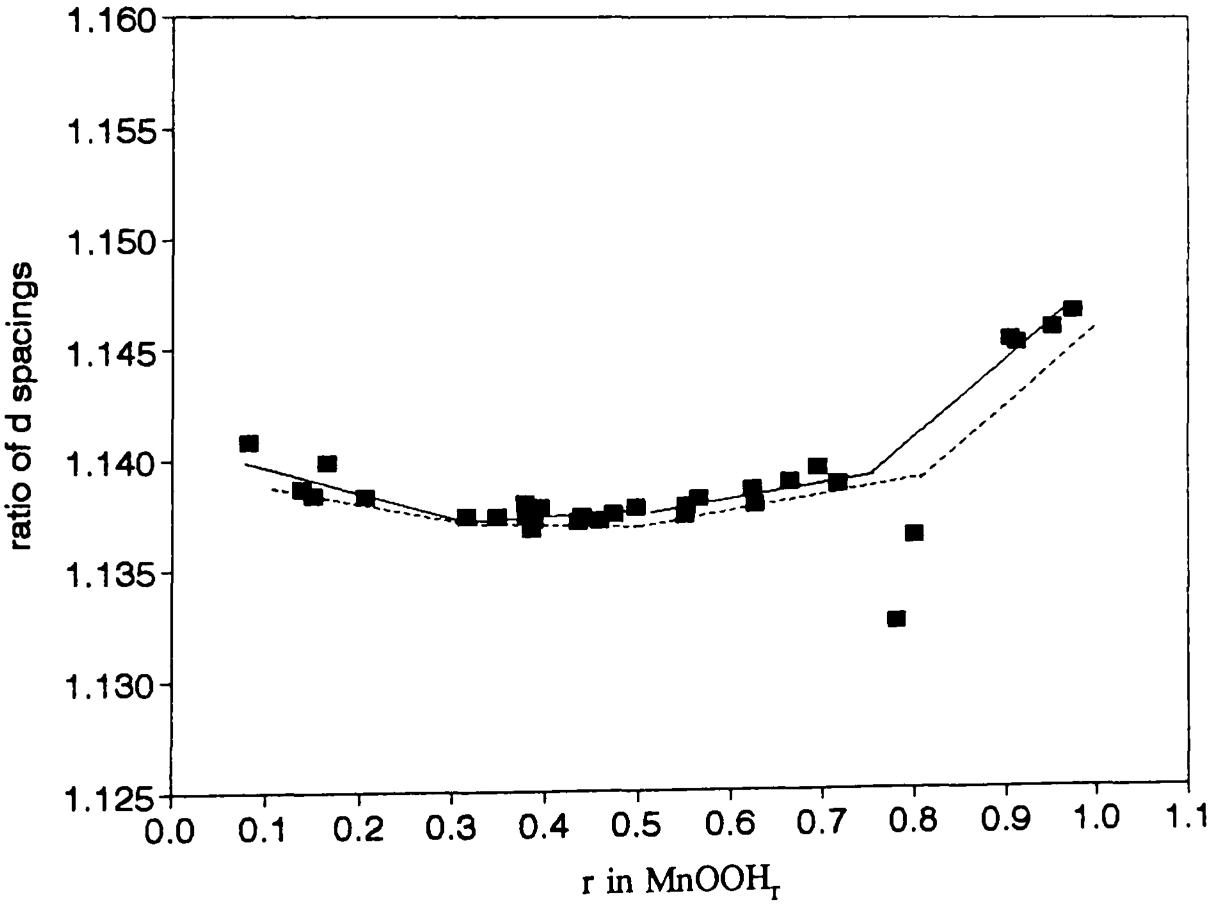

Figure 7-27 Ratio of the d spacings for peaks D/C for H insertion into IBA no.19. The dotted line indicates the same ratio derived from material R2.

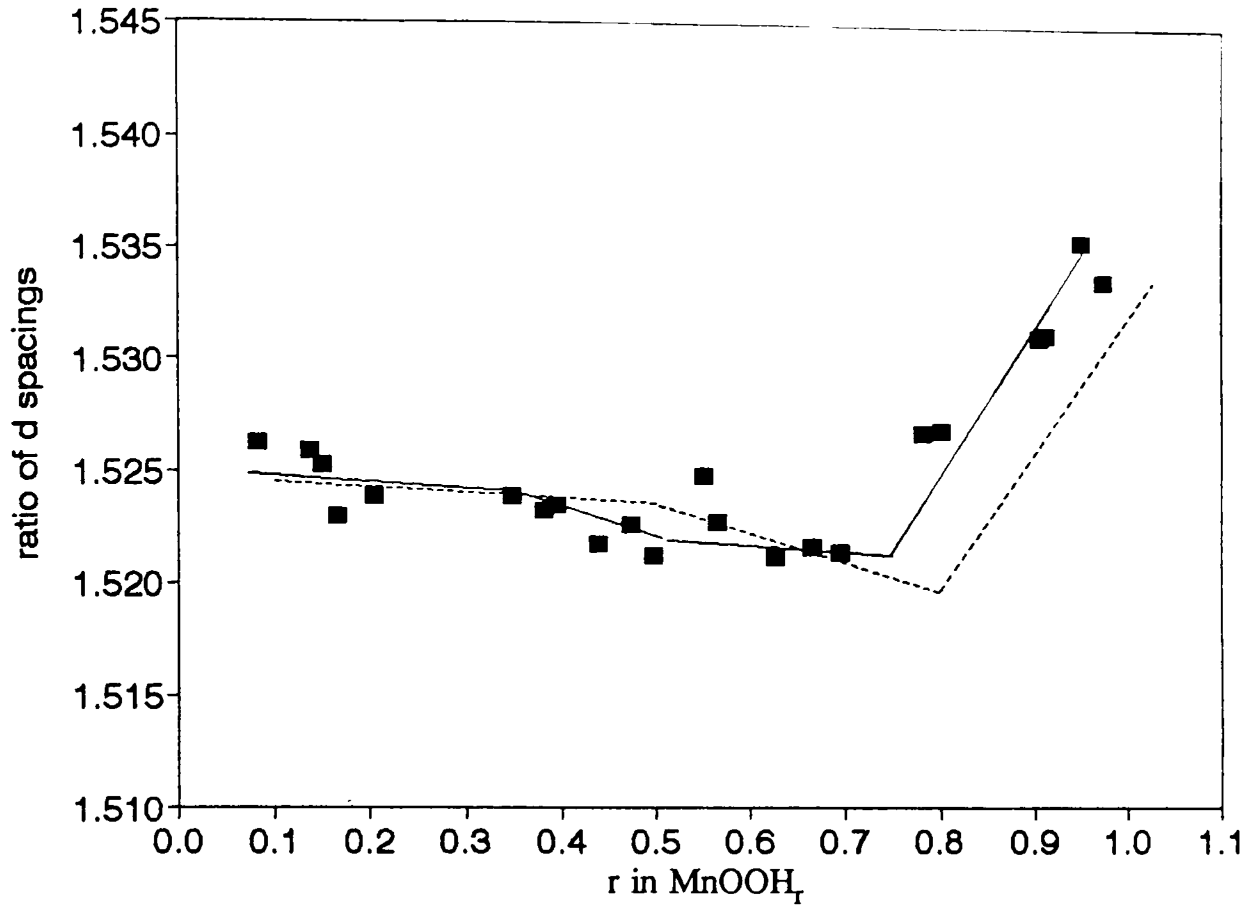

Figure 7-28 Ratio of the d spacings for peaks C/A for H insertion into IBA no.19. The dotted line indicates the same ratio derived from material R2.

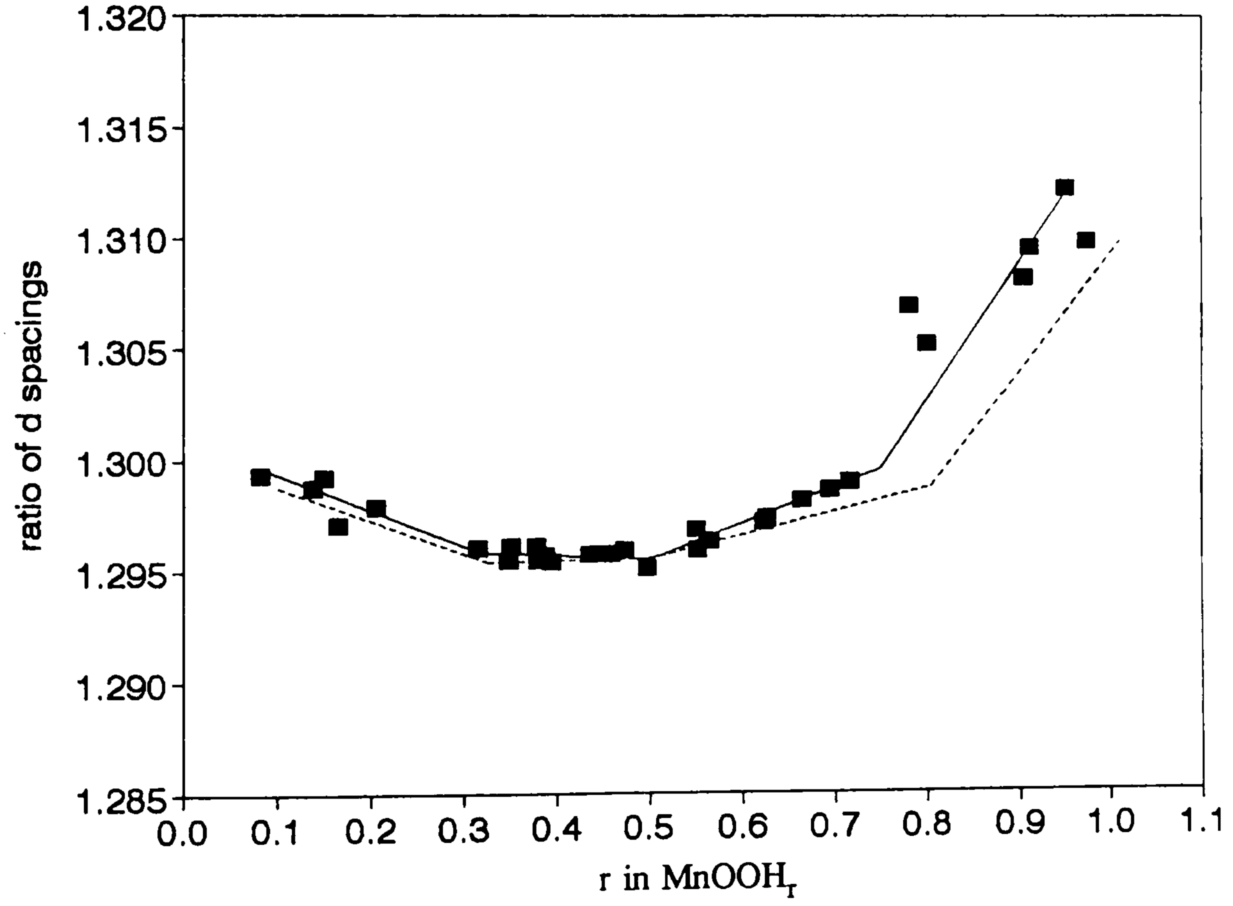

Figure 7-29 Ratio of the d spacings for peaks C/B for H insertion into IBA no.19. The dotted line indicates the same ratio derived from material R2.

to associate most probably is a consequence of the higher reaction temperature of the boiling propanol method of reduction compared to the ambient temperature reduction method employed by Fitzpatrick to prepare the R2 H inserted derivatives. Local heating when adding the 'non-aqueous' hydrazine hydrate suspension in large doses to the manganese dioxide may also account for the ability of this method to introduce heterogeneous behaviour. Any differences in figures 7-24, 7-25, 7-26, 7-27, 7-28, 7-29 compared to figures 6-11, 6-12, 6-13, 6-14, 6-15, 6-16 is thus believed to be induced by the reaction method rather than structural differences of which there is none.

One consequence of the precipitation of manganite is that the FTIR areas ar1, ar2, ar4 break at an earlier r in $MnOOH_r$ than those for R2 H insertion. Figures 7-30, 7-31, 7-32 clearly display that location of H starts at r=0.50 (figure 7-32) rather than at r=0.80 as found for R2, or r=0.75 as expected from the position of the peak d spacing ratio breaks. Clearly the position of the break in the graphs of absorption area versus r concurs with the onset of manganite precipitation and location of H within this phase. Beyond r=0.75 both manganite precipitation and $\delta_t$-MnOOH micro-domains are presumably responsible for the area of the FTIR absorption areas. Figures 7-30 and 7-31 (but not figure 7-32) support this conclusion in that the ar1 and ar2 against r slopes appear to increase beyond r=0.75.

This work employed a non-aqueous chemical H insertion method, as described in section 3.2. The manganite formation mentioned above is a consequence of the particular non-aqueous chemical H insertion method employed (see section 3.2). If, however, an aqueous method had been used the proportion of manganite would have been substantially increased as may be concluded from the work of Ohzuku and Hirai[95]. They used an aqueous hydrazine hydrate manganese dioxide suspension to insert H into a range of manganese dioxides similar to the range of materials used in this work. They claimed that IBA no.11 (very similar in its x-ray diffraction pattern to SBPA) reduced to groutite in a "single phase" process whereas IBA no.12 (Faradiser M) reduced to manganite also in "single phase". EMD (similar to IBA no.19 or R2), however, gave "mixed reduction products of groutite and manganite". The authors conclude that "The crystal structure of the reduction products by the hydrazine method seem to reflect the crystal structures of $MnO_2$ used.", and in the same paragraph that "From the experimental results, we have concluded that manganite was formed in a solid phase, not via the aqueous phase." Thus a progression of crystal structures from groutite,

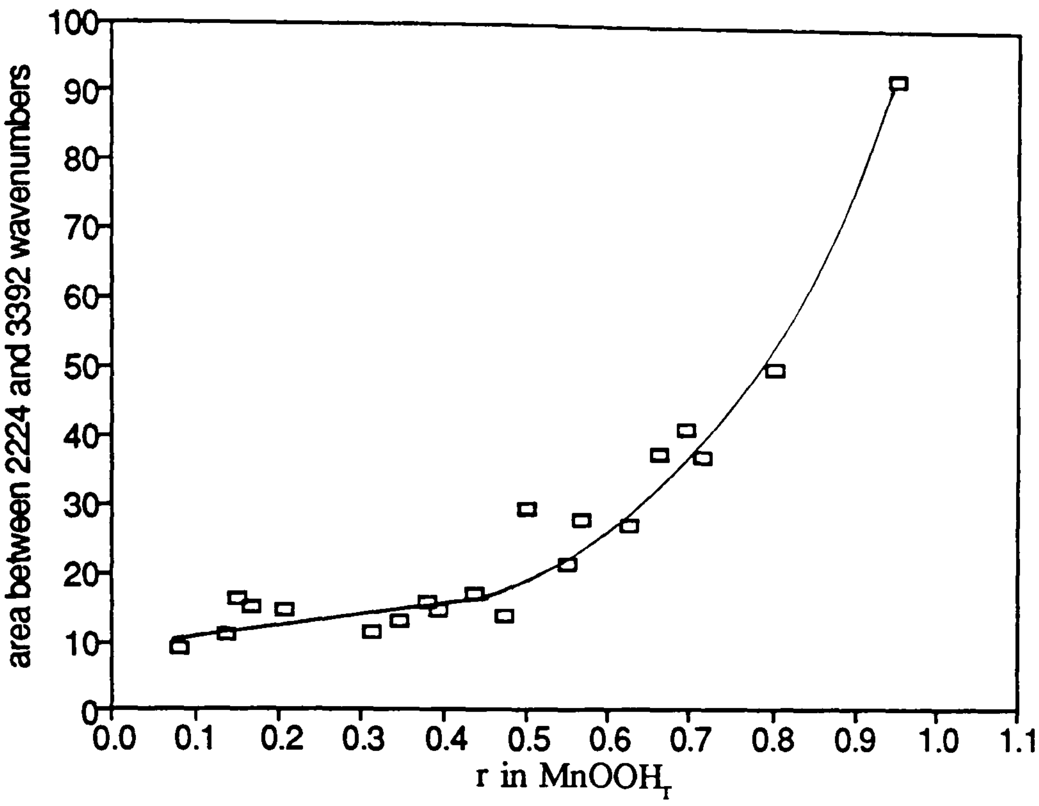

Figure 7-30 Change in integrated area of FTIR spectra minus background area, as defined by the ar1 boundaries shown in figure 5-13, with H insertion into IBA no.19.

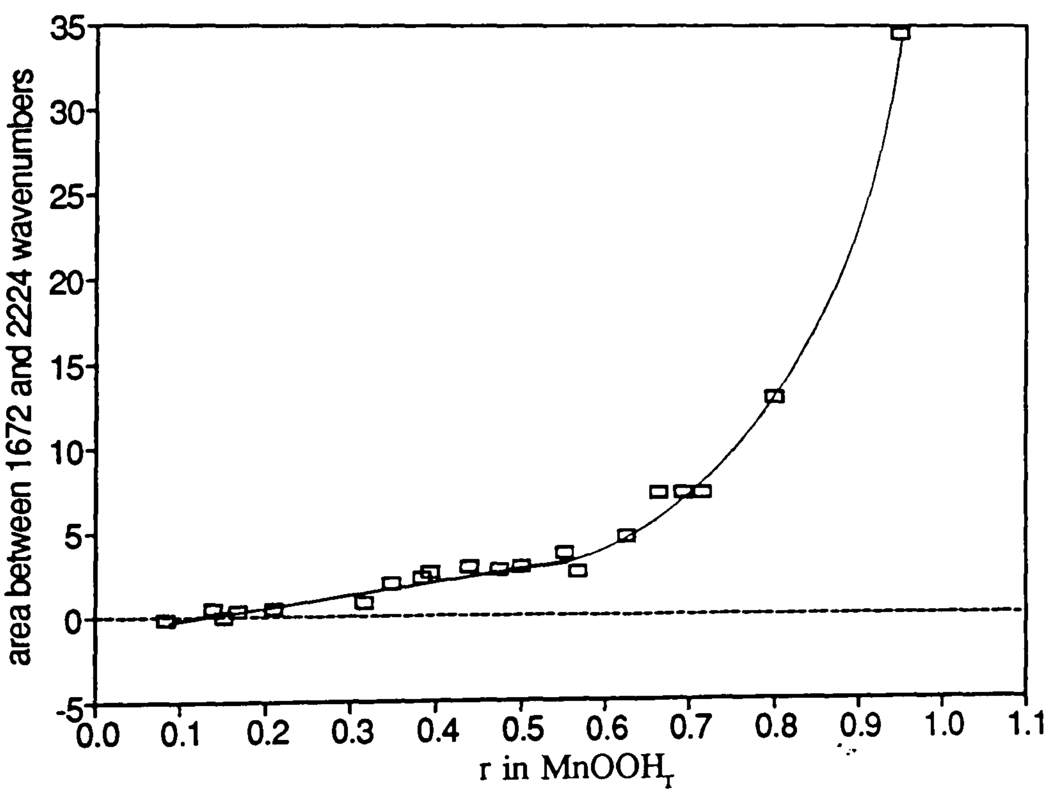

Figure 7-31 Change in integrated area of FTIR spectra minus background area, as defined by the ar2 boundaries shown in figure 5-13, with H insertion into IBA no.19.

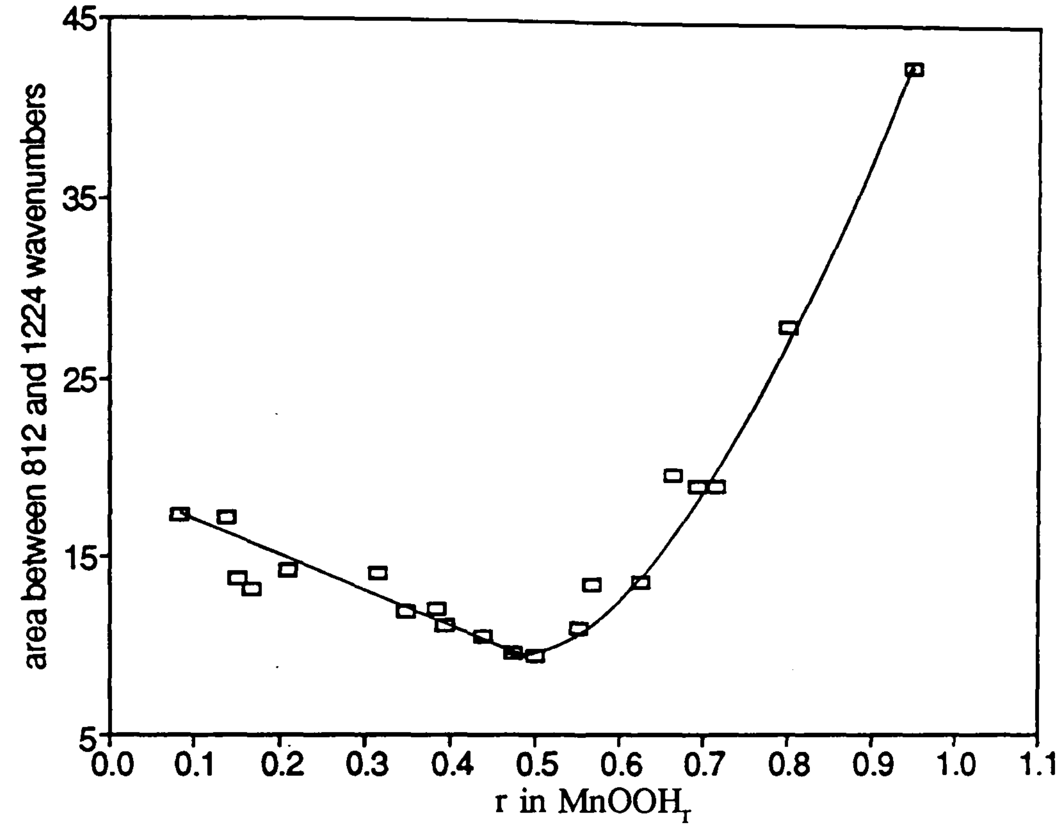

Figure 7-32 Change in integrated area of FTIR spectra minus background area, as defined by the ar4 boundaries shown in figure 5-13, with H insertion into IBA no.19.

groutite/manganite to manganite apparently related to the structure of the initial materials IBA no.11, EMD to Faradiser M was observed when reduction was performed. The products found in their work are not the same as found in this work (see section 4.2 and also following section for the product obtained for H insertion into F.M). Their results may be explained, not on the basis of the crystal structures of the initial materials, but rather on the basis of increasing specific surface area of the materials in the order IBA no.11, EMD, IBA no.12 and therefore an increased tendency for the H inserted material in question to dissolve and precipitate manganite. That the materials used by Ohzuku and Hirai have specific surface areas which increased in the order IBA no.11, EMD (as used), IBA no.12 is supported by the order of the areas listed in table 8.2 for the materials used in this work.The authors noted that the reduction product of IBA no.11 contained a small proportion of manganite which supports further the interpretation stated here for their results. Thus what was actually observed was an increased rate of manganite precipitation during the reduction reaction in line with increasing specific area of the initial material.

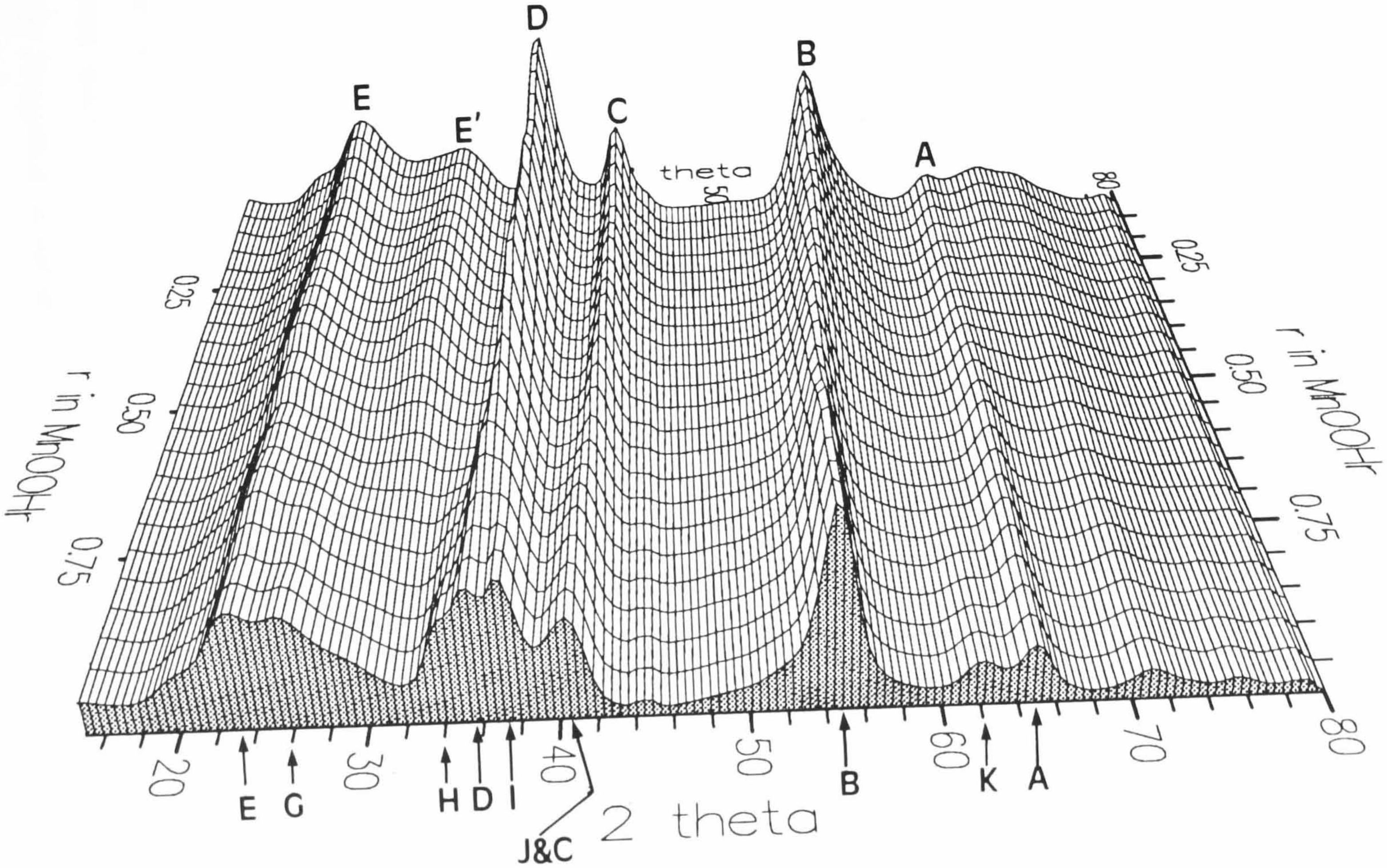

Figure 7-33 Pseudo-3D plot of the x-ray diffraction patterns resulting from H insertion into sample F.M. Peak labels as in figure 2-5 for the initial material and by analogy with figure 6-10 for the most reduced material.

## 7.4 Faradiser.M (abbrev. F.M).

A short account of the effects on the structure of inserting H in material F.M is offered. The primary reason for which is the difficulty associated in interpreting and measuring the effects on a small number of inherently broad peaks (compared to IBA no.19 or R2) which are almost certainly composed of overlapping maxima (see section 2.4.3).

Figure 7-33 summarises the observed changes that occurred to the x-ray diffraction pattern of this material when H was inserted. Smooth variations with regard to peak position and intensity are apparent i.e. there is no obvious evidence of heterogeneous reduction. Note, however, the gradual fading of the peak labelled E'. Consider also figure 7-34 which provides a selection of the data used to compile figure 7-33. 'New' peaks, characteristic of the most reduced product start to appear at $r \approx 0.70$. The final reduced material bears a striking resemblance to that obtained for H insertion into R2 or IBA no.19 with the obvious exception of peak E. The positions of the other 'new' and original peaks are almost exactly the same though their relative intensities are apparently quite different.

The peak positions of A, B, C, D are reported in figures 7-35, 7-36, 7-37, 7-38. With the exception of the peak labelled A, which was comparatively difficult to measure due to its weakness (see figure 7-34), the other peaks display striking 'S' shaped d spacing curves. As recognised in section 4.3.2 this type of change is one characteristic H-T peak shifts. The other characteristic is of a broadening and subsequent sharpening of the peak in question. Due to the close proximity of other maxima and that they are all probably combined maxima no attempt was made to measure the peak width, as it could not solely reflect this effect.

If the above suggestion were correct one would expect protons and electrons to be immobile within the structure across the whole H insertion range. FTIR evidence very nearly supports this proposition. Consider figures 7-39, 7-40, 7-41 which display the integrated absorbance areas, employing boundaries given in figure 5-13, as previously described. Clearly location of H occurred at an early H insertion level ($r \approx 0.20$).

Perhaps, however, both the FTIR behaviour and the 'S' shaped d spacing variation are caused by a heterogeneous process, in which the x-ray diffraction evidence

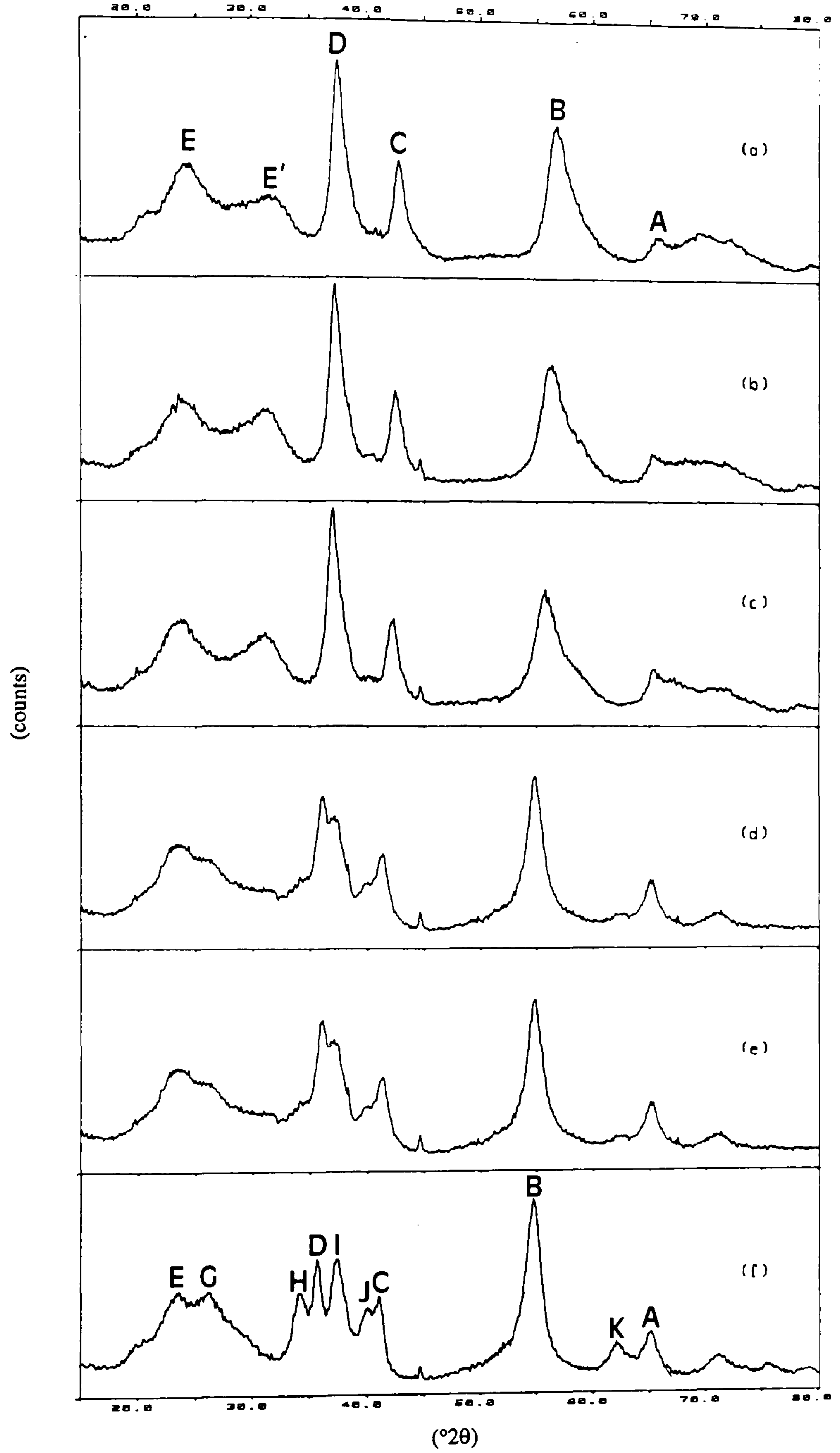

Figure 7-34 Selection of x-ray diffraction patterns representing the changes which occur on H insertion to material F.M. (a) $MnOOH_{0.112}$, (b) $MnOOH_{0.346}$, (c) $MnOOH_{0.462}$, (d) $MnOOH_{0.654}$, (e) $MnOOH_{0.798}$, (f) $MnOOH_{0.990}$. Labels as in figure 7-33.

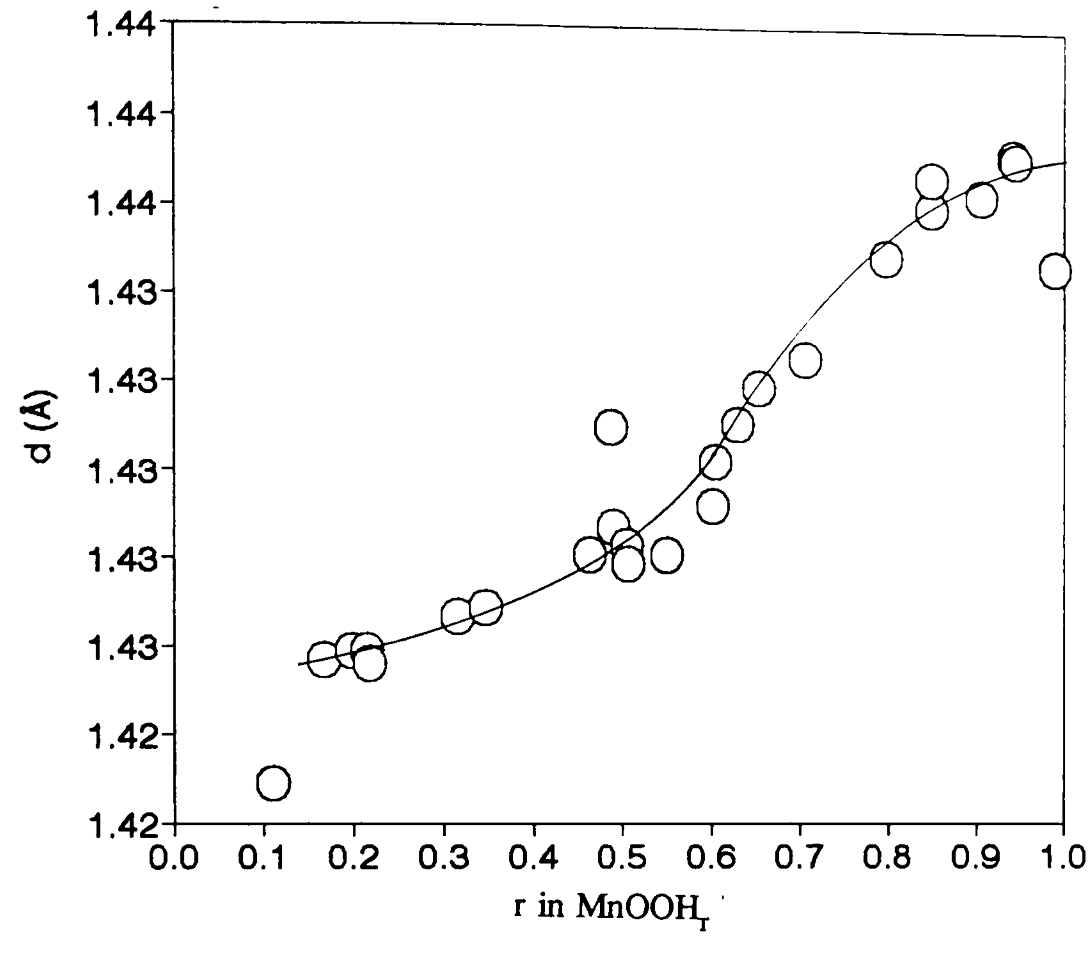

Figure 7-35 d or interplanar spacing variation of peak A with H insertion level for F.M.

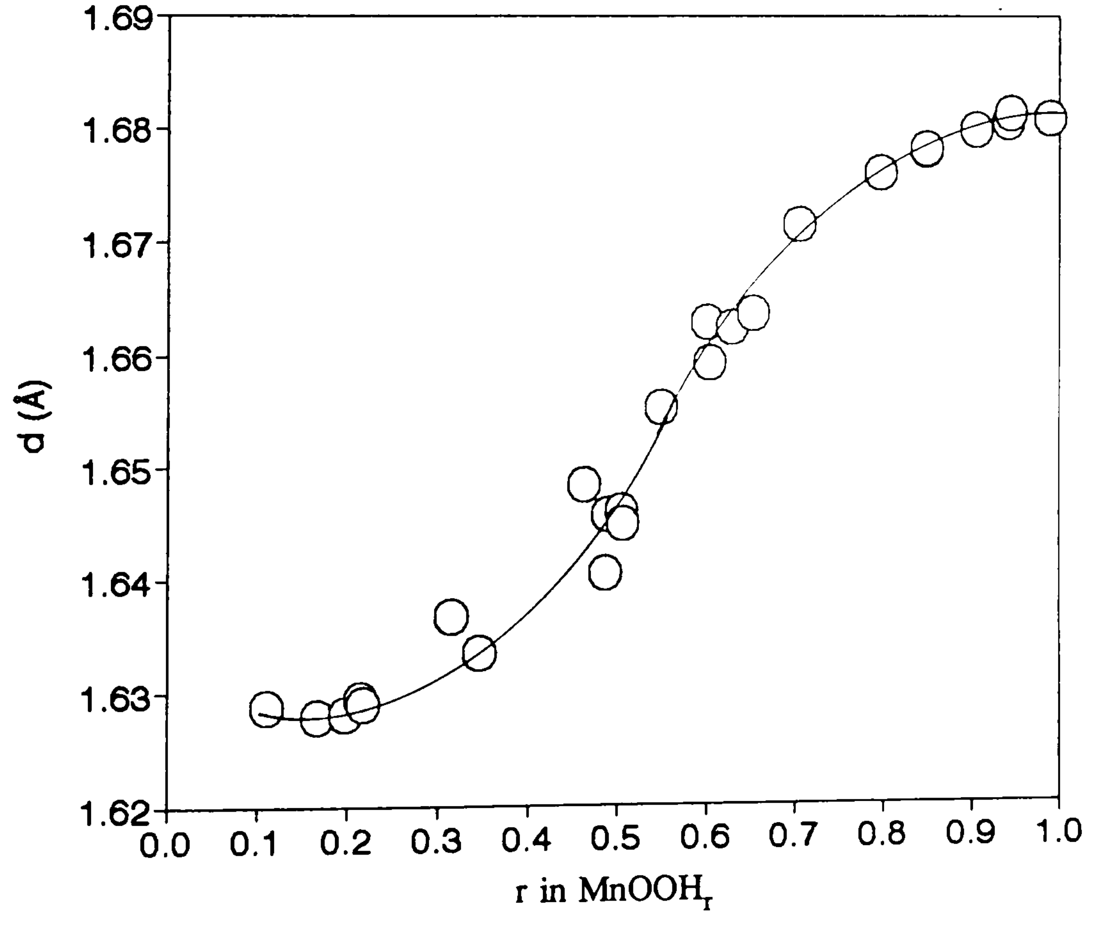

Figure 7-36 d or interplanar spacing variation of peak B with H insertion level for F.M.

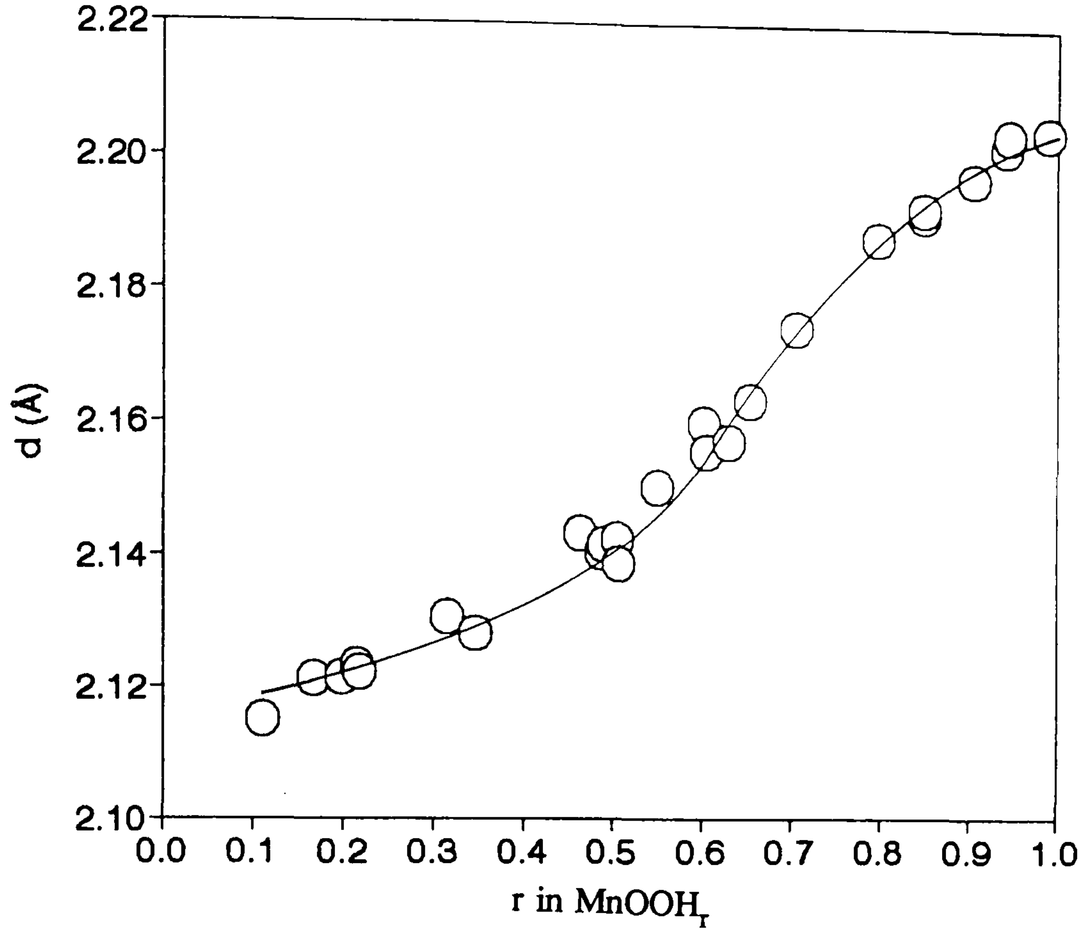

Figure 7-37 d or interplanar spacing variation of peak C with H insertion level for F.M.

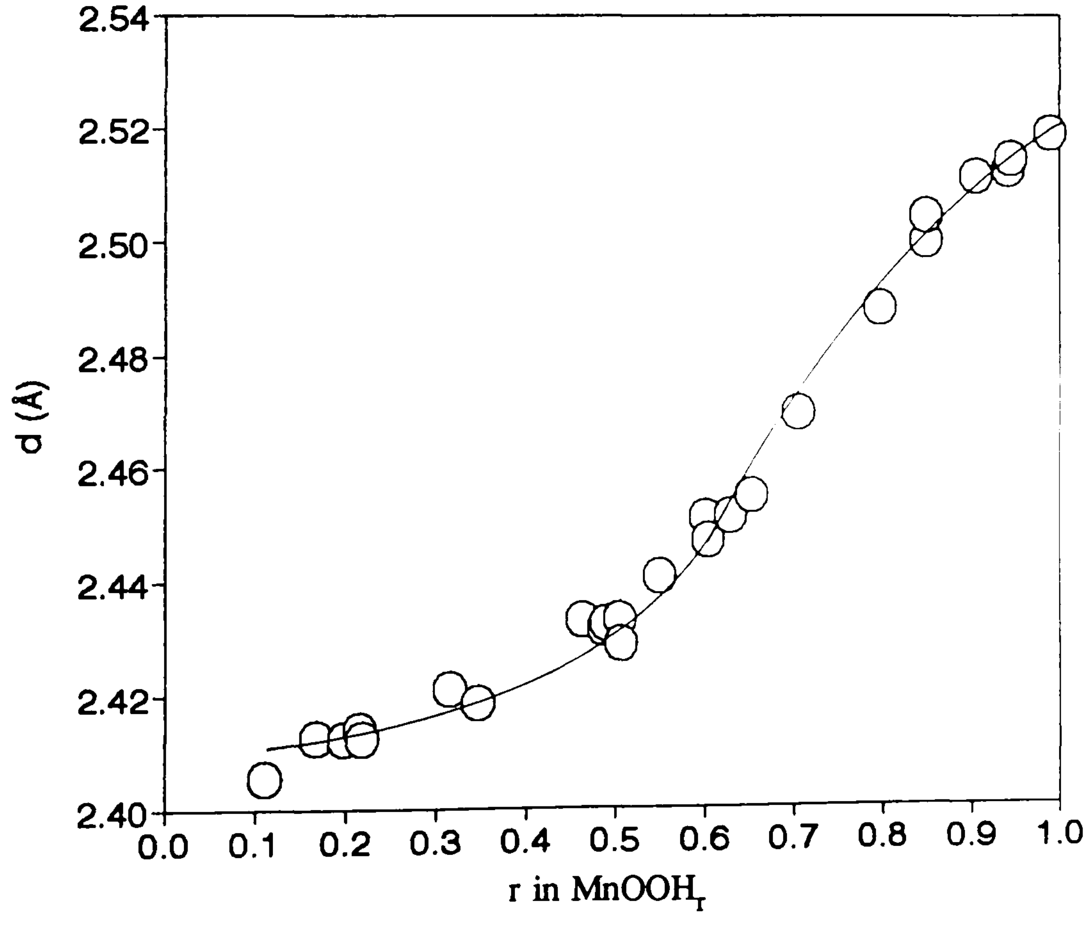

Figure 7-38 d or interplanar spacing variation of peak D with H insertion level for F.M.

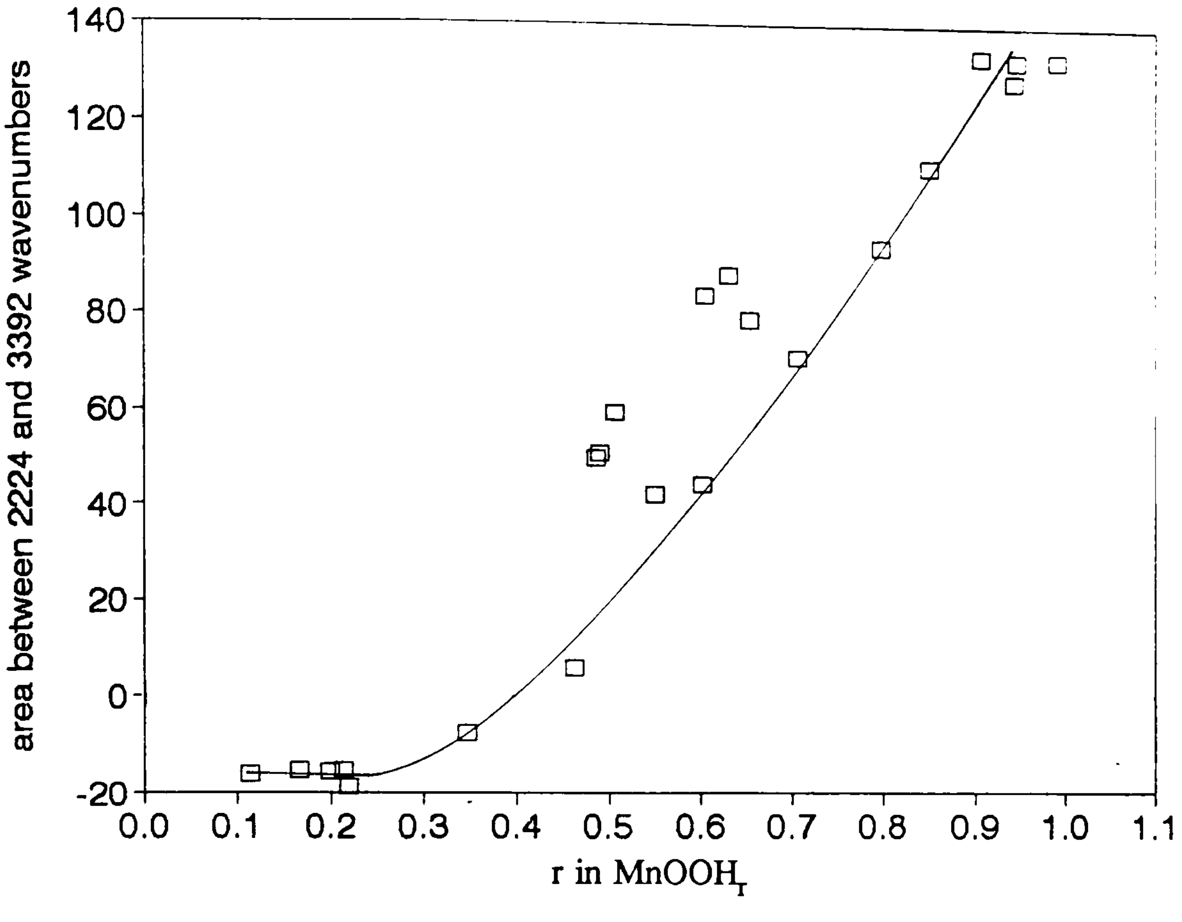

Figure 7-39 Change in integrated area of FTIR spectra minus background area, as defined by the ar1 boundaries shown in figure 5-13, with H insertion into material F.M.

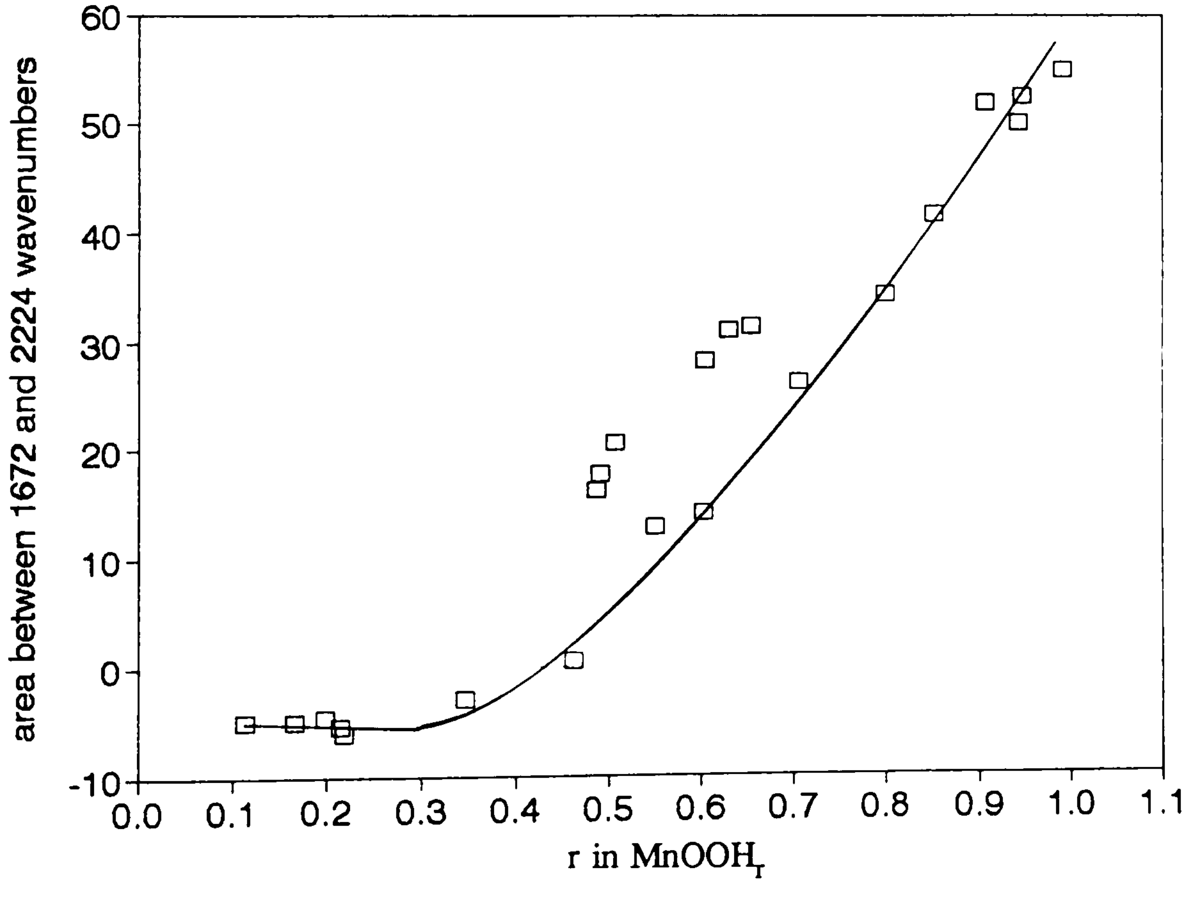

Figure 7-40 Change in integrated area of FTIR spectra minus background area, as defined by the ar2 boundaries shown in figure 5-13, with H insertion into material F.M.

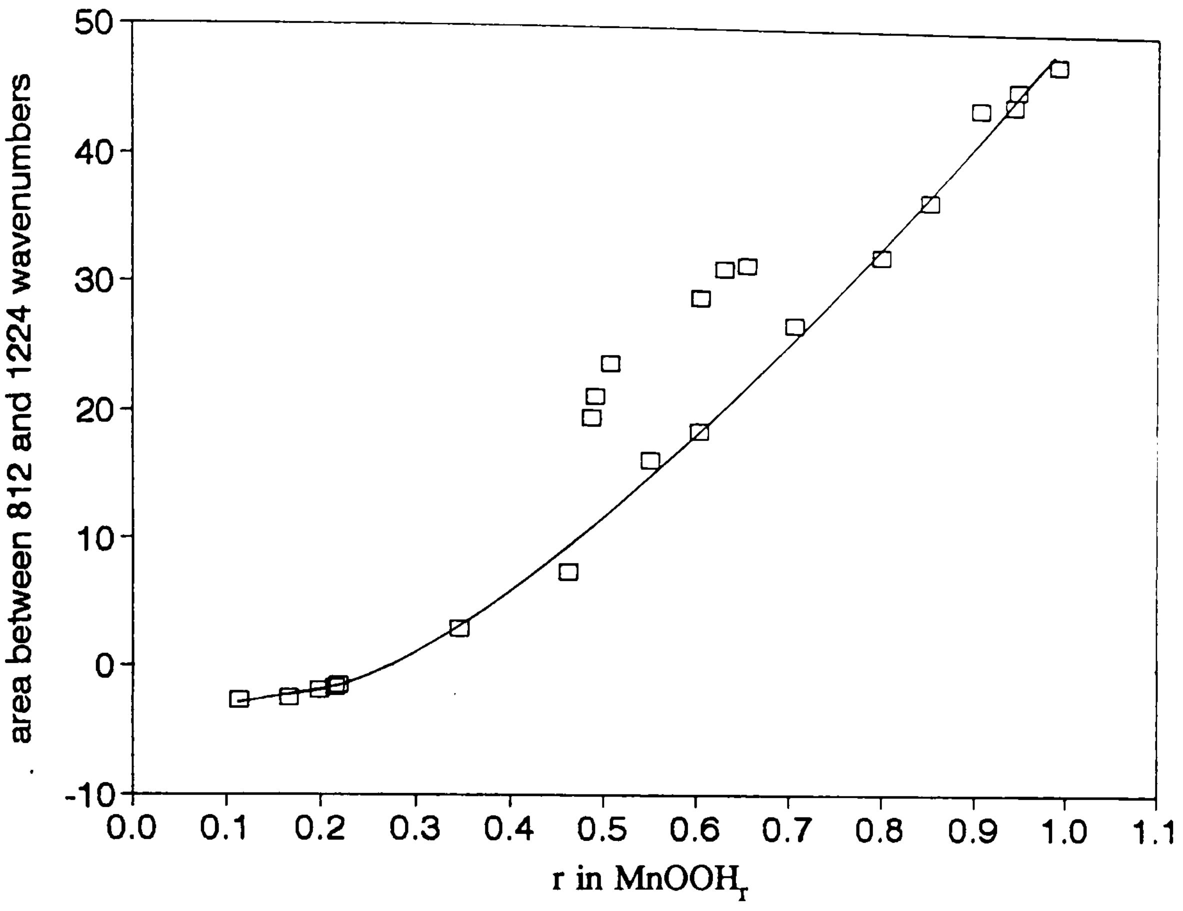

Figure 7-41 Change in integrated area of FTIR spectra minus background area, as defined by the ar4 boundaries shown in figure 5-13, with H insertion into material F.M.

becomes embedded in closely overlapping broad peaks such that single peaks are mostly apparent. Synthesizing an intermediate pattern with mixtures of patterns at r=0.20 (or the initial pattern, r=0.112) and the final reduced product (r=0.990) produces distinctly different appearances to that of an actual pattern of the same r value. Thus a heterogeneous process, (operating between these end members) was considered untenable.

On the evidence presented, it appears that an extended random layer structure (of the kind discussed in section 4.4.1) describes salient features of the peak d spacing variations presented and is also largely consistent with the FTIR evidence. The manganese dioxide is thus suggested to incorporate H by introduction of M(M') and G(G') type planar defects (at random locations) in an initial P(P') framework interspersed with a small fraction of R(R') type layers. M(M') (and G(G')) type layers replacing corresponding P(P') (and R(R')) type layers in an extended random layer model.

As noted earlier it is difficult to imagine how this might arise from strictly thermodynamic considerations. Possible explanations might envisage mobility of H with inbuilt restrictions allowing the protons and electrons to migrate but yet have a tendency to inhabit essentially P(P') layer defects forming a random distribution of M(M') planar defects.

## 7.5 Further conclusions.

It has been stressed that the onset of heterogeneous solid state reduction or precipitation of δ-MnOOH micro-domains is not solely connected to crystallographic differences exhibited by the $\gamma$-$\gamma_t$-$MnO_2$ series. Evidently the phenomena cited are two manifestations of the tendency of protons and electrons to 'freeze' at particular sites rather than obtain freedom as in a solid solution. It appears, however, that the following behaviour is unambiguously connected to the structural properties of the stated series.

Within the solid solution H insertion range a tendency towards anisotropic expansion is exhibited as one traverses in the $\gamma_t$-$\gamma$-$MnO_2$ series direction. Thus the materials SBPA and WSZ show distinct anisotropic behaviour, as demonstrated by the variation of the lattice parameters displayed in figures 5-7 and 7-9, in the observed (restricted) solid solution H insertion range. While EMD (represented by IBA no.19 or R2) displays within the solid solution range (free from δ-MnOOH micro-domains) almost isotropic behaviour, whereas IBA no.14, intermediate in the $\gamma$-$\gamma_t$-$MnO_2$ series, shows the first signs of anisotropy in comparison. It is reasonable to suppose that isotropic changes in lattice parameters would be expected for any conception of an ideal solid solution, in which the mobile species did not interact with the host crystal but rather formed a 'lattice gas'.

Such a description appears to apply to H insertion into commercial EMD where it has been shown[107] that the Gibbs free energy change of mixing ($\Delta G_{mix}$), as deduced directly from electrode potential measurements, at any composition was very close to that expected for ideal mixing (i.e. $\Delta H_{mix}=0$). Deviations from ideal mixing were successfully accounted for by use of an endless linear cluster model in which formation of small clusters of $H^+e^-$ pairs was observed which, it was posited, did not contribute fully to positional entropy. At high insertion levels larger clusters were formed which inevitably lead to the formation of crystalline micro-domains characteristic of the final product. Experimental evidence cited supporting the existence of these domains was the 'new' lines which appear in the x-ray diffraction pattern and indications of OH bond formation in the FTIR spectra of deeply H inserted EMD. This work has shown that such a suggestion is entirely consistent with the structural changes which occur to EMD as evidenced by the otherwise inexplicable x-ray diffraction behaviour which evolved with H insertion (with reference to chapter 6 in particular). Note that argument for the existence of such micro-domains arises in this work independently of the statistical thermodynamic considerations mentioned above and represents therefore a convergence of evidence and argument for such an interpretation.

Use of the word "micro-domain" is vindicated since the size of the domains that form must be of a similar order of magnitude to the wavelength of x-rays in order to produce the observed H-T effect (larger domains would simply lead to a superposition of x-ray patterns characteristic of the final H inserted product and that of the solid solution composition at which the domains form, and would therefore be indistinguishable from a heterogeneous process).

The micro-domains formed are for reasons given previously preferably termed δ-MnOOH micro-domains. These must not be confused with a previous suggestion by Giovanoli[2] that P(P') type layers were "microdomains of γ-MnOOH" which acted as nuclei for formation of γ-MnOOH during the chemical reduction of '$\varepsilon$-$MnO_2$'. A conclusion which is not supported by this work.

# 8 The stability of H inserted synthetic battery active manganese dioxide in 7M KOH.

## 8.1 Introduction.

The cathodic reduction of manganese dioxide in alkaline manganese cells has been the subject of numerous studies,[114-120] particularly in the period in which these primary batteries first appeared[121] (1960's). As a result it was discovered that manganese dioxide discharges (in the one electron range), as in Leclanché cells, by a solid state reaction characterised by a varying electrode potential in the manner theoretically described by Vetter[122]. It is now accepted that the solid state reaction is the insertion of $H^+$ and $e^-$ into manganese dioxide which may be represented:[123]

$$MnOOH_r + \Delta H^+ + \Delta e^- \rightarrow MnOOH_{r+\Delta} \qquad (8.1)$$

Where r reflects H insertion level which initially starts from a value, close to, but always greater than zero ($\approx$0.1) and finishes at the theoretical limit r=1.0. However, whether this limit is reached appears to depend on the nature of the discharge regime. On prolonged intermittent discharge regimes observations of cell potential indicate that the limit corresponds to r=0.8, which in turn corresponds to an oxidation level[124] of $MnO_{1.6}$. Bell and Huber[119] recognised that the H inserted $\gamma$-$MnO_2$ structure re-arranged to a different phase at high insertion levels (in alkaline manganese battery discharges) Tye[124] suggested that the solid solution is only metastable in KOH electrolyte which may explain the difference between alkaline manganese and Leclanché batteries (under intermittent discharge regimes) which in contrast to alkaline cells have a final solid state reduction product oxidation state $MnO_{1.5}$.

The instability of the solid solution has subsequently been confirmed by Holton *et al.*[125] At present this study represents the only investigation specifically on this topic. As suggested therein, (in the discussion published at the end of the paper), the metastability of H inserted battery active $MnO_2$ has consequences for the cycling capabilities of alkaline manganese rechargeable cells. The possibility of producing such cells is currently the subject of renewed research interest[126,127,128,129]. Such cells would be desirable for conserving energy[121] and the environment (in comparison to Ni-Cd batteries which rechargeable manganese dioxide batteries could replace). Already cells are marketed[127] but limited to small discharge depths (i.e. they are zinc limited) for which it is known manganese dioxide is rechargeable[130]. The discovery that H inserted battery active $MnO_2$ is only metastable in KOH has not been explicitly recognised in the recent work cited. The purpose of this study was primarily (a) to confirm for chemically prepared H inserted samples that a spontaneous reaction with KOH solutions occurs for the previously identified structural range of materials and (b) to correlate structural differences with different instability behaviour.

## 8.2 Experimental.

Observations of the electrode potential on the chemically produced H inserted samples from starting materials SBPA, IBA no.14, IBA no.19, R2 and F.M are reported in 7M KOH. Complementary x-ray diffraction and SEM analysis are presented.

### 8.2.1 Procedure.

1.00(g) of $MnO_2$ was added to 10(g) of 7M KOH and stored in an air box at 25(°C). Electrode potentials measured by the method described in section 3.6 were recorded at intervals of 1 week, 2 weeks, 3 weeks and 6 weeks unless otherwise stated. Potentials are reported versus an Hg/HgO reference electrode containing KOH electrolyte at the same molarity as the immersed $MnO_2$.

Samples for x-ray diffraction were prepared by one of two methods. Either the sample was vacuum filtered over sintered glass and washed with distilled water and sucked dry or the sample sucked without washing until a wet paste could be mounted in a diffraction holder. The difference between the two techniques could be accounted for by a large background scattering from the residual liquid in the paste method. Dry samples were ground in an agate pestle and mortar. SEM samples were also prepared by similar procedures.

## 8.3 Results of electrode potential measurements.

### 8.3.1 Faradiser M. (abbreviated F.M).

Figure 8-1 presents the measurements of electrode potential versus their initial oxidation state obtained on the F.M H inserted samples after 7 days immersion in 7M

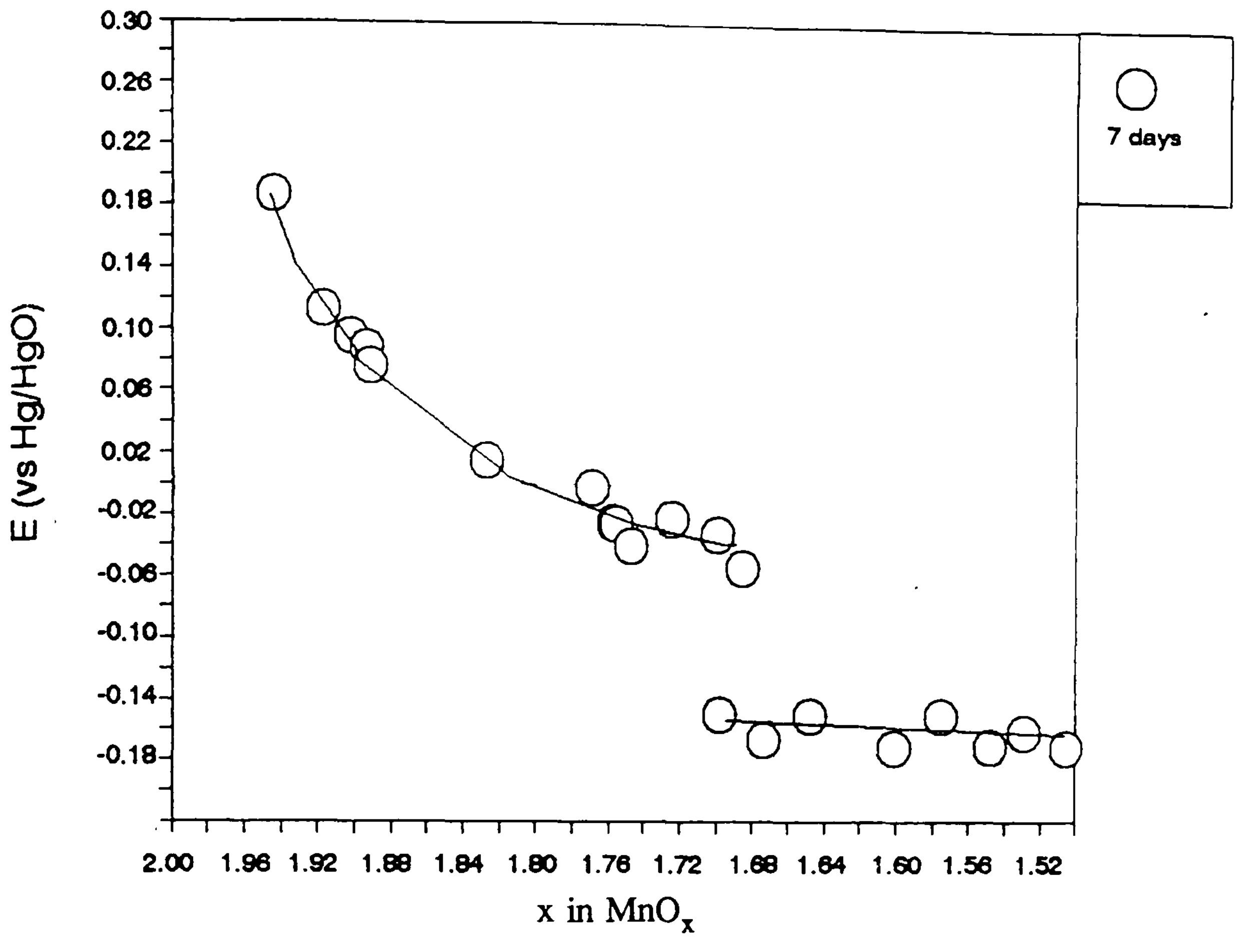

Figure 8-1 E(vs. Hg/HgO) versus x in $MnO_x$ for H inserted F.M samples after 7 days storage in 7M KOH.

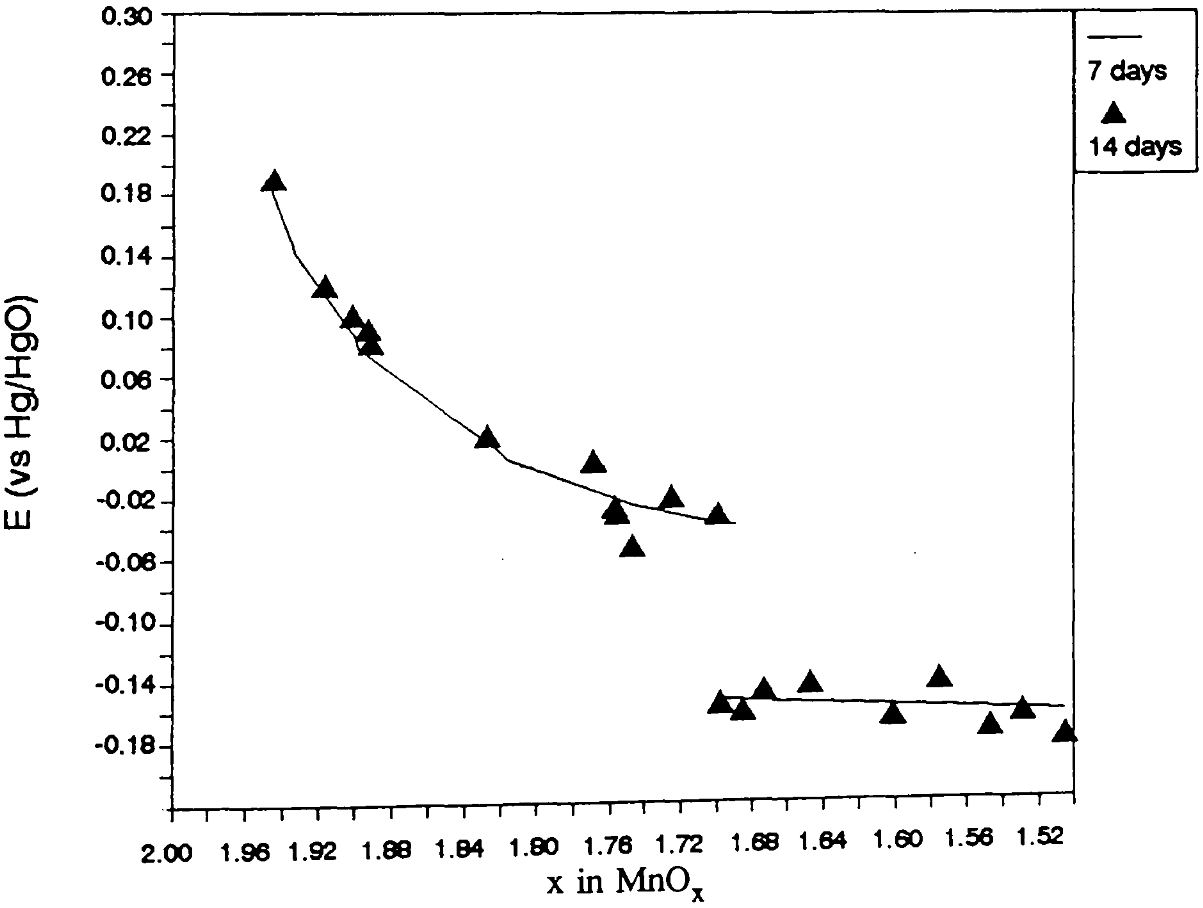

Figure 8-2 E(vs. Hg/HgO) versus x in $MnO_x$ for H inserted F.M samples after 14 days storage in 7M KOH.

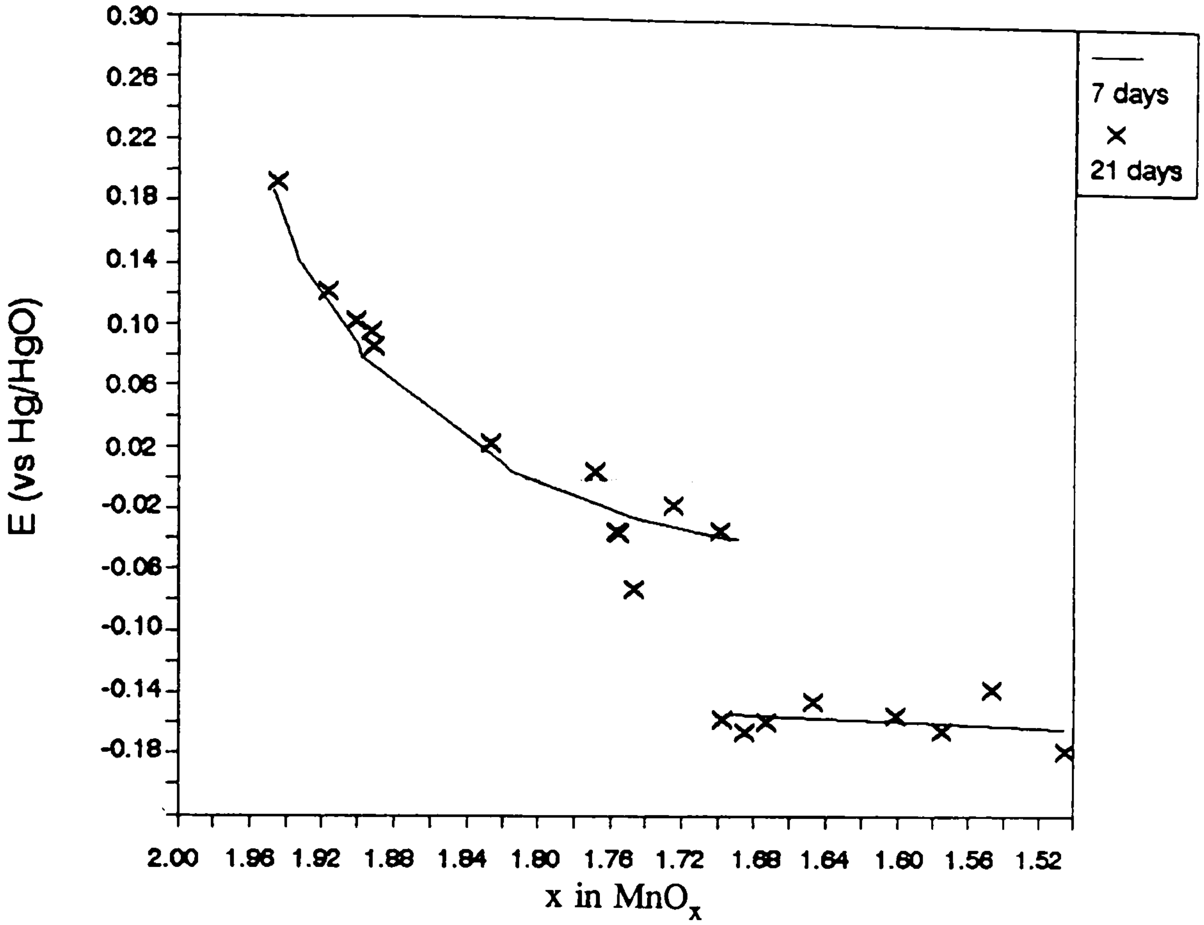

Figure 8-3 E(vs. Hg/HgO) versus x in $MnO_x$ for H inserted F.M samples after 21 days storage in 7M KOH.

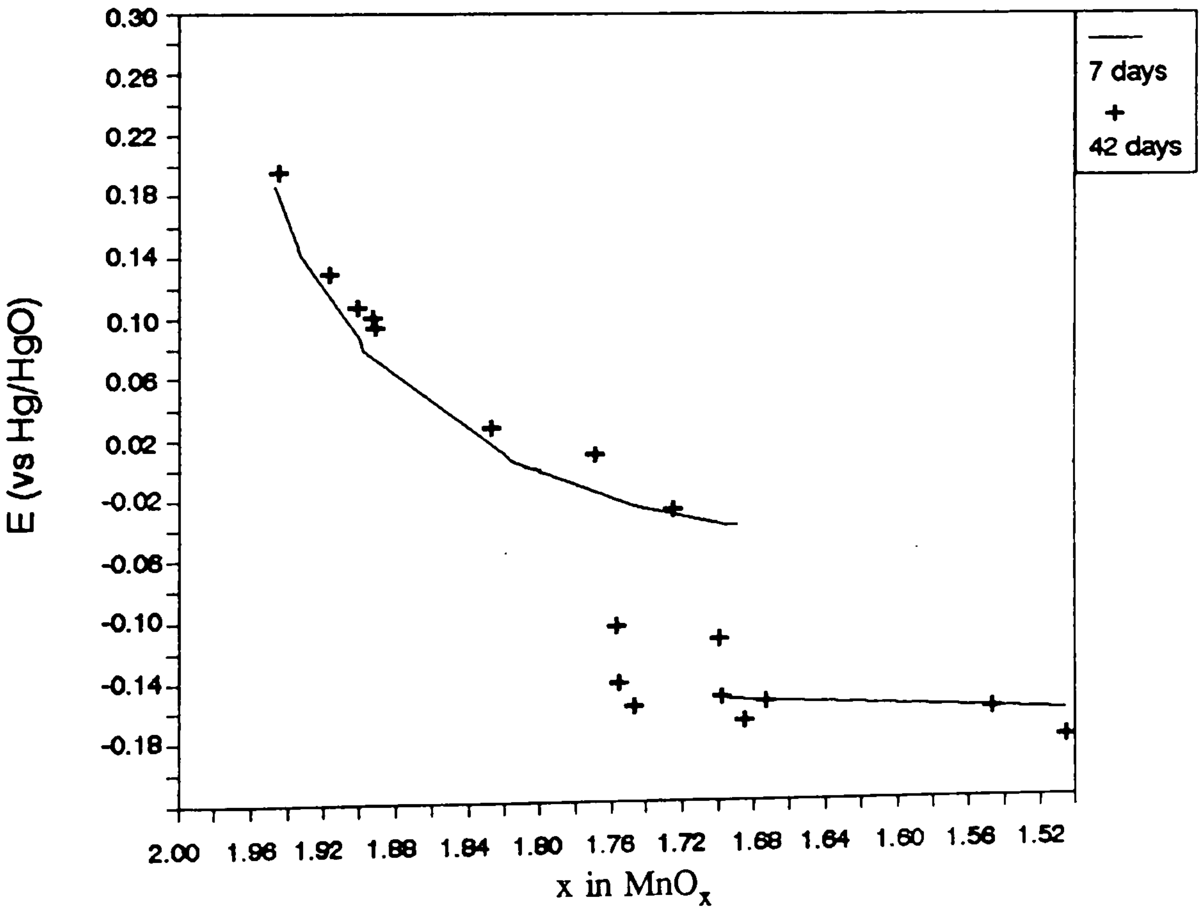

Figure 8-4 E(vs. Hg/HgO) versus x in $MnO_x$ for H inserted F.M samples after 42 days storage in 7M KOH.

KOH. Oxidation state was preferred in this instance since phases other than the oxyhydroxide phase may be present after storage[†]. Two potential zones are clearly distinguishable. One in which the potential falls from 0.188(V) at $MnO_{1.944}$ to -0.04(V) at $MnO_{1.67}$ in a continuous manner. The other is a region of nearly constant potential from $MnO_{1.70}$ to $MnO_{1.50}$. The average potential in this region is E(vs. Hg/HgO)=-0.16(V) (with the standard deviation $\delta_{n-1}$=0.01(V)). Note that the two regions apparently overlap. The magnitude of the potential drop between the two regions is therefore 0.12(V) or 120(mV). Figures 8-2, 8-3, 8-4 indicate slight changes to the potential on prolonged immersion of the H inserted manganese oxyhydroxides. In general a slow increase in potential is observed for all samples in the $MnO_{1.944}$ - $MnO_{1.76}$ zone and the constant potential region is extended i.e. $MnO_{1.76}$ - $MnO_{1.50}$.

### 8.3.2 IBA no.19 and R2.

Figures 8-5, 8-6, 8-7, 8-8 present the potential data recorded for the chemically H inserted compounds produced from material IBA no.19. In this case there also appears to be two regions, but their delineation is not clearly defined. This is because it seems that the region of constant potential is shorter than for the previous material. Furthermore prolonged immersion (6 weeks) does not appear to extend it. Supplementary data on a similar material viz R2, however, indicates that a continually developing flat potential region does develop with time, consult figures 8-9, 8-10, 8-11. Within the varying potential region selective increases and decreases occur leading to the potential versus x dependence indicated in figure 8-11 (dotted line). Again at least two regions of potential as a function of x may be identified. Namely $MnO_{1.950}$ - $MnO_{1.60}$ which has a varying potential and $MnO_{1.60}$ - $MnO_{1.50}$, constant potential. The average value for the horizontal potential for R2 and IBA no.19 is (from the long stored samples) E(vs. Hg/HgO)=-0.16(V).

### 8.3.3 IBA no.14.

The electrode potential versus x in $MnO_x$ for IBA no.14 H inserted samples after 7 days immersion in 7M KOH is presented in figure 8-12. A break in the potential versus x curve is once again observed, in this case at x≈1.60 in $MnO_x$. In the solid

---

[†] It also facilitates comparison with other work on the discharge of alkaline manganese batteries which is conventionally expressed in terms of oxidation state.

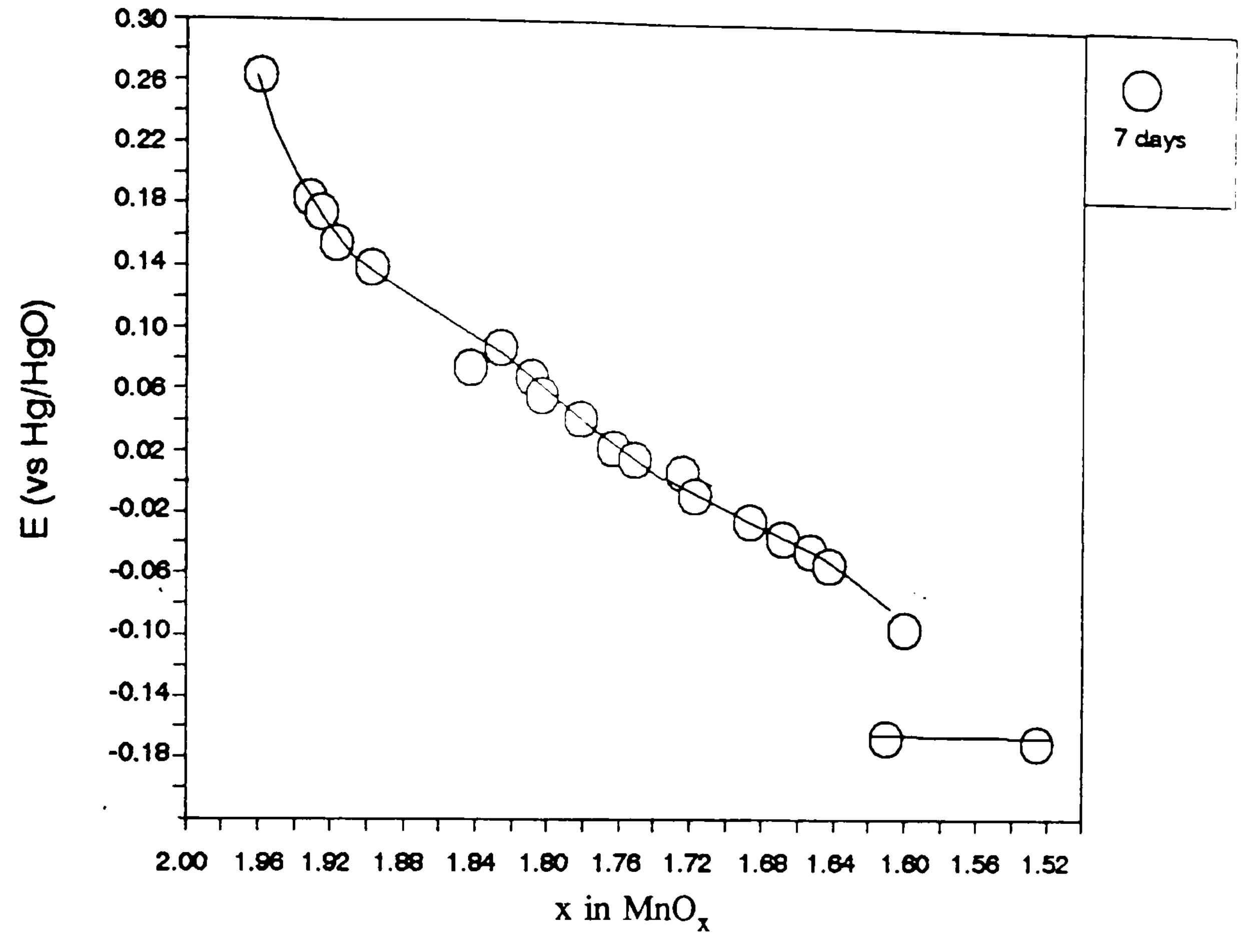

Figure 8-5 E(vs. Hg/HgO) versus x in $MnO_x$ for H inserted IBA no.19 samples after 7 days storage in 7M KOH.

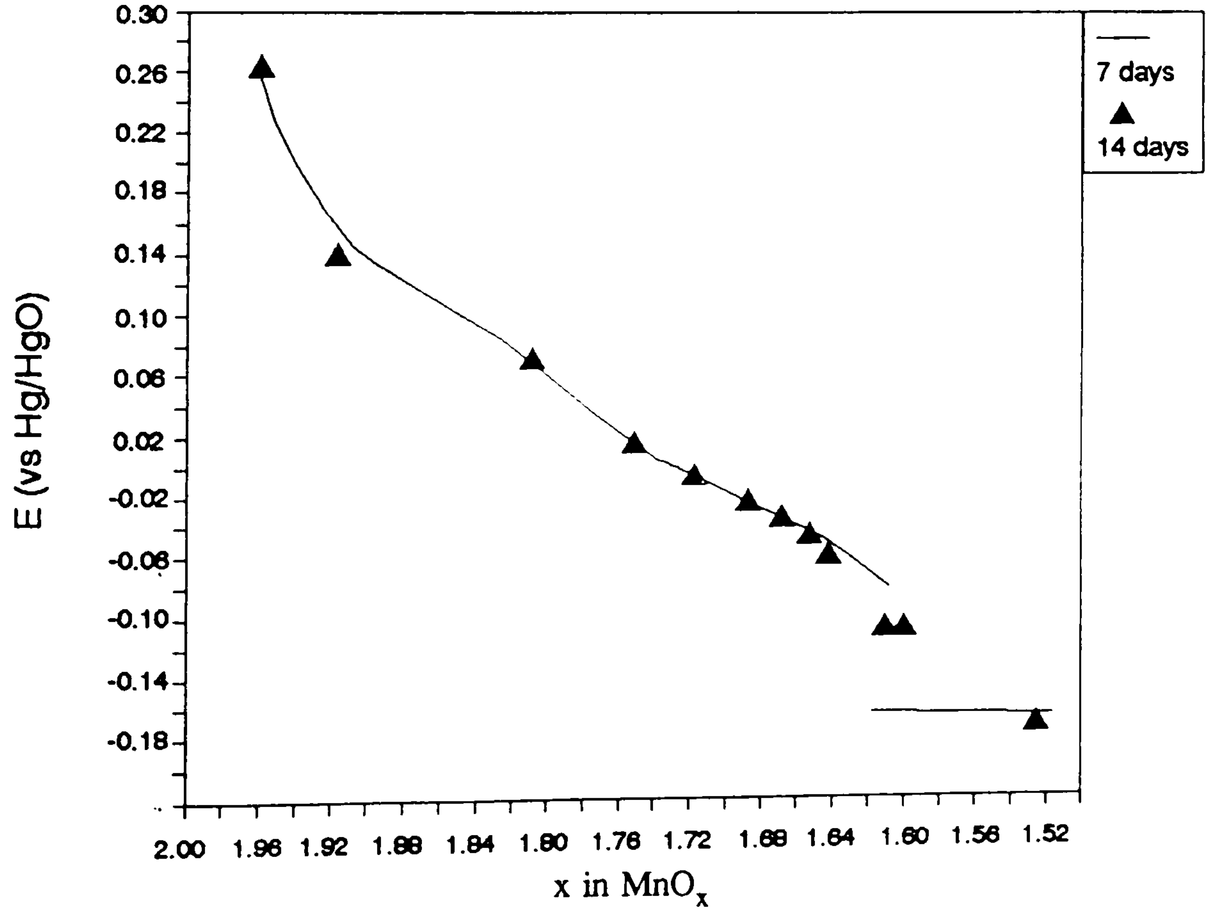

Figure 8-6 E(vs. Hg/HgO) versus x in $MnO_x$ for H inserted IBA no.19 samples after 14 days storage in 7M KOH.

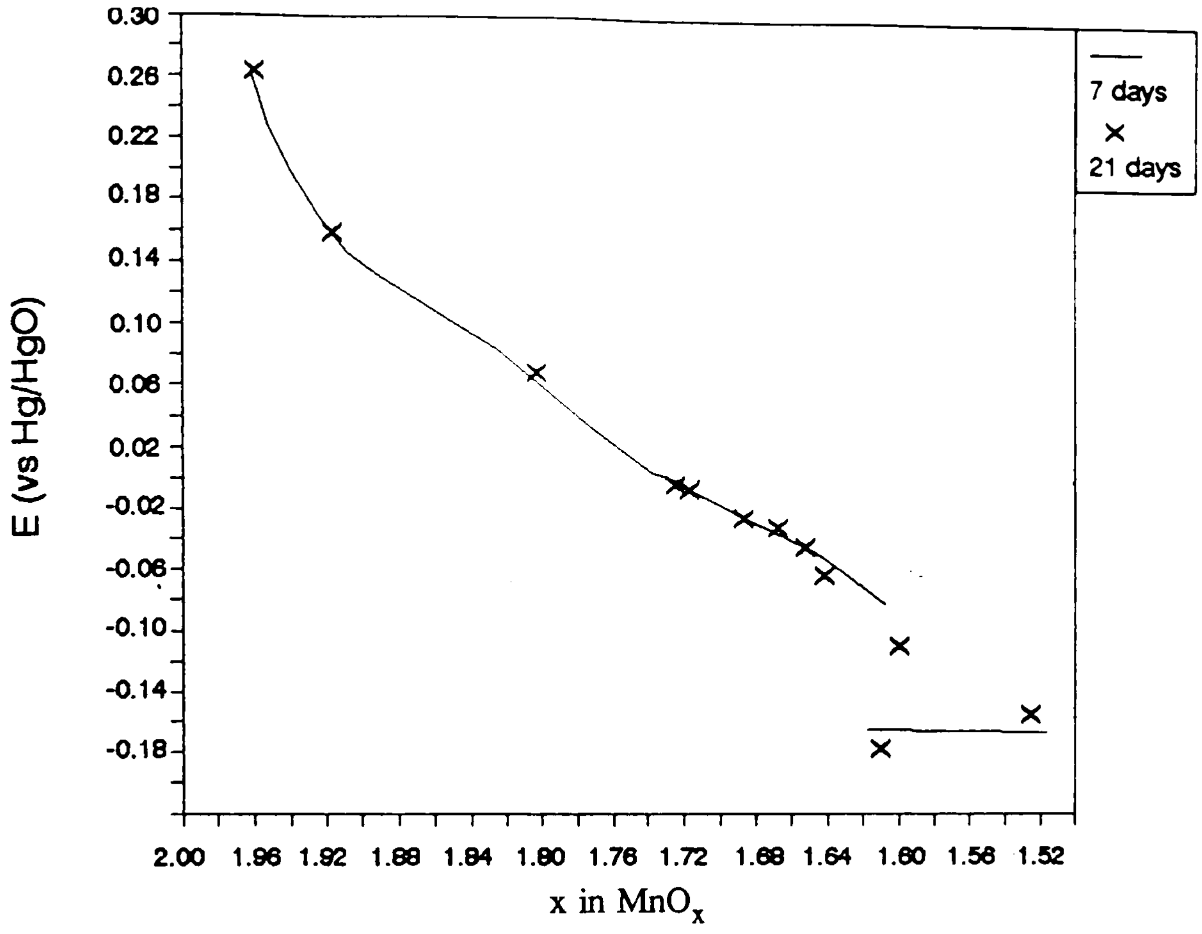

Figure 8-7 E(vs. Hg/HgO) versus x in $MnO_x$ for H inserted IBA no.19 samples after 21 days storage in 7M KOH.

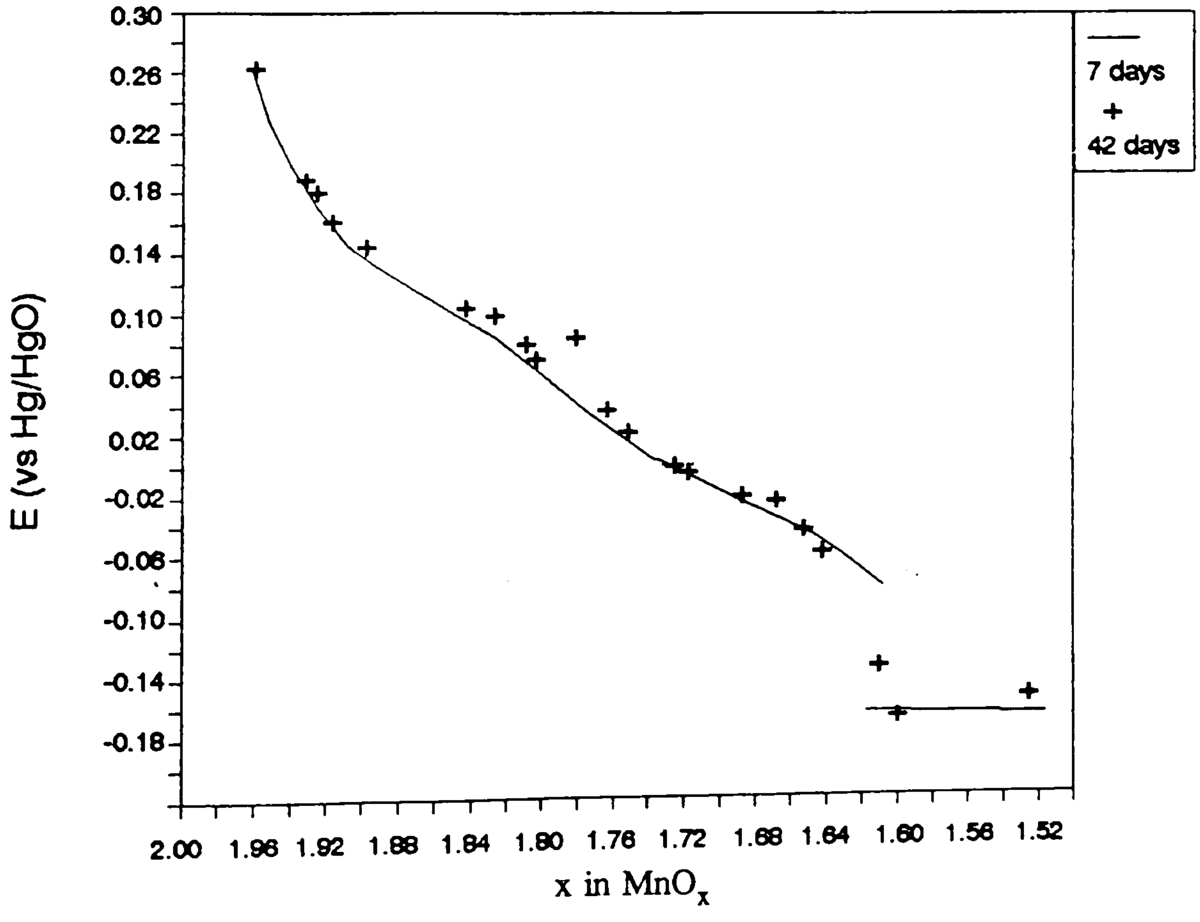

Figure 8-8 E(vs. Hg/HgO) versus x in $MnO_x$ for H inserted IBA no.19 samples after 42 days storage in 7M KOH.

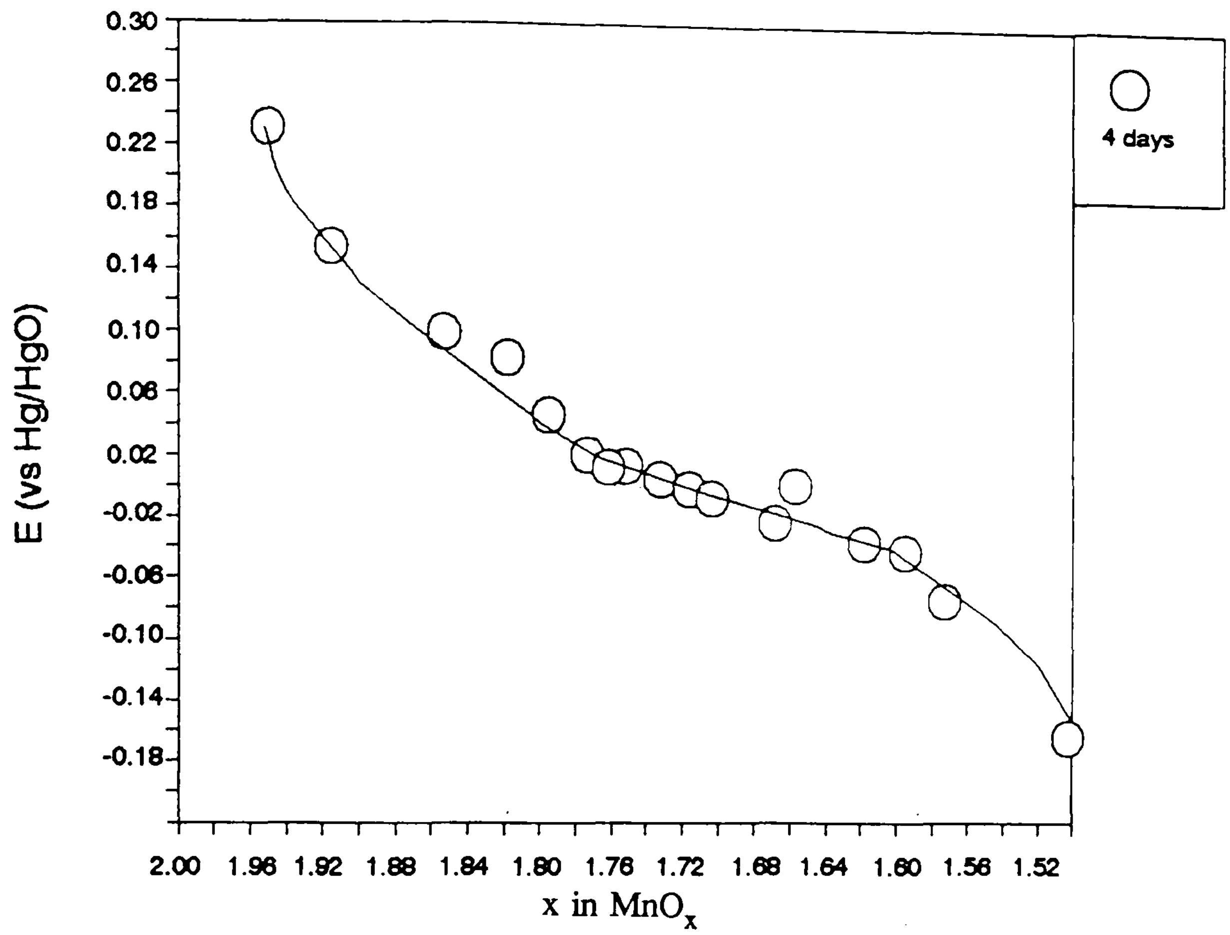

Figure 8-9 E(vs. Hg/HgO) versus x in MnO$_x$ for H inserted R2 samples after 4 days storage in 7M KOH.

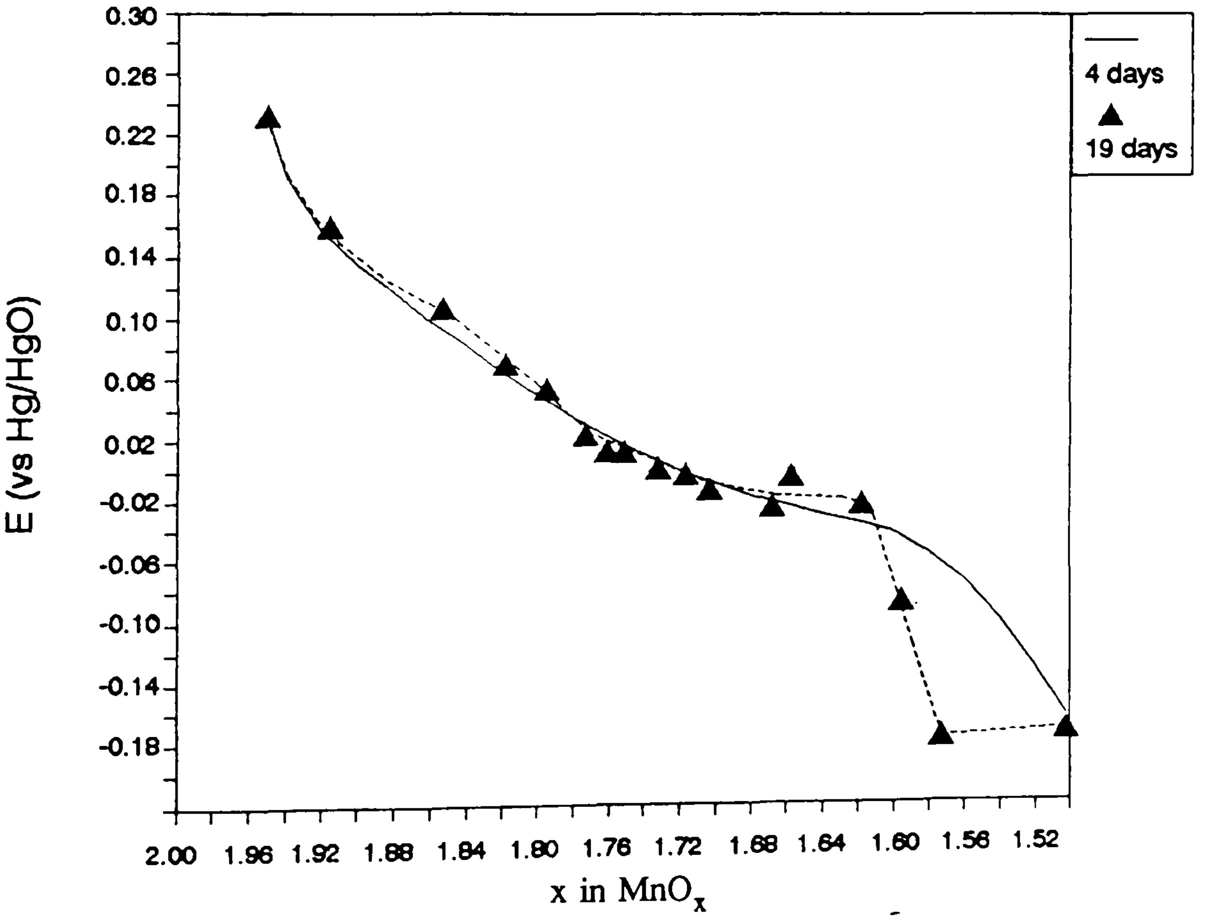

Figure 8-10 E(vs. Hg/HgO) versus x in MnO$_x$ for H inserted R2 samples after 19 days storage in 7M KOH.

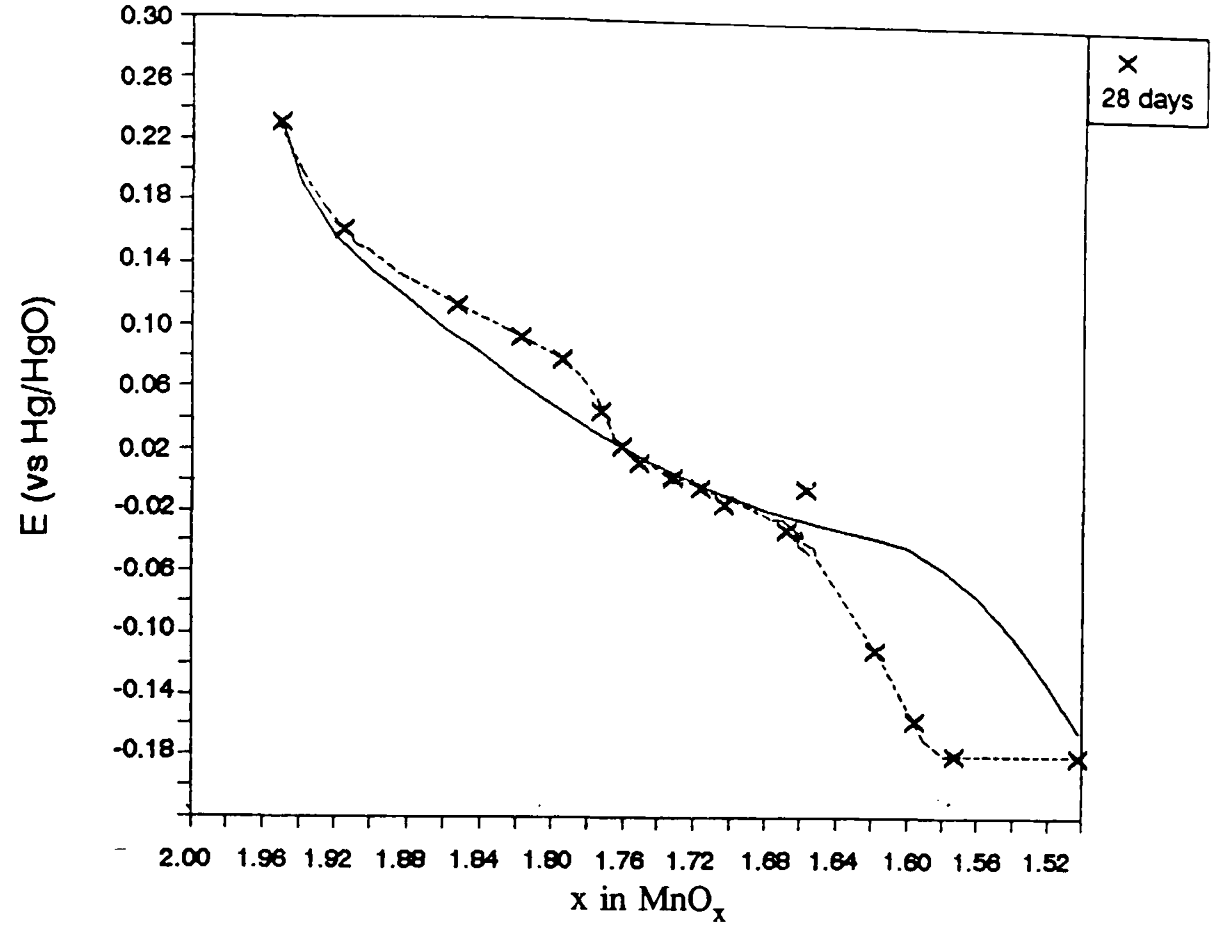

Figure 8-11 E(vs. Hg/HgO) versus x in $MnO_x$ for H inserted R2 samples after 28 days storage in 7M KOH.

solution potential range it is clear the overall shape is a combination of two different curves. The first extends from the initial potential to that at $MnO_{1.86}$ and the second from $MnO_{1.86}$ to $MnO_{x=1.60}$. If the break at x=1.60 in $MnO_x$ is due to instability of the H inserted oxide, it is probable that the second curve extends to $MnO_{1.50}$ in the absence of instability.

The lower end of the potentials in the region $MnO_{1.86}$ to $MnO_{1.60}$ appear to decrease towards the values between $MnO_{x=1.60}$ to $MnO_{1.50}$, as suggested by figures 8-13 and 8-14. Figure 8-15, however, does not confirm this trend. Those in the most reduced zone (i.e. from $MnO_{1.50}$ to $MnO_{x=1.60}$) fall towards -0.16(V) (average of results in this window for 42 days storage, with $\delta_{n-1}$=0.006(V)) which is the same as for the horizontal potential zones discovered for F.M and R2/IBA no.19 H inserted samples (sections 8.3.1 and 8.3.2).

### 8.3.4 SBPA.

The potential versus composition curve for this material is quite unlike the previous materials, see figure 8-16. An almost linear decrease in potential is observed

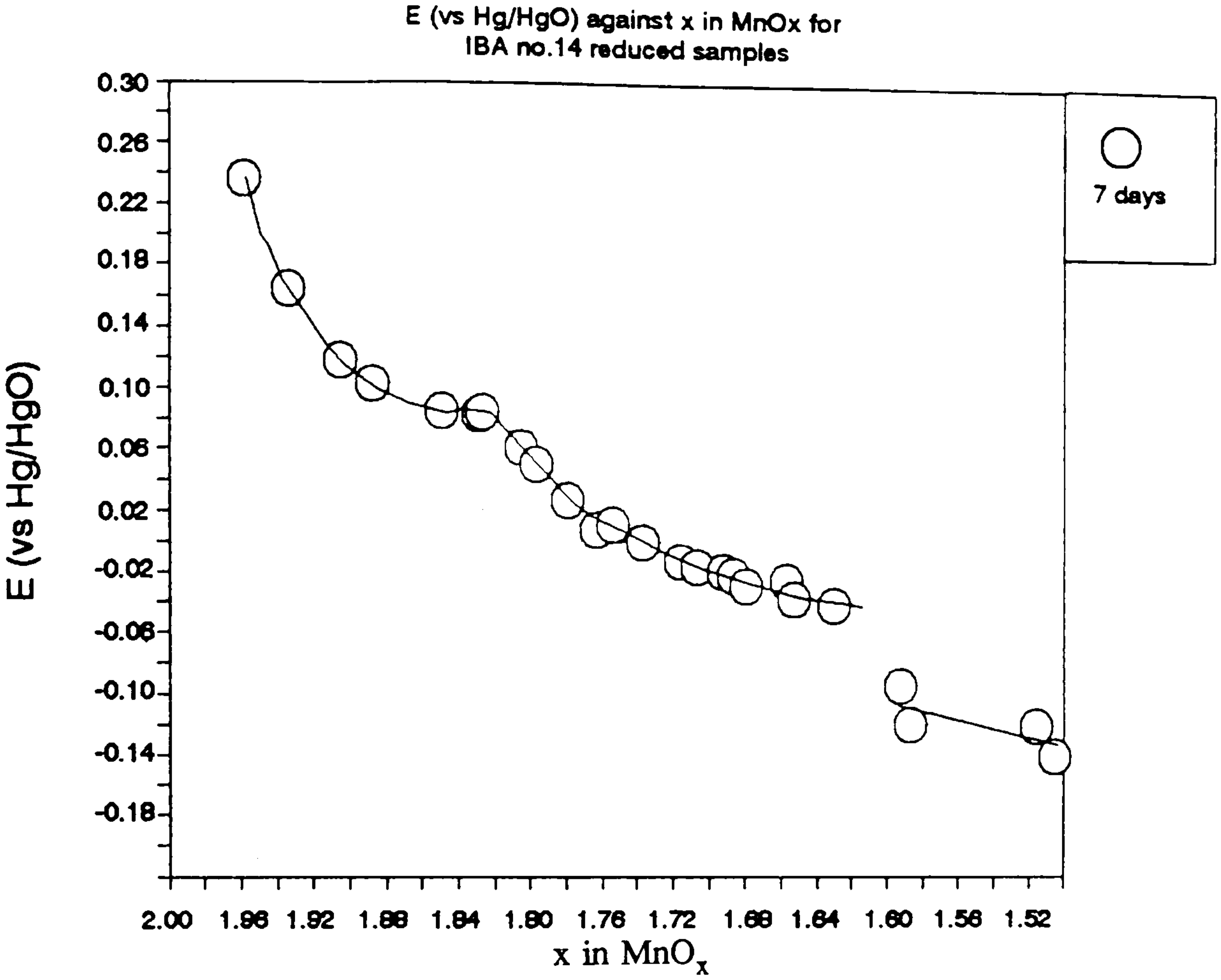

Figure 8-12 E(vs. Hg/HgO) versus x in MnO$_x$ for H inserted IBA no.14 samples after 7 days storage in 7M KOH.

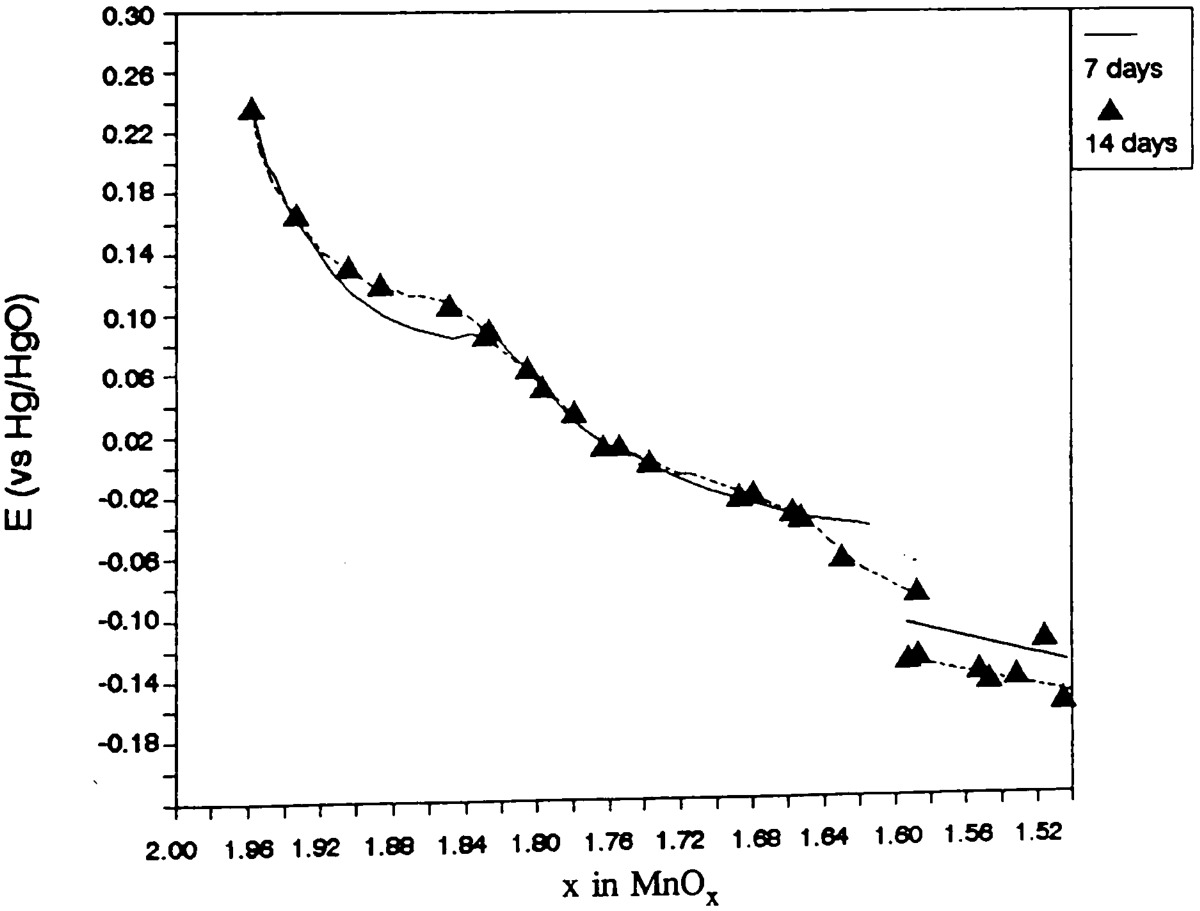

Figure 8-13 E(vs. Hg/HgO) versus x in MnO$_x$ for H inserted IBA no.14 samples after 14 days storage in 7M KOH.

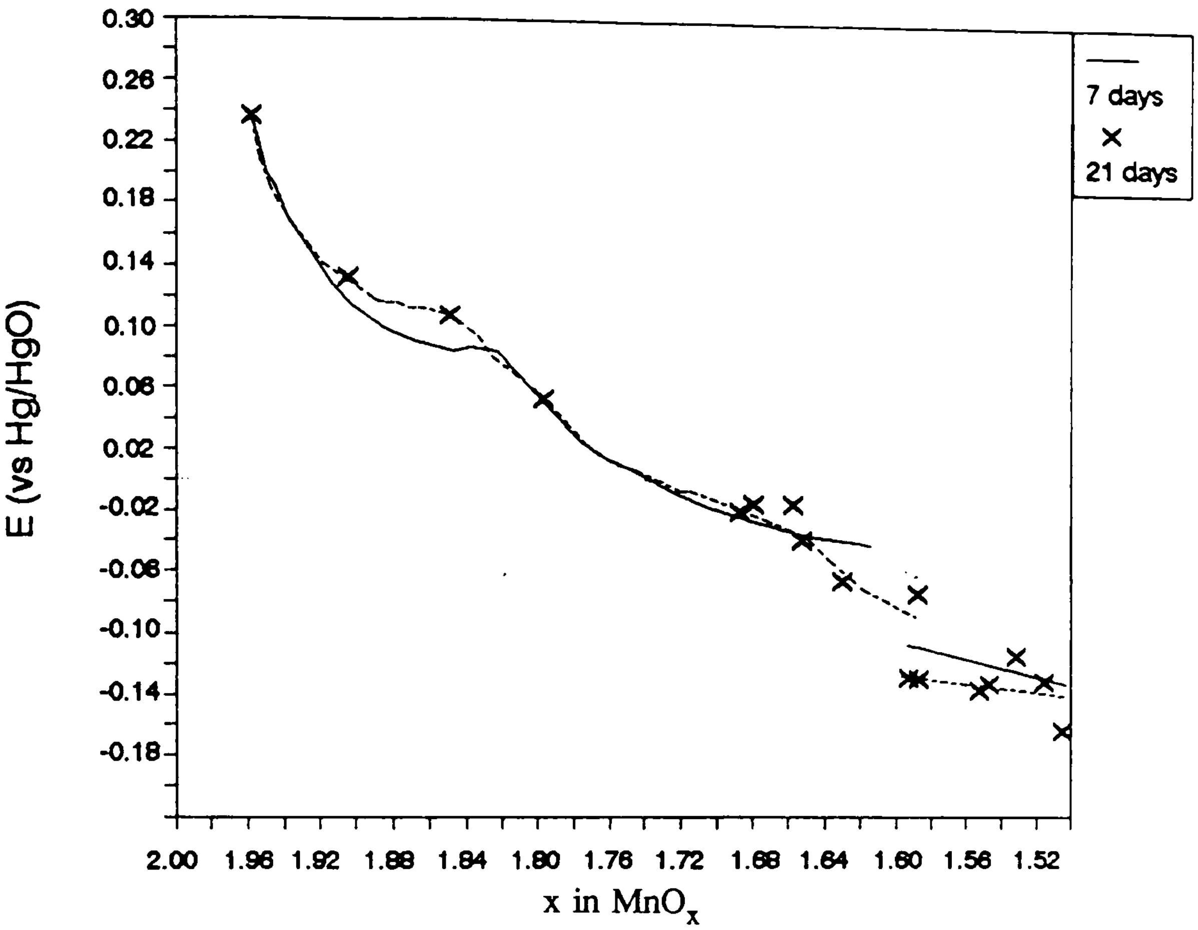

Figure 8-14 E(vs. Hg/HgO) versus x in MnO$_x$ for H inserted IBA no.14 samples after 21 days storage in 7M KOH.

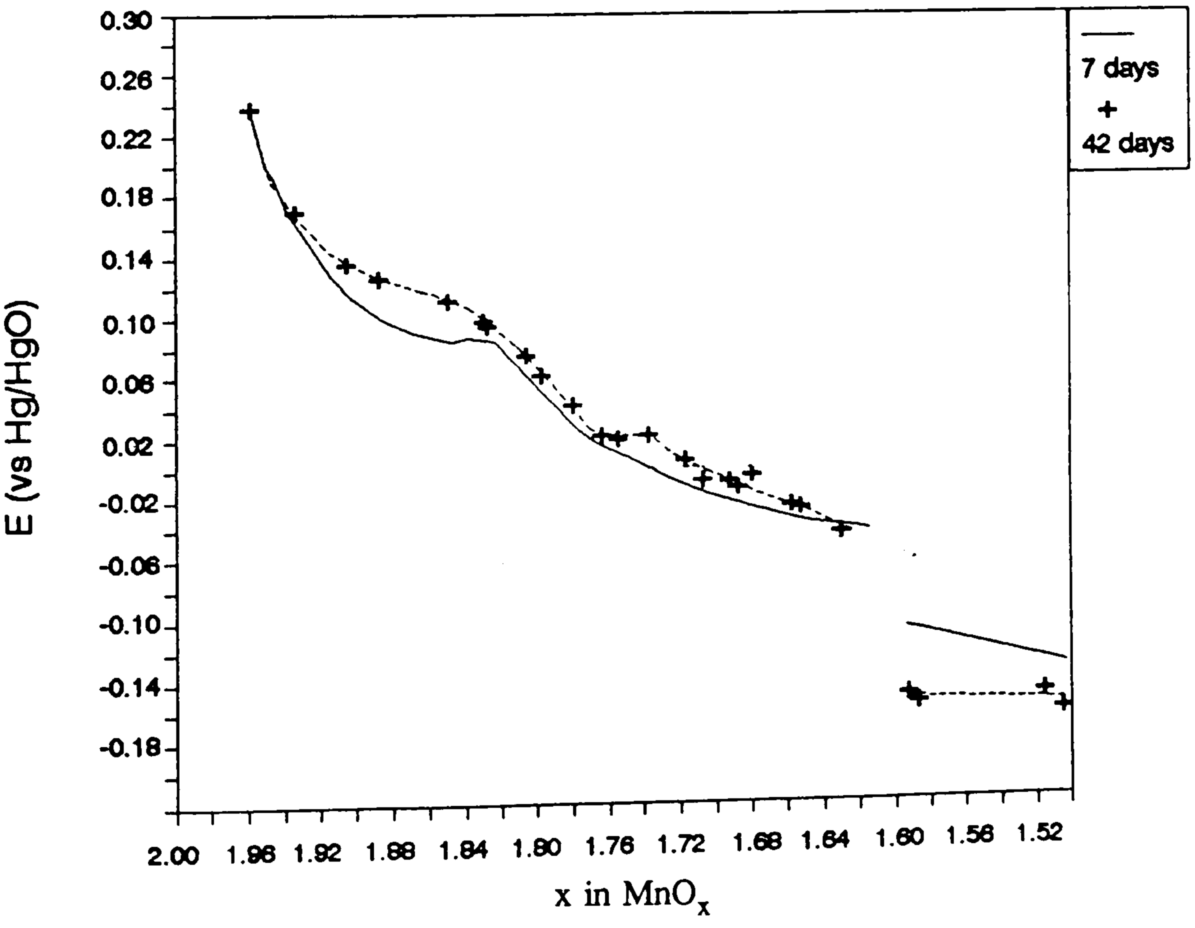

Figure 8-15 E(vs. Hg/HgO) versus x in MnO$_x$ for H inserted IBA no.14 samples after 42 days storage in 7M KOH.

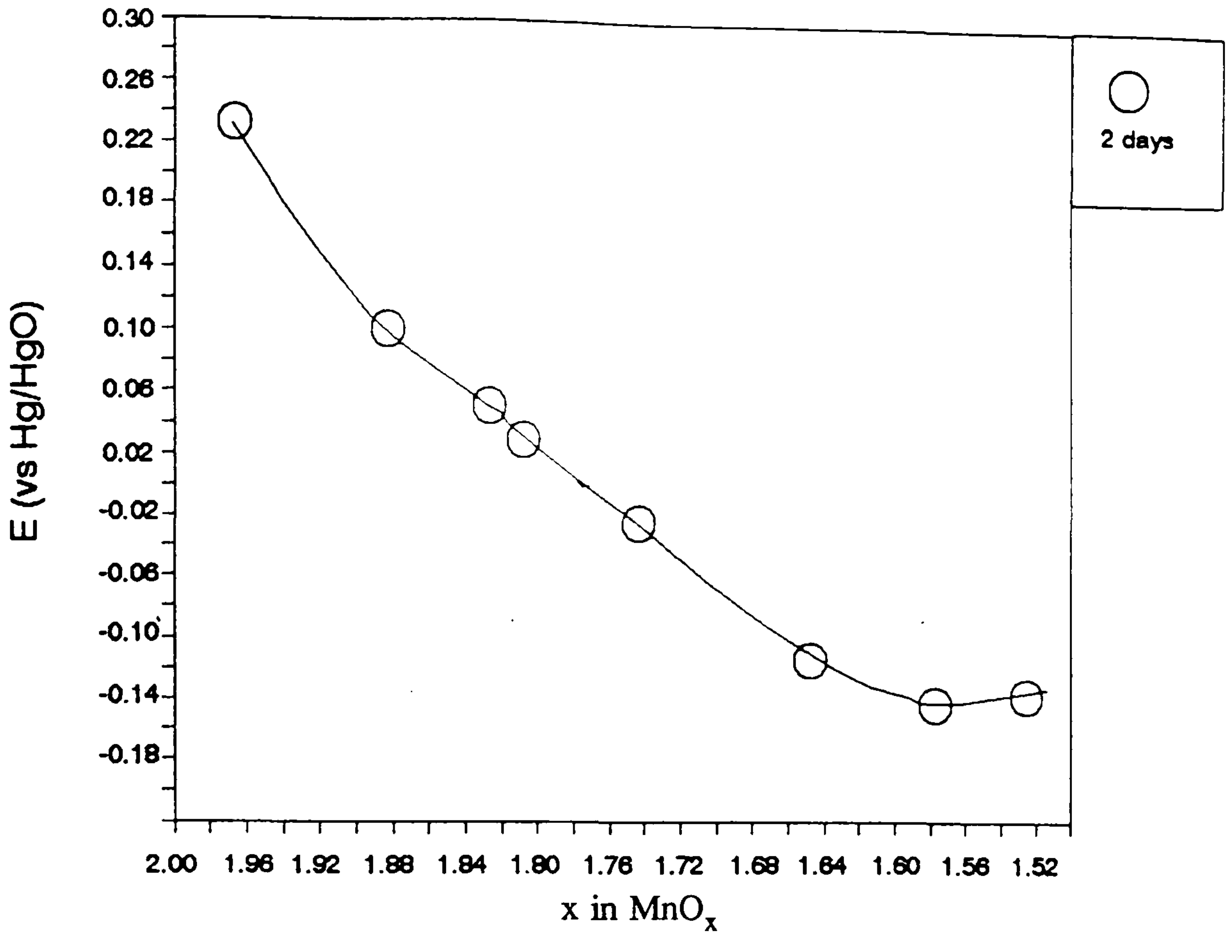

Figure 8-16 E(vs. Hg/HgO) versus x in $MnO_x$ for H inserted SBPA samples after 2 days storage in 7M KOH.

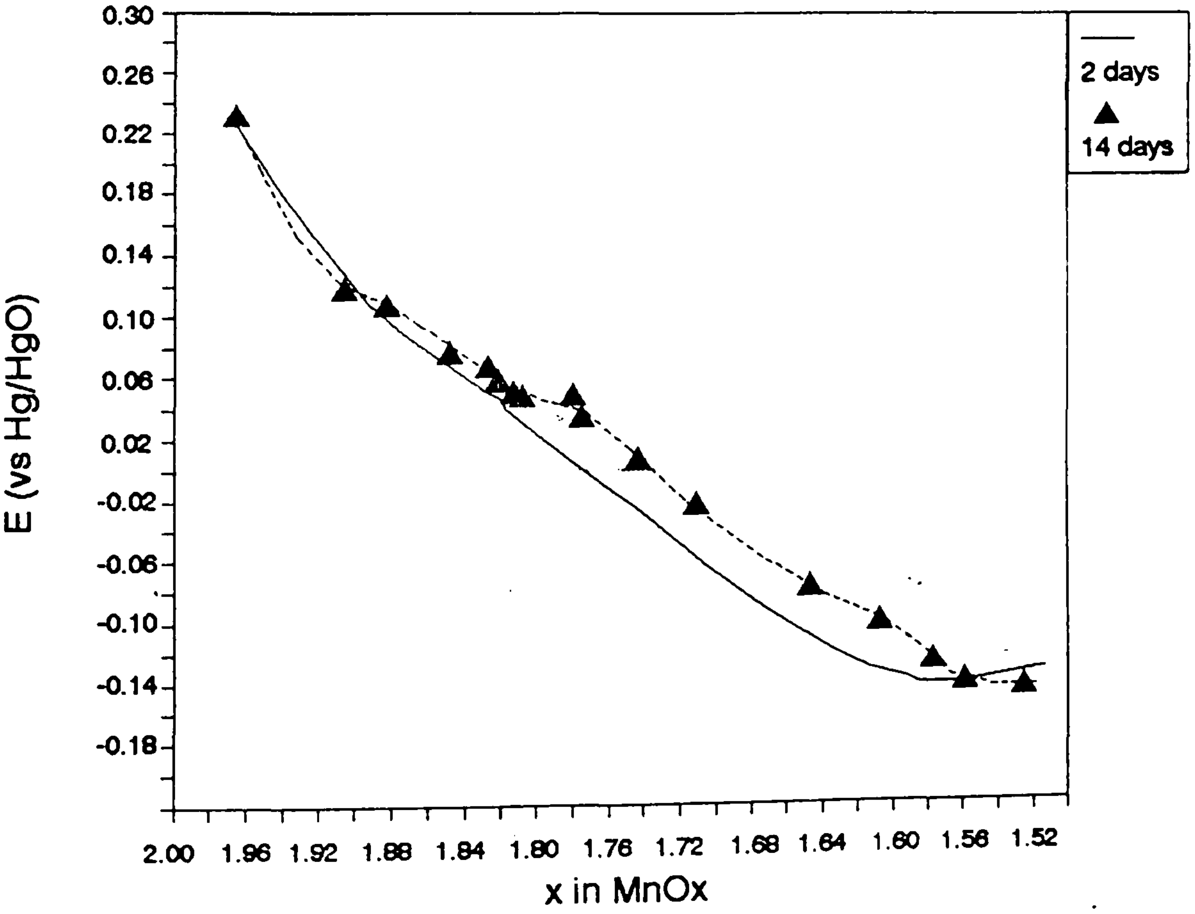

Figure 8-17 E(vs. Hg/HgO) versus x in $MnO_x$ for H inserted SBPA samples after 14 days storage in 7M KOH.

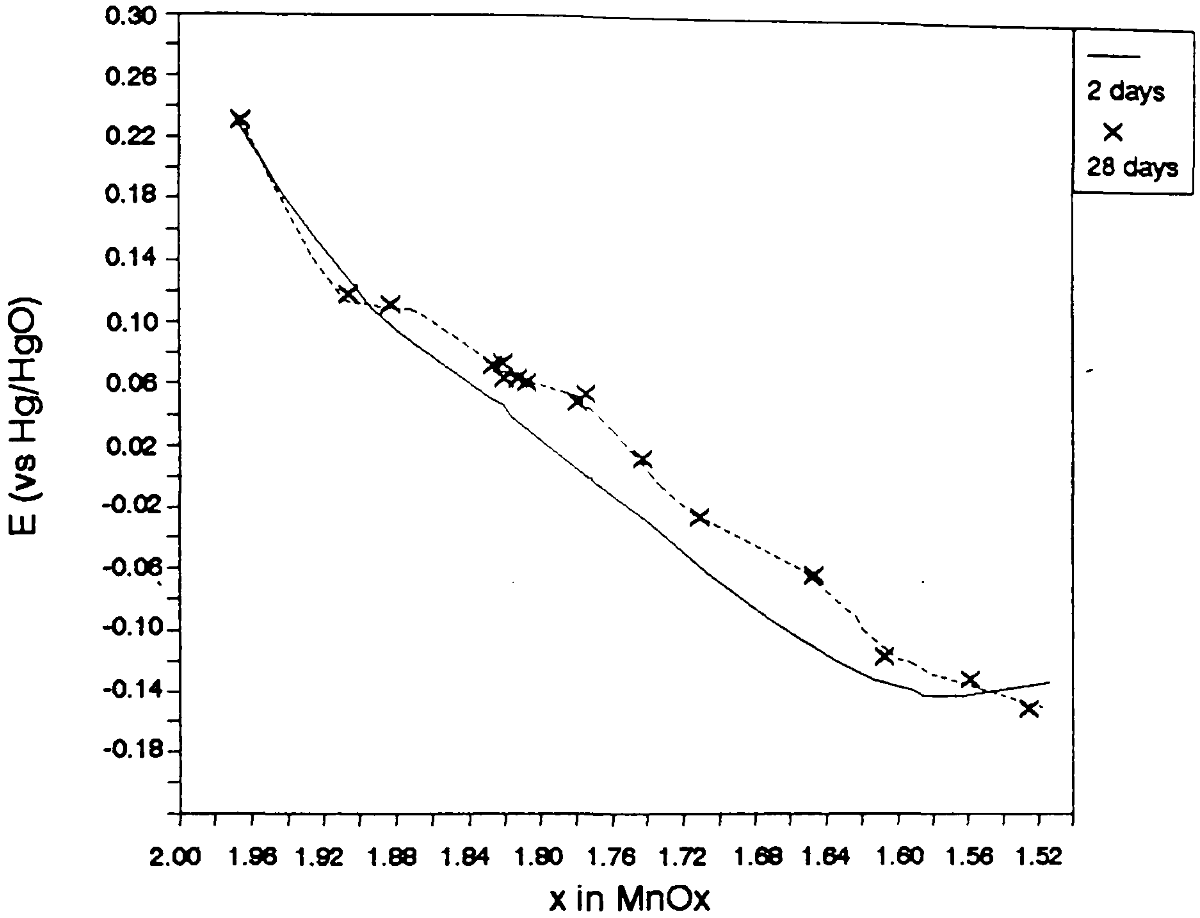

Figure 8-18 E(vs. Hg/HgO) versus x in $MnO_x$ for H inserted SBPA samples after 28 days storage in 7M KOH.

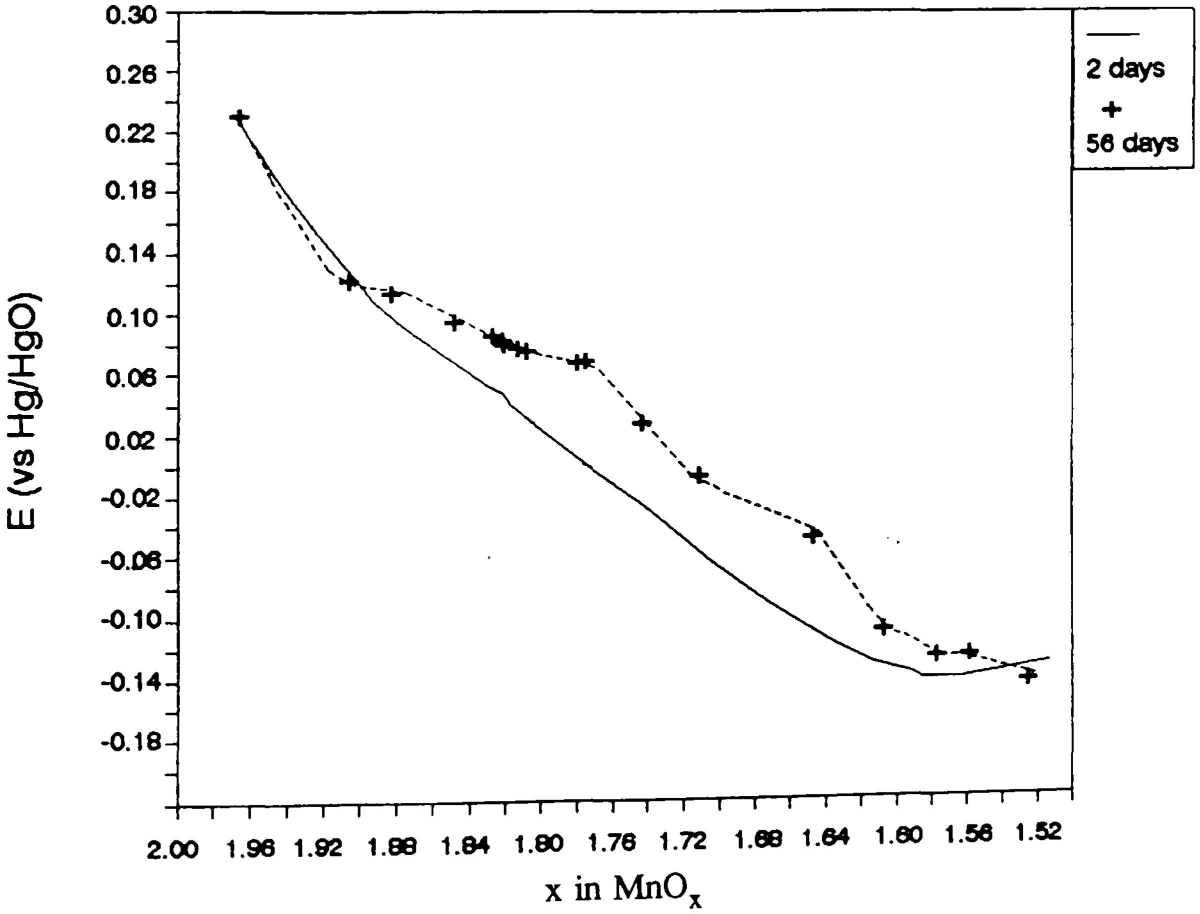

Figure 8-19 E(vs. Hg/HgO) versus x in $MnO_x$ for H inserted SBPA samples after 56 days storage in 7M KOH.

from $MnO_{1.966}$-$MnO_{1.58}$ from whereon a small horizontal region is observed. This gradually disappears with time, see figures 8-17, 8-18, 8-19 and a tendency for the potential versus x slope to increase is observed in the approximate composition range $MnO_{1.93}$ to $MnO_{1.76}$. A general tendency towards higher potentials is observed except for the initial (at $MnO_{1.961}$) which remains constant and the most reduced sample $MnO_{1.525}$, which decreases, the final value (i.e. after 56 days storage) is $-0.14_5$(V).

## 8.4 X-ray diffraction of samples stored in 7M KOH under air.

X-ray diffraction of the most H inserted samples of all the materials after storage indicate a gradual transformation into $\delta$-$MnO_2$ and apparently no other phases. Careful examination reveals that they are mixtures of the $MnOOH_r$ initial H inserted product, $\delta$-$MnO_2$, and $\gamma$-MnOOH as shall be presented in the following. Formation of $\delta$-$MnO_2$ has been reported previously in the discharge of alkaline manganese cells[131,132].

Consider figure 8-20 (a),(b) and (c) which indicate the changes which occurred to deeply H inserted samples of battery active manganese dioxide with 33 days storage in KOH under air (in a sealed container). The formation of $\delta$-$MnO_2$ is unambiguously identified by comparison with 8-20(d), which is a synthetic birnessite (see next paragraph). Other changes from the $\delta$-MnOOH patterns (i.e. before immersion in KOH) are probably explained by the inclusion of small amounts of $\gamma$-MnOOH as a comparison with 8-20(e) reveals. All the peaks in $\gamma$-MnOOH, however, are overlapped with $\delta$-MnOOH peaks except the small peak marked ($\gamma$). Furthermore the 100% $\gamma$-MnOOH peak is very close to the second most intense $\delta$-$MnO_2$ peak (compare 8-20 (d) and (e)). Thus its presence is difficult to detect unambiguously.

That the proportion of $\delta$-$MnO_2$ and $\gamma$-MnOOH increases with time is supported by figures 8-21 and 8-22 which indicate the state of very H inserted materials after periods of 3 weeks and 3 months storage. Note that the wet method of sample preparation was used which in this case produced a large liquid scattering contribution to the patterns.

Figure 8-23 compares three synthetically prepared $\delta$-$MnO_2$ compounds with a stored H inserted F.M compound showing little evidence of any residual initial (i.e. before immersion in KOH) H inserted material. The presence of $\delta$-$MnO_2$ is unambiguously identified by the peaks occurring at ~7(Å) (12.6(°2θ)) and ~3.5 (Å)

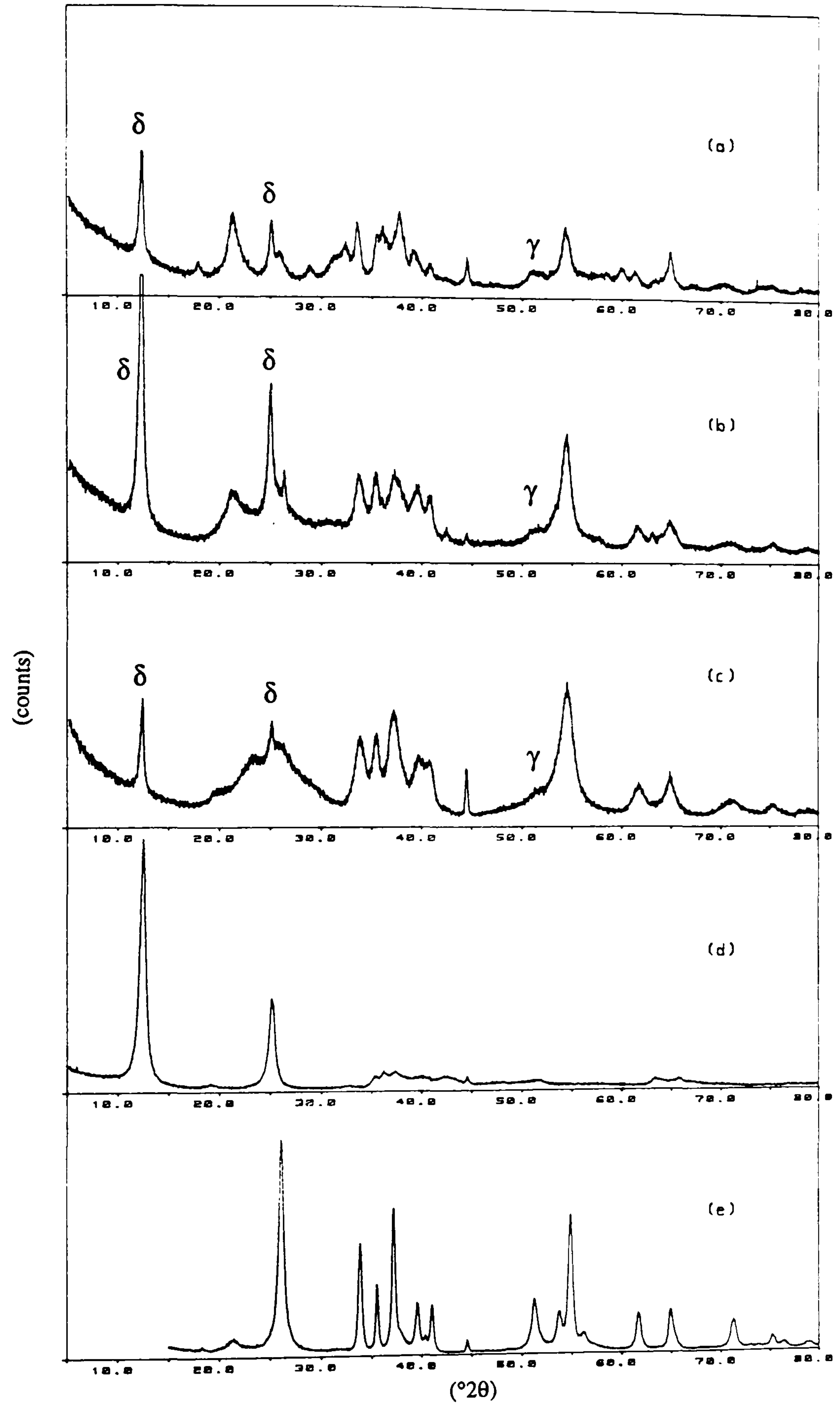

Figure 8-20 X-ray diffraction patterns of H inserted battery active manganese dioxide stored in 7M KOH under air for 33 days compared samples of synthetic birnessite and manganite. (a) H inserted SBPA, MnO$_{1.52}$, (b) H inserted R2, MnO$_{1.50}$, (c) H inserted F.M, MnO$_{1.50}$, (d) synthetic birnessite (same as in figure 8-23 (c)), (d) manganite produced from refluxing δ-MnOOH in water (same as in figure 3-4 (c)). Note that the intensity scale in (d) and (e) is 4× that of (a), (b) and (c). δ marks unambiguous δ-MnO$_2$ peaks and γ γ-MnOOH peaks.

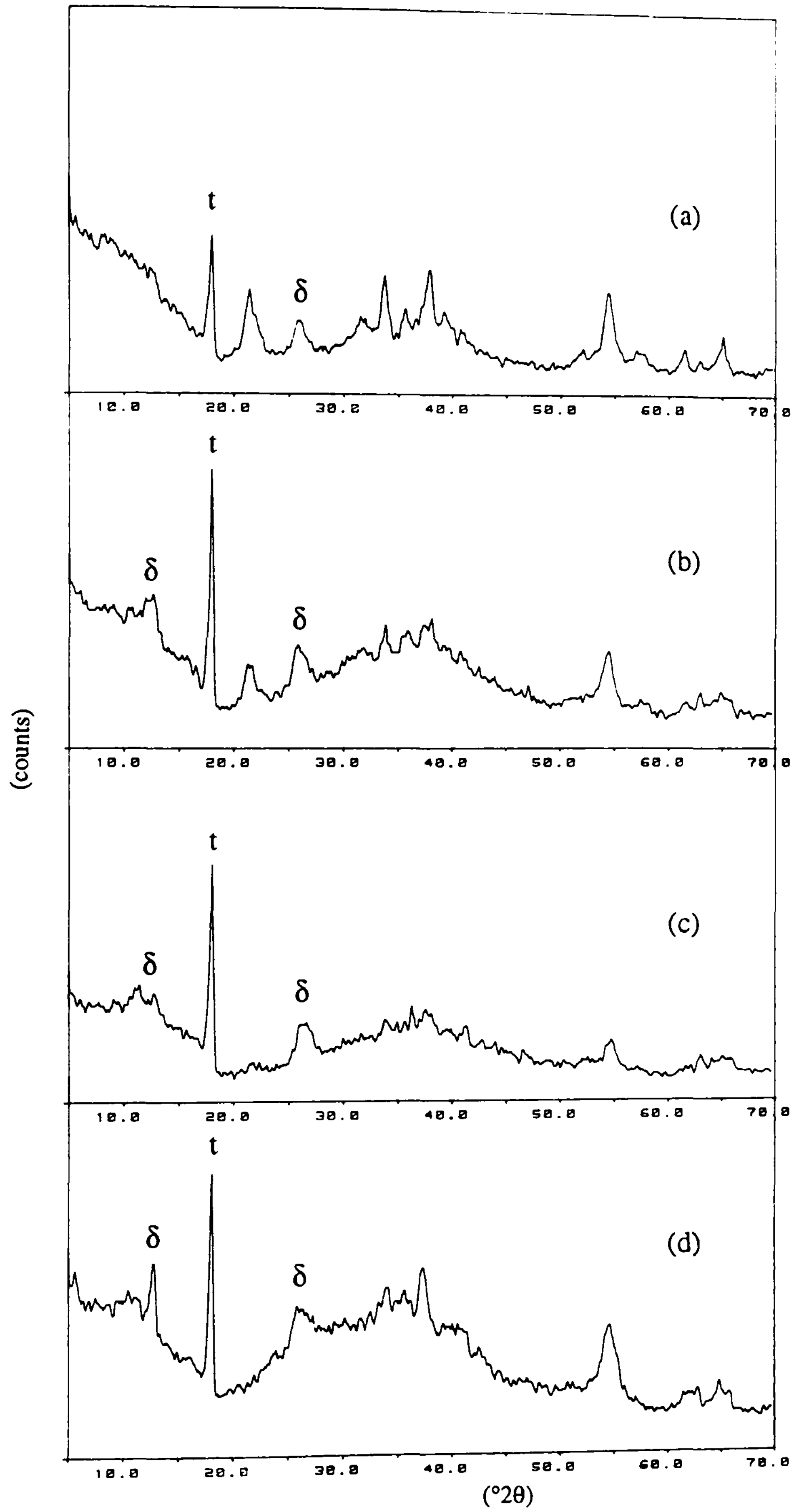

Figure 8-21 X-ray diffraction patterns of H inserted battery active manganese dioxide stored in 7M KOH under air for 3 weeks. (a) H inserted SBPA, $MnO_{1.607}$, (b) H inserted IBA no.14, $MnO_{1.593}$, (c) H inserted IBA no.19, $MnO_{1.600}$, (d) H inserted F.M, $MnO_{1.601}$. t - marks a teflon peak from the sample holder.

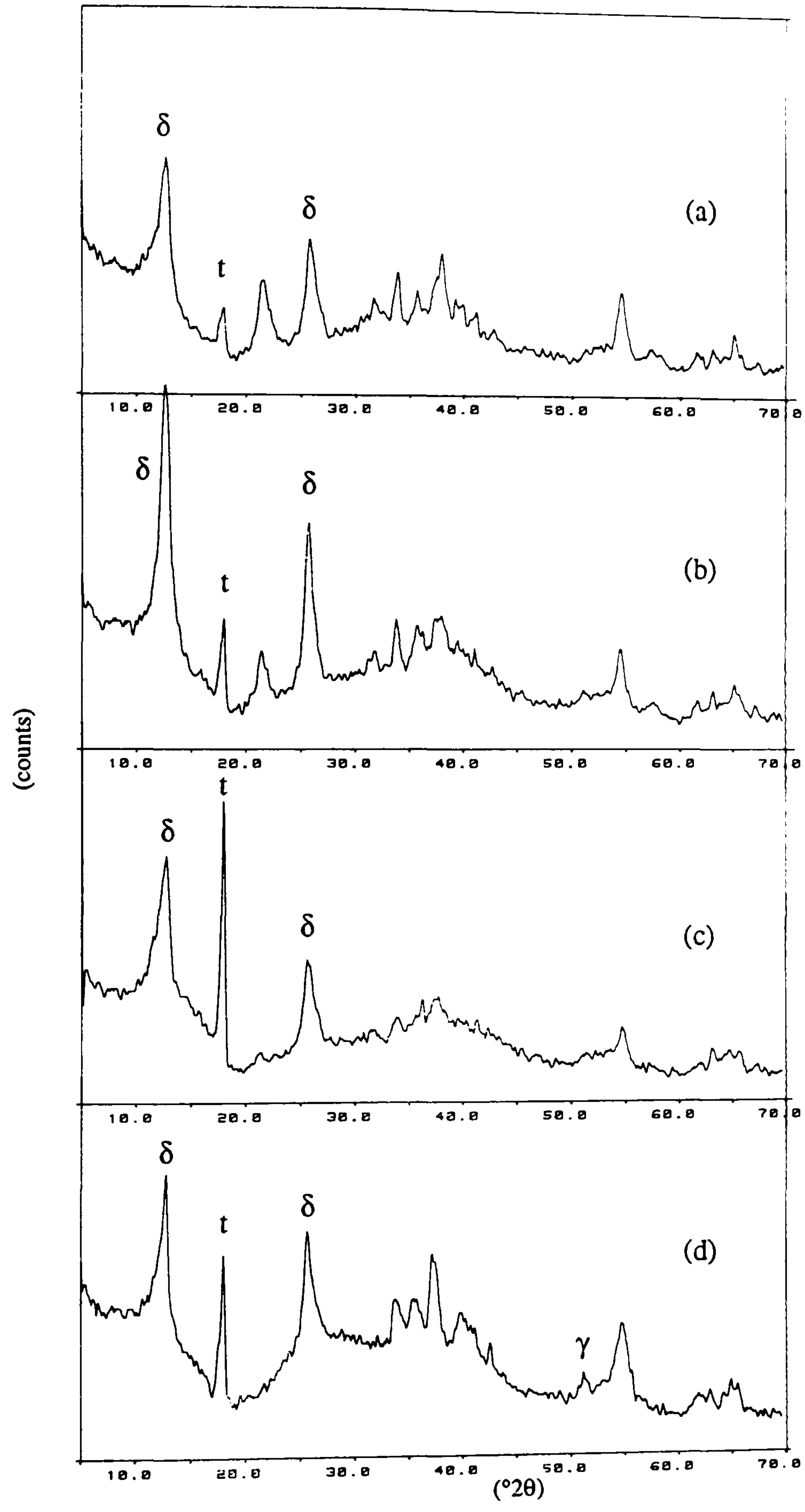

Figure 8-22 X-ray diffraction patterns of H inserted battery active manganese dioxide stored in 7M KOH under air for 3 months. (a) H inserted SBPA, $MnO_{1.607}$, (b) H inserted IBA no.14, $MnO_{1.593}$, (c) H inserted IBA no.19, $MnO_{1.600}$, (d) H inserted F.M, $MnO_{1.601}$. t - marks teflon from the sample holder.

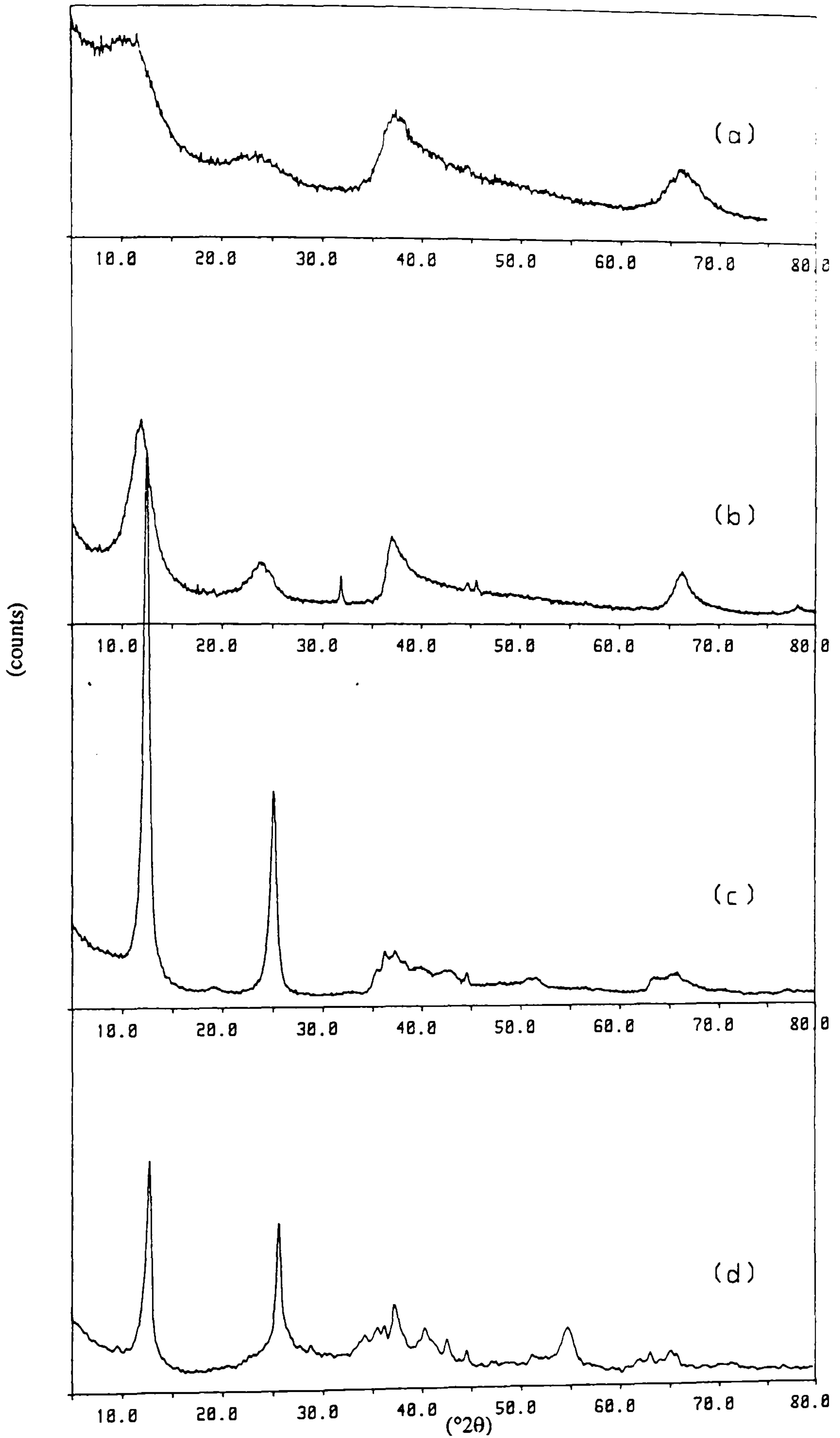

Figure 8-23 X-ray diffraction patterns of synthetic birnessite compared with a sample of H inserted manganese dioxide stored in KOH for 3 months. (a) obtained as a byproduct from an industrial synthesis (Boots) (b) preparation method unknown (c) produced by the method of Giovanoli Stähli and Feitknecht[134] (d) H inserted F.M ($MnO_{1.601}$) after 3 months storage in KOH under $N_2$.

(25.4(°2θ)).

'$\delta$-$MnO_2$' has been classified by Giovanoli as a member of the birnessite group or 7Å phyllomanganates[2,133] and is therefore not a true $MnO_2$ modification since these compounds usually contain other elements and when they do not the stoichiometry never[†] approaches $MnO_2$. '$\delta$-$MnO_2$' is therefore a misnomer but shall nevertheless be retained as is the convention in literature connected with batteries. Figure 8-23 (a)-(c) displays the variation in the x-ray pattern which can be encountered for this phase. (a) was obtained as byproduct from an industrial synthesis, (b) is also synthetic and labelled 100% pure $\delta$-$MnO_2$ (preparation method unknown) and (c) a K birnessite was prepared by the method of Giovanoli Stähli and Feitknecht[134] and is apparently more 'crystalline' product than (a) or (b). It is not known whether the occurrence of the small peaks in (b) and (c) represent impurities from the synthesis process or birnessite features. Birnessite is known to have a layer structure with the separation of the layers given by the d spacing of the 100% '7Å' peak, whose value depends on the ionic composition (i.e. whether K, Na or other ions are present in the structure). In this case 8-23 (b), in particular, suggests that the layers most probably have some degree of randomness in their orientation (in the plane of the layer) since the peak at ~38(°2θ) has a classical '2 dimensional' shape as exhibited by certain heat treated carbon blacks[135]. The other reflections are '3 dimensional' and therefore must be reflections representing directions perpendicular to the layers.

## 8.5 X-ray diffraction of samples stored in 7M KOH under an inert $N_2$ atmosphere.

Figure 8-24 shows a selection of H inserted F.M samples after 1 week storage in KOH contained in a nitrogen filled glove box at 25(°C). The experimental procedure was as follows. $N_2$ was bubbled for about 3 hours through a stock solution of 7M KOH which was then transferred via an airlock into the $N_2$ filled glovebox. The $MnOOH_r$ samples were degassed for 10 mins and the vacuum broken with nitrogen. Lids of the nalgene centrifuge tubes (containing the $MnOOH_r$) were quickly replaced and the tubes transferred to the $N_2$ filled glovebox. 10(ml) of KOH solution was subsequently added

---

[†] $Mn_7O_{13}.5H_2O$ with an oxidation level $MnO_{1.86}$ is the only member which does not contain any additional elements such as K or Na.

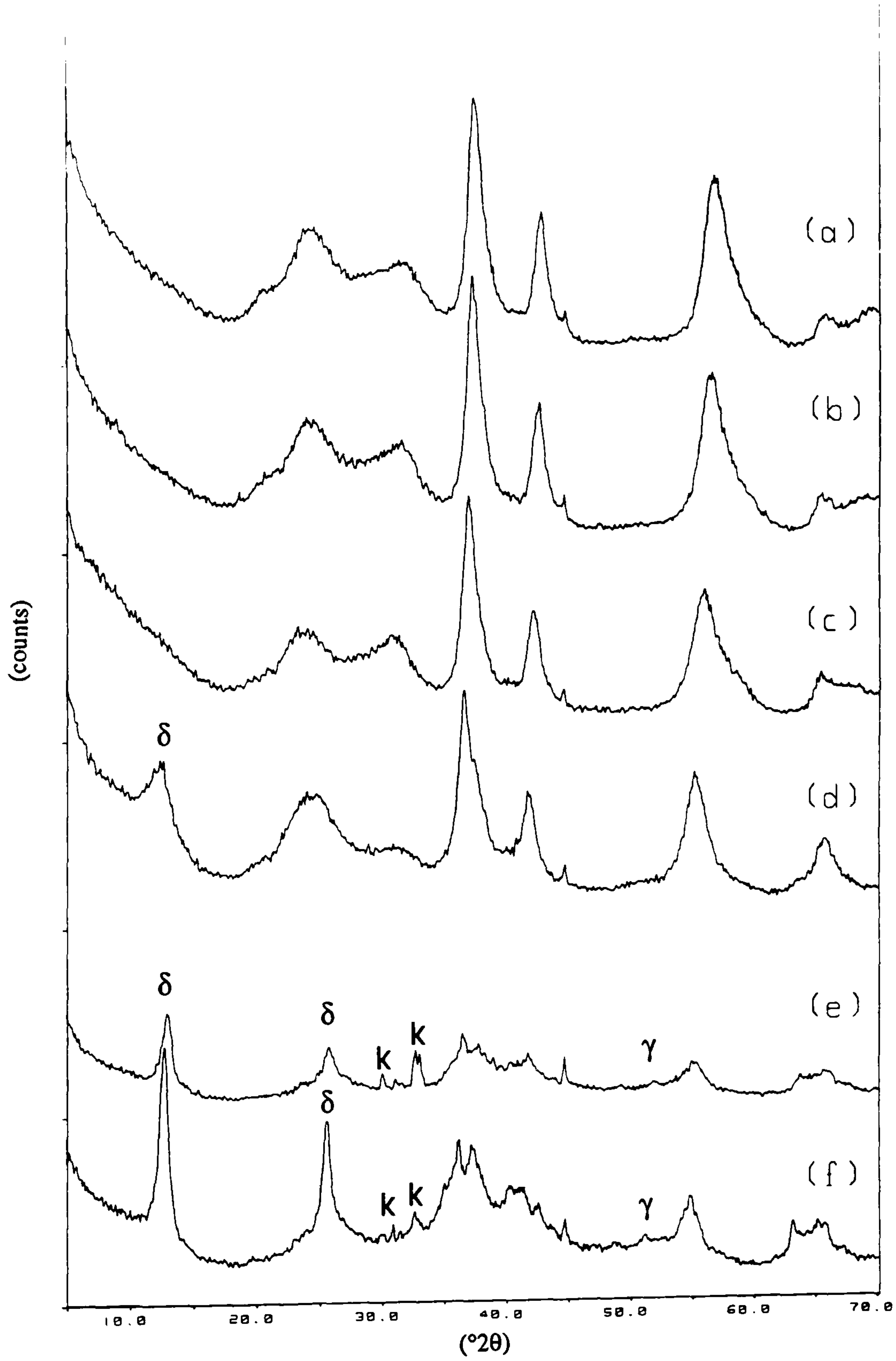

Figure 8-24 Selection of x-ray diffraction patterns representing the changes which occur with one weeks storage in 7 M KOH under $N_2$ to H inserted F.M . Samples prepared by 'wet' method. (a) $MnO_{1.944}$ (b) $MnO_{1.901}$ (c) $MnO_{1.827}$ (d) $MnO_{1.699}$ (e) $MnO_{1.647}$ (f) $MnO_{1.601}$. δ, k, γ, mark peaks which specifically belong to δ-$MnO_2$, α-KOH, or γ-MnOOH respectively.

to the samples (in the glovebox). Those for x-ray diffraction were removed as required, vacuum filtered, in a sintered glass crucible (porosity no.4) without washing and mounted as a paste in the x-ray diffraction holders. An x-ray diffraction scan was programmed to last only 30 mins. and the whole procedure from removal to obtaining a complete scan was approximately 40 mins. One unavoidable consequence of this procedure is a wide variation in the intensity of the observed x-ray patterns almost certainly due to a variable background intensity caused by liquid scattering. Evidence of this is particularly clear in 5 - 20(°2θ) Bragg angle range the curve of which is normally caused by air scattering and in this case a combination of air and water vapour scattering. The x-ray intensities are presented as recorded, all at the same intensity scale (figure 8-24). By comparing x-ray diffractograms of the starting compounds (i.e. before immersion in KOH) and those after storage in KOH the following compounds have been identified at the various oxidation states. In figure 8-24 (a) - (c) no change i.e. H inserted F.M, $MnOOH_T$, as described in section 7.4. (d) $\delta$-$MnO_2$ and $MnOOH_T$, (e) $\delta$-$MnO_2$, α-KOH and possibly γ-MnOOH. Marked on the diagram are those peaks which specifically identify the compounds listed. All other peaks may be due to a combination from the compounds listed. Account has to be taken of displacements in 2θ position from the real position due to misalignment of the surface of the paste as compared to that obtained with dry powders. Furthermore this changes as the paste drys, the surface displacing upwards out of the holder.

The presence of α-KOH is perhaps surprising but its presence is positively identified by the doublet occurring at[136] 32.2(°2θ) ($I/I_1$=100%) and 32.4(°2θ) ($I/I_1$=75%) whereas experimentally they occur at 32.6(°2θ) (100%) and 33.0(°2θ) (69%) which is within an experimental error of ±0.1(°2θ) a displacement of 0.5(°2θ). The other peaks listed in JCPDS card 21-645 (α-KOH) are all less than or equal to 20% of the maximum peak except for a peak occurring at 52.0(°2θ) which also has an analogue in observed pattern (but may also be contributed to by an H inserted F.M peak).

Figure 8-25 indicates the effect on the x-ray diffraction pattern of H inserted F.M with storage for 3 months in similar conditions. In this case also $\delta$-$MnO_2$ starts to appear between $MnO_{1.83}$ and $MnO_{1.70}$. The peaks in this case look considerably sharper indicating either a re-crystallisation has occurred or a continued growth of this phase. In each pattern where $\delta$-$MnO_2$ occurs (i.e. figure 8-25(d), (e)&(f)) the appearance of γ-MnOOH is now much more evident. There is also evidence of H inserted F.M

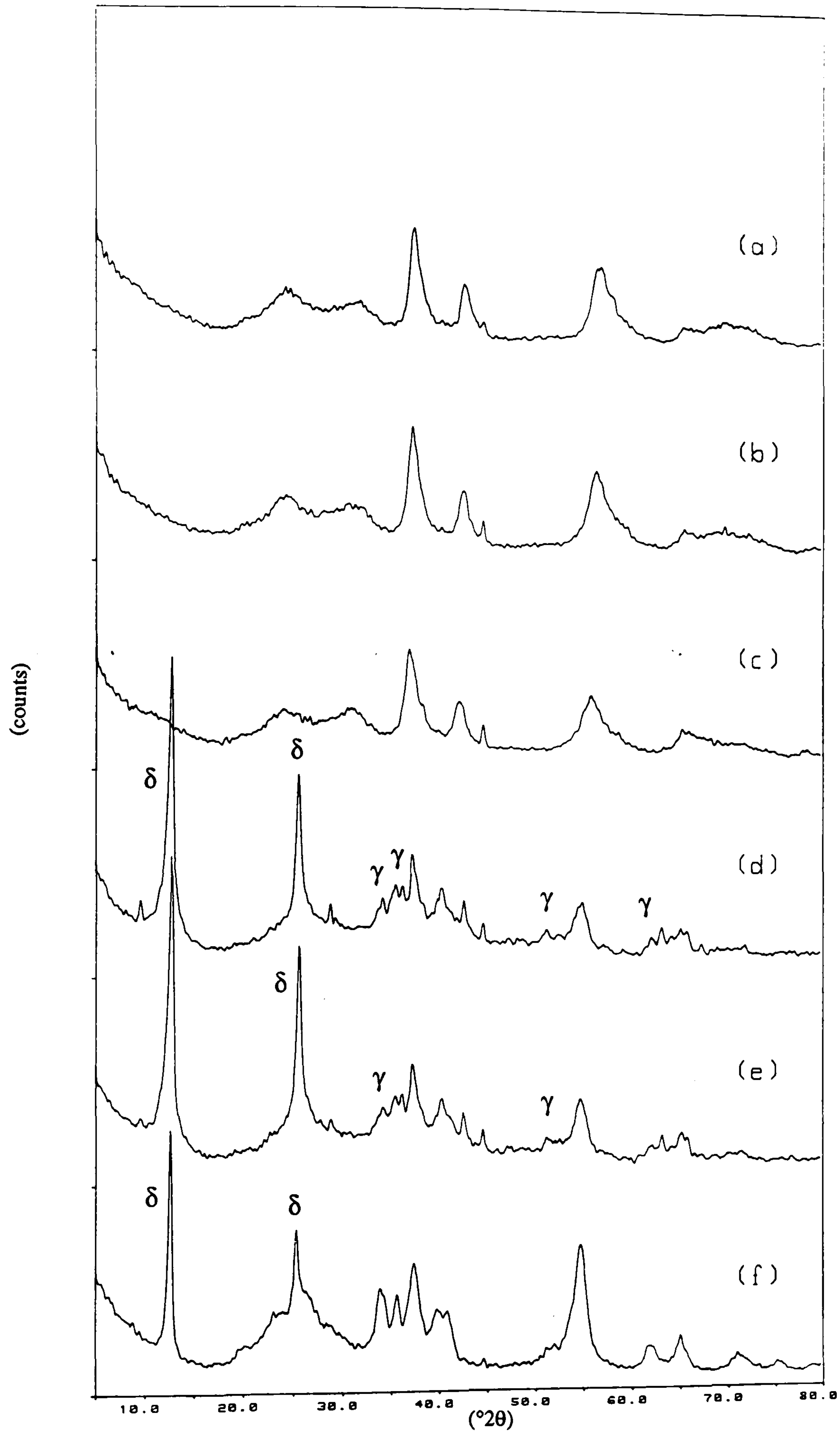

Figure 8-25 Selection of x-ray diffraction patterns representing the changes which occur with 3 months storage in 7 M KOH under $N_2$ to H inserted F.M . Samples prepared by 'wet' method. (a) $MnO_{1.944}$ (b) $MnO_{1.901}$ (c) $MnO_{1.827}$ (d) $MnO_{1.698}$ (e) $MnO_{1.601}$ (f) $MnO_{1.505}$. Peak labels as in figure 8-24.

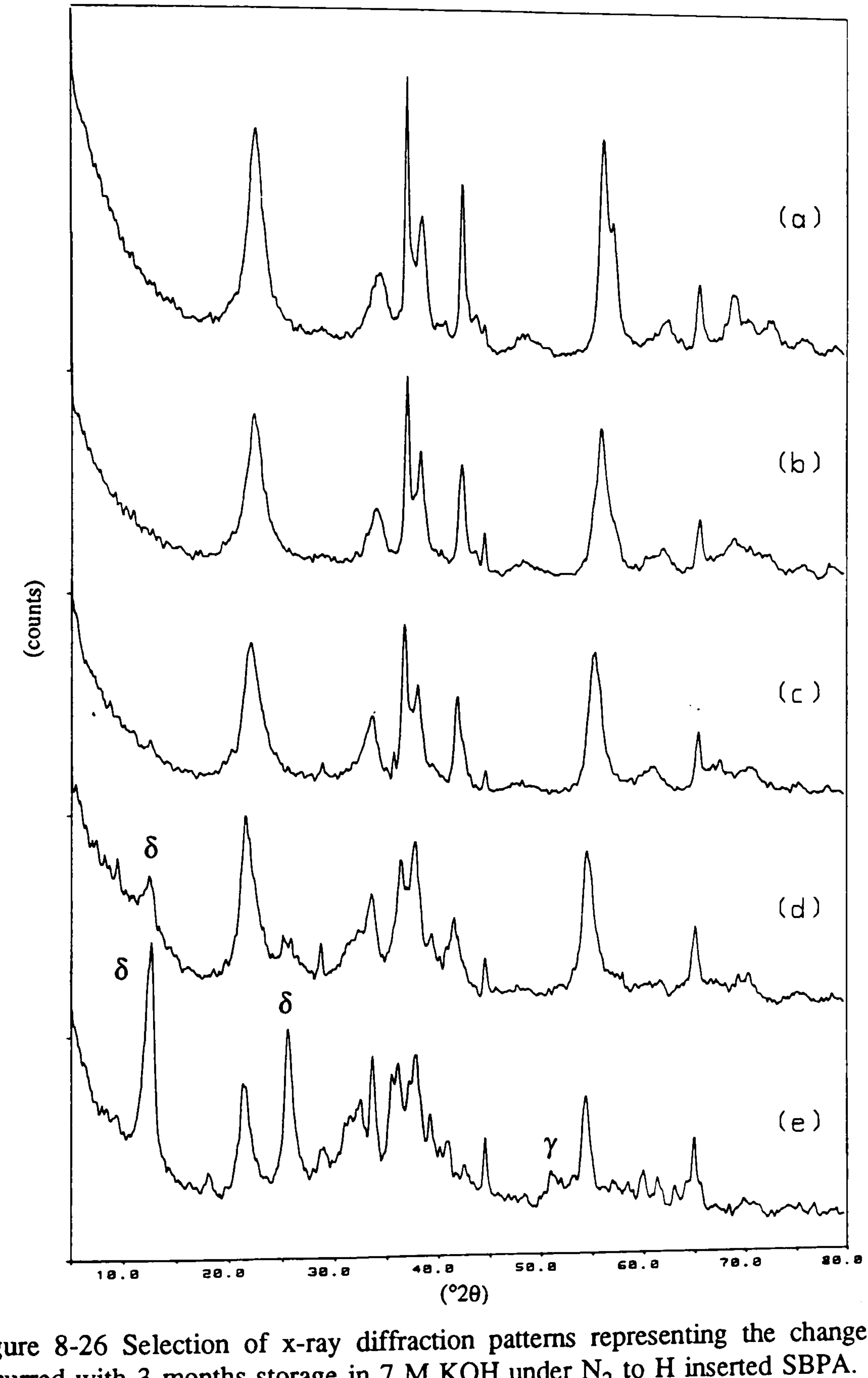

Figure 8-26 Selection of x-ray diffraction patterns representing the changes which occurred with 3 months storage in 7 M KOH under $N_2$ to H inserted SBPA. Samples prepared by 'wet' method. (a) $MnO_{1.966}$ (b) $MnO_{1.906}$ (c) $MnO_{1.808}$ (d) $MnO_{1.711}$ (e) $MnO_{1.525}$. Peak labels as in figure 8-24.

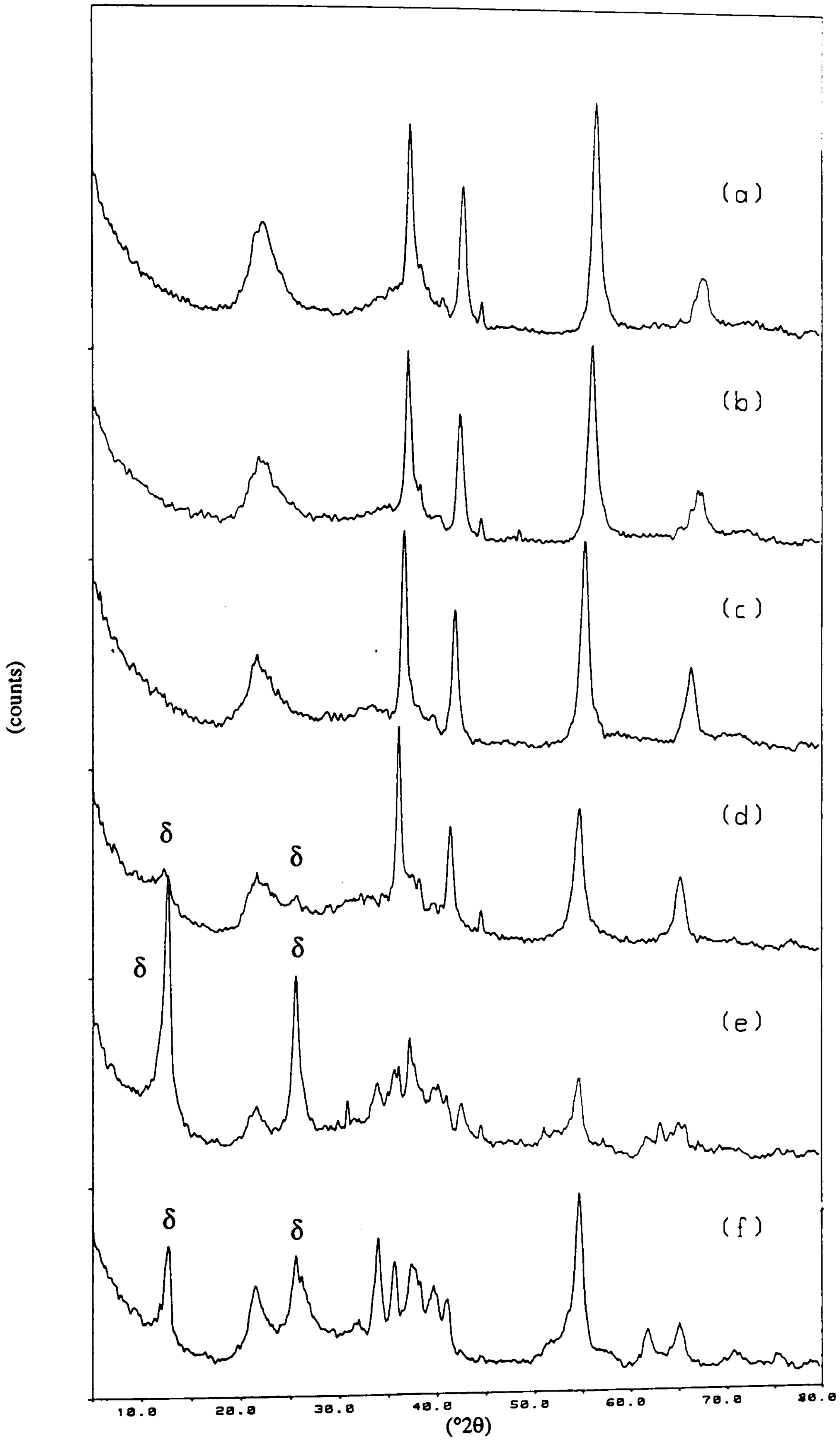

Figure 8-27 Selection of x-ray diffraction patterns representing the changes which occur with 3 months storage in 7 M KOH under $N_2$ to H inserted IBA no.19. Samples prepared by 'wet' method. (a) $MnO_{1.950}$ (b) $MnO_{1.897}$ (c) $MnO_{1.803}$ (d) $MnO_{1.687}$ (e) $MnO_{1.520}$ (f) $MnO_{1.544}$. Peak labels as in figure 8-24.

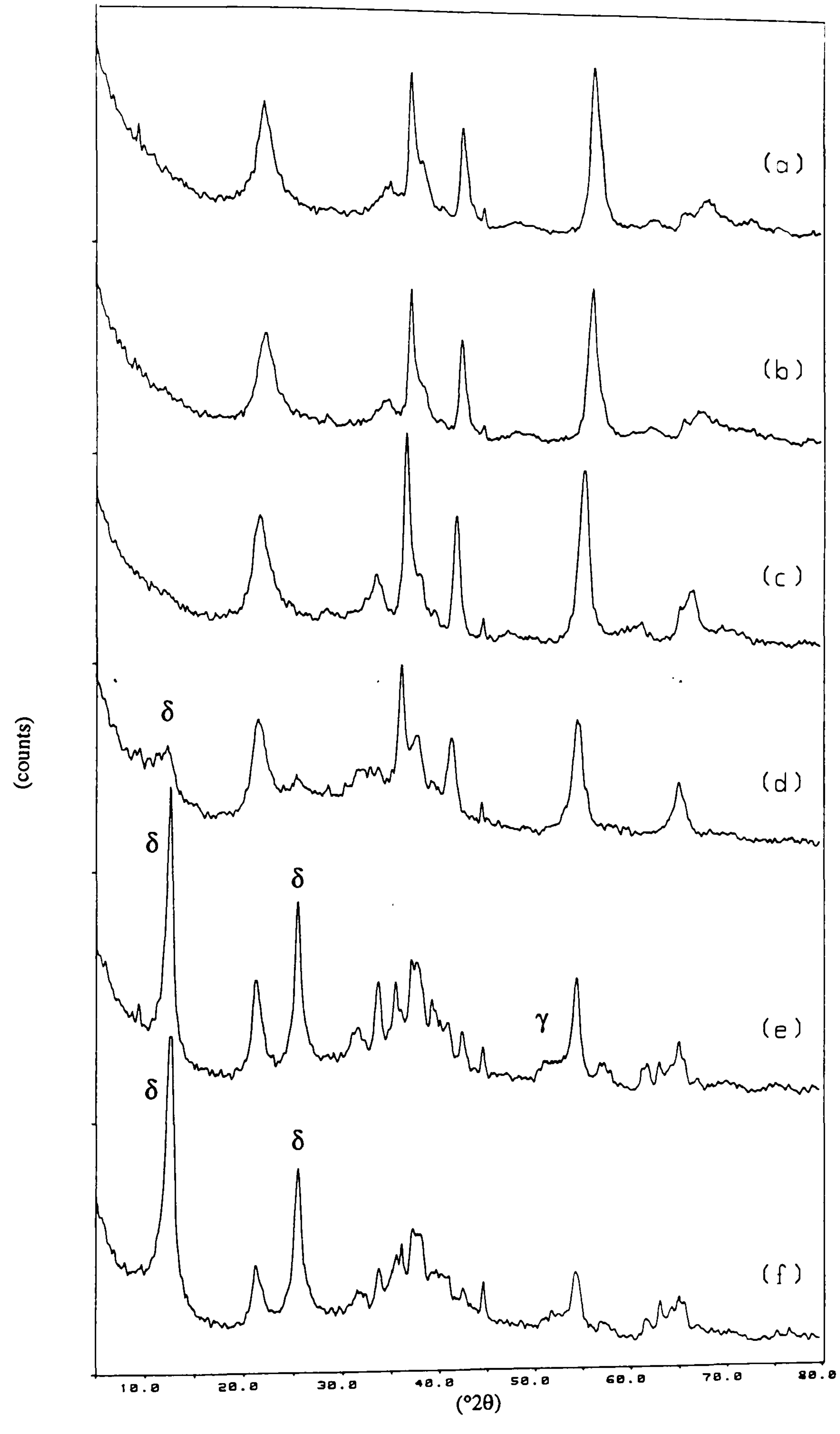

Figure 8-28 Selection of x-ray diffraction patterns representing the changes which occur with 3 months storage in 7 M KOH under $N_2$ to H inserted IBA no.14. Samples prepared by 'wet' method. (a) $MnO_{1.958}$ (b) $MnO_{1.905}$ (c) $MnO_{1.797}$ (d) $MnO_{1.687}$ (e) $MnO_{1.587}$ (f) $MnO_{1.505}$. Peak labels as in figure 8-24.

particularly in the most H inserted sample ($MnO_{1.505}$, see figure 8-25(f)). Figures 8-26, 8-27 and 8-28 present the x-ray diffraction patterns after 3 months storage in KOH under the conditions described above for the materials SBPA, IBA no.19 and IBA no.14 respectively. Careful examination reveals that changes from the H inserted product before immersion in KOH are explained by mixtures of $\delta$-$MnO_2$, $\gamma$-MnOOH the initial H inserted product and a slight amount of $\alpha$-KOH. Table 8.1 summarises where in the composition range x in $MnO_x$ in which $\delta$-$MnO_2$ was first detected. $\gamma$-MnOOH may also

Table 8.1 Summary of x in $MnO_x$ range in which $\delta$-$MnO_2$ first appears after prolonged storage in 7(M) KOH.

| Material | x range within which $\delta$-$MnO_2$ first appears when stored in KOH for 3 months. |
|---|---|
| F.M | 1.70 - 1.65 |
| IBA no.19 | 1.80 - 1.69 |
| IBA no.14 | 1.80 - 1.70 |
| SBPA | 1.74 - 1.69 |

be present but for small amounts of $\delta$-$MnO_2$ its presence is not easily detected. This is because the second most intense $\delta$-$MnO_2$ peak (d=3.49(Å), 25.52(°2θ)) nearly coincides with the 100% $\gamma$-MnOOH peak (d=3.41(Å), 26.13(°2θ))[97]. Evidence of a split peak is sometimes observed in the appropriate 2θ range, see for example figure 8-26.

It is noted at this stage that cementation occurred for all samples in which $\delta$-$MnO_2$ was detected. A solid 'plug' was eventually formed in the bottom of the nalgene test tubes for long stored H inserted samples.

## 8.6 SEM results on the same set of stored samples.

SEM on the same set of samples supports the presence of the potassium containing compounds identified by x-ray diffraction.

### 8.6.1 Initial appearance.

SEM photographs of the initial materials are presented in figures 8-29, 8-30, 8-31, 8-32, 8-33, 8-34. WSZ is included, although its stability in KOH solutions has not

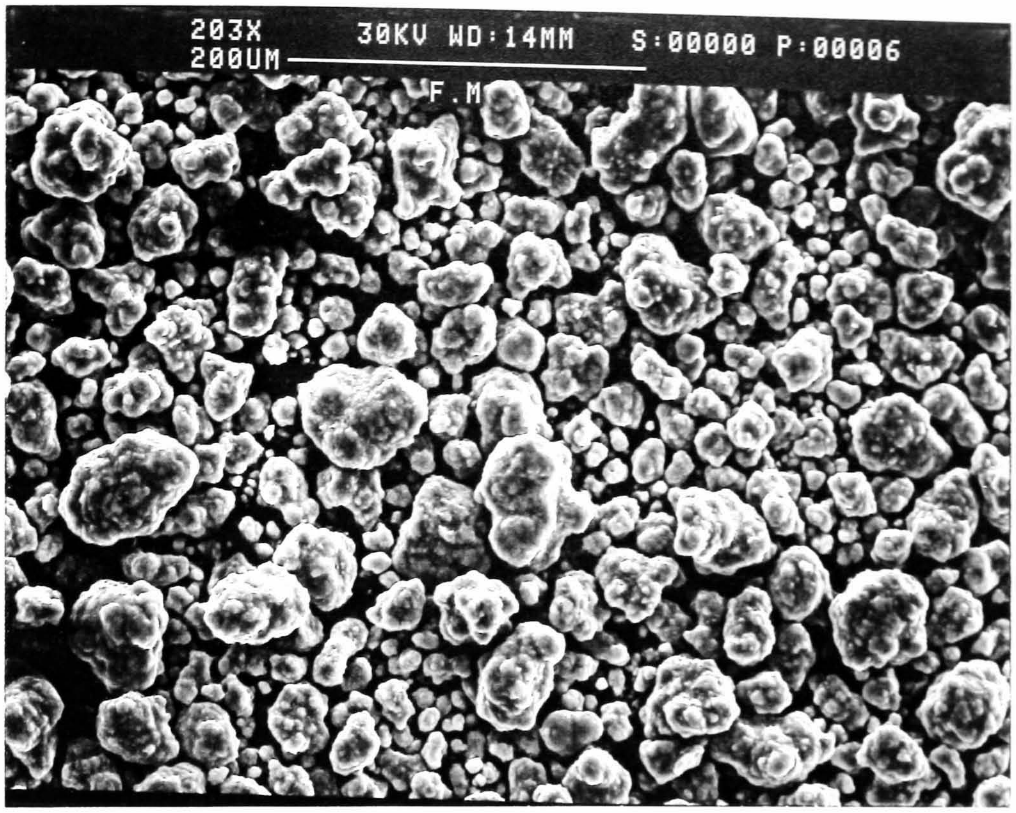

Figure 8-29 SEM photograph of initial manganese dioxide Faradiser M (abbrv. F.M).

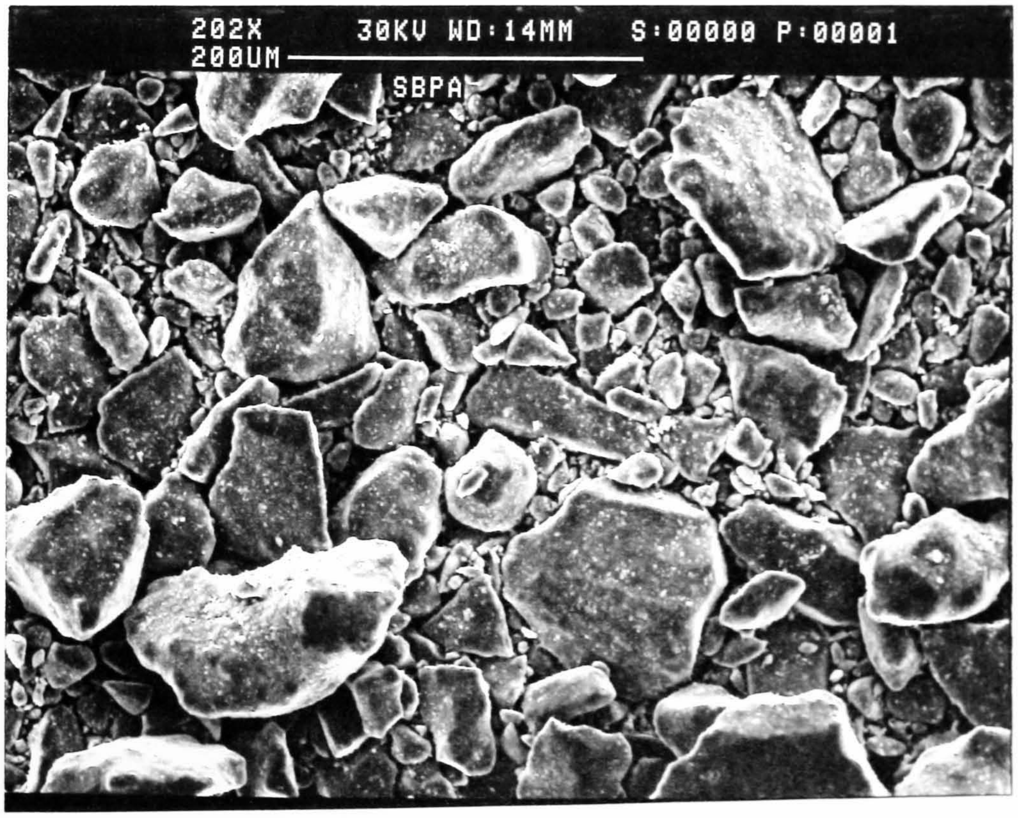

Figure 8-30 SEM photograph of initial manganese dioxide SBPA.

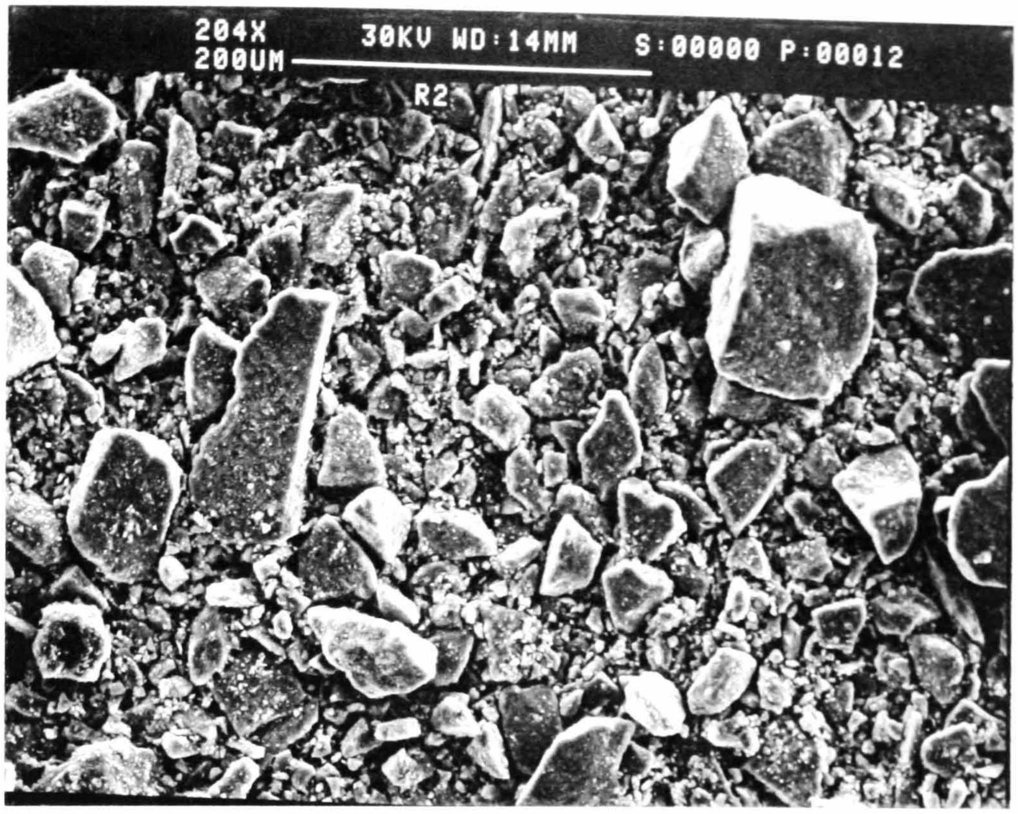

Figure 8-31 SEM photograph of initial manganese dioxide R2.

Figure 8-32 SEM photograph of initial manganese dioxide IBA no.19.

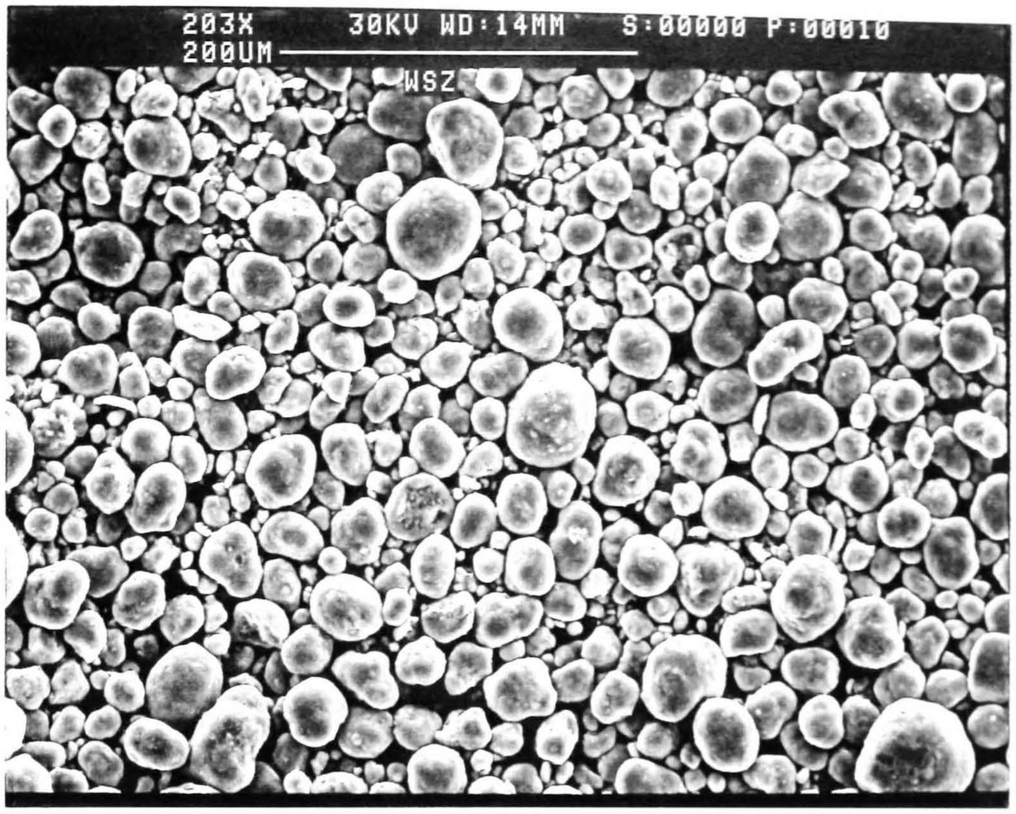

Figure 8-33 SEM photograph of initial manganese dioxide WSZ.

Figure 8-34 SEM photograph of initial manganese dioxide IBA no.14.

been included in this study. The potential versus composition of the same H inserted WSZ samples examined by x-ray diffraction in section 7.1 were measured by a fellow researcher J.Larcin and form part of his study[137]. The results obtained (in dilute KCl solution) indicate that the potential fell as expected for a solid solution to a reduction level r=0.4 whereby a nearly constant potential was observed. This observation supports the interpretation of the x-ray diffraction patterns presented in section 7.1. A different interpretation was preferred by Larcin which, however, does not concur with the persuasive x-ray diffraction results[†].

The SEM photographs (all photographed at the same magnification) highlight the difference in particle shape of the starting EMD's and CMD's (F.M and WSZ are both CMD's). Particularly striking is the completely differing appearances of IBA no.14 and WSZ which, as been previously shown, are only slightly separated in the $\gamma$-$\gamma_t$-$MnO_2$ structural series. The appearance of WSZ bears most resemblance to F.M although their x-ray diffraction patterns are quite different. Such differences in particle shape reflect the history of their production[138] rather than any structural differences. This statement is supported by figures 8-31, 8-32, 8-34 and 8-30 which are all EMDs with remarkably similar appearances despite their structures spanning the $\gamma$-$\gamma_t$-$MnO_2$ series.

Comparison of 8-31 and 8-32 suggests that the particle size of R2 will be on average smaller than that of IBA no.19 since R2 appears to contain a population of much smaller particles. An attempt to select an area which was judged to be representative of the particle size distribution of the whole sample was made.

### 8.6.2 Appearance after storage in 7M KOH.

Previously it has been shown (chapter 3) that the appearance of battery active manganese dioxide does not alter during solid state H insertion when viewed under the electron microscope. Thus the photographs of the starting materials presented previously (*vide supra*) represent impressions of the H inserted derivatives before immersion in 7M KOH.

Compare figure 8-35 which is of H inserted F.M ($MnO_{1.575}$) with figure 8-29 (both presented at the same magnification). Clearly a considerable transformation has

---

[†] The author wishes to point out that the conclusion reached by Larcin which involves postulating "undissociated MnOOH" as the thermodynamic component in an expression for the potential was arrived at without the benefit of the conclusions reached in section 7.1 concerning the x-ray diffraction evidence.

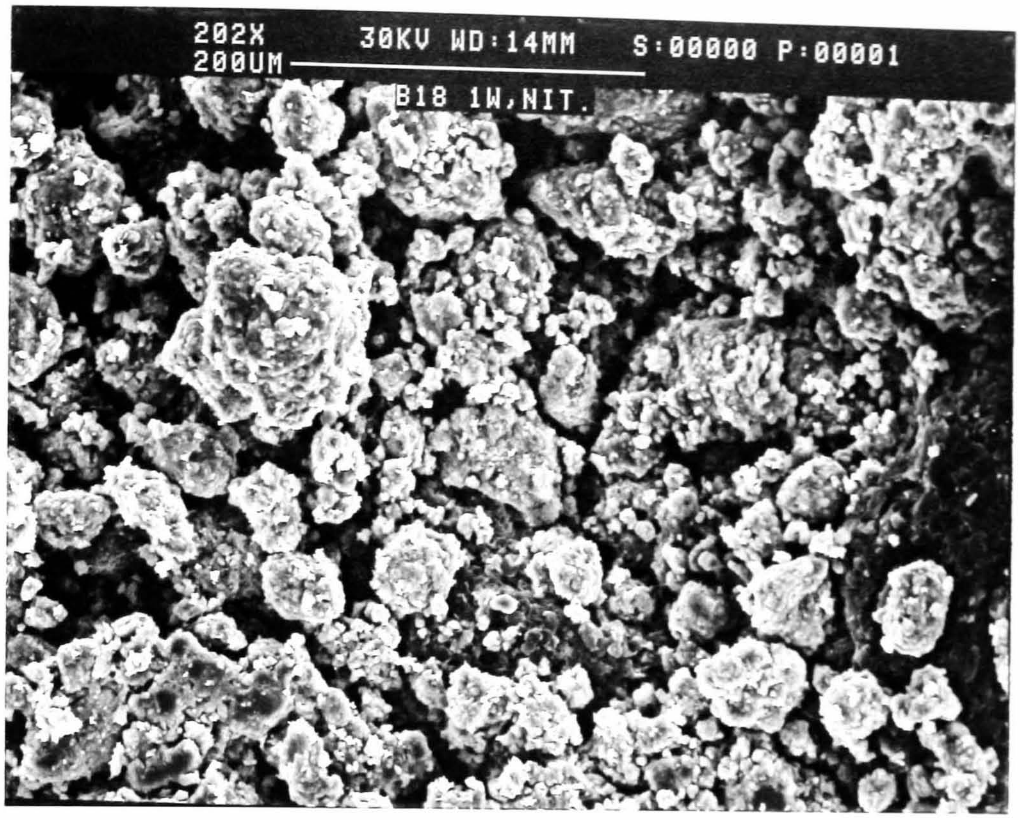

Figure 8-35 SEM photograph of H inserted F.M ($MnO_{1.575}$) after storage for 1 week in 7M KOH under $N_2$.

Figure 8-36 SEM photograph of H inserted F.M ($MnO_{1.575}$) (magnified area of figure 8-35) after storage for 1 week in 7M KOH under $N_2$.

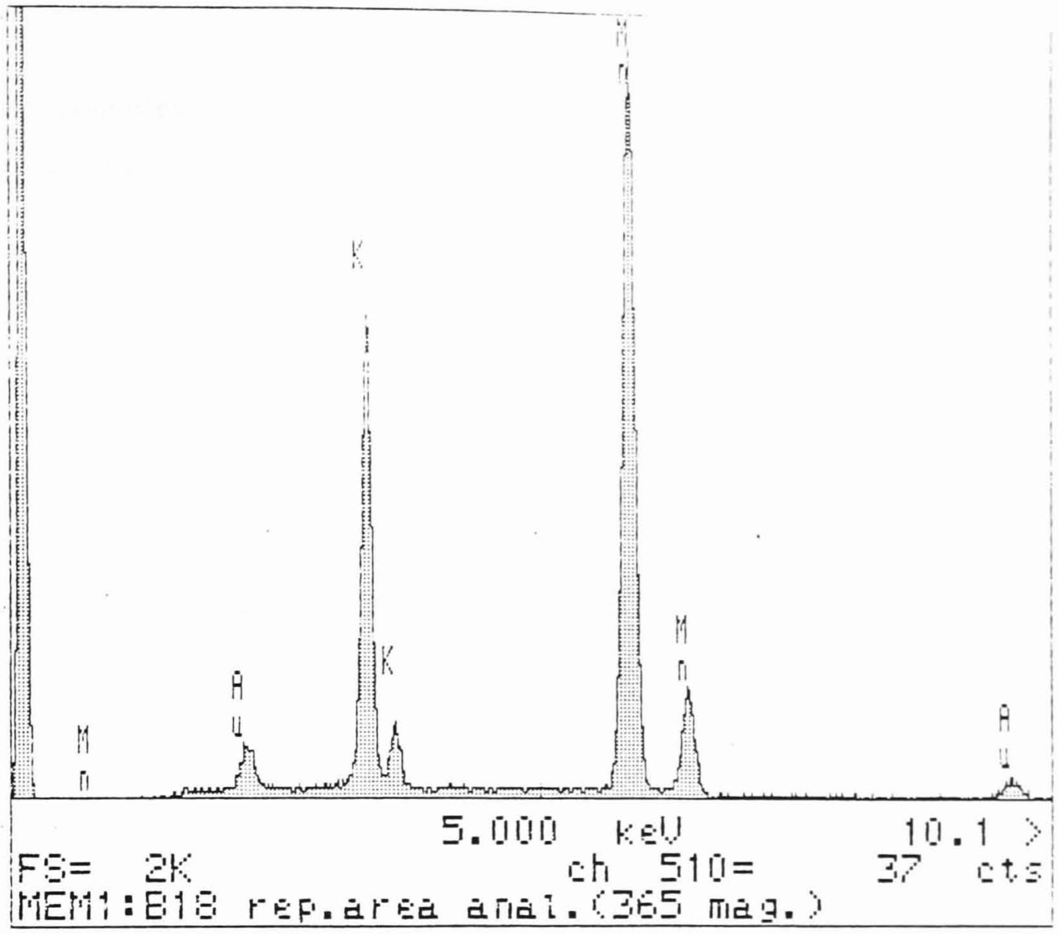

Figure 8-37 X-ray microanalysis of H inserted F.M sample ($MnO_{1.575}$) after storage in 7M KOH for 1 week under $N_2$. Mn,K and Au peaks are marked. The sample was gold coated to improve picture quality.

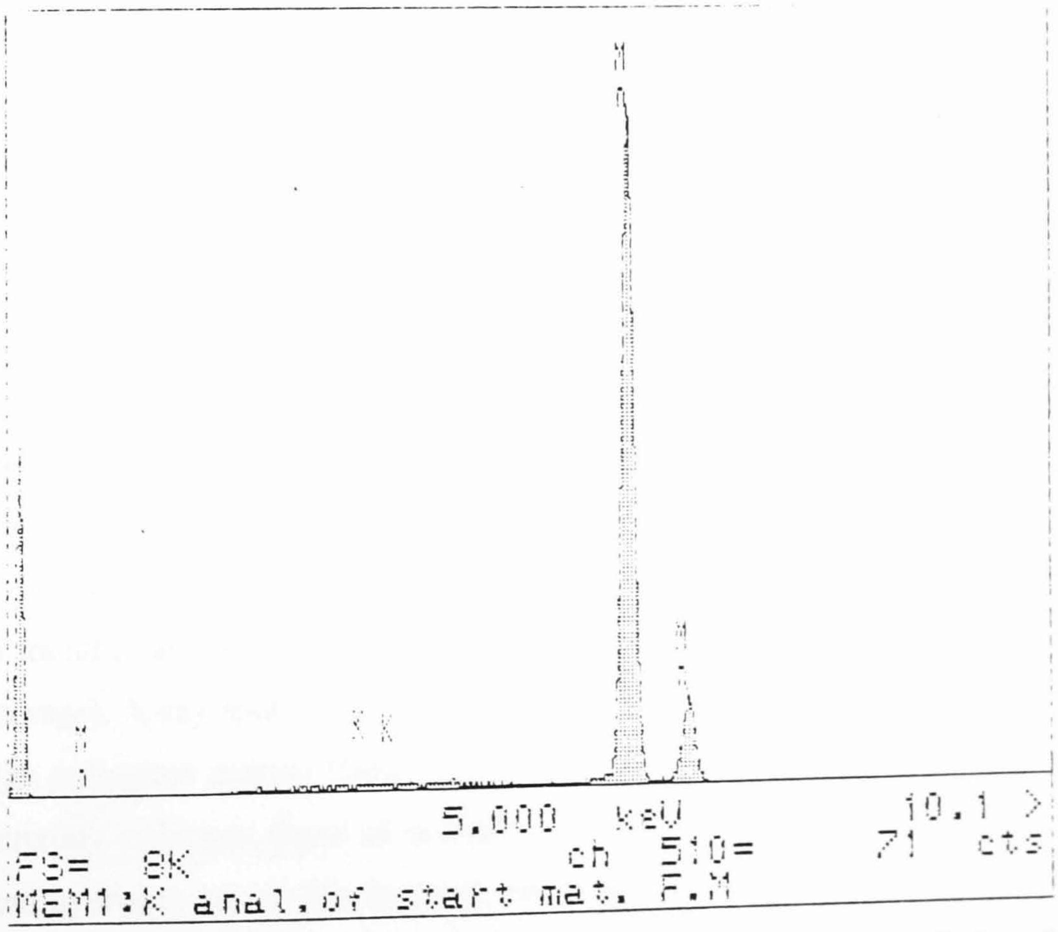

Figure 8-38 X-ray microanalysis of initial F.M manganese dioxide. The positions where K and Mn occur are marked.

taken place, consistent with growth of a different phase on the surface of the original material. Closer examination (figure 8-36) reveals an interesting plate-like growth. X-ray microanalysis of this area indicates a relatively high potassium content, see figure 8-37. That it is relatively high is clear by comparison with figures 8-38 and 8-39 which are of the starting material before and after 1 week storage in KOH under $N_2$. Since no change in either the appearance under the SEM or in the x-ray diffraction pattern occurred for the starting material it may be concluded that the observed small K content after storage is due to the known ion-exchange[139] properties of manganese dioxide.

The deposited platy material must therefore be the $\delta$-$MnO_2$ phase detected by x-ray diffraction in section 8.4. Figure 8-41 presents the appearance under the SEM of a H inserted sample of IBA no.19 ($MnO_{1.544}$) after 3 months storage in KOH under $N_2$. A crust of $\delta$-$MnO_2$ covers most of the initial reduced oxide. Some particles, however, appear to be relatively free. This suggests that the crust seperates on prolonged storage, as also suggested by figure 8-40 which is of H inserted SBPA ($MnO_{1.505}$). Cracking of the surface is evident. The re-appearance of $\delta$-MnOOH on prolonged storage is reported by Holton *et al.*[125] and is also noted in this work for certain samples (see section 8.5). Desai *et al.*[131] also drew attention to a similar phenomena in their study on the discharge of various manganese dioxides in alkaline media.

Similar results were obtained for very H inserted samples stored in KOH over air. Figure 8-42 indicates comparable crust development and cracked appearance as does figure 8-43. X-ray spot microanalysis confirms that the K content of crust is very much greater than the underlying particle. Figure 8-44 (crust analysis) and figure 8-45 (underlying particle analysis) is an example of such an analysis for the particle displayed in figure 8-43.

Finally if one examines figure 8-41 closely the bottom right hand corner reveals a small area with a quite different appearance to the surrounding material. Closer inspection reveals that it consists of a crystal growth of fine strands. Figure 8-46 shows a closeup found in another H inserted sample (H inserted IBA no.14, $MnO_{1.505}$ after 3 months storage). X-ray spot analysis of the fibres discloses almost no manganese and a very high potassium content (figure 8-47). Thus it is concluded that these fibres are almost certainly represent those of $\alpha$-KOH, detected by x-ray diffraction (Note that oxygen and hydrogen are, in this instance, not detectable by x-ray microanalysis.)

The results of the SEM analysis may be summarised as follows. SEM indicates

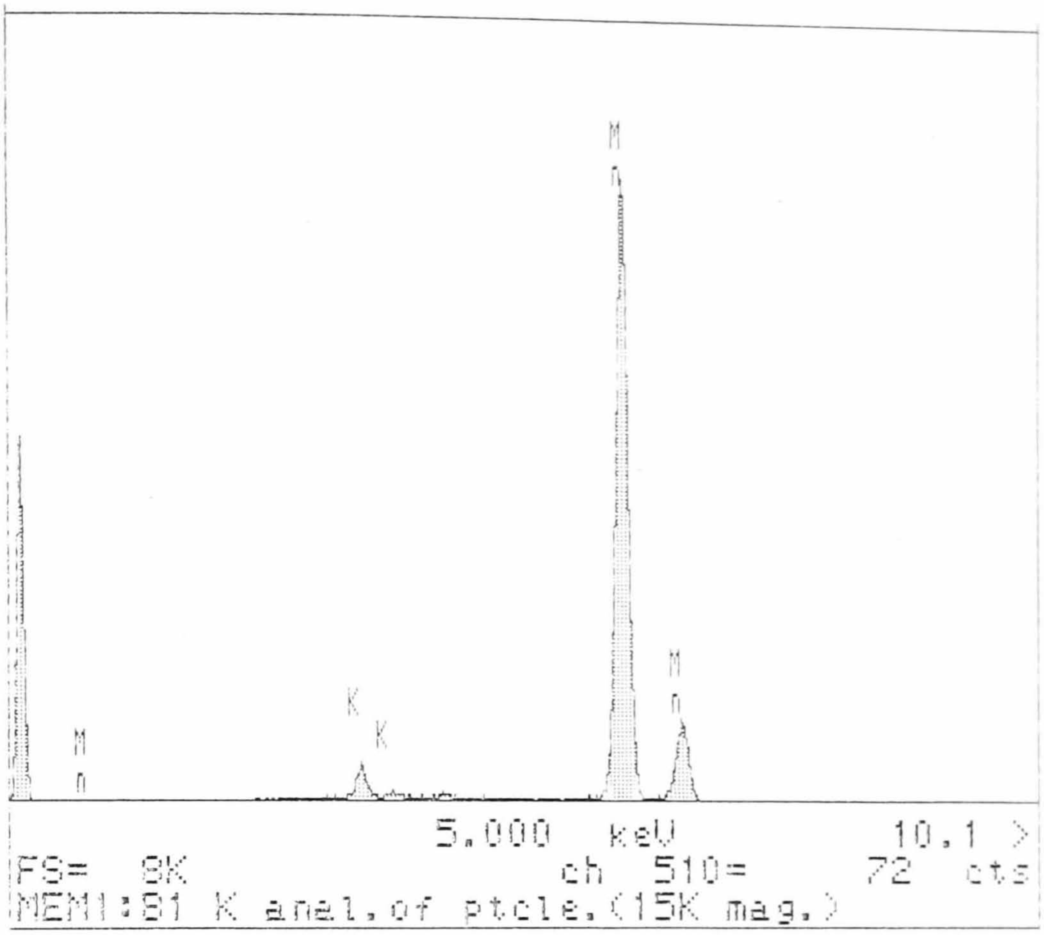

Figure 8-39 X-ray microanalysis of unreduced F.M sample ($MnO_{1.944}$) after storage in 7M KOH for 1 week under $N_2$. Mn and K peaks are marked.

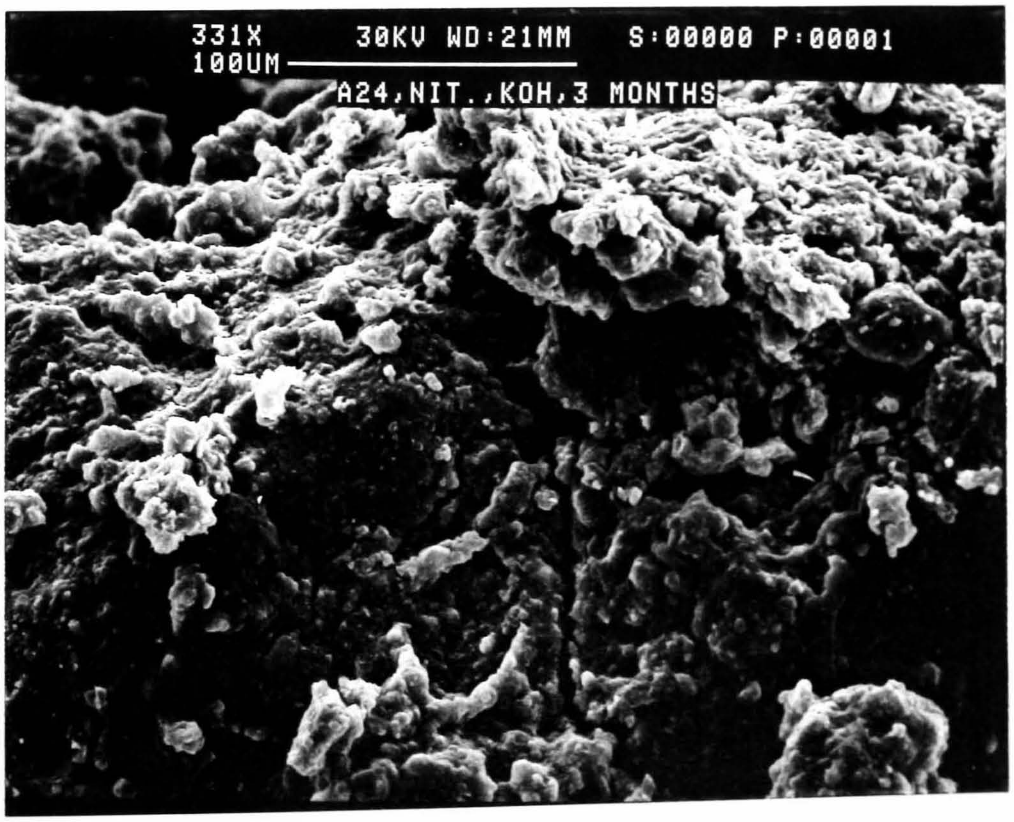

Figure 8-40 SEM photograph of H inserted SBPA sample ($MnO_{1.525}$) after storage in 7M KOH for 3 months under $N_2$.

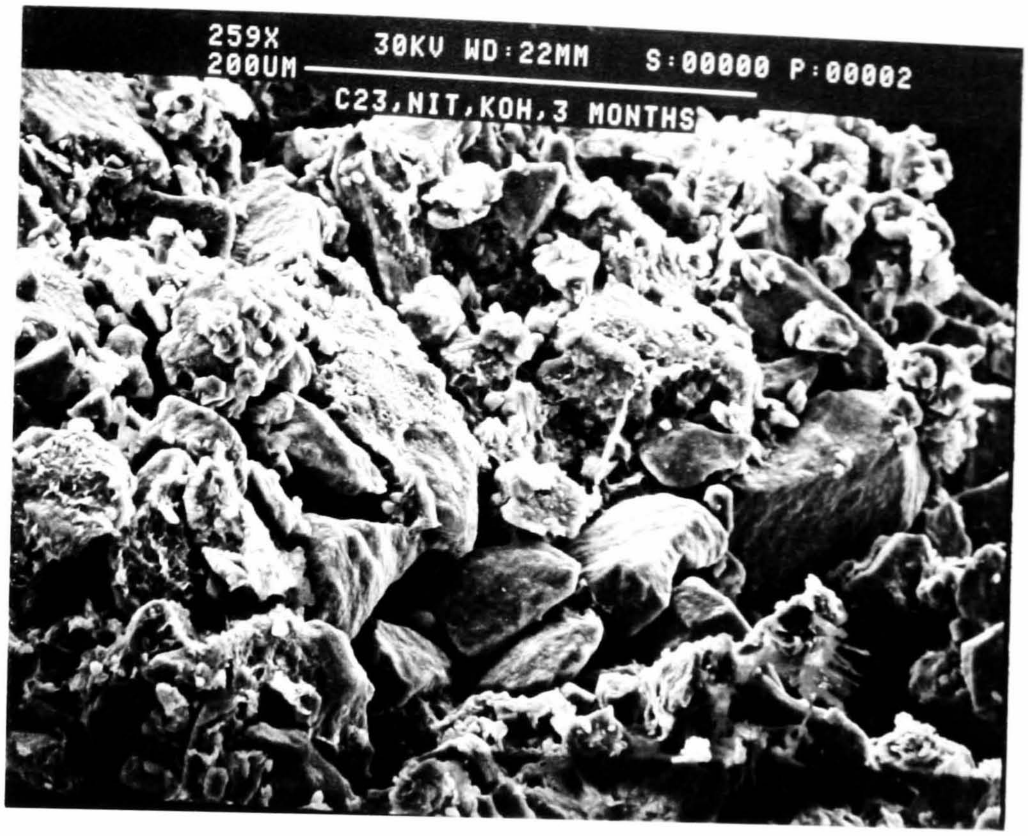

Figure 8-41 SEM photograph of H inserted IBA no.19 sample ($MnO_{1.544}$) after storage in 7M KOH for 3 months under $N_2$.

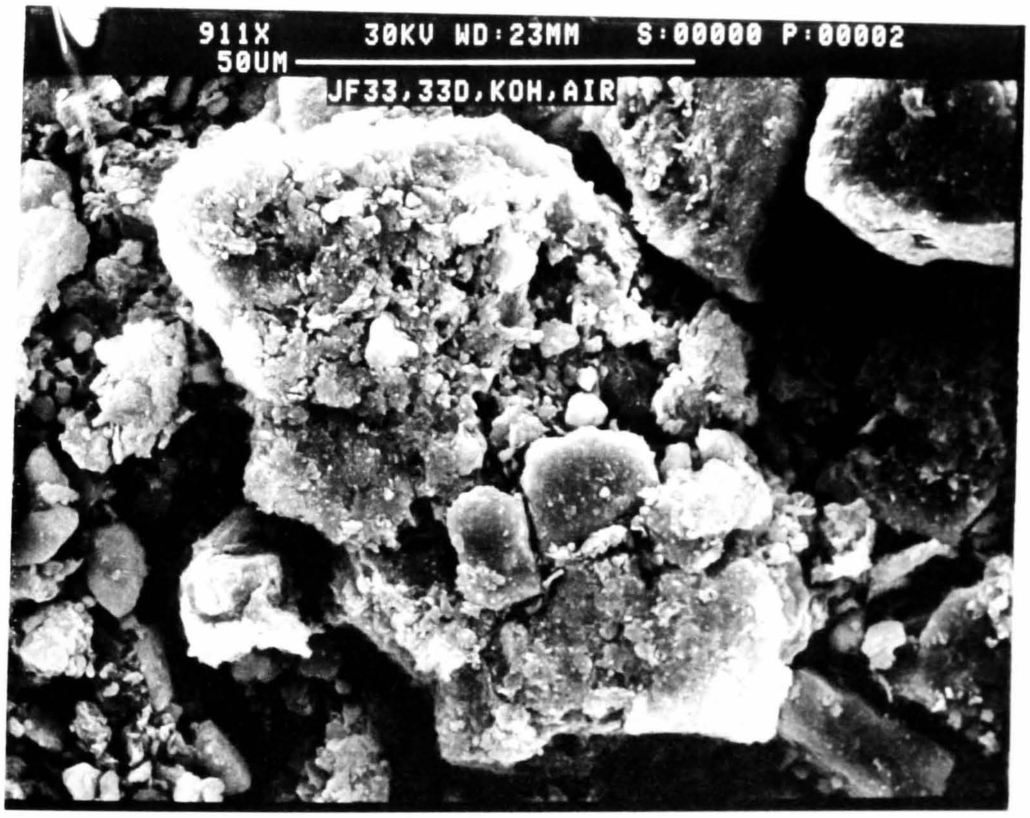

Figure 8-42 SEM photograph of H inserted R2 sample ($MnO_{1.505}$) after storage in 7M KOH for 33 days under air.

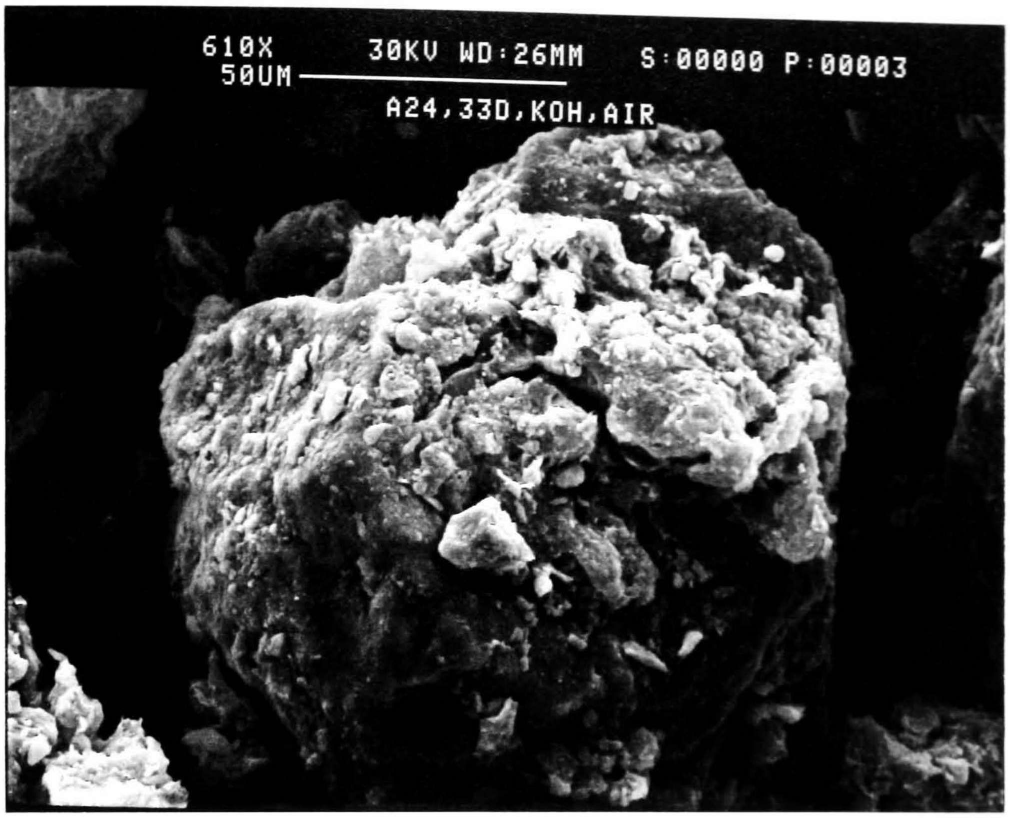

Figure 8-43 SEM photograph of H inserted SBPA sample ($MnO_{1.525}$) after storage in 7M KOH for 33 days under air.

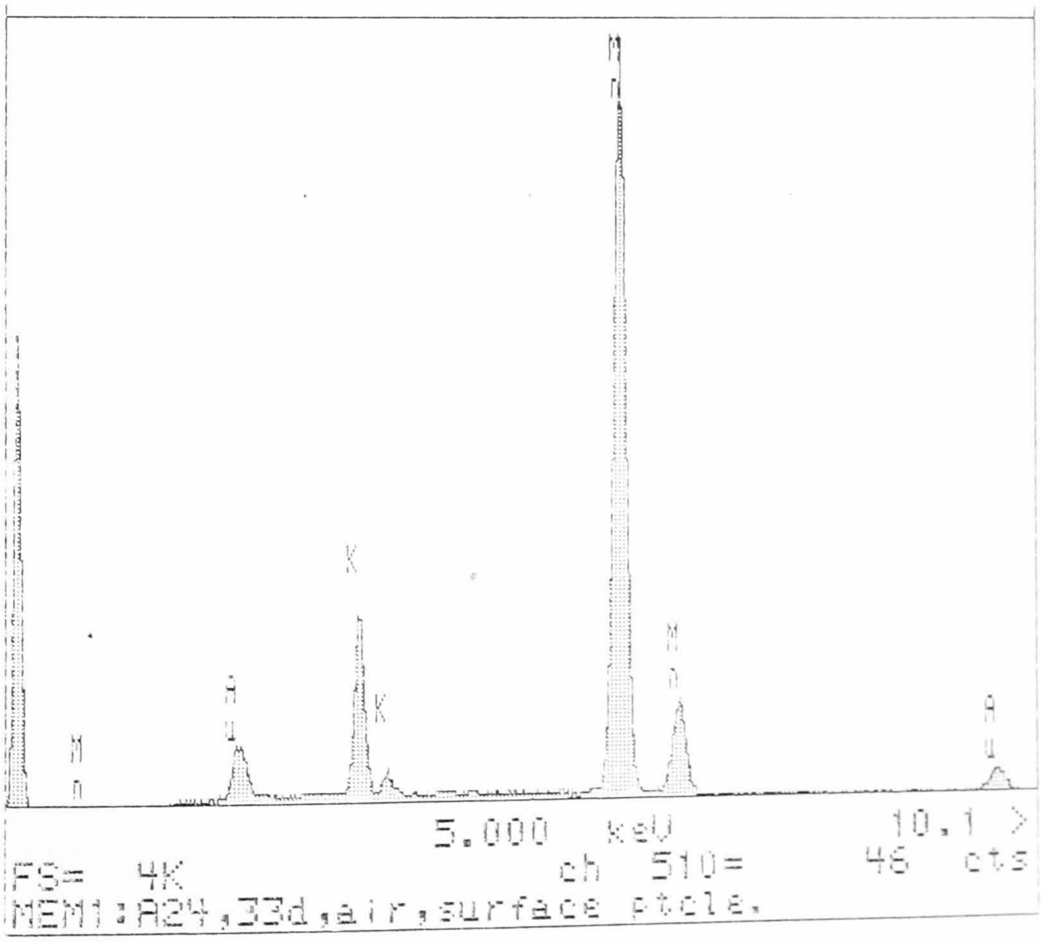

Figure 8-44 Spot x-ray microanalysis of crust surface shown in figure 8-43. K,Mn and Au peaks are marked.

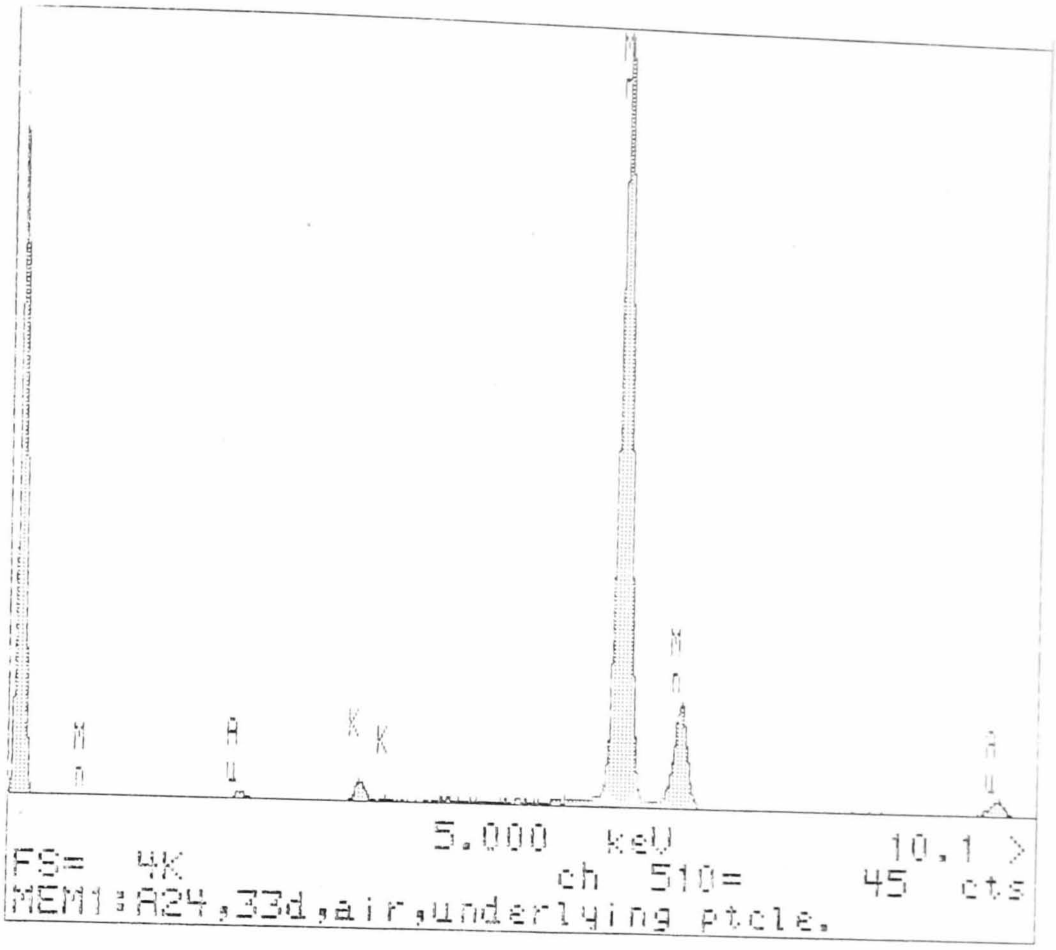

Figure 8-45 Spot x-ray microanalysis of underlying particle shown in figure 8-43. K,Mn and Au peaks are marked.

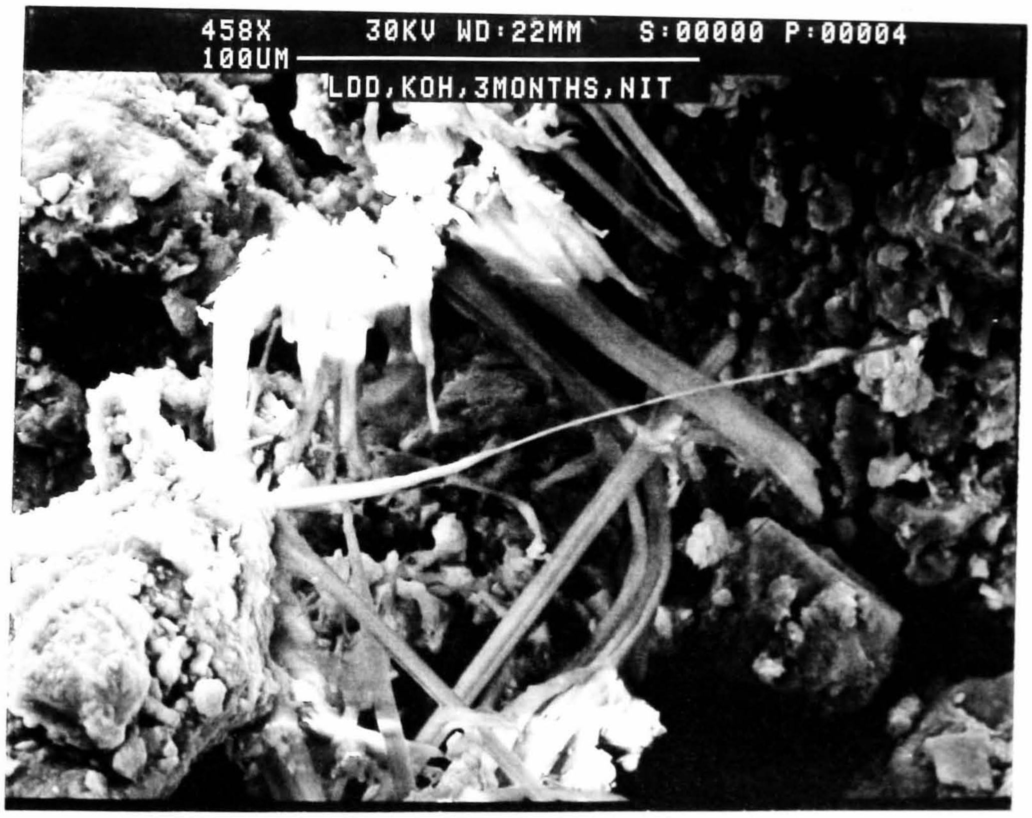

Figure 8-46 SEM photograph of H inserted IBA no.14 ($MnO_{1.505}$) after 3 months storage in 7M KOH, showing 'needle like' crystal growth.

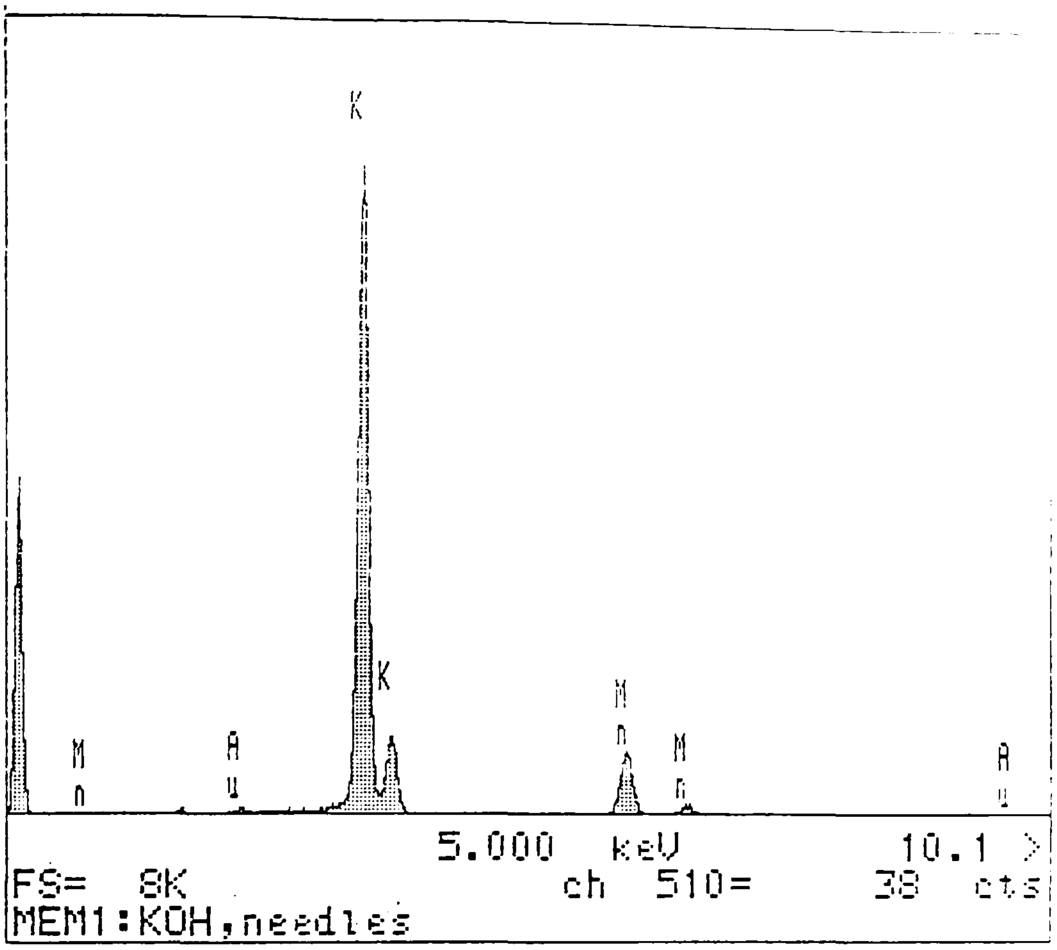

Figure 8-47 Spot x-ray microanalysis of 'needles' shown in figure 8-46. K,Mn and Au peaks are marked.

that the presence of $\delta$-MnO$_2$, as detected by x-ray diffraction, occurs as a deposit on the surface of the original reduced manganese dioxide. Where no $\delta$-MnO$_2$ was detected by x-ray diffraction no deposit was found on the H inserted particles. The presence of $\gamma$-MnOOH could not be confirmed. Its existence could have been detected if it had formed with a definite morphology as found previously for the product obtained from refluxing $\delta$-MnOOH in water, where it occurred as rod shaped particles (see section 3.2). The detection of $\alpha$-KOH by x-ray diffraction has been supported by the discovery of small amounts of K containing fibres.

## 8.7 Discussion.

As previously mentioned, no other work specifically concerned with metastability of H inserted manganese dioxide has emerged since the first work by Holton *et al.*[125] A complete description of the observations was obtained in that case. Attention is therefore focused on whether similar propositions apply to experimental data obtained herein.

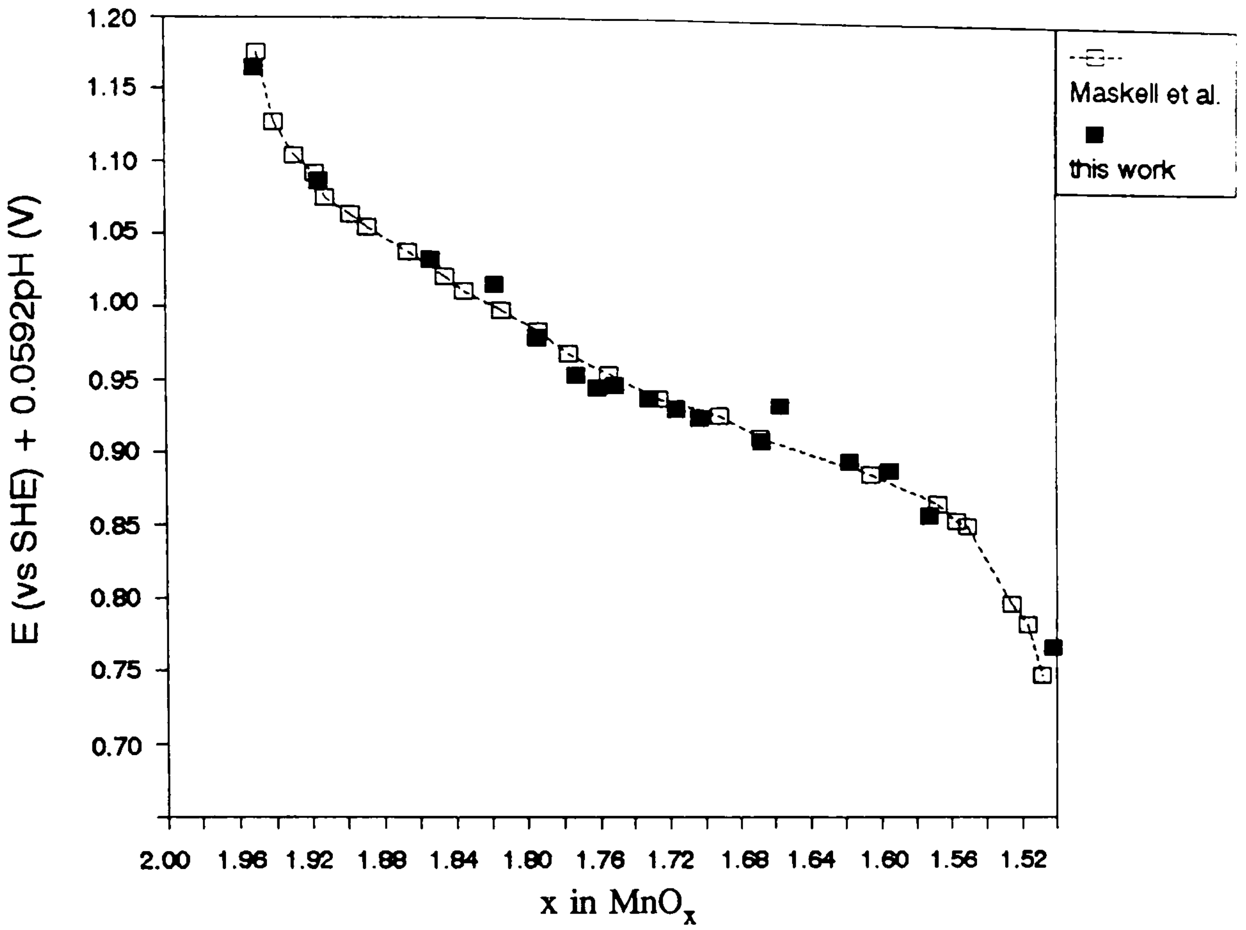

Figure 8-48 E(vs. SHE)+0.0592pH versus x in $MnO_x$ for H inserted R2 samples after 4 days storage in 7M KOH compared with potential data on the same manganese dioxide in ammonium chloride/zinc chloride solution from Maskell et al[140].

The potential as a function of x in $MnO_x$, obtained after four days immersion in 7M KOH (figure 8-9), was obtained from the same starting manganese dioxide as examined by Holton *et al.* viz the material coded R2 in their work and here. In this case H insertion into manganese dioxide was carried out with organic reductants in a non-aqueous environment whereas Holton *et al.* performed the reaction in an aqueous manganese dioxide concentrated KOH suspension. Although both methods insert H chemically different initial potential versus x dependencies are produced. Figure 8-48 plots E(vs. SHE) + 0.059pH for this work and that obtained from Maskell *et al.*[140] This expression removes differences in potential due to pH differences. To produce E(vs. SHE) + 0.059pH, 0.933(V) following Holton *et al.* was added to the experimental values (obtained as in their work against an Hg/HgO reference electrode in 7M KOH).

Figure 8-48 displays the same comparison as fig.2 in Holton *et al.*[125], which indicated the difference between the potential versus x in $MnO_x$ measured in ammonium chloride/zinc chloride electrolyte (from data obtained by Maskell *et al.*) and the data obtained therein. Whereas such a comparison signified a more rapid fall in potential than that expected for a solid solution (compared with the potential data from Maskell *et al.*)

from $MnO_{1.75}$ to $MnO_{1.63}$ followed by heterogeneous behaviour, satisfactory agreement over the whole composition range is found in this work when the same comparison is made (see figure 8-48). This provides evidence that the chemical insertion of H matches closely the battery process since the data obtained by Maskell *et al.* was obtained with the same starting material discharged in a Leclanché cell.

Thus the first potential curve (from the set indicated in figures 8-9, 8-10, 8-11) indicates that the potential dependence is that expected for a solid solution, which has been variously modelled on this basis. With regard to this problem (i.e. of modelling the potential variation of the manganese dioxide electrode versus composition) figure 8-12 is of interest. Most probably the break in this curve is due to instability and shall be discussed later†. Nevertheless, as mentioned earlier, it is evident that the initial potential variation with x is composed of two different curves, resulting in a distinct change in slope at $MnO_{1.86}$. Evidence has been cited for regarding the manganese dioxide electrode as composed of two solid solutions[141] in theoretical treatments for modelling the potential dependence as a function of x, though reference is made to the mid-reduction point ($MnO_{1.75}$) in these treatments[142]. It is perhaps pertinent to point out that the models refer to typical EMD, at the $\gamma_t$-$MnO_2$ end of the $\gamma$-$\gamma_t$-$MnO_2$ series, whereas IBA no.14 contains less microtwinning and is near but not at end of same series (section 2.4.4).

As established in chapter 5 the non-aqueous reduction of SBPA resulted in a solid state heterogeneous reaction beyond $r=0.40$ ($MnO_{1.80}$). Surprisingly this material exhibits an almost constant slope potential with x in $MnO_x$ as displayed in figure 8-16. No correlation with the convincing evidence for a heterogeneous reaction or at least change in reduction process was observed. At present the reason for this is unknown.

With storage in KOH solution a clear heterogeneous potential region develops for deeply H inserted materials confirming that such solid solutions are metastable in concentrated KOH. This is true for all materials except SBPA. The restricted heterogeneous range observed in R2 ($MnO_{1.60}$ - $MnO_{1.50}$) compared to that observed in Holton *et al.*[125] may be because 4 to 6 months storage was allowed in their work

---

† It is noted that this potential was obtained after 7 days storage rather than 4 days as for R2. Thus if one wishes to obtain the initial potential curve versus x expected for a solid solution measurements should be carried out within 4 days immersion. Experimentally it was also noted that irreproducible potentials are sometimes observed with chemically produced samples for storage times less than approximately 4 days, the cause of which is unknown.

whereas the maximum storage time reported here is six weeks, however, most of the potential changes were reported to occur in the first month of storage.

Other changes in potential which occur for instance in figure 8-11 in the region $MnO_{1.950}$ - $MnO_{1.60}$ may be viewed as a combination of two processes. The first is oxidation of the $MnO_x$ samples by dissolved $O_2$ in the KOH solution which leads to an apparent increase in potential with composition on storage. Secondly a tendency for the potentials to drop towards the heterogeneous potential level with storage time. This results in a distinct 'bump' at $MnO_{1.76}$ which correlates with the start of the heterogeneous potential reported by Holton *et al.* A similar 'bump' occurs at $MnO_{1.76}$ in figure 8-15 and 8-19 suggesting that the equilibrium heterogeneous potential region is independent of the material and starts at $MnO_{1.76}$. This is apparently consistent with figure 8-4 for material F.M but not with IBA no.19 which after 42 days storage in KOH shows little tendency towards instability or oxidation compared to the other materials. The reason for this is perhaps because IBA no.19 possesses a low specific surface area. Table 8.2 collects together selected data[143,144] regarding surface area measurements of all the materials examined which indicates that its value is similar to R2 but considerably higher than IBA no.14. Furthermore it indicates that F.M has a surface area very much larger than any of the other materials which suggests that the rate of reaction towards instability is related to the specific surface area of the manganese dioxide since F.M shows a large heterogeneous potential range after only 1 week of storage (see section 8.3.1). There may also be evidence that a seeding process is required to initiate

Table 8.2 BET specific surface area measurements for the materials considered in this part of the study.

| Material | BET surface area ($m^2g^{-1}$) | Reference source |
|---|---|---|
| IBA no.12† | 104 | 144 |
| R2 | 38 | 143 |
| IBA no.19 | 34 | 144 |
| IBA no.14 | 24 | 144 |
| SBPA | 22‡ | 51 |

†IBA no.12 is the same material as Faradiser M.
‡Obtained from figure 8 in ref.51 which displays the relationship between BET surface area and geometrical current density of deposition for SBP-EMD, which for material SBPA equals 1.2 ($Adm^{-2}$).

the instability reaction since δ-$MnO_2$ was produced in Holton *et al.*'s work during the reduction process and thus was already present before storage. The lack of δ-$MnO_2$ before storage could therefore account for the slowness of the reaction and hence restricted heterogeneous potential regions observed in this work particularly for R2 and IBA no.19. There is however an alternative and in the authors opinion more convincing argument.

A striking correspondence between the r in $MnOOH_r$ level at which H starts to locate in the solid solution and instability appears was observed for materials R2 and IBA no.19. Thus H was reported (see section 6.6) to become immobile in H inserted R2 beyond r=0.80 ($MnO_{1.60}$) which (see fig. 8-11) corresponds to the onset of a heterogeneous potential. This conclusion also accords with material IBA no.19 (see figure 8-8) in which H locates in the solid solution beyond r=0.75. Note that a small proportion of H becomes fixed in the manganite phase before this (see section 7.3). It is suggested that restricted mobility of H in the form of δ-MnOOH micro-domains may impose a 'strain' on the surrounding solid solution which in turn causes it to become unstable. This in turn suggests that location of H in the solid solution is the fundamental reason as to why alkaline manganese dioxide batteries only deliver useful power to a composition corresponding to $MnOOH_{0.8}$ under prolonged intermittent discharge regimes.

The correlation between H location and instability is not clearly maintained in the other materials however. Following the above argument, one would expect H inserted IBA no.14 to exhibit instability at a lower $MnOOH_r$ or higher $MnO_x$ than it does since H starts to locate at r=0.45 whereas instability appears to start at r~0.80 (or x~1.60). Furthermore if a heterogeneous solid state H insertion reaction occurred then the value of r at the surface would be higher than that of an average analysis, further promoting instability. H location, however, was not reported to lead to a heterogeneous solid state reduction for IBA no.14 but rather somewhere in between a random precipitation of δ-MnOOH micro-domains and a δ-MnOOH layer proceeding from the outside of a particle in a two phase reaction[†].

Heterogeneous solid state H insertion was reported for material SBPA beyond r=0.40, with H starting to become immobile at r=0.35. Instability would once again

---

[†] Note that H insertion into R2 led to a random precipitation within the solid solution and therefore r at the surface of a particle would be the same as the overall r of a particle.

therefore be expected at a lower r value than R2. This was not observed, nor was did the initial (i.e. shortly after immersion in KOH) potential reflect the heterogeneous solid state behaviour, as noted before.

In the case of F.M H location occurs at a very low H insertion level, see section 7.4, at r≈0.20. In this case the heterogeneous behaviour displayed in figure 8-4 is much greater than that of R2 or IBA no.19, ($MnOOH_{0.48}$ - $MnOOH_{1.00}$ or $MnO_{1.76}$ - $MnO_{1.50}$) with evidence that it may still be expanding (i.e. the instability reaction has not reached equilibrium) after 42 days storage. Following the previous suggestion F.M would not be suitable for alkaline manganese batteries because approximately only half the discharge capacity would be available.

The following reasons are proposed as to why the correlation between instability and H mobility described above was not observed in all the H inserted materials. The instability reaction may not have reached equilibrium, in any of the materials. Since F.M shows the greatest rate of change (and the highest surface area) one would expect that the materials with the lowest surface areas, namely SBPA and IBA no.14 (see table 8.2), to show the slowest rate of change. Also detection of a heterogeneous potential determining reaction may not be sensitive if the glassy carbon electrode happened to contact only one phase, namely the $\delta$-$MnO_2$ phase present as an outer-particulate crust†. On reflection grinding of each sample prior to each potential measure would have improved the contact with the inert electrode.

To summarise the discussion so far. The results obtained indicate that H inserted battery active manganese dioxide exhibits instability beyond a certain r in $MnOOH_r$ or $MnO_x$ value as detected by the presence of a heterogeneous potential and the appearance of $\delta$-$MnO_2$ and $\gamma$-MnOOH as detected by x-ray diffraction. $\alpha$-KOH which was also detected is assumed to be of secondary importance and probably results from the wet method of preparing the samples (see section 8.2).

The value of the heterogeneous potential E(vs. Hg/HgO) = 0.16(V) or E(vs. SHE)+0.0592pH = 0.77(V) corresponds approximately to the initial heterogeneous potential reported by Holton *et al.*[125], E(vs. SHE)+0.0592pH = 0.71(V) (determined from fig.2 in ref.125) attributed to a reaction involving $\gamma$-MnOOH and $Mn_3O_4$. In this case, however, no $Mn_3O_4$ was detected in any of the recorded x-ray diffraction patterns.

---

† X-ray diffraction on the other hand is an ideal technique to detect the precipitation of a crust of a crystalline phase since x-rays only penetrate the surface of a particle (see appendix B).

Cornell and Giovanoli[145] have reported that $Mn_3O_4$ spontaneously transforms to $\delta$-$MnO_2$ in alkaline solution (0.001-10M). The reaction involved dissolution of $Mn_3O_4$ followed by precipitation of $\delta$-$MnO_2$. Oxygen was also involved in the reaction but no difference in the phases present was detected when storage conditions were under $N_2$ rather than air (over the storage times reported, see section 8.5). That the storage conditions adequately excluded oxygen was indicated by storage of a sample of $Mn_3O_4$, using the same procedure outlined is section 8.5, which showed no change in its x-ray diffraction pattern in the storage times used for the $MnO_x$ samples.

The value of E(vs. SHE)+0.0592pH=0.71(V) was obtained by Holton *et al.* for the initial potential. On storage this changed to 0.76(V) which agrees closely to the value found in this work (0.77±0.01(V)). This higher potential was attributed to a heterogeneous reaction involving $\delta$-$MnO_2$ and $\gamma$-MnOOH. Following Holton *et al.* this may be written:

$$K_2Mn_4O_8.xH_2O + 2e^- \rightarrow 4(\gamma\text{-})MnOOH + 2K^+ + 4OH^- + (x\text{-}4)H_2O \qquad (8.2)$$

where $K_2Mn_4O_8$ is written as the ideal composition of $\delta$-$MnO_2$. $\delta$-$MnO_2$ is a phase of variable oxidation state[125] the lowest of which appears to be $MnO_{1.75}$ (i.e. $K_2Mn_4O_8$) and the highest $MnO_{1.86}$ (see footnote on p.241). The findings of this work support the conclusion of Holton *et al.* that battery active EMD solid solutions are unstable in KOH and disproportionate into $\delta$-$MnO_2$ and $\gamma$-MnOOH. This statement may now be extended to refer to structural members of the $\gamma$-$\gamma_t$-$MnO_2$ series. Including intercalated water as in equation (8.3) the disproportionation reaction may be written as follows:

$$2(1\text{-}y\text{-}z)KOH + 2MnOOH_{(y+z)} \rightarrow (1\text{-}y\text{-}z)K_2Mn_4O_8.2H_2O + 4(y+z\text{-}½)(\gamma\text{-})MnOOH \qquad (8.3)$$

where y is H insertion level beyond which disproportionation occurs. z varies between the limits

$$0 \leq z \leq 1\text{-}y.$$

and represents the degree of reduction beyond the level at which disproportionation starts (y). Note that equation 8.3 is only valid for $\delta$-$MnO_2$ of oxidation state $MnO_{1.75}$. This equation predicts, at equilibrium, that the amount of $\delta$-$MnO_2$ would decrease from a maximum amount at $MnOOH_y$ to zero at $MnOOH_{1.0}$ with the amount of $\gamma$-MnOOH adhering to the converse description. X-ray diffraction evidence does not support this description which indicates that the amount of $\delta$-$MnO_2$ increases with increasing reduction. However as noted in section 8.6.1 the reaction may not have proceeded to completion since initial H inserted manganese dioxide was detected by x-ray diffraction in many of the long stored samples (eg figure 8-25). It is possible that the reaction was stifled by the $\delta$-$MnO_2$ (and possibly $\gamma$-MnOOH) surface layer and therefore could not proceed further.

## 8.8 Conclusions.

A simplified reaction scheme to that proposed by Holton *et al.* accounts for the observed behaviour of $\gamma$-$\gamma_t$-$MnO_2$ H inserted oxides when stored in concentrated KOH. The differences can be attributed to the aqueous method of reduction. Thus formation of $\delta$-$MnO_2$ at high oxidation states ($MnO_{1.92}$), not found in this work, may be, as suggested therein (ref.125), due to equilibrium throughout the H inserted manganese dioxide being established through precipitation of $\delta$-$MnO_2$ via soluble $Mn^{3+}$ when small particles are unavoidably reduced more deeply than larger particles. $\delta$-$MnO_2$ may then subsequently be reduced to $Mn_3O_4$ and/or $\gamma$-MnOOH leading to more complicated reactions and subsequent changes on storage. Thus in Holton *et al.*'s work due to the fact that $\delta$-$MnO_2$ was produced during the initial reduction of the manganese dioxide in KOH its appearance during storage was not simply diagnostic of instability. This complication has been removed in this work and its appearance may now be taken as indicative of instability when H inserted battery active manganese dioxides are subjected to storage in concentrated KOH. $Mn_3O_4$ or $Mn(OH)_2$, compounds which have been attached to explanations[130,116] as to why battery active manganese dioxide has not been found to be fully rechargeable when deeply discharged (in the one electron range), have not been detected at any stage of the investigation.

The findings of this work may be summarised as follows.

(a) Electrode potentials as measured on materials produced by a non-aqueous chemical insertion technique from typical battery active manganese dioxide (i.e. near the $\gamma_t$ end of the $\gamma$-$\gamma_t$-$MnO_2$ series) and then placed in KOH are initially similar to those reported in ammonium chloride/zinc chloride solution. That is those expected from the composition of a solid solution when H was inserted.

(b) H inserted battery active manganese dioxides with r in $MnOOH_r \geq y$, where y appears to depend on the material and the method of H insertion, are found to be unstable when stored in concentrated KOH solution.

(c) Beyond $MnOOH_y$ disproportionation of the H inserted compounds into $\delta$-$MnO_2$

and $\gamma$-MnOOH occurred.

(d) H location within $\gamma_t$-$MnO_2$ (i.e. materials R2 and IBA no.19) solid solutions correlates with the observed instability of these materials (y=0.80 for R2 and IBA no.19).

(e) Faradiser M H inserted compounds are the most unstable, displaying the largest heterogeneous potential region (i.e. y=0.45) and the most rapid reaction with KOH.

(f) The rate of reaction of (c) appears linked to the specific surface area of the material and also perhaps to a need for seeding of the product phases.

# 9 Overall Conclusions and Further Work.

Returning to the question of the classification of manganese dioxide polymorphs (see page 1) the list must now be extended to include the $\gamma$-$\gamma_t$-$MnO_2$ series. This series is distinct from the $\gamma$-$MnO_2$ series in that the end members are not perfectly crystalline phases (nor are they stoichiometric). Nor is it a series which has only two end members, since $\gamma$-$MnO_2$ may have a p fraction extending from 0 (ramsdellite) to 1 (pyrolusite). Therefore $\gamma_t$-$MnO_2$ does not designate one particular defect structure but one which has a variable pyrolusite type layer fraction (p) and a large degree of microtwinning. F.M, IBA.no.19 and R2 may all, by this definition, be designated $\gamma_t$-$MnO_2$. In a completely analogous fashion the $Mn^{III}$ oxyhydroxide polymorphs must be extended to include the $\delta$-$\delta_t$-MnOOH series where similar comments apply. Thus the most H inserted F.M, IBA.no.19 and R2 may be designated $\delta_t$-MnOOH.

The results of this work lead to the following description for the structural changes which occurred when H was inserted into battery active manganese dioxide.

H insertion into the $\gamma$-$\gamma_t$-$MnO_2$ series produced dilation of the crystal structure in the manner expected for a solid solution in which $H^+$ and $e^-$ were mobile (see section 4.3) up until a certain r in $MnOOH_r$. This r appeared to depend on the rate at which H was inserted and the rate at which H diffused within the crystal structure. This is because regions of solid solution with high r in $MnOOH_r$ inevitably precipitate micro-domains of the end product. Once this has occurred an irreversible change has taken place (see below). If the rate of H insertion was 'slow' such that r was equalized throughout a particle these domains precipitated randomly throughout the crystal (as was observed for H insertion into R2 and IBA no.19, (see chap.6 and sect. 7.3). If, however, the H insertion was 'rapid' these micro-domains may form at the surface of a particle and gradually accumulate until a boundary between the solid solution and the precipitated end product ($\delta$ or $\delta_t$-MnOOH, depending on the initial material) had formed, subsequent H insertion would cause propagation this boundary into the bulk i.e. heterogeneous reduction. Exactly this description appears to have applied to H insertion into SBPA (sect. 5.4) and WSZ (sect. 7.1) with somewhere intermediate between these two descriptions for H insertion into IBA no.14 (sect. 7.2.1).

If the above were correct then it should be possible to insert H into, for example SBPA, without producing heterogeneous reduction and with an extended solid solution range. Alternatively rapid H insertion could produce heterogeneous reduction from a low H insertion level onwards. Clearly further research would be required to establish whether this was possible. Such work could also be directed towards the influence of the initial crystal structure on the formation of δ (or $\delta_t$)-MnOOH micro-domains. This work has already indicated that a tendency towards increased anisotropic expansion was exhibited in the solid solution H insertion range as one traversed the $\gamma$-$\gamma_t$-$MnO_2$ series. It may be that this signified a fundamental barrier towards extending the solid solution even with 'slow' H insertion. It should be noted that the formation of δ or $\delta_t$-MnOOH micro-domains at some deep H insertion level is considered inevitable. Further research towards verifying the existence of such micro-domains of δ (or$\delta_t$)-MnOOH and discovering the crystallographic site at which H locates (a question not addressed in this work) using alternative techniques could also be undertaken. Of these N.M.R. (Nuclear Magnetic Resonance) and neutron diffraction seem particularly suitable. Any technique which required use of a single crystal would however be difficult to apply to $\gamma_t$-$MnO_2$ because of the nature of its production which always produces small crystallites randomly orientated at a microscopic scale.

Although H insertion into F.M led to $\delta_t$-MnOOH, insertion of H proceeded in a quite different manner to the other materials. At very low H insertion levels H located or 'froze' in position ($r \approx 0.2$). This suggested an extremely short solid solution range ($\Delta r \approx 0.1$) which is reminiscent of H insertion into pyrolusite reported by Bode and Schmier[103], where a similar solid solution range was reported ($\Delta r \approx 0.1$). Heterogeneous reduction to manganite was thereafter reported. The reduction was performed using an aqueous hydrazine hydrate method. Recently this result has been confirmed[146] using hydrazine hydrate in a non-aqueous solvent (described in sect. 3.2.3). This would appear to reinforce the conclusion that F.M possesses a high pyrolusite type layer fraction ($\gamma_t$-$MnO_2$, $p \approx 0.7$, see sect. 2.4.3). Beyond $r \approx 0.2$ heterogeneous reduction was not thought to have occurred, rather it was suggested reduction proceeded in accordance with an extended random layer crystal (see sect. 7.4). It should be noted that F.M has by far the largest specific surface area of the materials studied and therefore the rate at which H was inserted must have been comparatively 'slow'.

In chapter 8 it was found that H inserted battery active manganese dioxide beyond a certain H insertion level was unstable when stored in concentrated KOH. A slow transformation into δ-$MnO_2$ and γ-MnOOH occurred confirming the reaction proposed by Holton *et al.*[125]

As mentioned previously (sect. 8.1) the instability of H inserted battery active manganese dioxide may explain the lower than expected discharge performance of alkaline manganese batteries on long period intermittent discharge regimes as first suggested by Tye[124], and have implications for attempts to produce rechargeable cells (see sect. 8.1). It appeared that the r in $MnOOH_r$ at which instability occurred depended on the r at which micro-domains of the final product were formed. Further research would be required to confirm this fundamental connection.

Evidence has been accumulated by Fitzpatrick and Tye[68] that changes in the x-ray diffraction pattern characteristic of the appearance of the final product (i.e. the formation of $\delta$ (or $\delta_t$)-MnOOH micro-domains) represented an irreversible solid state change. Future work establishing the fundamental r in $MnOOH_r$ at which H may be inserted into members of $\gamma$-$\gamma_t$-$MnO_2$ series without formation of $\delta$ (or $\delta_t$)-MnOOH micro-domains (or H location) and the relationship to the instability of these compounds in KOH would, according to the implications of this work, further the understanding required to produce improved alkaline manganese dioxide batteries.

## Appendix A

## A method to calculate p or m.

In order to calculate p (or m) (see section 4.1) it was first necessary to construct a table such as table 2.4 (or table 4.3) from measurements of peak positions on a diffraction pattern of $\gamma$-MnO$_2$. The table lists both the experimental ($\Delta q_1 = q_o - q_c$) and theoretical ($\Delta q_2 = q'_o - q_c$) values of $\Delta q$ for each peak. A function was then created reflecting the closeness to which observed values matched experimental (sum of residuals squared).

$$Q=\sum_{i=1}^{N}((\Delta q_1)-(\Delta q_2))^2$$

where i=peak number, N=total number of peaks

This function was then minimised by choosing appropriate values of $r_f$. This may be done in a stepwise fashion, that is calculating Q for values of $r_f$ stepped in small increments from 0 - 0.5 and noting the minimum or more appropriately using a numerical optimisation procedure. p (or m) may then be calculated for the value of $r_f$ corresponding to the minimum value of Q via equation (2.8).

The above operations are easily and conveniently carried out with a spreadsheet software package (e.g. Quattro Pro) running on a Personal Computer.

Results for materials in which analyzing for p or m by the above method is valid, i.e. materials near the $\gamma$ end of the $\gamma_t$-$\gamma$-MnO$_2$ series (so that the SdWIM is valid) are collected together in the following table. Also listed are the orthorhombic parameters for the prevailing ramsdellite type layers for each measure, required in the analysis for p or m.

Table A.1 Results for the determination of p,m and orthorhombic lattice parameters of $\gamma$-$MnO_2$ materials SBPA and WSZ and their most H inserted derivatives using the SdWIM.

| Material | No. | p | a | b | c |
|---|---|---|---|---|---|
| SBPA | 1 | 0.2096 | 4.4345 | 9.3443 | 2.8461 |
| | 2 | 0.2053 | 4.4380 | 9.3621 | 2.8511 |
| | 3 | 0.2034 | 4.4369 | 9.3420 | 2.8510 |
| | 4 | 0.1970 | 4.4414 | 9.3348 | 2.8506 |
| WSZ | 1 | 0.2300 | 4.4440 | 9.3450 | 2.8406 |
| | 2 | 0.2567 | 4.4541 | 9.2675 | 2.8508 |
| | 3 | 0.2358 | 4.4568 | 9.2901 | 2.8474 |
| | | m | | | |
| Most H inserted SBPA | 1 | 0.1281 | 4.5364 | 10.6402 | 2.8685 |
| | 2 | 0.1387 | 4.5381 | 10.6634 | 2.8703 |
| | 3 | 0.1500 | 4.5337 | 10.6437 | 2.8717 |
| Most H inserted WSZ | 1 | 0.1768 | 4.5238 | 10.5681 | 2.8687 |
| | 2 | 0.2009 | 4.5224 | 10.5949 | 2.8672 |
| | 3 | 0.1980 | 4.5332 | 10.5628 | 2.8681 |

| material | Av.p | Av.a | Av.b | Av.c |
|---|---|---|---|---|
| SBPA | 0.20±0.005 | 4.438±0.002 | 9.35±0.01 | 2.850±0.002 |
| WSZ | 0.24±0.01 | 4.45±0.006 | 9.30±0.04 | 2.84±0.005 |
| | m | | | |
| most H ins. SBPA | 0.14±0.01 | 4.536±0.002 | 10.65±0.01 | 2.870±0.002 |
| most H ins. WSZ | 0.19±0.01 | 4.52±0.005 | 10.58±0.02 | 2.868±0.001 |

## Appendix B

## A DIFFaX data file for calculating $\gamma$-$MnO_2$ to $\delta$-MnOOH diffraction patterns.

The following text contains an example data file required to produce an intergrowth structure with a composition corresponding to r=0.70 in $MnOOH_r$. All the calculated patterns in this work were calculated with this file (or a straightforward modification of it) as the input file for the computer program DIFFaX, written by Treacy Newsam and Deem[61]. For the meaning of each line in the file the reader should refer to the manual accompanying the program. The following points are noted for this file (listed below).

The origin of each layer is coincident with the bottom left hand oxygen (see figures 2-15(b) and C-1) at the zero z level. G(G') and M(M') layers are expanded by 14% in the b direction by means of the following transformation. Layers are transformed such that the puckered oxygen relationship, in a string of oxygens running parallel to the a axis (see figure C-1) maintains the same relative orientation but with an increased gap between each string of oxygens. This was achieved by displacing each string from the origin by an amount proportional to the original fractional axial distance in the b direction. Thus if the displacement required was D those oxygens occurring at ½ in the b direction were displaced ½D (and similarly for the remaining atoms, see figure C-1). Since the coordinates are referred to the original 'unit cell' this results in layer fractional coordinates greater than one in the b direction. The transformation described ensures that the oxygen positions at for example the sequence of layers RG' match at boundary. Note that at a G'R boundary a displacement of the 'unit cell' was required, which was taken into account by introducing a suitably expanded layer transition vector. Similar reasoning applies to the other possible layer transitions.

The stoichiometry r=0.70 was calculated from the probability of existence of each layer listed at the beginning of the file and equation (4.3). Note that the file listed (below) forms part of the calculated diffraction pattern sequence described as Case 2(b) described in section 4.4.1.

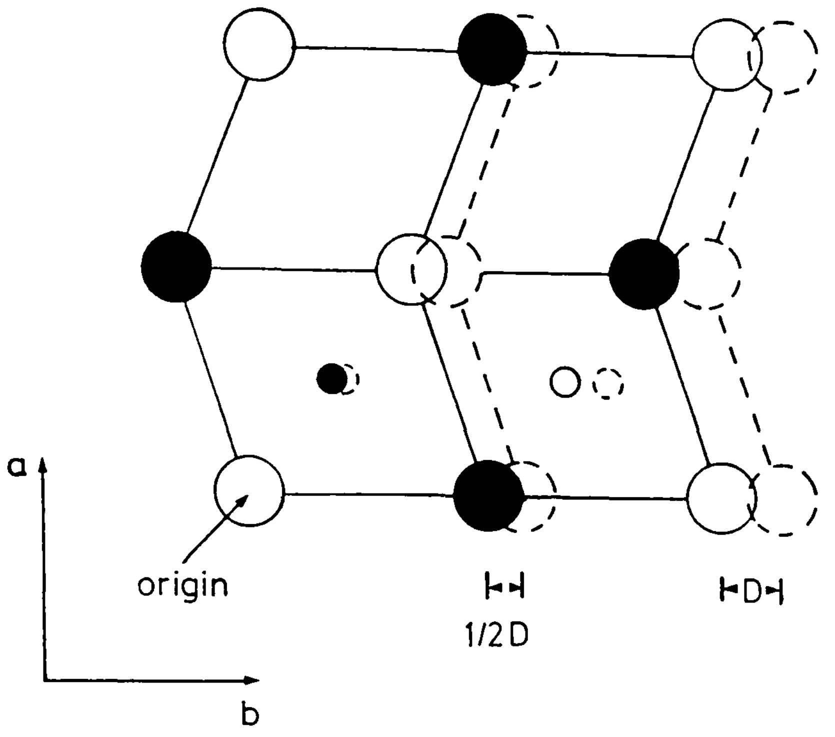

Figure C-1 Relationship of R layer to G layer. R layer (solid lines), c.f. figure 2-15, expanded by 14% in the **b** direction to form a G layer (dashed lines). Open and filled circles indicate z-levels of 0 and ½.

```
                         ---- start of file ----
{Data file for gamma-MnO2/MnOOH, with a random intergrowth of ramsdellite,}
{pyrolusite, groutite, manganite layers. Eight layers are required}
{RR’PP’GG’MM’ if the oxygen h.c.p. lattice is taken into account. This is}
{because eg. R and R’ (see de Wolff (1963) are not related by a true}
{translation, unless the oxygens are ignored. In this case the probability}
{of a pyrolusite layer is set to}
{BPorP’=0.06 or p=0.06}
{and that of groutite layer}
{BGorG’=0.56}
{and that of manganite}
{BMorM’=0.14}

INSTRUMENTAL                    {header for radiation data}
X-RAY                           {radiation type}
1.5418                          {x-ray wavelength}
GAUSSIAN 0.00 0.00 0.2 TRIM     {instrumental broadening}

STRUCTURAL                      {header for structural section}
4.5208 2.8687 4.6674 90.0       {unit cell dimensions}
UNKNOWN                         {note the unit cell is that of ramsdellite}
8                               {with b/2, and here transformed such that}
                                {c is the direction perpendicular to a layer}


LAYER 1                         {R or ramsdellite layer}
NONE
Mn4+ 1  0.250000  0.500000  0.166667  0.5  1.00
```

```
Mn4+ 2  0.2500000 0.000000  0.666667  0.5  1.00
O 1- 1  1.000000  0.000000  0.000000  1.0  0.25
O 1- 2  1.000000  0.500000  0.500000  1.0  0.50
O 1- 3  1.000000  0.000000  1.000000  1.0  0.25
O 1- 4  0.500000  0.500000  -.166667  1.0  0.50
O 1- 5  0.500000  0.000000  0.333333  1.0  1.00
O 1- 6  0.500000  0.500000  0.833333  1.0  0.50
O 1- 7  0.000000  0.000000  0.000000  1.0  0.25
O 1- 8  0.000000  0.500000  0.500000  1.0  0.50
O 1- 9  0.000000  0.000000  1.000000  1.0  0.25

LAYER 2                          {R' or ramsdellite layer}
NONE
Mn4+ 1  0.750000  0.500000  0.166667  0.5  1.00
Mn4+ 2  0.750000  0.000000  0.666667  0.5  1.00
O 1- 1  1.000000  0.000000  0.000000  1.0  0.25
O 1- 2  1.000000  0.500000  0.500000  1.0  0.50
O 1- 3  1.000000  0.000000  1.000000  1.0  0.25
O 1- 4  0.500000  0.500000  -.166667  1.0  0.50
O 1- 5  0.500000  0.000000  0.333333  1.0  1.00
O 1- 6  0.500000  0.500000  0.833333  1.0  0.50
O 1- 7  0.000000  0.000000  0.000000  1.0  0.25
O 1- 8  0.000000  0.500000  0.500000  1.0  0.50
O 1- 9  0.000000  0.000000  1.000000  1.0  0.25

LAYER 3                          {P or pyrolusite layer}
NONE
Mn4+ 1  0.750000  0.500000  0.166667  0.5  1.00
O 1- 1  1.000000  0.000000  0.000000  1.0  0.25
O 1- 2  1.000000  0.500000  0.500000  1.0  0.25
O 1- 3  0.500000  0.500000  -.166667  1.0  0.50
O 1- 4  0.500000  0.000000  0.333333  1.0  0.50
O 1- 5  0.000000  0.000000  0.000000  1.0  0.25
O 1- 6  0.000000  0.500000  0.500000  1.0  0.25

LAYER 4                          {P' or pyrolusite layer}
NONE
Mn4+ 1  0.250000  0.000000  0.166667  0.5  1.00
O 1- 1  1.000000  0.500000  0.000000  1.0  0.25
O 1- 2  1.000000  0.000000  0.500000  1.0  0.25
O 1- 3  0.500000  0.000000  -.166667  1.0  0.50
O 1- 4  0.500000  0.500000  0.333333  1.0  0.50
O 1- 5  0.000000  0.500000  0.000000  1.0  0.25
O 1- 6  0.000000  0.000000  0.500000  1.0  0.25

LAYER 5                          {G or groutite layer}
NONE
Mn3+ 1  0.250000  0.500000  0.190067  0.5  1.00
Mn3+ 2  0.2500000 0.0000000 0.760167  0.5  1.00
O 1- 1  1.000000  0.000000  0.000000  1.0  0.25
O 1- 2  1.000000  0.500000  0.570100  1.0  0.50
O 1- 3  1.000000  0.000000  1.140200  1.0  0.25
O 1- 4  0.500000  0.500000  -.166667  1.0  0.50
O 1- 5  0.500000  0.000000  0.403433  1.0  1.00
O 1- 6  0.500000  0.500000  0.973533  1.0  0.50
O 1- 7  0.000000  0.000000  0.000000  1.0  0.25
O 1- 8  0.000000  0.500000  0.570100  1.0  0.50
O 1- 9  0.000000  0.000000  1.140200  1.0  0.25
```

```
LAYER 6                         {G' or groutite layer}
NONE
Mn3+ 1  0.750000  0.500000  0.190067  0.5  1.00
Mn3+ 2  0.750000  0.000000  0.760167  0.5  1.00
O 1- 1  1.000000  0.000000  0.000000  1.0  0.25
O 1- 2  1.000000  0.500000  0.570100  1.0  0.50
O 1- 3  1.000000  0.000000  1.140200  1.0  0.25
O 1- 4  0.500000  0.500000  -.166667  1.0  0.50
O 1- 5  0.500000  0.000000  0.403433  1.0  1.00
O 1- 6  0.500000  0.500000  0.973533  1.0  0.50
O 1- 7  0.000000  0.000000  0.000000  1.0  0.25
O 1- 8  0.000000  0.500000  0.570100  1.0  0.50
O 1- 9  0.000000  0.000000  1.140200  1.0  0.25
LAYER 7                         {M or manganite layer}
NONE
Mn3+ 1  0.750000  0.500000  0.190067  0.5  1.00
O 1- 1  1.000000  0.000000  0.000000  1.0  0.25
O 1- 2  1.000000  0.500000  0.570100  1.0  0.25
O 1- 3  0.500000  0.500000  -.166667  1.0  0.50
O 1- 4  0.500000  0.000000  0.403433  1.0  0.50
O 1- 5  0.000000  0.000000  0.000000  1.0  0.25
O 1- 6  0.000000  0.500000  0.570100  1.0  0.25
LAYER 8                         {M' or manganite layer}
NONE
Mn3+ 1  0.250000  0.000000  0.190067  0.5  1.00
O 1- 1  1.000000  0.500000  0.000000  1.0  0.25
O 1- 2  1.000000  0.000000  0.570100  1.0  0.25
O 1- 3  0.500000  0.000000  -.166667  1.0  0.50
O 1- 4  0.500000  0.500000  0.403433  1.0  0.50
O 1- 5  0.000000  0.500000  0.000000  1.0  0.25
O 1- 6  0.000000  0.000000  0.570100  1.0  0.25
STACKING                          {header for stacking type}
RECURSIVE                         {statistical ensemble of crystallites}
INFINITE                        {infinite number of layers}

TRANSITIONS                        {header for transition data}
{1}
{RR}  0.00  0.0    0.0    0.0   {disallowed}
{RR'} 0.24  0.0    0.0    1.0
{RP}  0.06  0.0    0.0    1.0
{RP'} 0.00  0.0    0.0    0.0   {disallowed}
{RG}  0.00  0.0    0.0    0.0   {disallowed}
{RG'} 0.56  0.0    0.0    1.0
{RM}  0.14  0.0    0.0    1.0
{RM'} 0.00  0.0    0.0    0.0   {disallowed}

{2}
{R'R}  0.24  0.0   0.0    1.0
{R'R'} 0.00  0.0   0.0    0.0   {disallowed}
{R'P}  0.00  0.0   0.0    0.0   {disallowed}
{R'P'} 0.06  0.0   -.5    1.0
{R'G}  0.56  0.0   0.0    1.0
{R'G'} 0.00  0.0   0.0    0.0   {disallowed}
{R'M}  0.00  0.0   0.0    0.0   {disallowed}
{R'M'} 0.14  0.0   -.5    1.0

{3}
{PR}  0.24  0.0    0.5    0.5
```

```
{PR'}  0.00  0.0    0.0    0.0    {disallowed}
{PP}   0.00  0.0    0.0    0.0    {disallowed}
{PP'}  0.06  0.0    0.0    0.5
{PG}   0.56  0.0    0.5    0.5
{PG'}  0.00  0.0    0.0    0.0    {disallowed}
{PM}   0.14  0.0    0.0    0.5
{PM'}  0.00  0.0    0.0    0.0    {disallowed}

{4}
{P'R}  0.00  0.0    0.0    0.0    {disallowed}
{P'R'} 0.24  0.0    0.0    0.5
{P'P}  0.06  0.0    0.0    0.5
{P'P'} 0.00  0.0    0.0    0.0    {disallowed}
{P'G}  0.00  0.0    0.0    0.0    {disallowed}
{P'G'} 0.56  0.0    0.0    0.5
{P'M}  0.14  0.0    0.0    0.5
{P'M'} 0.00  0.0    0.0    0.0    {disallowed}

{5}
{GR}   0.00  0.0    0.0    0.0    {disallowed}
{GR'}  0.24  0.0    0.0    1.1402
{GP}   0.06  0.0    0.0    1.1402
{GP'}  0.00  0.0    0.0    0.0    {disallowed}
{GG}   0.00  0.0    0.0    0.0    {disallowed}
{GG'}  0.56  0.0    0.0    1.1402
{GM}   0.14  0.0    0.0    1.1402
{GM'}  0.00  0.0    0.0    0.0    {disallowed}

{6}
{G'R}  0.24  0.0    0.0    1.1402
{G'R'} 0.00  0.0    0.0    0.0    {disallowed}
{G'P}  0.00  0.0    0.0    0.0    {disallowed}
{G'P'} 0.06  0.0    -.5    1.1402
{G'G}  0.56  0.0    0.0    1.1402
{G'G'} 0.00  0.0    0.0    0.0    {disallowed}
{G'M}  0.00  0.0    0.0    0.0    {disallowed}
{G'M'} 0.14  0.0    -.5    1.1402

{7}
{MR}   0.24  0.0    0.5    0.5701
{MR'}  0.00  0.0    0.0    0.0    {disallowed}
{MP}   0.00  0.0    0.0    0.0    {disallowed}
{MP'}  0.06  0.0    0.0    0.5701
{MG}   0.56  0.0    0.5    0.5701
{MG'}  0.00  0.0    0.0    0.0    {disallowed}
{MM}   0.00  0.0    0.0    0.0    {disallowed}
{MM'}  0.14  0.0    0.0    0.5701

{8}
{M'R}  0.00  0.0    0.0    0.0    {disallowed}
{M'R'} 0.24  0.0    0.0    0.5701
{M'P}  0.06  0.0    0.0    0.5701
{M'P'} 0.00  0.0    0.0    0.0    {disallowed}
{M'G}  0.00  0.0    0.0    0.0    {disallowed}
{M'G'} 0.56  0.0    0.0    0.5701
{M'M}  0.14  0.0    0.0    0.5701
{M'M'} 0.00  0.0    0.0    0.0    {disallowed}
                                  ----- end of file ----
```

## Appendix C

## Maximum diffracted intensity for $MnO_2$.

Maximum intensity for a specimen is obtained if the thickness t of the specimen satisfies the following criteria[147]

$$t \geq \frac{3.2}{\mu}\frac{\rho}{\rho'}\sin\theta$$

where t - specimen thickness (cm)

$\rho$ - density of solid material ($gcm^{-3}$)

$\rho'$ - density of solid material including interstices ($gcm^{-3}$)

$\theta$ - diffracting angle (degrees)

$\mu$ - linear absorbtion coefficient ($cm^{-1}$)

Using the following data for the material coded R2. Mass absorbtion coefficients[148] Mn ($285cm^2g^{-1}$) and O ($11.5cm^2g^{-1}$), CuK$\alpha$ radiation; density[149] $\rho$=4.138($gcm^{-3}$), packing density $\rho'$=2.1 ($gcm^{-3}$) (measured from packing a ground sample of R2 in a diffraction holder) and $2\theta=65°$ (maximum angle diffraction peak of R2) then

$$\mu_{MnO2}=762.8(cm^{-1}),$$

which implies $\underline{t\geq 0.0044(cm) \text{ or } t\geq 44(\mu m)}$,

which is easily satisfied using a standard rectangular specimen holder (depth=0.20cm). Alternatively, since

$$I=I_o e^{-\mu x}$$

where I - Intensity of x-ray beam

$I_o$ - Incoming intensity of x-ray beam

x - depth of penetration of x-rays

then a 98% intensity drop in $MnO_2$ occurs in a distance of 21$\mu$m.

## References

1. British patent no.1637, (1866).
2. Giovanoli R., "Manganese Dioxide Symposium Vol.2", eds. B.Shumm Jr, H.M.Joseph and A.Kozowa, Tokyo, (1980).
3. Burns R.G., Burns V.M., "Manganese Dioxide Symposium Vol.2", eds. B.Shumm Jr, H.M.Joseph and A.Kozowa, Tokyo, (1980).
4. Hunter J.C., J.of Solid State Chem., **39**, 142-147, (1981).
5. Wells A.F., "Structural Inorganic Chemistry", 5th.edn., Clarendon Press, p.540, (1984).
6. Rogers D.B., Shannon R.D., Sleight A.W., Gillson J.L., Inorg.Chem., **8**, No.4, 841-849, (1969).
7. Baur W.H., Mat.Res.Bull., **16**, 339-345, (1981).
8. West A.R., Bruce P.G., Acta Cryst., B**38**, 1891-1896, (1982).
9. David W.I.F., Bruce P.G., Goodenough J.B., J.of Solid State Chem., **50**, 235-239, (1983).
10. Ohzuku T., Hirai T., "Progress in Batteries & Solar Cells", Vol.7, p.31-37, JEC Press Inc., (1988).
11. Fleischer M., Richmond W.E., Evans H.T., Amer.Miner., **47**, 47-58, (1962).
12. Ramsdell L.S., Am.Mineral., **17**, 143-149, (1932).
13. See reference 5 page 555.
14. Voinov M., Electrochim.Acta, **27**, 7, 833-835, (1982).
15. Wilson A.J.C., "X-ray Optics.*The Diffraction of X-rays by Finite and Imperfect Crystals.*", Methuen & Co.LTD.London, (1949).
16. Faulring G.M., Amer.Miner., **50**, 170-179, (1965).
17. Acharya B.S., Pradhan L.D., J.Appl.Cryst., **19**, 214-216, (1986).
18. Parida K.M., Kanungo S.B., Sant B.R., Electrochem. Acta, **26**, 435-443, (1981).
19. Kanungo S.B., Parida K.M., J.Electrochem.Soc.India, **33-3**, 219-226, (1984).
20. Zwicker W.K., Groeneveld Meijer W.O.J., Jaffe H.W., Amer.Miner., **47**, 246-267, (1962).
21. "Handbook of Manganese Dioxides Battery Grade", eds.Glover D., Schumm Jr., Kozawa A., The Int'l Battery Material Ass'n (IBA, Inc.), p.22, (1989).

22. Gabano J.P., Morignat B., Fialdes E., Emery B., Laurent J.F., Z.Phys.Chem., **46**, 359-372, (1965).

23. Ruetschi P., J.Electrochem.Soc., **131**, No.12, 2737-2744, (1984).

24. See reference 5 page 638.

25. Dachs H., J.Physical Soc. of Japan, **17**, B-11, 387-389, (1962).

26. Wyckoff R.W.G., "Crystal Structures", Vol.1, 2nd. edn., Interscience Publishers, chap.4 p.356, (1963).

27. Gruner, J.W., Amer.Mineral., **32**, 654-659, (1947).

28. Collin R.L., Lipscomb W.N., Acta Cryst., **2**, 104-106, (1949).

29. Feitknecht W., Marti W., Helv. Chimica Acta, **28**, 129, (1945).

30. Moore T.E., Ellis M., Selwood P.W., J.Am.Chem.Soc., **72**, (1950).

31. Bricker O., Amer.Miner., **50**, 1296-1355, (1965).

32. Feitknecht W., Oswald H.R., Feitknecht-Steinmann U., **43**, 7, 1947-1950, (1960).

33. Giovanoli R., Bernhard K., Feitknecht W., Helv.Chim.Acta, **51**, 355-366, (1968).

34. Ripert M., Poinsignon C., Chabre Y., Pannetier J., Phase Transitions, **32**, 205-209, (1991).

35. Chukhrov F.V., Gorshkov A.I., Sivtsov A.V., Dickov Ju.P, Beresovskaya V.V., Izvest. Akad. Nauk. S.S.S.R., Ser. Geol., **1**, 56-58, (1982).

36. Pannetier J., "Progress in Batteries & Battery Materials", **11**, ITE-JEC Press Inc., p51-55, (1992).

37. Freund F., Könen E., Preisler E., "Manganese Dioxide Symposium Vol.", eds. A.Kozowa and R.J.Brodd, Cleveland, (1975).

38. Li Jian-Bao, Koumoto K, Yanagida H., J.of.Mat.Science, **23**, 2595-2600, (1988).

39. Pannetier J., Chabre Y., Poinsignon C., ISSI Lett., **1**, No.2, 5-7, (1990).

40. Ripert M., Pannetier J., Chabre Y., Poinsignon C., Mat.Res.Soc.Symp.Proc., **210**, 359-365, (1991).

41. Brenet J., CITCE Conf., Madrid, (1956).

42. See for example reference 124 p.91.

43. de Wolff P.M., Visser J.W., Giovanoli R., Brütch R., Chimia, **32**, 257-259, (1978).

44. Charenton J.C., Strobel P., J.of Solid State Chem., **77**, 33-39, (1988).

45. Purcell K., Kotz J., "Inorganic Chemistry", Holt and Saunders, p.284, (1977).

46. Cullity B.D., "Elements of X-Ray Diffraction", 1st edn., Addison-Wesley, (1956).

47. See reference 46 page 44.

48. de Wolff P.M., Acta.Cryst., **12**, 341-345, (1959).

49. Byström A.M., Acta Chemica Scand., **3**, 163-173, (1949).

50. Byström A, Byström A.M., Acta Cryst., **3**, 146-154, (1950).

51. Preisler E., J.of Appl.Electrochem., **19**, 540-546, (1989).

52. Malpas D.G., Tye F.L., in "Handbook of Manganese Dioxides Battery Grade", eds.Glover D., Schumm Jr., Kozawa A., The Int'l Battery Material Ass'n (IBA, Inc.), chap.5, (1989).

53. Jones J., PhD thesis (unpublished).

54. Klug A., Alexander L.E., "X-ray Diffraction Procedures *For Polycrystalline and Amorphous Materials*", 2nd.edn., p.38, Wiley, (1974).

55. Strobel P., J Jean-Claude, R.Maria-Rodriguez, J.of Mat.Science, **21**, 583-590, (1986).

56. Preisler E., J.of Appl.Electrochem., **19**, 540-546, (1989).

57. Laudy J.H.A., de Wolff P.M., Appl.Sci.Res., **10**, Sect.B, 157-168, (1963).

58. Turner S., Busek P.R., Nature, **304**, 143-146, (1983).

59. Burns R.G., Battery Material Symposium I, Brussels, 341-354, (1983).

60. Hendricks S., Teller E., J.of Chem.Phys., **10**, 147-167, (1942).

61. Treacy M.M.J., Newsam J.M., Deem M.W., Proc.R.Soc.Lond., **433**, A, 499-520, (1991).

62. "International Tables for X-Ray Crystallography", Kynoch Press, (1974).

63. Clark J., David W., Hull S., Lecture presented at the Fourth Battery Material Symposium, York, (1989).

64. Desai B.D., Fernandes J.B., Kamat Dalal V.N., J. of Power Sources, **16**, 1-43, (1985).

65. "American Institute of Physics Handbook", 3rd edn., McGraw-Hill, (1972).

66. Pannetier J., Ripert M., Poinsignon C., (to be published).

67. Suzuki K., Ichihara M., Takeuchi S., Phil.Mag., **63**, A, No.4, 657-665, (1991).

68. Fitzpatrick J., Tye F.L., J.of Appl.Electochem., **21**, 130-135, (1991).

69. Harfenist M., Bavley A., Lazier W.A., J.Org.Chem., **19**, 1608-1616, (1954).

70. Gritter R.J., Wallace T.J., J.Org.Chem., **24**, 1051-1057, (1959).

71. Brady J.E., Humiston G.E., "General Chemistry", 4th edn., p.857, Wiley, (1986).

72. "Handbook of Chemistry and Physics", ed.R.C.Weast, 62nd edn., CRC press, (1981).

73. Maskell W.C., Shaw J.E.A., Tye F.L., Electrochim.Acta, **26**, 10, 1403-1410, (1981).

74. Lee J.A., Newnham C.E., Stone F.S., Tye F.L., J. of Solid State Chem.,**31**, 81-93, (1980).

75. Lingane J.J., Karplus R., Ind. Eng. Chem., Anal. Ed., **18**, 191-194, (1946).

76. Vetter K.J., Jeager N., Electrochim. Acta, **11**, 401-419, (1966).

77. Maskell W.C., Phd. thesis, (1976).

78. Koltoff I.M., Sandell E.B., Meehan E.J., Bruckenstein S., "Quantitative Chemical Analysis", 4th edn., p.816, (1969).

79. "Vogels Textbook of Quantitative Inorganic Analysis", 4th edn., revised by J.Basset, R.C.Denny, G.H.Jeffery and J.Mendham, Longman, p.359, (1978).

80. See reference 79 p.60.

81. Jenkins R., de Vries J.L., "An introduction to x-ray powder diffractometry", copyright Philips.

82. See reference 100 appendix 7, page 509.

83. See reference 54, page 284.

84. See reference 54 page 366.

85. West A.R., "Solid State Chemistry and its Applications", Wiley, p.369, (1984).

86. See reference 46 chap.11.

87. See ref. 100 p.359.

88. Ives D.J.G, Janz G.J., "Reference Electrodes, *Theory and Practice*", Academic Press, p.336, (1961).

89. Hills S., Vosburgh W.C., J.Electrochem.Soc., **104**, 1, 5-9, (1957).

90. Johnson R.S., Vosburgh W.C., J.Electrochem.Soc., **99**, 317-322, (1952).

91. Giovanoli R., Bernhard K., Feitknecht W., Helv. Chim. Acta, **51**, 2, 355-366, (1968).

92. Dent Glasser L.S., Ingram L., Acta Cryst.**B24**, 1233-1237, (1968).

93. Buerger M.J., Zeit.Kristallogr., **95**, 163-174, (1936).

94. Champness P.E., Mineralogical Magazine, **38**, 245-248, (1971).

95. Ohzuku T., Hirai T.,"Manganese Dioxide Electrode Theory and Practice for Electrochemical Applications", eds. B.Schumm, R.L.Middaugh, Grotheer M.P. and J.C.Hunter, The Electrochem. Soc. Inc., p.141-157, (1985).

96. JCPDS (Joint Committee on Powder Diffraction Standards) card 24-713.

97. JCPDS card 18-805

98. Ohzuku T., Kitagawa M, Hirai T., J.Electrochem. Soc., **136**, 11, 3169-3174, (1989).

99. Tye F.L., Electrochim. Acta, **21**, 415-420, (1976).

100. Cullity B.D. "Elements of X-Ray Diffraction", 2nd edn., Addison-Wesley, p.376, (1978).

101. See ref.85 p.367.

102. Bode H., Schmier A., Proceedings of the 3rd Int. Power Sources Symposium, ed. D.H.Collins, Pergamon Press, (1962).

103. Bode H., Schmier A., Chemie-Ing.-Techn., **38**, 6, 651, (1966).

104. Giovanoli R., Maurer R, Feitknecht W., Helv. Chim. Acta, **50**, 4, 1072-1080, (1967).

105. Potter R.M., Rossman G.R., Amer. Miner., **64**, 1199-1218, (1979).

106. Fitzpatrick J.F., PhD thesis, (unpublished).

107. Tye F.L. "Progress in Batteries & Battery Materials", **11**, ITE-JEC Press Inc., p.1-15, (1992).

108. Stumm W., Giovanoli R., Chimia, **30** (9), 423-425, (1976).

109. See reference 85 pages 183-184.

110. Wells A.F., "Structural Inorganic Chemistry", 3rd. edn., O.U.P., p.86-92, (1962).

111. Maskell W.C., Shaw J.A.E., Tye F.L., J.of Appl. Electrochem., **12**, 101-108, (1982).

112. Giovanoli R., Leuenberger U., Helv. Chim. Acta., **52**, 8, 2333-2347, (1969).

113. Alday J., MPhil thesis (unpublished).

114. Cahoon N.C., Korver M.P., J.Electrochem.Soc., **106**, 9, 745-750, (1959).

115. Kozowa A., Powers R.A., J.Electrochem.Soc., **113**, 9, 870-878, (1966).

116. Boden D., Venuto, Wisler D., Wylie R.B., J.Electrochem.Soc., **115**, 4, 333-338, (1968).

117. Kozowa A., Powers R.A., J.Electrochem.Soc., **115**, 122-126, (1968).

118. Kozowa A., Powers R.A., J.Electrochem.Technol., **5**, No.11-12, 535-542, (1967).

119. Bell G.S., Huber R, J.Electrochem.Soc., **111**, No.1, 1-6, (1964).

120. Kozowa A., Yeager J.F., J.Electrochem.Soc., **112**, 10, 959-963, (1965).

121. Kordesch K., Gsellmann J., Peri M., Tomantschger K., Chemelli R., Electrochim.Acta, **26**, 10, 1495-1504, (1981).

122. Vetter K.J., Z. Elektrochem. **66**, 577-586, (1962).

123. Atlung S., Manganese Dioxide Symposium, eds.A.Kozowa and B.J.Brodd, Cleveland, Ohio, (1975).

124. Tye F.L., "Electrochemical Power Sources", ed.M.Barak, Peter Peregrinus Ltd., p.50, (1980).

125. Holton D.M., Maskell W.C., Tye F.L., Power Sources 10 (ed. L.Pearce), p.247, The Paul Press Ltd, (1985).

126. Mondoloni C., Laborde M., Rioux J., Andoni E., Lévy-Clément C., J.Electrochem.Soc., **139**, 4, 954-959, (1992).

127. Wruck W.J., Reichman B., Bullock K.R., Kao W.-H., J.Electrochem.Soc, **138**, 12, 3560-3567, (1991).

128. Fletcher S., Galea J., Hamilton J.A., Tran T., Woods, R.,J.Electrochem.Soc., **133**, 7, 1277-1281, (1986).

129. Skowroński, J.M., J.Appl.Electrochem., **19**, 287-289, (1989).

130. McBreen J., Electrochim.Acta, **20**, 221-225, (1975).

131. Desai Buqui D., Dhume R.A.S., Kamat Dalal V.N., J.of Power Sources, **23**, 309-330, (1988).

132. Sugimori, M., Manganese Dioxide Symposium, eds. A.Kozowa and R.J.Brodd, The Electrochemical Soc., Cleveland.

133. Giovanoli R., Chimia, **23**, 12, 470-472, (1969).

134. Giovanoli R., Stähli E., Feitknecht W., Helv.Chim.Acta, **53**, 2, 209-220, (1970).

135. Warren B.E., Phys.Rev., **59**, 9, 693-698, (1941).

136. JCPDS card 21-645.

137. Larcin J., Phd. thesis (1991).

138. Giovanoli R., "Progress in Batteries & Solar Cells", Vol.9, JEC Press Inc. and IBA Inc., p.1-8, (1990).

139. Muller J., Tye F.L., Wood L.L., Batteries 2, ed. D.H.Collins, Peragamon Press, p.201-215, (1965).

140. Maskell W.C., Shaw J.E.A., Tye F.L., J.of Power Sources, **8**, 113-120, (1982).

141. Maskell W.C., Shaw J.A.E, Tye F.L., J.of Appl.Electrochem., **12**, 101-108, (1982).

142. Tye F.L., Electrochimica Acta, **30**, 1, 17-23, (1985).

143. St. Claire-Smith C., Lee J.A., Tye F.L., Manganese dioxide Symposium, eds A.Kozowa and R.J.Brodd, Cleveland, (1975).

144. Yamashita M., Ide M., Takemura H., Konishi K, Kozowa A., in "Handbook of Manganese Dioxides Battery Grade", eds.Glover D., Schumm Jr., Kozawa A., The Int'l Battery Material Ass'n (IBA, Inc.), chap.8, (1989).

145. Cornell R.M., Giovanoli R., Clays and Clay Minerals, **36**, 3, 249-257, (1988).

146. Gehain E.D., PhD thesis (1992).

147. See reference 54 p.294.

148. From appendix V reference 54.

149. Brown A.J., Tye F.L., Wood L.L., J. Electroanal. Chem., **122**, 337-346, (1981).